Thèse de doctorat présentée pour l'obtention du titre de
Docteur de l'Université de Lorraine

Mention « Géosciences »

par Yann FOUCAUD

Récupération du tungstène à partir d'un skarn à faible contraste de séparation – Apport de la modélisation moléculaire dans la flottation des minéraux calciques

Soutenue publiquement le 25 octobre 2019

Membres du jury :

Jan Miller, Professor, University of Utah (DME) ....Rapporteur
Jean-François Paul, Professeur, Université de Lille (UCCS) ....Rapporteur
Vanessa Fierro, Directrice de recherche, Université de Lorraine (IJL) ....Examinatrice
Martin Rudolph, Doctor-Engineer, HZDR ....Examinateur
Lev Filippov, Professeur, Université de Lorraine (GeoRessources) ....Directeur de thèse
Inna Filippova, Chercheuse, Université de Lorraine (GeoRessources) ....Co-directrice de thèse
Michaël Badawi, Maître de conférences, Université de Lorraine (LPCT)............................Invité
Sébastien Lebègue, Directeur de recherche, Université de Lorraine (LPCT).......................Invité

À Jean Foucaud (20/05/1928 – 30/08/2019)

Thesis abstract

Nowadays, skarns represent more than 40% of the global resources in tungsten, which has been classified as a critical raw material in the European Union. In particular, the Tabuaço deposit constitutes an archetype of tungsten skarns and contains high amounts of calcium minerals, including fluorite, apatite, and vesuvianite, in close association with scheelite ($CaWO_4$). According to their similar surface properties, the separation of these minerals by flotation with fatty acids is significantly difficult and, therefore, remains a scientific challenge. In this study, which has been conducted within the framework of the FAME H2020 European project, an economic, environment-friendly, and transferable process has been developed for the Tabuaço ore to demonstrate the feasibility of the tungsten skarns processing. In the froth flotation process, the Na_2CO_3/Na_2SiO_3 system has exhibited the best efficiency in terms of gangue minerals depression due to considerable synergistic effects that have been subsequently described by statistical, spectroscopic, and atomistic methods. Meanwhile, the influence of the ratios between different carboxylic acids in the collector formulations (Tall Oil Fatty Acids) has been assessed to improve the flotation selectivity. In addition, the enhanced gravity separation (Falcon centrifuge concentrator) has been investigated, optimised, and combined with the flotation to produce a marketable scheelite concentrate assaying 63% WO_3 with 59% recovery. Besides, to gain understanding in the molecular mechanisms involved in the flotation process, the fluorite and scheelite interfaces have been modelled using the density functional theory. This study has allowed to characterise the hydration state of these minerals, which display different affinities for water molecules. Furthermore, the adsorption of fatty acids on fluorite has been studied to unravel the adsorption mechanisms of these molecules on calcium minerals, confirmed by experimental investigations.

Résumé de la thèse

Aujourd'hui, plus de 40 % des ressources mondiales en tungstène sont contenues dans les skarns, dont le gisement de Tabuaço (Portugal) constitue un archétype. Ce minerai contient de fortes teneurs en minéraux calciques (fluorite, apatite et vésuvianite) en association fine avec la scheelite ($CaWO_4$) qui, étant donné leurs propriétés de surface proches, sont difficiles à séparer par flottation aux acides gras. Au cours de cette étude, ancrée dans le projet européen H2020 FAME, un procédé économique, écologique et transférable a été développé sur le minerai de Tabuaço afin de prouver la faisabilité minéralurgique de l'exploitation des skarns à tungstène, classé parmi les métaux critiques en Europe. En flottation, le système Na_2CO_3/Na_2SiO_3 a montré la meilleure efficacité en matière de dépression, obtenue grâce à des effets synergiques considérables. Ces derniers ont été décrits par des méthodes statistiques, spectroscopiques et atomistiques. En parallèle, l'influence des ratios entre différents acides carboxyliques au sein des formulations de collecteurs (huiles de tall) a été évaluée avec pour objectif d'améliorer la sélectivité de la flottation. La séparation par gravité augmentée (concentrateur centrifuge Falcon) a été examinée, optimisée puis combinée avec la flottation afin de produire un concentré commercialisable de scheelite titrant 63 % WO_3 pour 59 % de récupération. Par ailleurs, en vue d'appréhender les mécanismes moléculaires impliqués dans la flottation, les interfaces de la fluorite et de la scheelite ont été modélisées en utilisant la théorie de la fonctionnelle de la densité. Cette étude a permis de caractériser l'état d'hydratation des deux minéraux, qui présentent des affinités différentes pour les molécules d'eau. En outre, l'adsorption des acides gras sur la fluorite a été étudiée afin de fournir des éléments de réponse, confirmés expérimentalement, au sujet des mécanismes d'adsorption de ces molécules sur les minéraux calciques.

Remerciements

En premier lieu, je tiens à remercier Lev Filippov, mon directeur de thèse, pour la confiance et l'autonomie qu'il m'a accordées. Elles ont été très appréciables étant donné mon caractère mais aussi plus que nécessaires afin d'aborder sereinement des problématiques complexes associées à des thématiques novatrices, et, de fait, inconnues. Lev a cru en moi et m'a transmis autant que possible ce qu'il savait ; pour ces raisons, je lui en suis très reconnaissant. En outre, j'adresse mes remerciements les plus chaleureux à Inna Filippova, ma co-directrice de thèse, pour les heures qu'elle a passées à manipuler à mes côtés et pour les nombreuses discussions, heureusement pas toujours scientifiques, que nous avons pu avoir. Je remercie vivement Jan D. Miller et Jean-François Paul d'avoir accepté de rapporter ce travail de thèse ainsi que Martin Rudolph et Vanessa Fierro pour avoir bien voulu l'évaluer. Par ailleurs, j'aimerais vivement remercier Michaël Badawi et Sébastien Lebègue. Ils m'ont accordé leur confiance et m'ont donné l'opportunité de me lancer corps et âmes dans une thématique inconnue autant pour eux et que pour moi. Ils y ont cru ! Notre collaboration a porté ses fruits, permettant de sublimer nos travaux expérimentaux par l'addition d'une composante théorique et fondamentale.

Une thèse ne serait pas ce qu'elle est sans une équipe, un laboratoire, une atmosphère, qui sont, pour moi, des éléments indispensables à l'épanouissement intellectuel. Aussi, je tiens à remercier vivement tous ceux qui contribuent ou ont contribué à la bonne ambiance régnant au sein de l'équipe Valorisation du laboratoire GeoRessources. Tout d'abord, un grand merci à l'équipe technique de STEVAL, Bob, Fred, Pierric, Christophe et Eric qui, au-delà de leur position stratégique dans le bâtiment A, m'ont fourni un grand soutien logistique, technique et moral. Avec eux, Pabla et Alexandre « Kofi », les nombreuses discussions, rigolades, soirées et barbecues d'équipe me laisseront un souvenir impérissable ! Je tiens à adresser mes remerciements chaleureux à Zineb, qui m'a laissé sa place – stratégique, même si j'ai pris l'ancien fauteuil en cuir de Lev… Que de rigolades ! Merci aussi à Oumar pour tous les conseils utiles qu'il a pu me donner et que j'ai toujours plaisir à recroiser au bâtiment A. Bien entendu, je suis très reconnaissant à Anthony pour les nombreuses discussions dans le bureau, qui m'ont permis de trouver, au cours de ces trois années, l'inspiration requise pour ce travail de longue haleine. Le trio était complet avec Carlos, qui avait (presque) son bureau attitré, quand je n'avais pas de stagiaire – donc jamais, que je tiens à remercier vivement pour les nombreuses discussions et rigolades dans le bureau. Enfin, merci à Quentin qui a toujours gardé un pied à STEVAL malgré son éloignement géographique, grâce à notre collaboration fructueuse autour de ce petit bol tournant à 200 G. Des thésards partent, d'autres arrivent (depuis des contrées lointaines)… Puis sont élus… Puis déménagent… Et c'est ainsi je me suis retrouvé avec le père Mangold assis en face de moi – qui aurait cru qu'on pouvait rédiger une thèse en face d'un type aussi bruyant ? Pas Soumaya… Pour tout le soutien (humoristique, scientifique, mais aussi athlétique) qu'il m'apporte depuis déjà quelques mois, j'aimerais lui adresser un immense merci. Enfin, je remercie très chaleureusement Chloé, le lutin qui boulotte tout le temps, pour l'aide précieuse et indispensable qu'elle a pu m'apporter, surtout lors de la phase de rédaction. Je n'oublie pas les

List of publications

Foucaud, Y., Badawi, M., Filippov, L.O., Barres, O., Filippova, I.V., Lebègue, S. Synergistic adsorptions of Na2CO3 and Na2SiO3 on calcium minerals revealed by spectroscopic and ab initio molecular dynamics studies. Chemical Science. Under review.

Foucaud, Y., Badawi, M., Filippov, L.O., Filippova, I.V., Lebègue, S. A review of atomistic simulation methods for surface physical-chemistry phenomena applied to froth flotation. Minerals Engineering. Under review.

Foucaud, Y., Filippova, I.V., Dehaine, Q., Hubert, P., Filippov, L.O. Integrated Approach for the Processing of a Complex Tungsten Skarn Ore (Tabuaço, Portugal). Minerals Engineering. Accepted for publication.

Foucaud, Y., Dehaine, Q., Filippov, L.O., Filippova, I.V. Application of Falcon centrifuge as a cleaner alternative for complex tungsten ore processing. Minerals (2019), 9, 448. DOI: 10.3390/min9070448.

Foucaud, Y., Demeusy, B., Fabre, C., Filippova, I.V., Filippov, L.O. Optimisation of fast quantification of fluorine content using handheld LIBS. Spectrochimica Acta B 158 (2019), 105628. DOI: 10.1016/j.sab.2019.05.017.

Foucaud, Y., Filippova, I.V., Filippov, L.O. Investigation of the depressants involved in the selective flotation of scheelite from apatite, fluorite, and calcium silicates: focus on the sodium silicate/sodium carbonate system. Powder Technology 352 (2019), 501-512. DOI: 10.1016/j.powtec.2019.04.071.

Foucaud, Y., Badawi, M., Filippov, L.O. Comment on: Effects of crystal chemistry on sodium oleate adsorption on fluorite surface investigated by molecular dynamics simulation. Minerals Engineering 135 (2019), 156-159. DOI: 10.1016/j.mineng.2019.02.020.

Dehaine, Q., Foucaud, Y., Kroll-Rabotin, J.-S., Filippov, L.O. Experimental investigation into the kinetics of Falcon UF concentrator: Implications for fluid dynamic-based modelling. Separation and Purification Technology 215 (2019), 590-601. DOI: 10.1016/j.seppur.2019.01.048.

Foucaud, Y., Lebègue, S., Filippov, L.O., Filippova, I.V., Badawi, M. Molecular Insight into Fatty Acid Adsorption on Bare and Hydrated (111) Fluorite Surface. J. Phys. Chem. B, 2018, 122 (51), 12403–12410. DOI: 10.1021/acs.jpcb.8b08969.

Foucaud, Y., Badawi, M., Filippov, L.O., Filippova, I.V., Lebègue, S. Surface Properties of Fluorite in Presence of Water: An Atomistic Investigation. J. Phys. Chem. B, 2018, 122 (26), 6829–6836. DOI: 10.1021/acs.jpcb.8b02717.

Filippov, L.O., Foucaud, Y., Filippova, I.V., Badawi, M. New reagent formulations for selective flotation of scheelite from a skarn ore with complex calcium minerals gangue. Minerals Engineering 123 (2018), 85-94. DOI: 10.1016/j.mineng.2018.05.001.

Foucaud, Y., Lechenard, B., Marion, P., Filippova, I.V, Filippov, L.O. Geology, Textural Study, Ore Genesis and Processing of the Tabuaço Tungsten Deposit (Northern Portugal). Contributions to Mineralization (2018). DOI: 10.5772/intechopen.71674.

List of conferences, workshops, symposiums

Physical Separation '19, Falmouth (UK), 13-14th June 2019, Oral presentation.
Computational Modelling '19, Falmouth (UK), 11-12th June 2019, Oral presentation.
8° journées de l'Association Françaises d'Adsorption, Dijon (FR), 5-6th February 2019, Oral presentation.
XXIX° International Mineral Processing Congress, Moscow (RU), 17-21st September 2018, Oral presentation.
Geometallurgy 2018, London (UK), 19-20th April 2018, Oral presentation.
Mineral Engineering Conference '17, Wisła (Poland), 20-23th September 2017, Oral presentation.
New Achievements in Materials and Environmental Sciences '16, Nancy (FR), 7-9th November 2016, Oral presentation.

Table des matières

Tables des figures

Tables des tables

Résumé étendu de la thèse

1. Introduction

Le tungstène suscite un intérêt considérable au sein de l'Union Européenne depuis quelques années, au vu de son importance économique forte, de son faible taux de recyclage et de sa faible substituabilité (Audion and Labbé, 2012; European Commission, 2010). En outre, ce métal est sujet à des risques forts sur son approvisionnement, principalement dus au monopole que la Chine exerce sur le marché mondial (Pitfield et al., 2011). Actuellement, le tungstène primaire est toujours la principale source de tungstène pour l'élaboration de produits manufacturés tels que les alliages, les superalliages et le carbure de tungstène (Audion and Labbé, 2012; Pitfield et al., 2011). La scheelite ($CaWO_4$) et la wolframite [$(Fe,Mn)WO_4$] sont les deux minéraux exploités pour l'extraction du tungstène primaire. La scheelite est principalement extraite des skarns, qui proviennent de roches sédimentaires, essentiellement carbonatées, ayant subi un métamorphisme de contact (haute température, basse pression), accompagné d'un métasomatisme (transfert d'éléments chimiques) induits par l'intrusion d'un pluton granitique. Ces roches représentent, à l'heure actuelle, plus de 40 % des réserves mondiales en tungstène (Pitfield et al., 2011). Elle est très souvent concentrée par flottation bien que des séparations par gravité aient démontré de bonnes performances, essentiellement pour les particules grossières. Malgré leur valorisation complexe, les skarns à tungstène suscitent un intérêt grandissant dans la communauté mondiale, principalement depuis l'augmentation des cours du tungstène en 2007. Le gisement de Tabuaço se situe au Portugal, au nord de la Zone Centrale Ibérique du Massif Ibérique (Dehaine et al., 2019a), faisant lui-même partie de la chaîne varisque (voir Chapitre 1). L'occurrence de Tabuaço est encaissée dans des métasédiments du Cambrien, au niveau de la bordure nord du granitoïde varisque de Paredes-da-Beira-Tabuaço (Dias et al., 2014; Pinto et al., 2016). Un rapport NI 43-101, paru en 2011, a évalué les ressources à 2,7 millions de tonnes sur l'ensemble du gisement pour une teneur moyenne de 0,56 % WO_3, ce qui classe Tabuaço comme un gisement moyen de classe mondiale (Dawson, 1996). Cette étude se focalise sur le sous-gisement de São Pedro das Águias, qui représente 71 % des ressources de Tabuaço et se compose de deux couches d'une cinquantaine de mètres de puissance de métasédiments au sein desquelles se situent les minéralisations. Les deux couches, nommées Lower Skarn et Main Skarn, sont subparallèles au contact entre le granite et la Formation de Bateiras. Au sein des skarns, la scheelite est souvent finement disséminée et, étant donné la forte teneur en calcium du protolithe, associée avec des minéraux calciques comme la calcite, la dolomite, la fluorite et l'apatite (Jébrak et al., 2016; Kupka and Rudolph, 2018a; Yang, 2018). La maille de libération, généralement fine, rend difficile la valorisation de ces minerais par des séparations par gravité classiques telles que les tables à secousses, les jigs ou les spirales (Blazy and Joussemet, 2011; Das and Sarkar, 2018; Wells, 1991). La concentration par flottation est donc souvent privilégiée car elle permet la valorisation de minerais fins, jusqu'à moins de 10 µm, avec de forts débits et une efficacité relativement importante. De nos jours, peu d'options existent pour une flottation efficace et industrialisable de la scheelite (Kupka and Rudolph, 2018a; Yang, 2018). Les amines présentent de bonnes

performances de collection bien qu'ils soient connus pour collecter aussi les silicates, par leur physisorption sur les surfaces négativement chargées (Arnold et al., 1978; Hiçyìlmaz et al., 1993). Etant donné que les silicates représentent généralement la majorité des minéraux de gangue des skarns, l'emploi des amines semble très inadapté pour obtenir une bonne sélectivité en flottation. Les acides hydroxamiques, principalement l'acide benzohydroxamique, ont montré de très bonnes performances pour la flottation de la scheelite lorsqu'ils sont associés à du nitrate de plomb (Feng et al., 2017; Kupka and Rudolph, 2018a; Zhao et al., 2013). Néanmoins, l'usage industriel de composés à base de benzène et de plomb est strictement restreint voire interdit au sein de l'Union Européenne, ce qui rend cette méthode inapplicable pour des skarns européens. La dernière possibilité, dont les performances ne sont plus à démontrer étant donné son usage mondial, est la flottation aux acides gras, principalement l'oléate de sodium, qui s'avèrent très efficaces, peu coûteux et avec un faible impact environnemental (Agar, 1984; Miller and Misra, 1984; Pugh and Stenius, 1985; Rao et al., 1988; Yongxin and Changgen, 1983). À échelle industrielle, les huiles de tall, un sous-produit du procédé papetier Kraft, sont très utilisées, ce qui abaisse considérablement le coût des collecteurs. L'efficacité des acides gras est attribuée à l'adsorption des groupements carboxylates sur les atomes de calcium de la surface (Atademir et al., 1979; Filippova et al., 2014; Marinakis and Shergold, 1985a; Rao et al., 1988). Toutefois, les skarns à tungstène comme le gisement de Tabuaço présentent généralement de fortes teneurs en minéraux calciques, qu'ils soient des silicates ou des sels semi-solubles (fluorite, apatite, calcite et scheelite). Ainsi, la séparation de ces différents minéraux par flottation aux acides gras est difficile, étant donné l'adsorption de ces derniers sur les atomes de calcium en surface, qui induit une flottation non-sélective. Différentes solutions peuvent toutefois être mises en œuvre pour améliorer l'élimination des minéraux calciques au cours de la valorisation du skarn. La méthode de Petrov, développée à la fin des années 1930, permet d'augmenter la sélectivité de la flottation de la scheelite après le dégrossissage par chauffage de la pulpe à 80°C en présence de silicate de sodium concentré (Petrov, 1940). Toutefois, ce procédé, largement utilisé en Russie et en Chine, induit des coûts énergétiques élevés, qui ne sont pas acceptables en Europe. De plus, des déprimants peuvent être ajoutés en flottation afin d'augmenter le contraste de séparation entre la scheelite et les minéraux de gangue (Abeidu, 1973; Bo et al., 2015; Kupka and Rudolph, 2018a; Marinakis and Shergold, 1985b; Wang and Yu, 2007; Yang, 2018). Cependant, bien que les silicates soient aisément déprimés, peu de déprimants sont sélectifs entre la scheelite, la fluorite, l'apatite et la calcite. En outre, la sélectivité de flottation entre ces différents minéraux peut être améliorée en utilisant des mélanges d'acides gras comprenant des chaînes aliphatiques avec différentes structures.

Par ailleurs, les minéraux constitutifs des skarns à tungstène présentent généralement un large panel de densités : 2,7 pour la calcite, 3,2 pour la fluorite et l'apatite, entre 2,6 et 3,7 pour les silicates et 6,1 pour la scheelite. Ainsi, une séparation par gravité est envisageable pour éliminer les minéraux qui sont problématiques en flottation aux acides gras, principalement les sels calciques (fluorite, apatite et calcite). Cependant, la maille de libération fine rend difficile l'utilisation des séparations par gravité classiques (tables à secousses, spirales ou jigs). Depuis une vingtaine d'années, les minerais présentent des mailles de libération de plus en plus fines, ce

qui a conduit à une diminution significative de l'efficacité des séparations par gravité susmentionnées. Ceci a induit le développement d'appareils spécifiques comme les Séparateurs Multi-Gravité (MGS), les concentrateurs Knelson ou les concentrateurs Falcon afin d'obtenir une séparation par gravité efficace pour les particules fines (Blazy and Joussemet, 2011). Ces méthodes peuvent être appliquées sur des particules ultrafines, jusqu'à 3 µm (Burt, 1999; Das and Sarkar, 2018) et peuvent donc être utilisées pour les skarns comme le minerai de Tabuaço. Néanmoins, étant donné les faibles taux d'enrichissement obtenus avec ces équipements, ils sont souvent combinés avec d'autres étapes de séparation, notamment avec la flottation (Filippov et al., 2016).

Enfin, les skarns contiennent du fer, qui est généralement contenu dans les silicates ferromagnésiens comme l'épidote, la vésuvianite ou les grenats, tous formés lors du métamorphisme. Etant donné leur teneur en fer, ces silicates sont plus denses que les silicates non-ferromagnésiens et présentent une susceptibilité magnétique modérée, ce qui les rend paramagnétiques. Ainsi, une séparation magnétique à haute intensité est envisageable pour éliminer ces minéraux, pouvant représenter de très fortes teneurs dans les skarns comme celui de Tabuaço.

Globalement, les minéraux de gangue calciques contiennent souvent des éléments comme le phosphore, le silicium, le carbone et le fluor, qui sont considérés (avec le soufre) comme des éléments pénalisants des concentrés de scheelite ou du tungstène métal (Pastor, 2000; Pitfield et al., 2011; Yang et al., 2016). De plus, le manque de sélectivité en flottation conduit à une dilution de la scheelite dans le concentré, qui doit titrer au minimum 60 % WO_3 pour être traitable par hydrométallurgie (Pastor, 2000; Pitfield et al., 2011). L'élimination minéralurgique de la fluorite, de l'apatite, de la calcite et des silicates avant le traitement par hydrométallurgie est donc fondamentale. Cette étude présente une approche intégrée conduite sur le skarn à tungstène de Tabuaço, qui contient de la scheelite finement disséminée en association avec de la fluorite, de l'apatite et des silicates calciques. Les caractéristiques du gisement et du minerai sont discutées en se focalisant sur leurs implications dans le développement d'un procédé à faible impact environnemental et économiquement viable. Plusieurs options de valorisation, fondées sur la composition minéralogique du skarn, sont suggérées, testées, discutées, optimisées puis combinées afin de proposer un schéma de traitement global pour ce minerai, applicable pour d'autres skarns à tungstène dans le monde. Au cours de ce travail, les mécanismes moléculaires impliqués dans la flottation ont été étudiés. Pour cela, la théorie de la fonctionnelle de la densité a été utilisée car elle présente un bon compromis entre la précision obtenue sur les énergies/structures et les coûts de calcul. Cette méthode, fondée sur la mécanique quantique, est très largement employée dans le monde de la physico-chimie ; elle permet notamment de décrire précisément la réactivité chimique et la formation/destruction de liaisons chimiques. Des simulations moléculaires ont été conduites afin de comprendre les mécanismes moléculaires responsables des effets synergiques observés lorsque des réactifs sont utilisés en combinaison, notamment entre différents déprimants et différents collecteurs/co-collecteurs. De plus, l'hydratation des surfaces les plus exposées de la scheelite et de la fluorite, minéral le plus problématique en flottation, a été étudiée afin de décrire

l'état de la surface en présence d'eau. Les modalités d'adsorption des acides carboxyliques, collecteurs utilisés au cours de cette étude, ont donc été examinées car elles représentent, à l'heure actuelle, un sujet entre méconnu dans le domaine de la flottation.

2. Le skarn de Tabuaço

Les deux couches minéralisées du gisement de Tabuaço présentent des caractéristiques très contrastées en matière de géochimie, de composition minéralogique et de teneur moyenne en tungstène. Le Lower Skarn est plus riche en SiO_2 et en Fe_2O_3 quand le Main Skarn démontre des teneurs plus fortes en CaO, F, P_2O_5 et W. Ces différences sont probablement corrélées avec la distance au granite, le Lower Skarn étant plus distal que le Main Skarn. Elles peuvent aussi être attribuées à un contraste géochimique entre les protolithes : le Lower Skarn résulte du métamorphisme de roches plus riches en silice, le Main Skarn de roches plus calciques. Ce dernier est composé de silicates (85 ‰$_m$) principalement calciques (vésuvianite, zoïsite et grenat grossulaire) associés à de faibles pourcentages de feldspaths et de quartz. La fraction massique restante est constituée de fluorite, d'apatite et de scheelite. La roche présente des textures assez grenues avec des tailles de grains variant de quelques micromètres à plus d'un millimètre. La scheelite est majoritairement disséminée avec quelques micro-veines observables, qui recoupent les structures sédimentaires. Elle forme des cristaux xénomorphes de 5 à 300 µm avec une taille moyenne de 150 µm, qui définit la maille de libération pour le Main Skarn. De fines associations minérales sont observées entre la scheelite et la fluorite/vésuvianite avec une proportion importante de cristaux interpénétrés. De plus, une phase d'albitisation globale a affecté les couches minéralisées, essentiellement le Main Skarn, ce qui induit la présence fréquente de cristaux de scheelite rétromorphosés en albite. Le Lower Skarn contient quasi exclusivement des silicates (95 ‰$_m$) dont de la vésuvianite, du diopside (pyroxène calcique), de la zoïsite, du quartz et des feldspaths. Cette couche est plus pauvre en minéraux calciques et présente des teneurs bien plus faibles en fluorite, en apatite et en scheelite. Cependant, ce niveau contient des sulfures (arsénopyrite, pyrite et pyrrhotite), contrairement au Main Skarn. Les textures sont aussi beaucoup plus fines ; ainsi, la maille de libération de la scheelite est plus fine, estimée à 100-120 µm environ, par microscopie optique.

3. Implications pour les procédés minéralurgiques

Une teneur significative en sulfures induit traditionnellement une flottation préliminaire des sulfures (Tomas, 1985), ces derniers étant un pénalisant fort pour les concentrés de scheelite. Dans le Main Skarn, aucun sulfure n'est observé et, bien que quelques sulfures soient présents dans le Lower Skarn, le choix a été fait de ne pas réaliser de flottation des sulfures dans cette étude. Cependant, une attention tout particulière doit être accordée aux teneurs en soufre dans les concentrés de flottation.

Les couches minéralisées présentent toutes deux des mailles de libération fines, particulièrement pour le Lower Skarn. Cependant, la densité relativement forte de la scheelite induit un temps de résidence dans le broyeur généralement plus élevé que pour les minéraux de gangue. Ceci, associé

à la friabilité intrinsèque de la scheelite, a nécessité d'optimiser les paramètres du broyage afin de limiter autant que possible la production de particules fines (-10 µm).

La présente étude s'est focalisée sur la définition d'un procédé minéralurgique pour le Main Skarn, qui, au vu des teneurs en minéraux calciques (fluorite, apatite, silicates calciques…), représentait un défi bien plus important que pour le Lower Skarn. La suite des discussions se concentre donc sur le Main Skarn. En se fondant sur les différences de propriétés entre les différents minéraux constitutifs, plusieurs schémas de traitement ont pu être envisagés :

1. Une séparation par gravité qui, étant donné le contraste de densités entre les différents minéraux, éliminerait efficacement les silicates légers, modérément les sels calciques mais faiblement les silicates denses ;
2. Une séparation magnétique à haute intensité qui permettrait d'éliminer les minéraux paramagnétiques, c'est-à-dire les silicates denses ;
3. Une flottation avec des acides gras, qui concentrerait très bien la scheelite, les sels calciques et les silicates denses (car ils sont calciques). La sélectivité en flottation peut toutefois être modulée en utilisant des déprimants et en optimisant les formulations de collecteur.

La maille de libération rend la plupart des séparations par gravité classiques inefficaces pour la concentration de la scheelite (Burt, 1999; Das and Sarkar, 2018) et l'utilisation d'un concentrateur centrifuge Falcon, spécifiquement développé pour la valorisation des particules fines par gravité, a été suggérée pour le traitement du minerai de Tabuaço. Bien qu'une séparation magnétique fut aussi applicable pour ce skarn, les particules fines (-150+7 µm) ne pouvaient pas être traitées en séparation en voie sèche et ont donc été valorisées en voie humide, contrairement aux grossières (500-150 µm), qui ont été traitées en voie sèche. Ainsi, la séparation magnétique à haute intensité a été étudiée sur deux fractions granulaires différentes. Par ailleurs, la flottation a aussi été testée sur les fines particules (-150+7 µm) étant donné la maille de libération relativement fine. Les silicates représentent 85 %$_m$ du Main Skarn : l'utilisation d'amines pour la collection de la scheelite semblait inappropriée pour obtenir une bonne sélectivité et le choix a été fait d'utiliser des huiles de tall, essentiellement composées d'acides gras. Cependant, le Main Skarn présente des teneurs importantes en minéraux calciques (silicates ou sels), ce qui a rendu obligatoire l'optimisation des déprimants et des formulations de collecteur, ainsi que de leur dosage.

Dans un premier temps, le broyage a été adapté afin d'atteindre la maille de libération tout en évitant autant que possible les pertes en scheelite dans les fines. Pour remplir cet objectif, le broyeur à boulets a été alimenté par le refus du tamis de 150 µm, le passant court-circuitant le broyage. Après cette étape, le produit était tamisé à 150 µm et le refus re-broyé, ce qui constituerait la charge circulante d'un broyage en continu. À l'issue du broyage, les pertes en scheelite dans les fines (-7 µm), estimées par la teneur en WO$_3$ de la surverse de l'hydrocyclone après déschlammage, s'élevaient à 6,3 %. Etant donné la composition minéralogique, les

propriétés des minéraux et les précédentes discussions, quatre différentes options ont été suggérées pour le traitement du Main Skarn de Tabuaço:

1. Flottation directe ;
2. Séparation par gravité au Falcon SB ;
3. Séparation magnétique à haute intensité en voie humide ;
4. Séparation magnétique à haute intensité en voie sèche sur le (-500+150 µm).

Chaque option a été optimisée puis l'ensemble des possibilités ont été comparées en matière de performances de séparation, avec l'objectif global de combiner les meilleures options pour obtenir un concentré commercialisable de scheelite.

4. Déprimants en flottation

La flottation aux acides gras sans l'ajout de déprimants a conduit à une flottation non-sélective de la quasi-totalité des minéraux, dont la scheelite, la fluorite, l'apatite et les silicates : la teneur en WO_3 du concentré produit était encore très faible et la récupération en WO_3 était diminuée par la consommation du collecteur par tous les minéraux. Ainsi, l'usage de déprimants s'est avéré obligatoire pour atteindre des sélectivités acceptables. Plusieurs déprimants ont été testés au cours d'essais d'orientation afin d'identifier ceux présentant la meilleure sélectivité. Le silicate de sodium, même s'il a montré de bons résultats, s'est montré insuffisant, en particulier vis-à-vis de la fluorite. L'addition de sels métalliques (sels de fer, de zinc et d'aluminium) préalablement au silicate de sodium a été étudiée. De même, l'utilisation de molécules organiques (acide citrique, carboxylméthyl cellulose, tannin, sulfonate de lignine et amidon) en substitution du silicate de sodium a été envisagée. Parmi tous les déprimants testés, la combinaison entre le carbonate de sodium (Na_2CO_3) et le silicate de sodium (Na_2SiO_3) a présenté la meilleure efficacité, principalement attribuée à de forts effets synergiques entre les deux réactifs (Agar, 1984; Marinakis, 1980; Marinakis and Shergold, 1985b). Suite à ces essais d'orientation, le système Na_2CO_3/Na_2SiO_3 a été étudié plus en profondeur via un plan d'expériences. Na_2CO_3 utilisé seul n'affectait pas le ratio d'enrichissement en WO_3 et augmentait légèrement la récupération en WO_3, ce qui est probablement dû à la formation de complexes $Ca-CO_3$ en solution, diminuant la concentration de Ca^{2+} et augmentant ainsi la quantité de collecteur disponible pour collecter la scheelite. Na_2SiO_3 utilisé seul déprimait peu la scheelite et a permis d'atteindre des ratios d'enrichissement en WO_3 modérés, avant de déprimer la scheelite à trop fort dosage. Lorsque Na_2CO_3 a été ajouté préalablement à Na_2SiO_3, ce dernier a présenté un effet déprimant beaucoup plus fort, permettant d'atteindre des ratios d'enrichissement forts en WO_3. Néanmoins, la scheelite était lourdement déprimée pour des dosages trop importants en Na_2CO_3/Na_2SiO_3. Ces effets synergiques ont été étudiés plus précisément par des méthodes spectroscopiques (infrarouge et photoélectronique X) associées à de la modélisation moléculaire (par DFT) sur la fluorite (CaF_2), un minéral simple, facile à modéliser et qui n'absorbe pas en infrarouge dans les nombres d'onde considérés. Des spectres ont été acquis pour la fluorite traitée dans l'eau distillée, dans Na_2CO_3, dans Na_2SiO_3 et dans Na_2CO_3 suivi de Na_2SiO_3, à pH 10 quel que soit le système. De même, l'adsorption de $Si(OH)_4$ (la forme stable de Na_2SiO_3 en solution) sur la fluorite nue et sur

la fluorite traitée avec Na_2CO_3 a été étudiée par modélisation moléculaire. Les résultats ont montré que le $Si(OH)_4$ s'adsorbe sur la fluorite carbonatée avec une énergie d'adsorption beaucoup plus élevée que sur la surface nue (-180.8 kJ.mol^{-1} contre -100.7 kJ.mol^{-1}, respectivement). Ceci est expliqué par le transfert d'un proton de la molécule de $Si(OH)_4$ vers les groupements carbonates adsorbés sur la surface, qui transforme le $Si(OH)_4$ en $SiO(OH)_3^-$. Cette forme, anionique, dispose d'un excès d'électrons, ce qui rend l'adsorption très favorisée sur la surface. Ce transfert de proton est observable en infrarouge : le pic à 879 cm^{-1} présent lorsque la fluorite est conditionnée avec Na_2CO_3 seul, est déplacé à 842 cm^{-1} lorsque la fluorite est conditionnée avec Na_2CO_3 puis Na_2SiO_3. Ces deux pics sont attribués à Na_2CO_3 et $NaHCO_3$, respectivement, ce qui montre bien la formation de $NaHCO_3$ lorsque Na_2SiO_3 est ajouté sur une surface carbonatée. Ce résultat, généralisable aux minéraux calciques, est une avancée majeure dans le monde de la flottation : les effets synergiques entre Na_2CO_3 et Na_2SiO_3 sont connus et utilisés depuis des décennies [Petrov, dans son brevet de 1940, employait déjà le système Na_2CO_3/Na_2SiO_3 pour la flottation de la scheelite (Petrov, 1940)]. Ainsi, l'usage de Na_2CO_3 pour contrôler le pH permet de diminuer considérablement les dosages en Na_2SiO_3 en augmentant son effet déprimant (sur la fluorite et sur les autres minéraux de gangue calciques). Globalement, les conditions optimales qui ont permis de réaliser un compromis entre la teneur et la récupération étaient de 1 150 g/t de Na_2CO_3 et 1 225 g/t de Na_2SiO_3, pour 200 g/t de RBD15. L'essai réalisé dans ces conditions a produit un concentré de dégrossissage titrant 10,1 % WO_3 pour 93,2 % de récupération WO_3, pour une alimentation titrant 1,1 % WO_3. L'apatite et les silicates ont été correctement déprimés bien que la récupération en fluorite dans le concentré fut encore de 63,6 %.

5. Collecteurs en flottation

Malgré des doses considérables en déprimants (Na_2CO_3 et Na_2SiO_3), la fluorite restait mal déprimée et représentait encore la majorité de la masse du concentré de flottation, ce qui diluait dramatiquement la scheelite. L'approche d'optimisation des déprimants était donc limitée : la fluorite et la scheelite présentent des distances très similaires entre les atomes de calcium sur leur surface, ce qui induit une faible sélectivité des déprimants entre les deux minéraux, en particulier lorsqu'il s'agit de grandes molécules avec un fort taux de couverture. Les résultats précédents ont suggéré que les meilleurs déprimants identifiés, à des dosages optimisés, n'ont pas permis d'atteindre une sélectivité satisfaisante entre la scheelite et la fluorite. Ainsi, dans les conditions optimales de dépression, l'étude s'est focalisée sur les collecteurs : le RBD15, principalement composé d'acide oléique (mono-insaturé) et d'acide linoléique (bi-insaturé), ne présentait pas une sélectivité acceptable entre les deux minéraux. L'influence du pourcentage en acides résiniques dans les huiles de tall a été étudiée par microflotation et par flottation classique. Ils ont pour effet de réduire la sélectivité tout en augmentant les récupérations. Ceci est attribué à la diminution du contrôle exercé par les distances entre les atomes de calcium de la surface sur l'organisation de la couche d'adsorption. Les acides résiniques contiennent, en effet, des cycles dans leur chaine aliphatique et sont donc des molécules à fort encombrement stérique. Leur introduction dans les formulations implique que des sites d'adsorption (atomes de calcium) à la surface restent inoccupés (augmentation de la récupération par mise à disposition du collecteur)

et que la couche d'adsorption est moins bien organisée (perte de sélectivité). Ainsi, un compromis a été choisi, représenté par le RBD15, entre la sélectivité (faible teneur en acides résiniques) et la récupération (forte teneur en acides résiniques). Par ailleurs, selon cette même théorie, la diminution de l'encombrement stérique des molécules pouvait donc impliquer une augmentation de la sélectivité vis-à-vis de la scheelite. Ainsi, l'introduction d'acides gras saturés dans les formulations classiques (huiles de tall) a été testée et a démontré une augmentation considérable de la sélectivité entre la scheelite et la fluorite lors des essais de microflotation. Il est supposé que les acides gras saturés conduisent à une meilleure organisation de la couche d'adsorption, ce qui favorise l'influence des propriétés cristallographiques de surface, permettant d'exploiter les différences fines qui existent entre les deux minéraux. Toutefois, ces résultats positifs n'ont pas pu être observés sur le minerai de Tabuaço avec des formulations créées en laboratoire. Le LD, une nouvelle huile de tall contenant une proportion significative d'acides gras saturés, a été utilisé en remplacement du RBD15. Cette formulation commerciale a tout de même conduit à une augmentation considérable de la sélectivité en flottation vis-à-vis de la scheelite, probablement due à une organisation des acides gras au préalable, lors des étapes de distillation. Dans les conditions optimales de dépression déterminées précédemment, le dosage optimal de LD a été identifié à 600 g/t afin de réaliser un compromis entre la teneur et la récupération en WO_3. Dans ces conditions, le concentré de flottation titrait 14,5 % WO_3 pour 85.4 % de récupération en WO_3, pour une alimentation titrant 1,1 % WO_3. Par rapport au RBD15, le LD a induit une chute considérable de la récupération en WO_3 (de 93,2 % à 85,4 %) accompagnée d'une diminution appréciable de la récupération en fluorite ainsi que des récupérations des autres minéraux de gangue. Par ailleurs, l'introduction d'un alcool, l'isotridécanol, dans les formulations d'acides gras a été étudiée par flottation et par la théorie de la fonctionnelle de la densité. Il a été démontré que l'isotridécanol induit une augmentation considérable des teneurs en WO_3 dans les concentrés de relavage de flottation (peu au dégrossissage) avec toutefois une diminution de la récupération en WO_3. Ces effets sont plus prononcés pour le LD que pour le RBD15, probablement par des effets synergiques plus forts entre acides gras saturés et isotridécanol qu'entre acides gras insaturés et isotridécanol. Cependant, étant donné les récupérations en WO_3 largement diminuées et les coûts opératoires augmentés (dus à l'utilisation d'un co-collecteur), cette option n'a pas été sélectionnée pour la suite.

6. Concentration par gravité

Une autre option suggérée pour la valorisation du Main Skarn de Tabuaço était d'utiliser le contraste de densité considérable entre la scheelite (6,1) et la fluorite (3,2). En effet, cette dernière représentait le minéral le plus problématique en flottation avec une récupération encore élevée dans les conditions optimales de dépression et de collection. Pour ces raisons, l'usage d'un concentrateur Falcon (bols UF et SB) pour éliminer la fluorite par séparation par gravité avant ou après la flottation a été étudié. Un plan d'expériences a été mis en œuvre pour chaque bol, en prenant en compte la vitesse de rotation du bol, la densité de solides dans la pulpe, le débit d'alimentation et la pression de fluidisation (pour le Falcon SB). Les résultats ont montré que la vitesse de rotation et la pression de fluidisation sont les principaux paramètres qui influencent

les performances de la séparation en matière de ratio d'enrichissement WO$_3$, corrélé à l'élimination des minéraux de gangue, et de récupération en WO$_3$, pour le bol SB. Globalement, l'augmentation de la vitesse de rotation provoque une amélioration des récupérations en scheelite et en minéraux de gangue et ainsi une diminution de la teneur en WO$_3$ par dilution de la scheelite. En effet, l'augmentation de la vitesse de rotation induit une augmentation de la force centrifuge et donc un meilleur piégeage des particules au sein des gouttières du bol. Au contraire, l'augmentation de la pression de fluidisation implique une meilleure élimination des minéraux, essentiellement des minéraux de gangue mais aussi de la scheelite, et donc une augmentation de la teneur en WO$_3$. La pression de fluidisation exerce une force de traînée sur les particules, dirigée de manière radiale mais orientée vers l'intérieur du bol, c'est-à-dire de sens opposé à la force centrifuge. De plus, la force de traînée inhérente à la pression de fluidisation est de même norme pour l'ensemble des particules, quelle que soit leur densité, car elle dépend uniquement de la surface des particules, et donc de leur taille. Ainsi, la pression de fluidisation a tendance à éjecter les particules sur lesquelles la force centrifuge est la plus faible, à savoir les particules les moins denses. Elle induit donc une augmentation de la teneur en particules denses, ici la scheelite. Par ailleurs, la séparation avec le Falcon UF est principalement corrélée à la densité de pulpe et à la vitesse de rotation : une forte vitesse de rotation induit une longueur de piégeage des particules plus courtes et donc une augmentation non-sélective des récupérations. La densité de pulpe induit un effet inverse, expliqué par une sédimentation gênée/forcée. Globalement, le Falcon SB a présenté des performances de séparation nettement supérieures au Falcon UF, avec de meilleures récupérations en WO$_3$, teneurs en WO$_3$ et efficacités de déschlammage. Le Falcon SB a donc été sélectionné pour la suite. Une étape de séparation optimisée avec le Falcon SB a permis l'élimination de 84,7 % de la fluorite et de 79,7 % de l'apatite, pour une récupération en WO$_3$ de 75,8 %. De plus, le rendement poids dans le concentré était de seulement 15,8 %$_m$, ce qui signifie que près de 85 % de la masse totale a été éliminée au cours de la séparation avec un Falcon. Enfin, ce dernier a permis l'élimination de plus de 98 % des particules inférieures à 10 µm du minerai non-déschlammé. Néanmoins, les silicates denses (vésuvianite notamment) ont été faiblement éliminés et représentaient la majeure partie du concentré.

7. Séparation magnétique à haute intensité

La zoïsite, le grossulaire et la vésuvianite, présents en proportions considérables dans le Main Skarn de Tabuaço, contiennent du fer et du magnésium. Ainsi, plus de 70 %$_m$ du minerai est constitué par des minéraux paramagnétiques qui correspondent, de plus, aux silicates denses difficilement éliminés par le Falcon mais très efficacement par la flottation. La séparation magnétique représentait donc une option tout à fait envisageable pour éliminer les silicates denses, en complément de la flottation. Elle a été réalisée sur la fraction (-500+150 µm), avant le broyage, en voie sèche et, par ailleurs, en voie humide sur la fraction (-150+0 µm), qui représentait le même produit que l'alimentation de flottation. En voie sèche, la séparation a montré des résultats satisfaisants : la fraction magnétique était constituée des minéraux ferromagnésiens, qui correspondent aux silicates denses (vésuvianite, grossulaire et zoïsite), la fraction non-magnétique se compose des sels calciques (scheelite, fluorite et apatite) et des

silicates non-ferromagnésiens (quartz et feldspaths). Les récupérations en P_2O_5, en K_2O, en Fe_2O_3 et en F dans la fraction magnétique étaient de 13,7 %, 25,8 %, 59,6 % et 27,8 %, ce qui montre une bonne élimination des minéraux ferromagnésiens. Cet essai, réalisé dans des conditions favorisant la récupération en WO_3, démontre qu'une séparation magnétique à haute intensité en voie sèche permettrait de réduire la masse de 44,5 % avant le broyage avec des pertes acceptables en scheelite, de l'ordre de 6,0 %. De plus, les silicates ferromagnésiens, éliminés au cours de cette étape, sont connus pour être très abrasifs et résistants. Leur élimination préalable au broyage représenterait donc une option très positive sur les coûts opératoires. La séparation magnétique à haute intensité en voie humide a présenté des performances très inférieures par rapport à la voie sèche. Ici, le minerai a été déschlammé avant la séparation, ce qui a conduit à la perte de 7,9 % de la masse totale de scheelite qui s'est ajoutée aux 7,2 % de pertes dans la fraction magnétique, sans doute par entrainement particulaire. De manière globale, l'élimination des silicates ferromagnésiens et des minéraux de gangue en général était moins bonne en voie humide. Cette dernière option n'était pas envisageable au vu des faibles performances qu'elle présente.

8. Développement du procédé

Parmi toutes les options envisagées pour la valorisation du Main Skarn de Tabuaço, il est ressorti que :

- La flottation aux acides gras, après l'optimisation des déprimants et des formulations de collecteurs, a éliminé correctement les silicates (denses et légers) mais pas la fluorite ;
- Le séparateur Falcon, avec des paramètres opératoires optimisés, a éliminé efficacement la fluorite mais peu efficacement les silicates denses ;
- Une élimination des silicates denses était possible avant le broyage par séparation magnétique à haute intensité.

Au vu de ces conclusions, une combinaison entre le Falcon SB et la flottation aux acides gras était tout à fait envisageable. Par ailleurs, sur un schéma composé de flottation uniquement, l'influence d'un relavage devait être étudiée. Dans les conditions optimales de dépression, l'huile de tall classique (RBD15) a conduit à l'obtention d'une récupération en WO_3 plus forte malgré une teneur en WO_3 plus faible qu'avec la nouvelle formulation (LD). De plus, le dosage optimal pour cette dernière était de 600 g/t, contre seulement 200 g/t pour le RBD15, ce qui induirait des coûts opératoires plus importants lors de l'utilisation du LD. L'influence d'un relavage a donc été étudiée pour les deux collecteurs, dans les conditions optimales de dépression. Ainsi, cinq schémas de traitement globaux ont pu être proposés pour la valorisation du Main Skarn de Tabuaço :

1. Dégrossissage + relavage dans les conditions optimales de dépression, avec le RBD15 ;
2. Dégrossissage + relavage dans les conditions optimales de dépression, avec le LD ;
3. Falcon SB + Dégrossissage dans les conditions optimales de dépression, avec le RBD15 ;
4. Falcon SB + Dégrossissage dans les conditions optimales de dépression, avec le LD ;
5. Dégrossissage dans les conditions optimales de dépression, avec le RBD15 + Falcon SB.

Globalement, les schémas incorporant uniquement de la flottation ont produit des concentrés ayant une teneur en WO_3 plus élevée quand le LD est utilisé, avec des récupérations en WO_3 similaires (Schémas 1 et 2). Le Falcon a produit un pré-concentré avec une teneur et une récupération en WO_3 considérablement plus faibles que le concentré de flottation. Cependant, la majorité de la fluorite, de l'apatite et des fines ont été éliminées par la séparation avec le Falcon SB, ce qui a impliqué une efficacité très importante de l'étape de flottation réalisée sur ce pré-concentré. En effet, ce dernier était constitué essentiellement de scheelite et des silicates denses, très bien éliminés par flottation, induisant ainsi un ratio d'enrichissement en WO_3 très élevé. Après une seule étape de Falcon SB et de flottation au RBD15, le concentré titrait 38,1 % WO_3 pour 62,5 % de récupération globale en WO_3, à partir d'une alimentation titrant 1,1 % WO_3. Les résultats ont été très similaires lorsque le RBD15 a été remplacé par le LD, ce qui peut être attribué au fait que la majorité de la fluorite avait été éliminée par le Falcon. Cette élimination préalable a écrasé les différences de sélectivité entre les deux collecteurs, produisant ainsi des concentrés très semblables en matière de teneur. Toutefois, le LD a amélioré sensiblement la récupération en WO_3, probablement grâce à des dosages plus élevés (600 g/t) par rapport au RBD15 (200 g/t).

Le schéma inverse (flottation puis Falcon) a aussi été testé ; le concentré final, après une étape de flottation et de Falcon, titrait 25,9 % WO_3 pour 55,9 % de récupération globale en WO_3. Cette option présentait cependant moins d'avantages : (1) quand la flottation est réalisée en tête, le minerai doit être déschlammé au préalable, ce qui requiert l'usage d'un hydrocyclone, impliquant plus d'opérations et des pertes en scheelite dans les fines ; (2) étant donné que le Falcon induit des coûts opératoires plus faibles, les débits les plus importants doivent être traités avec le Falcon plutôt qu'en flottation ; (3) les collecteurs ne se désorbent pas des surfaces des particules après la flottation, ce qui perturbe les mécanismes de séparation dans le bol du Falcon en rajoutant une tension de surface aux particules.

Etant donné les récupérations et teneurs en WO_3, le schéma 4 (Falcon → Flottation avec LD) a été considéré comme la meilleure option pour la valorisation du Main Skarn de Tabuaço. Une étape de Falcon optimisée suivie d'une étape de flottation au LD a produit un concentré final titrant 37,8 % WO_3 avec 72,6 % de récupération globale en WO_3. Plusieurs étapes de relavage en flottation ont été testées sur ce concentré, sans aucun ajout de réactif. Logiquement, les relavages successifs ont permis d'augmenter la teneur en WO_3 malgré une diminution modérée de la récupération en WO_3. Après quatre étapes de flottation réalisées sur le pré-concentré produit avec le Falcon, le concentré final titrait 62,9 % WO_3 pour 59,4 % de récupération globale en WO_3, à partir d'une alimentation titrant 1,1 % WO_3, ce qui constituait un concentré commercialisable de scheelite. La récupération en WO_3 sera largement améliorée lorsque le procédé sera adapté en fonctionnement continu, c'est-à-dire à échelle pilote, étant donné que les stériles, qui contiennent encore des quantités non-négligeables de scheelite, seront recyclés dans les étapes précédentes. De plus, des études sur les stériles du Falcon SB, qui représentaient 24,0 % de la masse totale en scheelite, pourraient être entreprises pour augmenter la récupération globale en WO_3.

Le schéma de traitement global, développé dans cette étude, pourra être adapté aux performances attendues : les paramètres opératoires adoptés pour le Falcon SB peuvent être définis afin de favoriser l'élimination des minéraux de gangue (donc la teneur en WO_3) ou la récupération en WO_3. De plus, le nombre d'étapes de flottation réalisées sur le pré-concentré par Falcon SB peut aussi être optimisé pour favoriser la teneur en WO_3 (beaucoup d'étapes de flottation) ou la récupération en WO_3 (peu d'étapes de flottation). De manière globale, le schéma de traitement proposé dans cette étude permettrait de :

- Produire un concentré commercialisable de scheelite (62,9 % WO_3) ;
- Limiter la consommation énergétique, 55 % de la masse étant éliminée avant le broyage ;
- Limiter les coûts opératoires liés aux réactifs, 85 % de la masse étant éliminée avant la flottation ;
- Limiter la consommation d'eau, pour la même raison ;
- Utiliser uniquement des réactifs à faible impact environnemental en flottation (Na_2CO_3, Na_2SiO_3, huile de tall) et à température ambiante étant donné que les minéraux problématiques sont rejetés avant la flottation ;
- Adapter le schéma de traitement aux spécifications imposées sur le produit ou aux performances visées (favoriser la teneur ou la récupération en WO_3).

9. Propriétés de surface de la fluorite et de la scheelite en présence d'eau : une étude atomistique

En parallèle du développement du procédé, une étude plus fondamentale a été entreprise afin de comprendre les mécanismes moléculaires impliqués dans l'adsorption des réactifs de flottation sur les minéraux et parfois responsables d'effets synergiques observés expérimentalement. En premier lieu, les états d'hydratation de la surface (111) de la fluorite ainsi que des surfaces (001) et (112) de la scheelite ont été examinés à l'aide de la théorie de la fonctionnelle de la densité en utilisant une correction des interactions de van der Waals, à 0 K et 300 K. Les résultats ont montré que l'eau s'adsorbe sous forme moléculaire sur un seul atome de calcium de surface pour la fluorite et la scheelite (001) et entre deux atomes de calcium de surface pour la scheelite (112). Les énergies d'adsorption calculées sont de $\Delta E_{ads} \approx$ -55 kJ.mol^{-1} pour la fluorite, de $\Delta E_{ads} \approx$ -87 kJ.mol^{-1} pour la scheelite (001) et de $\Delta E_{ads} \approx$ -127 kJ.mol^{-1} pour la scheelite (112), ce qui indique que l'adsorption de l'eau est bien plus favorable sur la scheelite que sur la fluorite. De plus, l'adsorption d'eau dissociée est favorable sur les deux surfaces de scheelite avec, cependant, une adsorption exothermique pour la surface (112). Cela démontre une forte capacité des surfaces de la scheelite à être hydroxylées, ce qui conduit donc à un pH d'hydroxylation plus bas pour la scheelite que pour la fluorite. Par ailleurs, étant donné que ces deux minéraux sont semi-solubles, la substitution des anions de surface par des groupes OH$^-$ a été étudiée ; au vu des énergies de réaction fortement positives, elle semble défavorisée. Ensuite, l'interaction des surfaces avec plusieurs molécules d'eau a été examinée à 0 K et confirmée à 300 K par des simulations en dynamique moléculaire *ab initio*. Sur la fluorite, la moitié des atomes de calcium sont occupés par des molécules d'eau adsorbées alors que, sur la surface (001) de la scheelite, chaque atome de calcium est occupé par deux molécules d'eau. Sur la surface (112), chaque atome

de calcium présente une molécule d'eau adsorbée et une molécule d'eau partagée entre deux atomes de calcium de la surface, ce qui conduit à trois molécules d'eau adsorbées sur deux atomes de calcium au total. Ceci est cohérent avec la réactivité plus importante des atomes de calcium pour la scheelite induite par l'existence de deux liaisons rompues par atome de calcium au lieu d'une seule pour la fluorite. Cette différence de réactivité conduit donc à l'adsorption de deux molécules d'eau par atome de calcium sur la surface, ou trois molécules d'eau sur deux atomes de calcium de la surface pour les surfaces (001) et (112) de la scheelite, respectivement, quand une seule molécule d'eau est adsorbée pour deux atomes de calcium sur la surface de la fluorite. Ceci explique probablement l'hydrophobie naturellement élevée de la surface (111) de la fluorite, qui présente des angles de contact considérables (Jańczuk et al., 1993; Kowalczuk et al., 2017; Zhang et al., 2015). Par ailleurs, dans le modèle de Langmuir, l'adsorption en phase liquide comprend la désorption préalable des molécules d'eau pré-adsorbées avant l'adsorption de la molécule à proprement parler. Ainsi, les énergies d'adsorption des molécules d'eau sur la scheelite plus élevées que sur la fluorite impliquent probablement une difficulté plus importante pour les réactifs de flottation pour s'adsorber sur les surfaces de scheelite. Globalement, les résultats sur les états d'hydratation contribuent à une meilleure compréhension des propriétés de la fluorite et de la scheelite en phase aqueuse et sont cruciales pour caractériser l'adsorption des collecteurs de flottation. En particulier, l'étape suivante au cours de ce travail a été d'étudier les aspects fondamentaux de l'adsorption des acides gras sur différents minéraux calciques, principalement sur la fluorite, afin de mieux appréhender les mécanismes moléculaires impliqués dans leur adsorption.

Ces aspects ont été examinés par des simulations atomistiques (en DFT) menées à 0 K et à 300 K, en conditions hydratées et sèches sur la surface (111) de la fluorite. En premier lieu, les acides gras sous leur forme acide s'adsorbent sur la surface de la fluorite avec ΔE_{ads} = -78.2 kJ.mol^{-1} malgré une adsorption endothermique sous forme dissociée. Par ailleurs, les acides gras sous leur forme carboxylate peuvent s'adsorber directement sous leur forme anionique ou associés avec un cation de sodium (Na$^+$) pour leur neutralisation. Ainsi, en conditions non-hydratées, un carboxylate seul, c'est-à-dire sans Na$^+$, fait une chimisorption avec une configuration en bidentate binucléaire alors que, lorsqu'il est associé avec un Na$^+$, il s'adsorbe soit sur les atomes de calcium de la surface, soit sur le Na$^+$, ce dernier faisant office de cation-pont entre le carboxylate et la surface. De plus, l'anion carboxylate peut s'adsorber en réalisant un échange anionique avec un ion fluorure de la surface, ce qui s'est toutefois avéré endothermique. Globalement, en conditions non-hydratées, les trois premières formes sus-décrites sont possibles pour l'adsorption du carboxylate. La configuration de la chaîne aliphatique lors de l'adsorption a ensuite été étudiée : pour des longueurs de chaîne typiquement utilisées en flottation, l'adsorption à plat est favorisée, c'est-à-dire avec la chaîne sub-parallèle à la surface et interagissant avec cette dernière par des forces de dispersion. A 300 K, les mêmes conclusions peuvent être tirées avec des énergies d'adsorption relativement similaires, légèrement modifiées en raison de la température. Les mécanismes d'adsorption ont été aussi étudiés en conditions hydratées, systématiquement à 300 K pour la détermination des géométries et à 0 K pour le calcul des énergies d'adsorption. Les résultats ont permis de démontrer que, en solution, la liaison

entre le carboxylate et un Na^+ est thermodynamiquement favorisée, malgré une possible énergie d'activation. De plus, le Na^+ s'adsorbe favorablement sur la surface de la fluorite, avec ΔE_{ads} = -144.8 kJ.mol^{-1}, ce qui indique que des Na^+ sont probablement adsorbés sur la plupart des atomes de fluor de la surface. Ainsi, les Na^+ en solution sont soit liés aux carboxylates, soit adsorbés sur la surface de la fluorite. De plus, en conditions hydratées, il a été démontré que les chaînes aliphatiques restent verticales au cours de l'adsorption : l'adsorption à plat n'est plus favorisée car des molécules d'eau sont adsorbées sur la surface. Par ailleurs, trois modes d'adsorption ont été mis en évidence pour les carboxylates en conditions hydratées :

- L'anion carboxylate en configuration monodentate (ΔE_{ads} = -66.3 kJ.mol^{-1}) ;
- Le carboxylate de sodium ponté sur la surface par le Na^+, lui-même adsorbé sur les atomes de fluor de la surface (ΔE_{ads} = -154.2 kJ.mol^{-1}) ;
- Un échange anionique entre un fluor de surface et l'anion carboxylate (ΔE_r = -106.4 kJ.mol^{-1}).

Pour confirmer ces résultats, des calculs via la méthode de la théorie des perturbations de la fonctionnelle de la densité ont permis de simuler des spectres infrarouges à partir des géométries déterminées à 300 K en conditions hydratées. Les résultats ont montré que les adsorptions en bidentate binucléaire et en monodentate conduisent à l'obtention du pic du groupe carboxyle à 1575 et 1535 cm^{-1}, respectivement. Ces deux pics ont été largement observés dans la littérature et ont été attribués à la précipitation de dicarboxylate de calcium sur la surface. De plus, l'adsorption du carboxylate de sodium sur le Na^+ faisant office de cation-pont conduit à l'obtention de la bande du groupe carboxyle à 1558 cm^{-1} qui a aussi été très observée par les auteurs, alors qu'elle est située à 1586 cm^{-1} pour l'échange d'anions. Globalement, l'adsorption des carboxylates sous leur forme anionique ou pontés sur des cations Na^+ semble principalement contrôlée par la concentration de Na^+ en solution.

Chapter 1

Introduction

1. Scope of the study

1.1 Tungsten: an overview

Tungsten is a transition metal with the symbol W and atomic number 74, part of the same family than molybdenum and chromium. Its name comes from the former Swedish in which scheelite, the calcium tungstate, was named *tungsten*, *i.e.* "heave stone". Tungsten displays very interesting properties for industrial applications. First, it is one of the densest metals on Earth with a specific gravity of 19.3, very similar to that of gold and significantly higher than that of other transition metals. Besides, it exhibits a melting point of 3 422°C, which constitutes the highest melting point among all the metals (only exceeded by graphite). Along with its thermal dilatation coefficient, the lowest among all the metals, this makes tungsten an excellent refractory material. Furthermore, it displays a substantial hardness (7.5 on the Mohs's scale), especially when it is combined with carbide anions in tungsten carbide (WC), which exhibits a hardness of 9.0. Tungsten has a low abundance in the Earth's crust, around 1.3 ppm, which is significantly lower than the other lithophile elements but about the same as that of tin (2 ppm) and molybdenum (1.2 ppm). Rarely found under its metal form, tungsten is mostly encountered bond to oxygen atoms (tungstate anions) although it can form sulphides.

1.2 Properties, applications, and prices

The aforementioned interesting properties of tungsten induce a wide range of industrial applications for this metal, including the production of tungsten carbide (55%), tungsten alloys and supra-alloys (25%), metal tungsten (13%), and chemical compounds (7%) (U.S. Geological Survey, 2019). In particular, cemented tungsten carbide are traditionally used for machining of metallic items and products where they constitute the friction parts of drills and mills. Besides, tungsten alloys and supra-alloys are commonly used for refractory metallic pieces in aircraft engines, munitions, or metallurgical furnaces. Since cemented tungsten carbide cannot be recovered, the tungsten recycling rate is around 20-25% (Audion and Labbé, 2012), which represents a considerably low value compared to other metals. Moreover, the noticeable properties of tungsten induce a difficult substitution for this element: it can be substituted with molybdenum, titanium, or niobium in carbides and alloys while metal tungsten can be replaced with depleted uranium. However, most of these substitutions decrease, rather than replace, the amount of tungsten used and generally induce health problems (for uranium), increased cost, or significant loss of product performances (U.S. Geological Survey, 2019).

Before the 20th century, tungsten was marginally used for industrial applications. Its consumption significantly raised with the development of heavily armoured warships, penetrative ammunitions, and automotive industry at the beginning of the 20th century. Tungsten inflation-adjusted price has remained constant in average over the 20th century (Figure 1). Nonetheless, it exhibited considerable peaks (Figure 1), in particular in 1915-1918 (World War I), 1951-1956 (Korean War), 1973-1978, and 2005, with a moderate raise during the World War II. In the 1980s, an extra tungsten production ensured by China led to a tremendous decrease of the

tungsten price (Audion and Labbé, 2012). Subsequently, most of the European tungsten mines, including the Salau French mine, closed, and very few tungsten mines in the world remained in operation. Since these closures, China has held a monopoly on the global tungsten production and has maintained the tungsten price significantly low. Nevertheless, in 2005, some exportations quotas were applied by China on its tungsten production (Audion and Labbé, 2012), inducing a global increase of the tungsten price and, therefore, a gain of interest for tungsten exploration in the rest of the world, including in the European Union (EU).
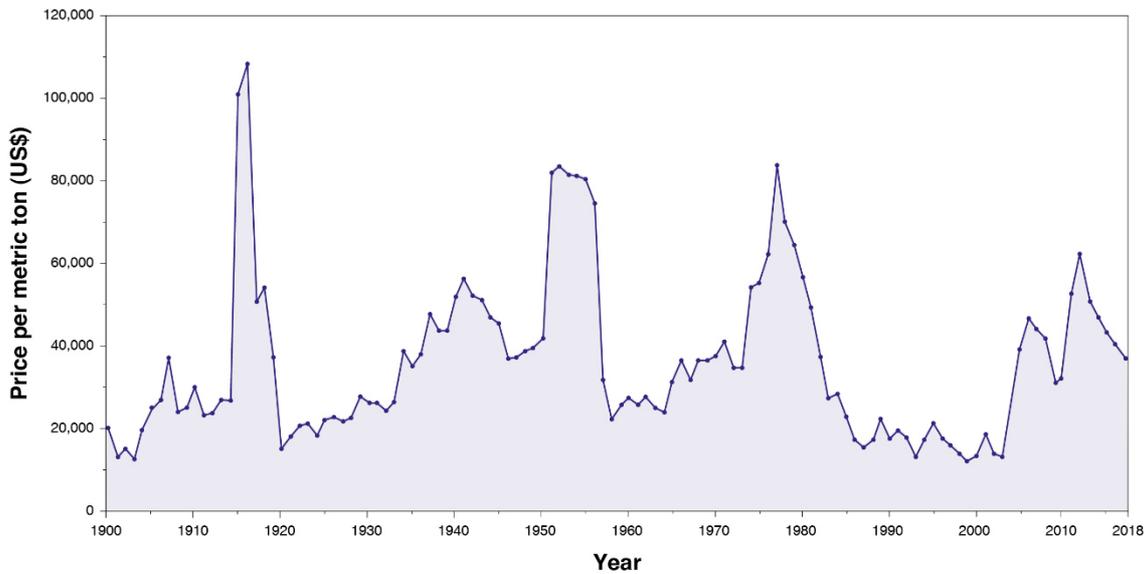
Figure 1. Evolution of the tungsten inflation-adjusted price per metric tonne from 1900 to actual (source: Metalary website).

1.3 Tungsten deposits and resources

Several tungsten minerals have been reported in the literature but only scheelite ($CaWO_4$) and wolframite [$(Fe,Mn)WO_4$] are of economic importance and nowadays exploited for primary tungsten extraction (Pitfield et al., 2011; Schmidt, 2012a, 2012b; Yang, 2018). Wolframite is a continuous solid series between ferberite ($FeWO_4$) and hubnerite ($MnWO_4$); the Fe/Mn ratio in the mineralised rock defines the dominance of one on another. Four major types of tungsten ore deposits have been reported in the literature: skarns, veins/stockworks, porphyries, and stratabound deposits (Jébrak et al., 2016; Pitfield et al., 2011; Schubert et al., 2006; Werner et al., 1998). As an overview, the typical WO_3 grades, deposit sizes, tungsten-bearing mineral(s), and mines of the four major types of tungsten ore are summarised in Table 1. Notably, skarn ores exhibit low tonnages and moderately high grades compared to the three other tungsten deposits, mainly the porphyries deposits.

Table 1. The four major types of tungsten ore deposits with typical deposit sizes, WO_3 grades, tungsten minerals and mines, adapted from (Pitfield et al., 2011; Schubert et al., 2006; Werner et al., 1998; Yang, 2018).

Deposit type	Deposit sizes (t)	Typical grade (%WO_3)	Tungsten mineral(s)	% of total	Mines
Skarn	$10^4 - 5 \times 10^7$ t	0.3 – 1.4	Scheelite	41	Cantung (Canada); Los Santos (Spain); Vostok-2 (Russia)
Vein/stockwork	$10^5 - 10^8$ t	Variable	Wolframite	35	Pasto Bueno (Peru); Panasqueira (Portugal); San Fix (Spain); Chollja (Bolivia);
Porphyry	$10^7 - 10^8$ t	0.1 – 0.4	Wolframite Scheelite	21	Xingluokeng (China); Yangchuling (China); Northern Dancer (Canada); Climax (USA)
Stratabound	$10^6 - 10^7$ t	0.2 – 1.0	Scheelite	3	Mittersill (Austria); Damingshan (China); Mount Mulgine (Australia)

At the moment, the world tungsten production is mainly ensured by China, which produced, in 2018, more than 80% of the 82,000 t of tungsten produced worldwide (U.S. Geological Survey, 2019). More than ten major tungsten mines, with annual output over 1,300 t of WO_3, are reported in China, most of them being located in southern China (Audion and Labbé, 2012; Pitfield et al., 2011; Werner et al., 1998; Yang, 2018). In particular, the Xianglushan and Shizhuyuan deposits represent the two largest tungsten mines in China, with over 5,700 and 5,500 t of WO_3 produced each year, respectively (Yang, 2018). Some other countries such as Vietnam, Russia, and a few European countries produce low amounts of tungsten (Figure 2). Vietnam operates one of the largest tungsten mine worldwide, the Nui Phao mine, which reserves have been estimated to 66 million tonnes of ore with an average grade of 0.2% WO_3 (Masan Resources, 2012). Besides, Russia has been mining the Vostok-2 sulphide-scheelite skarn ore since 1969, with around 1 million tonnes of remaining ore with a high average grade of around 1.7% WO_3 (Soloviev and Krivoshchekov, 2011). Despite the decrease of tungsten price in the 1980s, Austria and Portugal succeeded in maintaining the Mittersill and Panasqueira mines in operation. They produced, in 2018, 980 t and 770 t of tungsten, respectively, which represents a very minor part of the world production (Figure 2). Recently, considering the significant increase of tungsten price in the middle of the 2000s, new tungsten mining projects have been developed in the world, including in the EU (Suárez Sánchez et al., 2015). In particular, the Los Santos mine (Spain) started operations in 2008 and produced, in 2018, 750 t of tungsten, with estimated reserves of 3.6 million tonnes with an average grade of 0.2% WO_3 (Wheeler, 2015). Furthermore, operations started in the Hemerdon mine [United Kingdom (UK)] in 2015, which reserves have been estimated at 35.7 million tonnes of ore at 0.2% WO_3 (Yang, 2018). Nonetheless, despite a production of 900 t of tungsten in 2018, the Hemerdon mine ceased trading operations in October 2018, mainly due to a decrease of tungsten price along with poor processing performances.
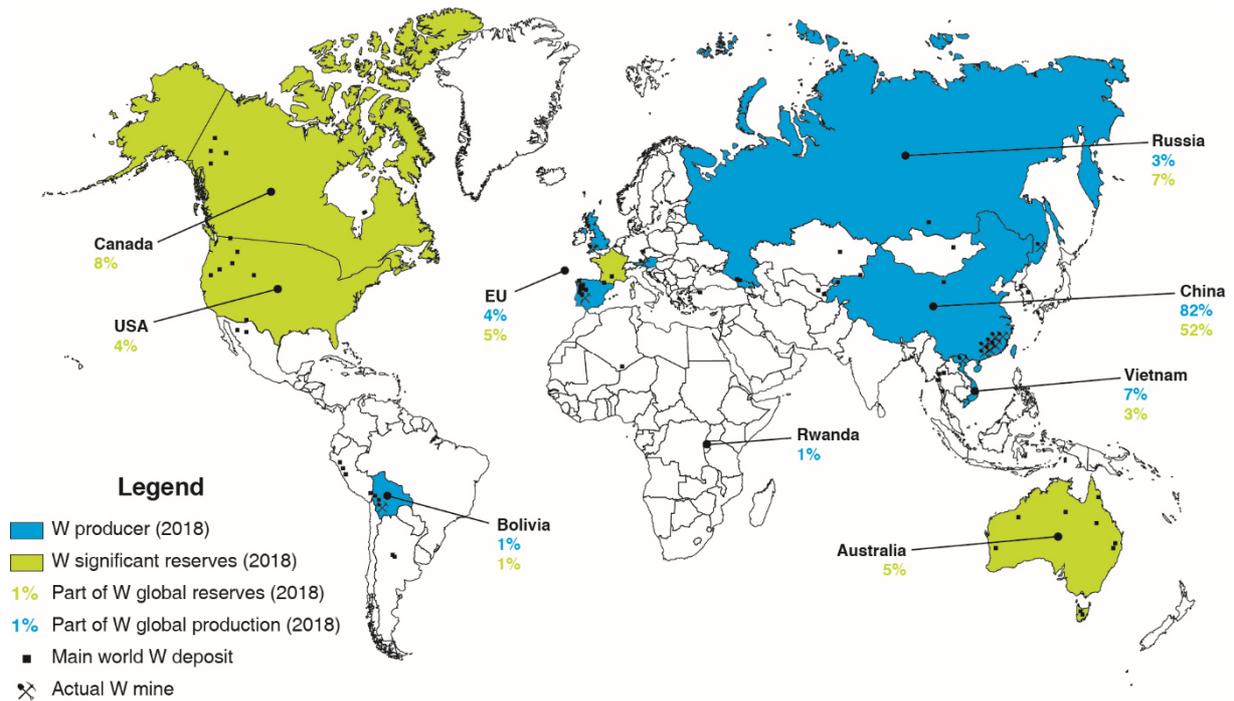
Figure 2. World map of main W world deposits, W mines, W producers and countries with significant W reserves and their respective part in the global W reserves/production in 2018, built with data from (Audion and Labbé, 2012; U.S. Geological Survey, 2019).

Overall, the EU tungsten production amounts to less than 3,000 t while its consumption is estimated at about 10,000 t per year, with a slight continuous increase predicted for the next decade (Yang, 2018). Therefore, increasing the tungsten primary production as well as the tungsten recycling rate is crucial to afford the EU independency in terms of tungsten consumption. Nowadays, the global tungsten reserves and resources are estimated at 3.3 million tonnes (U.S. Geological Survey, 2019) and 4.0 million tonnes (Pitfield et al., 2011; Yang, 2018), respectively, with around 52% in China (Figure 2). Nevertheless, many tungsten occurrences have been reported in the EU, including in the UK, Spain, Austria, Portugal, and France (Figure 3), some of which exhibiting significant resources and being suitable for exploitation.

Figure 3. Reported tungsten occurrences in the EU according to the main databases, adapted from (Lauri et al., 2018).

1.4 A Critical Raw Material in the EU

The EU has become deeply dependant on the importation of raw materials over the past decades, including metals that can be strategic for its economy or its defence as tungsten. This dependence is mainly attributed to the high global competition and strict regulations existing on the extraction of raw materials, although the EU has many occurrences and deposits that could be exploited (European Commission, 2008). Besides, the production of some raw materials is held by a small number of countries, which are then considered in a monopoly situation regarding the global production. For instance, in 2018, Brazil produced, 88% of the global niobium supply while China ensured 82% of the tungsten production, 71% of the rare-earth elements (REE) production, and 61% of the fluorite production (U.S. Geological Survey, 2019). Additionally, some of these countries are considered as politically unstable or can present a significant willing for environmental protection, which can result in a decrease of their exportation quotas in the future and, therefore, an important supply risk for the EU (Dewulf et al., 2016; European Commission, 2008).

Within that background, the EU launched in 2008 the "European Raw Material Initiative", which aimed at identifying critical raw materials for the EU. The criticality of each raw material was assessed by considering its supply risk (including its recycling rate), its economic importance, and the environmental country risk (Dewulf et al., 2016; European Commission, 2008). This latter is related to the risks that measures might be taken by countries with the willing of

protecting the environment, therefore endangering the supply of raw materials to the EU (Dewulf et al., 2016; European Commission, 2008). This methodology has been applied to the 78 main raw materials identified in the EU and, as a consequence, 14 raw materials were defined as critical raw materials (CRM) for the EU, in 2011 (European Commission, 2010). This list was updated in 2014 by adding six other raw materials (European Commission, 2014) and in 2017 to attain a total number of CRM of 27 in the EU (European Commission et al., 2017). Traditionally, the raw materials are displayed in a diagram that presents their supply risk as a function of their economic importance. Criteria are defined on the two properties, allowing to define an area of high supply risk and high economic importance (Figure 4). The raw materials that are comprised in this zone are considered as CRM, including tungsten (Figure 4), which has been classified as a CRM since 2011. This is attributed to the monopoly that has been held by China since the 1980s on the tungsten production, combined with a significant economic importance, a low substitutability, and a low recycling rate.
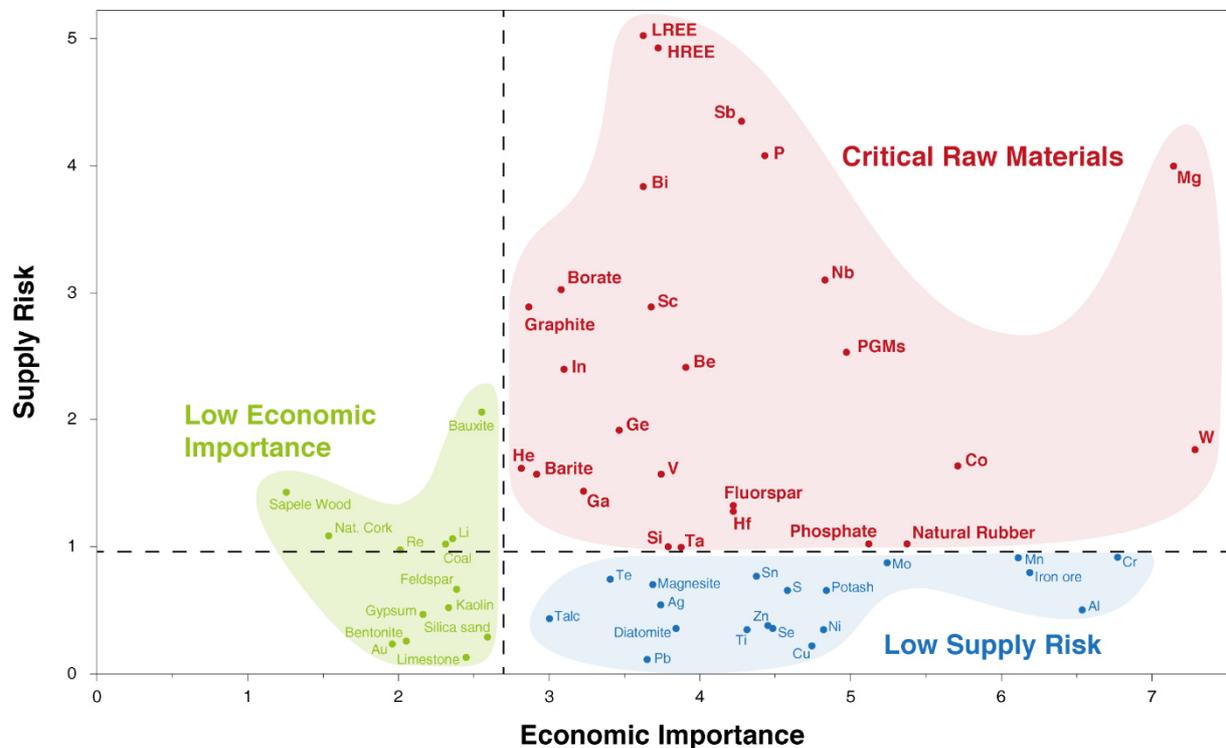
Figure 4. Criticality diagram based on the economic importance and supply risk, adapted from (European Commission, 2010; European Commission et al., 2017).

Considering the aforementioned "European Raw Material Initiative", the European Commission suggested policies to relaunch the CRM mining industry in the EU for the close future. The United States of America (USA) launched a similar programme aiming at identifying CRM for the US economy (U.S. Department of the Interior, 2018). In both European and US Raw Material Initiatives, tungsten has been classified as a CRM (European Commission et al., 2017; U.S. Department of the Interior, 2018) and has, therefore, drawn significant worldwide attention over the past few years.

1.5 The FAME European project: relaunch the tungsten extraction

From the 1st of January 2015, the FAME (Flexible and Mobile Economic Processing Technologies) European project, funded by the European Commission through the H2020 research and innovation programme, started with the global objective to relaunch the European mining industry for tungsten, tin, and lithium. In particular, the European Commission wanted to stimulate the investments in the mining field as well as to develop the competitiveness of the mining companies while creating jobs. For that, FAME distinguished Research and Innovation (R&I) on three different ore types (skarn, greisen, and pegmatite) to develop their respective processing flowsheets for mineral liberation (grinding, comminution, and sorting), flotation, and hydrometallurgical treatment (Figure 5). In order to find the most suitable approach for the mineral wealth and physio-chemical properties of these three ore types, mineralogical investigations were carried out. Some key deposits were identified and considered as study cases for the 17 industrial and academic partners involved in the framework of FAME, including University of Lorraine. Indeed, FAME was an industry-driven network R&I project comprising research-oriented small and medium size enterprises (SME). These allowed to unlock the most promising domestic raw material resources, *i.e.* primary ores. FAME brought together the experiences, visions, and exploitable know-how of industry, scientific research institutes, and academia. This developed new business fields and enterprises in the raw material sector. In particular, the Tabuaço tungsten deposit was selected as a typical tungsten skarn; while some partners performed the mineralogical characterisation, University of Lorraine was in charge of the process development and intensification, *i.e.* work packages 3, 4, and 5 (Figure 5). The global objective, during the four years of the project, was to suggest an adaptable and mobile flowsheet for the processing of the Tabuaço ore, based on the mineralogical composition of the ore as described in the work package 2. The challenge was important: within the four major tungsten deposit types, skarns represent nowadays more than 40% of the global tungsten reserves (Pitfield et al., 2011; Schubert et al., 2006; Werner et al., 1998). However, despite significantly high WO_3 grades, most skarn ores are still considered complex for mineral processing: the development of efficient, environment-friendly, and mobile processing routes for tungsten skarns beneficiation is therefore of paramount interest.
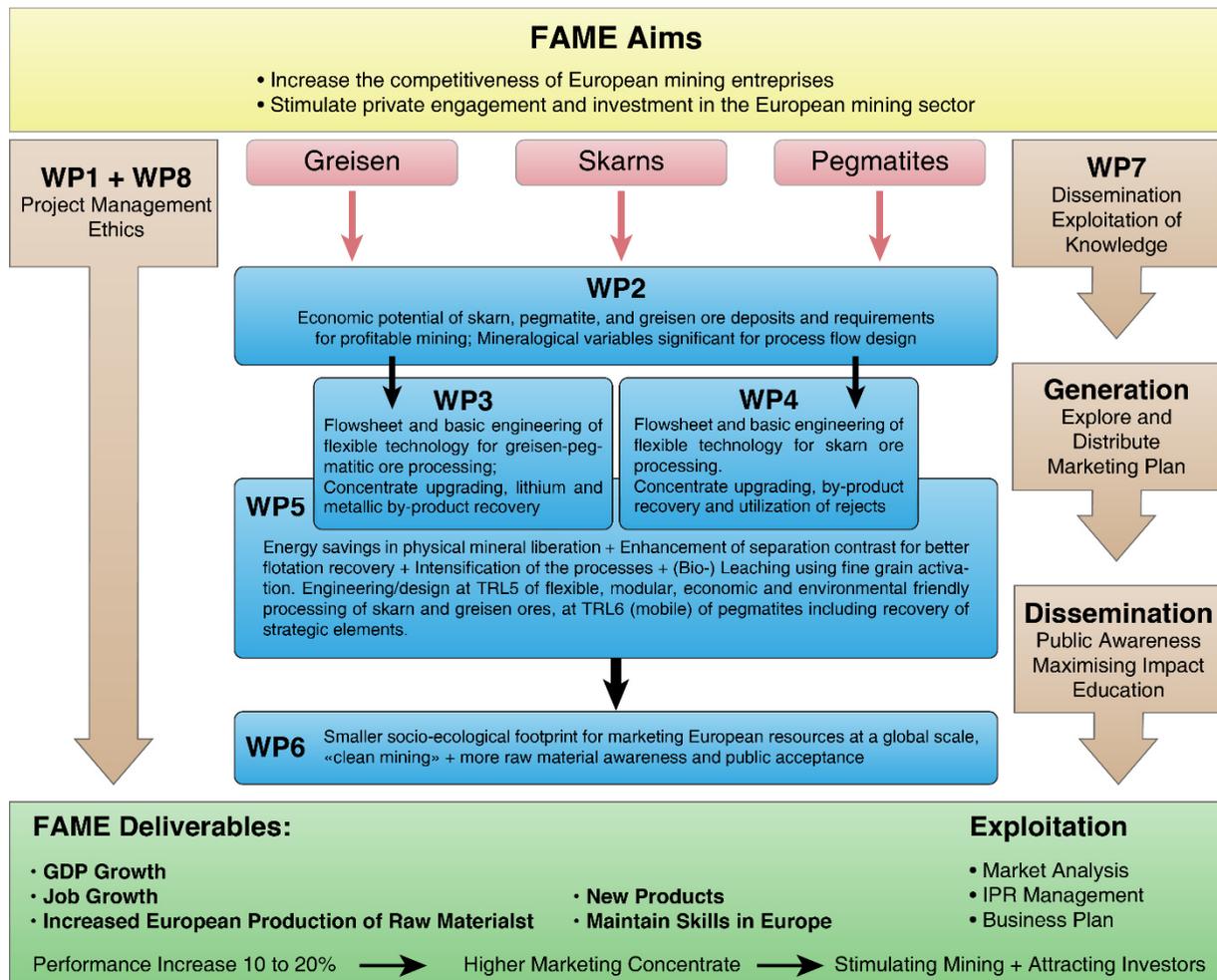
Figure 5. Progress diagram of the FAME project presenting the different objectives, work packages (WP), deliverables and socio-economic implications.

1.6 Tungsten skarns

1.6.1 What is a skarn?

Skarn deposits are one of the most abundant ore types in the Earth's crust and have been intensively studied over the past decades (Meinert et al., 2005). Around 150 publications pear year contain the term "skarn", which indicates a high constant interest of researchers and industrials for such deposits. Initially, skarns were defined by their mineralogical composition usually dominated by calc-silicates such as pyroxene or garnets, due to significant amounts of calcium in protolithic rocks (Dawson, 1996; Einaudi and Burt, 1982; Kwak, 1987; Meinert et al., 2005; Misra, 2000). However, skarns can also be considered in a more broadly way, as rocks produced by the replacement of calcite or dolomite marble regardless the presence of calcic or magnesian silicates (Kwak, 1987). Skarn deposits occur throughout a wide range of geological backgrounds, from Precambrian to Cenozoic, although most economic deposits are young and associated with magmatic-hydrothermal activity associated with plutonism in orogenic belts (Einaudi and Burt, 1982). Traditionally, skarns are formed during contact metamorphism associated with a variety of metasomatic processes involving fluids of magmatic, metamorphic,

meteoric, and/or marine origin (Meinert et al., 2005). Hence, most skarns are encountered adjacent to plutons albeit they can occur along faults, major shear zones, and various other structural backgrounds (Figure 6). Skarns can be classified by considering several major criteria, *e.g.* their calcite/dolomite initial content (calcic versus magnesian skarns), their Fe^{3+}/Fe^{2+} ratio (oxidised versus reduced skarns), or their distance to the pluton (proximal versus distal skarns), to name but a few (Einaudi and Burt, 1982; Kwak, 1987; Meinert et al., 2005). Overall, though some skarns occur in not-calcic rocks, most of tungsten skarns are hosted in rocks with significant contents of calcium (and/or magnesium) since this element is essential for scheelite deposition in the ore. This induces a common dominance of calcium minerals associated with scheelite in such ores.
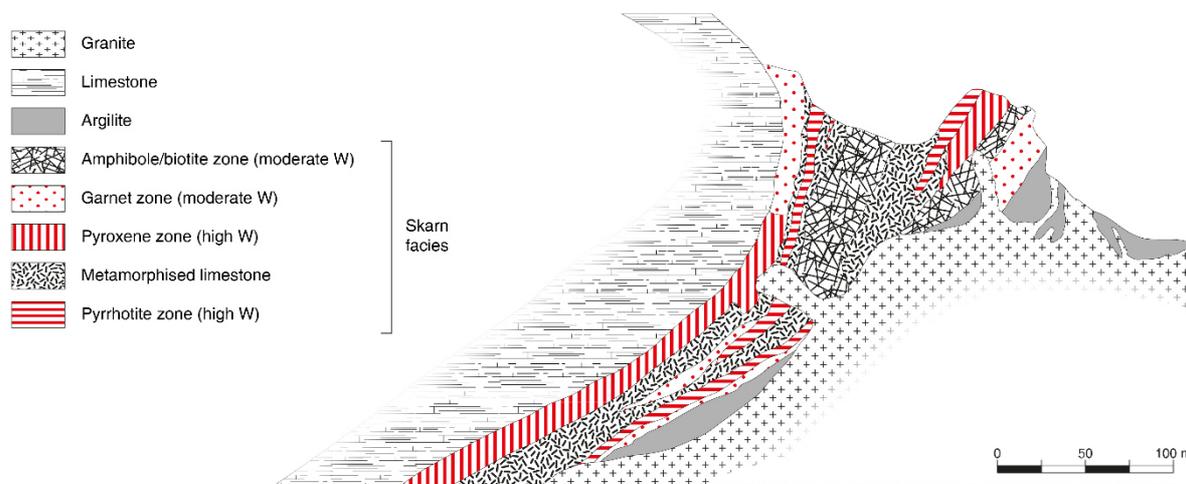
Figure 6. Cross-section of a typical tungsten skarn (Cantung skarn) showing the granite, the limestone, and the different skarn facies at their interface, including the tungsten-bearing lithologies, modified from (Dawson, 1996).

1.6.2   The economic importance of skarns

Mining of skarn deposits dates back at least 4,000 years and clear evidences of the mining of skarns can be encountered in the ancient Chinese, Greek, and Roman empires (Meinert et al., 2005). Historically, skarns have been mined for a large variety of metals, including iron, tin, tungsten, copper, zinc (along with lead), molybdenum, and gold (Dawson, 1996; Einaudi and Burt, 1982; Kwak, 1987; Meinert, 1992; Meinert et al., 2005). Considering actual economic deposits, skarns display either too low grades (for iron) or tonnages, *e.g.* for lead, zinc, or copper (Kwak, 1987) and, therefore, are no more exploited. Nonetheless, tungsten skarns commonly display average WO_3 grades ranging from 0.3% to 1.5%, which is significantly higher than for the other major types of tungsten deposits (see section 1.3, Table 1, and Figure 7). Hence, despite lower tonnages compared to other major types of tungsten deposits (Table 1), many tungsten skarns are of economic importance. They have been continuously exploited for decades (Figure 7), supplying most of the world's tungsten (>70%) during some periods such as in the 1980s (Kwak, 1987). Nowadays, China ensures 82% of the world tungsten production (U.S. Geological Survey, 2019) with a considerable part of the Chinese tungsten coming from skarn deposits

(Audion and Labbé, 2012). Indeed, the Xianglushan and Shizhuyuan world class tungsten deposits, which account for more than 11,000 tonnes (14%) in the annual global tungsten production, are considered as tungsten skarns (Cheng, 2016; Dai et al., 2018; Lu et al., 2003). Additionally, the Nui Phao and Vostok-2 mines, which together produce 10% of the world tungsten, are also mining tungsten skarns (Masan Resources, 2012; Soloviev and Krivoshchekov, 2011) Hence, these latter represent a significant part in the current tungsten production, while some authors estimate that they account for more than 40% of the global tungsten reserves (Pitfield et al., 2011; Schubert et al., 2006; Werner et al., 1998). Within this context, the Tabuaço deposit, defined as a typical tungsten skarn in the FAME project, exhibits estimated resources of 2.7 million tonnes of ore with an average WO_3 grade of 0.6%, which corresponds to a middle-sized world tungsten skarn (Figure 7). Besides, many tungsten skarns have been reported in the world, including in the EU; some are currently exploited while the other largest ones were exploited in the second half of the 20th century (Figure 7).
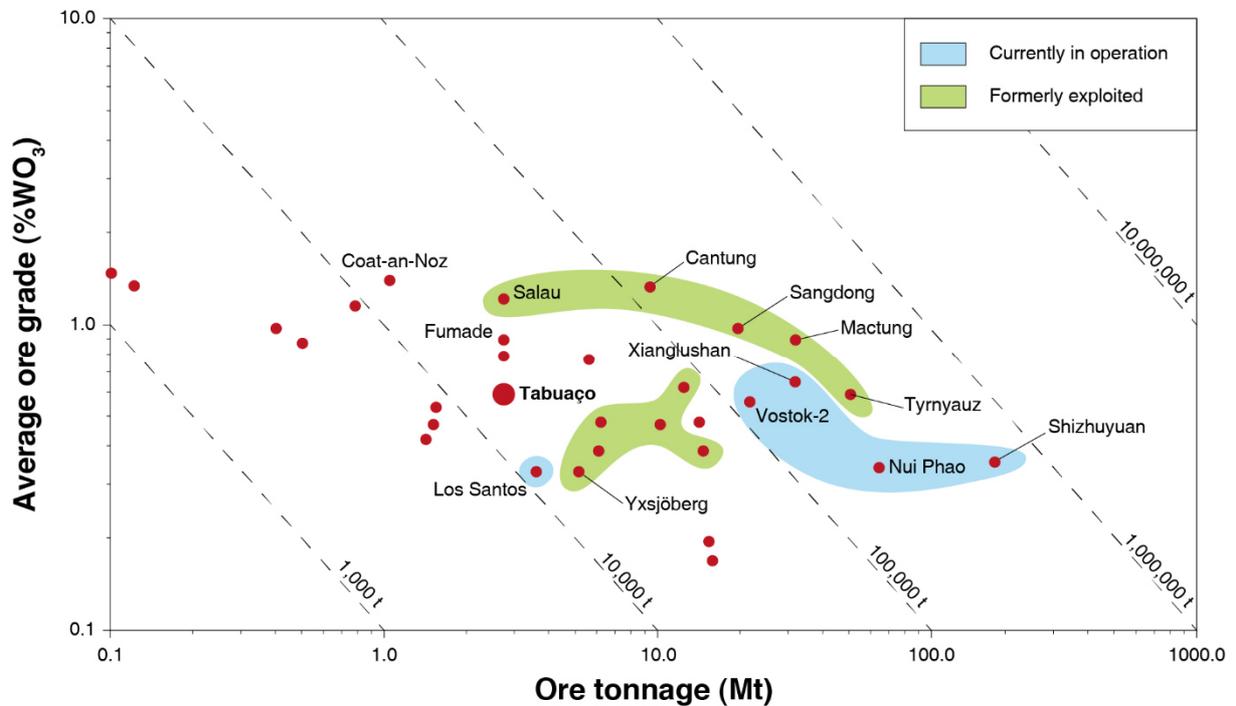
Figure 7. Grade versus tonnage of significant tungsten skarn deposits in the world, currently or formerly in operation, including the Tabuaço deposit, modified and updated from (Dawson, 1996).

1.6.3   The Tabuaço deposit: a middle-sized tungsten skarn

The Tabuaço tungsten deposit is located in Northern Portugal, at the north of the Central Iberian zone of the Iberian Massif that is part of the Variscan belt (Figure 8a). As with many other scheelite-skarn occurrences, the Tabuaço deposit is hosted in Cambrian metasediments, at the northern margin of Variscan granitoids such as the Paredes da Beira-Tabuaço (PBT) granite (Dias et al., 2014; Pinto et al., 2016), see Figure 8b. It comprises two sub-deposits called Aveleira and São Pedro das Águias. The present study concerns the latter, which accounts for 71% of the

global Tabuaço deposit resources. São Pedro das Águias sub-deposit consists in a ~100 m thick layer of metasedimentary rocks in which two mineralised zones are included (Figure 8c). A NI 43-101, published in 2011, indicated and inferred resource of 2.7 million tonnes with a 0.6% WO$_3$ average grade, ranking Tabuaço as a middle-sized world-class tungsten deposit (Dawson, 1996). The two mineralised layers, called "Lower Skarn" and "Main Skarn", are sub-parallel to the contact between the PBT granite and the Bateiras Formation, which exhibits numerous other lower-sized scheelite-skarns occurrences (Figure 8b).
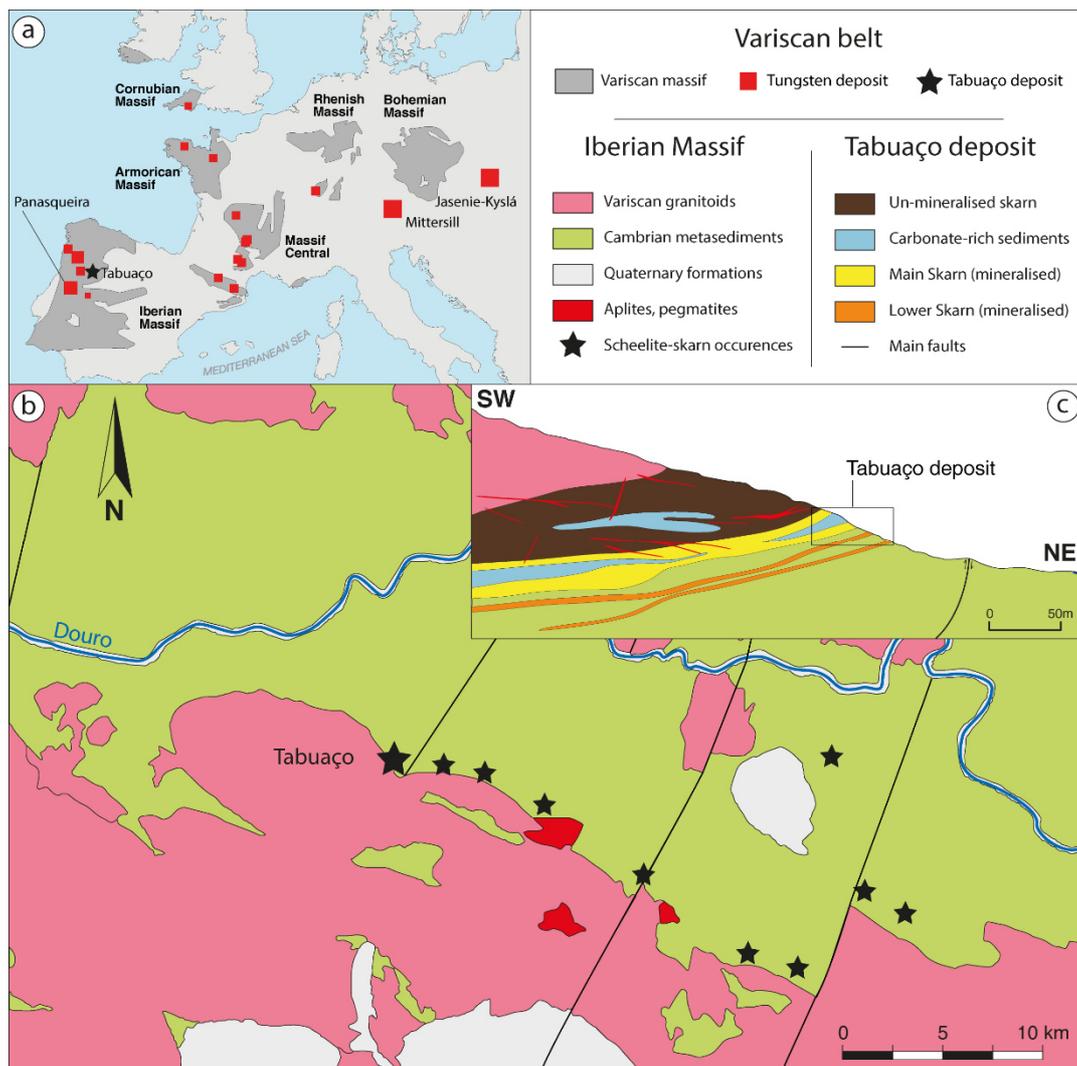
Figure 8. (a) Location of the Tabuaço deposit and other European tungsten deposits associated with the Variscan belt, modified after (Dehaine et al., 2019a); (b) structural map of the Tabuaço deposit and associated scheelite-skarns occurrences; (c) SW-NE cross section of the Tabuaço deposit built from the drilling campaign conducted by Colt Resources in 2015.

1.6.4   Processing problematics and options

Considering the high economic potential of skarn ores, the classification of tungsten as a CRM resulted in a global resurgence of interest for these deposits (Kupka and Rudolph, 2018a; Suárez Sánchez et al., 2015; Yang, 2018). However, most authors working on tungsten skarns, either in

the geology or in the mineral processing fields, have reported moderately complex gangues for the tungsten extraction, in particular for the ore dressing stage. Indeed, skarns generally occur in limestones protoliths, which induce high amounts of calcium and, therefore, the formation of calcium-bearing minerals. Due to these metallogenetic processes, scheelite is found in fine-grained mineralisation disseminated thorough the orebody and commonly associated with calcium silicates such as garnet, pyroxene, epidote, vesuvianite, wollastonite as well as with calcium salts such as fluorite (CaF_2), apatite [$Ca_5(PO_4)_3(OH,Cl,F)$], and calcite ($CaCO_3$) (Cheng, 2016; Dai et al., 2018; Dawson, 1996; Einaudi and Burt, 1982; Jébrak et al., 2016; Kwak, 1987; Lu et al., 2003; Meinert, 1992; Meinert et al., 2005). The Tabuaço deposit, as a typical tungsten skarn, displays all the aforementioned characteristics (low liberation size, calcium silicates, and calcium salts as gangue minerals), see Figure 9 and Chapter 2. Therefore, it constitutes an ideal study case and this work can be generalised for most tungsten skarns.
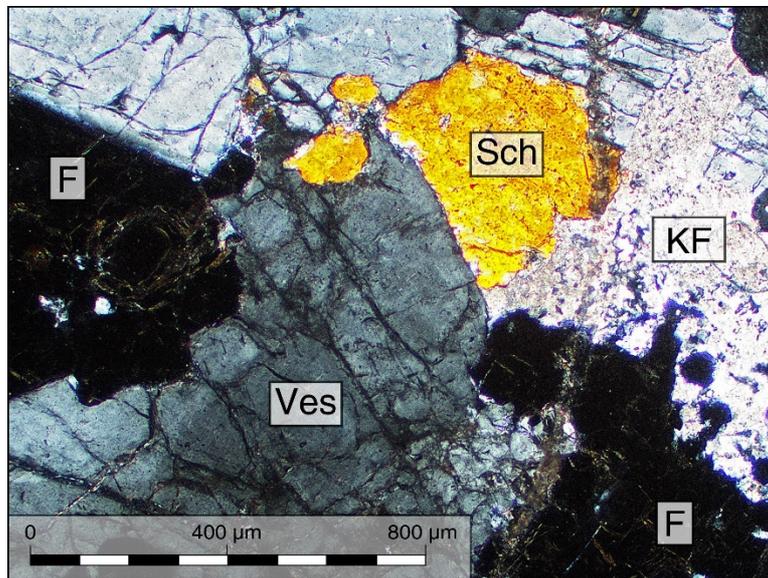
Figure 9. A thin section of a coarse-grained zone from Tabuaço deposit, observed with an optical microscope under a cross-polarised light, exhibiting the typical mineralogical association composed of calcium silicates, calcium salts, silicates, and moderately fine-grained scheelite. Sch = Scheelite; F = Fluorite; Ves = Vesuvianite; KF = Potassium Feldspar.

The minerals commonly contained in tungsten skarns, including the Tabuaço skarn, exhibit a large range of specific gravities: 2.7 for calcite, 3.2 for fluorite and apatite, and 6.1 for scheelite while silicates have specific gravities between 2.6 and 3.7, depending on the geological context. Hence, it allows one to perform a gravity separation to eliminate the lightest minerals, *i.e.* mostly the calcium-bearing semi-soluble salts (calcite, apatite, and fluorite). Nonetheless, the fine liberation size makes it difficult to process these ores by classical gravity separation methods, *e.g.* shaking tables, jigs, or spirals (Blazy and Joussemet, 2011; Das and Sarkar, 2018; Wells, 1991). The froth flotation technique is preferred since it enables the beneficiation of fine-grained ores, down to 10 µm, with relatively high throughputs (Kupka and Rudolph, 2018a; Yang, 2018). However, the flotation separation of scheelite from fluorite, apatite, and calcite has been

intensively investigated over the past decades and remains, in the 21st century, one of the most challenging problem in the froth flotation field.

Besides, the gangue calcium-bearing minerals often comprise elements such as P, Si, C, and F that are considered (along with sulphur) as penalising elements either for the scheelite concentrates processed by hydrometallurgy or for the final metal-tungsten product (Pastor, 2000; Pitfield et al., 2011; Yang et al., 2016). Moreover, tungsten is traditionally extracted from scheelite concentrates by the hydrometallurgy process that requires >60% WO$_3$ in the concentrates (Pastor, 2000; Pitfield et al., 2011) while skarn ores usually assay between 0.5% and 1.5% WO$_3$ (Figure 7). Hence, removal of fluorite, apatite, calcite, and calcium-bearing silicates prior to any hydrometallurgical treatment is of paramount interest. The development of an efficient mineral processing flowsheet for the removal of the abovementioned minerals from a given skarn ore allows to make this skarn of economic potential, *i.e.* exploitable.

2.   Literature review

The beneficiation of wolframite and scheelite ores generally consists of pre-concentration after crushing and grinding, followed by successive purification stages to produce a concentrate assaying 65-75% WO$_3$ to meet the product specifications imposed by the international trading (Lassner and Schubert, 1999; Pastor, 2000). Both wolframite and scheelite are brittle and, therefore, tend to form fine particles during the milling stage. Traditionally, the comminution is carefully designed to avoid overgrinding with regular and appropriate classifying stages all over the process. Wolframite is dense (specific gravity of around 7.3) and paramagnetic, which enables the sole use of physical separations in the processing routes, *i.e.* gravity and magnetic separations (Yang, 2018). Scheelite is diamagnetic and, therefore, magnetic separations are most of the time unsuitable for scheelite ores, which, also, generally display finer liberation sizes. Hence, scheelite is usually beneficiated by sole froth flotation or by a combination of gravity separation and froth flotation (Kupka and Rudolph, 2018a; Yang, 2018), since it is also significantly dense (specific gravity of around 6.1). Nonetheless, skarn deposits commonly exhibits fine textures and, consequently, fine liberation size along with complex gangues (Dawson, 1996; Jébrak et al., 2016; Kwak, 1987; Meinert et al., 2005; Misra, 2000), *i.e.* gangue minerals that display similar surface properties to that of scheelite. Although the two main processing options for tungsten skarns, namely the gravity separation and froth flotation, are suitable for Tabuaço and other complex tungsten skarns, they have to be thoroughly investigated and adapted to the skarn characteristics.

2.1 Gravity concentration of scheelite ores

Gravity concentration is one of the oldest and most used methods in mineral processing over the world. It consists in the separation of minerals based on their difference in specific gravity by their differential displacement in the gravity field (Burt and Mills, 1984). Before the development of the froth flotation, in the late 19th century, gravity concentration was the main method used for ore dressing since the metal-bearing minerals commonly exhibit higher specific gravity than

the gangue minerals. Nonetheless, the development of more selective methods based on chemical or physico-chemical properties induced a significant decrease of the interest drawn for gravity concentration techniques (Burt, 1999; Burt and Mills, 1984). Compared to these latter, the new methods, *i.e.* froth flotation and hydrometallurgy, however induce higher operating costs, high complexity, and possible environmental issues due to the processing of finer particles and to the use of chemical reagents (Richards et al., 2000; Richards and Palmer, 1997). Therefore, gravity separation has remained a widely used method in mineral processing routes and is still highly preferred for most of the exploited ores nowadays, for its low operating costs, its environment-friendliness, and its high throughput units. Some metallic minerals such as wolframite, cassiterite, or columbite-tantalite are exclusively or mainly beneficiated by gravity separations techniques (Burt, 1999; Burt and Mills, 1984; Yang, 2018). When flotation is implemented in the processing routes, it is frequently combined with gravity separation to perform a purification of the gravity pre-concentrates (Yang, 2018), as for the former Salau French tungsten mine (Tomas, 1985) or the Bernic Lake tantalum operations in Canada (Burt et al., 1995).

2.1.1 Principle

Gravity concentration is based on the movement of minerals of different density in response to different force fields, including the gravity field as well as various fluid-related forces that are specific to each gravity concentrator's type (Burt and Mills, 1984). Based on these characteristics, four main categories can be defined for the gravity concentrators:

- Density: a fluid with an intermediate density between that of the minerals that have to be separated is used. The particles with a density lower than that of the fluid float while the dense particles sink. The density of the medium can be modulated to produce an "apparent" density. All the dense medium separation devices are included in this category.
- Stratification: pulsation/suction cycles in the fluid, following a vertical plane, induce a stratification of the particles as a function of their density. This category is mostly represented by the jigs but however displays a wide range of devices.
- Flowing film: a pulp film containing the particles flows along a plane and the particles settle differentially in the flowing film as a function of their density. In such devices, mostly represented by spirals and sluices, a centrifugal force can supplement the natural gravity force field.
- Shaking: a horizontal shear force is superimposed on the flowing film to improve the separation mechanisms of a simple flowing film separator. This force can be oscillating (shaking table) or orbital (Crossbelt concentrator).

Besides, when particle size is too low, the settling kinetics can be very low, which induces that the time required for effective separation is impracticably long (Das and Sarkar, 2018). Since conventional gravity separations are not able to afford such long residence times, they are, therefore, not suitable for fine particles (Das and Sarkar, 2018). Nevertheless, it is of paramount

interest to recover fine particles as they usually contain significant amounts of fully liberated valuable minerals. Hence, in the 1990s, advanced gravity concentrators have been developed to address this problem. Such devices subject particles to a centrifugal force field to increase their relative settling velocities in the flowing film, which constitutes an enhancement of the settling mechanism intensity without modifying the mechanism itself (Burt, 1999). Moreover, some devices provide an additional counter-current flow to generate a hindered bed condition for particle settling (Epstein, 2005). The advanced gravity concentrators have been specifically designed for fine particles gravity processing and are constituted by the Knelson and Falcon concentrators along with the Kelsey Jig and Multi Gravity Separator (Das and Sarkar, 2018).

2.1.2   A wide variety of equipment available

Since gravity concentration has been used for centuries in mineral processing, a very large range of equipment is available from the four different abovementioned categories. However, they do not operate with the same performances, objectives, costs, throughputs, and, mostly, particles size (Burt, 1999; Burt and Mills, 1984; Das and Sarkar, 2018). In particular, Figure 10 illustrates the different working particle sizes of several common gravity separation apparatus. Density, stratification, and flowing film devices traditionally operate for particle coarser than 100 μm (Figure 10), which appears unsuitable for tungsten skarn since a significant amount of the scheelite can be comprised in the -100 μm size fraction (Pitfield et al., 2011; Yang, 2018). Indeed, most of the classical gravity separation devices (jigs, shaking tables, spirals…) exhibit a significant decrease in the separation performances when the particle size decreases, due to higher settling times (Das and Sarkar, 2018). Hence, centrifuge devices are particularly suitable for fine particles while they remain employable for moderately coarse particles (Figure 10), which constitutes an interesting range of working particle sizes. In particular, Falcon concentrator displays a wide working particle size range (Figure 10) along with significant performances (Burt et al., 1995; Burt and Mills, 1984) and high throughputs for industrial devices (Sepro, 2015a, 2015b). Considering these criteria, the use of Falcon concentrator was selected for the Tabuaço tungsten skarn, with the global objective to demonstrate the suitability of such devices to concentrate scheelite by rejecting the calcium salts that are usually problematic during the froth flotation process.
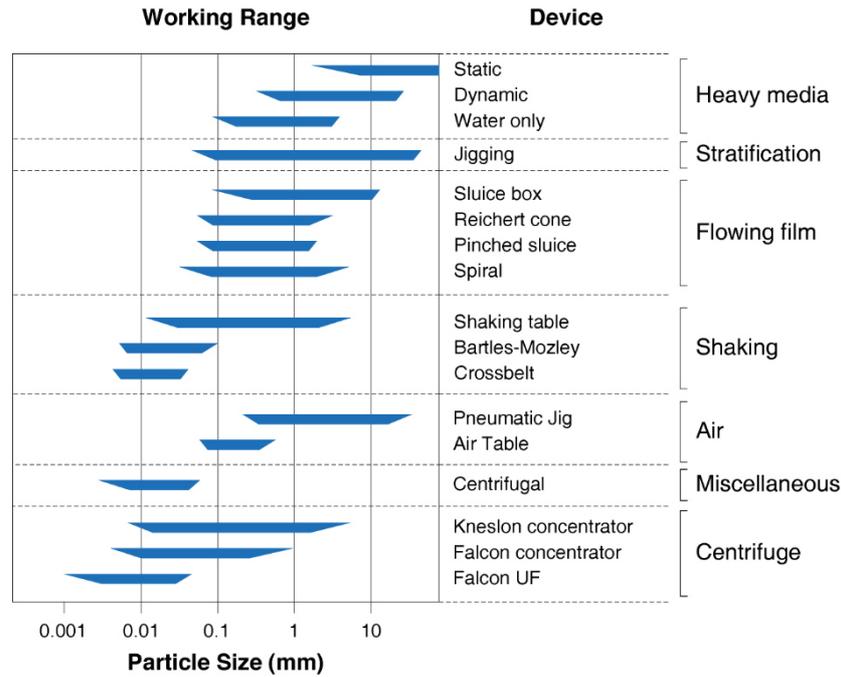
Figure 10. Working particle size range of various gravity concentration devices, from (Burt, 1987; FLSmidth, 2015; Sepro, 2015a, 2015b).

2.1.3 Falcon centrifugal concentrator

Falcon concentrators consist in a conical bowl capable of spinning at high rotation speed (up to 600 G), enabling the separation of fine particles based on their density (Falconer, 2003). The slurry is fed at the bottom-centre of the bowl and flows upwards along the bowl wall due to combined effect of bowl opening angle and centrifugal force (Figure 11). A retention zone delimited just before the bowl outlet retains the dense particles inside the bowl while the light particles are flushed over the top of the separator with the process water (McAlister and Armstrong, 1998). Three Falcon types are available industrially, namely, Falcon SB (Semi-Batch), Falcon C (Continuous), and Falcon UF (UltraFine), which differ by the way particles are trapped in the retention zone (Figure 11). Falcon SB series use fluidised annular grooves upstream of the bowl outlet to avoid compaction and adjust the retention capacity by injection of counter pressure water through the concentrate ridges. Falcon C series are operated on a continuous basis without any water addition due to subdivisions into hoppers with air operated valves to control the flow in the retention zone. Falcon UF concentrator series use a smooth bowl with a retention zone delimited by a slight reduction in diameter at the outlet, specifically designed to recover ultrafine particles (-3 µm). The bowl can be equipped with a variable lip in the retention zone to adjust its capacity (Sepro, 2015a). No fluidisation counter-pressure is applied in these concentrators to prevent flushing out fine particles. Both Falcon SB and UF are operated in semi-batch mode and must be stopped before saturation of the bowl to avoid concentrate losses by erosion or by unselective separation (Filippov et al., 2016; Laplante and Nickoletopoulos, 1997).

33
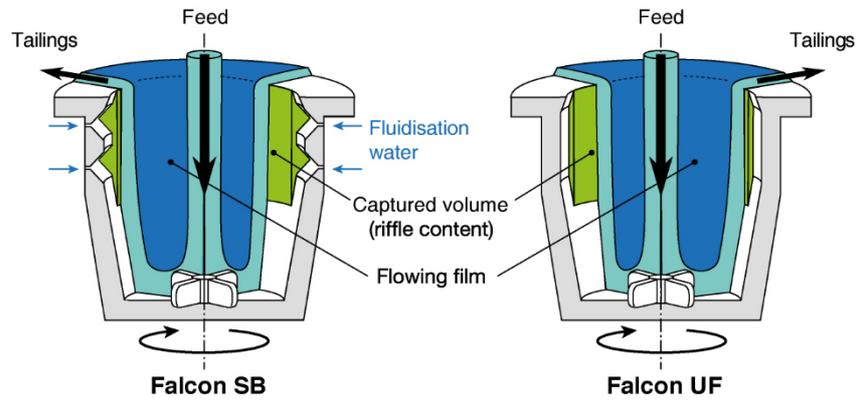
Figure 11. Falcon L40 SB (left) and UF (right) bowl schematics cross-sections, adapted from (Filippov et al., 2016; Kroll-Rabotin et al., 2010).

Thanks to its design oriented towards ultrafine particles recovery, Falcon UF has been successfully employed to recover both metal-bearing heavy minerals (tin, tungsten, tantalum, chrome, and cobalt) as well as native metals (gold, silver) with particle sizes down to 3 µm (Sepro, 2015a). Such performance however is material/ore-dependent and may vary from one mining operation to the other. Recently, fundamental modelling studies through numerical simulation methods such as Discrete Element Methods (DEM) or Computational Fluid Dynamics (CFD) have looked into the separation mechanisms as well as the influence of feed properties and operating parameters for Knelson concentrators (Fatahi and Farzanegan, 2017, 2018; Ma et al., 2018, 2019). The separation process within Knelson and Falcon concentrators bowls relies on two main mechanisms, differential settling of particles in the flowing film along the inside wall of the bowl (Abela, 1997; Buonvino, 1993; Honaker et al., 1996; Laplante and Nickoletopoulos, 1997; Laplante et al., 1994) and selective reorganisation of the particles in the retention zone through fluidisation (Ancia et al., 1997; Majumder and Barnwal, 2006), the latter being the predominant mechanism in Knelson concentrators (Das and Sarkar, 2018). However, since Falcon UF is not fluidised, this second separation mechanism is unlikely to occur in the smooth UF bowls as illustrated by the presence of a layer of denser material at the surface of the concentrate bed through the entire height of the bowl (Deveau, 2006). Hence, it is believed that there should be no reorganisation of particles in the concentrate bed, which leads to the model assumption that all the particles entrapped before saturation belong to the concentrate (Kroll-Rabotin et al., 2010). Based on a mechanistic understanding of the separation physics within those bowls, (Kroll-Rabotin, 2010; Kroll-Rabotin et al., 2010, 2013) derived a physical model of the Falcon UF concentrator for diluted suspensions by solving a simplified particle transport equation analytically:

$$C_p = \max\left(0, min\left(\frac{4\pi}{9}\lambda_0 Q^{-1}\omega^2(\rho_p - \rho_f)d_p^2\rho_f^{-1}\nu^{-1}R_{min}R_{max}H_{bowl}, 1\right)\right) \tag{1}$$

in which C_p is the recovery to the concentrate, Q, and ω are the operating parameters (volume flow rate, and rotation rate), d_p and ρ_p are the particles properties (size and density), ρ_f and v are the fluid density and kinematic viscosity, R_{min}, R_{max} and H_{bowl} are the dimensions of the bowl and λ_0 is a calibration constant. A full description of the forces acting on a particle within the Falcon UF bowl, as well as a detailed derivation of the model can be found in the literature but will not be further detailed here (Kroll-Rabotin, 2010; Kroll-Rabotin et al., 2010).

In 1986, a first commercial unit of Falcon concentrator was installed for fine gold particles concentration (Napier-Munn, 1997). Since that, it has been widely used for gold recovery with good performances (Alp et al., 2008; Laplante et al., 1996; Lins et al., 1992; Zhang, 1998) as well as for fine coal cleaning (Honaker, 1998; Honaker et al., 1996; Tozsin et al., 2018; Zhu et al., 2017a, 2017b), for tantalum ores (Burt et al., 1995; Deveau, 2006), copper ores (Aydogan and Kademli, 2019), wolframite ores (Lu et al., 2016; Schmidt, 2012b; Yue et al., 2018), and cassiterite ores (Abd El-rahman et al., 2009; Angadi et al., 2015, 2017; Yue et al., 2018). Besides, Falcon concentrators are also widely used for recycling processes (Duan et al., 2009; Zhang et al., 2018) or for mine tailings reprocessing (Filippov et al., 2016), which constitute key approaches to improve environmental outcomes (Edraki et al., 2014). Considering the wide use of Falcon concentrators for the beneficiation of minerals with specific gravities similar to that of scheelite, the use of such separators represents a suitable option for tungsten skarns, including the Tabuaço skarn.

2.2 Froth flotation of scheelite

Scheelite is mostly encountered in skarn deposits (and stratabound deposits) exhibiting fine textures, which commonly induce fine scheelite liberation size. Moreover, scheelite tends to form fine particles during the comminution stages, which can imply high WO_3 losses during physical separations. For these reasons, scheelite has traditionally been beneficiated by froth flotation since the 1930s, when this process became a powerful route for fine particles processing. In particular, scheelite flotation was thoroughly investigated during the World War II in the USA and USSR since the tungsten demand was significantly high for military applications. However, scheelite flotation has been widely spread in the 1970s, which resulted in a sudden increase in the scientific interest for scheelite flotation and, hence, in the publication of many studies dealing with this topic (Kupka and Rudolph, 2018a). Due to the depletion of wolframite reserves in China along with the European Metal policy, scheelite flotation has gathered considerable interest in the world over the past few years (Kupka and Rudolph, 2018a; Pitfield et al., 2011; Suárez Sánchez et al., 2015; Yang, 2018).

2.2.1   Surface properties of scheelite

Scheelite is an ionic mineral composed of Ca^{2+} cations and WO_4^{2-} anions, occurring in in the $I4_1/a$ space group (tetragonal system). The most exposed surfaces have been extensively studied by means of atomistic calculations as well as of various experimental methods. Scheelite cleaves mostly forming the (112) and (001) surfaces since they exhibit the lowest surface dangling bond

densities (Gao et al., 2016b, 2013; Hu et al., 2012; Li and Gao, 2017; Mogilevsky et al., 2004). The average W-O bond length is 1.777 Å compared to 2.458 Å for the Ca-O bond length. Consistently, this induces significant differences in bond energies between W-O (610 kJ.mol^{-1}) and Ca-O (130 kJ.mol^{-1}) (Neiman, 1996). Hence, during the cleavage process, most WO_4^{2-} anions remain intact while the Ca-O bonds break, resulting in a surface constituted of large polyatomic WO_4^{2-} anions bonded with Ca^{2+} cations (Figure 12). The (001) and (112) cleavage surfaces exhibit two dangling bonds per calcium atom (Figure 12). As each calcium atom is eight-coordinated in the scheelite lattice, the (001) and (112) surfaces comprise six-coordinated calcium atoms, which results in a significant reactivity of the surface calcium atoms.
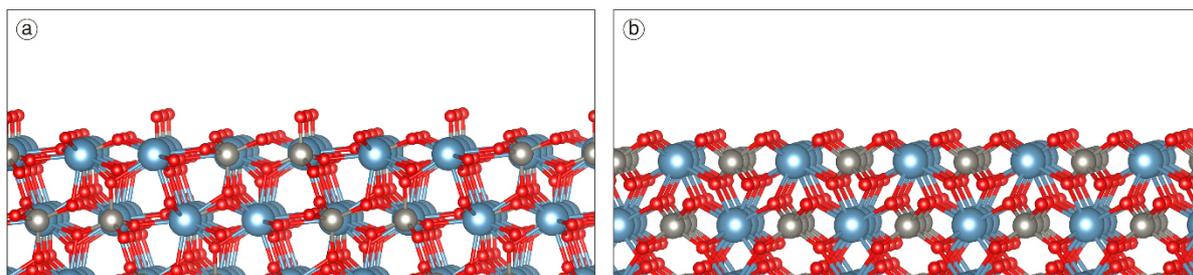
Figure 12. The two main exposed surfaces during scheelite cleavage, namely the (112) surface (a) and the (001) surface (b), based on the literature cited in the text. These surfaces exhibit two dangling bonds per calcium atom while each calcium atom is eight-coordinated in the scheelite lattice.

Considering the significant electronegativity difference existing between WO_4^{2-} and Ca^{2+}, scheelite is a sparingly soluble polar salt type mineral. Hence, it exhibits a significant free energy value at its surface, which induces a favoured adsorption of water molecules or hydroxyl anions on its surface, making it hydrophilic (Gao et al., 2016b; Hu et al., 2012; Wills et al., 2015). Some authors investigated the solubility of scheelite in water at room temperature (25°C). The solubility product remains roughly constant at pH>6 with a value of 8.9 x 10^{-9} (Marinakis and Kelsall, 1987) or 4.9 x 10^{-10} (Atademir et al., 1979), which substantiates the semi-soluble behaviour. The solubility increases significantly below pH 6 (Arnold and Warren, 1974; Atademir et al., 1979; Marinakis and Kelsall, 1987), which can be mainly attributed to the displacement of the dissolution equilibrium by the formation of isopolytungstate species (polymerised tungstate) in solution (Marinakis and Kelsall, 1987). Interestingly, the molar concentration of WO_4^{2-} above pH 6 is significantly higher than that of Ca^{2+}, resulting in an excess of WO_4^{2-} anions near the surface, *i.e.* in the inner plane. This probably explains the negative zeta potential of scheelite over the whole pH range (Arnold and Warren, 1974; Atademir et al., 1979; Gao et al., 2016b; Hicyilmaz and Özbayoglu, 1992; K. I. Marinakis and Kelsall, 1987; Ozcan and Bulutcu, 1993) although high Ca^{2+} concentrations can conduct to a zero zeta potential. This is attributed to increased amounts of Ca^{2+} ions in the inner plane that balance the WO_4^{2-} provided by the preferential dissolution of scheelite (Atademir et al., 1979; Hicyilmaz and Özbayoglu, 1992).

2.2.2   Collection of scheelite

Two main surface properties can be exploited for the adsorption of flotation collectors on scheelite: the existence of surface calcium atoms with two dangling bonds (Gao et al., 2016b, 2013; Hu et al., 2012; Li and Gao, 2017; Mogilevsky et al., 2004), *i.e.* under-coordinated (Figure 12) and the negative zeta potential over the whole pH range (Arnold and Warren, 1974; Atademir et al., 1979; Gao et al., 2016b; Hicyilmaz and Özbayoglu, 1992; K. I. Marinakis and Kelsall, 1987; Ozcan and Bulutcu, 1993). These two properties suggest the use of anionic and cationic collectors, respectively, which can both be employed for scheelite flotation.

Anionic collectors

Anionic collectors are composed of a polar group that exhibits a negative charge, available to establish a chemical bond with under-coordinated surface cations of many minerals, including scheelite. Hence, anionic collectors are widely used for a large range of minerals (Bulatovic, 2007; Leja, 1981). Notably, the negatively-charged atoms of the polar group are traditionally adapted to the target mineral: oxygen atoms (oxhydril) for oxide minerals and sulphur atoms (sulfhydryl) for sulphide minerals (Bulatovic, 2007; Fuerstenau and Healy, 1972; Fuerstenau and Palmer, 1976; Leja, 1981). Therefore, oxhydril collectors are generally used for scheelite (Figure 13), which is an oxide mineral. Most oxhydril collectors correspond to the basic form of an acid-base couple, since the existence of an extra valence electron, *i.e.* a negative charge, located on the polar group of the collector is induced by the deprotonation of the acidic form.
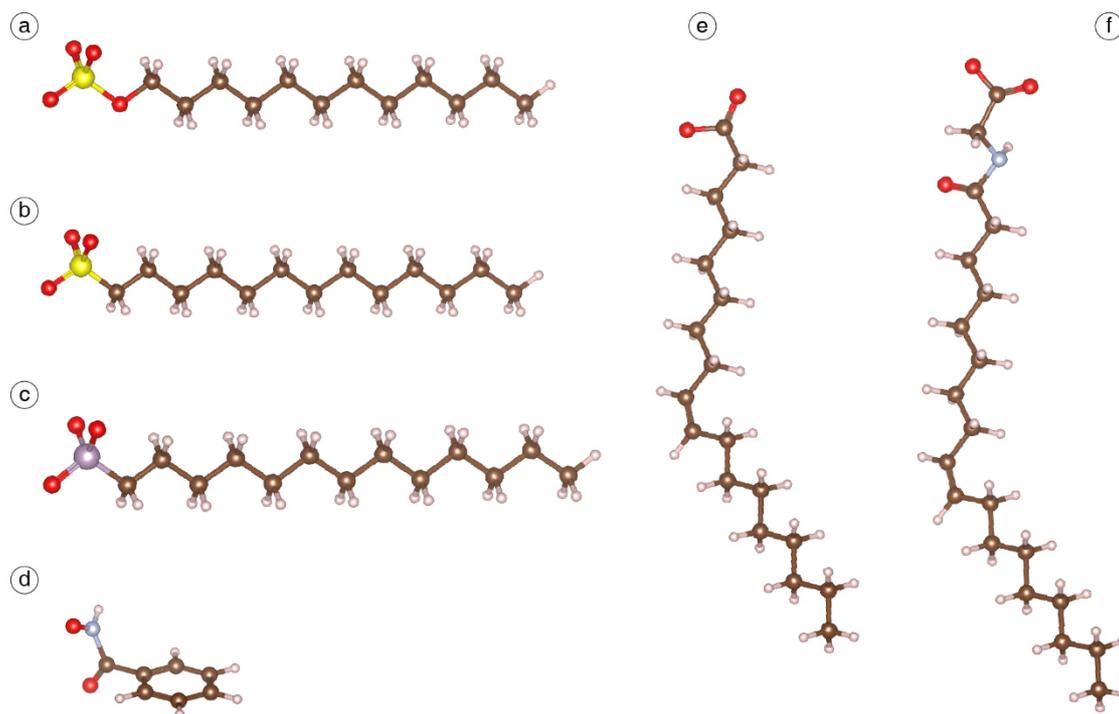
Figure 13. The different anionic collector families used for scheelite flotation: sulphates (a), sulphonates (b), phosphonates (c), hydroxamates (d), carboxylates (e), and sarcosinates (f). The marron, white, red, yellow, purple, and blue-grey balls represent the carbon, hydrogen, oxygen, sulphur, phosphorous, and nitrogen atoms, respectively.

a. Sulphates, phosphates, and their derivatives

Some authors have investigated the use of sulphate collectors such as sodium dodecyl sulphate (SDS) for scheelite flotation (Atademir et al., 1981; Grosman, 1962; Grosman and Sukhoval'skaya, 1955; Marinakis and Kelsall, 1987). Nevertheless, they reported a significant lack of selectivity between scheelite and other calcium minerals such as calcite (Atademir et al., 1981; Marinakis and Kelsall, 1987). The adsorption of sulphates is related to an exchange between a surface tungstate anion, WO_4^{2-}, and the collector molecule (Atademir et al., 1981), which is supported by the solubility results previously discussed (Atademir et al., 1979; Marinakis and Kelsall, 1987). Albeit these collectors have been poorly investigated for scheelite flotation over the past decades, they have been extensively studied for other calcium salts such as fluorite. Interestingly, SDS provided high performances for fluorite flotation (Sørensen, 1973), which are mainly attributed to a chemisorption onto surface calcium atoms (González-Martín et al., 1996; Mielczarski et al., 1983; Shergold, 1972; Sørensen, 1973). Furthermore, the calcium sulphate salts exhibit a significant solubility compared to other anionic collectors salts, indicating that no precipitation occurred at the studied concentrations (Fuerstenau and Palmer, 1976). Hence, such collectors are promising despite the crucial lack of selectivity displayed throughout the flotation tests. Besides, sulphonate collectors, which display a chemical structure very similar to that of

sulphate collectors (Figure 13), demonstrated acceptable performances for calcium minerals flotation, including scheelite (Fukazawa, 1977; Gao et al., 2015a) and fluorite (Chen et al., 2019; Zheng et al., 2018). However, as for sulphates, sole sulphonates provided poor selectivity between scheelite and other calcium minerals despite good recoveries (Gao et al., 2015a).

In phosphonates molecules, the sulphur atom from a sulphonate is replaced with a phosphorous atom (Figure 13). Nonetheless, while sulphur establishes two double-bonds with the surrounding oxygen atoms, phosphorous forms only one double-bond (Figure 13c). As for sulphates, phosphonates are used in basic conditions to favour the anionic form, *i.e.* the phosphonate, rather than the acidic form (Marinakis and Kelsall, 1987). The adsorption studies conducted with phosphonate suggested that a chemisorption occurs between the polar group and the surface calcium atoms of scheelite and calcite (Marinakis and Kelsall, 1987). However, considering the very close calculated adsorption energies of phosphonate on scheelite (-42.9 kJ.mol^{-1}) and on calcite (-38.8 kJ.mol^{-1}), the adsorption selectivity and, therefore, the flotation selectivity are traditionally very low using these collectors (Marinakis and Kelsall, 1987).

b. Hydroxamates

Hydroxamates, the anionic forms of hydroxamic acids, have been also significantly used for two decades, mainly because of their noticeable chelating abilities. Basically, their polar group contain a carbon atom linked to an oxygen and a nitrogen, these latter being linked to an oxygen atom, which can be both deprotonated to form the anionic forms (Figure 13d). The use of hydroxamic acids has been deeply investigated in the literature by many research articles published between 2000 and 2019 (Feng et al., 2017; Han et al., 2017; Pradip and Fuerstenau, 1985, 1983; Tian et al., 2018; Wei et al., 2019, 2018; Yue et al., 2018; Zhao et al., 2015, 2013). First, Zhao and co-workers (2013) demonstrated that cyclohexylhydroxamate (CHA) exhibits performances significantly better than benzohydroxamate (BHA) for scheelite collection (Zhao et al., 2013). Nonetheless, the flotation recovery was not as high as with other collectors such as fatty acids and hydroxamates commonly suffer from a lack of selectivity (Zhao et al., 2013). Hence, most studies have shown that BHA must be combined with lead ions to increase notably the flotation selectivity, providing an acceptable separation of scheelite from gangue minerals, including the calcium salts (Feng et al., 2017; Tian et al., 2018; Wei et al., 2019, 2018; Zhao et al., 2015). The activation mechanism is mainly related to the specific adsorption of Pb^{2+} ions onto scheelite surfaces, since the lead tungstate species are known to be thermodynamically stable. In addition, the chelation ability of BHA is significantly higher on lead ions compared to calcium ions, especially because these latter are included in the crystallographic structure.

c. Sarcosinates

The acyl sarcosinates represent another family of collectors that were developed in the early 1990s by the chemical reaction between a fatty acid and an amino-acid (Schubert et al., 1990). They exhibited very good performances for fluorite flotation from calcite-rich gangues albeit some specific depressants were used to depress calcite (Schubert et al., 1990). The oleoyl sarcosine

(Figure 13f), which is synthesised from the oleic acid, also displayed satisfactory performances for scheelite flotation from a siliceous gangue (Ozcan et al., 1994; Ozcan and Bulutcu, 1993). Nevertheless, this molecule provided a poor selectivity between scheelite and calcite and modifiers had to be added in a first stage of conditioning to reach an acceptable separation. This method was applied to an ore assaying 0.3 % WO_3, which was first conditioned with alkyloxine (400 g/t) at pH 8, then with 50 g/t of quebracho to depress calcite, and finally with 200 g/t of oleoyl sarcosine as scheelite collector (Ozcan et al., 1994). This flowsheet afforded good separation performances since the authors obtained a concentrate assaying 56.1% WO_3 with 79.4% WO_3 recovery. Nonetheless, the ore considered by Ozcan and co-workers (1994) comprised only calcite as calcium salt, strongly depressed by the use of quebracho. In addition, sarcosinates have been successfully used for fluorite collection (Schubert et al., 1990), indicating a significant affinity of these collectors for fluorite, as well as for scheelite (Ozcan et al., 1994). This is mainly due to the adsorption mechanisms, which are reported to be very similar to that of fatty acids since the polar group of sarcosinates contain a carboxylate group (Xian-Ping et al., 2017).

   d. Carboxylates

Carboxylates, which correspond to the anionic form of carboxylic acids (Figure 13e), are the most used collectors worldwide for the collection of a large range of oxide (and fluoride) minerals, including silicate and sparingly soluble minerals. These latter are composed of an alkaline-earth, a lanthanide, or a transition metal associated with a mono- or a polyatomic anion. On the one hand, the valuable metal can correspond to the cation, as it is the case for rare earth elements [in monazite, $(La,Ce,Nd)PO_4$, or in bastnäsite, $(La,Ce,Nd)CO_3$], barium (in barite, $BaSO_4$), or strontium (in celestite, $SrSO_4$). On the other hand, the valuable metal can correspond to the cation that forms the polyatomic anion, as niobium, tantalum, tungsten, or boron, which constitute niobate-/tantalite-based minerals (*e.g.* columbite, $(Fe,Mn)Nb_2O_6$), tungstate-based minerals (*e.g.* scheelite and wolframite), and borate-based minerals (*e.g.* colemanite, $Ca_2B_6O_{11}, 5\ H_2O$), respectively. Besides, the metallic commodity can be the whole anion of the semi-soluble salt such as F^- and PO_4^{3-}, extracted from fluorite and apatite, respectively. All the abovementioned minerals have been successfully collected by carboxylates (Bulatovic, 2015, 2010; Fuerstenau and Palmer, 1976; Leja, 1981; Wills and Finch, 2016) as well as many silicates (Fuerstenau and Palmer, 1976), including andalusite/kyanite (Jin et al., 2019), spodumene (Xu et al., 2016, 2017a; Zhu et al., 2018), feldspars (Xu et al., 2016, 2017a, 2017b), activated quartz (Fuerstenau and Palmer, 1976; Gaudin and Fuerstenau, 1956), muscovite (Alekseev and Morozov, 1975), and beryllium silicates (Walsh and Vidal, 2009). In addition, pure oxides such as cassiterite (Angadi et al., 2015) or hematite (Nakhaei and Irannajad, 2018) have been collected using fatty acids with satisfactory performances. These collectors have been traditionally used for scheelite collection and, considering their low cost, high efficiency, and environment-friendliness, they will be employed in the present work. Consequently, their adsorption mechanisms are discussed in a dedicated part, hereafter (see section 2.2.3).

Cationic collectors

Considering the significantly negative zeta potential of scheelite on the whole pH range, cationic collectors have a high potential for scheelite collection since they are known to adsorb through electrostatic interactions. Among the cationic collectors, amines are the most commonly used for the collection of silicates, oxides, and various other minerals including scheelite. In the literature, some authors have investigated the use of amines for scheelite flotation. In particular, Arnold and co-workers (1978) studied the floatabilities of scheelite and calcite with amines by microflotation as well as their separation by microflotation tests performed on mixtures. They concluded that, despite the good floatabilities of each mineral, the flotation separation of scheelite from calcite remained very difficult using amines (Arnold et al., 1978). Moreover, Atademir and co-workers (1981) demonstrated very good scheelite recovery using dodecylamine hydrochloride which, however, was not suitable for industrial application due to the high silicates contents in traditional ores (Atademir et al., 1981). Later on, Hiçyìlmaz and co-workers (1993) tested several different amines and showed that amine D acetate (a dodecylamine neutralised with acetate radicals) provided acceptable scheelite recoveries (91%) but poor selectivity between scheelite and calcite (Hiçyìlmaz et al., 1993). Recently, Gao and co-workers (2015) have investigated the use of dodecylamine (DDA) for the flotation separation of scheelite from calcite with a strong focus on adsorption mechanisms (Gao et al., 2015b). Interestingly, they showed that, at low pH, electrostatic bonds are established between positively charged amine (NH_3^+ head group) and WO_4^{2-} surface sites (Gao et al., 2015b). Also, DDA adsorbs better on scheelite than on calcite by creating a more compact monolayer, therefore enhancing the contact angle of scheelite (Gao et al., 2015b). Besides, the use of quaternary ammonium salts (QAS) as collectors for scheelite has also been investigated (Hu et al., 2011; Yang et al., 2015). Such molecules afforded good scheelite flotation performances along with very good selectivity between scheelite and other calcium minerals such as calcite. For instance, dioctyl dimethyl ammonium bromide was used on a mixture of calcite and scheelite at pH 8 and exhibited high selectivity as well as high scheelite recovery, which were significantly better than those obtained with oleic acid (Hu et al., 2011). Similar performances were attained with didecyl dimethyl ammonium and trioctylmethylammonium chlorides (Yang et al., 2015).

Collector mixtures

To increase selectivity between scheelite and the other calcium minerals, one can use collector mixtures, including anionic/anionic, cationic/non-ionic, and anionic/non-ionic reagents mixtures. In particular, the use of a mixture of sodium oleate and fatty alcohols, *i.e.* a non-ionic reagent, provided interesting performances for gypsum separation from a gangue comprising calcium minerals (Filippova et al., 2014). A similar mixture, involving sodium oleate and a fatty alcohol, conducted to an efficient flotation separation of scheelite from calcite (Filippov et al., 1993; Filippov and Filippova, 2006). It is assumed that mixing ionic and non-ionic reagents allows to reduce the electrostatic repulsions existing between the ionic groups of anionic collectors by introducing, in the adsorption layer, non-ionic compounds. These latter are supposed to adsorb

on the cationic sites by means of electrostatic interactions and/or hydrogen bonding. In addition, while reducing the polar repulsions, they also maintain significant hydrophobic chain-chain interactions inside the adsorption layer (Filippov et al., 2019, 2012, 1993; Filippov and Filippova, 2006; Filippova et al., 2014) since they are composed of aliphatic chains of 10 to 16 carbon atoms. They induce higher quantities of collector adsorbed onto a mineral from another (Figure 14), due to a better organisation of the adsorption layer. All the abovementioned studies clearly noticed significant variations in flotation selectivity and/or recoveries of various minerals. Similar results were observed using a combination of sodium oleate and polyoxyethylenes reagents (Chen et al., 2018; Chen Chen et al., 2017).
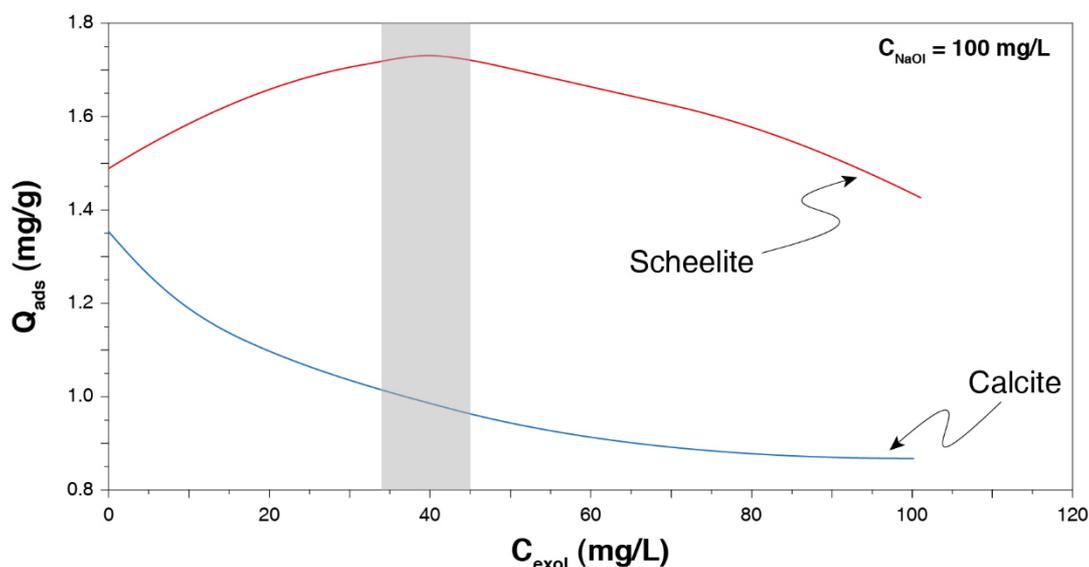
Figure 14. Effect of the quantity of an alcohol reagent (Exol-B) on the sodium oleate adsorption onto scheelite and calcite, adapted from (Filippov and Filippova, 2006). The optimum zone is displayed in grey, which roughly corresponds to a 2.5:1 mass ratio.

Besides, a similar methodology was applied for anionic/anionic reagents mixtures by Yin and Wang (2014), who blended BHA and sodium oleate and observed an increase in the scheelite recovery, without yet performing any test on a real ore (Yin and Wang, 2014).
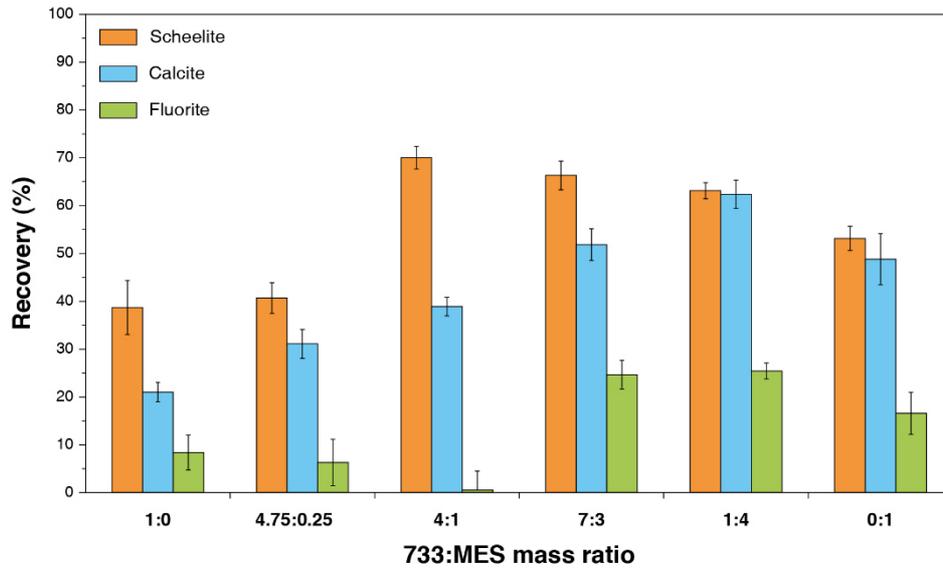
Figure 15. Effect of mass ratio of a fatty-acids collector combined with methyl ester sulfonate on flotation behaviour of scheelite, fluorite, and calcite, adapted from (Gao et al., 2015a).

Another mixture of two different anionic collectors was studied recently on an ore: Gao and co-workers (2015) blended a sulphonate with a fatty-acid-based mixture with interesting results in terms of scheelite/fluorite selectivity (Figure 15). They produced a concentrate assaying 65.8% WO_3 with 66.0% WO_3 recovery. This mixture not only improved selectivity compared to sole sodium soap but it also reduced the quantity of sodium soap and water glass required, with, finally, a high tolerance to water hardness (Gao et al., 2015a). Overall, some of the collector mixtures that have been investigated in the literature are summarised in Table 2.

Table 2. Collector mixtures in calcium minerals flotation.

Collector	Collector modifier	Material floated	References
Fatty acids	Alkylphenol ethoxylate	Apatite	(Lovell, 1976)
Sodium oleate	Sodium sulphosuccinate/sulphosuccinamate	Apatite	(Pinto et al., 1991)
Potassium oleate	Ethoxylated sulphonate	Apatite/dolomite	(Somasundaran et al., 1991)
Sodium sulphosuccinamate	Alcohol	Cassiterite	(Filippov and Houot, 1997)
Sodium oleate	Alcohol	Scheelite, calcite, apatite	(Filippov et al., 2019, 1993; Filippov and Filippova, 2006; Filippova et al., 2014)
Sodium dodecanoyl sarcosinate	Alkylammonium chloride	Fluorite	(Helbig et al., 1998)
Sodium oleate	Polyoxyethylenes	Scheelite	(Chen et al., 2018; Chen Chen et al., 2017)
Sodium oleate	BHA	Scheelite	(Yin and Wang, 2014)
Fatty acids	Sodium sulphonate	Scheelite	(Gao et al., 2015a)

2.2.3   Adsorption of carboxylates on calcium minerals

The high collection ability of carboxylates for a large range of minerals is mainly related to their significant affinity for metallic cations (alkali-earth, lanthanide, or transition metals). Traditionally, carboxylate collectors are called fatty acids since they are composed of a carboxylic group and a linear aliphatic chain with between 12 and 18 carbon atoms that frequently comprises unsaturations (Leja, 1981). They occur naturally under their acidic form in many vegetal organisms such as trees (mostly pine) or oleaginous plants (olive, colza, peanuts…), which store their energy in the form of lipid molecules. For their use in the froth flotation process, fatty acids are usually treated with a strong base (mainly sodium hydroxide, but also potassium hydroxide) to form carboxylates anions. Most short-chain carboxylic acids exhibit pKa value of *ca.* 4.8 (Kanicky and Shah, 2002). For instance, the pKa value of ethanoic acid (two carbon atoms in the chain) is 4.74 when it is dissolved in water. The pKa values increase with the carbon chain length of the carboxylic acid until four carbon atoms, since the electronic effects are not felt beyond two or three carbon atoms (Kanicky and Shah, 2002). Albeit intramolecular interactions become negligible beyond four carbon atoms in the aliphatic chain, the pKa values can be modified by intermolecular interactions. Indeed, some authors measured pKa values as high as 8 to 10 for long-chain fatty acids (Heikkila et al., 1970; Kanicky et al., 2000; Kanicky and Shah, 2002), which is mainly induced by the aforementioned intermolecular interactions. The availability of the proton is decreased by the existence of hydrogen bonds between the carboxyl groups of different molecules. Consistently, the lower is the distance between the aliphatic chains of the molecules, the higher is the pKa (Kanicky and Shah, 2002). Nonetheless, most of these studies were conducted at high concentrations (>0.1 mol.L^{-1}), which induce high intermolecular interactions resulting in increased pKa values. In froth flotation or microflotation systems, the fatty acids concentrations usually employed are significantly lower than those values, generally inferior to 1×10^{-4} mol.L^{-1}. It can be assumed that, at these concentrations, most fatty acids molecules are under monomeric forms in solution (Young and Miller, 2000), which induces negligible intermolecular interactions in solution (Mielczarski et al., 1999). The pKa values of fatty acids commonly used in flotation can therefore be considered as equivalent to that of short-chain fatty acids, *i.e.* of *ca.* 4.8.

The fatty acids deprotonation results in a significant increase of their solubility: authors reported higher solubility products of metal soaps in solution compared to fatty acids, these latter being nearly zero at room temperature (Khuwijitjaru et al., 2002; Leja, 1981), although a significant decrease in the solubility of carboxylate salts occurs when the chain length increases (Fuerstenau and Miller, 1967). Besides, the deprotonation allows to add an extra valence electron, *i.e.* a negative charge, on the polar group (-COO$^-$), which enables a chemisorption of the carboxylate onto surface metallic cations. In solution, four major species have been reported for the oleic acid/oleate species, depending on the pH and the total concentration (Figure 16). They can be under RCOO$^-$, (RCOO)$_2^{2-}$, (RCOO)$_2$H$^-$, and RCOOH forms, the two first being the most dominant at alkaline pH and for usual concentrations in flotation (Miller and Misra, 1984).
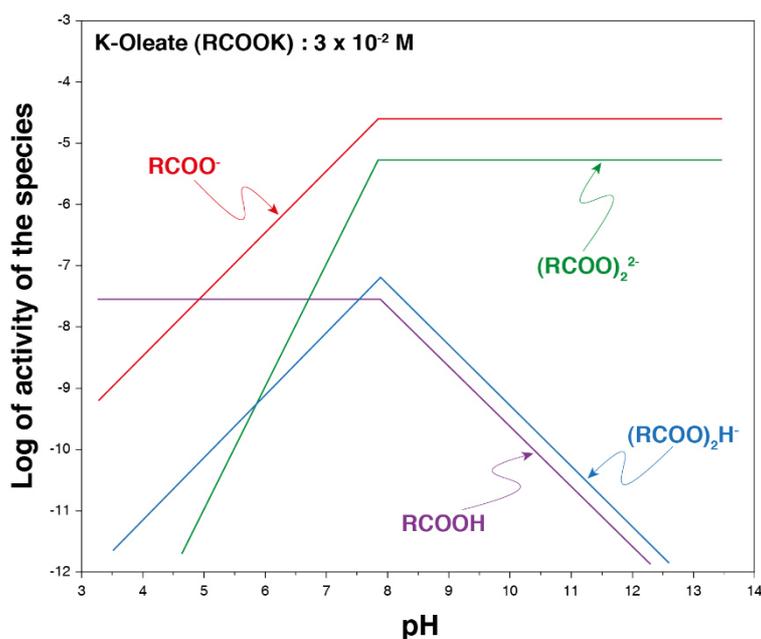
Figure 16. Species distribution diagram for an aqueous (potassium) oleate solution, adapted from (Miller and Misra, 1984).

For one century, the *cis*-octadec-9-enoic acid, also named oleic acid, has been the most used carboxylic acid in the flotation worldwide (Bulatovic, 2007; Kupka and Rudolph, 2018a; Leja, 1981), for its high natural abundance and its low melting point (induced by its unsaturation). Hence, it displays low operating costs and ease to work with. Nevertheless, many other fatty acids, with different chain lengths and unsaturation degrees, are used, most of the time in mixture with oleic acid. Indeed, this latter is difficult to purify from vegetal extracts (trees or oleaginous compounds) and is, therefore, commonly associated with other abundant fatty acids such as the saturated lauric acid (12 carbon atoms), myristic acid (14 carbon atoms), palmitic acid (16 carbon atoms), and stearic acid (18 carbon atoms), or the unsaturated linoleic acid (18 carbon atoms, two unsaturations) and linolenic acid (18 carbon atoms, three unsaturations). Thus, most fatty-acid-based collectors are mixtures of the aforementioned fatty acids in different proportions. In particular, Tall Oil Fatty Acids (TOFA) are fatty acids mixtures derived from the saponification and the distillation of pine resin (Logan, 1979). These by-products of the paper Kraft process represent a significant amount of the fatty acids used for froth flotation at industrial scale. In such mixtures, the classical above-described fatty acids are also associated with rosin acids, large-sized hydrophobic terpene-derived compounds among which abietic, pimaric, and palustric acids are dominant (Logan, 1979). Albeit authors suggested that rosin acids do not adsorb onto minerals surfaces (Pearse, 2005), their impact on the flotation of sparingly soluble minerals has not been studied at the moment. As well, the influence of the ratios between the classical fatty acids, in particular saturated/unsaturated or long chain/short chain, has not been investigated in the current literature.

For decades, the adsorption states of carboxylate species onto semi-soluble salts, especially calcium minerals, have been discussed based on a large range of experiments such as spectroscopic

and adsorption studies. Unravelling the molecular mechanisms that take place at the mineral-water interface in the presence of carboxylates is of paramount interest to find the most selective and/or most efficient carboxylate-based collectors formulations. Considering this high importance, many authors have investigated the adsorption of fatty acids, particularly sodium oleate, onto calcite (Filippova et al., 2018; Fuerstenau and Miller, 1967; Marinakis and Shergold, 1985a; Pugh and Stenius, 1985; Rao et al., 1988; Somasundaran, 1969; Young and Miller, 2000), fluorite (Free and Miller, 1997, 1996; Kellar et al., 1992, 1991; Lovell et al., 1974; Lu and Miller, 2002; Marinakis and Shergold, 1985a; Mielczarski et al., 2002, 2000, 1998, 1999; Rao et al., 1991a; Sivamohan et al., 1990), apatite (Lu et al., 1998; Mielczarski et al., 1993; Rao et al., 1990; Yehia et al., 1993), and scheelite (Mizuniwa et al., 1979; Rao and Forssberg, 1991) with however a strong focus on calcite and fluorite. Since the aforementioned semi-soluble calcium minerals display similar behaviour regarding their interactions with fatty acids, they are discussed together hereafter. All the adsorption studies clearly show two distinct regions in the adsorption isotherms (Figure 17): oleate adsorption on calcite occurs as a submonolayer in Region I and, for higher oleate concentrations, as multilayers in Region II (Marinakis and Shergold, 1985a; Young and Miller, 2000). In this latter region, the adsorption density exhibits a plateau (maximum) followed by a decrease, attributed to the formation of dimers and micelles in solution, respectively (Young and Miller, 2000). This form of adsorption isotherms for calcite has also been observed for fluorite by several authors (Gutierrez, 1979; Hu et al., 1986a; Kellar et al., 1991).
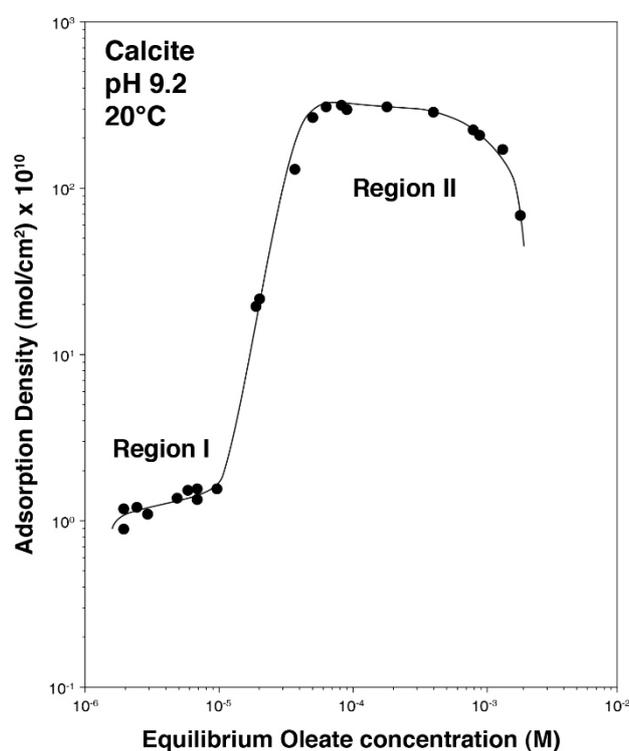
Figure 17. Typical oleate adsorption isotherm for calcite at 20°C and pH 9.2, which has also been observed for the other semi-soluble calcium salts such as fluorite and apatite, slightly adapted from (Young and Miller, 2000).

Most authors interpreted Region I as chemisorbed oleate and Region II as surface-precipitated calcium dioleate (Hanumantha Rao and Forssberg, 1991; Hu et al., 1986b; Peck, 1963; Peck and Wadsworth, 1965; Rao et al., 1991a; Sivamohan et al., 1990). The oleate concentrations for which Region II formation begins display variations between considered studies, from 1×10^{-6} mol.L^{-1} (Marinakis and Shergold, 1985a) to 1×10^{-4} mol.L^{-1} (Somasundaran, 1969). Considering a solubility product of calcium dioleate of 1×10^{-15}-10^{-16} (Fuerstenau and Miller, 1967; Hu et al., 1986a; Irani and Callis, 1960) and a Ca^{2+} concentration of around 1-2 $\times 10^{-4}$ mol.L^{-1} at the thermodynamic equilibrium (Marinakis and Shergold, 1985a; Pugh and Stenius, 1985; Rao et al., 1991b), an oleate concentration as low as 1×10^{-6} mol.L^{-1} would be enough to precipitate calcium dioleate on the surface. In addition, the Ca^{2+} concentration probably exhibits a significant gradient between the surface vicinity and the water bulk, supporting the assumption of calcium dioleate surface precipitation. Zeta potential measurements also substantiates this statement since the zeta potential of calcite conditioned with high oleate concentrations was found close to that of calcium dioleate (Mishra et al., 1980; Rao et al., 1988).

Meanwhile, the carboxyl (COO$^-$ or COOH) stretching vibrations in Fourier transform infrared (FTIR or IR) spectroscopy, which are located in the 1300-1800 cm^{-1} domain, provide crucial information about the adsorption geometry. In particular, the wavenumber of the asymmetric stretching vibration of COO$^-$ has been intensively studied since 1965, when Peck and Wadsworth suggested that a monolayer of oleate chemisorbed on fluorite and barite surfaces was characterised by a single absorption IR band at around 1550 cm^{-1} (Peck and Wadsworth, 1965). Other studies, conducted since that, have substantiated this conclusion by observing the single absorption at around 1550 cm^{-1} (Free and Miller, 1996; Jang and Miller, 1993; Kellar et al., 1991). This band has been observed at various wavenumbers between 1549 cm^{-1} (Free and Miller, 1996; Kellar et al., 1991; Sivamohan et al., 1990) and 1555 cm^{-1} (Peck and Wadsworth, 1965; Rao et al., 1991b; Sivamohan et al., 1990), depending on the method and the studied mineral. Most FTIR studies performed on calcium minerals displayed this single band for low sodium oleate equilibrium concentrations, *i.e.* for low surface coverage. In particular, Rao and co-workers (1991) recorded IR spectra that corresponded to different adsorption densities, from very low surface coverage to a bilayer (Rao et al., 1991b). At low adsorption densities, they observed two bands at 1560 and 1557 cm^{-1}. The first one disappeared while the second one shifted to 1555 cm^{-1} when the oleate concentration was increased (Rao et al., 1991b). For higher surface coverages, the single band at 1555 cm^{-1} was obscured by a doublet at 1540 and 1574 cm^{-1}. Finally, a single band at 1558 cm^{-1} was observed when the sodium oleate concentration raised to reach a statistical bilayer (Rao et al., 1991b), although this latter has not been described by most authors working on the same topic (Young and Miller, 2000). To help in the interpretations, the IR spectra of pure sodium oleate and pure calcium dioleate were recorded in various studies (Eileen Ross L. Espiritu et al., 2018; Hu et al., 1986b; Lovell et al., 1974; Rao et al., 1991a). Interestingly, a single band was systematically observed at 1559-1561 cm^{-1} for pure sodium oleate (Eileen Ross L. Espiritu et al., 2018; Lovell et al., 1974; Rao et al., 1991a) and a doublet at 1540-1542 cm^{-1} and 1577-1580 cm^{-1} for calcium dioleate (Hu et al., 1986b; Lovell et al., 1974; Rao et al., 1991a). Hence, the observations from (Rao et al., 1991b) were discussed in the light of the aforementioned

pure compounds. First, the band at 1560 cm^{-1} observed for very low adsorption densities was ascribed to physically adsorbed sodium oleate while the band at 1555 cm^{-1}, observed at slightly higher adsorption densities, was attributed to chemisorbed oleate on the surface calcium atoms. This latter interpretation was shared by (Hu et al., 1986a; Kellar et al., 1992, 1991; Lovell et al., 1974; Miller et al., 1989; Peck and Wadsworth, 1965; Rao et al., 1990) and later on by (Free and Miller, 1996; Jang and Miller, 1993; Lu et al., 1998; Lu and Miller, 2002; Young and Miller, 2001, 2000). Then, the doublet, observed for high oleate concentrations, was ascribed to calcium dioleate precipitation on the surface by most authors, considering the significant similarity between this doublet and the doublet of pure calcium dioleate spectra. This conclusion was substantiated by various experiments such as vigorous shakings or ultrasound treatments, which induced a disappearance of the doublet in favour of the single band at 1555 cm^{-1} (Rao et al., 1991b). Nonetheless, some results were confusing: at low adsorption densities, the single band at 1562 cm^{-1} was observed (Lovell et al., 1974), previously attributed to sodium oleate, while Rao and co-workers (1991) observed the three abovementioned adsorption bands (Rao et al., 1991a). Besides, Filippova and co-workers (2018) recently investigated the effect of sodium oleate concentration on the IR bands. They did not observe any band at 1555 cm^{-1}, the IR spectra displaying no peak at very low concentrations and the doublet, previously attributed to surface precipitated calcium dioleate, at moderate to high concentrations (Filippova et al., 2018). For decades, these results have been controversial, considering the significant number of articles, suggested mechanisms, and interpretations regarding the adsorption states (Lu and Miller, 2002). In particular, Mielczarski and co-workers suggested, in 1993, different interpretations for the three IR bands observed for fatty acids adsorbed onto calcium minerals (Mielczarski et al., 1993). They stated that the IR absorption bands do not depend on the adsorption mechanism but rather on the organisation of the adsorption layer on the surface (Mielczarski et al., 1993). In particular, the doublet at 1540 and 1572 cm^{-1} was attributed to a well-organised close-packed structure constituted by two different structural forms (conformations) for the adsorbed carboxylates. Later on, the same authors used polarised FTIR measurements to substantiate their previous conclusions. In their results, the band at 1536 cm^{-1} was ascribed to oleate molecules adsorbed onto surface calcium atoms in a bidentate mode, while the band at 1576 cm^{-1} corresponded to the unidentate mode (Mielczarski et al., 1998). Besides, the peak at 1560 cm^{-1} was attributed to calcium-sodium oleate surface species, rarely occurring (Mielczarski et al., 1999). They systematically observed either the sole doublet or the doublet combined with the band at 1563 cm^{-1} (Mielczarski et al., 1999). The latter study clearly demonstrated that the conditioning time plays a key role in the fatty acids adsorption onto calcium minerals since the authors observed either appearing/disappearing bands or variations in the relative intensities of the absorption bands (Mielczarski et al., 1999). At low coverage, they observed, in some cases, the band at 1556 cm^{-1}, which was obscured by the doublet at 1538 and 1574 cm^{-1} when the oleate concentration increased (Mielczarski et al., 2000). The post-conditioning under a moderate vacuum induced the disappearance of the doublet in favour of the singlet. In addition, washing in deionised water during 44 min after conditioning with sodium oleate did not change anything regarding the IR doublet (Mielczarski et al., 2002), which supported their previous suggestions.

Indeed, one minute of contact between a sodium oleate solution at a moderate concentration (3.3 x 10^{-5} mol.L^{-1}) and fluorite was enough to exhibit the abovementioned doublet (Mielczarski et al., 2002). One minute seems short to form a calcium dioleate precipitate considering the significantly slow kinetics of fluorite dissolution, the fact that fluorite was not equilibrated with water prior the oleate introduction, and the slow kinetics of the calcium dioleate precipitate formation. Hence, the assumption of adsorption of oleate species onto surface calcium atoms was significantly supported by these experiments. Moreover, washing with stream desorbed the oleate species since the doublet disappeared (Mielczarski et al., 2002), which also substantiated the suggestion of chemisorbed oleate on surface calcium atoms. Nonetheless, the same authors demonstrated that two pure fluorite samples from different locations did not provided the same responses: for short conditioning time (two minutes), the first one exhibited the doublet (1537 and 1575 cm^{-1}) while the second one the singlet at 1558 cm^{-1} (Mielczarski et al., 2002). This arises strong scientific questioning regarding the influence of the surface topography since the two samples were very similar in terms of crystallography and chemical composition.

The adsorption mechanisms of carboxylates onto calcium minerals remain a large scientific problematic at the moment. Some authors mentioned the chemisorption of oleate species followed by the surface precipitation of calcium dioleate while other researchers suggested the sole chemisorption of oleate species onto surface calcium atoms. Moreover, different mechanisms were introduced for the adsorption of these latter species on the surface, including the adsorption through a sodium cation itself adsorbed onto negatively charged surface sites (Rao et al., 1990). Besides, most authors agreed on the decrease in the wavenumbers of the -CH$_2$ stretching vibrations due to stronger van der Waals interactions between the aliphatic chains (Kellar et al., 1991; Mielczarski et al., 2000). Hence, free rotation around C-C bonds in the aliphatic chains has been suggested for this phenomenon, going from a -*gauche* state to a -*trans* state when the oleate concentration increases (Kellar et al., 1991). These adsorption studies were combined with either molecular modelling or calorimetric measurements. Notably, the adsorption energy of oleate onto fluorite was calculated by molecular modelling of -70 kcal.mol^{-1} for the bidentate mode and of -65 kcal.mol^{-1} for the unidentate mode (Mielczarski et al., 2002). Nonetheless, this study didn't consider the prior adsorption of water on surface: in the Langmuir adsorption model, the whole adsorption process comprises the water desorption prior to the collector molecule adsorption. More realistically, the adsorption energies were calculated by means of calorimetry and found of 2.4 kcal.mol^{-1} (Miller et al., 1989) or 2.8 kcal.mol^{-1} (Hu et al., 1986a) for Region I (chemisorbed oleate) and of -5.3 kcal.mol^{-1} (Miller et al., 1989) or -6.7 kcal.mol^{-1} (Hu et al., 1986a) for Region II (surface precipitated calcium oleate). Later on, Free and Miller (1997) calculated an activation energy of 42.1 kJ.mol^{-1} for the adsorption of oleate onto fluorite by means of kinetics studies (Free and Miller, 1997).

In the 1980s, some authors noticed that the adsorption of oleate onto mineral surfaces resulted in a significant oxygen consumption (Miller and Misra, 1984; Hu et al., 1986a). Based on these previous results, several studies were conducted on the adsorption of sodium oleate on various minerals, including fluorite. In particular, for high temperatures and/or high oxygen potentials

in solution, the C=C double bond of the adsorbed sodium oleate species exhibited a significant reactivity, which induced a decrease in the intensity of the =CH band in FTIR spectroscopy (Brandao, 1982; Brandao and Poling, 1988; Hu et al., 1986a, 1986b; Kellar et al., 1992; Miller and Misra, 1984; Plaksin, 1959). This decrease was correlated with the apparition of a broad band at 1090 cm^{-1} that has been assigned to C-O-C bonds (Hu et al., 1986b; Kellar et al., 1992; Miller and Misra, 1984). Interestingly, this phenomenon was not observed for the surface precipitated calcium dioleate and seemed limited to the first chemisorbed layer, highlighting a possible surface catalysis of the polymerisation reaction (Kellar et al., 1992).

2.2.4 Depressants for common gangue minerals

Sodium silicate

With an estimated annual world consumption of 4 Mt in 1990 (Lagaly et al., 2000), alkali silicate reagents are among the most used inorganic reagents worldwide. These environment-friendly reagents have been intensively studied over the past decades (Baral et al., 2017; Nakamura and Ogawa, 2012; Pedone et al., 2007) since they commonly serve as a basis for the production of a large range of silica-containing materials (Kahlenberg, 2010; Lagaly et al., 2000; Shelby, 2005; Varshneya, 1994). Besides, their interesting properties induce a wide range of industrial applications as additives, including detergents, foundries, adhesives, surface coatings, and water treatment (Lagaly et al., 2000; Shelby, 2005; Swenson and Adams, 2003; Varshneya, 1994). For decades, sodium silicate (Na_2SiO_3) has been one of the most common reagents used in the froth flotation process (Leja, 1981) where it plays two key roles. First, it increases the efficiency of the flotation process since it prevents slime coating/aggregating by decreasing the particle-particle interactions (Bulatovic, 2007; Leja, 1981). Also, due to its high affinity for gangue minerals, mostly silicates, it adsorbs onto their surfaces and prevents the adsorption of the collector, *i.e.* it depresses them, keeping them hydrophilic. Therefore, Na_2SiO_3 is commonly used in the flotation separation of rare earth minerals (Filippov et al., 2016), zinc minerals (Ejtemaei et al., 2012), iron minerals (Rao et al., 2011), scheelite ($CaWO_4$) (Kupka and Rudolph, 2018a; Yang, 2018), fluorite (Song et al., 2006; Zhou et al., 2013), apatite (Qi et al., 1993; Sis and Chander, 2003), and many other minerals. Worldwide researchers have extensively investigated the behaviour of Na_2SiO_3 in aqueous solutions. It is assumed that it dissociates into silica tetrahedra (SiO_4) which can be under SiO_4^{4-}, $SiO_3(OH)^{3-}$, $SiO_2(OH)_2^{2-}$, $SiO(OH)_3^-$, and $Si(OH)_4$ forms depending on the solution pH and the total silica concentration (Bass and Turner, 1997; Engelhardt et al., 1975; Halasz et al., 2007; Jansson et al., 2015; Marinakis, 1980; Marinakis and Shergold, 1985b). Moreover, some authors demonstrated that silica tetrahedra can polymerise, also depending on the pH, the total silica concentration, and the SiO_2:Na_2O ratio, a high ratio inducing a high polymerisation degree (Bass and Turner, 1997; Dimas et al., 2009; Jansson et al., 2015; Lentz, 1964; Marinakis, 1980; Nordström et al., 2011). In dilute solutions (~ 1.10^{-3} mol.L^{-1}) and for low to moderate SiO_2:Na_2O ratio, traditionally used in flotation, the main species of Na_2SiO_3 are $Si(OH)_4$ for pH<9.4, $SiO(OH)_3^-$ for 9.4<pH<12.6, and $SiO_2(OH)_2^{2-}$ for pH>12.6 (Han et al., 2016; Marinakis, 1980) although this latter pH is rarely attained in the flotation process (Figure 18).

Also, it is assumed that the polymerisation reaction depends strongly on the $SiO(OH)_3^-$ and $SiO_2(OH)_2^{2-}$ concentrations in solution (Marinakis, 1980; Roller and Ervin, 1940). To limit operating costs, most flotation processes worldwide are performed at pH 7-11, which induces that the silica monomers are dominant, under both $Si(OH)_4$ and $SiO(OH)_3^-$ forms.
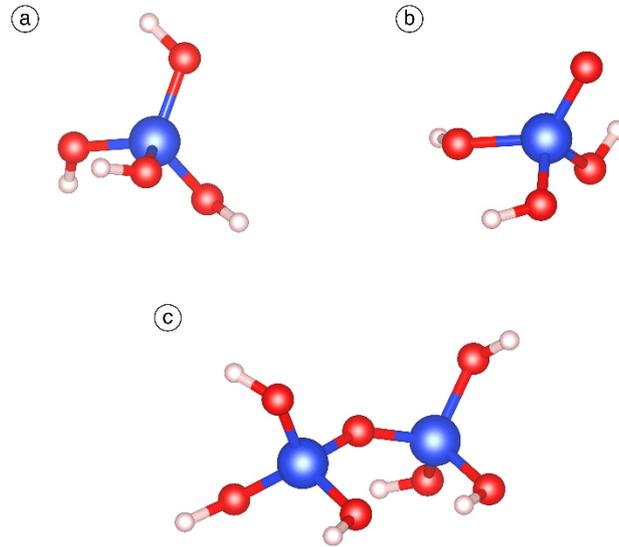
Figure 18. Most dominant forms of Na_2SiO_3 in aqueous solutions for realistic froth flotation conditions: (a) acidic monomer, $Si(OH)_4$, (b) basic monomer, $SiO(OH)_3^-$, and (c) acidic dimer, $Si_2O(OH)_6$. The blue, red, and white balls represent the silicon, oxygen, and hydrogen atoms, respectively.

The above-mentioned silica species in aqueous solution are assumed to interact strongly with the surface cations, *i.e.* Ca^{2+} in the case of calcium salts. Depending on the surface calcium speciation (Ca or Ca-OH) and the most dominant silica species in solution, silica adsorption can result in the formation of Ca-Si(OH)$_4$ or Ca-O-Si(OH)$_3$ on the surface (Marinakis, 1980; Marinakis and Shergold, 1985b). However, various adsorption mechanisms have been suggested, including the physical adsorption of silica gel and water glass (Cheng et al., 1963), silicate ions (Fuerstenau et al., 1972; Glembotskii and Uvarov, 1964), colloidal silica and polymeric silicic acid (Nikiforov and Skobeev, 1968) besides from chemisorption (Fuerstenau et al., 1972; Marinakis, 1980; Marinakis and Shergold, 1985b). Besides, the soda amount as well as the age of the Na_2SiO_3 solution is likely to play a role in the depressing effect of Na_2SiO_3 (Berlinskii, 1962; Marinakis, 1980; Marinakis and Shergold, 1985b).

Sodium carbonate

Sodium carbonate (Na_2CO_3) is mostly described as a buffering pH modifier (Bulatovic, 2010) as well as a pulp dispersant (Kupka and Rudolph, 2018b), and eventually as a depressant (Zheng and Smith, 1997). Some authors highlighted positive synergistic effects when Na_2SiO_3 is used in flotation pulps where the pH is controlled beforehand by Na_2CO_3 (Agar, 1984; Kupka and

Rudolph, 2018a). In other terms, the prior addition of Na_2CO_3 induces a higher efficiency of Na_2SiO_3 in terms of gangue minerals depression, which allows a better flotation selectivity and, hence, higher metal grades in the flotation concentrates (Kupka and Rudolph, 2018b; Martins and Amarante, 2013). At the moment, very few studies have been conducted on the Na_2CO_3/Na_2SiO_3 system in flotation and the synergistic effects exhibited by this reagent combination are still poorly understood. Recently, Kupka and Rudolph (2018) suggested that fluorite would be first depressed followed by calcite, silicates, and scheelite when Na_2CO_3 dosage is increased, with negligible dependence on the pH and the other pH modifiers used (Kupka and Rudolph, 2018b). The effect of Na_2CO_3 can be related to the precipitation of calcium ions in suspension (Bahr et al., 1968; Kupka and Rudolph, 2018b) as well as a surface carbonation of the calcium minerals (Bahr et al., 1968; Miller and Hiskey, 1972; Rahimi et al., 2017). Indeed, the precipitation of calcium ions probably decreases the gangue minerals activation induced by their adsorption (Kupka and Rudolph, 2018b). Besides, the formation of calcium carbonate onto gangue minerals surfaces (silicates, apatite, fluorite…) possibly results in a better depression of these minerals by Na_2SiO_3, which is known to strongly depress calcite (Kupka and Rudolph, 2018b).

Metallic salts

Studies have demonstrated that the addition of metallic cations, such as Fe^{3+}, Al^{3+}, Pb^{2+}, Zn^{2+},… in the flotation process allows to modulate the selectivity of the separation (Abeidu, 1973; Detienne, 1978; Feng et al., 2017; Hanna and Somasundaran, 1976; Mercade, 1975; Oliveira and Sampaio, 1988; Patil and Nayak, 1985; Raatz, 1992; Schubert et al., 1990), see Figure 19. However, using sole metallic salts results in a limited improvement of the flotation performances (Hiçyìlmaz et al., 1993). Combined with Na_2SiO_3, these cations are assumed to form strongly hydrophilic hydrosols, which depress gangue minerals efficiently (Changgen and Yongxin, 1983). In particular, Patil and Nayak (1985) efficiently depressed calcite by using a hydrosol composed of Na_2SiO_3 and ferrous sulphate with no negative impact on scheelite (Patil and Nayak, 1985). Interestingly, they noted an increase in the flotation recovery when the two reagents were added simultaneously. The use of iron salts combined with Na_2SiO_3 systematically conducted to an increase of the flotation selectivity in favour of scheelite (Dean and Schack, 1964), which could be attributed to a specific adsorption of iron compounds (mostly hydroxides) on scheelite along with a strong depression of calcite by Na_2SiO_3. Nevertheless, the mechanisms involved in the depression/activation phenomena observed when Na_2SiO_3 is combined with metallic cations is poorly understood.
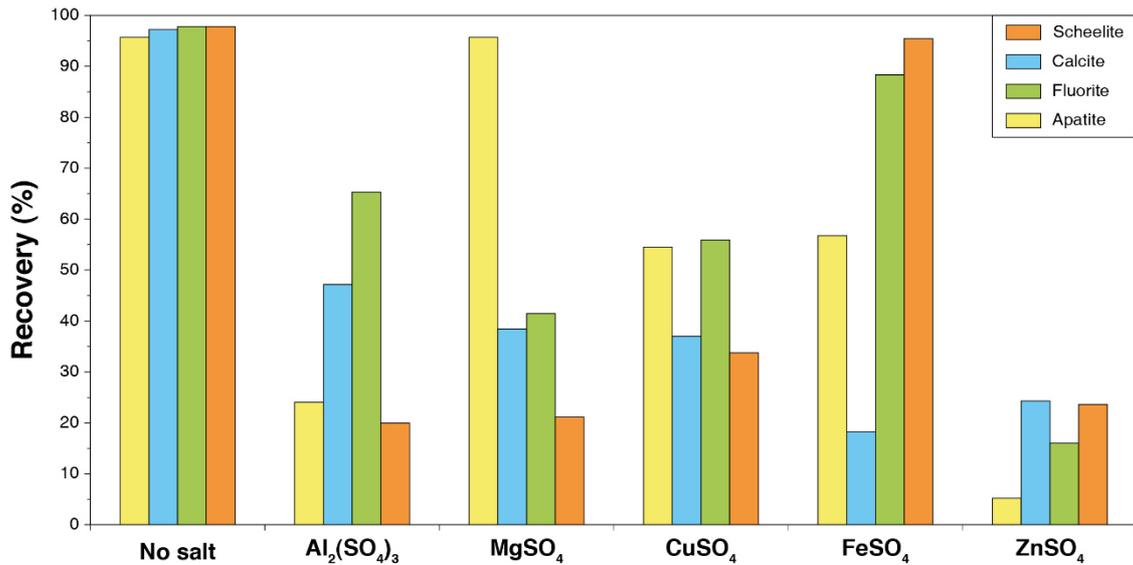
Figure 19. Combined effect of polyvalent metallic cations (300 g/t) and Na_2SiO_3 (1.5 kg/t) on the flotation recovery of calcium salts, adapted from (Hanna and Somasundaran, 1976) and (Kupka and Rudolph, 2018a). Tests were performed with 2 kg/t Na_2CO_3 and 100 g/t oleic acid at pH 9.1-9.5.

Organic molecules

Moreover, organic polymers such as tannins and starch (Liu et al., 2016; Ozcan and Bulutcu, 1993; Rutledge and Anderson, 2015), as well as chelating agents, *e.g.* citric acid (Bulatovic, 2015; Gao et al., 2016a) are known to depress calcium-bearing minerals in some cases. It has been demonstrated that organic molecules adsorb by interactions between their polar groups (-OH or –COOH) and the surface cations such as Ca^{2+} (Filho et al., 2000; Filippov et al., 2013; Somasundaran, 1969; Wang and Somasundaran, 2005). These interactions can be of various types, including chemisorption of -COO⁻ group onto calcium atoms, physisorption of -OH or -COOH groups onto the same cations, or hydrogen bonding between -OH or -COOH groups and hydroxylated surface cations $[Ca(OH)^+]$. In particular, starch is widely known to strongly depress silicate minerals and calcite (Bulatovic, 2010), as well as quebracho, following the above-described mechanisms.

Phosphate derivatives

Phosphate derivatives such as sodium hexametaphosphate $[(NaPO_3)_6]$, sodium phosphate (Na_3PO_4), sodium pyrophosphate $(Na_4P_2O_7)$, and 1-Hydroxyethylidene -1,1-diphosphonic acid (HEDP) (J. Wang et al., 2018) are also widely used inorganic depressants for scheelite flotation from calcite and fluorite (Bel'kova et al., 1993; Bulatovic, 2015; Liu et al., 2016; Yongxin and Changgen, 1983). The depressing effect of phosphate derivatives have been extensively discussed, with however contradictory results (Kupka and Rudolph, 2018a). Indeed, some authors successfully used phosphate derivatives to depress calcite and fluorite in scheelite flotation (Changgen and Yongxin, 1983; Yongxin and Changgen, 1983) while other researchers employed them to depress apatite in fluorite flotation (Bulatovic, 2015) or in scheelite flotation (Bel'kova

et al., 1993). Phosphate derivatives are known to chelate Ca^{2+} ions in solution leading to a surface depletion in terms of calcium ions faster for fluorite and calcite than for scheelite (Changgen and Yongxin, 1983). However, Gao and co-workers (2018) rather suggested a chemisorption of phosphate derivatives onto surface calcium atoms (Gao et al., 2018), which exhibit a higher density and activity for calcite than for scheelite.

2.3 Atomistic simulation methods applied to froth flotation

2.3.1   Importance of molecular modelling for flotation

Liberations sizes in most ores are nowadays low enough to make unable the use of classical physical separation methods, making the froth flotation mandatory to concentrate the target mineral(s). Also, the average ore grades are decreasing over time (Calvo et al., 2016; Mudd, 2007), which can be mostly attributed to the depletion of the high grade deposits, although some authors interpret this decline as innovation and improvements in extractive technologies (Drielsma et al., 2016). Along with the ore grades decline, ores displaying high separation contrast between the constitutive minerals will also decline. Since the froth flotation is mandatory for most ores, the gangue complexness as well as the low grades will be overcome by increasing the flotation performances, *i.e.* the selectivity between minerals and the flotation recovery. Hence, understanding the molecular mechanisms involved in the adsorption of flotation reagents (depressants, activators, and collectors) is of paramount interest since they are still poorly apprehended. The determination of adsorption energies and structural configurations allows to adapt the reagents used during the flotation process to the ore mineralogical association. Moreover, it brings clarity in the comprehension of the synergistic effects that are commonly exhibited when reagents are used in combination. New reagents formulations can be developed based on the adsorption energies calculated from molecular simulations, which allow to improve the flotation selectivity or recovery. Because of the presence of a liquid phase, the molecular mechanisms are difficult to investigate with experimental methods, mainly when similar reagents are used in mixtures, which makes the molecular modelling a powerful tool. In particular, this methodology could bring new insights in the molecular mechanisms involved in the fatty acids adsorption onto calcium minerals since this topic has been widely debated over the past decades (see section 2.2.3).

Over the past few years, molecular modelling has gathered interest to understand the key mechanisms that are the basis of the froth flotation process. This increase can be assessed by expressing the number of original research articles that have included the words "flotation" and "molecular simulations" over the fifteen last years (Figure 20a).
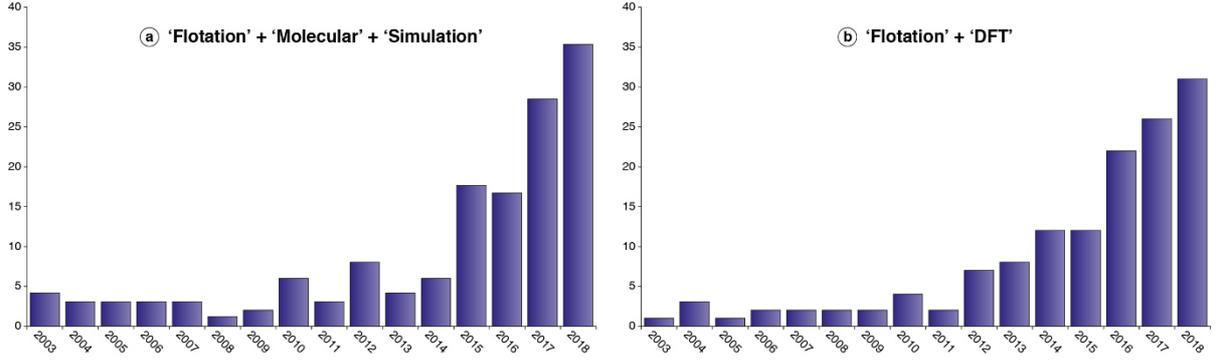
Figure 20. Number of research articles per year over the past fifteen years including the words "flotation", "molecular", and "simulation" (a) and including the words "flotation" and "DFT" (b) from Web of Science.

The energy of systems describing the adsorption processes can be calculated using highly accurate methods based on quantum mechanical descriptions such as Hartree-Fock, post-Hartree-Fock, and density functional theory (DFT) (Evans et al., 2017; Sholl and Steckel, 2009). Besides, energies and structures can be determined using classical potentials-based simulations that require accurate force fields and are not able to fully describe quantum mechanisms such as chemical bond cleavage or formation (Evans et al., 2017). Most of the abovementioned articles used DFT (Figure 20b), which exhibits the best compromise between accuracy and computational demand among the current molecular modelling methods (Sholl and Steckel, 2009). Hereafter, the different molecular simulation methods existing nowadays in theoretical physics and chemistry are critically reviewed. A global method for modelling the interactions between flotation reagents and mineral surfaces is suggested.

2.3.2 Quantum mechanical simulations

In quantum simulations, it is assumed that all the bonds and interactions between atoms are related to the electrons, which can be described using the Schrödinger equation, considered as time-independent to simplify the problem:

$$\hat{H}_T \psi(R_1, \dots R_n, r_1, \dots, r_n, \sigma_1, \dots, \sigma_n) = E\psi(R_1, \dots R_n, r_1, \dots, r_n, \sigma_1, \dots, \sigma_n) \qquad (2)$$

Where $\hat{H}$ represents the total Hamiltonian operator of the system, ψ the wave function that is a function of the spatial coordinates of nuclei (R) and electrons (r) and the spin of electrons (σ) that will be ignored for the rest of the discussion, and E the total energy of the system. In Eq. 2, the Hamiltonian operator can be expressed as the sum of total kinetic energy operator and the Colombian interactions. The kinetic energy operator takes into account the electrons kinetic energy operator, $\hat{T}_e$, and the nuclear kinetic energy operator, $\hat{T}_n$, while the Colombian interactions include the electron-electron repulsion ($\hat{V}_{e-e}$), the electron-nucleus attraction ($\hat{V}_{n-e}$), and the nucleus-nucleus repulsion ($\hat{V}_{n-n}$) operators:

$$\hat{H}_T = \hat{T}_e + \hat{T}_n + \hat{V}_{n-e} + \hat{V}_{e-e} + \hat{V}_{n-n} \tag{3}$$

Hence, the time-independent Schrödinger equation depends on 4N+3M variables, where N is the number of electrons and M the number of nuclei, which makes nearly impossible a numerical resolution. To reduce the number of variables involved in the Schrödinger equation, the Born-Oppenheimer approximation is commonly used, in which the nuclei are considered immobile since their mass is significantly higher than the electrons (around 1800 times). Therefore, the nuclear kinetic energy operator can be neglected while the nucleus-nucleus Colombian interaction is constant. It induces that the total energy of the system corresponds to the sum of the total electronic energy of the system and a constant term representing the nucleus-nucleus interaction term.

In the Born-Oppenheimer approximation, the electron-electron repulsion term, $\hat{V}_{e-e}$ still does not have a simple analytical solution for systems with more than two electrons. The Hartree-Fock method (Hartree and Hartree, 1935; Slater, 1930) was developed to solve this problem, in which the wave function is expressed as a Slater determinant and the Schrödinger equation is solved self-consistently to minimise the total energy of the system (Epstein, 2014; Nesbet, 2002). Although the exchange is correctly described by this method, the correlation is not taken into account, which induces an energy overestimation. Hence, post-Hartree-Fock methods (Cramer, 2004; Jensen, 2007) were developed to take into account correlation terms, resulting in accurate energy determinations but high computational costs that make this method viable only for small systems.

Besides, Hohenberg and Kohn demonstrated that the total energy E_0 of a system in its fundamental state can be expressed as a functional that depends only on the electronic density (Hohenberg and Kohn, 1964). In this formalism, the total energy of the system (E) is the sum of the kinetic energies of the electrons $T[\rho]$, the repulsive Colombian electron-electron interactions $J[\rho]$, the electron-nucleus interaction potential $V_{ne}(\vec{r})$, and a term corresponding to the electron-electron exchange-correlation effects $E_{ncl}[\rho]$:

$$E[\rho] = T[\rho] + J[\rho] + E_{ncl}[\rho] + \int V_{ne}(\vec{r})\rho(\vec{r})d\vec{r} \tag{4}$$

To propose a practical mean to solve this equation, Kohn and Sham suggested a method (Kohn and Sham, 1965) based on an imaginary system in which the electrons do not interact between themselves and move in a potential V_s that is chosen so that the calculated electronic density of the imaginary system is equal to the real electronic density.

The unknown terms are gathered in a quantity called the exchange-correlation energy, $E_{xc}[\rho]$, which cannot be determined analytically in the Kohn-Sham equations. A number of exchange-correlation functionals have been developed to calculate the exchange-correlation

energy, for instance in the local density approximation (LDA) or in the generalised gradient approximation (GGA). LDA approximates the system by a uniform homogenous electrons gas (Hafner, 2008; Perdew and Zunger, 1981) while GGA takes into account the gradient density and, thus, is more accurate for systems exhibiting significant density variations (Johnson et al., 1993; Perdew et al., 1996; Perdew and Wang, 1992). Besides, GGA is known to not describe precisely dispersion interactions, which represent a part of van der Waals forces (Evans et al., 2017). Consequently, methods have been intensively developed to correct the dispersion interactions by adding a term in the exchange-correlation functional with various degrees of accuracy [see for instance (Bučko et al., 2016, 2014, 2013a, 2013b, 2010; Grimme, 2006; Grimme et al., 2010)]. Dispersion interactions should be included in the DFT calculations since the adsorption of flotation reagents, mostly collectors, is partly led by hydrophobic interactions between the aliphatic chains (Cases and Villieras, 1992).

Overall, DFT simplifies a 3N-dimensional problem (where N is the number of electrons) to a 3-dimensional problem with a high accuracy and a relatively low computational cost. Hence, it enables the electronic structure calculations of crystals and molecules in liquid or gas phases for relatively large systems. More than 15,000 papers including DFT are published each year in various fields including condensed matter physics (Bučko et al., 2010; Csonka et al., 2009; Lebègue and Eriksson, 2009; Srour et al., 2018), interface phenomena (Bučko et al., 2017; Chebbi et al., 2017; Chibani et al., 2018; Jabraoui et al., 2019), catalysis (Badawi et al., 2013, 2009; M. Badawi et al., 2011; Michael Badawi et al., 2011)… This method displays now a very good reproducibility that has been assessed recently on 71 elemental crystals (Lejaeghere et al., 2016) as well as very good agreement with high-precision experiments (Losch et al., 2018). The global development of high-performance computing (HPC) allows to perform DFT calculations on systems with up to 1500-2000 atoms in around 50 Å³ cells (Evans et al., 2017).

2.3.3   Molecular dynamics simulations techniques

DFT calculations are used to determine the structure and energy of a system in its ground-state and, hence, describe neither the atoms movements nor the thermal motion. For that, molecular dynamics (MD) simulations must be used: they produce dynamical trajectories for a system composed of N particles by integrating Newton's equations of motion:

$$m_i \frac{d^2 r_i}{dt^2} = f_i = -\frac{\partial}{\partial r_i} U(r_1, r_2, ..., r_n) \tag{5}$$

Where f_i represents the external forces acting on the particle i of mass m_i and position r_i, which corresponds to the negative of the gradient of the potential energy of the system. The external forces are calculated at each time step, which should be small enough to describe correctly the fastest intramolecular vibrational motions, so usually around 1 fs. The forces can be calculated either by means of DFT, which is called the *ab initio* molecular dynamics (AIMD) simulations, or by means of force fields (FF), which is called classical molecular dynamics (CMD) simulations.

Both of these simulations are performed at constant number of particles (N), volume of the simulation cell (V), and temperature (NVT), pressure (NVP), or energy (NVE). For that, various thermostats or barostats, respectively, are available (González, 2011; Hünenberger, 2005) and enable the comparison between the simulation results and experiments. Notably, the Nosé-Hoover thermostat is among the most widely used thermostats since it considers the heat bath as a part of the system, with an additional artificial variable and an associated mass (Hoover, 1985; Shūichi Nosé, 1984; Shuichi Nosé, 1984). Both CMD and AIMD will be discussed with upsides and downsides given for each method along with successful examples of use.

Classical molecular dynamics (CMD) simulations

CMD are based on force fields, which enable the calculation of the external forces acting on each particle for the integration of Newton's equations of motion. Force fields represent an expression of the energy of a system as a function of the coordinates of its particles (González, 2011). They include several terms that can be divided into three main groups: intramolecular, intermolecular, and special terms. The first ones mainly describe the bonds, angles, torsions, etc., the second ones refer to Coulombic and van der Waals interactions between atoms, while the special terms may include cross-terms or reactivity terms. Many different force fields have been developed over the past decades, among which some were designed to simulate the liquid/solid interfaces such as OPLS (Jorgensen et al., 1996) or COMPASS (Sun, 1998). Most force fields were developed based on *ab initio* calculations, which were used to determine the parameters acting on each term. The force field choice should be adapted to the modelled system since each force field exhibits particular strengths and weaknesses, depending on the parametrisation. However, most force fields do not include any term for the reactivity, *i.e.* bond creation or destruction, which cannot be described accurately by simple force models since they result from electronic processes (Evans et al., 2017). However, CMD simulations supply a relatively accurate description of the physisorption phenomena, which represent a significant part of the molecular mechanisms involved in the flotation process. Moreover, reactive force fields such as the ReaxFF (van Duin et al., 2001) have been developed over the past decades to include chemical reactivity. They are based on high accurate *ab initio* calculations and allow continuous bond formation/breakage on, nonetheless, a restricted number of atom types at the moment (van Duin et al., 2001). Overall, CMD can be performed on systems containing millions of atoms (Evans et al., 2017, 2015; Freddolino et al., 2006; González, 2011; Kadau et al., 2006; Klepeis et al., 2009; Schulz et al., 2009) with total simulations times reaching the order of microseconds, which enables the investigation of macroscopic properties such as the diffusion of molecules in liquid phase.

Ab initio molecular dynamics (AIMD) simulations

In Eq. 5, the external forces acting on the particles can be determined by a DFT calculation since the total energy of the system can be easily related to the total forces. This allows to perform a MD simulation at finite-temperature with a DFT calculation for each time step. However, the quantum chemical calculation realised at every time step limits significantly the system size (Kühne, 2014). Nowadays, AIMD simulations are one of the most powerful methods

for energy and structure determination as they associate the high accuracy of DFT and the temperature/pressure control of molecular dynamics simulations. Since the electrons are included, the chemical bonds can break and form, which enables the study of chemical-based molecular processes and reactivity. Today, with the development of HPC, AIMD simulations can reach total simulations times of 100 ps and up to 500 atoms with acceptable accuracy and computational costs. This allows to work with explicit solvents if the considered cells and the adsorbed molecule(s) are small enough. As all the molecular modelling methods, AIMD simulations determine the total energy of the system and, hence, one can calculate adsorption energies at finite temperature. This is usually performed by averaging the internal energy of each system (surface alone, molecule alone, and surface with the adsorbed molecule) on total simulation times of 100 ps with however eliminating the first 10 ps of simulations, which are considered as a thermalisation period.

2.3.4   General methods for liquid/solid adsorption modelling

Surfaces exposed

Prior to the froth flotation process, a size reduction stage is performed to enable the transport of mineral particles by air bubbles. This crushing and milling stages cleave bonds existing between cations and anions in the mineral and generate new mineral surfaces. Minerals are cleaved following their usual cleavage planes, well described in the literature, which correspond to the surfaces with the lowest surface energy, *i.e.* the lowest surface density of broken bonds (Gao et al., 2014; Whittaker, 1982) . Hence, a complete study has to be performed to investigate the most exposed surfaces for each mineral since all the adsorption processes will involve those surfaces (Gao et al., 2019, 2017, 2012; Hu et al., 2012). This investigation requires the calculation of surface energy for each different surface with accuracy and is usually performed by DFT or by HF methods.

In practice, different surfaces have to be generated from a bulk previously relaxed by first principles methods (DFT or HF), including the common cleavage planes that are usually well described in the crystallography area. Then, the different generated surfaces should be relaxed and the surface energy (in J.m^{-2}) is calculated using:

$$E_{surf} = \frac{E_{slab} + \frac{N_{slab}}{N_{bulk}} * E_{bulk}}{2A} \tag{6}$$

Where E_{slab} and E_{bulk} are the energies of the surface slab and the bulk cell, respectively, N_{slab} and N_{bulk} are the number of atoms contained in the slab and bulk unit cells, respectively, and A the slab area.

After the milling/crushing stages, the surface exposure follows a probability law that can be related to the surface energy differences between all the surfaces. However, at the moment,

molecular modelling of the adsorption of flotation reagents cannot be performed on too many different surfaces since it would represent high computational costs. Hence, an assessment has to be done on the main exposed surface(s), which is/are selected for the following adsorption studies. The surface behaviour determination should constitute the first work to perform: for example, *ab initio* studies confirmed successfully that the (104) surface is the most exposed for calcite (Gao et al., 2012, 2017), the (001) and (112) for scheelite (Cooper and de Leeuw, 2003; Gao et al., 2013), and the (001) and (210) for barite (Bittarello et al., 2018).

Hydration

The froth flotation process and, most of the time, the prior milling stage are performed in aqueous conditions. It induces that the surfaces generated during the milling stage are exposed to water molecules before being in contact with flotation reagents. Hence, these latter, when added to the pulp, interact with hydrated surfaces, *i.e.* surfaces on which water molecules are already adsorbed. Therefore, the molecular modelling of the adsorption of flotation reagents has to be preceded by a deep study of the surface hydration mechanisms. Overall, several molecular mechanisms are at play at the mineral/water interface:

1. Adsorption of molecular water
2. Adsorption of dissociated water, leading to a hydroxylation of surface cations
3. Substitution of a surface anion by a hydroxyl group (OH⁻)
4. Influence of the surface on several water layers at the interface

To consider mechanisms 1 and 2, the adsorption energy of a lone water molecule should be calculated and compared with the adsorption energy of a dissociated water molecule, where the H atom is set on a surface anion while the HO group is placed on a surface cation. The point 3 should be investigated by considering the following reaction, with A being the surface anion:

$$\text{Surface-A} + \text{H}_2\text{O} = \text{Surface-OH} + \text{HA} \tag{7}$$
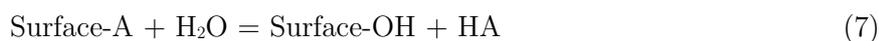
The four systems should be relaxed with their energy calculated, summed for each member of the equation (left and right), and compared with each other to assess the preference of the anion substitution. Finally, the point 4 should be investigated by increasing the surface coverage: from a lone water molecule, one should add sequentially water molecules to reach a 100% coverage prior to add a second and a third water molecules layer. The final step is to conduct a simulation with the cell full of water molecules with a calculated density of $1 \, \text{kg.dm}^{-3}$. The four above-mentioned possible hydration mechanisms can be investigated either at 0 K or at a finite temperature using DFT (static or AIMD, respectively). Besides, the points 1 and 4 can be addressed by CMD simulations since they involve no reactivity (bond creation/breakage).

The hydration mechanisms of widely known mineral surfaces have been intensively investigated over the past fifteen years by atomistic simulations. Various sulphides were studied by DFT simulations (M. Badawi et al., 2011; J. Chen et al., 2014; Haider et al., 2014; Li et al., 2019;

Long et al., 2016b) to bring clarity in the hydration mechanisms, mostly accompanied by oxidation phenomena. In addition, oxide minerals were deeply investigated since they represent an important source for non-base metals and mineral commodities. The hydration mechanisms of calcium/magnesium carbonates were described by CMD simulations (Fenter et al., 2013; Perry et al., 2007; Wolthers et al., 2012), see Figure 21, by the HF method (Villegas-Jiménez et al., 2009), and, mainly, by DFT calculations (de Leeuw and Parker, 1998, 1997; Escamilla-Roa et al., 2013; Goverapet Srinivasan et al., 2017; Lopez-Berganza et al., 2015) including AIMD simulations (Ghatee and Koleini, 2017). Other sparingly soluble salts were also deeply investigated with atomistic simulations to consider hydrated surfaces for the flotation reagents adsorption, such as scheelite (Cooper and de Leeuw, 2003; de Leeuw and Cooper, 2003a), fluorite (De Leeuw et al., 2000; Khatib et al., 2016), apatite (Pareek et al., 2009, 2008; Ulian et al., 2018; Zahn and Hochrein, 2003), and rare-earth-elements-bearing minerals (Goverapet Srinivasan et al., 2017, 2017; Srinivasan et al., 2016; Stack et al., 2018). Metallic oxides/hydroxides such as rutile (TiO_2) (Heydari et al., 2019), manganite [$MnO(OH)$] (Xia et al., 2007), corundum (Al_2O_3) (Janeček et al., 2014), pyrochlore (Bjørheim et al., 2012), goethite [$FeO(OH)$] (Aquino et al., 2007; Y. Chen et al., 2017; de Leeuw and Cooper, 2007), and hematite (Fe_2O_3) (de Leeuw and Cooper, 2007; Souvi et al., 2013) were also studied since they are known to form hydroxylated species at their surfaces in the presence of water molecules. In particular, some surfaces can be hydroxylated and hydrated at the same time, with specific terminations (Souvi et al., 2017). The same phenomenon occurs for silicates with various crystallographic structures, which constitute the most common gangue minerals in ores. Hence, their consideration in atomistic studies enables their better rejection by optimising the flotation reagents. The hydration mechanisms of many silicates, *e.g.* olivine (Kerisit et al., 2013; Liu et al., 2019; Prigiobbe et al., 2013) or various phyllosilicates (Peng et al., 2016; Wang et al., 2005; Wungu et al., 2012), have been investigated with however a high number of studies focussing on quartz (SiO_2) (Du and de Leeuw, 2006; Rignanese et al., 2004; Skelton et al., 2011; X. Wang et al., 2018). Interestingly, Skelton and co-workers (2011) compared different force fields for CMD simulations, used AIMD calculations to determine the best force field, and compared the water structure at the vicinity of the surface with experimental data (Skelton et al., 2011). Along with hydration, interactions between electrolytes in the aqueous phase and mineral surfaces can be described by molecular modelling methods, mainly to investigate the depressing or activating effect of some ions such as phosphate anions (Ahmed et al., 2019), metallic cations (Liu et al., 2014, 2019; Sarvaramini et al., 2016b), and alkali/alkali-earth cations (Guichen et al., 2018; Pfeiffer-Laplaud and Gaigeot, 2016; Sakuma et al., 2011). Overall, an accurate determination of the hydration state of a mineral is a crucial prerequisite for the investigation of reagents adsorption on a realistic surface.
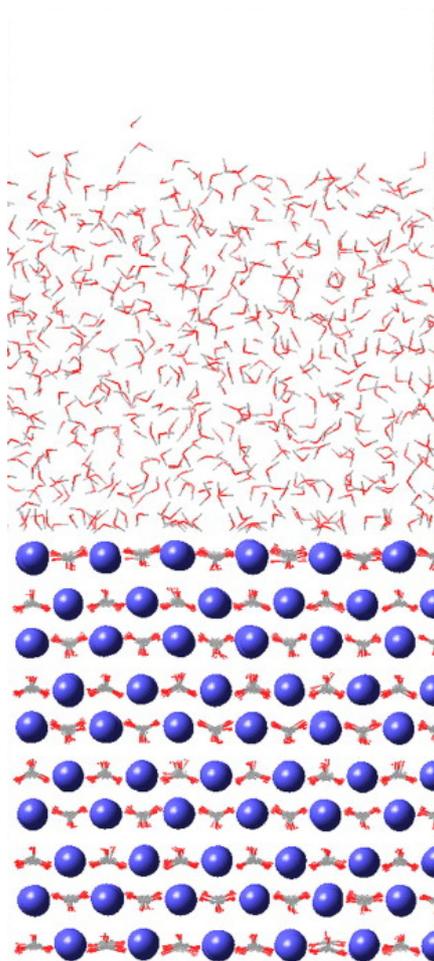
Figure 21. Snapshot of MD simulations using force fields to investigate the hydration mechanisms of calcite surface, adapted from (Perry et al., 2007).

Adsorption of flotation reagents

a. On sulphide minerals

Considering their high importance for base metals (copper, zinc, lead…), sulphide minerals [pyrite (FeS$_2$), chalcopyrite (CuFeS$_2$), sphalerite (ZnS), galena (PbS),…] have been intensively and firstly studied by atomistic simulations to gain understanding in the molecular mechanism that are at the basis of flotation. Several researchers have used DFT calculations to study the surface oxidation mechanisms of sulphides minerals (Figure 22) such as galena (J. Chen et al., 2017), sphalerite (Chen and Chen, 2010), pyrite (Sun et al., 2004), and chalcopyrite (Xiong et al., 2018), since oxidation reactions are known to affect the collector adsorption. Most of them combined DFT with spectroscopic and other experimental techniques to bring insights from *ab initio* molecular modelling or to validate the developed models. Besides, the adsorption of the most widely used collectors for sulphides (xanthates, thiophosphate, carbamate) have been investigated by DFT for pyrite (Hung et al., 2003, 2004), for galena (J.-H. Chen et al., 2014; Long et al., 2016b), chalcopyrite (Jiao et al., 2015; Ma et al., 2017; Sarvaramini and Larachi, 2017; Zhao et al., 2016), and sphalerite (Jiao et al., 2015; J. Liu et al., 2018; Liu et al., 2014,

2013; Long et al., 2016a; Sarvaramini et al., 2016b) with some concerns on the activation of sulphides by metallic ions such as Pb^{2+} (Sarvaramini et al., 2016b) or Cu^{2+} for sphalerite (Liu et al., 2014). Since all the sulphides collectors are anionic, the use of DFT is compulsory to describe accurately the chemical bonding between the surface cations and the collectors anions (O or S). Moreover, the low electronegativity difference existing between sulphur and cations comprised in sulphides (Cu, Fe, Pb, Zn, Ni...) induce a strong-covalent component for their bond, which makes the use of DFT mandatory for such systems.
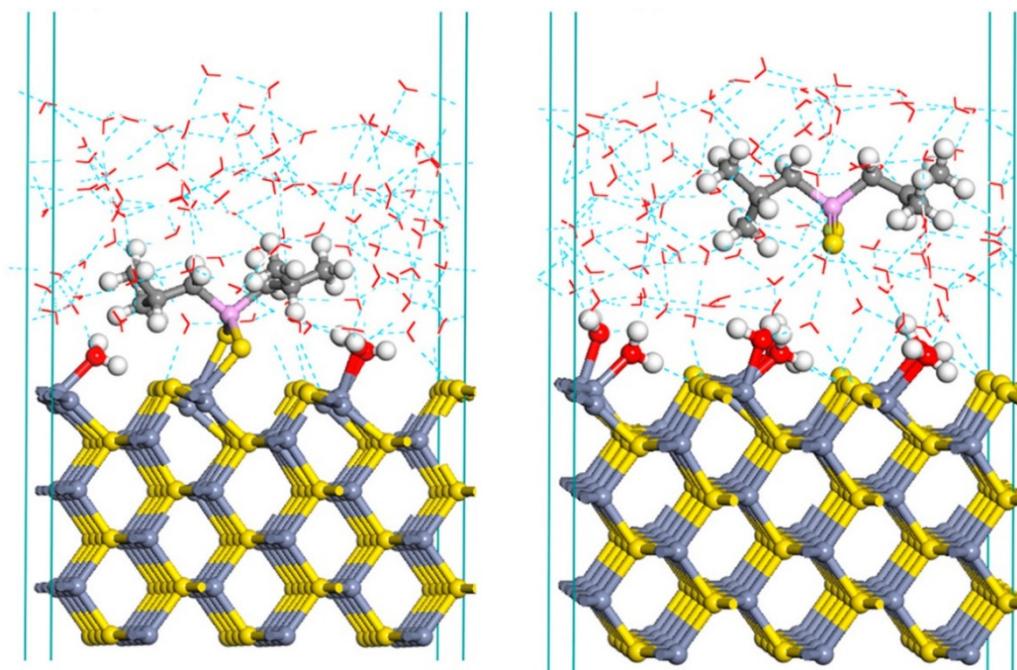
Figure 22. Adsorption of solvated diisobutyl dithiophosphinate on sphalerite surface: most stable adsorbed configuration (left), non-adsorbed solvated collector (right), adapted from (Sarvaramini et al., 2016b).

b. On silicate minerals

Few studies exist which focus on the adsorption of flotation reagents onto silicates since these latter are usually gangue minerals that have to be rejected and, thus, not collected in flotation. However, reverse flotation processes, in which silicates are collected, have been increasingly used over the past decades to purify the final metallic concentrate after the main separation, *e.g.* for iron ores (Araujo et al., 2005; Veloso et al., 2018). Hence, cationic collectors, mostly amines, adsorption have been studied by CMD and DFT simulations on quartz (Huang et al., 2014; Liu et al., 2015; Rath et al., 2014a) which was in accordance with the generated experimental data (flotation tests and microcalorimetry results). The efficiency of new formulations such as ether and ester derivatives of primary aliphatic amines could be investigated, predicted and discussed based on DFT calculations (Rath et al., 2014a). Besides, some silicates are collected in flotation since they represent either a metal-bearing mineral or an industrial mineral. Hence, the adsorption of amines onto such minerals was investigated by DFT calculations, *e.g.* on muscovite (Wang et al., 2014; Xu et al., 2013) or on kaolinite (Xia et al., 2009). Moreover, the adsorption

of anionic collectors, mostly fatty acids, was investigated by molecular modelling for quartz (Li et al., 2017) that can be activated by alkali-earth cations (Guichen et al., 2018), but mostly for various valuable silicates that have a significant affinity for fatty acids such as feldspars (Xu et al., 2017a, 2017b) or spodumene (Fushun et al., 2014; He et al., 2014; Xu et al., 2017a; Yu et al., 2015; Zhu et al., 2018). Since silicates are usually gangue minerals, the molecular modelling of depressants adsorption onto their surfaces has been investigated by DFT (Han et al., 2016) although very few studies are currently reported.

c. On oxide and fluoride minerals

Oxide minerals were also strongly investigated by atomistic simulations to gain understanding in the flotation reagents adsorption mechanisms. As for sulphides, anionic collectors are widely used for oxides and require the use of DFT to describe correctly chemisorption, although the covalent component is lower for oxides: except silicates, most of them include alkali, alkali-earth, or rare-earth elements as cations, which display higher electronegativity difference with oxygen compared to transition metals and sulphur. Otherwise, anionic collectors can be studied under their neutral, *i.e.* protonated, form to avoid the problem of reactivity. In this case, researchers have demonstrated that a physisorption occurs, based on electrostatic interactions between the collector polar group and the surface cation. Actually, one of the main limitation using DFT periodic codes is that the system has to be electrically neutral, inducing that either an extra-electron or a counter-ion that will give an electron to the anionic reagent must be added to the system.

The adsorption of anionic collectors has been mainly investigated on semi-soluble salt minerals since they constitute sources for some critical raw materials. For instance, researchers have studied the adsorption mechanisms of anionic collectors, mostly carboxylate and hydroxamate, by DFT onto rare-earth minerals (E.R.L. Espiritu et al., 2018; Espiritu et al., 2019; Sarvaramini et al., 2016a), onto scheelite (Cooper and de Leeuw, 2004; Yin et al., 2015; Zhao et al., 2013), cassiterite (SnO_2) (Gong et al., 2017; J. Liu et al., 2017; Tian et al., 2018), apatite (Mkhonto et al., 2006; Xie et al., 2018), hematite (Chernyshova et al., 2011; Rath et al., 2014b), and fluorite (de Leeuw and Cooper, 2003b). In addition, AIMD simulations can be performed to assess the influence of the temperature on the adsorption mechanisms (bond lengths and angles, molecule steric configuration, adsorption energy, adsorption geometry…). Notably, the adsorption of fatty acids under their anionic form can be impacted by the temperature. Finally, water molecules should be added under the form of an explicit solvent to consider the effect of the liquid phase on all the studied parameters.

The use of molecular modelling in flotation is tremendously increasing and will be, in the future, a crucial tool to attain the flotation performances required for the processing of low-grades fine-grained complex ores by predictive calculations. In particular, it can allow to unravel the synergistic effects observed empirically in flotation experiments and to gain understanding in the fundamentals of flotation reagents adsorption onto mineral surfaces.

3. Objectives

Considering the above-described literature and the mineralogical composition of the Tabuaço skarn, presented in Chapter 2, the processing of this tungsten skarn can be based on a Falcon gravity separation and a flotation separation. Nowadays, few routes exist for efficient industrial-scale scheelite flotation in presence of gangue calcium salts and silicates. Though amine collectors demonstrated acceptable performances, they are known to float silicates due to their physisorption on negatively-charged surfaces. Since silicates represent 85%-95% of the Tabuaço ore, the use of amines seems unsuited to attain a good selectivity. Another method consists of the utilisation of hydroxamic acids, mainly benzohydroxamic acid, in combination with lead cations. Nevertheless, in the EU, benzene-based compounds are forbidden and the industrial use of lead is strictly restricted, making this method impossible to apply for the Tabuaço deposit. The last proofed and widely used route was the flotation with fatty acids as collectors, especially sodium oleate, which are very efficient, cheap, and environment-friendly. Their high efficiency is attributed to the chemisorption of the carboxylate group onto surface calcium atoms (see section 2.2.3). However, tungsten skarns, including the two mineralised layers of Tabuaço deposit, particularly the Main Skarn (see Chapter 2), commonly display high amounts of calcium-bearing minerals, either calcium silicates or calcium semi-soluble salts (fluorite, apatite, calcite, and scheelite), these latter exhibiting similar surface properties (Table 3).

Table 3. Calculated calcic sites densities and surface Ca-Ca distance on the main cleavage planes for each studied mineral.

Mineral	Cleavage planes (according to literature)		Ca-Ca distance (Å)	$d(Ca^{2+})$ $(Ca/Å^2)$
Scheelite	(112)	(Gao et al., 2013; Hu et al., 2012)	3.87	4.01×10^{-2}
	(001)	(Gao et al., 2013; Hu et al., 2012)	5.22	3.67×10^{-2}
Fluorite	(111)	(Parks and Barker, 1977)	3.86	7.75×10^{-2}
Apatite	(001)	(Chang et al., 1996)	3.96	4.58×10^{-2}
Calcite	(101)	(Chang et al., 1996)	4.05	3.38×10^{-2}
	(104)	(Chang et al., 1996)	4.05	4.58×10^{-2}

Flotation separation of calcium minerals with fatty acids is difficult: their chemisorption onto the surface calcium atoms along with the similar surface properties between the minerals (Table 3) generally induce a non-selective flotation. The flotation selectivity can be improved by using the Petrov's process: developed in the 1930s and still very used in Russia and China, it consists of heating the rougher flotation concentrate at 80°C with a considerable Na_2SiO_3 concentration (Petrov, 1940). Nonetheless, it implies significant energetic costs and would not be suitable for the EU. Besides, different solutions can be undertaken to improve the elimination of calcium-bearing minerals during the mineral processing stage while maintaining a high level of environment-friendliness:

(1) The minerals commonly contained in tungsten skarns, including the Tabuaço skarn, exhibit a large range of specific gravities: 2.7 for calcite, 3.2 for fluorite and apatite, and 6.1 for scheelite while silicates have specific gravities between 2.6 and 3.7, depending on the geological context. Hence, it allows one to perform a gravity separation to eliminate the minerals that are problematic in flotation with fatty acids, mostly the calcium-bearing semi-soluble salts (calcite, apatite, and fluorite). Based on the literature review (see section 2.1), Falcon concentrators can achieve an efficient density separation on skarn ores such as the Tabuaço ore. Therefore, the Falcon separation should be deeply investigated in terms of separation mechanisms and optimised to maximise the rejection of the problematic calcium salts.

(2) Additionally, skarns commonly contain iron that is found within the ferromagnesian silicates of the protolith. After the thermometamorphism stage, iron is often included in the newly-formed dense silicates such as vesuvianite, epidote, and garnets. Due to the iron they contain, these silicates, which are denser compared to the non-ferromagnesian silicates, exhibit significant magnetic susceptibility, ranking them in the paramagnetic minerals class. Hence, a high intensity magnetic separation is possible to eliminate these minerals that can represent high amounts in the tungsten skarns, including the Tabuaço skarn.

(3) In flotation, depressants can be added to enhance the separation differential between scheelite and the troublemaking minerals. Nevertheless, although silicates are quite easily depressed, very few depressants are selective between scheelite and fluorite, apatite, and calcite. Hence, intensive developments should be done to find efficient and environment-friendly depressing conditions as well as to gain understanding in the adsorption mechanisms of the selected depressants onto calcium minerals.

(4) Considering the similar surface properties between scheelite and the other calcium minerals, the modulation of flotation collectors appears very difficult to separate scheelite from the other calcium minerals. According to recent developments, the flotation selectivity regarding the above-mentioned gangue minerals can be enhanced using collector mixtures (anionic/anionic or anionic/non-ionic), which exhibited satisfactory results in terms of flotation selectivity. Therefore, these collector mixtures should be intensively investigated to modulate the flotation selectivity in favour of scheelite and to gain understanding in the synergistic effects that they can exhibit.

The four above-mentioned points should be thoroughly investigated in this work to develop an efficient, adaptable, integrated, and environment-friendly process for the Tabuaço tungsten skarn. Besides, the froth flotation process is led by the adsorption of various reagents, organic or mineral, at the liquid/solid interface, with the objective of selectively rendering the target mineral(s) hydrophobic to recover it in the froth phase. Collectors, which contain a polar group and a non-polar aliphatic chain, can be adapted in terms of chain length, unsaturation, and ramification, as well as functionalised polar group. Moreover, all reagents can be combined to improve the flotation performances (selectivity or target mineral(s) recovery). All these optimisations are difficult to investigate by experimental methods and molecular modelling is a

powerful tool to gain understanding in the adsorption mechanisms of flotation reagents at the mineral surfaces. Two main methods are widely used, force-fields-based (CMD) and *ab initio* simulations (DFT), with significant differences in accuracy, considered phenomena, computational costs, system sizes and simulation times. One should adapt the atomistic method to the flotation system, mostly to the collector. In the present study, *ab initio* atomistic simulations will be applied to gain understanding in the fundamentals of fatty acids adsorptions onto calcium minerals and to unravel the synergistic effects highlighted when different reagents are combined together (either depressants or collectors).

Materials and methods

1. The Tabuaço Skarn ore

    1.1 Sampling

A diamond drill campaign was performed by Colt Resources on the Tabuaço deposit to establish the 3D geological model of the ore body. Based on these preliminary studies, a sampling campaign was organised to acquire around 500 kg on each outcropping skarn layer (Main and Lower Skarns) for mineralogical characterisation and subsequent metallurgical test work (Figure 23). The acquired samples were as representative as possible of the two outcropping layers and it was assumed that they were also representative of the whole deposit.
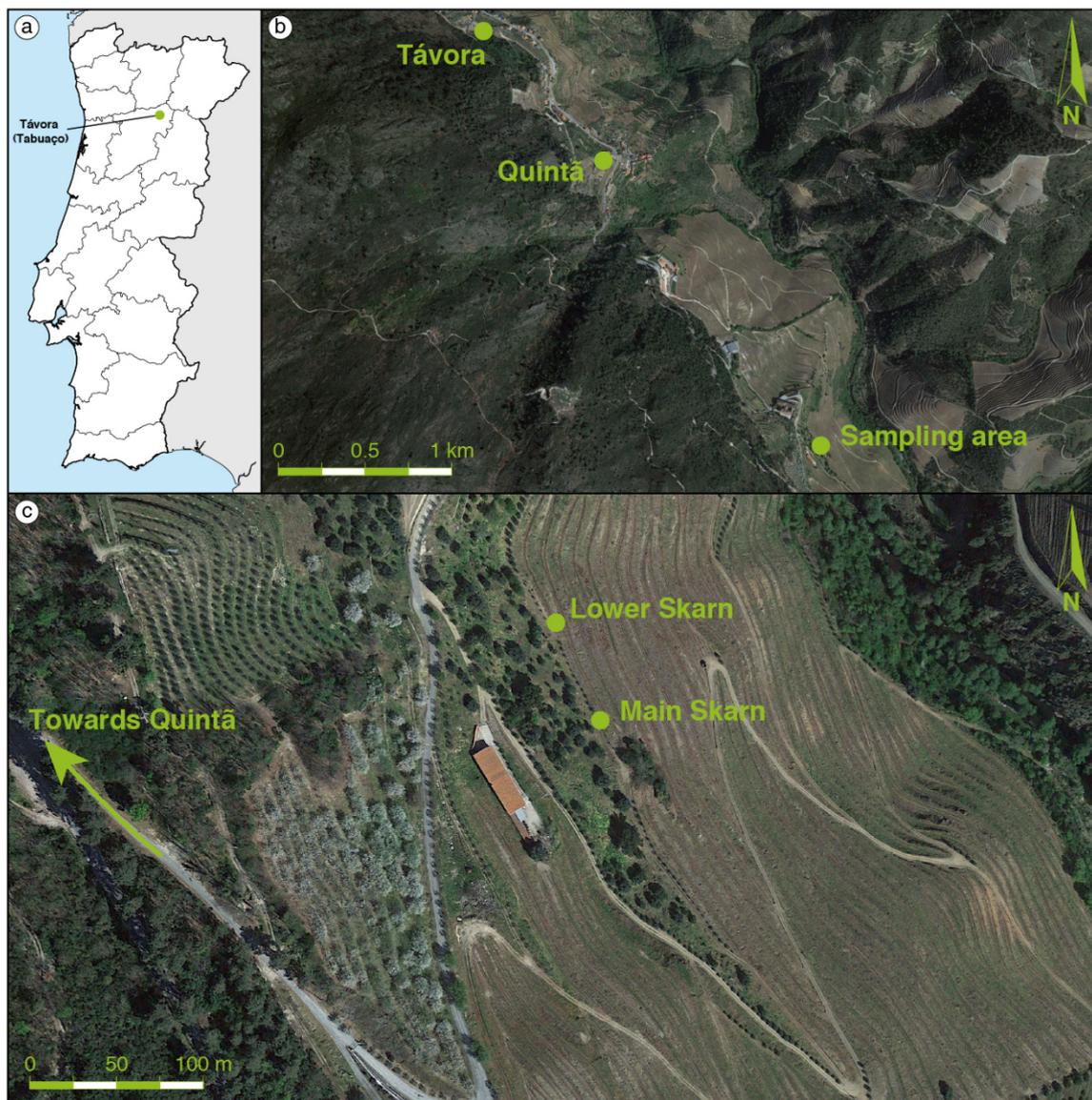
Figure 23. Location of the sampling area and the two sampled outcrops. **a.** Location of Távora, part of Tabuaço city, in Portugal. **b.** Location of the sampling area in relation to Távora and Quintã, the two closest towns, part of Tabuaço city. **c.** Exact locations of the two sampled outcrops, corresponding to the Lower Skarn and Main Skarn, in relation to the road going to Quintã. Satellite images from Google Earth.

1.2 Chemical analyses

Prior any crushing, milling, or separation tests, the Tabuaço Main and Lower Skarn layers were characterised in terms of chemical contents. For this characterisation, chemical analyses were carried out by Inductively Coupled Plasma – Mass Spectrometer (ICP-MS) for the trace elements and by Inductively Coupled Plasma – Optical Emission Spectrometer (ICP-OES) for the major elements. Fluorine was analysed by direct potentiometry using a fluoride-ion sensitive electrode (ISE) and CO_2 with a C-S analyser. All these analyses were performed on representative pulverised samples at the accredited *Service d'Analyses des Roches et des Minéraux* (SARM-CNRS, Nancy, France).

Besides, for all the separation tests performed in this study, the products (concentrates and tailings) were systematically dried, weighted, riffle-split to sample representative aliquots, and analysed in terms of chemical contents. Some of the preliminary tests performed during this work along with samples used in the above-mentioned characterisation were analysed by Inductively Coupled Plasma – Mass Spectrometer (ICP-MS) for the trace elements and by Inductively Coupled Plasma – Optical Emission Spectrometer (ICP-OES) for the major elements. The chemical contents of these samples were also measured by Energy Dispersive X-Ray fluorescence spectroscopy (ED-XRF) using a Niton™ XL3t (Thermo Scientific) portable analyser. This latter allowed to analyse W, K, Fe, Ca, P, and Si contents with a good accuracy on heavy elements and a moderate accuracy for lighter elements such as Si. The samples analysed by ICP-MS/OES and by ED-XRF were selected to display a wide range of chemical contents. Based on these results, correlations were established between the chemical contents measured by ICP-MS/OES and those measured by ED-XRF spectroscopy. The calibration models are presented in Figure 24. The model functions were chosen to optimise both the squared correlation coefficient (R^2) and the root mean square error (RMSE). Three models were simple linear regressions and two models included quadratic terms (Figure 24). The last calibration curve, for tungsten, was defined on a very large domain, ranging from around 0% to around 55% W. Therefore, a power model suited best the raw data and was selected, with however a power close to 1. All the six developed models exhibited very good correlations with $R^2>0.99$ and very low absolute average errors (AAE), see Figure 24. This value traditionally assesses the error that can be done when the content is predicted by the model, a low value thereby indicating a low error on the prediction.

71
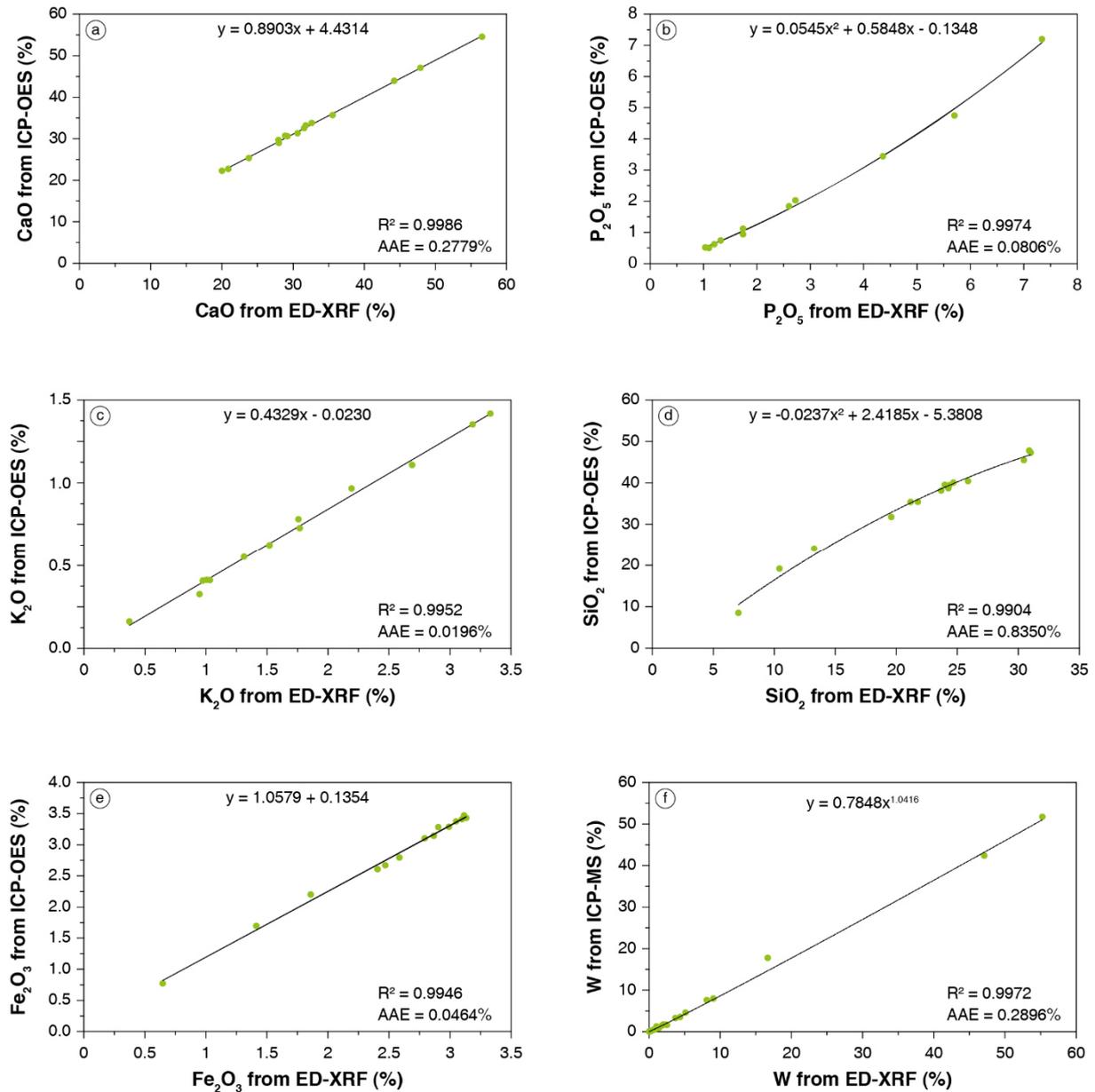
Figure 24. CaO (a), P_2O_5 (b), K_2O (c), SiO_2 (d), Fe_2O_3 (e), and W (f) contents measured by ICP-OES/MS as a function of the same contents measured by ED-XRF using a Niton™ XL3t (Thermo Scientific) portable analyser. The graphs display the model developed on the data, their squared correlation coefficient (R^2), and their absolute average error (AAE). This latter value assesses the error that can be done when predicting the content with the model.

All the chemical analyses performed for separations presented hereafter were carried out by ED-XRF and corrected using the calibrations presented in Figure 24. It allowed very fast analyses, since the ED-XRF spectroscopy commonly operates on powdered rocks, *i.e.* non-dissolved rocks, with a good accuracy induced by the calibration. The corrected WO_3, P_2O_5, SiO_2, Fe_2O_3, and K_2O contents (and recoveries) were used as proxies to assess the separation performances in terms of scheelite, apatite, undifferentiated silicates, iron-bearing silicates (which are also the dense silicates), and feldspars (which represent the major part of the light and non-iron-bearing silicates), respectively. Besides, since the most problematic mineral in flotation

was fluorite, the F content must have been known fast and accurately to assess the flotation performances in terms of fluorite. Hence, 100 samples, selected from flotation tests and corresponding to flotation products (non-floated and floated), were analysed by ISE. These samples were also analysed by ED-XRF and their corrected WO_3, P_2O_5, SiO_2, K_2O, and CaO contents were used to develop a multivariate calibration. The Partial Least Squares Regression (PLS-R) methodology was employed to generate a model that predicted the F content from the corrected WO_3, P_2O_5, SiO_2, K_2O, and CaO contents measured by ED-XRF. The nonlinear estimation by iterative partial least squares (NIPALS) algorithm was used. The developed model was a multilinear function:

$$F = 0.9291 * CaO + 0.3178 * WO_3 - 0.3378 * P_2O_5 + 20.3919 * K_2O - 0.1667 * SiO_2 - 24.8677 \quad (8)$$

where F is the predicted F content and CaO, WO_3, P_2O_5, K_2O, and SiO_2 are the contents measured by ED-XRF and corrected according to the models developed. The final graph showing the predicted F contents as a function of the F contents measured by ISE is presented in Figure 25. For all the separations tests presented in this work, the F contents and, then, the F recoveries, in the products were calculated by using Eq. 8.
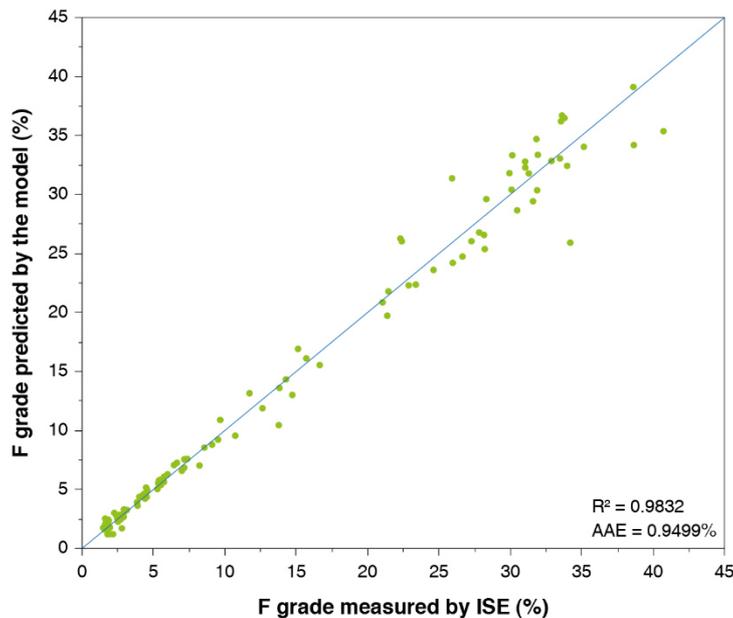
Figure 25. F contents predicted by the multivariate calibration as a function of the F contents measured by ISE. The blue line represents the y = x curve. AAE: Absolute Average Error, which assesses the error that can be done when predicting the F content with the model.

1.3 Mineralogical analyses

Textures and mineralogical associations were determined by optical microscopy, using a Nikon OptiPhot-2 that operates with transmitted polarised or cross-polarised light. The microscope was equipped with a camera to record high-resolution micrographs. Also, all the mineralogical observations and determinations were confirmed by electron microscopy, using a Hitachi S-4800 scanning electron microscope (SEM) operated with an acceleration voltage of

15 kV. This apparatus was equipped with a ED-XRF modulus, which allowed semi-quantitative *in-situ* non-destructive chemical analyses to estimate the chemical formulas of the minerals identified by optical microscopy. A CAMECA SX100 Castaing electron microprobe with an acceleration voltage of 15 kV was employed to determine the accurate structural formulas of all the minerals identified by optical and electron microscopy. Besides, X-ray diffraction (XRD) analyses were performed on the Lower Skarn and Main Skarn levels. The diffractometer used was a Bruker D8 Advance, which was operated with a cobalt anode (1.789 Å), a voltage of 35 kV, and a current of 45 mA. All the XRD data were interpreted using the DIFFRAC.EVA software, supplied by Bruker.

1.4 Particle size analyses

Particle size analyses were performed following two distinct techniques depending on the use of the size fraction. When the contents of each size fraction had to be separated for further analyses, particle size analysis was performed using a Rotap apparatus and a standard laboratory wet and dry sieving procedure (ISO 2591-1:1988). Alternatively, more detailed particle size analyses were obtained by laser light scattering using a Helium-Neon Laser Optical System Mastersizer 3000 (Malvern instruments Ltd.). The samples were introduced in a beaker coupled with a Hydro Extended Volume (EV), equipped with a dip-in centrifugal pump and a stirrer, until the desired obscuration level (up to 20%) was reached. The dispersed sample then passed through the measurement area of the optical bench, where a laser beam illuminated the particles. The obtained particle size distributions were systematically the average of 5 duplicate measurements.

1.5 Mineralogical characterisation of the ore

1.5.1   Geochemistry of the mineralised layers

First, chemical analyses, according to the procedure described in section 1.2, were carried out on the two skarn units, which are significantly different in terms of geochemistry: the Lower Skarn exhibits higher contents in SiO_2, in Fe_2O_3, and in MgO but lower contents in CaO, in F, in P_2O_5, and in WO_3 (Table 4). These differences can be related to their distance to the granite intrusion since the Lower Skarn is further away from the granite than the Main Skarn (see Chapter 1). It can also be attributed to significant differences in the protoliths chemistry: the Lower Skarn probably derives from a more-siliceous rock while the Main Skarn from a more-calcareous rock (Table 4).

1.5.2   Optical microscope analyses

Based on the optical microscope observations, the Main Skarn is composed of silicates (85 wt.%), mostly calcium-bearing silicates (vesuvianite, zoisite, and grossular) and, to a lesser extent, feldspars and quartz (Figure 26).
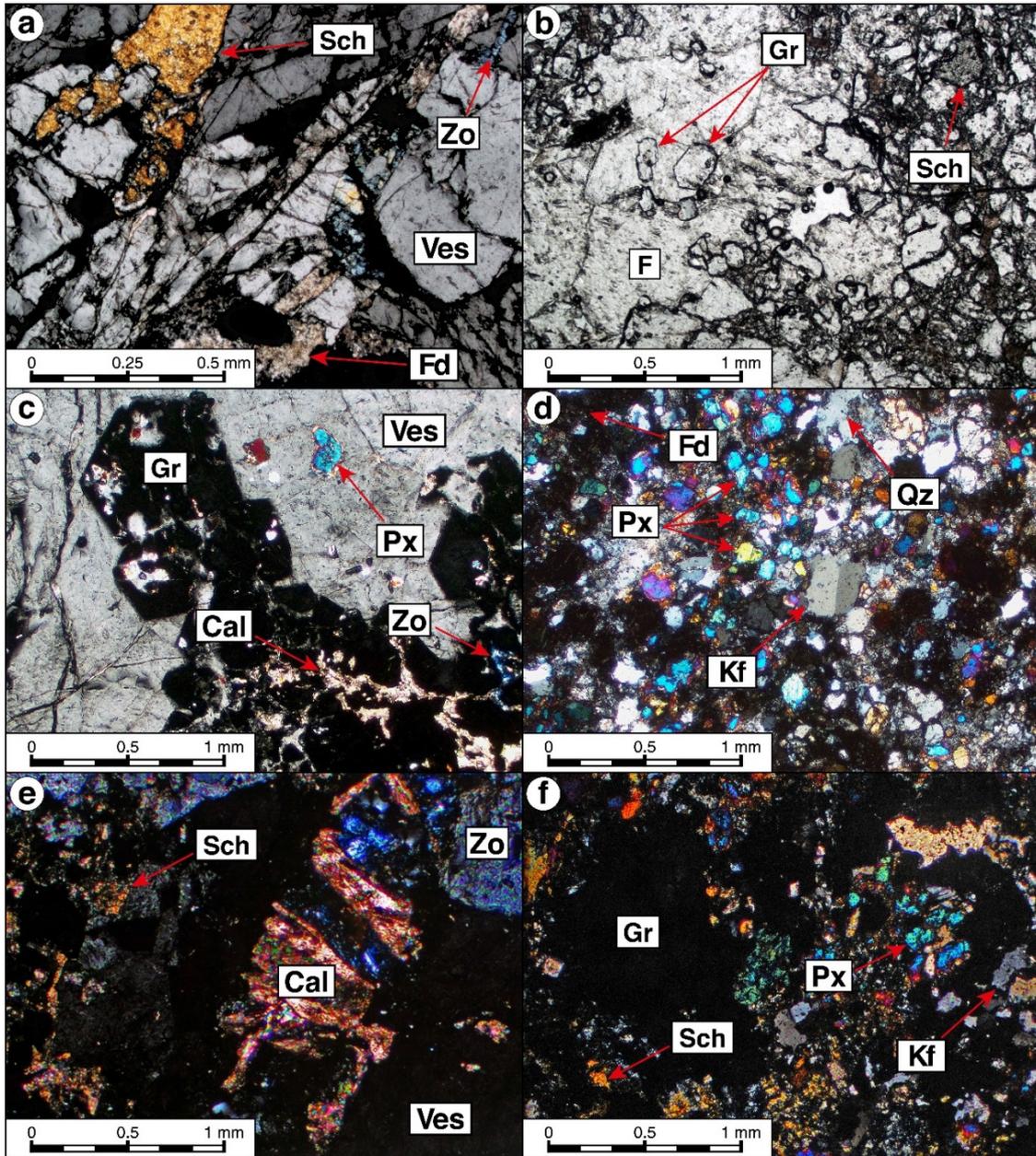
Figure 26. Micrographs of thin sections of Main Skarn layer (a, b, and c) and Lower Skarn layer (d, e, and f) observed under cross-polarised light (a, c, d, e, and f) and polarised light (b) with optical microscopy. Sch = Scheelite; F = Fluorite; Ves = Vesuvianite; Zo = Zoisite; Gr = Grossular; Px = Pyroxene; Cal = Calcite; Qz = Quartz; Fd = undetermined feldspars; Kf = K-feldspars.

The remaining fraction comprises fluorite, apatite, and scheelite. The calcium-bearing silicates such as vesuvianite, grossular, and zoisite constitute common gangue minerals in skarns since they form at high calcium and silica activities in fluids (Dawson, 1996; Kwak, 1987). Zoisite is part of the epidote group (calcic alumino-silicate) while grossular represents the alumino-calcic pole of garnets, which are both usually encountered in tungsten skarns (Dawson, 1996; Kwak, 1987). Besides, the Main Skarn presents massive coarse-grained textures with grain sizes varying from few micrometres to more than one centimetre. Scheelite is often finely disseminated and

75

rarely laminated, overprinting sedimentary structures. It forms 5 to 300 µm anhedral crystals with an average size of 150 µm, which constitutes the liberation size for the Main Skarn. Very close mineral associations are exhibited between scheelite and fluorite/vesuvianite with a significant proportion of intergrowth crystals. Moreover, pervasive albitisation of the skarn horizons, principally the Main Skarn, affects the whole mineralogical association including scheelite and can induce significant proportions of intergrowth crystals.

The Lower Skarn contains mostly silicates (95 wt.%) including significant amounts of vesuvianite, grossular, calcic pyroxene (diopside/hedenbergite), zoisite, quartz, and feldspars (Figure 26). This layer is poorer than Main Skarn in terms of calcium-bearing salts, displaying low levels of fluorite, apatite, and scheelite. However, higher contents of calcite are exhibited in this facies as well as a few sulphides, mainly arsenopyrite, pyrite, and pyrrhotite. Sulphides were not identified in the Main Skarn level, which is also very poor in terms of pyroxene compared to the Lower Skarn level. This latter displays finer textures (Figure 26) and, thus, finer scheelite liberation size, estimated at around 100-120 µm by optical microscopy.

1.5.3 X-ray diffraction

On the Main Skarn level, XRD analyses allowed to identify precisely scheelite, fluorite, fluorapatite, and possibly calcite in terms of semi-soluble salts. Moreover, vesuvianite, grossular, pyroxene (most probably diopside), and zoisite have been clearly identified as well as the three feldspars (anorthite, albite, and orthoclase), chamosite (part of the chlorites group), muscovite, and quartz. The same minerals were identified in the Lower Skarn with, however, probably different relative amounts compared to the Main Skarn since the relative intensities of the peaks are significantly different between the two diffractograms. Hence, XRD analyses confirmed the mineralogical composition determined previously by optical microscopy.

1.5.4 Summary

The geological, geochemical, and mineralogical characteristics of the two mineralised levels are summarised in Table 4. Most of the mineralogical identifications were confirmed by Castaing electron microprobe, which also allowed to determine structural formulas for all the minerals encountered in the Tabuaço skarn. Besides, the molybdenum content in scheelite, which constitutes a solid solution with the calcium molybdate (powellite, $CaMoO_4$), has been measured with the Castaing electron microprobe and is very low, with an average of 0.029 % MoO_3. Molybdenum is a strong pollutant for the metal-tungsten products and has to be as low as possible. Hence, the molybdenum content in scheelite is crucial and determines the deposit quality: molybdenum and tungsten exhibit similar behaviours during the hydrometallurgy stage and, when molybdenum is included in scheelite, it cannot either be separated from tungsten during the mineral processing stage.

Table 4. Summary of the main geological, geochemical, and mineralogical characteristics of the Main and Lower skarns.

Characteristics		Main Skarn	Lower Skarn
Geological			
Mineralisation		Disseminated and laminated scheelite	Disseminated scheelite
Protolithic geochemistry		CaO>SiO$_2$	CaO<SiO$_2$
Average scheelite grain size		180 µm	120 µm
Geochemical		wt.%	wt.%
WO$_3$		1.13	0.28
SiO$_2$		41.17	47.25
Al$_2$O$_3$		17.83	17.14
Fe$_2$O$_3$		2.41	6.06
MgO		1.82	2.31
CaO		27.28	21.38
Na$_2$O		1.72	1.86
K$_2$O		1.11	0.94
P$_2$O$_5$		1.05	0.33
F		4.05	1.47
Mineralogical		wt.%	wt.%
Vesuvianite	Ca$_{10}$(Mg,Fe)$_2$Al$_4$(SiO$_4$)$_5$(Si$_2$O$_7$)$_2$(OH)$_4$	55	35
Feldspars	(Na,K)AlSi$_3$O$_8$	15	10
Fluorite	CaF$_2$	10	3
Zoisite	Ca$_2$(Al,Fe)$_3$(SiO$_4$)$_3$(OH)	5	10
Grossular	Ca$_3$(Al,Fe)$_2$(SiO$_4$)$_3$	5	3
Clay minerals	N/A	5	5
Fluorapatite	Ca$_5$(PO$_4$)$_3$F	3	1
Quartz	SiO$_2$	1	10
Muscovite	KAl$_2$(AlSi$_3$O$_{10}$)(OH,F)$_2$	1	1
Pyroxene	Ca(Mg,Fe)Si$_2$O$_6$	1	20
Scheelite	CaWO$_4$	1	0.50
Calcite	CaCO$_3$	<1	2

1.6 Ore preparation for separation tests on Main Skarn

Based on the above-mentioned mineralogical characterisation, the Main Skarn seemed the most challenging level since it displayed a complex gangues with significant amounts of fluorite, apatite, and calcium silicates along with a moderately low liberation size. Hence, all the developments presented hereafter were carried out on the Main Skarn level while very few tests were performed on the Lower Skarn (not presented here). The liberation size was estimated at 150 µm by optical microscopy for the Main Skarn. It indicated that the comminution stage had to be adapted to roughly reach this particle size, at which most particles are constituted by only one mineral. Hence, the samples were crushed in three successive jaw crushers and a gyratory

crusher to produce a -4+0 mm fraction (Figure 27). To avoid any over-grinding, the ground material was sieved and only the +150 µm material was then fed to a laboratory ball mill to reach the liberation size (Figure 27). This latter was fed with 1 kg of +150 µm material, 10 kg of steel balls of various sizes, and 500 g of tap water, *i.e.* at 66 wt.% solids in pulp, for each milling stage that lasted 6 min. Some of the separation tests performed in this work had to be conducted on deslimed products, in particular flotation and wet magnetic separation tests (Figure 27). For these tests, the -150+0 µm product, after milling, was deslimed using a 50 mm hydrocyclone. A vortex finder of 11 mm and an apex aperture of 3 mm was used, with a theoretical cut size of 7 µm. The hydrocyclone was fed at a constant pressure of 2 bar and a constant pulp flowrate of 20 L.min^{-1} with a pulp density of 5 wt.% solids. Besides, since the desliming efficiency of the Falcon concentrator was investigated in the present study, the feed, corresponding to the -150+0 µm product, was not deslimed prior the Falcon tests.
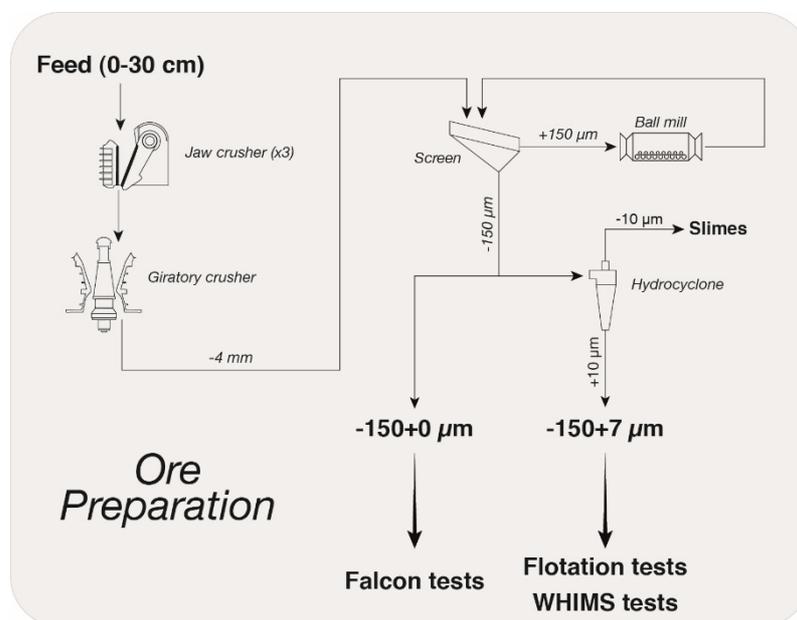
Figure 27. Schematic diagram showing the ore comminution for preparation of -150+0 µm and -150+7 µm products, used for metallurgical test work, from the Main Skarn blocs sampled in Tabuaço.

1.7 Material characterisation for separation tests

The products were characterised in terms of particle size distributions (PSD) and chemical contents per size fraction after the crushing the stage, to adapt the milling, and after the milling stage to assess the minerals distributions in the different size fractions for the separation tests. The PSD of the -4+0 mm product, corresponding to the crushed ore obtained after the gyratory crusher is presented in Figure 28a. This product exhibited a d_{80} of around 2.2 mm and a d_{20} of around 150 µm indicating that, after the crushing stage, 20 wt.% of the total product was finer than 150 µm (Figure 28a). Moreover, around 10 wt.% of the product was finer than 63 µm (Figure 28a), which represented an acceptable value considering the global objective to avoid the production of fine particles that could comprise significant amount of scheelite.
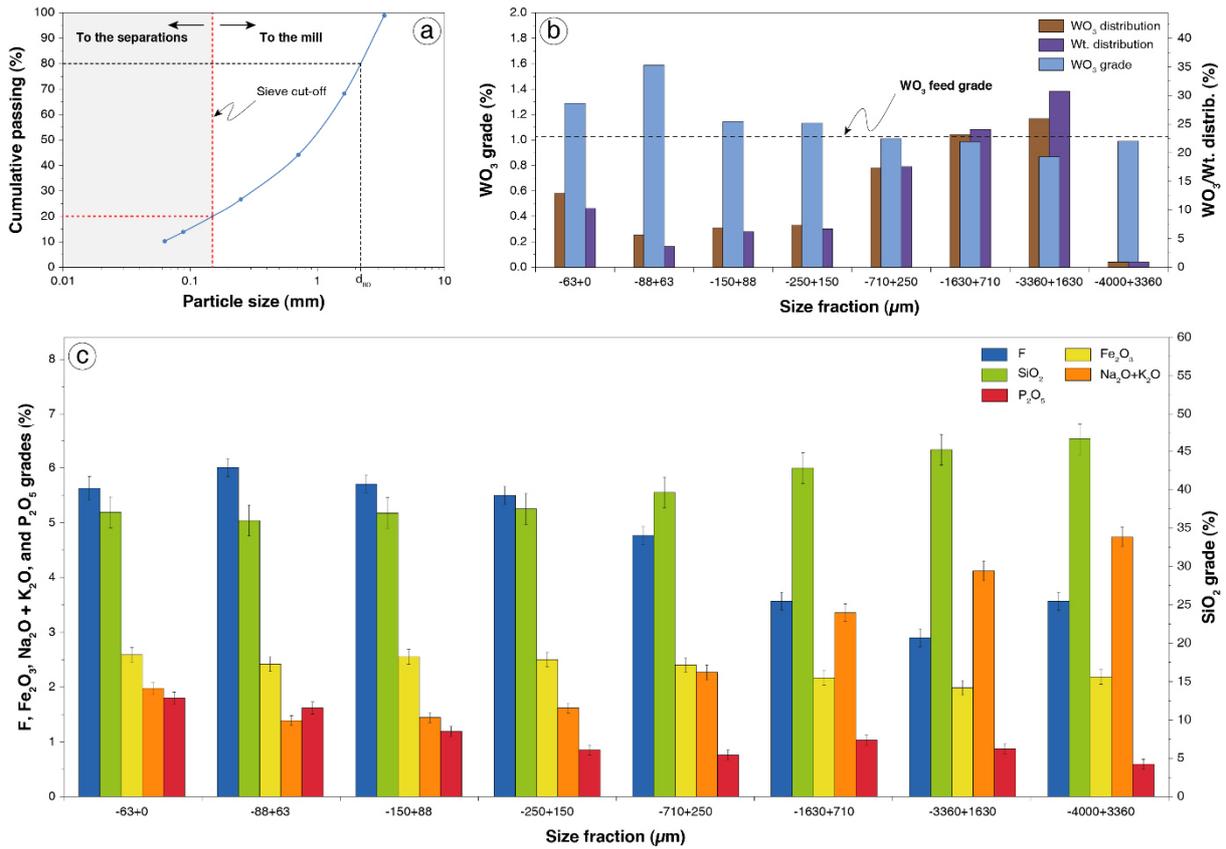
Figure 28. **a.** PSD of the Main Skarn Tabuaço ore after the crushing stage and before the milling stage. The size cut-off applied by the sieve before the crushing stage is displayed as well as the d_{80} of the product, corresponding to the size which 80 wt.% of the particles are finer than. **b.** WO_3 grade, WO_3 distribution, and wt.% retained for each size fraction of the crushed product (0-4 mm), after the gyratory crusher. Since the WO_3 grade was measured by ICP-MS, the error bars are not displayed considering the accuracy of this method. **c.** F, SiO_2, Fe_2O_3, $Na_2O + K_2O$, and P_2O_5 grades in each size fraction of the crushed ore, assessing the distributions of the main gangue minerals in the different size fractions. The error bars represent the average error claimed for each analysis method (ISE for F, ICP-AES for the other), which is roughly equivalent to 5% of the given value.

Besides, the WO_3 grade, WO_3 distribution (recovery) and wt.% retained for each size fraction of the crushed ore are presented in Figure 28b. The two finest size fractions, namely the -63+0 µm and the -88+63 µm exhibited significantly higher WO_3 grade although, considering their low wt.% retained, they represented together only 20% of the WO_3 total distribution. Based on Figure 28a and b, the -150+0 µm fraction, containing the -63+0 µm, -88+63 µm, and -150+88 µm fractions represented 20 wt.% of the total product and more than 20% of the total WO_3 distribution. Hence, the -150+0 µm size fraction was sent directly to the separation tests to avoid over-grinding of the above-mentioned 20% of the total scheelite content, considering the significant trend of scheelite to form fine particles. The ball mill was subsequently fed with the remaining 80 wt.% of the crushed product, as displayed in Figure 27. In addition, the gangue minerals distributions in the crushed ore were assessed by measuring the F, Fe_2O_3, $Na_2O + K_2O$, and P_2O_5 grades in each size fraction. They are presented in Figure 28c. Interestingly, F and

79

P_2O_5 contents, which represented the fluorine and the apatite contents, were significantly higher in fine fractions than in coarse fractions (Figure 28) while a reverse trend was observed for SiO_2 and $Na_2O + K_2O$ contents. This indicated that the silicate minerals were resistant during the crushing stage and tended to form coarse particles. Meanwhile, the Fe_2O_3 content was roughly constant over the different size fractions. Hence, it could be concluded that apatite, fluorite, and scheelite, display similar behaviours during the comminution, probably attributed to the fact that they are calcium salts with lower bond energies for Ca-O compared to Si-O in the case of silicates.

The above-described -4+0 mm product was then milled according to Figure 27, *i.e.* with the -150+0 µm size fraction sent directly to separation tests before milling. The PSD and chemical contents per size fractions for scheelite and other gangue minerals are displayed in Figure 29, for the deslimed ore, used for flotation/magnetic separation tests, and the non-deslimed ore, used for Falcon tests. The d_{80} of both products were around 100 µm (Figure 29a), which was acceptable considering the liberation size, estimated at around 150 µm. Consistently, the WO_3 grade was higher in the finest fractions (Figure 29b), due to the trend of scheelite to form fine particles, except for the hydrocyclone overflow (-7+0 µm), which could be attributed to the influence of the density on the hydrocyclone separation mechanisms. Around 8.5% of the scheelite content was distributed in the (-7+0 µm) (Figure 29b), which was considered as lost according to Figure 27 in flotation/magnetic separations tests. Nevertheless, this product was enriched in terms of alkaline ($Na_2O + K_2O$), SiO_2, and Fe_2O_3 contents (Figure 29c), probably due to the above-mentioned phenomenon in the hydrocyclone. Besides the hydrocyclone overflow, the P_2O_5 and F contents were higher in the finest particles, indicating the same trend than observed before regarding fluorite and apatite (Figure 29c). Albeit $Na_2O + K_2O$ and Fe_2O_3 were higher for the -20+7 µm size fraction, they globally increased with the particle size, as well as the SiO_2 content (Figure 29c).
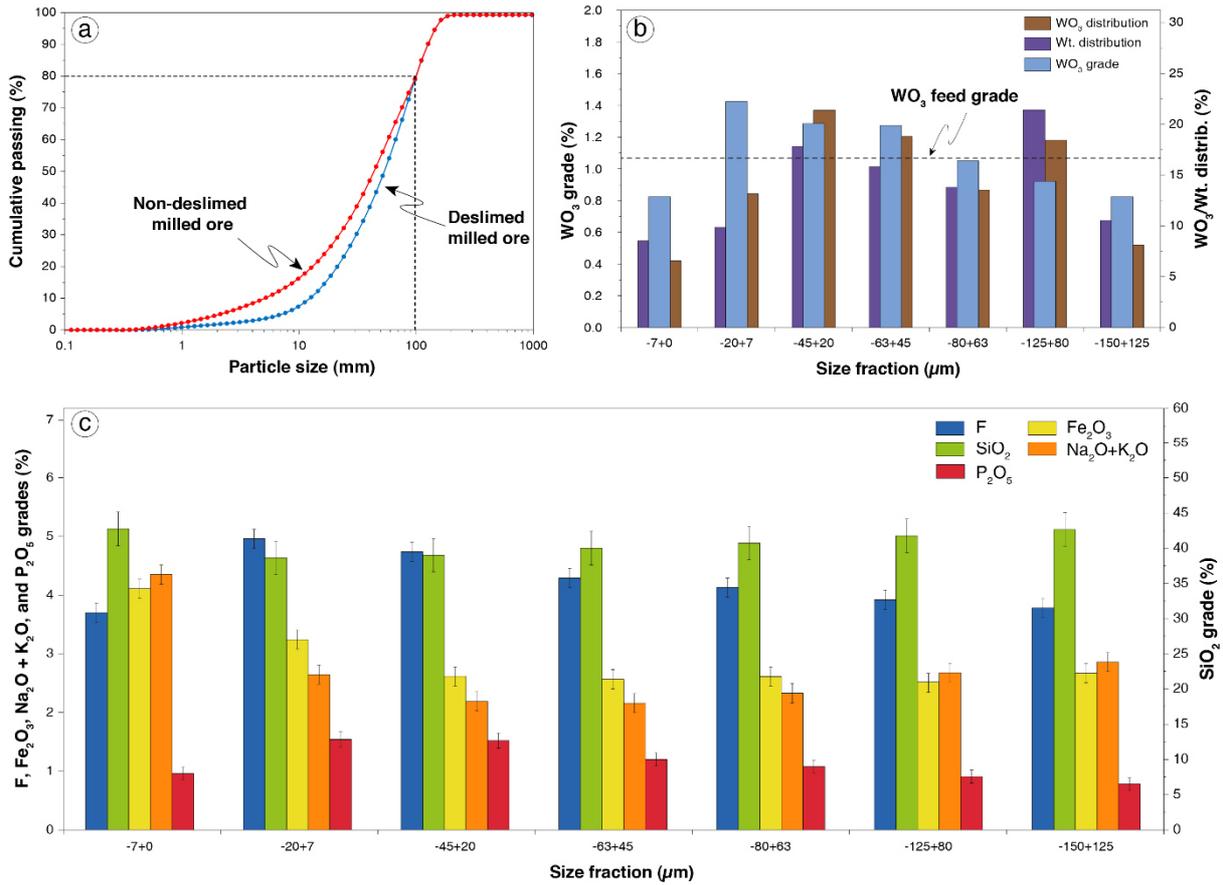
Figure 29. **a.** PSD of the Main Skarn Tabuaço ore after the milling stage, for the deslimed ore and the non-deslimed ore (used for Falcon tests). The dashed line shows the d_{80} of the two products. **b.** WO_3 grade, WO_3 distribution, and wt.% retained for each size fraction of the milled product (-150+0 µm). Since the WO_3 grade was measured by ICP-MS, the error bars are not displayed considering the accuracy of this method. **c.** F, SiO_2, Fe_2O_3, $Na_2O + K_2O$, and P_2O_5 grades in each size fraction of the milled ore, assessing the distributions of the main gangue minerals in the different size fractions. The error bars represent the average error claimed for each analysis method (ISE for F, ICP-AES for the other), which is roughly equivalent to 5% of the given value. For **b** and **c**, the -7+0 µm product corresponds to the hydrocyclone overflow when the ore was deslimed.

1.8 Scheelite beneficiation tests

1.8.1   Falcon gravity separation

The Falcon concentrator used in this work was a Falcon L40 laboratory model (Sepro Mineral Systems, Canada). Tests were performed with the two bowl types, *i.e.* the 4" smooth-walled Falcon UF bowl and the Falcon SB bowl (for further explanations, see Chapter 1), to compare their efficiency. During the tests, the feed slurry, constituted by the -150+0 µm product, was kept homogeneous and the feed flowrate, called pulp flowrate hereafter, maintained constant (Figure 30). In addition, a by-pass was placed at the output of the feed tank to allow operating in closed circuit during feed preparation, for pulp density adjustment and flowrate control. Feed

81

dry weight was set at 500 g for both Falcon UF and Falcon SB, based on saturation tests (not presented here), which allowed to set the maximum feed weight to work with to avoid saturation of the bowl
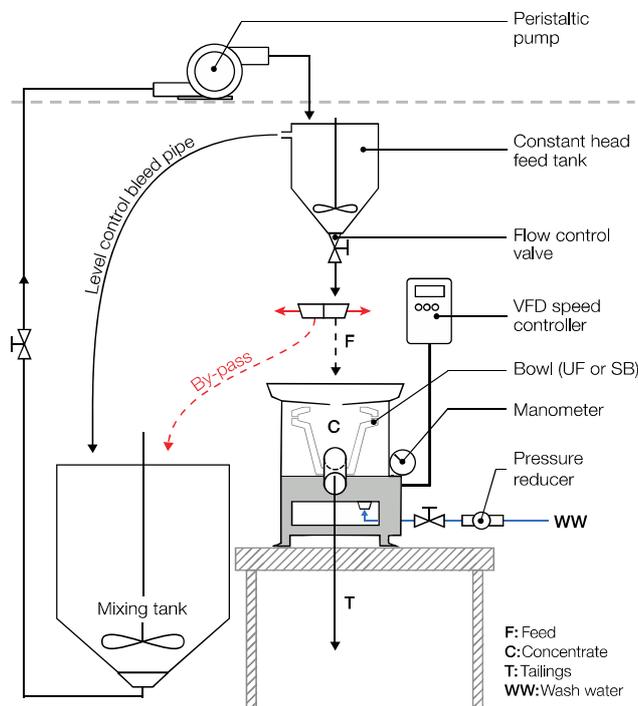
Figure 30. Experimental setup for Falcon L40 testing. Note that wash water (WW) is only used for Falcon SB testing.

1.8.2   Froth flotation

Reagents

In the present study, many different flotation reagents were tested to define optimal flotation conditions for the Tabuaço Main Skarn ore. First, sodium hydroxide (NaOH) and sodium carbonate (Na_2CO_3) were used as pH modifiers to compare their effects on flotation performances. They were of technical quality (>99%) and were supplied by Sigma Aldrich. The same NaOH was also used for collector preparation. Then, several types of depressants were tested in flotation to efficiently depress the gangue minerals with a strong focus on fluorite. Organic molecules [tannin, carboxymethyl cellulose (medium), lignin sulfonate, citric acid, and starch (from corn)], sodium silicate (Na_2SiO_3), and metallic cations [$FeSO_4$, $ZnSO_4$, and $Al(NO_3)_3$] were used as depressants, in some instances in combination with each other. They were all of technical quality (>99%) and all supplied by Sigma Aldrich except citric acid (Fisher Chemicals), tannin (VMR Prolabo), $FeSO_4$ (VMR Prolabo), $ZnSO_4$ (ACROS), and $Al(NO_3)_3$ (Fisher Chemicals). The Na_2SiO_3 used in this study was a solution at 35.1% $Na_2O + SiO_2$, with a $Na_2O:SiO_2$ ratio of 0.3:1. However, all the dosages given hereafter are in pure Na_2SiO_3. Besides, the flotation collectors used in the present study were fatty acids, *i.e.* carboxylic acids with linear aliphatic chains containing between 12 and 18 carbon atoms. Four

different commercial Tall Oil Fatty Acids (TOFA), by-products of the Kraft paper process, were used as collectors for the flotation tests. The three first TOFA were RBD2, RBD15, and RBD30, supplied by MeadWestvaco, composed of oleic acid, linoleic acid, and negligible amounts of palmitic and linolenic acids (for further details about their composition, please report to Chapter 5). The second collector, named LD, was roughly the same but with a significantly higher quantity of saturated fatty acids, namely palmitic and stearic acids. The fatty-acid-based collectors were prepared in aqueous conditions at alkaline pH to obtain the dominance of the carboxylate form, *i.e.* deprotonated (anionic) form, of fatty acids (for further explanations, see Chapter 1). The pKa of these latter being around 5, a solution at pH moderately alkaline was enough to obtain the anionic forms of fatty acids. This alkaline pH was obtained via the addition of the above-mentioned sodium hydroxide in slight excess compared to the fatty acids considering the deprotonation reaction. Moreover, the solution was heated to 60°C during all the preparation process to increase the kinetics of the deprotonation reaction by raising the fatty acids solubility. Besides, pure isotridecanol (>99.5%), supplied by CECA, was used as a co-collector. For all the reagents preparations, deionised water was used (R = 18.2 MΩ·cm). In some instances, A65 (polypropylene glycol), supplied by Solvay, was used as a frother.

Tests

The flotation tests were realised in Agitair® LA-500 rotor-stator apparatus with a 1.5 L cell (Figure 31) fed with 500 g of -150+7 µm material, according to Figure 27 (for the material characterisation, see section 1.7). The rotational speed in the cell was set at 900 rpm during conditioning and flotation, with a solid-liquid ratio of 33 wt.%. The samples were conditioned in the cell with tap water at pH 9.5-10 for 1 min, with the depressant for 2–5 min (depending on the depressant type), and with the collector for 3 min. In tests involving the addition of metallic cations and sodium silicate, the cations were systematically added to the mixture prior to Na_2SiO_3. In tests involving LD, 5 g/t of A65 were introduced 1 min before the beginning of the flotation process. The pH was maintained to 9.5-10 during the whole conditioning stage by adding NaOH. The tests (conditioning and flotation) were carried out at room temperature (20-26°C). During the flotation process, the airflow was set at 0.27 m^3/h and the froth was recovered at 2 s intervals for 3 min. Repeatability tests were performed and allowed to determine an average error made on the flotation tests. This error was used to calculate the error bars displayed on the results graphs.
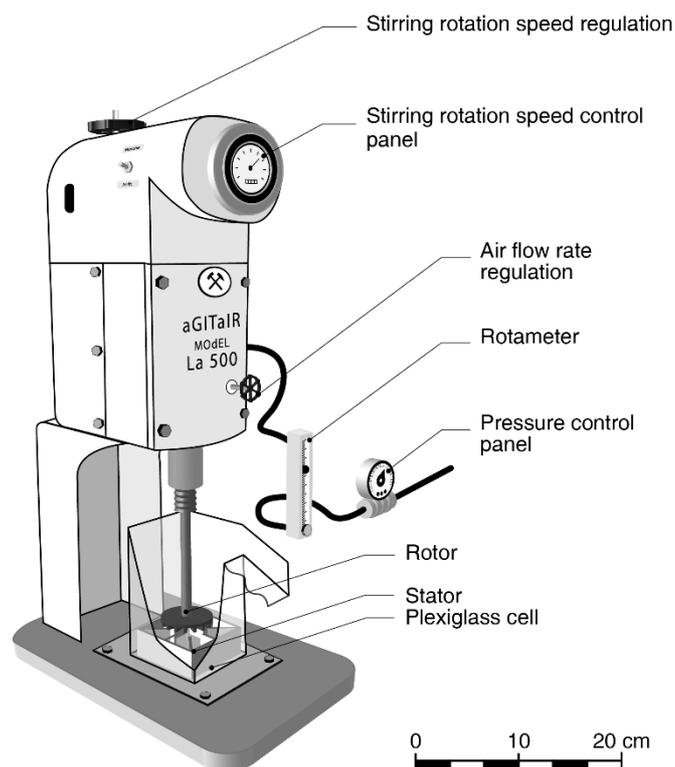
Figure 31. Diagram of the 1.5 L Agitair® LA-500 used for the laboratory scale batch flotation experiments.

1.8.3   High intensity magnetic separation

Among the metallurgical test work conducted to define a processing route for the Tabuaço Main Skarn, high intensity magnetic separation was investigated to reject paramagnetic minerals. Tests were performed in both dry and wet conditions. In dry conditions, the tests were conducted using a PermRoll® magnetic separator equipped with a neodymium-iron-boron permanent magnet (≈ 1 T) on the -500+150 µm fraction, corresponding to a part of the non-milled product. The angle of the separation flap and the feed belt speed were adjusted to maximise the scheelite recovery since it constituted an investigated option to reject gangue minerals prior to the milling stage rather than to enrich the ore. The wet magnetic separation was performed on the flotation feed, namely, the -150+7 µm product, with a plate type JONES® magnetic separator, operated with an electromagnetic induction of 1 T. The middling particles were mixed with the non-magnetic fraction to maximise the scheelite recovery, as for the dry magnetic separation.

1.9 Design of experiments methodology

The design of experiments (DOE) methodology allows to study the influence of k parameters at l levels for one or several response(s) (Montgomery, 2013) and to model these responses from the studied parameters. When the number of levels is higher than or equal to three, this methodology can efficiently describe the non-linear phenomena as interactions between two flotation reagents (Box and Wilson, 1951; Goupy and Creighton, 2007). Some design of experiments such as

Box-Behnken, Central Composite Design, and Response Surface Design are specifically designed for parameter optimisation by developing second-order models:

$$y = a_0 + \sum_{i=1}^{k} a_i x_i + \sum_{i=1}^{k-1} \sum_{j=i+1}^{k} a_{ij} x_i x_j + \sum_{i=1}^{k-2} \sum_{j=i+1}^{k-1} \sum_{l=j+1}^{k} a_{ijl} x_i x_j x_l + \cdots + a_{ijl\ldots n} x_i \ldots x_n + \sum_{i=1}^{k} a_{ii} x_i^2 + \varepsilon \qquad (9)$$

where the x_i are the measurable variables (factors); a_0, a_i, $a_{ij..}$, and a_{ii} are the constant, linear, interaction, and quadratic model coefficients, respectively; and ε is a residual. The coefficients and the residual are determined using the least square method on the experimental results (Goupy and Creighton, 2007; Montgomery, 2013). The DOE and response surface methodologies have been used in many different fields (Campatelli et al., 2014; Djoudi et al., 2007; Kincl et al., 2005) and applied to mineral processing systems (Dehaine et al., 2017; Ebadnejad et al., 2013; El-Midany and Ibrahim, 2011; Honaker et al., 1996; Kökkılıç et al., 2015; Tripathy et al., 2010).

In this work, all the experimental designs were generated using the JMP® statistical software D-optimal design tool (SAS institute) following the usual procedures (Goupy and Creighton, 2007; Montgomery, 2013). The same software was used to perform the data processing and statistical analyses, systematically realised on coded variables. Thus, a Student test was performed on each calculated model coefficient with a confidence level of 95% to select the significant coefficient. The analysis of variance (ANOVA) was used to assess the model significance and eliminate the non-significant coefficients from the final models. The validation of the models was performed through the relationships between the experimental and predicted results. For this statistical analysis, both the correlation coefficient (R^2) and the root mean squared error (RMSE) were studied, which are defined in Eq. 10 and 11, respectively:

$$R^2 = 1 - \frac{\sum_{i=1}^{n}(y_i - \hat{y}_i)^2}{\sum_{i=1}^{n}(y_i - \bar{y})^2} \qquad (10)$$

$$RMSE = \sqrt{\frac{1}{n}\sum_{i=1}^{n}(y_i - \hat{y}_i)^2} \qquad (11)$$

Where y_i represents the observed values; $\hat{y}_i$ are the values that are predicted by the models; and $\bar{y}$ is the mean of the observed values. In Eq. 10, the numerator corresponds to the sum of squared errors (SSE) while the denominator represents the total sum of squares (TSS).

2. Fundamental studies of the flotation reagents adsorption

2.1 Pure minerals

Pure crystals of scheelite, fluorite, calcite, and apatite were acquired from China, Mexico, Madagascar, and Madagascar, respectively. They were hammered and ground in an agate mortar, alternating with dry sieving to prevent from over-grinding. Chemical analyses were carried out by Inductively Coupled Plasma Optical Emission Spectrometry (ICP-OES) for major

elements and Mass Spectrometry (ICP-MS) for the trace elements as well as by ISE for fluorine, at the *Service d'Analyses des Roches et des Minéraux* (SARM-CNRS, Nancy, France). They are presented on Table 5. After the grinding stage, the pure minerals were dry sieved to produce a -100+40 µm and a -40+20 µm size fractions that were used for microflotation tests and spectroscopic studies, respectively.

Table 5. Chemical compositions in major elements of the pure minerals used; L.D. = Limit of Detection.

Mineral	CaO (%)	P_2O_5 (%)	SiO_2 (%)	MgO (%)	Al_2O_3 (%)	Fe_2O_3 (%)	Na_2O (%)	K_2O (%)	MnO (%)	W (%)	F (%)
Scheelite	19.8	1.63	0.72	<L.D.	<L.D.	<L.D.	<L.D.	<L.D.	<L.D.	63.71	<L.D.
Fluorite	70.1	<L.D.	2.69	<L.D.	0.05	<L.D.	<L.D.	<L.D.	<L.D.	0.01	44.59
Calcite	55.2	<L.D.	<L.D.	0.29	0.06	0.05	<L.D.	0.02	<L.D.	<L.D.	<L.D.
Apatite	49.1	33.68	11.27	0.03	0.03	0.06	0.05	0.02	<L.D.	<L.D.	2.07

2.2 Reagents

Fundamentals tests such as microflotation tests, spectroscopic tests, or thermal desorption tests, were performed on pure minerals systems (unary or binary systems). For fundamentals studies about collectors (microflotation and FTIR), pure fatty acids with different chain structures were used: octadecanoic acid, *i.e.* stearic acid (18 carbon atoms, saturated), (9Z)-octadec-9-enoic acid, *i.e.* oleic acid (18 carbon atoms, 1 unsaturation), (9Z,12Z)-octadeca-9,12-dienoic acid, *i.e.* linoleic acid (18 carbon atoms, 2 unsaturations), and tetradecanoic acid, *i.e.* myristic acid (14 carbon atoms, saturated). These fatty acids, their characteristics, and the main possible variations on the fatty acids aliphatic chains are displayed in Figure 32. All the fatty acids used were of high purity (>99.5%) and supplied by Sigma Aldrich. Furthermore, to represent rosin acids in microflotation tests, pure abietic acid was used, also supplied by Sigma Aldrich. No depressants were used for microflotation tests. As for flotation tests, the fatty acids preparation as well as the pH adjustment were performed using sodium hydroxide of technical quality (>99%). Besides, for fundamentals studies about depressants (FTIR and XPS), the same NaOH, Na_2SiO_3, and Na_2CO_3, of high quality (>99%), than for flotation tests were used, supplied by Sigma Aldrich. All the reagents were prepared following the same procedures as described in section 1.8.2, in deionised water.
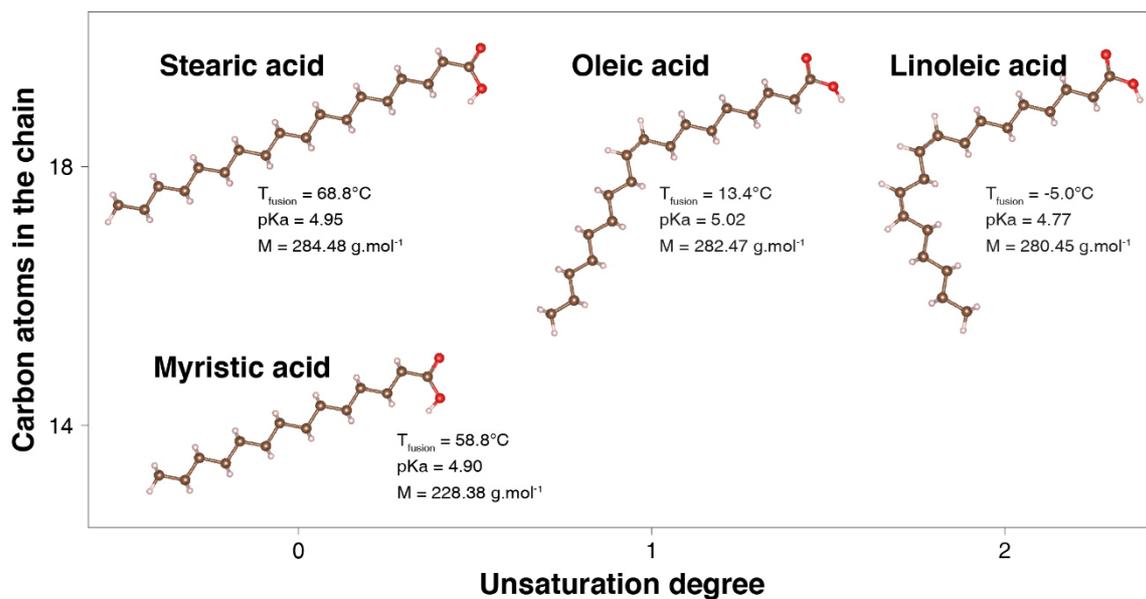
Figure 32. The main fatty acids used in this study, their main characteristics, and the possible variations for fatty acids chain (unsaturation degree and number of carbon atoms in the aliphatic chain). The pKa values are given for 25°C.

2.3 Microflotation tests

For microflotation tests, a 300 mL Hallimond tube, which is presented on Figure 33, has been used. Each microflotation test was carried out on 1 g of pure mineral, or on 0.5 g of each mineral when binary mineral mixtures were studied. The minerals were first conditioned for 5 min in 50 mL of deionised water followed by 5 min with the collector(s) in 100 mL of solution, at room temperature (25°C). The total flotation time was 5 min, also at room temperature (25°C), under stirring by a magnetic bar rotating at 500 rpm. This latter was surrounded by a glass coating to avoid any particle adsorption or bubble coalescence on the polytetrafluoroethylene coating that is traditionally used for magnetic bars. The microflotation tests were performed with nitrogen, under a constant flow rate of $1.9 \cdot 10^{-3} \cdot m^3 \cdot h^{-1}$ at a pressure of $18.9 \cdot 10^3$ Pa. Floated and non-floated products were filtrated, dried in an oven, and weighed to calculate the minerals recoveries. In the case of binary minerals mixtures, the two products were analysed by ED-XRF spectrometry to calculate the recovery of each mineral in each product.

Water level (300 mL)

Seal

Closing shell

Floated disharge spigot

Four fingers clamp on
retort stand

Magnetic glass stir bar
(25*6 mm)

Sintered glass (Porous)

Gas inlet flexible pipe

Magnetic stirrer device

Stir bar rotation speed
control wheel

0   2.5   5 cm
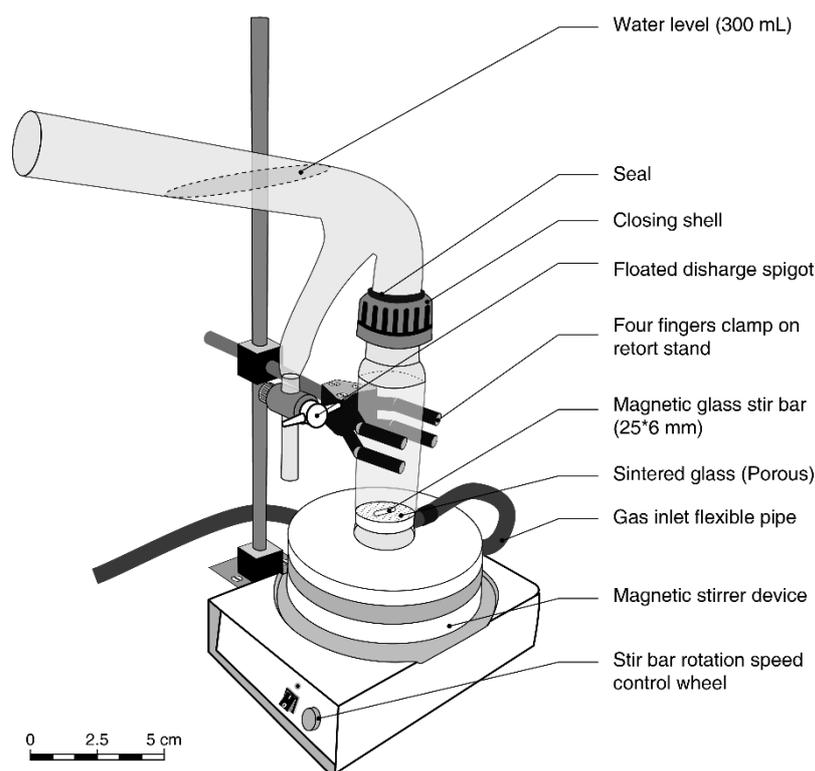
Figure 33. Diagram of the 300 mL Hallimond tube used for the microflotation experiments.

2.4 Spectroscopic studies

2.4.1   Fourier Transform Infrared Spectroscopy

The Fourier Transform Infrared (FTIR) spectroscopy is one of the most method used worldwide to identify molecules, organic or mineral, in gas and liquid phases. Different techniques have been developed to adapt FTIR measurements to the wanted system (bulk liquid, bulk gas, interfaces…). In particular, the diffuse reflectance method (DRIFTS) allows to maximise the surface signal by concentrating the surface-reflected IR beam to the IR detector. This method has been intensively used by various researchers over the past decades to investigate the adsorption of flotation reagents onto mineral surfaces (see Chapter 1). Hence, the diffuse reflectance method was used for all the FTIR analyses conducted in the present study. The spectra were recorded using a Bruker IFS 55 spectrometer equipped with a large-band mercury-cadmium-telluride (MCT) liquid-nitrogen-cooled detector and associated with a diffuse reflectance attachment (Harrick Corporation). The IR spectra were acquired in the mid-infrared range between 4000 cm^{-1} and 600 cm^{-1} with a spectral resolution of 2 cm^{-1}. Dry mineral samples were analysed most of the time with a dilution in potassium bromide powder of spectroscopic grade (used as a reference) to the 1:50 ratio. However, for the adsorption of depressants (in Chapter 4), to maximise the surface signal, the samples were not diluted in KBr for analyses.

2.4.2   X-Ray Photoelectron Spectroscopy

X-Ray photoelectron spectroscopy (XPS) supplements very well the FTIR spectroscopy. When an X-Ray beam is sent on a sample (a mono-crystal or a powder), the irradiated atoms emit a photoelectron, which is a core electron that is characteristic of the considered atom. The kinetic energy of this emitted electron is measured, and the electrons of a given kinetic energy are quantified using a detector. All the experiments are performed in ultrahigh vacuum to avoid any influence of the air onto the electron movement in the apparatus. The kinetic energy of the electrons allows to identify the atoms, their oxidation state, and their chemical environment since these two latter parameters affect the core electron binding energy. Moreover, the atomic species can be quantified with a relative accuracy, albeit atomic ratios are preferred for accurate quantification. Interestingly, XPS allows to investigate only few nanometres on the surface, which represents around a dozen atomic layers. It maximises the surface signal and provides crucial chemical information (oxidations, bonds, atoms) about the surface. In the present study, the XPS spectra were acquired using an X-ray photoelectron spectrometer Kratos Axis Ultra DLD, equipped with a monochromatic Al Kα X-ray source (1,486.7 eV) operated at 120 W (8 mA and 15 kV). The global spectra were recorded with a resolution of 1.0 eV and a pass energy of 160 eV while the high-resolution spectra were acquired with a resolution of 0.1 eV and a pass energy of 20 eV. For carbon and oxygen, the resolution was decreased to 0.05 eV. The hybrid mode was employed, using a magnetic-electrostatic lens and a charge neutraliser since the samples were not conducting. After the acquisition, the adventitious carbon was used as a reference with the C-C bonds binding energy set at 284.6 eV. The software Vision 2.2.10, supplied by Kratos Analytical (Manchester, UK), was employed to process the data.

2.4.3   Conditioning

Spectroscopic tests (XPS or FTIR) were conducted with 0.5 g or 1 g of -40+20 µm fraction of pure minerals (described in section 2.1). For the control sample, *i.e.* without the addition of any reagent, the pure mineral was treated in deionised water (R = 18.2 M$\Omega \cdot$ cm) during 15 min. For minerals conditioned with flotation reagents, unless the conditioning time varied (and therefore it will be given in the appropriate sections), the minerals were in contact with the reagent solution during 15 min, under lateral vigorous shaking conditions, in an adapted vial. The conditioning solution was constituted by 5 mL for 0.5 g of mineral and by 10 mL for 1 g of mineral. When several reagents were added at the same time, the experimental procedure was the same. After the conditioning stage, the mineral sample was filtrated using ashless filter paper and rinsed three times with deionised water. During the whole experimental process, the pH was adjusted by adding NaOH or HCl solutions at 1 x 10^{-1} mol.L^{-1}. When reagents were used sequentially, the 0.5 g of mineral was first conditioned in 5 mL of the first solution during 15 min and the conditioning solution was eliminated. Then, the sample was washed three times with deionised water and conditioned with 5 mL of the second solution during additional 15 min. The same solid/liquid separation and washing procedure was applied at the end of the conditioning stage.

3. DFT

3.1 Structural model

In the present study, a primitive cubic cell of fluorite has been used as the starting point (Cheetham et al., 1971). The cell was optimised through full relaxation to obtain lattice parameters a = b = c = 5.462 Å. It is known that the (111) surface is the most exposed surface for fluorite crystals (Bennewitz et al., 1997; De Leeuw et al., 2000; Parks and Barker, 1977). Following previous studies, a (111) cleavage surface was created from the fully relaxed bulk. The same methodology was applied for scheelite, with the (112) and (001) surfaces, corresponding to the most exposed surfaces, generated from the fully-relaxed lattice.

3.2 Calculation settings

The total energy and structure of the systems were determined by density functional theory calculations (Hohenberg and Kohn, 1964; Kohn and Sham, 1965; Tasker, 1980), using the Vienna *ab initio* simulation program (VASP) (Kresse and Hafner, 1993). The semilocal Perdew−Burke−Ernzerhof (PBE) exchange-correlation functional proposed by Perdew and co-workers (Perdew et al., 1996), in the generalised gradient approximation (GGA), was employed. The electron-ion interactions were described using the projector augmented wave (PAW) method (Blöchl, 1994; Kresse and Joubert, 1999) and the Kohn-Sham equations (Kohn and Sham, 1965) were solved self-consistently (Kresse and Furthmüller, 1996) until the energy difference between cycles became lower than 10^{-7} eV. The plane wave cut-off energy was set to 500 eV. A Methfessel Paxton smearing (Methfessel and Paxton, 1989) of $\sigma = 0.1$ eV was applied to occupations, to help the total energy convergence. The structural relaxations were performed until all forces were smaller than 0.03 eV/Å. All the calculations were realised using the Γ-point only due to the large size of the cell. To describe precisely the interactions involved in the adsorption of molecules, van der Waals (vdW) forces were taken into account. Since they are not included in the PBE functional, the D2 (Grimme, 2006) and the D3 (Grimme et al., 2010) corrections of Grimme were used. The *ab initio* molecular dynamics calculations were performed using the same computational parameters. A Nosé-Hoover thermostat was used (Hoover, 1985; Shūichi Nosé, 1984; Shuichi Nosé, 1984) with a temperature set to 300 K. The time step was 1 fs and 100,000 steps were realised permitting to reach a total simulation time of 100 ps. For the *ab initio* molecular dynamics calculations, only the D2 correction method of Grimme (Grimme, 2006) was used.

3.3 Energy calculation

To understand the adsorption of molecules on the mineral surface, three calculations were performed for each system, giving the following energies:

- E_{Surf}: the total energy of the mineral slab alone;
- E_X: the total energy of the adsorbent molecule alone in vacuum;
- E_{Surf-X}: the total energy of the mineral slab with adsorbed molecule(s).

The adsorption energy was determined using:

$$\Delta E_{ads} = E_{Surf-X} - E_{Surf} - E_X \tag{12}$$

The contribution of dispersion energy in the adsorption energy was determined in a similar way:

$$\Delta E_{disp} = E_{disp\ Surf-X} - E_{disp\ Surf} - E_{disp\ X} \tag{13}$$

When n molecules were adsorbed simultaneously, the adsorption energy per molecule was determined using:

$$\Delta E_{ads/molecule} = \frac{E_{Surf-nX} - E_{Surf} - n \times E_X}{n} \tag{14}$$

$$\Delta E_{disp/molecule} = \frac{E_{disp\ Surf-nX} - E_{disp\ Surf} - n \times E_{disp\ X}}{n} \tag{15}$$

Besides, when exchange, substitution, or adsorption of a molecule from the bulk of water, a reaction was considered and the total energy of each member of the equation was calculated. On *ab initio* molecular dynamics simulations, calculations of internal adsorption energies were realised using the above-mentioned equations, based on the average energy of each system computed for the last 90 ps of the simulation to exclude the thermalisation period.

Gravity concentration of a complex skarn ore

1. General introduction

Enhanced gravity separators, which use additional centrifugal force to enhance the separation, are the most common gravity concentration techniques used for fine particles processing. Centrifugal separators can be seen as a ramification of the flowing film gravity concentrators category which employs centrifugal force to enhance the relative settling velocities of particles components. These separators are mainly represented by the Knelson and Falcon concentrators as well as the Kelsey Jig and Multi Gravity Separator (MGS). The two latter devices actually use one additional separation mechanism, *i.e.* stratification for the Kelsey jig and shaking for the MGS. Falcon concentrators consist in a conical bowl capable of spinning at high rotation speed (up to 600 G's), enabling the separation of fine particles based on their density (for further details, please report to Chapter 1).

Considering the significant contrast of minerals specific gravities existing in the Tabuaço skarn along with the significant amounts of scheelite in the finest size fractions (see Chapter 2), the use of a Falcon concentrator was a suitable option. Moreover, it would allow to reject the problematic gangue minerals prior to flotation and, therefore, improve the subsequent flotation performances. Recently, authors demonstrated that Falcon concentrators, as other centrifugal separators, allow to eliminate efficiently the fine particles (-10+0 µm), also called slimes (Dehaine et al., 2019b). Desliming, which is recommended for the froth flotation stage since fine particles (-10+0 µm) are known to disturb the process, is usually performed using hydrocyclones. These apparatus operate a particle-size-based separation and do not usually concentrate the dense minerals, even if a pre-concentration of dense minerals in the underflow is sometimes observed (Dehaine and Filippov, 2015). This section investigates the use of a Falcon concentrator prior to flotation to perform both a pre-concentration and a desliming stage on a W-skarn ore. The main objective of this study is to propose an optimised Falcon separation prior to flotation to reject the penalising gangue minerals and, as a side objective, to deslime the ore. Such developments would lead to the reduction of the overall environmental impacts of skarn ore processing by allowing the use of cleaner reagents, *i.e.* fatty acids, and by decreasing the tonnage processed by flotation and, consequently, the reagents consumption. **This work has been published under the title "Application of Falcon centrifuge as a cleaner alternative for complex tungsten ore processing" in Minerals, 9, 448.**

2. Methods

   2.1 Performance assessment

The global mineralogical assemblage can be divided into 4 different mineral groups displaying specific density ranges (Table 6). Assuming that all minerals contained in each density range behave similarly during the separation, the separation performances are estimated using one proxy by minerals group.

The light silicates fraction is dominated by K-feldspar (see Chapter 2), which displays a density very similar to those of other light silicates such as quartz and Na-feldspar (Table 6). Therefore, the potassium oxide (K_2O) content could be used as a proxy to estimate the separation performances for this group of minerals. The gangue calcium-bearing salts group contains apatite and fluorite (Table 6), the elimination of which is crucial to improve the downstream flotation process. These minerals have very close densities (Table 6) and their elimination could be approximated using the phosphorous oxide (P_2O_5) content in the sample, apatite being the only P-bearing mineral in the ore (see Chapter 2). The dense silicates group comprises pyroxenes, garnets, vesuvianite, and zoisite, which all contain iron and calcium (Table 6). To assess the rejection performances for this mineral group, the iron oxide (Fe_2O_3) content was used as these minerals are the only Fe-bearing minerals in the Tabuaço ore (see Chapter 2). Finally, the W content could be used to quantify scheelite recovery as no other W-bearing mineral was reported in this ore. Although most of the clay minerals reported contain potassium and iron, they could be classified as light silicates since their densities are close to 2.6. Considering the small amounts of phyllosilicates in the ore, their contribution in terms of iron could be neglected.

Table 6. Mineralogical composition of the Tabuaço W-skarn showing the relative abundances along with the chemical formulas, and the densities of the minerals which are classified into four different groups.

Mineral	Formula	Abundance (wt.%)	Density (g · cm⁻³)	Group
Vesuvianite	$Ca_{10}(Mg,Fe)_2Al_4(SiO_4)_5(Si_2O_7)_2(OH)_4$	45	3.30	Dense silicates
Epidote (zoisite)	$Ca_2(Al,Fe)_3(SiO_4)_3(OH)$	15	3.20	Dense silicates
Fluorite	CaF_2	10	3.18	Calcium salts
Feldspars	$(K,Na)AlSi_3O_8$	15	2.65	Light silicates
Phyllosilicates	-	1-5	2.65	Light silicates
Garnet (grossular)	$Ca_3(Al,Fe)_2(SiO_4)_3$	1-5	3.70	Dense silicates
Fluorapatite	$Ca_5(PO_4)_3F$	3	3.18	Calcium salts
Pyroxene (diopside)	$Ca(Fe,Mg)Si_2O_6$	1	3.20	Dense silicates
Quartz	SiO_2	1	2.65	Light silicates
Scheelite	$CaWO_4$	1	6.10	Target mineral

2.2 Design of experiments

In this chapter, the DOE methodology has been used to gain understanding on the influence of the operating parameters on the separation efficiency, for the two types of Falcon bowls (UF and SB), and to optimise the separation in terms of gangue minerals rejection. Hence, Central Composite Designs (CCD) with two centred points were generated to investigate the influences of the rotary speed, the pulp flowrate, and the solid pulp density, plus the fluidisation pressure for the Falcon SB only, in order to optimise the Falcon separation (Table 7). The levels were defined in accordance with results of preliminary tests and the operating range recommended by the manufacturers. The rotary speed could only vary between 20 and 78 Hz for the Falcon L40, pulp density was chosen as low as possible (2% being the lowest realistically possible pulp density), the feed flowrate levels were chosen as low as possible to avoid settling in the feed and as high as possible to avoid the feed to overflow from the Falcon feeder, and the levels for the fluidisation pressure where chosen in accordance with the manufacturer guidance with regard to the sample maximum particle size. Since the chosen levels defined a large experimental domain, the axial value of the CCD was set to 1, which induced that each axial point was located on one boundary of the domain.

Table 7. Independent factors and corresponding levels for the experimental designs. * Falcon SB only.

Factors	Symbol	Levels			Coded-variables
		Low (-1)	Centre (0)	High (+1)	
Rotary speed (Hz)	ω	30	50	70	$x_1 = (\omega - 50)/20$
Pulp density (wt. % solid)	$\%_s$	2	6	10	$x_2 = (\%_s - 6)/4$
Pulp flowrate (kg $\cdot$ min^{-1})	Q	1	2	3	$x_3 = (Q - 2)/1$
Fluidisation pressure (PSI)*	f	1	2	3	$x_4 = (f - 2)/1$

The main objective was to use the Falcon concentrator as a pre-concentrating apparatus, to produce a W pre-concentrate from the complex Tabuaço scheelite-containing ore to feed a fatty-acid flotation circuit. An optimised elimination of gangue minerals and fine particles (-10+0 µm) was required to ensure the selectivity of the subsequent flotation process. Therefore, K_2O, Fe_2O_3, and P_2O_5 recoveries were used as indicators to estimate the rejection of the corresponding gangue mineral groups. The WO_3 recovery characterised the separation performance in terms of target mineral recovery, and was kept as high as possible. Finally, to compare the desliming action of Falcon concentrators to that of a classical hydrocyclone, the "desliming efficiency" (D_{eff}) was defined as the ratio of the amount of -10+0 µm particles in the tailings over the amount of -10+0 µm particles in the feed. In total, 5 performance indexes were considered. Overall, moderate and tight objectives were defined for the Falcon separation indexes *i.e.*, the 5 studied responses, which are detailed in Table 8. The tight criterion, if reached, would represent a significant improvement in skarn ore processing since high calcium gangue minerals and fine particles eliminations would increase tremendously the efficiency of the flotation process while reducing reagents consumption.

Table 8. Moderate and tight objectives based on the five studied responses for the Falcon separation performances.

Response	Criterion	
	Moderate	Tight
WO_3 recovery	70%	75%
P_2O_5 recovery	40%	25%
K_2O recovery	40%	20%
Fe_2O_3 recovery	40%	20%
Desliming efficiency	60%	90%

3. Results and discussion

3.1 Falcon UF

3.1.1   Design of experiments results

The experimental results were used to determine the second order response models, after Eq. 9. These models represent the expression of the studied responses (WO_3 recovery, K_2O recovery, P_2O_5 recovery, Fe_2O_3 recovery, and D_{eff}) as a function of the codded operating variables. The significance of each developed model was estimated through an analysis of variance (ANOVA). A first F-test was conducted on the models, with all the factors and their interactions. The critical F-value for the 0.05 significance level was calculated using the degrees of freedom of the models (10) and the residuals (5) for the first run, which is $F_{(10,5)} = 4.74$. The significance of each factor was assessed by comparing the calculated F-value for each factor to the critical F-value. For each model, the non-significant factors were eliminated from the models one by one, the coefficients were re-calculated, and the ANOVA was performed again after each elimination. Finally, only the significant factors were included in the final models and the ANOVA was conducted again on the final models to assess their significance. The calculated F-values for each final model are significantly higher than the critical F-values, which are, for a 0.05 significance level, $F_{(3,12)} = 3.49$ for the R_W, R_K, and R_{Fe} models, $F_{(2,13)} = 3.81$ for the R_P model, and $F_{(1,14)} = 4.60$ for the D_{eff} model, inducing low p-values.

The accuracy of the models was assessed by the relationships between the observed experimental values and the predicted results (Table 9). The R^2 and the RMSE were used to illustrate the accuracy and the strength of these relationships (Table 9). The correlation coefficients are quite high for the gangue minerals recoveries (>0.8) but significantly lower for the WO_3 recovery and the desliming efficiency for which $R^2 = 0.5801$ and $R^2 = 0.5435$, respectively, indicating that the models accuracy is relatively low.

Table 9. Summary of fit (actual vs predicted) for the five studied responses for the Falcon UF.

	R_W	R_K	R_P	R_{Fe}	D_{eff}
R^2	0.5802	0.9420	0.8810	0.9121	0.5492
RMSE	5.5592	2.7470	4.3503	3.5020	5.0488
F	5.5300	64.9100	48.1000	41.5300	17.0600
P	0.0128	<0.0001	<0.0001	<0.0001	0.0010

3.1.2 Interpretation of the models

For each model, a Student's *t*-test was performed on each coefficient to assess the significance of their impact on the results. All the non-significant factors have been eliminated to obtain the final models, which induces that all the remaining factors have a *p*-value below 0.05, *i.e.* the chosen significance level. The final models can be expressed as a function of the coded variables:

$$R_W = 87.52 - 3.90x_1 + 3.89x_2 - 7.47x_1^2 \tag{16}$$

$$R_K = 39.21 - 5.62x_1 + 10.08x_2 - 3.71x_3 \tag{17}$$

$$R_P = 49.26 - 8.08x_1 + 10.81x_2 \tag{18}$$

$$R_{Fe} = 45.41 - 6.58x_1 + 10.06x_2 - 2.89x_3 \tag{19}$$

$$D_{eff} = 63.65 - 6.59x_2 \tag{20}$$

The WO_3 recovery depends significantly on the rotary speed (linear and quadratic terms) and on the pulp density. The rotary speed affects negatively the WO_3 recovery for the linear and quadratic terms while the pulp density acts positively on this response. The intercept is high (87.52), which indicates a high WO_3 recovery at the centre of the experimental domain. As the entrapment of a particle is directly linked to its settling length in the bed (Kroll-Rabotin, 2010; Kroll-Rabotin et al., 2013, 2011, 2010), scheelite settles probably very fast at the considered operating conditions. The gangue minerals recoveries (proportional to K_2O, P_2O_5, and Fe_2O_3 recoveries) show similar trends: as the WO_3 recovery, they are all affected by a significant negative effect of the rotary speed whereas the pulp density displays a high positive coefficient. The increase of the rotary speed results in the application of a higher G-force and then of a higher cut-off density (Kroll-Rabotin et al., 2013, 2010), which induces a better rejection of light particles as well as, to a lesser extent, dense particles. The effect of the pulp density can be linked to the differential settling, which is the main separation mechanism occurring in the bowl. When the pulp density is too high, forced settling of light particles may occur, attributed to the superposition of particles with different densities in the flowing film (Burt and Mills, 1984; Burt, 1987). It affects the sedimentation length of both light and dense particles inducing that the light ones are trapped while they should not be. Moreover, the flowrate acts negatively on the K_2O and Fe_2O_3 recoveries. This result can be attributed to the presence of phyllosilicates in light silicates and dense silicates groups, since their characteristic shape can result in stronger

entrainment phenomenon (Burt, 1987; Burt and Mills, 1984; Kademli and Gulsoy, 2012). Moreover, it can also be linked to the erosion mechanisms in the bowl that are undoubtedly stronger for higher pulp flowrates and might affect more significantly the light minerals. Overall, for the gangue mineral recoveries, the pulp density has a higher effect in absolute value than the rotary speed, indicating a strong control of the settling mechanisms on the separation. The coefficients have the same magnitude between the three gangue minerals groups but some differences can be discussed. The constant term, indicating the value of the response at the centre of the domain, is the lowest for the light silicates (39.21), the highest for the calcium minerals (49.26), and intermediate for the dense silicates (45.41). However, following Table 6, the dense silicates display higher densities than the calcium minerals and, then, their constant term should be higher. This phenomenon could be attributed to the existence of iron-bearing silicates (biotite, iron-bearing chlorites, iron-bearing clay minerals, etc.) that are lighter than the calcium minerals. Also, the densities considered for the calcium minerals could be inaccurate, as they have been measured for ideal minerals, from reference tables. The negative coefficient affecting the rotary speed is the lowest for the light silicates (-5.62), the highest for the calcium minerals (-8.08) and intermediate for the dense silicates (-6.58), in absolute values, which is in accordance with the previous discussion. Additionally, the recovery is low at the centre of the domain for the light silicates, which results in a low term affecting the rotary speed for the light silicates. The same trend is followed by the other two responses, as the rotary speed is the main parameter influencing the density cut (Kroll-Rabotin et al., 2013).

The desliming efficiency is significantly affected by a negative effect of pulp density. It means that a high pulp density induces the trapping of fine particles in the concentrate bed, which could be attributed to the forced settling occurring for fine particles as well as for light particles. Moreover, it could also be linked to the second separation mechanism occurring in the bowl, namely the erosion of the concentrate bed. Indeed, with 500 g of feed material, once the concentrate bed is formed, erosion phenomenon are likely to occur. It was shown that the erosion phenomenon is linked to the shear forces induced by the flow of the pulp at the surface of the concentrate bed. Consistently, the shear forces are higher when the pulp density increases due to the interaction between particles and the concentrate bed surface, that are not taken into account in the current physical separation model of the Falcon yet. Also, the suggested model for the lift forces strongly depends on the particle size which results in a higher erosion rate for coarse particles. This phenomenon could explain the lower desliming efficiency when the pulp density is increased. However, regarding the accuracy of the model, the interpretations are difficult.

3.1.3   Optimisation and validation

Following the models for the different responses, the iso-response graphs presented in Figure 34 display the gangue minerals recoveries as a function of the operating parameters. No iso-response graph and no performance objective were established for D_{eff} as it is affected by only one parameter. Optimum operating conditions were selected based on the models determined previously, through the iso-responses graphs (Figure 34). The areas attaining the moderate

performances objectives are indicated in Figure 34 while the tight objectives are attained only for WO_3 recovery (Figure 34). None of the studied responses reaches an extremum on the domain. The WO_3 recovery is maximum at intermediate rotary speed and high pulp density but satisfies the performances objectives in the whole experimental domain. The K_2O recovery is minimum at high rotary speed, high pulp flowrate, and low pulp density (Figure 34b, c, and d). The other gangue mineral recoveries (P_2O_5 and Fe_2O_3) are minimum at high rotary speed and low pulp density (Figure 34e, f, g, and h). Since the WO_3 recovery attains the performances objectives on the whole experimental domain, the gangue minerals recoveries can be minimised while the WO_3 recovery remains higher than 70% (and matches the moderate performances objectives), which however results in WO_3 losses: the similar trends followed by the gangue minerals and scheelite induce that a compromise has to be done between the WO_3 recovery and the gangue minerals rejection.
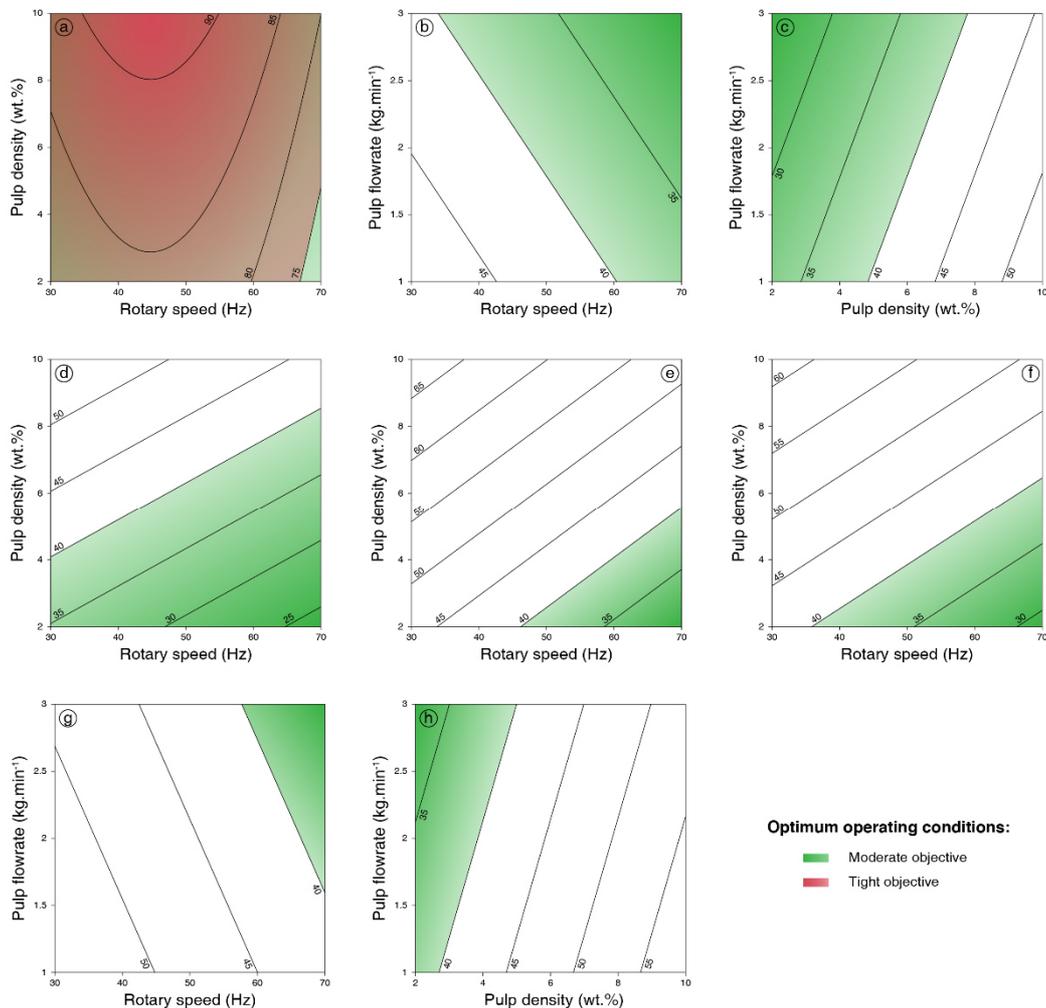
Figure 34. 2-D contour plots for WO_3 recovery (a), K_2O recovery (b, c, and d), P_2O_5 recovery (e), and Fe_2O_3 recovery (f, g, and h) for the Falcon UF models as a function of the operating parameters. The coloured zones correspond to values that satisfy the performance objectives defined in Table 8.

Global iso-responses graphs have been built for the five considered responses as a function of the operating parameters to select the optimum operating conditions taking into account all the responses (Figure 35). Zones corresponding to the operating conditions for which the responses comply with the moderate objective are indicated on the graphs. Thus, the moderate objective can be reached by maximising the pulp flowrate and the rotary speed (3 kg · min^{-1} and 70 Hz, respectively) while minimising the pulp density (2 wt.% solid).
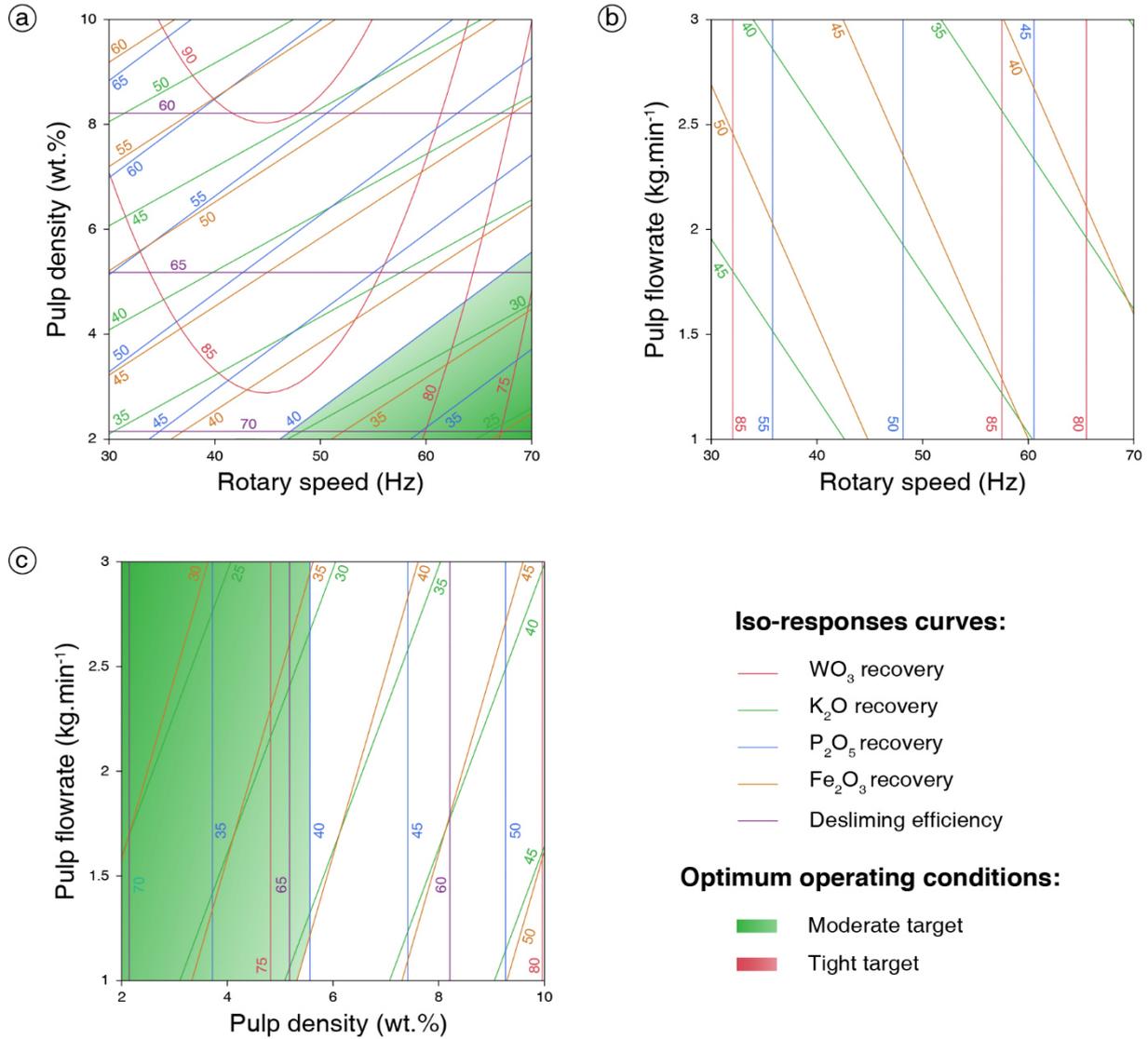
Figure 35. 2-D contour plots for the five studied responses (WO$_3$, K$_2$O, Fe$_2$O$_3$, and P$_2$O$_5$ recoveries and desliming efficiency) for the Falcon UF models as a function of the operating parameters. Targets represent zones where the objectives set on all the studied responses, defined in Table 8, are reached.

Since the pulp flowrate has little influence on the separation, inducing that the performances with Falcon UF mainly depend on the rotary speed and the pulp density, the WO$_3$ enrichment ratio and the WO$_3$ recovery could be expressed as a function of these two latter parameters. The pulp flowrate was maximised, according to Figure 35, to build the response surfaces presented in

Figure 36, which allow to summarise the above-mentioned effects: decreasing the pulp density induces lower WO_3 recoveries but higher WO_3 enrichment ratios, *i.e.* gangue minerals rejection, while decreasing the rotary speed induces higher WO_3 recoveries along with lower WO_3 enrichment ratios (Figure 36).
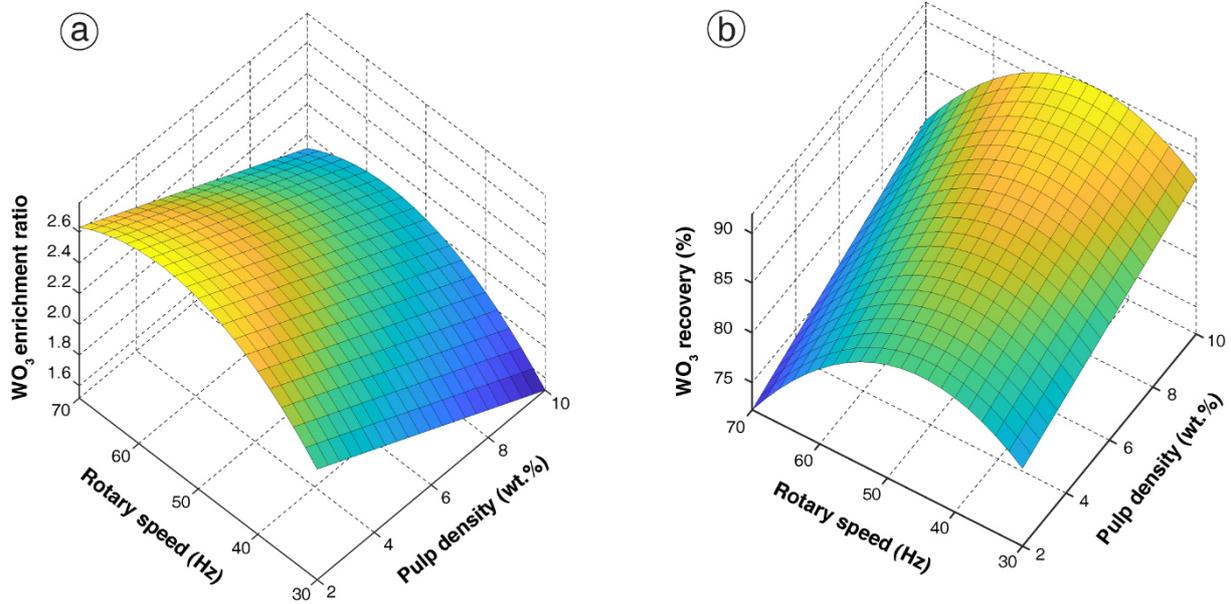
Figure 36. Response surfaces presenting the WO_3 enrichment ratio (a), proportional to the gangue minerals rejection, and the WO_3 recovery (b) as a function of the two main parameters affecting them, *i.e.* the rotary speed and the pulp density, for Falcon UF. To establish these surfaces, the pulp flowrate was set to the optimal value, *i.e.* 3 kg · min^{-1} (maximum value).

To validate the developed models, a series of tests with the optimised operating conditions was performed. This experience was reproduced four times to assess the experimental variability. For each response, the mean and the standard deviation were calculated based on the four reproduced experiences, see Table 10. The experimental standard deviation was also expressed as a percentage of the experimental value. The error between the predicted values and the average obtained values for the studied responses was used to assess the validity of the model. The experimental errors are low, indicating a good reproducibility of the experiments. The errors between the predicted and the observed values are acceptable for most responses ($<10\%$) with the exception of the W recovery.

Table 10. Validation test for the Falcon UF based on a test with optimised parameters ($\omega = 70$ Hz; $\%_S= 2$ wt.%; $Q = 3$ kg · min^{-1}) repeated four times.

	R_W	R_K	R_P	R_{Fe}	D_{eff}
Mean	63.73	24.19	25.45	22.62	72.51
Absolute experimental standard deviation	1.94	1.30	1.89	1.26	1.46
Predicted by the model	72.26	19.80	30.37	25.89	70.24
Model absolute error	8.53	-4.39	4.92	3.27	-2.27

3.2 Falcon SB

3.2.1 Design of experiments results

As for the Falcon UF, the experimental results of the Falcon SB tests were used to define the second order response functions, after Eq. 9. These functions represent the expression of the responses (WO_3 recovery, K_2O recovery, P_2O_5 recovery, Fe_2O_3 recovery, and D_{eff}) as a function of the operating parameters. The same methodology than for the Falcon UF was applied here. The critical F-value for a 0.05 significance level was calculated using the degrees of freedom of the models (19) and the residuals (6) for the first run, which is $F_{(19,6)} = 3.88$. After the elimination of the non-significant coefficients, the calculated F-values for each final model are significantly higher than the critical F-values, which are, for a 0.05 significance level, $F_{(5,20)} = 2.71$ for the R_W model and $F_{(2,23)} = 3.42$ for the R_K, R_P, and R_{Fe} models, and $F_{(3,22)} = 3.05$, inducing low p-values.

The models accuracies were estimated by the relationships between the observed experimental results and the predicted values. The R^2 and the RMSE were used to illustrate the accuracy and the strength of these relationships, see Table 11. The correlation coefficients are very similar for all the minerals recoveries and for the desliming efficiency, around 0.7, which is acceptable.

Table 11. Summary of fit (actual vs predicted) for the five studied responses for the Falcon SB.

	R_W	R_K	R_P	R_{Fe}	D_{eff}
R^2	0.6989	0.6523	0.6904	0.7125	0.6921
RMSE	6.2631	3.3917	3.4524	2.9182	2.6222
F	364.1500	21.5800	25.6500	28.5000	16.4900
P	0.0001	<0.0001	<0.0001	<0.0001	<0.0001

3.2.2 Interpretation of the models

A Student's t-test was performed on each coefficient of each model to assess the significance of their impact on the results. All the non-significant factors have been eliminated to obtain the final models, which induces that all the presented values have a p-value below 0.05. The final models are expressed as a function of the coded variables:

$$R_W = 77.33 + 6.57x_1 - 3.25x_2 - 3.52x_4 + 4.37x_1x_4 - 7.69x_4^2 \tag{21}$$

$$R_K = 14.59 + 3.82x_1 - 3.61x_4 \tag{22}$$

$$R_P = 24.58 + 3.87x_1 - 4.36x_4 \tag{23}$$

$$R_{Fe} = 20.19 + 3.82x_1 - 3.52x_4 \tag{24}$$

$$D_{eff} = 97.16 - 2.94x_1 + 2.02x_4 - 4.49x_1^2 \tag{25}$$

The WO$_3$ recovery depends on the rotary speed, the pulp density, the fluidisation pressure (linear and quadratic), and the interaction between the speed and the fluidisation pressure. All the coefficients have close absolute values. However, they are negative for the pulp density and for the fluidisation pressure (linear and quadratic) but positive for the two other parameters. It induces that the pulp density and the fluidisation pressure have a negative effect on the WO$_3$ recovery. In the Falcon SB bowl, the separation depends mainly on two mechanisms: the differential settling in the flowing film (Kroll-Rabotin et al., 2013, 2011, 2010, p.; Laplante and Nickoletopoulos, 1997) and the reorganisation of the trapped particles in the gutters (Ancia et al., 1997; Majumder and Barnwal, 2006). It can be assumed that, before reaching the gutters, the particles are subject to a differential settling that can be described by the same physical model than for the Falcon UF bowl despite different bowl geometries. Consistently, the rotary speed increases the scheelite recovery as the settling length of scheelite particles is decreased when the G-force is increased. Moreover, a hindered settling phenomenon appears at high pulp density (Burt, 1987; Burt and Mills, 1984) resulting in a decrease of the scheelite recovery and then a negative coefficient for the pulp density. The negative coefficient for the fluidisation pressure can be attributed to a low selective particles rejection when the fluidisation pressure increases, inducing scheelite losses.

The gangue minerals recoveries follow the same trends, due to their similar densities which are also very similar to the scheelite behaviour. The rotary speed acts positively while the fluidisation pressure acts negatively, roughly with the same absolute values. A high rotary speed induces a non-selective entrapment as it decreases the settling lengths of all the minerals. In the trapping gutters, the fluidisation pressure has an opposite direction compared to the gravity force. Hence, the entrapment of a particle in the gutters depends on the force balance between the gravity force, which is a function of the density and the size of the particle, and drag the force induced by the fluidisation pressure. This latter, which has been intensively described for Knelson concentrators, is mainly proportional to the particle area (Coulter and Subasinghe, 2005; Ghaffari and Farzanegan, 2018, 2017; Laplante et al., 1996). Then, this balance results in a rejection of light particles from the gutters, inducing the negative coefficient for the fluidisation pressure on the gangue mineral recoveries. Consistently, the scheelite and the gangue minerals follow very similar trends considering the rotary speed and the fluidisation pressure. The absolute values of the coefficients are still different, which can be attributed to their density contrast. It indicates that the scheelite particles are subject to the same force balance and that reaching a better rejection of gangue mineral particles will lead to higher scheelite losses. Overall, the constant terms, as well as the absolute values of the coefficients affecting each operating parameter, can be related with the actual densities of each minerals group.

The desliming efficiency is negatively impacted by the rotary speed (linear and quadratic terms) and positively affected by the fluidisation pressure, in the same order of magnitude. The increase of rotary speed leads to the entrapment of fine particles as their settling length is decreased while the fluidisation pressure flushes them out from the gutters. The high constant term means that most of the fine particles are rejected with no dependence on the operating parameters in the

considered experimental area. The force balance between the gravity force and the fluidisation force significantly disfavours the entrapment of fine particles. Indeed, the weight force, responsible for the entrapment of the particle, is correlated to the particle volume and, hence, depends on d^3, where d is the particle diameter. The pressure force is mainly related to the particle area that is in contact with the water counter-pressure and should be proportional to the particle surface, whose dependence on the particle size is only at a power of 2 (Coulter and Subasinghe, 2005; Ghaffari and Farzanegan, 2018, 2017; Laplante et al., 1996).

3.2.3 Optimisation and validation

The Falcon SB design yielded more complex models, since, following the equations and the iso-responses graphs (Figure 37), the recoveries of the different minerals, including scheelite, are affected very similarly by the operating parameters. A little loss of recovery is acceptable as the industrial Falcon concentrators are known to be much more efficient than the laboratory-scale Falcon concentrators in terms of recoveries (Burt, 1999; Das and Sarkar, 2018). The graphs in Figure 37 present zones corresponding to optimum operating conditions that satisfy the moderate and tight objectives presented in Table 8.
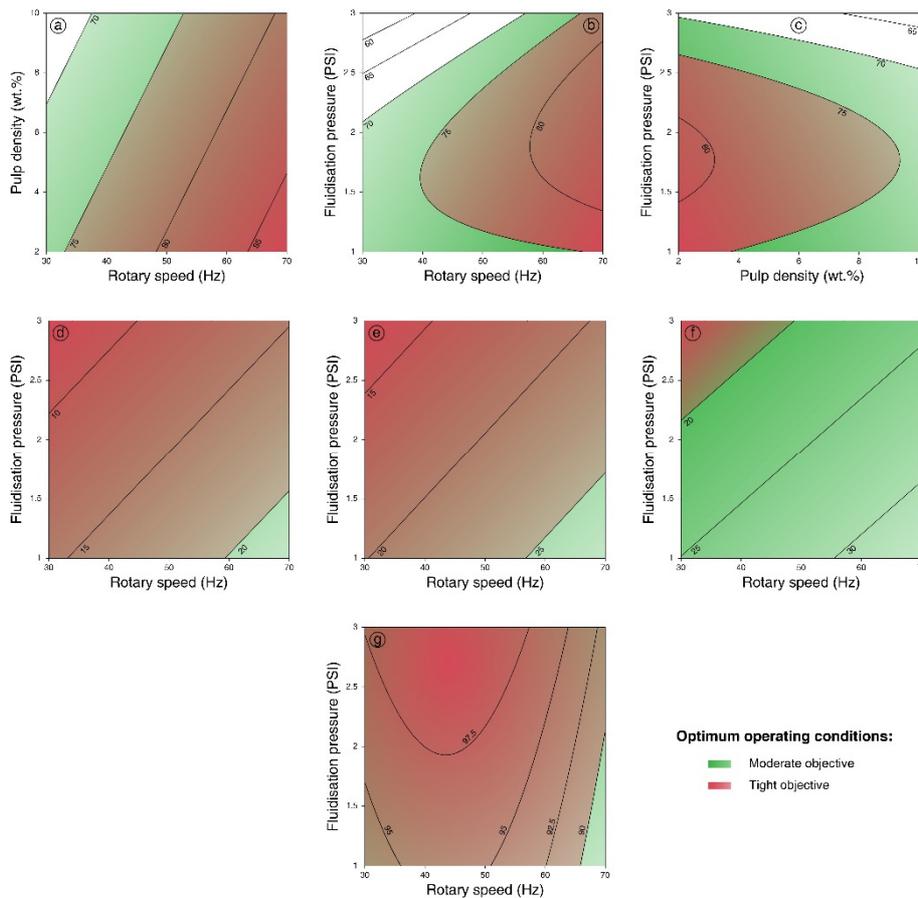
Figure 37. 2-D contour plots for WO_3 recovery (a, b, c), K_2O recovery (d), P_2O_5 recovery (e), Fe_2O_3 recovery (f), and desliming efficiency (g) for the Falcon SB models as a function of the operating parameters. The green and the red zones correspond to values which satisfy respectively the moderate and the tight performance objectives defined in Table 8.

Optimum operating conditions were selected based on the models determined previously and on Figure 38. A compromise had to be made between the WO_3 recovery and the WO_3 grade. The global objective was to eliminate the gangue minerals that are problematic for flotation, meaning that the gangue minerals recoveries had to be minimised as much as possible. Hence, following the iso-responses graphs (Figure 38), the pulp density should be minimised (2 wt.% solid), the fluidisation pressure should be maximised (3 PSI) whereas intermediate rotary speed must be defined (58 Hz) to reach a compromise between WO_3 recovery, gangue minerals recoveries, and desliming.
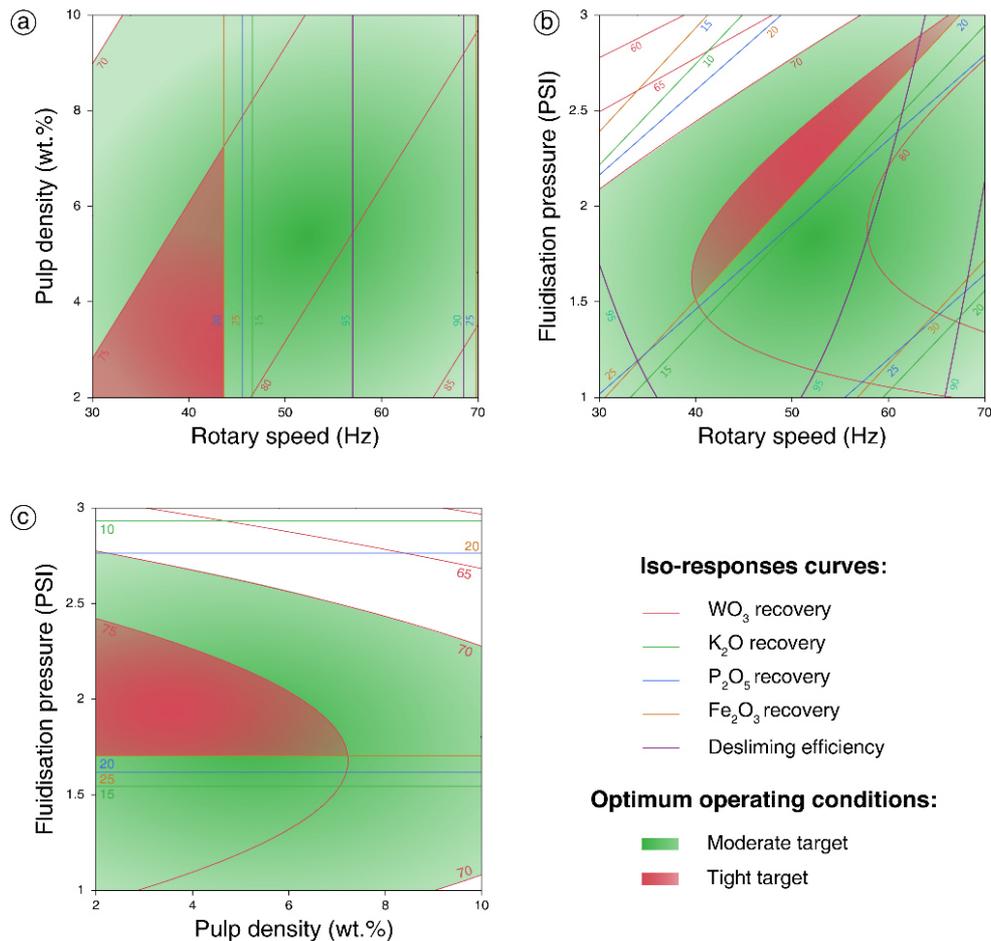
Figure 38. 2-D contour plots for the 5 studied responses (WO_3, K_2O, Fe_2O_3, and P_2O_5 recoveries and desliming efficiency) for the Falcon SB models as a function of the operating parameters. Targets represent zones where the objectives set on all the studied responses, defined in Table 8, are reached.

Since the separation is mainly led by the rotary speed and the fluidisation pressure, the WO_3 enrichment ratio and the WO_3 recovery could be expressed as a function of these two latter parameters. The pulp density was minimised, according to Figure 38, to build the response surfaces presented in Figure 39, which allow to summarise the above-mentioned effects: decreasing the fluidisation pressure induces higher WO_3 recoveries but lower WO_3 enrichment ratios, *i.e.* gangue minerals rejection, while decreasing the rotary speed induces lower WO_3

recoveries along with higher WO₃ enrichment ratios (Figure 39). The surfaces however display parabolic trends, highlighting the fact that intermediate values had to be chosen for rotary speed.
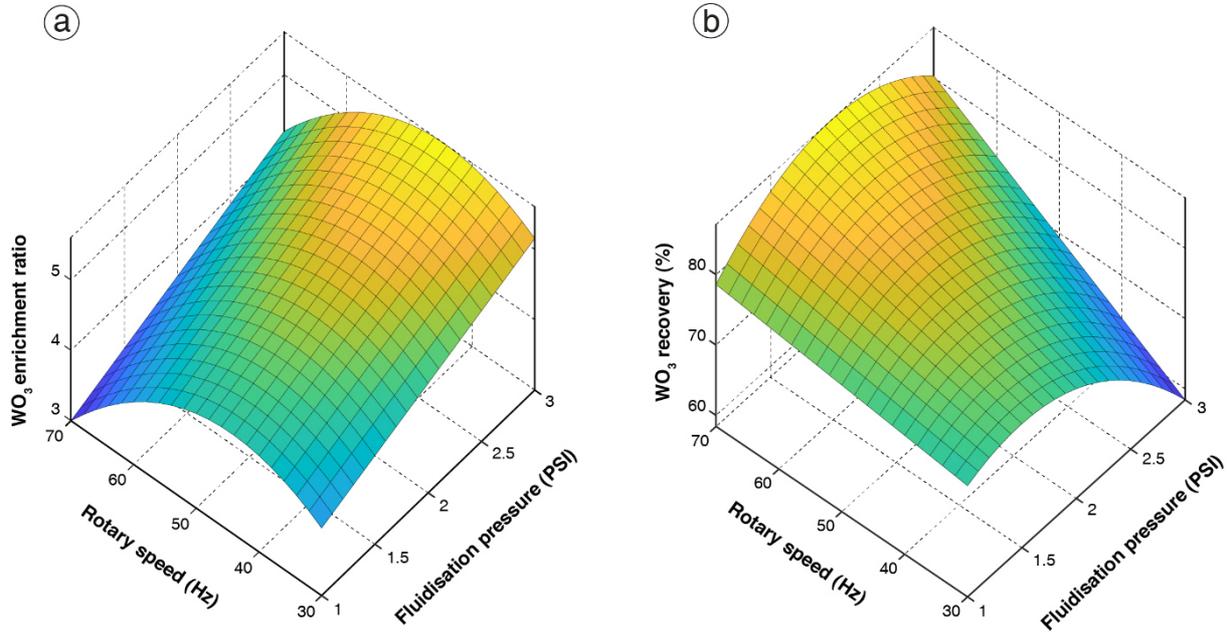
Figure 39. Response surfaces presenting the WO₃ enrichment ratio (a), proportional to the gangue minerals rejection, and the WO₃ recovery (b) as a function of the two main parameters affecting them, *i.e.* the rotary speed and the fluidisation pressure, for Falcon SB. To establish these surfaces, the pulp density was set to the optimal value, *i.e.* 2 wt.% (minimum value), while the pulp flowrate has no effect on these responses.

A test with the optimised operating parameters was performed and reproduced seven times to assess the experimental variability (Table 12). The experimental errors are quite low, indicating a good reproducibility of the experiments. The errors between the predicted and the observed values are very low, indicating a good accuracy of the five developed models.

Table 12. Validation test for the Falcon SB based on a test with optimised parameters (ω = 58 Hz; $\%_S$ = 2 wt.%; Q = 3 kg · min⁻¹; f = 3 PSI) repeated seven times.

	R_W	R_K	R_P	R_{Fe}	D_{eff}
Mean	71.61	12.63	22.62	17.15	98.78
Absolute experimental standard deviation	3.52	1.29	3.16	1.24	0.06
Predicted by the model	73.74	12.51	21.77	18.20	97.29
Model absolute error	2.07	-0.12	-0.85	1.05	-1.49

3.3 Discussion on experimental results

Based on Figure 35, the Falcon UF does not allow to reach the tight objectives defined in Table 8 while Figure 38 shows that they are reached for very specific operating conditions with the Falcon SB. It demonstrates a higher ability of Falcon SB for the gangue minerals elimination

compared to Falcon UF. Further comparisons of the two bowls in terms of gangue minerals elimination and desliming efficiency are presented in Figure 40, using previous results from the DOE. First, the grade-recovery graph for WO_3 (Figure 40a) shows that Falcon SB allows obtaining WO_3 recoveries ranging from 50% to 86% with WO_3 enrichment ratios ranging from 1.83 to 7.92. Due to its optimised bowl design and the addition of a fluidisation pressure, the Falcon SB displays better performances than the Falcon UF despite a slight decrease in WO_3 recoveries (Figure 40a). This latter produces concentrates with WO_3 recovery ranging from 60% to 92% and WO_3 enrichment ratio ranging from 1.30 to 2.88 (Figure 40a). As a comparison, the underflow of a classical hydrocyclone stage with a 10 µm cut-off displays a 1.2 WO_3 enrichment ratio for 92% WO_3 recovery (Figure 40a). These losses are in accordance with the homogeneous distribution of scheelite in the size fractions.

The desliming efficiency of each apparatus is also presented as a function of the WO_3 recovery (Figure 40b). Desliming is very efficient with Falcon SB as the desliming efficiency ranges from 80 to 98%, far better than those obtained with a hydrocyclone (Figure 40b). Indeed, the desliming efficiency with hydrocyclone is 48%, which is around the values obtained with the Falcon UF (Figure 40b). The high desliming performances obtained with both bowls suggest that Falcon concentrators can be used as a pre-concentrating and a desliming apparatus, prior to fatty-acid flotation, therefore substituting to hydrocyclones in flotation feed preparation circuits.

The WO_3 enrichment ratio is expressed as a function of the yield in Figure 40c. The yields are comprised between 8% and 33% for the Falcon SB and between 29% and 63% for the Falcon UF. Such values are very well correlated with the WO_3 enrichment ratio, as the Figure 40c shows: the highest WO_3 enrichment ratios correspond to the lowest yields. Hence, a pre-concentration stage with a Falcon concentrator, in particular the Falcon SB, would lead to a significant decrease of the pulp subjected to the flotation stage, reducing the energy, water, and reagents consumptions. The selectivity curve shown in Figure 40d expresses the WO_3 recovery as a function of yield. While the hydrocyclone displays a very poor selectivity, as expected, the Falcon SB is more selective than the Falcon UF, exhibiting lower yields for roughly equivalent WO_3 recoveries (Figure 40d).
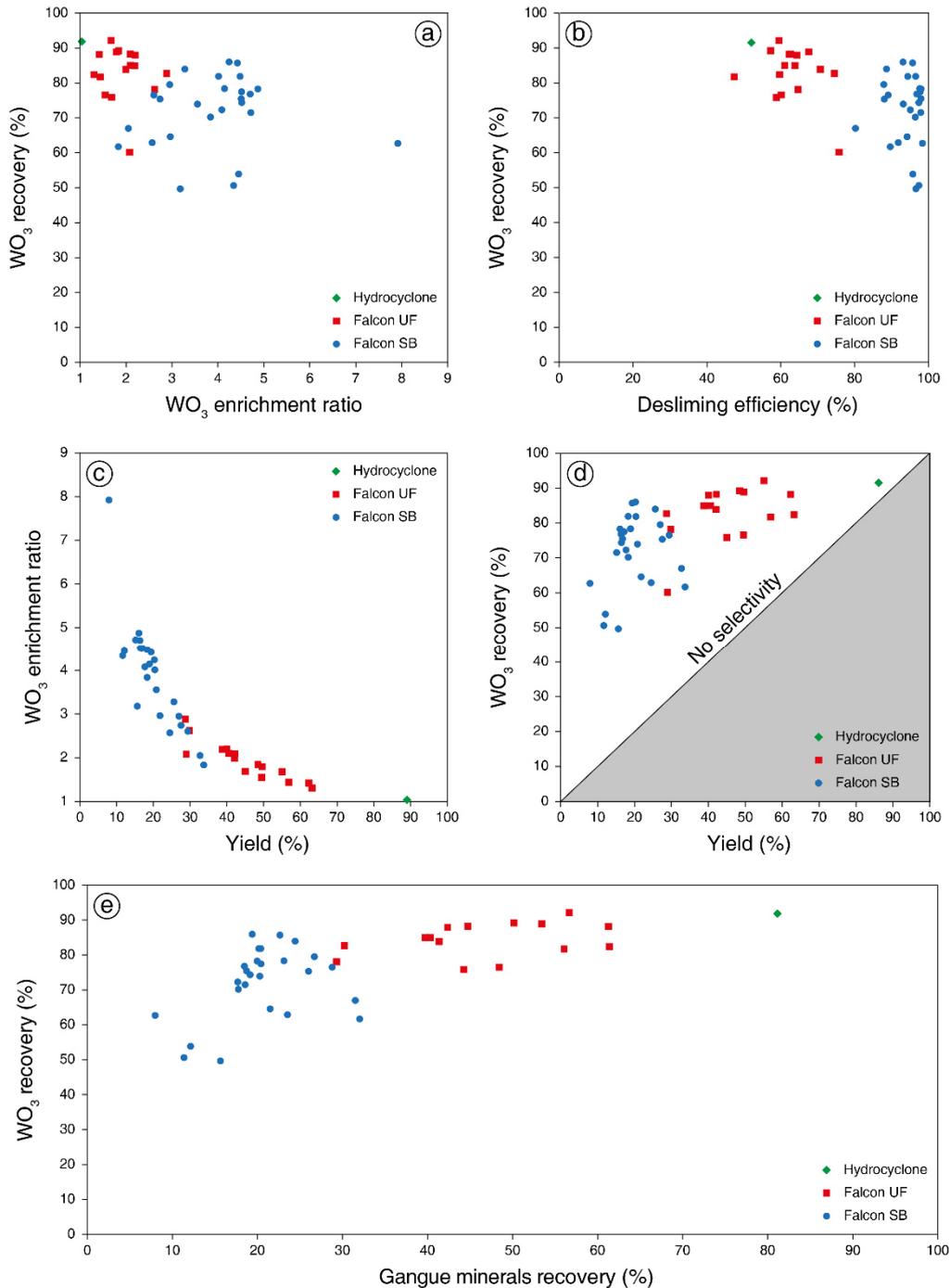
Figure 40. Comparison between a Falcon UF, a Falcon SB, and a classical hydrocyclone in terms of separation performances using the DoE results. **a.** WO₃ recovery versus WO₃ enrichment ratio (grade-recovery curve); **b.** WO₃ recovery versus desliming efficiency; **c.** WO₃ enrichment ratio versus yield; **d.** WO₃ recovery versus yield (selectivity curve); **e.** WO₃ recovery versus gangue minerals recovery.

Another selectivity curve, displaying the WO₃ recovery as a function of the gangue minerals recoveries is shown in Figure 40e. Overall, for the best tests in terms of gangue minerals elimination, 89% of the apatite, 89% of the fluorite, and 93% of the silicates (light + dense) are rejected from the concentrate. This crucial result indicates that apatite and fluorite, which are

known to be highly problematic in fatty-acid flotation, could be eliminated by a Falcon pre-concentrating stage prior to flotation.

The rotary speed has a negative effect on the gangue mineral recoveries for the Falcon UF but a positive effect for the Falcon SB. Moreover, the pulp density has very little effect on the recoveries for the Falcon SB and a significant positive effect on the gangue mineral recoveries for the Falcon UF. This may indicate a difference in the separation mechanisms between the two bowls. In the Falcon UF, the separation is mostly governed by the differential settling of the particles in the flowing film, before the concentration zone in the upper part of the bowl. It means that the parameters affect the separation performance by influencing the differential settling mechanisms: the rotary speed decreases the settling length of the particles while the pulp density impels either a hindered or a forced settling of particles. In the Falcon SB, the separation seems mostly lead by the forces balance between the centrifugal force, increasing with the rotary speed, and the fluidisation pressure. The differential settling occurring in the flowing film before the particles reach the gutters seems to have little influence on the separation performance, indicating that the actual separation happens in the gutters.

4. Conclusions

Gravity concentration of a complex W-skarn has been investigated using a Falcon concentrator with the global aim of eliminating the calcium-bearing minerals that are known to be problematic during fatty-acid flotation. Furthermore, the desliming efficiency was studied to enable the utilisation of the Falcon concentrator as a pre-concentrating and desliming apparatus, prior to flotation. Thus, the influence of the operating parameters on the Falcon UF and Falcon SB performances were modelled using the DOE methodology. It allowed to set the best conditions to attain the elimination of 75% and 77% of the total amount of apatite and fluorite with the Falcon UF and Falcon SB, respectively. The Falcon SB exhibited better performances with up to 98% of fine particles rejected from the pre-concentrate, a WO_3 recovery higher than 70%, a WO_3 enrichment ratio higher than 4.5, and a yield of around 15%. Given the good elimination of calcium-bearing minerals and fine particles, the pre-concentrate could directly undergo a flotation process with fatty acids as the lack of selectivity between the calcium-bearing minerals would not be a problem anymore. Also, it allowed to reject 85% of the global yield by the gravity pre-concentration, leading to a decrease of 7 times of the reagents consumed in the flotation stage, as well as reducing the energy consumption. Since the choice was made to maximise the gangue minerals rejection, the Falcon separation induced around 30% of WO_3 losses in the tailings compared to around 10% of WO_3 losses for a classical hydrocyclone stage. A scavenger Falcon stage could be suggested to reduce these losses, which would anyhow be significantly decreased by up-scaling the laboratory scale Falcon UF and SB to an industrial Falcon C. Indeed, Falcon UF and SB, used at laboratory scale in this study, are operated in semi-batch and thus are not commonly used at industrial scale in continuous operations since they need to be installed in parallel circuits. For this reason, the Falcon C is more widely used in the industry, operating high pulp flowrates that are, unfortunately, not suitable for laboratory test work. However,

according to Sepro Mineral Systems (Sepro, 2015a, 2015b), the Falcon C efficiency at industrial scale can be assessed based on laboratory tests performed with semi-batch-operated Falcon SB/UF. Overall, replacing hydrocyclones by Falcon concentrators (SB or C) in flotation feed preparation circuits could lead to higher process performances while reducing the environmental impacts by allowing the replacement of usual ecotoxic reagents by the environment-friendly fatty acids, reducing the reagent and energy consumptions.

Investigation of the depressants for scheelite flotation from a complex tungsten skarn ore: focus on the sodium carbonate/sodium silicate system

1. General introduction

Different processing options are suitable to increase the separation contrast between scheelite and other gangue minerals, including calcium minerals. Separation of calcium minerals by flotation is very difficult because they all exhibit Ca atoms on their surface as well as similar Ca-Ca distance on the surfaces, Ca sites densities, and potentially anions, WO_4^{2-}, CO_3^{2-}, and PO_4^{3-} (see Chapter 1). Indeed, since fatty acids are known to chemisorb onto the surface Ca^{2+} ions, they display a lack of selectivity, inducing global flotation of the calcium minerals. In the previous chapter, the use of a Falcon concentrator was investigated to reject the calcium minerals, mostly the calcium salts, prior to flotation. However, the Falcon operating parameters were defined by doing a compromise between the calcium salts rejection and the scheelite recovery, which induced significant scheelite losses (see Chapter 3). These losses are common for gravity separations, which are known to be considerably less efficient than flotation. Hence, the increase of the selectivity in the froth flotation process would be an interesting achievement since it would allow to concentrate scheelite with lower losses compared to gravity separation. For a constant hydrodynamic regime, *i.e.* the same flotation cell, stirring conditions, pulp density, pulp viscosity, and aeration, the flotation selectivity depends totally on the adsorption selectivity. This selectivity can be modulated by the use of depressants, which are added prior to the flotation collector and prevent the adsorption of this latter on the gangue minerals. In the literature, the efficient flotation of scheelite from other calcium-bearing minerals has been reached using specific depressants, see Chapter 1.

A large investigation, presented in this chapter, has been conducted to define the optimal depressing conditions for the Tabuaço Main Skarn ore. In particular, based on the literature, several widely known flotation depressants were tested and their performances were compared in terms of WO_3 grade and recovery. Na_2CO_3 and Na_2SiO_3 exhibited the best performances for scheelite flotation, mainly attributed to high synergistic effects between the two reagents. Hence, their dosages were optimised following the DOE method, which also allowed to deeply investigate their linear effects as well as the synergistic effects existing between them. Finally, spectroscopic studies were combined with AIMD simulations to gain understanding in the molecular mechanisms resulting in the significant synergistic effects highlighted by the DOE method. This work has been partly published in **Powder Technology 352 (2019), under the title "Investigation of the depressants involved in the selective flotation of scheelite from apatite, fluorite, and calcium silicates: focus on the sodium silicate/sodium carbonate system"**. Moreover, the last part of this chapter is under review in the **Chemical Science journal**.

2. Investigation of the depressants involved in the selective flotation of scheelite from apatite, fluorite, and calcium silicates

   2.1 Introduction

As described in Chapter 1, the main depressant used in the selective separation of scheelite from gangue minerals is Na_2SiO_3. This depressant traditionally exhibits better efficiency when it is

used in conjunction with Na_2CO_3. Studies have also demonstrated that the addition of metallic cations, such as Fe^{3+}, Al^{3+}, and Pb^{2+} combined with Na_2SiO_3 in the flotation process can enhance the selectivity of the separation. Besides, organic polymers such as tannins and starch, as well as chelating agents, *e.g.* citric acid, are known to depress calcium-bearing minerals in some cases. Most of the time, these depressants have been tested in microflotation tests or in binary mixtures that are not realistic and cannot represent a real ore. Indeed, the adsorption of such reagents onto mineral surfaces can be affected by the presence of several minerals in the same solution, since the depressants will adsorb onto the mineral on which the adsorption is the most favoured.

In this first part, the use of several depressants was investigated to enhance the separation contrast between scheelite and gangue minerals (apatite, fluorite, and silicates) on the Tabuaço ore, which mineralogical composition has been presented in Chapter 2. It allowed to study accurately the adsorption selectivity of the reagents onto minerals since all the flotation tests were performed on the Tabuaço ore, in which a dozen of different minerals have been identified. First, sole Na_2SiO_3 was tested in the flotation process and, then, its combination with metallic cations (Fe^{2+}, Al^{3+}, and Zn^{2+}) or with Na_2CO_3. Besides, several organic molecules (starch, lignin sulfonate, citric acid, tannin, and carboxymethyl cellulose) were tested in the flotation process as a substitute for Na_2SiO_3.

2.2 Results and discussions

2.2.1 Sodium silicate

As stated previously, the most used depressant for gangue minerals, in particular for silicates, is Na_2SiO_3 and, therefore, was tested on the Tabuaço ore with the global objective to reach a selective flotation of scheelite from gangue minerals. Flotation tests were performed with various dosages of Na_2SiO_3, with the classical TOFA collector (RBD15) at a concentration set to 200 g/t. To discuss the effects of Na_2SiO_3 on the minerals depression, the WO_3, P_2O_5, F, and SiO_2 recoveries were calculated and are presented in Figure 41. The Na_2SiO_3 dosages represent pure Na_2SiO_3 dosages, since the commercial Na_2SiO_3 solution used here contains only 33% of pure Na_2SiO_3.
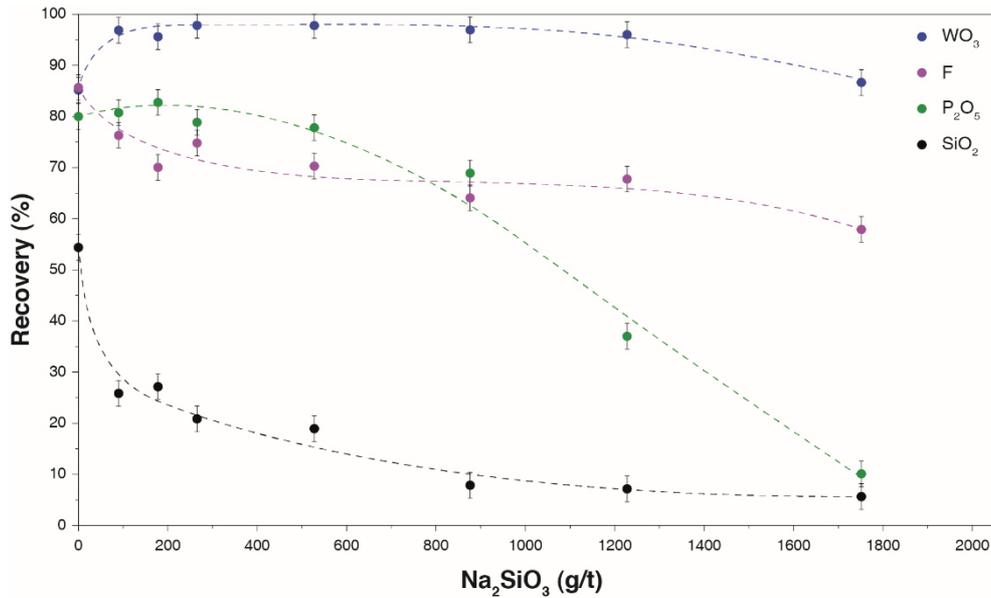
Figure 41. WO_3, F, P_2O_5, and SiO_2 recoveries as a function of Na_2SiO_3 dosage.

Na_2SiO_3 has a little influence on scheelite flotation until 1,775 g/t, at which scheelite is slightly depressed (Figure 41). Without Na_2SiO_3, scheelite recovery is significantly lower, which can be attributed to the consumption of collector by other minerals (gangue minerals such as silicates) leading to a decrease of the WO_3 recovery. Apatite is depressed efficiently at 1,225 g/t and more of Na_2SiO_3 (Figure 41) while scheelite is not significantly impacted at this dosage. Moreover, silicate minerals undergo a strong depression, increasing with the quantity of Na_2SiO_3 added, but really efficient at 875 g/t. From this dosage, the SiO_2 recovery is lower than 10%, which represents an acceptable value for a rougher stage. Fluorite exhibits the same behaviour than scheelite in terms of depression by Na_2SiO_3: the amounts of Na_2SiO_3 required for fluorite depression also depress scheelite. This can be attributed to the very similar calcium site densities (see Chapter 1) on the mineral surfaces between scheelite and fluorite, since the depression of calcium minerals by Na_2SiO_3 is mostly linked to the adsorption of silica species [$Si(OH)_4$, $SiO(OH)_3^-$] onto surface calcium atoms (Azizi and Larachi, 2018; Fuerstenau et al., 1972; Marinakis, 1980; Marinakis and Shergold, 1985b). The best flotation test, *i.e.* with 1,225 g/t of Na_2SiO_3, produces a concentrate assaying 6.2% WO_3 with 95.1% WO_3 recovery, from a feed assaying 1.1% WO_3. However, for this test, the concentrate assays 2.7% P_2O_5 with 39.2% P_2O_5 recovery, which still represent high values indicating that apatite is not enough depressed. Also, SiO_2 recovery is still 7.7%. Increasing the Na_2SiO_3 dosage results in an unsuitable depression of scheelite, which highlights that Na_2SiO_3 does not allow to completely depress silicates since a high Na_2SiO_3 concentration conducts to its adsorption onto scheelite. Overall, the depression of silicates by Na_2SiO_3 is mainly related to the formation of $Si-O-Si(OH)_3$ onto silicon surface atoms (Fuerstenau et al., 1972). Considering the binding energies of Si-O and Ca-O, the formation of $Si-O-Si(OH)_3$ is probably much more favoured than the formation of $Ca-O-Si(OH)_3$, occurring for calcium minerals surfaces. This can explain the low depressing effect of Na_2SiO_3 onto calcium salts (apatite, scheelite, and fluorite) since they exhibit no silicon atom on their surfaces. Overall, the use of lone Na_2SiO_3 allows to enhance significantly the separation contrast between scheelite,

apatite, and silicates. However, this increase is not enough since the recoveries of undesirable minerals are still high. Moreover, Na_2SiO_3 is not efficient concerning fluorite, suggesting that other depressants must substitute Na_2SiO_3 or be combined with it to improve the depression of gangue minerals, including fluorite.

2.2.2 Combination of sodium carbonate and sodium silicate

NaOH, previously used to set the pH to 10 was substituted with Na_2CO_3, which, based on the literature, can exhibit interesting synergistic effects with Na_2SiO_3 (Agar, 1984; Kupka and Rudolph, 2018b). A test was then performed at the optimal Na_2SiO_3 dosage defined previously and adding 1,150 g/t Na_2CO_3 prior to the addition of Na_2SiO_3.
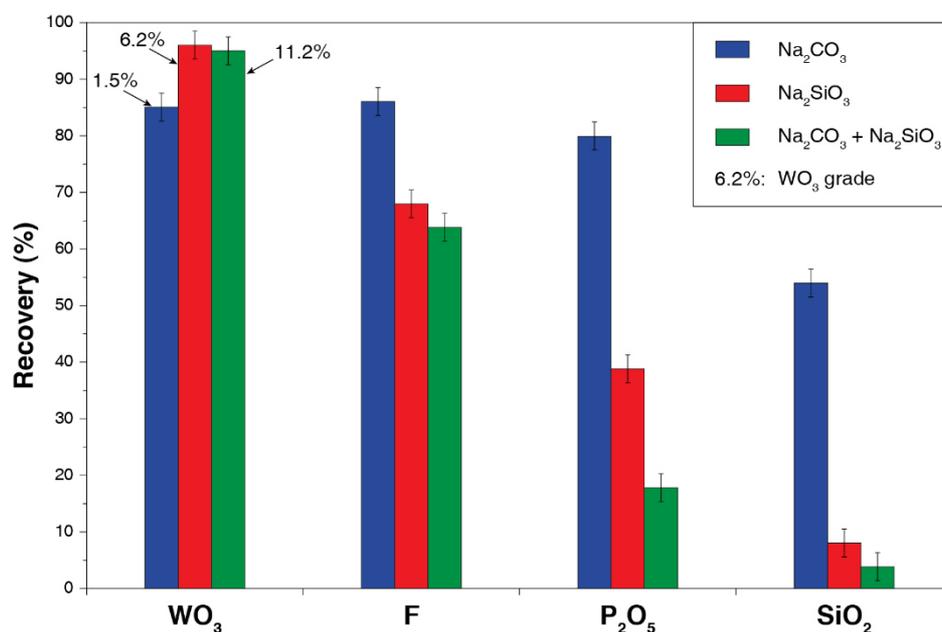
Figure 42. WO_3, F, P_2O_5, and SiO_2 recoveries for Na_2CO_3 used alone, Na_2SiO_3 used alone, and both reagents used in combination.

The flotation selectivity is significantly enhanced regarding silicates, apatite, and, to a lesser extent, fluorite (Figure 42). The SiO_2 and P_2O_5 recoveries decrease significantly, being divided by 2 compared to the test with lone Na_2SiO_3. This allows to increase the WO_3 grade of the rougher concentrate to 11.2% WO_3 without impacting the WO_3 recovery. Used alone, sodium carbonate is a pH modifier which exhibits no impact on the flotation except to not depress the gangue minerals, leading to a consumption of collector by other species than scheelite, which results in a decrease of WO_3 recovery (Figure 42). These synergistic effects are difficult to interpret in terms of surface molecular mechanisms. They could be related to the formation of a $CaCO_3$ layer on the calcium minerals surfaces (Bahr et al., 1968; Miller and Hiskey, 1972; Rahimi et al., 2017) when Na_2CO_3 is used, resulting in a better depression by Na_2SiO_3 that is known to have a high affinity for calcite (Bo et al., 2015; Gao et al., 2015a; Kupka and Rudolph, 2018b). Nonetheless, these effects should be thoroughly investigated by specific experimental methods, allowing to unravel the mechanisms involved in these observed synergistic effects.

2.2.3   Combination of sodium silicate and metallic cations

Previous studies have reported that Na_2SiO_3 exhibits a strong depressing effect on silicates as well as on apatite and calcite, increased when it is used in combination with different metallic cations (see Chapter 1). Thus, the addition of zinc, iron, and aluminium salts, prior to the addition of a constant optimal Na_2SiO_3 dosage (1,225 g/t) determined previously, was investigated. Lead cations are also very efficient in the scheelite flotation process. However, lead is a strong water pollutant and thus, it was not tested in this present work. Although the addition of 1,000 g/t aluminium nitrate before the addition of the referential 1,225 g/t Na_2SiO_3 improves the depressions of the silicates, apatite, and fluorite, it also strongly depresses the scheelite (Figure 43). This indicates that the aluminium salt is non-selective, even if Al^{3+} ions are known to form an AlF_3 complex. However, this complexation occurs at pH ~5.5, while this study has been conducted at pH 9. Moreover, *ab initio* modelling has proven that Al adsorption (weak bonding) on the fluorine atoms of the fluorite surface is negligible (Rietjens, 1998). Besides, the combination of 500 g/t iron sulphate with 1,225 g/t of Na_2SiO_3 significantly improves the depressant effect of Na_2SiO_3 on apatite and, to a lesser extent, that on fluorite (Figure 43). When the amount of iron sulphate is increased to 1,000 g/t, all the minerals are depressed. Hence, the selectivity between scheelite and fluorite is not enhanced with the addition of iron sulphate.
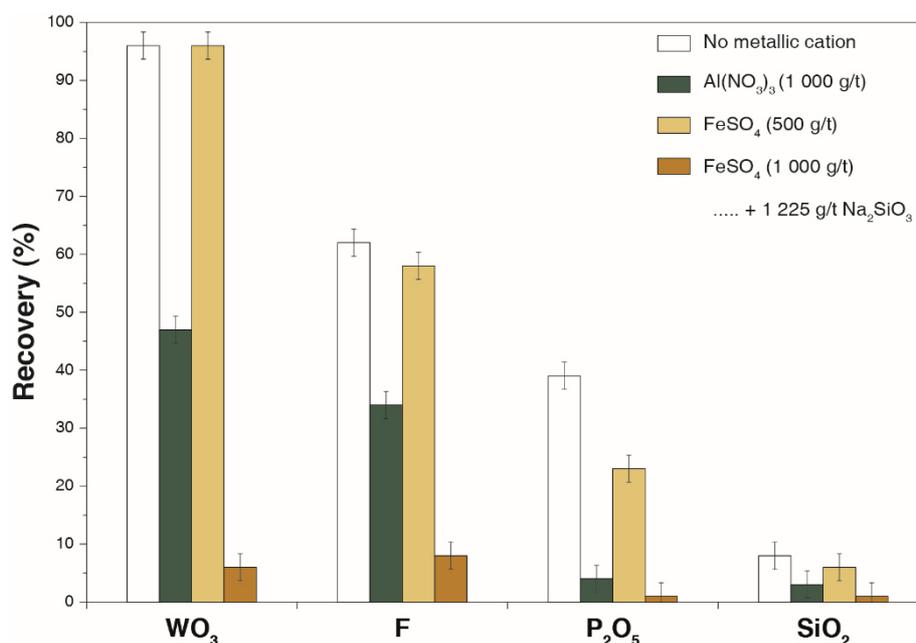
Figure 43. Scheelite, fluorite, apatite, and silicate recoveries versus the addition of aluminium and iron cations in various quantities prior to the addition of 1,225 g/t Na_2SiO_3.

Considering these results, tests with different concentrations in $ZnSO_4$ have been performed to assess the influence of the metallic cations concentration in solution prior to the addition of Na_2SiO_3. Compared to the addition of sole Na_2SiO_3, the combination of 75 g/t zinc sulphate with 1,225 g/t Na_2SiO_3 leads to better apatite flotation, while scheelite, fluorite, and silicates are only

slightly more depressed. No selectivity is reached, while increasing the zinc sulphate quantity induces the global depression of all the minerals, including scheelite (Figure 44).
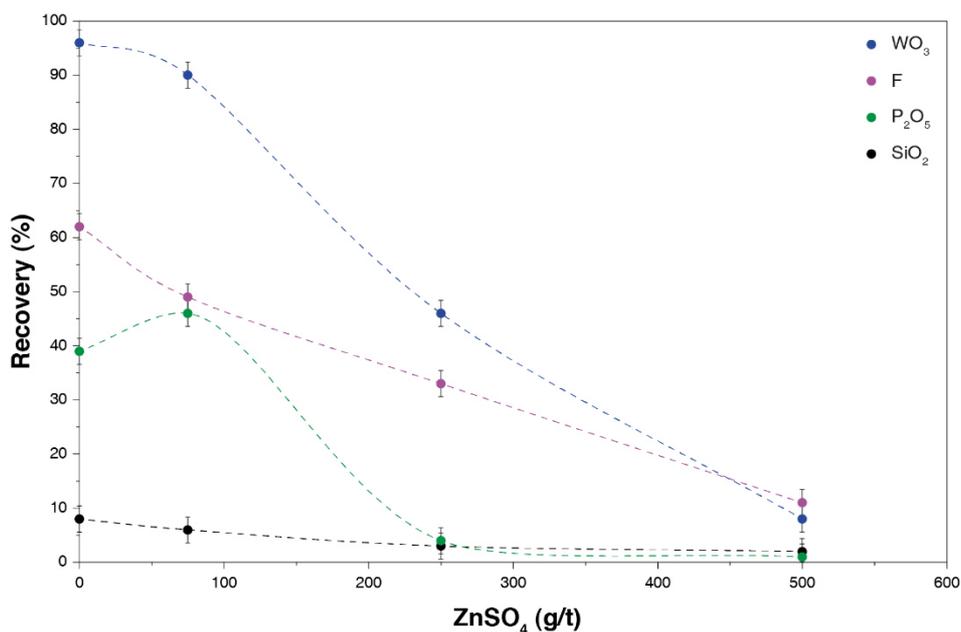
Figure 44. WO_3, F, P_2O_5, and SiO_2 recoveries as a function of the $ZnSO_4$ dosage added prior to Na_2SiO_3.

Reported changes in the zeta potentials, when metallic cations are added in the flotation process, suggest that depression by metallic cations can be linked to their adsorption onto the minerals surfaces (Mercade, 1975; Raatz, 1992; Torem et al., 1992; Wang and Yu, 2007; Zachara et al., 1988). At alkaline pH, the metallic cations are assumed to adsorb, via hydroxo-complexes, onto the mineral surfaces (Raatz, 1992; Rakotonarivo et al., 1985). This prevents the adsorption of the collector onto the surface calcium ions. Moreover, free metallic cations in solution can interact strongly with the carboxylate, decreasing the availability of the collector. The interactions between metallic cations and Na_2SiO_3 is not well understood. Some authors assume the formation of hydroxo-metallic-silicate colloids that adsorb onto the mineral surface, leading to depression by preventing the collector adsorption (Feng et al., 2017; Mercade, 1975). However, the interactions between metallic cations and Na_2SiO_3 seem very small. Indeed, low quantities of metallic cations do not significantly alter the depression so that Na_2SiO_3 is the main depressing factor (Figure 44). High quantities of metallic cations strongly depress all the minerals, proving that the effect of Na_2SiO_3 is no more significant than the effect of polyvalent cations (Figure 44). In order to study deeply the interactions between Na_2SiO_3 and metallic cations, a test was performed with 750 g/t of $FeSO_4$ (intermediate quantity) added prior 1,225 g/t of Na_2SiO_3 and compared with the test where the two reagents were premixed prior to their addition. The premixing results in a depression of all minerals, including scheelite: the WO_3 recovery is decreased from 98.3% (successive addition) to 13.2% (premixed addition). Premixing Na_2SiO_3 and metallic cations probably leads to the production of metal ion-Na_2SiO_3 polymer (Wei et al., 2018) that exhibits a strong non-selective depressing effect.

2.2.4   Organic molecules

Over the past decades, researchers have highlighted the depressant effect of organic molecules and polymers for various minerals, including silicates, calcite, and fluorite (see Chapter 1). Hence, in the approach that aimed at defining the best depressing conditions for the Tabuaço ore, some widely used organic molecules have been tested in batch scale flotation tests. All the tested organic molecules exhibit similar behaviour (Figure 45), which leads to an efficient silicate depression and a moderate depression for apatite, fluorite, and scheelite; however, no selectivity is observed. The surface anions/hydroxyl groups are involved in H-bond formation with the hydroxyl groups (either their oxygen or their hydrogen atom) of the organic molecules (Filippov et al., 2013; Lee et al., 2013; Wang and Somasundaran, 2005), while the surface cation, *e.g.* calcium atoms establish bonds with their carboxyl groups (Burdukova et al., 2008; Filho et al., 2000; Somasundaran, 1969; Wang and Somasundaran, 2005).
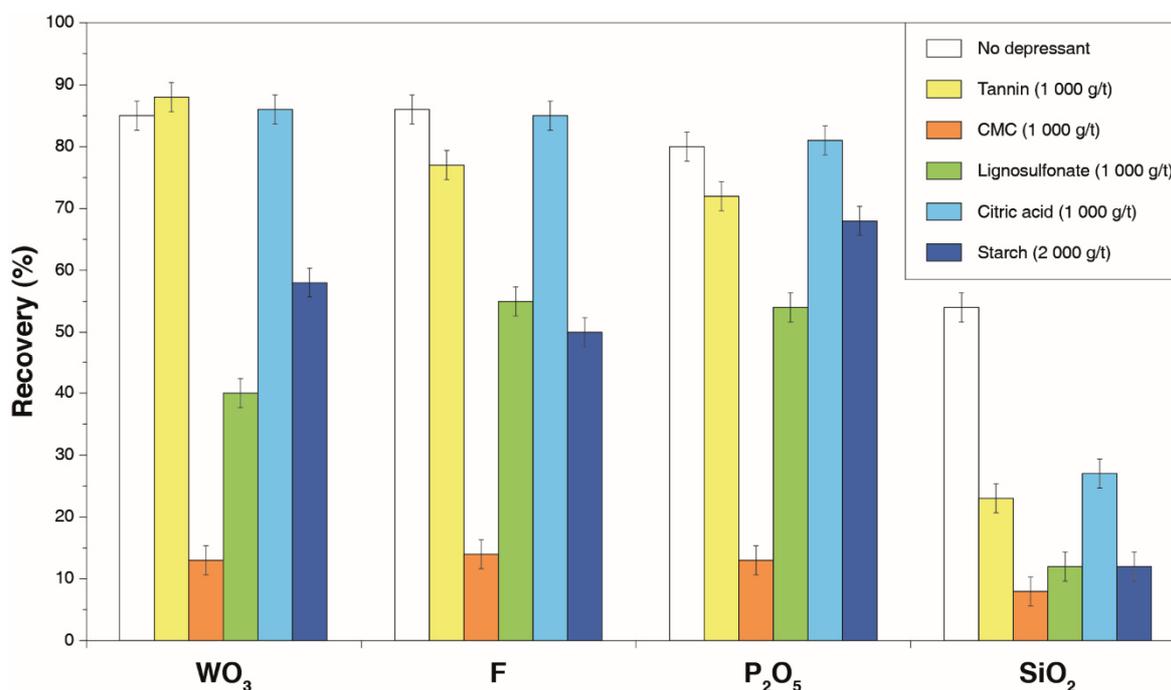
Figure 45. Scheelite, fluorite, apatite, and silicate recoveries versus the addition of tannin, carboxymethyl cellulose, lignosulfonate, citric acid, and starch.

Moreover, these molecules are large with high surface coverage, which may erase all the differences in the crystallographic properties of the minerals. Citric acid is known to form a complex with Ca^{2+} ions at alkaline pH (Gao et al., 2016a; X. Liu et al., 2017); nevertheless, no selectivity is observed during complexation with the calcium ions present in apatite, fluorite, and scheelite (Figure 45). None of the molecules tested in this study afford the selective separation of scheelite from fluorite and apatite.

2.3 Conclusion

Different depressants were tested to attain the selective depression of gangue minerals from scheelite, to eliminate them from the scheelite concentrate, which would enhance the WO_3 grade and eliminate penalising elements from the concentrate. The efficiencies of the different depressants in terms of WO_3 recovery and grade in the flotation concentrate are summarised in Figure 46. First, sole Na_2SiO_3 afforded an efficient depression of silicate minerals and a moderate depression of apatite, with however very poor selectivity between scheelite and fluorite. Then, Na_2SiO_3 was compared to different organic molecules, namely tannin, CMC, lignosulfonate, citric acid, and starch. All these molecules exhibited very low selectivity compared to sole Na_2SiO_3. Next, the addition of various metallic cations (Al^{3+}, Zn^{2+}, and Fe^{2+}) followed by Na_2SiO_3 demonstrated little improvement in the selectivity, with significant loss in scheelite. On the other hand, the addition of 500 g/t iron sulphate displayed an increase in apatite depression with no decrease in WO_3 recovery. However, the results were not better than those afforded when Na_2CO_3 was added prior to the addition of Na_2SiO_3.
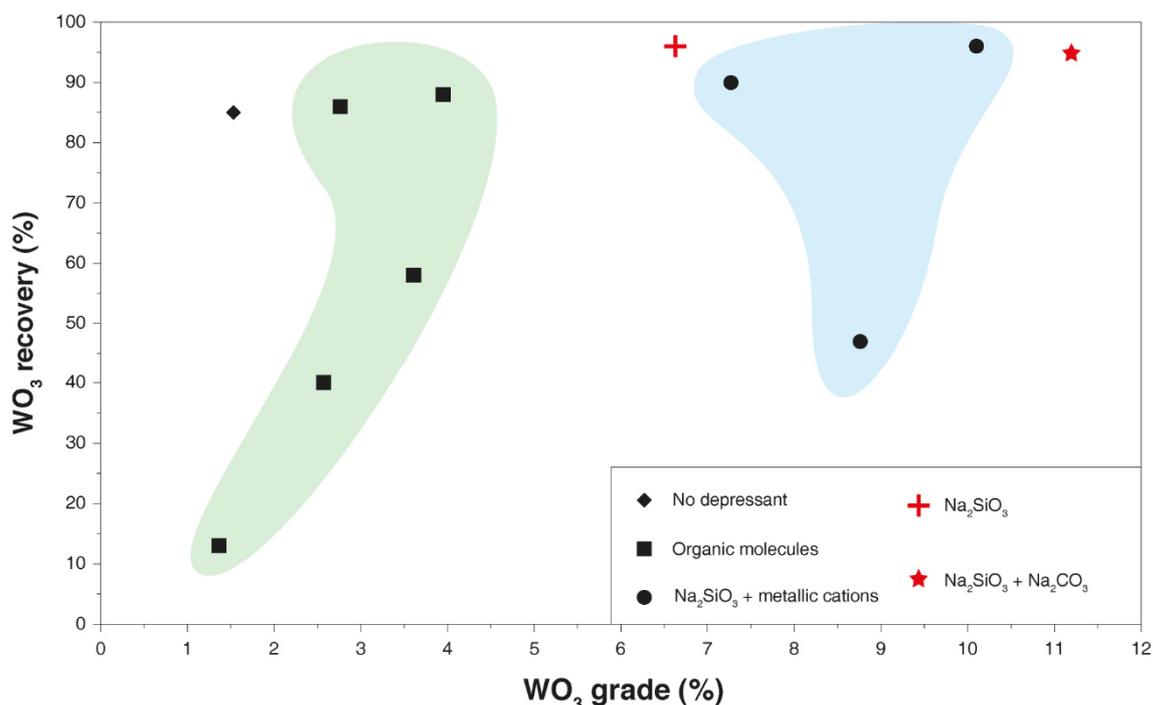
Figure 46. WO_3 recovery as a function of WO_3 grade for the different tested depressants.

3. The Na_2CO_3/Na_2SiO_3 synergistic depressing system in the flotation of scheelite from fluorite, apatite, and calcium minerals

3.1 Introduction

In the previous part, a preliminary investigation was conducted to find a depressing system suitable for selective flotation of scheelite from fluorite, apatite, and calcium minerals. Among all the tested depressants, the use of Na_2CO_3 as the pH modifier combined with Na_2SiO_3 afforded

the best performances for scheelite flotation in terms of WO_3 recovery and grade. Under aqueous conditions, Na_2CO_3 totally dissociates to form the carbonate ion (CO_3^{2-}), a weak base involved in the HCO_3^-/CO_3^{2-} couple (pKa = 10.2). For this reason as well as for its buffering effect, Na_2CO_3 is commonly used in the froth flotation process as a pH modifier (Bulatovic, 2010; Kupka and Rudolph, 2018b). Its addition prior to Na_2SiO_3 produces positive synergistic effects on gangue minerals depression, which have been observed and used by researchers over the past decades (see Chapter 1). These effects have also been observed in the present study, since the WO_3 grade in the concentrate increased from 6.2% to 11.2% when Na_2CO_3 was used as the pH modifier instead of NaOH (see section 2.2.2). Nevertheless, the influence of both reagents, including their synergy, on the minerals floatabilities, are still poorly understood. Hence, the DOE methodology was used to characterise thoroughly the Na_2CO_3/Na_2SiO_3 system and to understand the mechanisms involved in the depression of all the minerals, including scheelite. Moreover, since DOE method traditionally allows to optimise the studied responses, it was used to define optimal Na_2CO_3 and Na_2SiO_3 dosage to maximise the flotation separation performances (WO_3 recovery and grade). For this study, the Response Surface Methodology (RSM) was used with the number of levels was set to four, so that a total of 16 experiments were performed. The main objectives were to model and gain understanding in the effect of each parameter and their interactions as well as optimising the depressants combination for the flotation process. Preliminary flotation tests were performed to set the limits and levels of the experimental area (Table 13). They were included in the results to establish the best model. A student test was performed on each calculated model coefficient with a confidence level of 95% to select the significant coefficient. The analysis of variance (ANOVA) was used to assess the model significance and eliminate the non-significant coefficients from the final models.

Table 13. Independent factors and corresponding levels of the experimental designs for both the un-coded and coded variables.

Factors	Levels				Coded variables
	1	2	3	4	
[Na_2SiO_3] (kg/t)	0.526	0.877	1.228	1.754	$x_1 = ([Na_2SiO_3] - 0.9893)/1.6667$
[Na_2CO_3] (kg/t)	0	1.333	2.667	4	$x_2 = ([Na_2CO_3] - 1.7778)/2$

3.2 DOE results

The experimental results served as a basis to determine the second order response functions, based on Eq. 9. These functions represent the expression of the studied responses, namely the WO_3 enrichment ratio and the WO_3, P_2O_5, F, and SiO_2 recoveries. After the first modelling step, the ANOVA was performed on each model to estimate their significance. The F-test was performed on the models, with a 0.05 significance level. The critical F-value was then calculated, considering the degrees of freedom of the models and the residuals. This value was then compared to the calculated F-values of the models. For each model, the critical F-value was significantly lower their F-value, suggesting that the p-values were very low. This indicated that the

probability that the model could be adjusted as a simple mean was very small. The non-significant coefficients for the 0.05 significance level were not included in the final models. The coefficients were recalculated and the ANOVA was performed again. The validation of the models was performed through the relationships between the experimental and predicted results. For this statistical analysis, both the R^2 and the RMSE were studied (Table 14).

Table 14. Summary of fit for validation using the correlation coefficients (R^2) and root errors (RMSE).

	WO$_3$ ratio	WO$_3$ recovery (%)	P$_2$O$_5$ recovery (%)	F recovery (%)	SiO$_2$ recovery (%)
R^2	0.9647	0.9482	0.8705	0.9065	0.9126
RMSE	0.6970	2.8096	12.4389	4.5439	2.5325

3.3 Interpretation of the models

For all the models, the Student's t-test was performed on each coefficient to determine whether they significantly impact the results. Since the non-significant coefficients were eliminated from the models, for all the values, P is <0.05, the chosen significance level. For the WO$_3$ enrichment ratio (G) and the WO$_3$ (R_W), P$_2$O$_5$ (R_P), F (R_F), and SiO$_2$ (R_S) recoveries, the final models as a function of the coded variables are:

$$G = 8.76 + 4.17x_1 + 1.28x_2 + 2.12x_1x_2 - 1.43x_1^2 - 1.35x_2^2 \tag{26}$$

$$R_W = 91.40 - 12.01x_1 - 6.05x_2 - 9.21x_1x_2 - 4.77x_1^2 \tag{27}$$

$$R_P = 45.78 - 48.31x_1 \tag{28}$$

$$R_F = 59.73 - 16.87x_1 - 6.14x_2 - 10.58x_1x_2 \tag{29}$$

$$R_S = 3.89 - 8.84x_1 - 1.97x_2 + 9.94x_1^2 \tag{30}$$

The WO$_3$ enrichment ratio is affected by positive linear effects for both reagents. However, the Na$_2$CO$_3$ displays a low coefficient (1.28) compared to that observed for Na$_2$SiO$_3$ (4.17). The quadratic effects for these factors negatively influences the WO$_3$ enrichment ratio, with coefficients of -1.43 and -1.35, respectively. Moreover, the interactional effect between the two parameters is significant, with a positive coefficient of 2.12. This indicates the presence of positive synergistic effects on the WO$_3$ enrichment ratio when a combination of the two reagents is employed. Additionally, the opposite coefficients for the linear (positive) and quadratic (negative) effects indicates that an extremum exists for the WO$_3$ enrichment ratio, even if it is not reached in the studied experimental domain. This extremum should be a maximum, as the sign of the quadratic coefficients determine the directional changes of the function and are negative in this case. However, reaching this extremum would require the use of excessive amounts of depressant, which would be unrealistic in terms of industrial operating costs.

The WO_3 recovery is negatively affected by the linear effects of the Na_2SiO_3 (x_1) and Na_2CO_3 (x_2) concentrations. The absolute value of the effect of the latter concentration is lower (-6.05) than that of the Na_2SiO_3 coefficient (-12.01). The quadratic effect for the Na_2SiO_3 concentration (-4.77), which is negative and quite strong, is significant. Both the quadratic and the linear effects are negative, implying the absence of an extremum for the WO_3 recovery. The interactional effect between the two reagent concentrations is significant, with a negative effect on the WO_3 recovery (-9.21). These results suggest the existence of negative synergistic effects on this response.

The P_2O_5 recovery only depends on the Na_2SiO_3 concentration, with a very high negative linear effect (-48.31). Na_2CO_3 does not play a significant role in the P_2O_5 recovery. The F recovery is affected negatively by the linear effects of both the Na_2CO_3 and Na_2SiO_3 concentrations. This latter exhibits a much stronger effect (-16.87) than the Na_2CO_3 (-6.14). The interactional effect between the two reagents is significantly negative (-10.58). Overall, the F recovery follows a very similar trend to that of the WO_3 recovery. Except for the quadratic effects, which are insignificant, all the coefficients display the same signs and similar absolute values for the WO_3 and F recoveries. The SiO_2 recovery presents a small constant term (3.89), indicating a very low recovery at the centre of the experimental domain. Significant negative linear effects of the Na_2SiO_3 and Na_2CO_3 concentrations affects the SiO_2 recovery. Surprisingly, the quadratic effect of the sodium silicate concentration is significant and positive. Accordingly, a minimum is reached in the experimental domain.

3.4 Discussions

3.4.1 Scheelite recovery

The two reagents present close molecular weights so that the different coefficients can be compared in terms of molecular mechanisms. Thus, the discussion can be based on the response surfaces. First, the predicted WO_3 recovery, which is proportional to the scheelite recovery, is plotted as a function of the two reagent concentrations (Figure 47). Scheelite is not depressed at low Na_2SiO_3 concentrations, since the silica species probably display a better adsorption affinity to the silicate minerals. The use of Na_2CO_3 with low Na_2SiO_3 quantities leads to a mild increase in the WO_3 recovery (Figure 47). This can be attributed to a depletion in the free calcium ions in the solution due to the formation of Ca-CO_3 complexes, thereby increasing the availability of the collector (Detienne, 1978; Kupka and Rudolph, 2018b). A reverse trend is observed when the Na_2SiO_3 concentration is increased (Figure 47). Previous studies have reported carbonation of the surfaces by adsorption of excess CO_3^{2-} ions (Miller and Hiskey, 1972). This carbonation probably occurs in the whole experimental domain but only high CO_3^{2-} concentrations induce sufficiently strong surface carbonation. Moreover, only high Na_2SiO_3 concentrations lead to scheelite depression. This occurs by the adsorption of the $Si(OH)_4$ and $SiO(OH)_3^-$ species, *i.e.* the most dominant forms of silica in solution, onto the $CaCO_3$ layer that formed on the surface, whereby the silicate species are known to better depress calcite over scheelite (Bo et al., 2015; Gao et al., 2015a; Kupka and Rudolph, 2018b; Marinakis and Shergold, 1985b). Even though the molecular structures of silica species and CO_3^{2-} ion are similar, their behaviour is significantly

different. Indeed, the adsorption of the silica species onto scheelite depresses the mineral, while the adsorption of CO_3^{2-} ions exhibits very little impact on scheelite flotation. This can be attributed to calcite formation on the mineral surface (Bahr et al., 1968; Miller and Hiskey, 1972; Rahimi et al., 2017), allowing the collector to adsorb as well on this surface as onto that of scheelite.
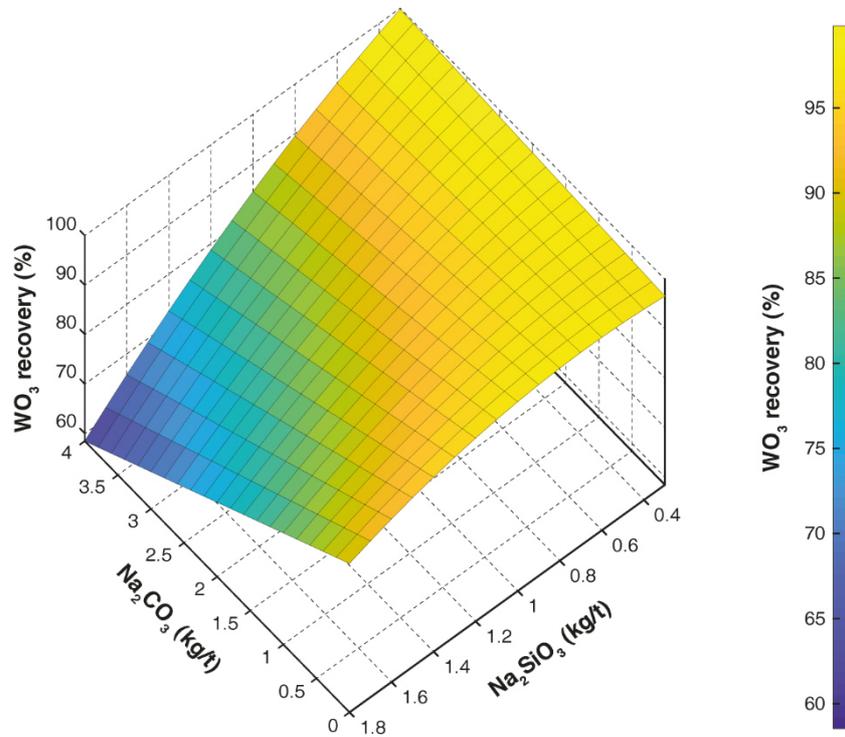
Figure 47. Response surface plot showing the WO_3 recovery as a function of the Na_2SiO_3 and Na_2CO_3 concentrations.

3.4.2   Apatite recovery

The P_2O_5 recovery is proportional to the apatite recovery and depends only on a constant term and the linear effect of Na_2SiO_3. Thus, the response surface is a plane and has not been plotted. Apatite has a strong affinity to carbonate ions, which often substitute the PO_4^{3-} anions to create francolite (Fleet and Liu, 2008; Kent et al., 2017; Mcarthur, 1985). This result can then be explained by the existence of a $CaCO_3$ layer already formed on the apatite either by the substitution of PO_4^{3-} by CO_3^{2-} or by the adsorption of CO_3^{2-} ions on the mineral surface. The whole comminution process was performed in tap water, which is in equilibrium with the atmosphere in terms of CO_3^{2-} ions. This suggests that the added Na_2CO_3 does not display a significant effect on the floatation process. On the other hand, Na_2SiO_3 exhibits a strong negative impact on the apatite recovery. These observations are in accordance with the existence of a calcium carbonate layer on the surface, as Na_2SiO_3 is known to depress calcite very efficiently (Bo et al., 2015; Gao et al., 2015a; Marinakis and Shergold, 1985b).

3.4.3   Fluorite recovery

The F recovery is proportional to the fluorite recovery, assuming that all the fluorine atoms are contained in the fluorite. The behaviour of the fluorite recovery is very similar to that observed for the scheelite recovery (Figure 48). This is attributed to the very similar surface properties of the two minerals: scheelite (112) and fluorite (111), the most exposed surfaces, exhibit very close Ca–Ca distance despite significantly different surface calcium densities (see Chapter 1). Hence, the depression mechanism previously suggested for scheelite, whereby surface carbonation produces a better efficiency for Na_2SiO_3, can also be applied to fluorite, demonstrating a strong control of the Ca-Ca distance on the depression mechanism. This similar behaviour indicates that the separation of scheelite and fluorite by flotation remains a challenge. However, some studies have reported an acceptable selectivity between these two minerals using specific depressants such as sodium alginate or polyacrylate (W. Chen et al., 2017; Zhang et al., 2017), which display molecular structures more complex than those of Na_2CO_3 and Na_2SiO_3. The combination of these two reagents presents very low selectivity between scheelite and fluorite, even though the fluorite recovery is significantly lower in the entire studied domain (Figure 48).
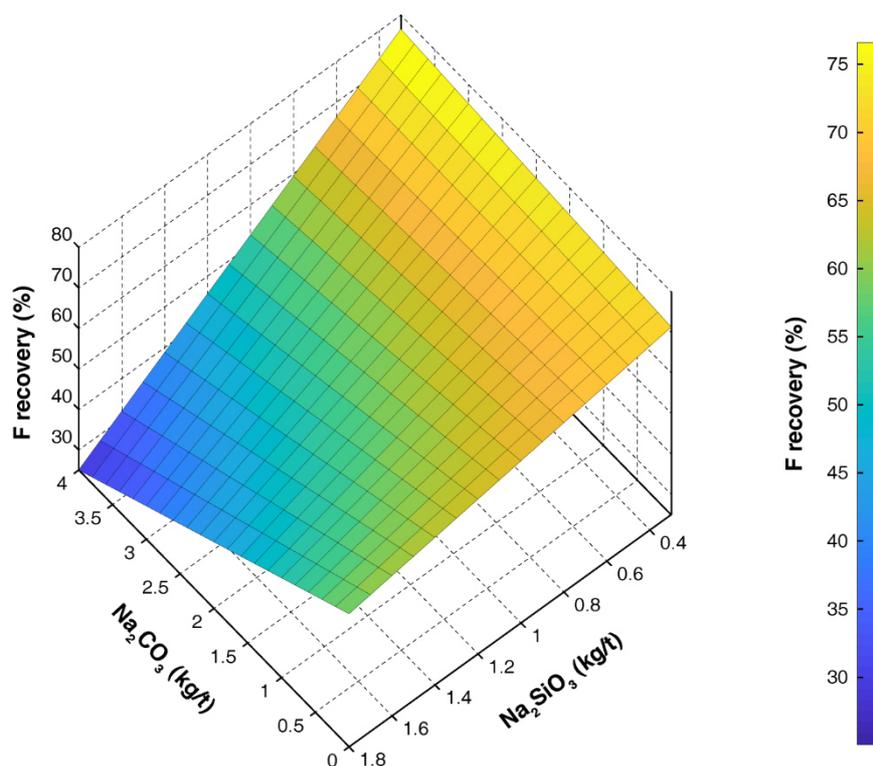
Figure 48. Response surface plot presenting the F recovery as a function of the Na_2SiO_3 and Na_2CO_3 concentrations.

Finally, the SiO_2 recovery has been plotted as a function of Na_2SiO_3 and Na_2CO_3 (Figure 49). This is proportional to the recovery of all the silicate minerals, without any distinction between them. Global recoveries are very low on the experimental domain, indicating poor floatability of the silicates with fatty acids. Nevertheless, the absence of sodium silicate can induce very high

SiO_2 recoveries ≥ 50 %, as presented previously (see section 2.2.1). The Na_2CO_3 concentration displays very little effect but its increase improves silicate depression (Figure 49). This is attributed to the low surface carbonation of the calcium-bearing silicates. However, this carbonation is probably very weak due to the high Ca–Ca distances and the complex crystallographic structures exhibited by the silicate minerals. Besides, the silica species in solution [$Si(OH)_4$ and $SiO(OH)_3^-$] exhibit a powerful effect on the silicates. An increase in the Na_2SiO_3 concentration leads to a high depression of the silicates, with a high slope, whereby the SiO_2 recovery approaches 0% (Figure 49). On the other hand, high Na_2SiO_3 concentrations improve the SiO_2 recovery, with the minimum being reached in the experimental domain (Figure 49). This can be attributed to calcium salts (mainly scheelite and fluorite) depression by Na_2SiO_3, leading to a higher availability of the collector.
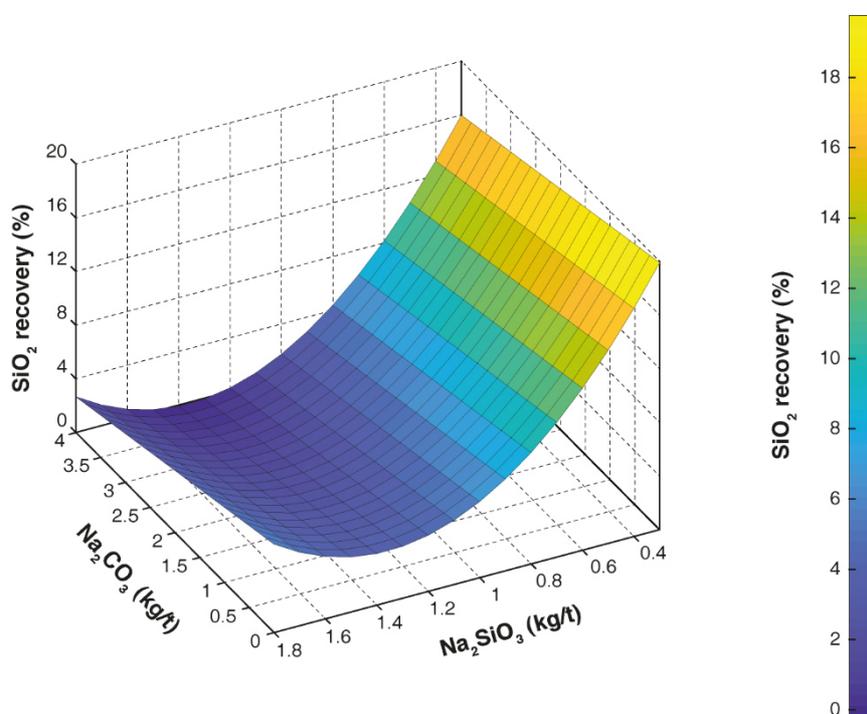
Figure 49. Response surface plot showing the SiO_2 recovery as a function of the Na_2SiO_3 and Na_2CO_3 concentrations.

3.4.4   Scheelite enrichment ratio

The WO_3 enrichment ratio represents the WO_3 grade and subsequently, the scheelite grade of the concentrate. No maximum is reached in the experimental domain (Figure 50). The best enrichment ratio is observed for high concentrations of both Na_2CO_3 and Na_2SiO_3. According to previous studies, this result is not surprising, as carbonation of the surfaces is induced by Na_2CO_3, allowing a much more efficient depression of gangue minerals by Na_2SiO_3 (Marinakis and Shergold, 1985b; Miller and Hiskey, 1972). Thus, all the minerals undergo carbonation, but with different strengths. This carbonation is only efficient at sufficiently high Na_2SiO_3 concentrations.
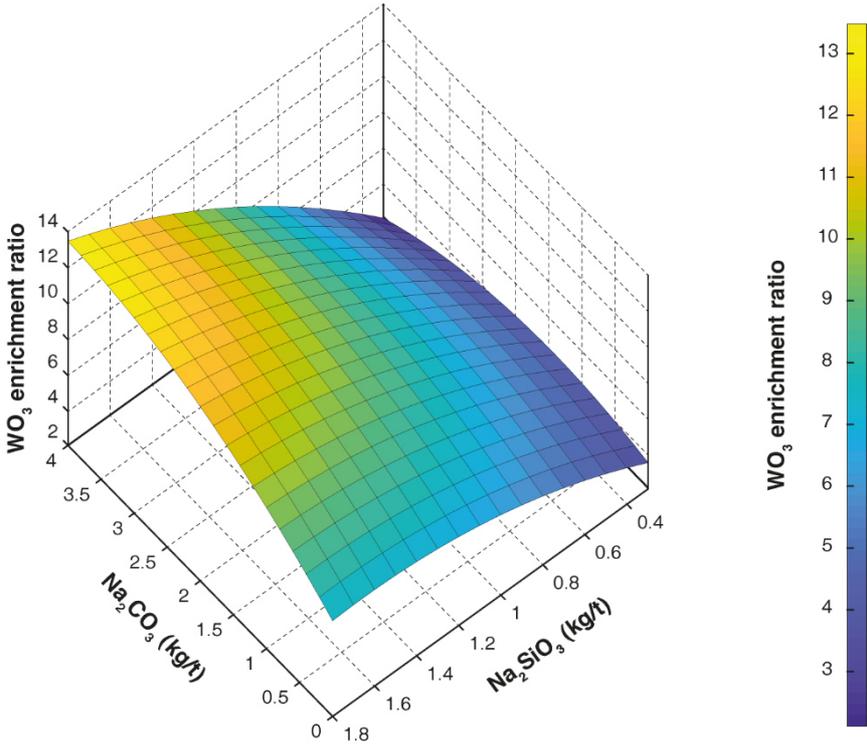
Figure 50. Response surface plot of the WO$_3$ enrichment ratio as a function of the Na$_2$SiO$_3$ and Na$_2$CO$_3$ concentrations.

The WO$_3$ enrichment ratio mainly depends on the gangue mineral recoveries, as their elimination during flotation produces an increase in the WO$_3$ grade in the concentrate. The WO$_3$ enrichment ratio is linearly correlated (Figure 51) with the gangue mineral recoveries, all the coefficients being significant. On the other hand, apatite exhibits a smaller effect on the WO$_3$ ratio compared to fluorite and silicates (Figure 51). The strength of these effects is attributed to the grade of the studied minerals in the feed, with the apatite representing 2% of the ore, while the fluorite assays 10% and silicates >80%. However, the fluorite and silicates are affected by similar coefficients (Figure 51). This indicates that only some of the silicates, probably the calcium-bearing silicates, are problematic in the flotation process and that the fluorite poses a greater problem in flotation.
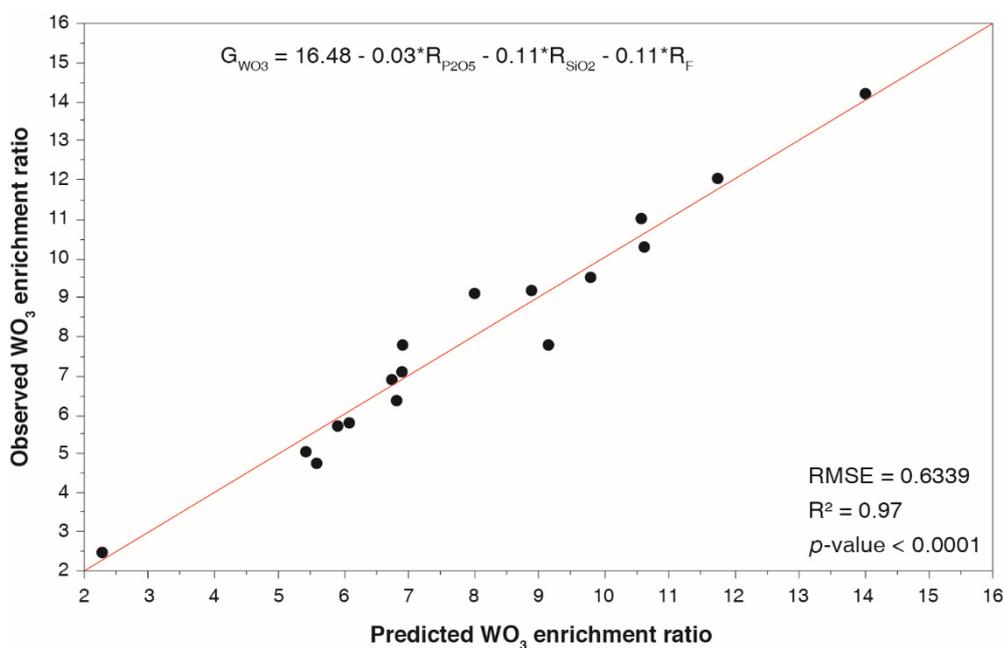
Figure 51. Observed versus predicted values for the WO_3 enrichment ratio modelled as a function of P_2O_5, SiO_2, and F recoveries; the formula is included on the top of the figure.

3.4.5   Relationships between the different responses

The predicted WO_3 recovery is correlated to the predicted WO_3 enrichment ratio through an exponential model (Figure 52a). The WO_3 recovery significantly falls when the enrichment ratio is enhanced. An increase in the ratio is only possible with a significant decrease in the WO_3 recovery. As the WO_3 recovery approaches zero, the WO_3 enrichment ratio approaches 16.48, a value corresponding to the constant value of the equation displayed in Figure 52a. Hence, under these experimental conditions, it is impossible to increase the ratio above this value. The presence of a significant amount of mixed particles can explain this relationship; however, this would favour a linear correlation, as the enrichment ratio would increase despite the loss in mixed particles. Moreover, the d_{80} of the flotation feed is 120 µm, while the liberation size is 150 µm. Hence, a most probable explanation could be attributed to the lack of selectivity of the studied depressants. Their increase at low concentrations significantly enhances the WO_3 enrichment ratio. However, at higher concentrations, the WO_3 recovery falls dramatically, which is attributed to either the $CaCO_3$ layer becoming stable or silica species adsorption onto the scheelite, without any consideration of the presence of the $CaCO_3$ layer.

Similar trends are also observed when the WO_3 recovery is plotted as a function of the different gangue mineral recoveries (SiO_2, F, and P_2O_5). First, the F recovery is very well correlated to the WO_3 recovery through two types of models (Figure 52b). The linear correlation is again explained by the very similar surface fluorite and scheelite properties. However, the depressants affect the fluorite more than the scheelite (Figure 52b). Another model can be developed through the exponential function (Figure 52b). This model better represents the experimental conditions and presents lower RMSE and higher R^2 values. This is due to the fluorite, which cannot be

completely (100%) depressed without significantly impacting the scheelite. Notably, even under these conditions, the carbonation of the mineral and the subsequent adsorption of silica species are more favourable for fluorite than for scheelite, with fluorite being depressed more strongly. However, a significant amount of locked scheelite-fluorite particles could also explain this global trend.
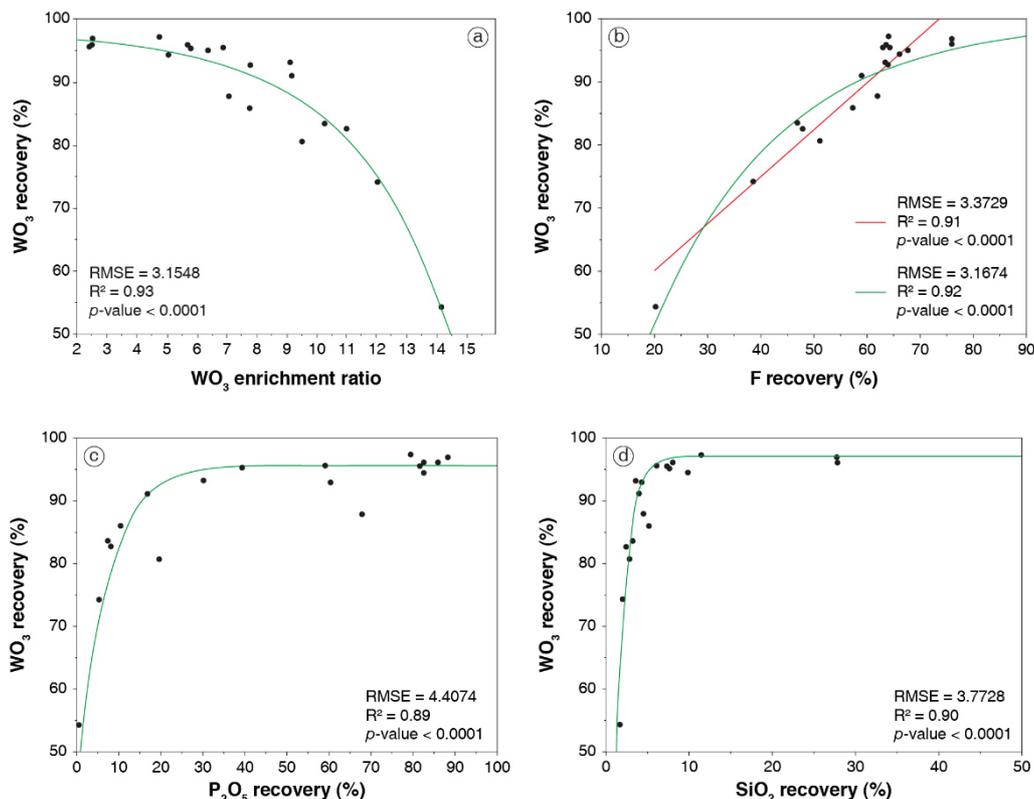
Figure 52. Modelled WO_3 recovery as a function of the modelled WO_3 enrichment ratio (a), of the modelled F recovery (b), of the modelled P_2O_5 recovery (c), and of the modelled SiO_2 recovery (d).

The WO_3 recovery plotted as a function of P_2O_5 recovery is also fitted by an exponential model. In this case, the depression of the apatite occurs without significantly impacting the scheelite recovery (Figure 52c). The scheelite is strongly affected at P_2O_5 recoveries <20% (Figure 52c). The CO_3^{2-} ions do not play a role in the apatite depression and the Na_2SiO_3 is the only reagent involved. This global trend implied that the silica species preferentially adsorb onto the apatite, a process favoured by spontaneous surface carbonation, until a given concentration is reached. Once this concentration is exceeded, the silica species begin to adsorb onto the scheelite. However, this behaviour can also be explained by the existence of locked scheelite-apatite particles, involving 10–20% of the total apatite and 30–40% of the total scheelite although these are relatively high values.

The same phenomenon is observed, with a more pronounced effect, when WO_3 recovery is plotted as a function of SiO_2 recovery (Figure 52d). In this case, the SiO_2 recovery decreases, mainly by the depressing action of the silica species, without impacting the WO_3 recovery. This suggests

that the chemical affinity of the silica species for the silicate minerals is significantly higher than that for scheelite. The WO_3 recovery falls dramatically at Si recoveries <10% (Figure 52d). This indicates that the scheelite is depressed by silica species adsorption onto the free or carbonated scheelite surface. This adsorption can be due to the silica species concentration in solution being too high, displacing the chemical equilibrium in favour of their adsorption onto the surface. Additionally, the last 10% of the silicate minerals that are difficult to depress are assumed to comprise only one silicate type, which displayed poor affinity to the silica species or high affinity to the collector. This drop can also be attributed to the existence of locked scheelite-silicate particles, involving 10% of the total amount of silicates and at least 40% of the total amount of scheelite. However, these values seem to be very high and are therefore improbable.

3.5 Optimisation of the depressant concentrations and validation

3.5.1   Optimisation of the concentrations

To optimise the proposed method, the WO_3 enrichment ratio and WO_3 recovery models have been plotted on iso-response graphs to establish the influence of the two factors on the two main responses (Figure 53). A desirable area has been defined with lower limits imposed on the WO_3 recovery (90%) and WO_3 enrichment ratio (9). This area corresponds to the optimal flotation conditions of the two studied reagents and is located at the centre of the experimental domain (Figure 53). As previously demonstrated, the WO_3 recovery and WO_3 enrichment ratio are anti-correlated. Moreover, since the cost of the reagents represents an important part of the operating costs, the lowest reagent concentrations inside this field can be chosen to define the optimal flotation conditions: 1,225 g/t sodium silicate and 1,150 g/t sodium carbonate, approximately corresponding to a 1:1 ratio.
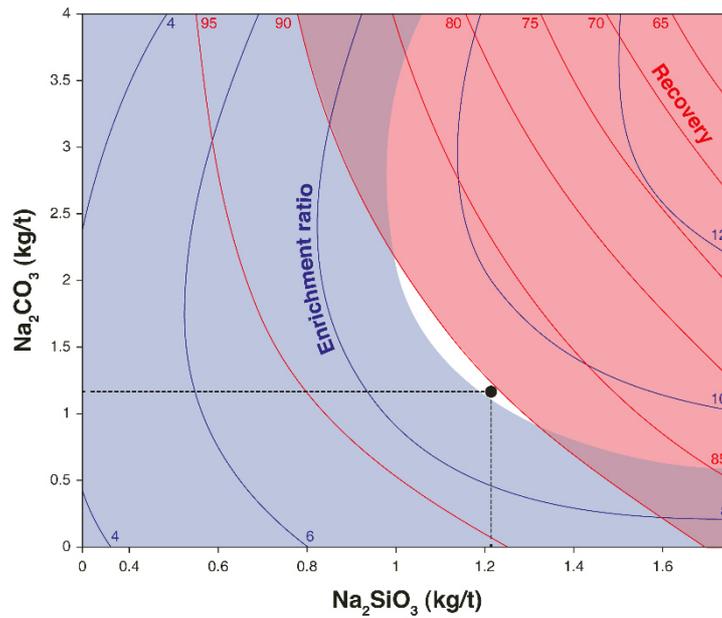
Figure 53. Iso-response surface of the WO_3 enrichment ratio and WO_3 recovery as a function of sodium silicate and sodium carbonate. The area in white is the optimal field where the best quantities are defined: ~1,225 g/t sodium silicate and 1,150 g/t sodium carbonate.

3.5.2 Validation tests

To validate the models, one test from the design of experiments was randomly selected and duplicated. Moreover, the test under the optimal conditions, determined through the DOE, was performed and used for the critical validation of the models. For both tests, the predicted values are compared to the experimental results and the relative errors are then calculated (Table 15). The calculated values agree with the obtained data, suggesting that the models can predict the responses quite adequately, even when the relative errors are high.

Table 15. Validation tests showing the experimental results, predicted results, and relative errors.

Conditions (g/t)	WO_3 enrichment ratio			WO_3 recovery (%)			P_2O_5 recovery (%)		
	Actual	Fitted	Error (%)	Actual	Fitted	Error (%)	Actual	Fitted	Error (%)
1,225; 1,150	10.05	9.13	10.1	93.2	90.30	3.2	25.2	31.87	-20.1
500; 0	2.446	2.82	-13.3	95.6	95.86	-0.3	88.1	92.19	-4.5

Conditions (g/t)	F recovery (%)			SiO_2 recovery (%)		
	Actual	Fitted	Error (%)	Actual	Fitted	Error (%)
1,225, 1,150	63.6	57.80	10.0	2.4	2.64	-9.1
500; 0	75	73.1	2.6	25.0	28.8	-13.2

3.6 Conclusions

Different depressants were tested to attain the selective depression of gangue minerals from scheelite, to eliminate them from the scheelite concentrate. Among all the tested depressants, the results were not better than those afforded when Na_2CO_3 was added prior to the addition of sodium silicate. A DOE was consequently used to study this system. The following facts were highlighted:

➢ Strong synergistic effects between the two reagents, mainly on scheelite and fluorite. These effects are attributed to surface carbonation that makes $Si(OH)_4/SiO(OH)_3^-$ adsorption more favourable;

➢ Inefficiency of the effect of sodium carbonate on apatite, probably caused by spontaneous carbonation of the mineral surfaces (formation of francolite or adsorption of dissolved CO_2 under the CO_3^{2-} form);

➢ Very high affinity of sodium silicate for the silicates minerals, comparatively inducing little effect from sodium carbonate. The complex crystallographic structures of the silicates may hinder surface carbonation;

➢ Strong correlations between the responses that can be attributed to locked particles or the chemical affinity of the silica species for the different minerals. The former explanation is quite unlikely considering the amount of scheelite that would be involved.

Overall, the DOE allowed the setting of the best experimental conditions in terms of reagent concentration, thereby leading to optimised gangue mineral depression in the flotation process. These conditions were established as: 1,150 g/t Na_2CO_3 with 1,225 g/t Na_2SiO_3. This proposed method produced a concentrate assaying 10.1% WO_3 with 93.2% WO_3 recovery. However, the fluorite recovery was still 63.6%, which is considered high. Besides, the Na_2CO_3/Na_2SiO_3 system was deeply characterised by the DOE method, which is an empirical statistical method that does not allow to understand finely the molecular mechanisms leading to the observed synergistic effects. Since these latter are poorly understood and not described in the literature, spectroscopic studies seems mandatory to gain understanding in the molecular mechanisms that explain these high synergistic effects.

4. Synergistic adsorptions of Na_2CO_3 and Na_2SiO_3 on calcium minerals revealed by spectroscopic and *ab initio* molecular dynamics studies

    4.1 Introduction

At the moment, very few studies have been conducted on the Na_2CO_3/Na_2SiO_3 system in flotation and the synergistic effects exhibited by this reagent combination are still poorly understood. Some authors have successfully investigated surface reactivity and synergistic adsorptions/reactions by FTIR (Li et al., 2018; X. Liu et al., 2018; Ogawa et al., 2014; Zhou et al., 2019), by XPS (Lovat et al., 2019; Píš et al., 2019; Shen et al., 2012), and by AIMD (Ogawa et al., 2014; Kristoffersen et al., 2018) with couplings between the above-mentioned techniques.

In the following part, a combination of DRIFTS, XPS, and AIMD simulations is used to gain understanding in the molecular mechanisms involved in the Na_2SiO_3 adsorption onto bare surfaces and surfaces prior treated with Na_2CO_3. The most stable species of Na_2SiO_3 in solution at the pH commonly used in the flotation process, *i.e.* $Si(OH)_4$ and $SiO(OH)_3^-$, are considered hereafter. The experimental details for these three methods are presented in Chapter 2. Fluorite (CaF_2), a simple cubic calcium-bearing mineral, was chosen for this study since it is considered as an archetype of minerals that can be depressed by Na_2SiO_3, as demonstrated in the previous part (see section 3.4.3).

4.2 Results

4.2.1   Carbonation of CaF_2 in presence of Na_2CO_3

The DRIFT spectrum of CaF_2 treated with 5.10^{-2} mol.L^{-1} of Na_2CO_3 displayed bands at 2492, 1775, 1650, 1439, 879, and 842 cm^{-1} that are not present on the spectrum of CaF_2 conditioned in water only (Figure 54a). The bands located at 2492, 1775, 1439, and 879 cm^{-1} are ascribed to CO_3^{2-} in either Na_2CO_3 or $CaCO_3$ (Miller and Wilkins, 1952), which cannot be distinguished from each other. The band at 842 cm^{-1} is attributed to $NaHCO_3$ as well as the band located at 1650 cm^{-1}, which overlapps the band corresponding to water molecules, around 1620-1640 cm^{-1} for CaF_2 conditioned in water. Considering the low intensity of the band at 842 cm^{-1}, $NaHCO_3$ is in minority in the adsorbed layer compared to $CaCO_3$ and/or Na_2CO_3. However, at pH 10, HCO_3^- is present in the same amount than CO_3^{2-} in solution since the pKa of HCO_3^-/CO_3^{2-} is 10.2. Hence, it can be assumed that CO_3^{2-} is more likely to adsorb on the CaF_2 surface than HCO_3^-. Overall, the DRIFT results do not allow to determine the nature of the carbonate layer formed on the CaF_2 surface, considering the significant amounts of both Na^+ and Ca^{2+} available in solution. Indeed, some authors demonstrated that the CaF_2 dissolution rate is significant, which implies that the thermodynamic equilibrium is reached in only one hour (Roche, 1973). Assessing a solubility product of 7×10^{-11} for CaF_2 (Marinakis and Shergold, 1985a), the amount of Ca^{2+} ions available in solution is high enough to form a $CaCO_3$ layer onto the surface. However, it can be assumed that the formation of the carbonate layer is quite fast and can prevent the mineral dissolution.
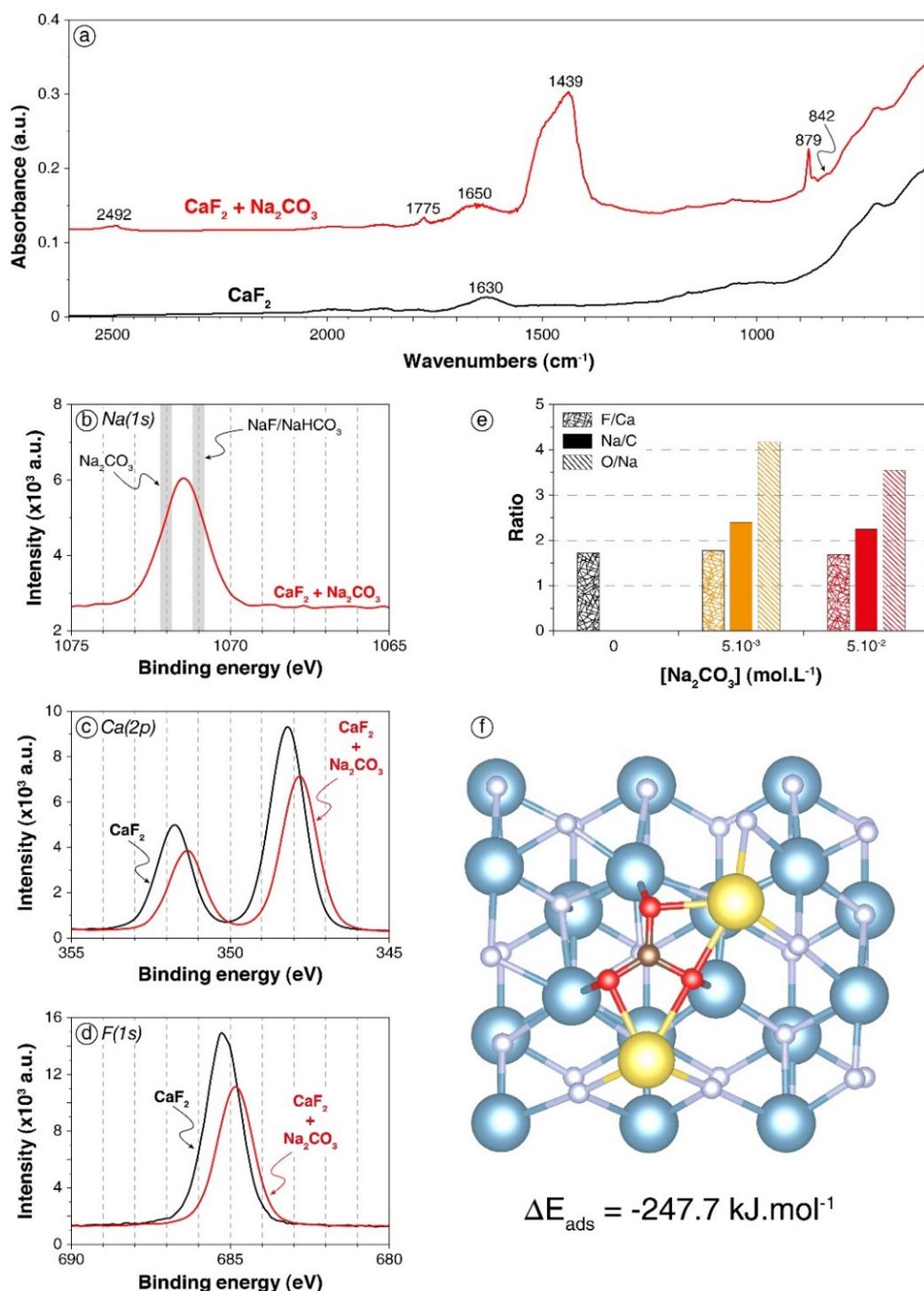
Figure 54. Carbonation of CaF_2 surface by Na_2CO_3 addition. Black and red IR/XPS spectra represent pure CaF_2 conditioned in deionised water or in a 5.10^{-2} mol.L^{-1} Na_2CO_3 solution, respectively. **a**. DRIFT spectra **b**. XPS Na(1s) spectrum, with the common binding energies of Na-O and Na-F bonds [from (Briggs, 1981)]. **c**. XPS Ca(2p) spectra. **d**. XPS F(1s) spectra. **e**. F/Ca, Na/C, and O/Na ratios of CaF_2 conditioned in deionised water (black), in a 5.10^{-3} mol.L^{-1} Na_2CO_3 solution (orange), and in a 5.10^{-2} mol.L^{-1} Na_2CO_3 solution (red). **f**. Snapshot of a top view of the (111) CaF_2 surface with a Na_2CO_3 molecule adsorbed onto the surface after 35 ps of AIMD simulation. The blue, grey, red, maroon, and yellow balls represent the calcium, fluorine, oxygen, carbon, and sodium atoms, respectively.

To confirm the previous conclusions and to gain understanding in the molecular mechanisms involved in the CaF_2 surface carbonation, XPS analyses were performed on CaF_2 conditioned in deionised water, in a 5.10^{-2} mol.L^{-1} Na_2CO_3 solution, and in a 5.10^{-3} mol.L^{-1} Na_2CO_3 solution, at pH 10. First, for CaF_2 conditioned in deionised water, calcium, fluorine, and oxygen are identified along with polluting elements such as C, corresponding to adventitious carbon, and Si (3.0 at.%), which presence has been previously highlighted by chemical analyses (see Chapter 2). The O(1s) spectrum exhibits two components with binding energies of 532.1 eV (11.1 at.%) and 533.2 eV (3.4 at.%) that are attributed to adsorbed carbonate and water molecules, respectively, which is in accordance with the DRIFT spectrum of pure CaF_2 (Figure 54a). Besides, the F/Ca atomic ratio of 1.73 indicates that the surface is depleted in terms of fluorine atoms since the theoretical F/Ca ratio should be 2. This can be attributed to the fact that the (111) surface, which is the main cleavage plane for fluorite (Parks and Barker, 1977; Tasker, 1980), exhibits seven-coordinated calcium atoms while they are eight-coordinated in the fluorite crystal. This under-coordination induces that the first atomic layer is constituted by only seven fluorine atoms along with two calcium atoms, which results in a surface F/Ca ratio of 1.75, in agreement with the ratio measured here. Overall, no hydroxyl groups as well as no sodium atoms are identified onto pure CaF_2, indicating that the fluorite surface is not hydroxylated at pH 10.

The two different Na_2CO_3 concentrations led to similar trends for XPS that are, consistently, more pronounced for 5.10^{-2} mol.L^{-1}. The following discussion will then focus on results with the highest concentration. First, sodium atoms are identified (4.5 at.%) with a Na(1s) binding energy of around 1071.5 eV (Figure 54b): this corresponds to an intermediate value between Na-O bonds of Na_2CO_3 species (Briggs, 1981) and Na-F bonds of NaF or Na-O bonds of $NaHCO_3$, which binding energy is known to be lower. However, DRIFTS results demonstrate the absence of $NaHCO_3$ (Figure 54a), which induces that the binding energy of 1071.5 eV corresponds to an intermediate value between Na-O bonds of Na_2CO_3 and Na-F bonds. Besides, the Ca($2p_{3/2}$) and ($2p_{1/2}$) binding energies are shifted from 348.2 eV and 351.8 eV for pure CaF_2 to 347.8 eV and 351.3 eV, respectively, for CaF_2 + Na_2CO_3 (Figure 54c). This shift is attributed to the presence of Ca-O bonds that have lower binding energies than Ca-F bonds (Briggs, 1981). Moreover, the F(1s) binding energy is shifted from 685.2 eV for pure CaF_2 to 684.8 eV for CaF_2 + Na_2CO_3 (Figure 54d), demonstrating the existence of the aforementioned F-Na bonds, along with F-Ca bonds (Briggs, 1981). The O(1s) spectrum presents two components with binding energies of 531.7 eV (15.9 at.%) and 533.6 eV (0.8 at.%) for 5.10^{-2} mol.L^{-1} Na_2CO_3. The first one is attributed to C-O bond of Na_2CO_3 (Hammond et al., 1981) while the second one can be ascribed to C-O bond of $NaHCO_3$, which is present in very small amounts as the DRIFTS results demonstrate (Figure 54a). However, the second component, with a binding energy of 533.6 eV, exhibited on the O(1s) spectrum for 5.10^{-2} mol.L^{-1} Na_2CO_3 is absent for 5.10^{-3} mol.L^{-1} Na_2CO_3. This demonstrates that the CO_3^{2-} ions are more likely to adsorb onto CaF_2 since, at low Na_2CO_3 concentration, no HCO_3^- species are identified on the surface. Besides, the F/Ca ratio is not significantly affected by the addition of Na_2CO_3 (Figure 54e) regardless the concentration. The Na/CO_3 ratio is 2.40 at low Na_2CO_3 concentration and 2.25 at high Na_2CO_3 concentration, indicating that the layer formed onto the surface is Na_2CO_3 with an excess of Na^+, probably

absorbed along with OH^- ions, which however decreases when Na_2CO_3 concentration was increased. Overall, Na_2CO_3 adsorbs onto CaF_2 mostly under Na_2CO_3 form (Figure 54e), establishing Ca-O and Na-F bonds with the surface atoms (Figure 54b, c, and d). Small amounts of $NaHCO_3$ are exhibited at high Na_2CO_3 concentration, which is in accordance with the DRIFTS results (Figure 54a).

AIMD simulations confirm that, when a Na_2CO_3 molecule is set onto the CaF_2 (111) surface, it adsorbs with each oxygen atom establishing an O-Ca bond with a different calcium atoms (Figure 54f). Their average lengths on the whole simulation are 2.36, 2.36, and 2.43 Å with a standard deviation of around 0.10 Å. Each sodium atom establishes two Na-F bonds with surface fluorine atoms with $d_{Na-F1} = 2.41$ Å and $d_{Na-F2} = 2.45$ Å (Figure 54f). Also, each sodium atom is bonded to two oxygen atoms of the CO_3^{2-} ion with $d_{Na-O1} = d_{Na-O2} = 2.35$ Å in average. The Na_2CO_3 molecule adsorbs with $\Delta E_{ads} = -247.7$ kJ.mol^{-1} including $\Delta E_{disp} = -91.3$ kJ.mol^{-1}, which indicates a considerably favoured adsorption as well as high induced dipole-induced dipole forces. This theoretical result is in agreement with both DRIFTS and XPS results that allows to identify carbonate and Ca-O/Na-F bonds on the surface, respectively.

4.2.2   Adsorption of Na_2SiO_3 on CaF_2 bare surface

Compared to CaF_2 treated in deionised water only, CaF_2 treated in a 5.10^{-2} mol.L^{-1} Na_2SiO_3 solution exhibits two weak broad bands at 1510 and 1405 cm^{-1} (Figure 55a), which probably correspond to a surface carbonation (HCO_3^- and CO_3^{2-}, respectively). Moreover, a broad band between 1200 and 900 cm^{-1} with a maximum at 1080 cm^{-1} is present (Figure 55a), which can be attributed to the Si-O asymmetric stretching vibration. Some authors demonstrated that the Si-O asymmetric stretching vibration wavenumber in silica is affected by the proportion of non-bonding oxygen atoms (Bass and Turner, 1997; Gaggiano et al., 2013; Halasz et al., 2007; Jansson et al., 2015). Monomers exhibit wavenumbers around 850 cm^{-1} while highly polymerised silica can display wavenumbers as high as 1300 cm^{-1} for the Si-O asymmetric stretching vibration (Bass and Turner, 1997; Gaggiano et al., 2013; Jansson et al., 2015). Moreover, the proportion of H^+ or Na^+ ions bonded to the terminal oxygen atoms, which depends on the pH and the Si/Na ratio, is also known to shift the wavenumbers of this vibration (Halasz et al., 2007). Based on the literature, the broad band between 1200 and 900 cm^{-1} is difficult to interpret: it can be attributed either to moderately polymerised adsorbed silica or to free silica monomers adsorbed under basic form, *i.e.* $SiO(OH)_3^-$. Furthermore, the adsorption of the silica tetrahedra on the surface, regardless their form, probably shifts the wavenumbers of the Si-O asymmetric stretching vibration.

For low Na_2SiO_3 concentration (5.10^{-3} mol.L^{-1}), small amounts of sodium atoms (0.84 at.%) along with silica atoms (5.7 at.% compared to 3.0 at.% for pure CaF_2) are identified by XPS, indicating the adsorption of Na_2SiO_3 onto CaF_2. The Na(1s) binding energy is 1071.9 eV, which mostly corresponds to Na-O bonds (Figure 55b). Hence, it can be assessed that the adsorbed Na atoms are mainly bonded to silica tetrahedra under anionic form. Moreover, the F(1s) as well as the Ca(2p) binding energies are not affected by the adsorption of Na_2SiO_3 at low concentration

(Figure 55c and d), indicating a physisorption of silica tetrahedra onto CaF_2 surface. The Si(2p) spectrum exhibits two main components (Figure 55e) at 102.1 eV (1.2 at.%) and 103.2 eV (4.5 at.%), which can be attributed to Si-O bonds and Si-O-Si bonds, respectively (Barr, 1978; Carniato et al., 2007; Merlen et al., 1990). The low-energy component (102.1 eV) can be ascribed to a Si-O bond in which the oxygen atom is either partly charged (Si-O$^-$) or stabilised by a sodium atom (Si-O-Na) or a calcium atom (Si-O-Ca), as Na and Ca exhibit lower electronegativity than Si (Pauling, 2000), inducing lower Si(2p) binding energy. Furthermore, the high-energy component (103.2 eV) can also be related to Si-O-H bonds since H and Si display similar electronegativity (Pauling, 2000). Overall, the Si(2p) spectrum is difficult to discuss considering the influence of chemical environment onto binding energies, since the chemical environment of the oxygen atom (Si-O$^-$, Si-O-H, Si-O-Na, Si-O-Ca, and Si-O-Si) affects significantly the Si(2p) binding energies. The F/Ca ratio is not affected by the Na_2SiO_3 adsorption at low concentration, indicating no chemical modification of the surface (Figure 55f). Moreover, the O/Si ratio is 3.61 and the O/Na ratio is 24.35 (Figure 55f), which correspond to a global formula of $Si_{6.75}O_{24.35}NaH_{20.70}$, very close to $Si(OH)_4$. Hence, at low Na_2SiO_3 concentrations, the silica adsorbs mostly under monomeric protonated form, *i.e.* $Si(OH)_4$.
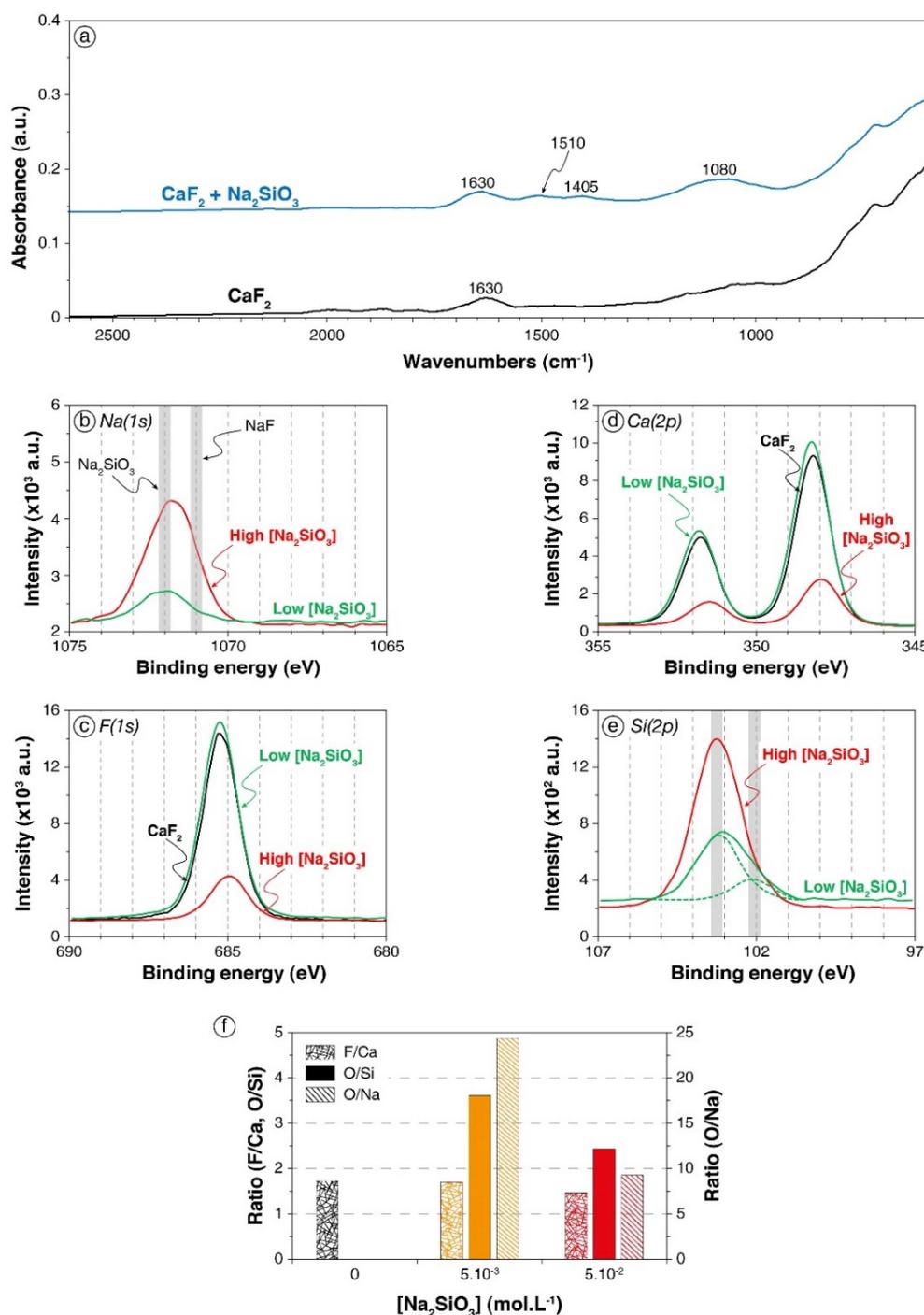
Figure 55. Adsorption of Na_2SiO_3 onto CaF_2 surface. **a.** Infrared spectra of CaF_2 conditioned in deionised water (black) and in a 5.10^{-2} mol.L^{-1} Na_2SiO_3 solution (blue). **b.** XPS Na(1s) spectra of CaF_2 conditioned in a 5.10^{-3} mol.L^{-1} (green) and a 5.10^{-2} mol.L^{-1} (red) Na_2SiO_3 solutions, with the common binding energies of Na-O and Na-F bonds [from (Briggs, 1981)]. **c.** XPS F(1s) spectra, same legends than above. **d.** XPS Ca(2p) spectra, same legends than above. **e.** XPS Si(2p) spectra, same legends than above, with the common binding energies of SiO_2 and Si-O-X bonds (Barr, 1978; Carniato et al., 2007; Merlen et al., 1990). **f.** F/Ca, O/Si, and O/Na ratios of CaF_2 conditioned in deionised water (black), in a 5.10^{-3} mol.L^{-1} Na_2SiO_3 solution (orange), and in a 5.10^{-2} mol.L^{-1} Na_2SiO_3 solution (red). The ratios were calculated with the corresponding component for O and Si.

139

At high Na_2SiO_3 concentration, sodium (4.2 at.%) and silica (16.1 at.%) are also identified. No significant change in Na(1s) and F(1s) binding energies are displayed compared to low Na_2SiO_3 concentration (Figure 55b and c). However, the Ca($2p_{3/2}$) and ($2p_{1/2}$) binding energies are shifted from 348.2 eV and 351.8 eV for pure CaF_2 to 348.0 eV and 351.5 eV, respectively (Figure 55d). Though low significance, it could correspond to the formation of Ca-O bonds. The Si(2p) exhibits an only component at 103.2 eV (Figure 55e) that is ascribed to polymerised silica tetrahedra that induce binding energy close to that of the quartz (Briggs, 1981). Besides, the F/Ca ratio significantly decreases from 1.73 for pure CaF_2 to 1.47 for CaF_2 conditioned with high Na_2SiO_3 concentration (Figure 55f). Since no calcium atoms are present in deionised water, this decrease is attributed to a surface depletion in terms of fluorine atoms. Considering the apparition of Ca-O bonds discussed previously, it can be assessed that silica tetrahedra substitute fluorine atoms on the surface. The O/Si ratio is 2.45 (Figure 55f), which indicates the adsorption of silica under polymerised forms onto CaF_2. Also, the O/Na ratio is 9.30 which still indicates that protonated forms are dominant onto the surface (Figure 55f). The global formula was $Si_{3.80}O_{9.30}NaH_{2.4}$, which corresponds to moderately polymerised silica under protonated and anionic forms. To investigate the adsorption of Na_2SiO_3 as well as the increase of Na_2SiO_3 concentration, four different phenomena have been studied by AIMD simulations:

1. The adsorption of monomeric protonated forms of silica, *i.e.* $Si(OH)_4$;
2. The adsorption of anionic forms of silica, *i.e.* $SiO(OH)_3^-$;
3. The increase of the surface coverage with protonated monomers;
4. The adsorption of polymerised forms of silica, *i.e.* $Si_2O(OH)_6$.

The lone molecule of $Si(OH)_4$ adsorbs under its molecular form with ΔE_{ads} = -100.7 kJ.mol^{-1} including ΔE_{disp} = -46.4 kJ.mol^{-1} (Figure 56a and b), which confirms the physisorption suggested by XPS at low Na_2SiO_3 concentrations (Figure 56c). Three oxygen atoms are bonded to three surface calcium atoms (Figure 56b) with average Ca-O bond lengths of 2.65 Å, 2.78 Å, and 2.65 Å. The hydrogen atoms of the three –OH groups establishes H-bonds with surface fluorine atoms (Figure 56b), which average lengths were all of 1.66 Å. For the adsorption of $SiO(OH)_3^-$ form, a sodium atom was added on the surface near the $SiO(OH)_3^-$ molecule to keep the cell electrically neutral. During the simulation, the non-protonated oxygen atom ejects a fluorine atom from the surface and establishes three O-Ca bonds with three different surface calcium atoms, substituting an F$^-$ in the upper fluorine atoms layer (Figure 56d). The ejected fluorine atom re-adsorbs onto a surface calcium and the sodium atoms:

$$\text{Surf-F} + \text{NaSiO(OH)}_3 = \text{Surf-SiO(OH)}_3 + \text{NaF} \tag{31}$$

The average distances between the non-protonated oxygen and the three surrounding calcium atoms are 2.54 Å. One protonated oxygen atom establishes an O-Ca and an O-Na bonds with d_{O-Ca} = 2.72 Å and d_{O-Na} = 2.27 Å. The adsorption energy is ΔE_{ads} = -196.5 kJ.mol^{-1} including ΔE_{disp} = -56.9 kJ.mol^{-1}: the anionic form of silica tetrahedron, *i.e.* $SiO(OH)_3^-$, adsorbs with significantly higher energy in absolute value compared to the $Si(OH)_4$ form.
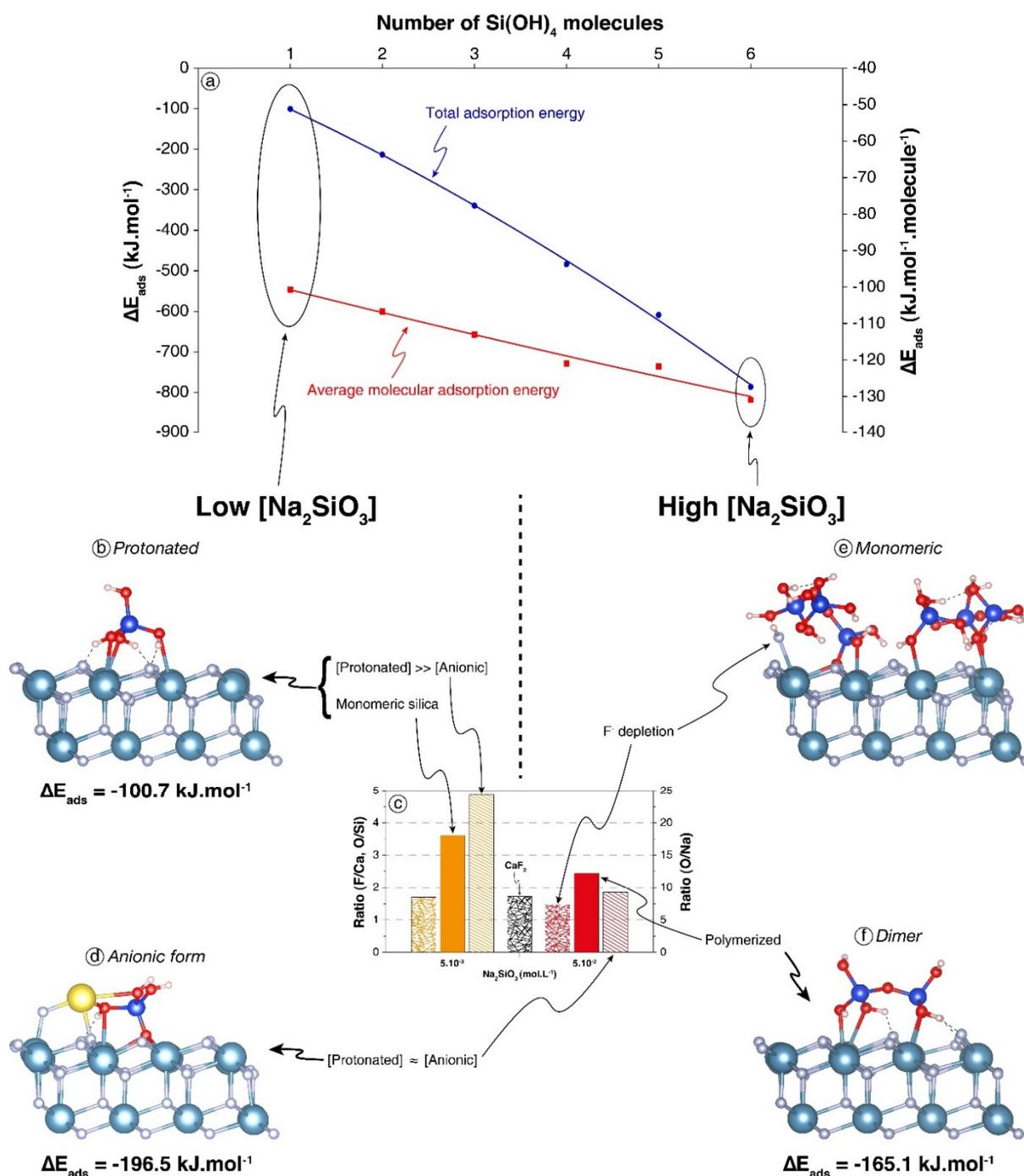
Figure 56. **a.** Total and molecular adsorption energies as a function of surface coverage for $Si(OH)_4$ molecules onto bare CaF_2 surface. **b.** Snapshot of a side view of the (111) CaF_2 surface with a $Si(OH)_4$ molecule adsorbed after 50 ps of AIMD simulation. **c.** F/Ca, O/Si, and O/Na ratios of CaF_2 conditioned in different conditions, please report to Figure 55f for legends. **d.** Snapshot of a side view of the (111) CaF_2 surface with a $NaSiO(OH)_3$ molecule adsorbed after 50 ps of AIMD simulation. **e.** Snapshot of a side view of the (111) CaF_2 surface with six $Si(OH)_4$ molecules (100% coverage) adsorbed after 50 ps of AIMD simulation. **f.** Snapshot of a side view of the (111) CaF_2 surface with a $Si_2O(OH)_6$ molecule adsorbed after 50 ps of AIMD simulation. The light blue, grey, red, dark blue, and yellow balls represent the calcium, fluorine, oxygen, silicon, and sodium atoms, respectively. Dashed lines represent hydrogen bonds.

141

To assess the influence of total silica concentration in solution, the surface coverage was successively increased to reach six $Si(OH)_4$ molecules, *i.e.* 100% coverage (Figure 56a and e). From two to five molecules, the adsorption configuration is roughly the same than with one $Si(OH)_4$ molecule, establishing however two Ca-O bonds instead of three. The molecules interact with each other when they co-adsorb, inducing a slight increase of adsorption energies in absolute values, from -100.7 $kJ.mol^{-1}.molecule^{-1}$ for one molecule to -121.8 $kJ.mol^{-1}.molecule^{-1}$ for five molecules (Figure 56a). When added, the sixth molecule of $Si(OH)_4$ forms spontaneously $SiO(OH)_3^-$ and substitutes a surface fluorine atom (Figure 56e), which recombines with the proton to form HF on the surface:

$$Surf\text{-}F + 6\ Si(OH)_4 = Surf\text{-}SiO(OH)_3 + HF + 5\ Si(OH)_4 \qquad (32)$$

This reaction, which induces an increase in absolute value of the adsorption energy to -131.1 $kJ.mol^{-1}.molecule^{-1}$, is in agreement with XPS results that demonstrate a depletion in fluorine atoms and the existence of Ca-O bonds when the Na_2SiO_3 concentration is high (Figure 56c).

$Si_2O(OH)_6$ adsorbs under its molecular form establishing four Ca-O bonds between four terminal (non-bonding) oxygen atoms and four different surface calcium atoms with $d_{O\text{-}Ca} = 2.53$ Å for three bonds and $d_{O\text{-}Ca} = 3.65$ Å for the last bond (Figure 56f). Moreover, as for the $Si(OH)_4$ monomer, hydrogen atoms of the –OH groups establish hydrogen bonds with surface fluorine atoms (Figure 56b and f). Energetically speaking, the dimer adsorbs with $\Delta E_{ads} = -165.1$ $kJ.mol^{-1}$ including $\Delta E_{disp} = -70.4$ $kJ.mol^{-1}$, which represents a significant lower adsorption energy in absolute value compared to two monomers, regardless their acid-base form.

4.2.3 Adsorption of Na_2SiO_3 on CaF_2 carbonated surface

The DRIFT spectrum of CaF_2 treated with 5.10^{-2} $mol.L^{-1}$ of Na_2CO_3 and 5.10^{-2} $mol.L^{-1}$ of Na_2SiO_3 sequentially is significantly different from the spectra of CaF_2 conditioned with each reagent alone (Figure 57a). First, the bands located at 2492 cm^{-1} and at 1775 cm^{-1}, previously attributed to $Na_2CO_3/CaCO_3$, are no more present when the two reagents are used together. Moreover, compared to CaF_2 conditioned with Na_2CO_3 only, the band at 879 cm^{-1}, ascribed to $Na_2CO_3/CaCO_3$, is significantly weaker while the band located at 842 cm^{-1}, attributed to $NaHCO_3$, exhibits a higher intensity (Figure 57a). It indicates a higher amount of adsorbed $NaHCO_3$ when CaF_2 is conditioned with $Na_2CO_3 + Na_2SiO_3$. Also, CaF_2 conditioned only with Na_2CO_3 displays one band at 1439 cm^{-1} and another at 1650 cm^{-1} while two peaks are present in each aforementioned zone for CaF_2 conditioned with $Na_2CO_3 + Na_2SiO_3$: two bands located at 1732 and 1667 cm^{-1} and two other bands at 1470 and 1383 cm^{-1} are exhibited (Figure 57a), corresponding to both carbonate and hydrogencarbonate species. Furthermore, the band corresponding to Si-O asymmetric stretching vibration is narrower and shifted to 1057 cm^{-1} with a shoulder at 1023 cm^{-1} when CaF_2 is conditioned with $Na_2CO_3 + Na_2SiO_3$ (Figure 57a). According to the literature, it can be attributed either to higher amount of $SiO(OH)_3^-$ form rather

than $Si(OH)_4$ form for silica tetrahedra or to lower amount of polymerised silica onto the surface (Bass and Turner, 1997; Gaggiano et al., 2013; Jansson et al., 2015). Considering the higher amounts of $NaHCO_3$, it can be assessed that one or both of the following reactions occurs on the surface:

$$Si(OH)_4 + CO_3^{2-} = SiO(OH)_3^- + HCO_3^- \tag{33}$$

$$Si_2O(OH)_6 + CO_3^{2-} + H_2O = SiO(OH)_3^- + Si(OH)_4 + HCO_3^- \tag{34}$$
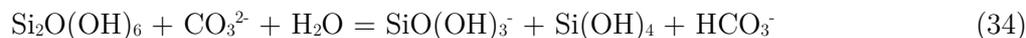
in which the CO_3^{2-} ion is part of the Na_2CO_3 or $CaCO_3$ layer formed on the CaF_2 surface.

XPS analyses were also conducted on CaF_2 conditioned with low reagents concentrations, *i.e.* 5.10^{-3} mol.L^{-1} for each, or with high reagents concentrations, *i.e.* 5.10^{-2} mol.L^{-1}. For low reagents concentrations, sodium atoms are identified (5.0 at.%) with $Na(1s)$ binding energies of 1071.3 eV, which is significantly lower than 1071.6 eV or 1071.9 eV displayed for $CaF_2 + Na_2CO_3$ and $CaF_2 + Na_2SiO_3$, respectively (Figure 57b). This shift can be attributed to the formation of $NaHCO_3$ onto the surface since this latter exhibits lower $Na(1s)$ binding energy than Na_2CO_3 (Briggs, 1981). Moreover, the peak at 533.6 eV exhibits on the $O(1s)$ spectrum for $CaF_2 + Na_2CO_3 + Na_2SiO_3$, which is absent for $CaF_2 + Na_2CO_3$ and $CaF_2 + Na_2SiO_3$, corresponded to $NaHCO_3$ (Shchukarev and Korolkov, 2004). The O/Si ratio is 4.03, which is slightly higher than 3.61 exhibited for Na_2SiO_3 alone at the same concentration, indicating a possible depolymerisation of silica species on the surface induced by the carbonate layer.

When the reagents concentrations are increased to 5.10^{-2} mol.L^{-1}, the surface chemical responses are very similar to those observed at low reagents concentrations. Interestingly, the $Si(2p)$ spectrum displays two components, at 103.1 eV (5.6 at.%) and 102.3 eV (4.6 at.%), while only one component at 103.2 eV is identified on $CaF_2 + Na_2SiO_3$ at the same concentration (Figure 57d). Although the interpretations for $Si(2p)$ spectra are difficult, the component at 103.1 eV was previously ascribed to Si-O-Si, *i.e.* polymerised silica, while the component at 102.3 eV was ascribed to Si-O-Na, *i.e.* non-polymerised and deprotonated silica.

To confirm these results, AIMD simulations were conducted on a carbonated surface. A complete layer of Na_2CO_3 was set on the (111) CaF_2 surface: a natrite supercell was created and fully relaxed at 0 K before generating the (110) surface, which presents crystallographic properties very close to the (111) fluorite surface. The natrite slab was then set on the (111) fluorite slab so that the CO_3^{2-} anions and the Na^+ cations corresponded spatially to Ca^{2+} cations and F^- anions, respectively. This carbonated surface was then used for the adsorption of Na_2SiO_3 onto carbonated surface at 300 K. As for bare CaF_2 surface, the adsorption of three different species have been investigated: (1) the protonated monomer, *i.e.* $Si(OH)_4$; (2) the basic form of the monomer, *i.e.* $NaSiO(OH)_3$; (3) the protonated form of the dimer, *i.e.* $Si_2O(OH)_6$.
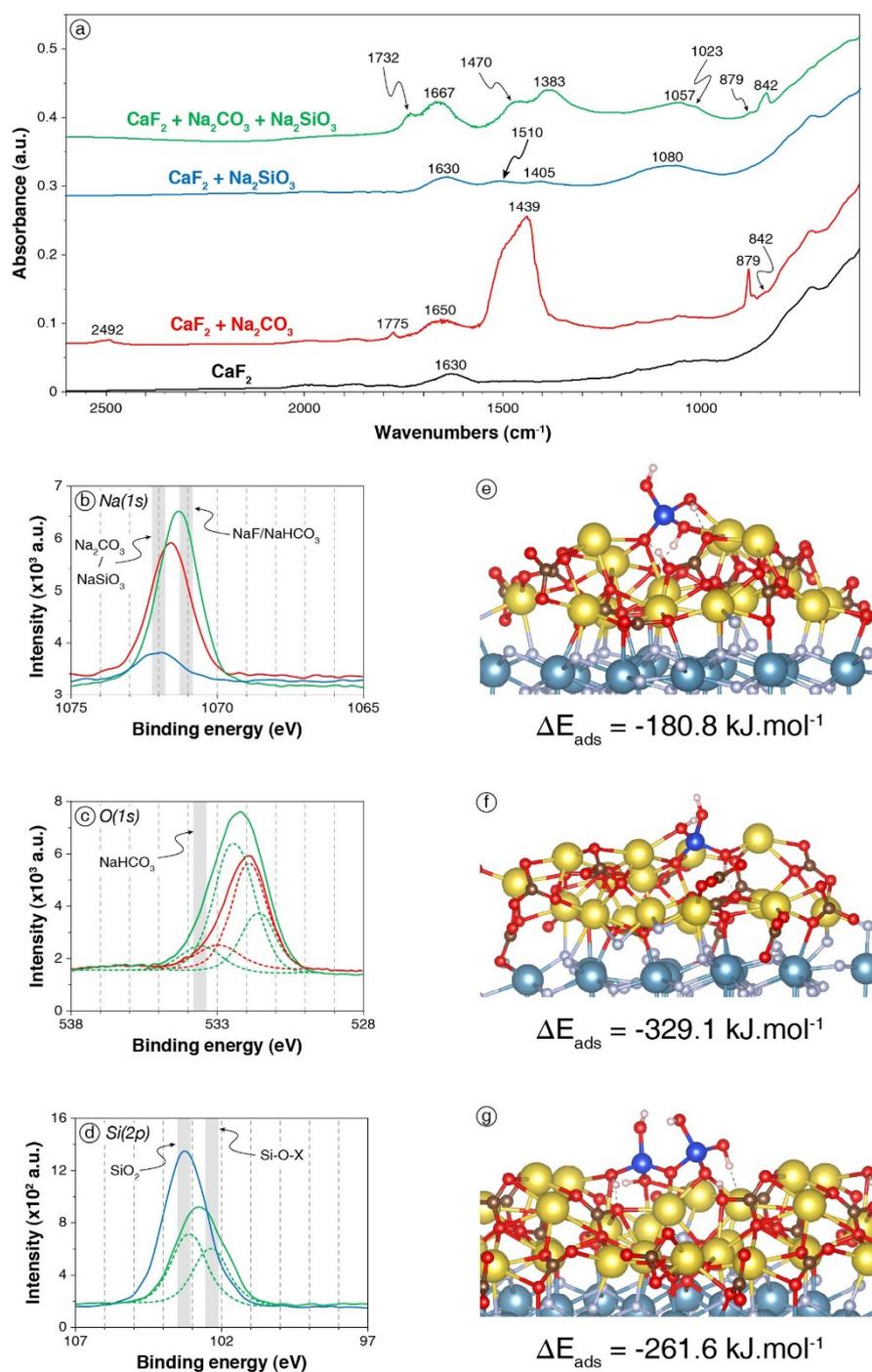
Figure 57. Adsorption of Na$_2$SiO$_3$ onto carbonated CaF$_2$ surface. **a.** Infrared spectra of CaF$_2$ conditioned in deionised water (black), in a 5.10^{-2} mol.L^{-1} Na$_2$CO$_3$ solution (red), in a 5.10^{-2} mol.L^{-1} Na$_2$SiO$_3$ solution (blue), and in 5.10^{-2} mol.L^{-1} Na$_2$CO$_3$ solution prior to in a 5.10^{-2} mol.L^{-1} Na$_2$SiO$_3$ solution (green). **b.** XPS Na(1s) spectra of the three last aforementioned samples. **c.** XPS O(1s) spectra, same legend than above. **d.** XPS Si(2p) spectra of CaF$_2$ conditioned in a 5.10^{-3} mol.L^{-1} Na$_2$SiO$_3$ solution (blue) and in 5.10^{-3} mol.L^{-1} Na$_2$CO$_3$ solution prior to in a 5.10^{-3} mol.L^{-1} Na$_2$SiO$_3$ solution (green). Snapshots of a side view of the carbonated (111) CaF$_2$ surface with a Si(OH)$_4$ molecule (**e**), a NaSiO(OH)$_3$ molecule (**f**), and a Si$_2$O(OH)$_6$ molecule (**g**) adsorbed onto the surface, after 50 ps of AIMD. For balls legends, please report to Figure 54 and Figure 55. Dashed lines represent hydrogen bonds.

The $Si(OH)_4$ molecule placed onto the carbonated (111) CaF_2 surface adsorbs establishing five Na-O bonds with two Na-O bonds formed by two different oxygen atoms and one Na-O bond by the last oxygen atom (Figure 57e) with average bond lengths comprised between 2.36 and 2.88 Å. Each hydrogen atom establishes a hydrogen bond with an oxygen atom of the Na_2CO_3 layer. Besides, sometimes during the simulation, a proton is transferred from the $Si(OH)_4$ molecule to a CO_3^{2-} anion of the Na_2CO_3 surface layer (Figure 57e). After few picoseconds, it is transferred back to the $Si(OH)_4$, indicating that the two configurations coexist on the surface with similar energy. This reaction on the surface is in nice agreement with the formation of $NaHCO_3$ previously demonstrated by DRIFTS and XPS (Figure 57a, b, c, and d). Overall, $Si(OH)_4$ adsorbs onto the carbonated surface with $\Delta E_{ads} = $ -180.8 kJ.mol^{-1} including $\Delta E_{disp} = $ -45.0 kJ.mol^{-1} compared to $\Delta E_{ads} = $ -100.8 kJ.mol^{-1} including $\Delta E_{disp} = $ -46.4 kJ.mol^{-1} onto the bare surface.

The $NaSiO(OH)_3$ molecule placed onto the carbonated (111) CaF_2 surface adsorbs with the deprotonated oxygen atom establishing four Na-O bonds with average bond lengths comprised between 2.34 and 2.70 Å (Figure 57f). Moreover, each protonated oxygen atom establishes one Na-O bond with the Na_2CO_3 layer with similar bond lengths. The hydrogen atoms form hydrogen bonds with surface oxygen atoms while the sodium atom also adsorbs onto the Na_2CO_3 layer. Overall, the $NaSiO(OH)_3$ molecule adsorbs with $\Delta E_{ads} = $ -329.1 kJ.mol^{-1} including $\Delta E_{disp} = $ -73.7 kJ.mol^{-1}, which is significantly higher than for the bare surface.

The $Si_2O(OH)_6$ molecule set on the carbonated surface adsorbs with three non-bonding and the bonding oxygen atoms each establishing two Na-O bonds with average bond lengths comprised between 2.30 and 2.80 Å (Figure 57g). Also, one proton is transferred durably from $Si_2O(OH)_6$ to a CO_3^{2-} anion of the surface, forming the $Si_2O_2(OH)_5^-$ species (Figure 57g). Episodically during the simulation, a second proton is transferred between the adsorbed molecule and the surface, forming the $Si_2O_3(OH)_4^{2-}$ molecule. Overall, the dimer adsorbs with $\Delta E_{ads} = $ -261.6 kJ.mol^{-1} including $\Delta E_{disp} = $ -87.9 kJ.mol^{-1}, which represents significantly higher adsorption energies in absolute values compared to the bare surface.

XPS and DRIFTS results demonstrate that the prior treatment with Na_2CO_3 can induce a depolymerisation of silica onto the surface. Hence, a $Si_2O(OH)_6$ molecule was set onto bare and carbonated surfaces along with an H_2O molecule, which is mandatory to enable the depolymerisation reaction. However, this reaction is not observed spontaneously. Overall, based on the previous results, the following conclusions can be drawn, at pH 10:

- Conditioning with Na_2CO_3 induces the formation of a carbonate layer at CaF_2 surface;
- Na_2SiO_3 adsorbs on CaF_2 surface under both $Si(OH)_4$ and $SiO(OH)_3^-$ forms, with significant amount of polymerised forms of silica at the studied concentrations;
- The CO_3^{2-} ions comprised in the surface carbonate layer accept a proton from silica: $NaHCO_3$ is formed while deprotonated and/or depolymerised silica forms become dominant on the surface. The deprotonated forms of silica adsorbs better than the protonated forms, which can explain the synergistic effects observed between the two reagents.

4.3 Discussion

Considering the experimental and theoretical results, the Na_2CO_3 layer formed on the surface induces a proton exchange between the silica molecules and the carbonated surface, even at low coverage (1 molecule, *i.e.* 16.7% coverage). This proton exchange occurs for the acid forms of the monomer $[Si(OH)_4]$ and dimer $[Si_2O(OH)_6]$, and, hence, probably for all the n-mers. It results in the formation of the basic, *i.e.* anionic, forms of these molecules, which adsorbs with significantly higher adsorption energies compared to their acid forms (Table 16). This proton exchange is observed for bare surface only for high surface coverage (6 molecules, *i.e.* 100% coverage). These results explain the positive synergistic effects on the gangue minerals depression observed when the reagents are used in combination: the prior surface carbonation allows to form the anionic species of silica molecules by a surface acid-base reaction. It induces a chemisorption of these molecules onto the surface for low coverage while a high coverage is needed to observe the same phenomenon on bare surface. Increasing the solution pH would also lead to observe the same phenomenon by increasing the amount of anionic silica species in solution. However, it would also result in hydroxylation of the surface cations, which would prevent the collector adsorption on all surfaces, including on the target mineral surface.

Table 16. Summarising table of the adsorption energies and surface reactions as a function of the surface coverage and the surface carbonation.

Molecule	Number	Surface	ΔE_{ads} (kJ.mol^{-1}.molecule^{-1})	ΔE_{disp} (kJ.mol^{-1}.molecule^{-1})	Comments
$Si(OH)_4$	1	Bare	-100.7	-46.4	-
$Si(OH)_4$	6	Bare	-131.1	-49.4	Formation of HF by surface substitution of F$^-$ by SiO(OH)$_3^-$
$NaSiO(OH)_3$	1	Bare	-196.5	-56.9	Formation of NaF by surface substitution of F$^-$ by SiO(OH)$_3^-$
$Si_2O(OH)_6$	1	Bare	-165.1	-70.4	-
$Si(OH)_4$	1	Carbonated	-180.8	-45.0	Partial formation of SiO(OH)$_3^-$ by proton exchange with the surface
$NaSiO(OH)_3$	1	Carbonated	-329.1	-73.7	-
$Si_2O(OH)_6$	1	Carbonated	-261.6	-87.9	Formation of Si$_2$O(OH)$_5^-$ and partial formation of Si$_2$O(OH)$_4^{2-}$ by proton exchanges with the surface

4.4 Conclusions

In this part, a combination of surface spectroscopic methods (DRIFTS and XPS) and AIMD simulations was used to gain understanding in the adsorption mechanisms of Na_2SiO_3 on fluorite, which represents an archetype of salt-types minerals. In particular, the synergistic effects observed when Na_2SiO_3 is used in combination with Na_2CO_3 in the froth flotation process were investigated. Both experimental and theoretical results demonstrated that Na_2CO_3 adsorbs onto fluorite and forms a carbonate layer on the surface. Also, they proved that $Si(OH)_4$, the most stable form of Na_2SiO_3 in dilute aqueous solutions at pH<9.4, physisorbs with

$\Delta E_{ads} = $ -100.7 kJ.mol^{-1} while SiO(OH)$_3^-$, stable for pH>9.4, chemisorbs onto the surface by substituting a fluorine atom, with $\Delta E_{ads} = $ -196.5 kJ.mol^{-1}. The dimer, Si$_2$O(OH)$_6$, representing polymerised forms stable for higher silica concentrations, physisorbs with $\Delta E_{ads} = $ -165.1 kJ.mol^{-1}, which is significantly lower than two monomers. The surface carbonation, induced by the prior addition of Na$_2$CO$_3$, leads to an acid-base reaction on the surface that results in the formation of the deprotonated forms of silica, regardless the polymerisation degree, *i.e.* SiO(OH)$_3^-$, Si$_2$O$_2$(OH)$_5^-$, and Si$_2$O$_3$(OH)$_4^{2-}$. Also, experimental studies demonstrated that the surface carbonation leads to a silica depolymerisation onto the surface. The anionic forms adsorbed with higher adsorption energies in absolute values compared to acid forms, as well as the monomers compared to the dimers. The formation of anionic forms onto bare surface needs either high silica coverage or high solution pH to be observed. Hence, at a moderate pH, lower amount of Na$_2$SiO$_3$ is needed when the surface is carbonated to produce the same effect, explaining the strong synergistic effects highlighted when the Na$_2$SiO$_3$ is used in combination with Na$_2$CO$_3$. Also, the deprotonation in solution by a pH increase would lead to a hydroxylation of all the surfaces and then a global depression of all the minerals including the target mineral. This work allowed to gain understanding in the depressing effect of the combination of Na$_2$SiO$_3$ and Na$_2$CO$_3$ and could lead to a reduction of the Na$_2$SiO$_3$ amounts used worldwide in the flotation industry by using Na$_2$CO$_3$ instead of NaOH to control the pH.

5. General conclusion

In this chapter, among the different depressants were tested to attain the selective depression of gangue minerals from scheelite, which would enhance the WO_3 grade and eliminate penalising elements from the concentrate. Among all the investigated depressants, the combination of Na_2CO_3 added prior to the addition of Na_2SiO_3 afforded the best results in terms of WO_3 recovery and gangue minerals rejection. This combination was then studied in deeper detail by using the DOE methodology to assess the effect of each reagent as well as their interactions. It allowed to highlight strong synergistic effects between the two reagents, mainly on scheelite, fluorite, and, to a lesser extent, silicates. These effects were attributed to surface carbonation that makes $Si(OH)_4/SiO(OH)_3^-$ adsorption more favourable. Overall, the DOE allowed the setting of the best experimental conditions in terms of reagent concentration, thereby leading to optimised gangue mineral depression in the flotation process. These conditions were established as: 1,150 g/t Na_2CO_3 with 1,225 g/t Na_2SiO_3. This proposed method produced a concentrate assaying 10.1% WO_3 with 93.2% WO_3 recovery. However, the fluorite recovery was still 63.6%, which is considered high. Besides, the Na_2CO_3/Na_2SiO_3 system was deeply characterised by spectroscopic studies (FTIR and XPS) combined with state-of-the-art AIMD simulations, which both demonstrated that the prior surface carbonation induce an acid-base reaction on the surface involving the silica species. Hence, $Si(OH)_4$ is transformed to $SiO(OH)_3^-$ by the loss of a proton in favour of surface a CO_3^{2-} ion, leading to a significantly more favoured adsorption of the silica species [-100.7 $kJ.mol^{-1}$ for $Si(OH)_4$ on the bare surface, -180.8 $kJ.mol^{-1}$ on the carbonated surface]. This allows to unravel the molecular mechanisms responsible for the strong synergistic effects that have been observed for decades between Na_2CO_3 and Na_2SiO_3. Also, it highlights the benefits of using DFT simulations for understanding molecular mechanisms involved in the flotation process.

Fatty acids used as collectors for selective scheelite flotation from a complex tungsten skarn ore

1. Introduction

As stated previously, different processing options are suitable to increase the separation contrast between scheelite and other gangue minerals, including calcium minerals. In Chapter 3, the use of a Falcon concentrator was investigated to reject the calcium minerals, mostly the calcium salts, prior to flotation. However, the Falcon operating parameters were defined by doing a compromise between the calcium salts rejection and the scheelite recovery, which induced significant scheelite losses. Hence, in Chapter 4, the depressants in scheelite flotation were investigated, which resulted in the determination and optimisation of the depressing conditions for the Tabuaço skarn. For these previous works, the collecting parameters were maintained constant: a simple TOFA (RBD15) at a dosage of 200 g/t was used for all the flotation tests since it exhibited good performances in terms of WO_3 grade and recovery during preliminary orientation tests. Furthermore, the pH was arbitrarily set to 9.5-10 as scheelite traditionally displays a good floatability in this pH range. Nonetheless, although the selected depressants, *i.e.* Na_2CO_3 and Na_2SiO_3, are the best among all the tested molecules, they still exhibit a lack of selectivity between scheelite and fluorite. The flotation performances depend not only on the depressing conditions but on all the above-mentioned parameters that were maintained constant for the depressants optimisation. Hence, the separation contrast between scheelite and gangue minerals could also be improved by changing the pH, collector type(s), collector structure(s), and collector dosage. The present chapter presents studies that have been conducted most of the time with the depressing conditions maintained constant at their optimised levels for the investigation and optimisation of the collection conditions to further improve the scheelite flotation selectivity. Microflotation tests were performed to study the influence of the pH, the collector concentration, and the collector formulations. Then, batch scale flotation tests were conducted to characterise the above-mentioned developments on the Tabuaço skarn ore. In addition, FTIR analyses were performed to gain understanding in the molecular mechanisms involved in the phenomena observed in the flotation tests. A part of this work has been published in **Minerals Engineering 123 (2018), under the title "New reagent formulations for selective flotation of scheelite from a skarn ore with complex calcium minerals gangue"**.

2. Microflotation tests

> 2.1 Effect of pH on the scheelite and fluorite floatabilities

First, the floatability of each mineral as a function of pH was assessed with sodium oleate, the most common fatty acids used for calcium minerals flotation. Previous orientation tests allowed to set a collector concentration at 1×10^{-5} mol.L^{-1} for scheelite and at 5×10^{-6} mol.L^{-1} for fluorite. Then, with this constant sodium oleate concentration, microflotation tests were performed on each mineral separately at various pH values (4.5, 6, 8, 9.5, and 11). The results are presented in Figure 58.
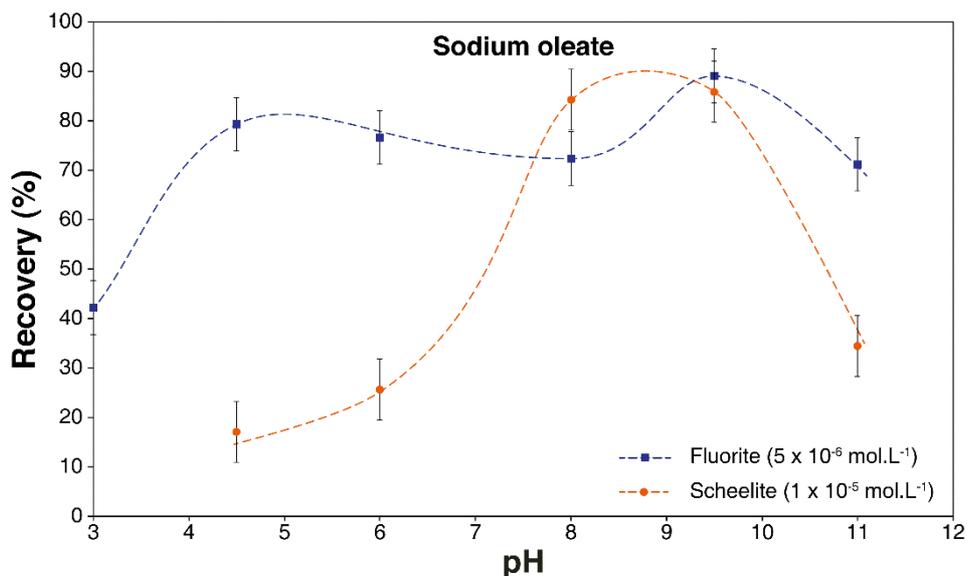
Figure 58. Microflotation recoveries of fluorite and scheelite as a function of the conditioning and flotation pH, with sodium oleate at set concentration.

2.1.1 On scheelite

For scheelite, recoveries are low in acidic conditions, *i.e.* for pH 4.5 and 6, which can be attributed to the dominance of the acidic form (R-COOH) of the collector since the pKa of oleic acid/oleate is 5.0. This result is in agreement with the literature as fatty acids mainly physisorb onto surface calcium atoms when they are under their acidic form (Fuerstenau and Healy, 1972). The floatability increases with the pH to reach a maximum around pH 8 – 9.5, which matches the predominance of the deprotonated (R-COO⁻) collector form. It is attributed to the chemisorption of the carboxylate forms of fatty acids on the surface calcium atoms, which is known to occur with significantly higher adsorption energies (Bachér et al., 2015; Changgen and Yongxin, 1983; Fuerstenau and Healy, 1972; Marinakis and Shergold, 1985a). When the pH is increased to 11, the floatability considerably decreases, which can be attributed to the high activity of hydroxide ions (OH⁻) in solution. It probably leads to a significant surface hydroxylation, *i.e.* to the adsorption of OH⁻ onto surface calcium atoms that are consequently unavailable for the collector adsorption: it corresponds to a competitive adsorption between OH⁻ and -COO⁻.

2.1.2 On fluorite

Fluorite exhibits the same trends, with however lower amplitudes (Figure 58): the floatability is roughly constant between pH 4.5 and pH 9.5 and decreases significantly for pH<4.5 and slightly for pH>10, which corresponds to the same phenomena displayed by scheelite. At pH 4.5, fluorite still has a good floatability, which can be attributed to the coexistence of both acidic and carboxylate forms. This coexistence is known to enhance the flotation performances by the formation of molecular-anionic complexes (Miller and Misra, 1984), which reduce the polar repulsion between the carboxylate forms in the adsorption layer. Nevertheless, this phenomenon is not observed for scheelite, which displays a significantly lower floatability compared to fluorite

on all the studied domain. Their floatabilities are yet very similar at pH 8 and 9.5, although the total amount of collector used was two times higher for scheelite than for fluorite. Also, the specific gravities of fluorite and scheelite are 3.2 and 6.1, respectively, which induces that, for a same size fraction, scheelite exhibits two times less specific surface than fluorite. Based on these discussions, the poor floatability of scheelite with sodium oleate might be ascribed to its high specific gravity, which possibly enhances the detachment probability by increasing the weight force. It can also be impelled by its lower surface calcium atoms density: it induces a decrease of the lateral interactions between the collector aliphatic chains, which results in a less compact adsorption layer and then a higher wettability. Finally, surface calcium atoms probably display reactivity differences between scheelite and fluorite since they are six-coordinated for the former and seven-coordinated for the latter on their respective most exposed surfaces. Overall, pH 9-10 corresponds to the optimal scheelite floatability and, therefore, should be selected for the further flotation tests albeit it also represents the maximum in the fluorite floatability.

2.2 Effect of concentration on the scheelite and fluorite floatabilities

2.2.1   On fluorite

Influence of the unsaturation degree

According to the previous results, the following microflotation tests were performed at pH 9.5, which was the optimal pH for fluorite and scheelite flotation. The floatabilities of the two minerals were evaluated as a function of the collector concentration, for the different collectors studied. First, the influence of the unsaturation degree on the fluorite floatability was investigated with a constant chain length of 18 carbon atoms (Figure 59a). At similar collector concentrations, flotation recoveries are the highest for oleate, intermediate for linoleate and, finally, the lowest for stearate. The low efficiency of stearate can be attributed to the low solubility of saturated fatty acids, since the fatty acids solubility is known to decrease when the unsaturation degree decreases (Fuerstenau and Miller, 1967; Leja, 1981). This commonly results in a low mobility of saturated fatty acids in solution and then a low availability of these molecules for the adsorption. Due to its additional unsaturation, linoleate is more soluble than oleate but however exhibits lower fluorite recoveries at low to moderate concentrations. This indicates that the fatty acids solubility is not the only parameter influencing the fluorite floatability. Besides the solubility, the three fatty acids differ in their global geometrical configuration, which is induced by the unsaturation degree: the *-cis* double bond(s) of oleate and linoleate result in chains that bend at the position of the *-cis* double bond (Kanicky and Shah, 2002). This provides a higher steric hindrance when the unsaturation degree increases and then a higher packing area for the unsaturated fatty acids: stearic acid (or stearate) can pack down to 20 Å² while the packing areas are approximately 41 Å² for oleic acid (Kanicky and Shah, 2002; Tomoaia-Cotişel et al., 1987) and 48 Å² for linoleic acid (Kanicky and Shah, 2002; Peltonen and Rosenholm, 1989; Tomoaia-Cotişel et al., 1987).
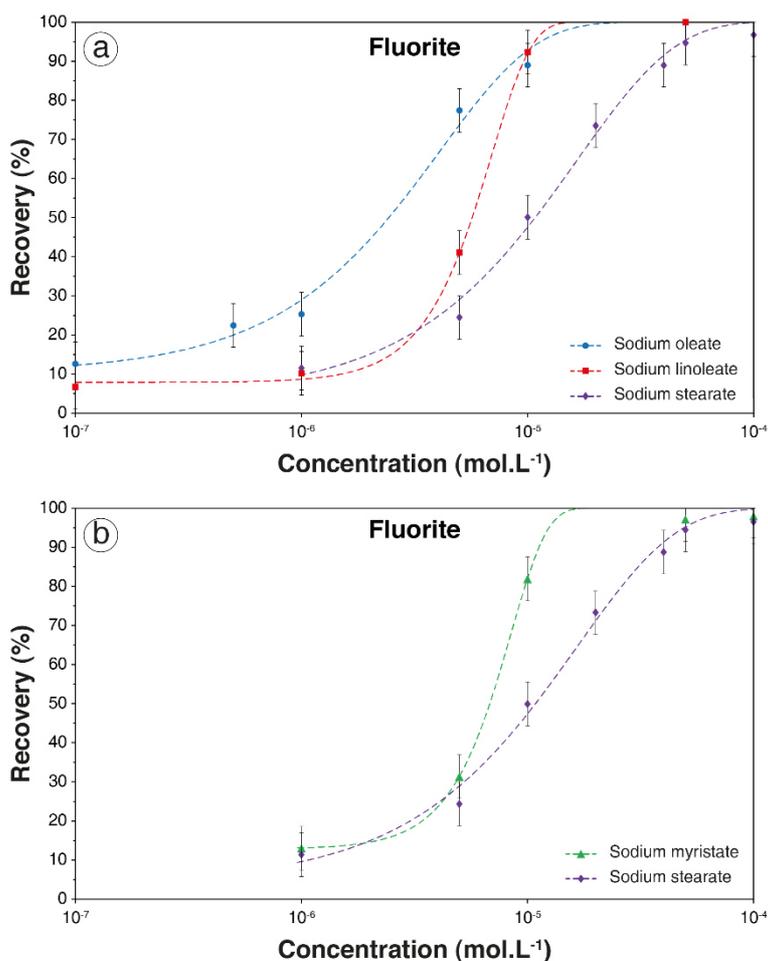
Figure 59. Fluorite floatability (microflotation recoveries) as a function of the collector concentration for collectors having different unsaturation degrees for a constant chain length (a) or different chain lengths for a constant unsaturation degree (b).

Considering these values, it can be assessed that the adsorption layer is tightly organised with saturated fatty acids and more loosely assembled when the unsaturation degree increases. This results in higher amount of saturated fatty acids needed to reach the same surface coverage compared to unsaturated fatty acids, *i.e.* lower floatabilities with saturated fatty acids for a given concentration. Nonetheless, the differences in fluorite recoveries between oleate and linoleate are erased at higher collector concentration, *e.g.* 1 x 10^{-5} mol.L^{-1}, at which they exhibit similar recoveries. This is induced by different recoveries curve slope between the three different collectors tested: the slope increases with the unsaturation degree (linoleate>oleate>stearate), which can be related to two chemical phenomena. First, the fatty acids solubility increases with the unsaturation degree: when the amount of collector in solution is increased, the added molecules are more available to adsorb when they are unsaturated. Moreover, apart from their higher solubility, the slope increase with unsaturation degree can be explained by the double bonds reactivity: authors demonstrated that polymerisation of the fatty acids aliphatic chains can occur via an oxidation of the double bonds resulting in an oxygen linking between the chains (Brandao, 1982; Hu et al., 1986b, 1986a; Kellar et al., 1992; Miller and Misra, 1984).

Influence of the chain length

Besides, the influence of the chain length on the fluorite floatability was investigated with saturated fatty acids (Figure 59b). Myristate and stearate exhibit very similar behaviours with close floatabilities at low concentrations (1 x 10^{-6} and 5 x 10^{-6} mol.L^{-1}). At moderate concentrations, myristate displays a better efficiency than stearate while, at higher concentrations, they provide similar recoveries. Accordingly, myristate exhibits the highest slope, which, considering their same unsaturation degree and, hence, packing area, can only be attributed to the higher solubility of myristate due to its lower chain length. Therefore, it can be assessed that the slope of the recovery curve is only controlled by the solubility of the fatty acids.

2.2.2   On scheelite

The influence of the unsaturation degree on the scheelite floatability was also investigated, with a constant chain length of 18 carbon atoms (Figure 60a). Oleate and linoleate display very similar efficiency and slope, while stearate provides poor efficiency and lower slope, which can be attributed to its low solubility. This highlights the differences in terms of surface properties (Ca^{2+} density and Ca^{2+}-Ca^{2+} distance) between scheelite and fluorite, as well as their specific gravity contrast. Moreover, the influence of chain length on the scheelite floatability was also investigated, with a constant unsaturation degree of 0 (Figure 60b). Myristate exhibits lower efficiency compared to stearate: the shorter aliphatic chain of myristate probably results in a lower surface tension at the air/solid interface, which enhances the bubble-particle detachment probably. Nonetheless, this phenomenon was not observed for fluorite, considering its significantly lower specific gravity. Hence, considering these results, the short chain fatty acids seems an unsuitable option for the scheelite selective flotation since it provides a poor hydrophobation that does not compensate the high specific gravity of scheelite.
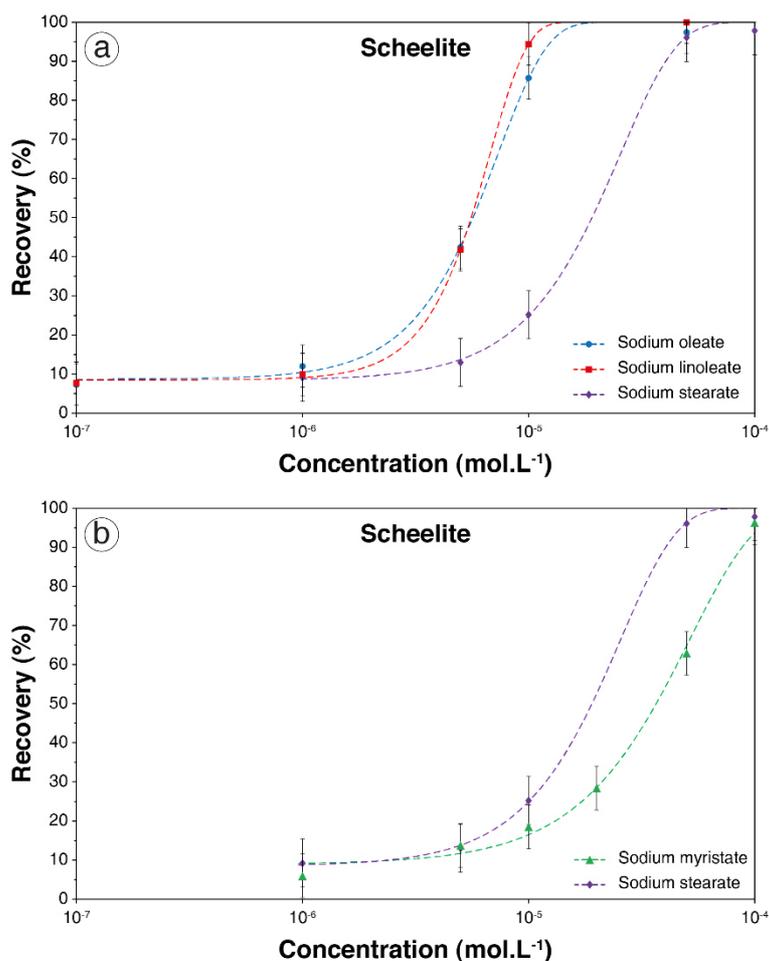
Figure 60. Scheelite floatability (microflotation recoveries) as a function of the collector concentration for collectors having different unsaturation degrees for a constant chain length (a) or different chain lengths for a constant unsaturation degree (b).

2.2.3   A comparison

Fluorite and scheelite floatabilities measured and discussed previously can also be expressed as a function of each collector concentration to compare the two minerals behaviours without being mixed (Figure 61). On each graph of Figure 61, the physical-chemical properties of the fatty acid are the same (solubility and packing areas), which allows to compare thoroughly the two minerals. The lower floatability of scheelite compared to fluorite with oleate can be explained by the higher specific gravity of scheelite (6.1 rather than 3.2), which induces a higher bubble-particle detachment probably during microflotation tests. This phenomenon is strictly the same for stearate with however a lower floatability difference between the two minerals. Moreover, myristate exhibits the highest floatability difference between fluorite and scheelite, which can also be attributed to a higher bubble-particle detachment probability for scheelite combined with the lower surface tension induced by its short chain. Interestingly, linoleate displays very similar floatabilities between the two minerals. This is probably related to the significant steric hindrance of linoleate molecules that erases the surface properties differences

between scheelite and fluorite. Therefore, linoleate induces a more loosely organised adsorption layer due to its two double-bonds (which result in two bending in the aliphatic chain).
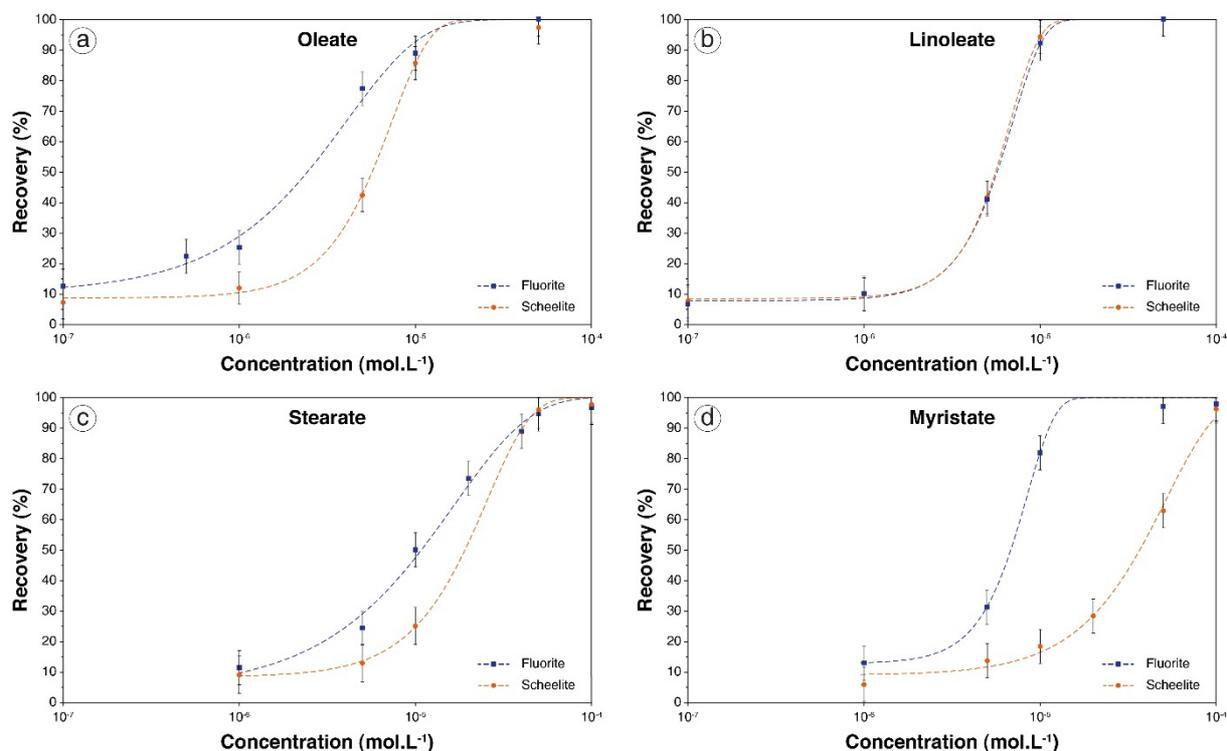
Figure 61. Fluorite and scheelite floatabilities as a function of the four studied collectors concentrations, namely oleate (a), linoleate (b), stearate (c), and myristate (d).

2.2.4 The selectivity of sole fatty acids

Microflotation performed on pure minerals allows to assess the floatability of a given mineral but with no consideration of the adsorption selectivity. Indeed, when the collector is added to the solution, an equilibrium exists between the amount of molecules adsorbed and the amount of molecules in solution, these latter being however in minority (Cases and Villieras, 1992). Besides, when a flotation collector is added in pulp with an ore, an equilibrium is established between the solution and all the minerals on which the collector is able to adsorb. Hence, the minerals affinities for the collector(s) strongly govern the surfaces/solution equilibrium since the collector adsorption will be favoured on the mineral that exhibits the higher affinity for the collector. As the present study aims at increasing the collector adsorption selectivity for scheelite mixtures of 50 wt.% scheelite and 50 wt.% fluorite were created and used in microflotation tests. It allowed to compare the floatabilities of the two minerals when they are conditioned in the same solution and, then, to discuss thoroughly the collector adsorption selectivity. First, the sole four fatty acids were used with increasing concentration and the results are presented in Figure 62. Fluorite systematically exhibits higher floatabilities than scheelite, which can be attributed to the higher specific gravity of scheelite, to a lower surface calcium sites density, and to higher surface Ca-Ca distance. This could also be attributed to water molecules adsorbed with higher adsorption energies in the case of scheelite, which could induce a higher difficulty for the collector to adsorb

on the surface (see Chapter 7). However, some differences can be observed between the four studied fatty acids. In particular, sodium linoleate displays the lowest floatability contrast, while sodium myristate shows the highest one, in favour of fluorite. Sodium stearate, albeit its lower availability in solution, affords an acceptable fluorite floatability but a poor scheelite floatability, similarly to sodium myristate, while sodium oleate provide an intermediate selectivity, between that of sodium linoleate and sodium stearate. This observation can be related to the minerals surface properties: as stated previously, the packing areas are closely correlated to the unsaturation degree, and hence, they are in the order linoleate>oleate>stearate/myristate. This is the same order than the floatabilities contrast between fluorite and scheelite. This demonstrates that the control of the surface Ca-Ca distance and surface calcium sites density have on the adsorption selectivity decreases when the unsaturation degree increase. This can be attributed to a looser adsorption layer when the unsaturation degree is increased due to the higher steric hindrance for unsaturated fatty acids. Overall, no positive selectivity can be provided by sole fatty acids on model systems, *i.e.* without any depressants. Nonetheless, the selectivity in favour of fluorite, systematically observed, could be reduced by increasing the unsaturation degree of the fatty acids, in particular by using sodium linoleate. Moreover, saturated fatty acids, which have been supposed to play a positive role in the increase of the flotation selectivity in favour of scheelite (see section 3.3), clearly exhibit a significant adsorption selectivity for fluorite.
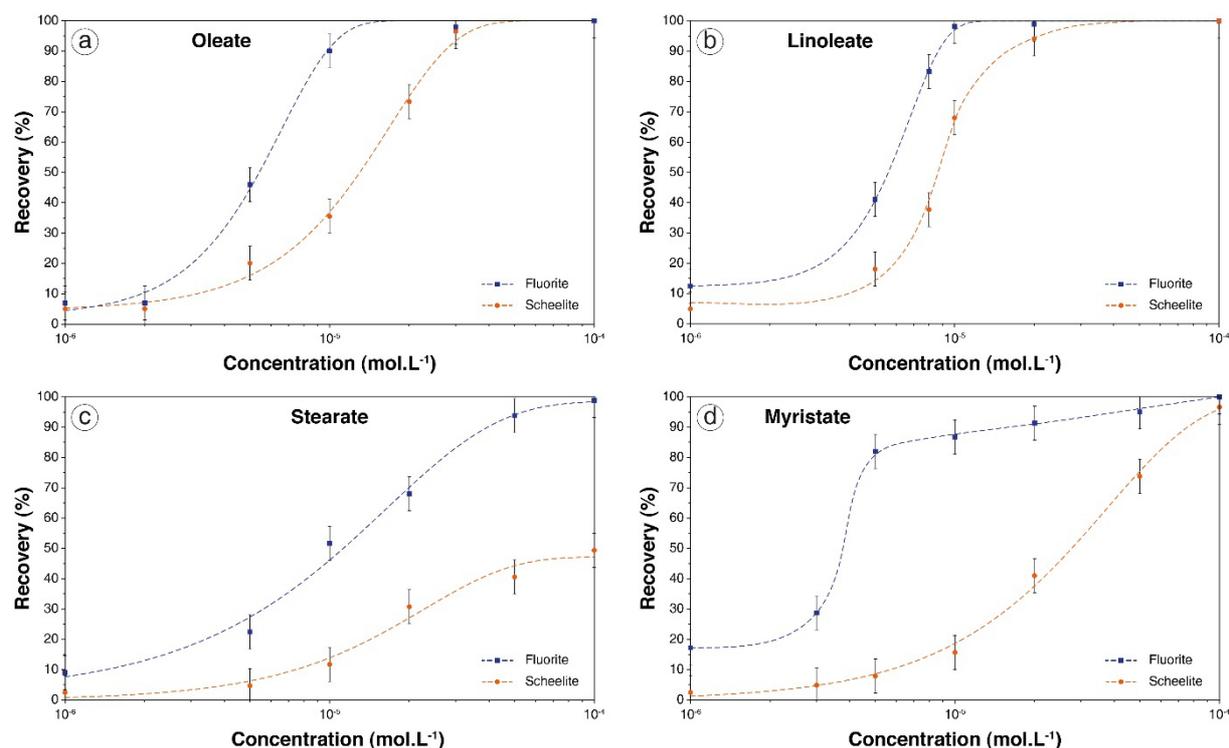
Figure 62. Fluorite and scheelite microflotation recoveries from binary mineral mixtures (50 wt.% fluorite + 50 wt.% scheelite) using sodium oleate (a), sodium linoleate (b), sodium stearate (c), and sodium myristate (d) at various concentrations.

2.3 Effect of fatty acids mixing

For decades, collectors with different polar functions, chain lengths, or chain structures have been used together in formulations. Indeed, most industrial fatty-acid-based formulations as TOFA are mixtures since it is very difficult to purify the different fatty acids. Hence, the effect of fatty acids mixing on the selectivity should be investigated. According to the previous results, fatty acids used alone demonstrate poor selectivity between scheelite and fluorite, always in favour of fluorite, see previously. The selectivity in favour of scheelite is inversely related with the saturation degree: sole saturated fatty acids exhibit the worst selectivity in favour of scheelite while sole linoleate somewhat provides similar floatabilities between scheelite and fluorite. For a constant chain length, the only difference existing between the fatty acids is their unsaturation degree, which result in different packing area, as mentioned previously. Hence, the Ca-Ca distance on the minerals surfaces controls the adsorption and the organisation of the adsorption layer, which is, additionally, led by the fatty acids packing area. The modulation of the organisation of the adsorption layer, induced by mixing fatty acids with different chain structures, could change the selectivity in favour of scheelite. Consequently, a DOE was generated with different proportions in each of the four fatty acids, maintaining the total collector concentration constant. Binary, tertiary, and quaternary mixtures were used. To estimate the separation performances, a selectivity index was introduced following:

$$Selectivity_{A/B} \ index \ = \ \frac{Recovery_A \ - \ Recovery_B}{2 \ \times Recovery_{Total}} \tag{35}$$

Where A was scheelite and B fluorite, and where the recoveries were calculated by measuring the W content in ED-XRF analyses. This selectivity index is zero when an equal amount of each mineral was floated, -1 when all fluorite and no scheelite was floated, and +1 when all scheelite and no fluorite was floated. The selectivity index was then selected as the studied response in the model since the global objective of this study was to improve the selectivity between scheelite and fluorite. Overall, all the coefficients of the linear terms and the second-order interactions terms are significant while the third-order and fourth-order interactions are not significant and have been eliminated from the model. As a consequence, the response can be displayed on response surfaces (Figure 63). First, on the whole domain studied, the selectivity index is always negative, which indicates that fluorite has a higher floatability than scheelite. For all fatty acids mixtures, at very low and high concentrations of both fatty acids, the selectivity index is the higher. This can be explained by two main phenomenon: at very low collector concentrations, the selectivity differences are probably erased since each mineral exhibits very poor floatability; at high collector concentrations, the adsorption layer on fluorite is possibly complete and, therefore, collector is made available to adsorb on scheelite surfaces. In addition, the selectivity index is maintained at moderate values on the y = x curve, indicating that a 1:1 ratio is favourable to a higher selectivity in favour of scheelite. At high concentrations of reagents used solely (ratio 1:0 or 0:1), the selectivity index is dramatically low: this confirms that mixing fatty acids increases the selectivity in favour of scheelite since, for a constant total amount of collector,

the selectivity is higher for a 1:1 ratio rather than for a 1:0 or a 0:1 ratio. Albeit the selectivity index displays similar behaviour regarding the different fatty acids, some differences can be observed. Notably, the mixture of myristate and stearate does not afford any selectivity in favour of scheelite while the mixture of stearate and linoleate exhibit slightly higher selectivity index than other mixtures. The most significant synergistic effects are displayed by the oleate-linoleate and linoleate-stearate mixtures. Hence, for a total collector concentration maintained constant, using collector mixtures containing at least one unsaturated fatty acid (oleate or linoleate), allows to attain higher selectivity indexes than using sole collector. Furthermore, the behaviours of sole fatty acids, observed in section 2.2.4, are totally different when they are mixed, probably due to strong synergistic effects existing between them. Indeed, while sole saturated fatty acids provided the poorest selectivity in favour of scheelite, mixing them with unsaturated seems to increase the selectivity for scheelite. These results are crucial for the following studies: TOFA, which are the main collectors used in this work, usually comprise mixtures of different fatty acids, mostly oleic and linoleic acids, due to their natural origin. The above-mentioned results exhibited positive synergistic effects between fatty acids with different chain lengths and saturation degrees, which could be exploited for the design of a new collector formulation that would be more selective for scheelite.
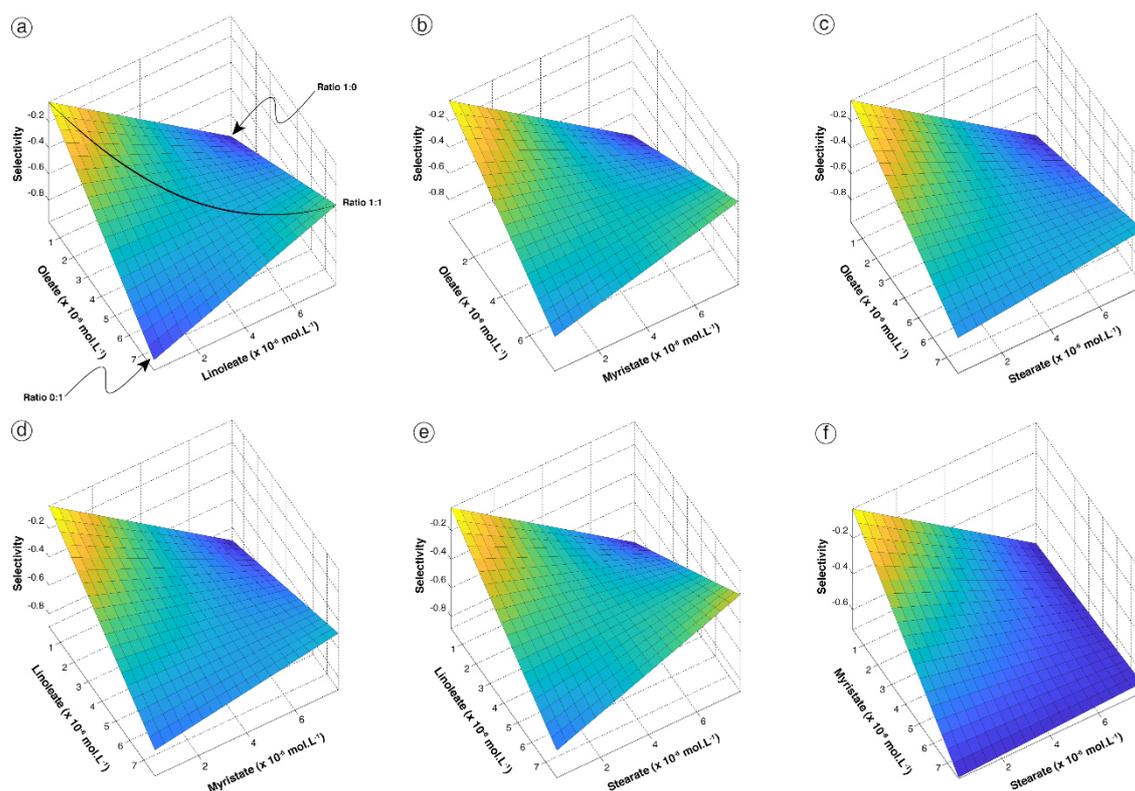
Figure 63. Responses surfaces displaying the selectivity index for scheelite modelled as a function of the four fatty acids concentrations in microflotation tests performed on mineral mixtures. For each surface, the concentrations of the two non-represented fatty acids were set to zero.

2.4 Effect of rosin acids content

As mentioned previously, many commercial fatty-acid formulations used for industrial applications are TOFA, which generally include significant amounts of rosin acids. These terpene derivative molecules have non-linear aliphatic chains with around 20 carbon atoms. The most common rosin acids in fatty-acid formulations are palustric, pimaric, and abietic acids, which all contain a carboxylic acid group and several non-aromatic cycles combined together (Figure 64).
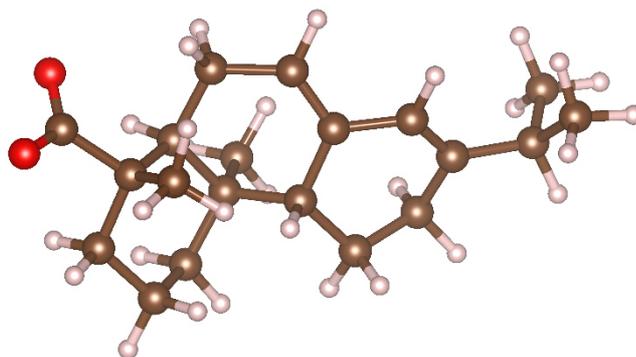
Figure 64. Abietate molecule, the carboxylate form of the abietic acid, which, considering the slight differences between the different rosin acids, represents all the rosin acids.

The influence of the rosin acids content in the collector formulations was first assessed by microflotation tests. For this study, pure abietic acid was used to represent the rosin acids. In addition, the total fatty acids concentration was set to 5×10^{-6} mol.L^{-1}, the ratio between oleate and linoleate was maintained constant, equal to 1, and the ratio between abietate and (oleate + linoleate) was modified. The effect of this latter on scheelite, fluorite, apatite, and calcite floatabilities is displayed on Figure 65. At a ratio oleate/linoleate kept constant to 1:1, when the ratio abietate/(oleate + linoleate) is increased, *i.e.* more abietate is introduced in the system, the selectivity decreases significantly (Figure 65). For a ratio oleate:linoleate:abietate = 1:1:1 and 1:1:2, the four minerals exhibit similar floatabilities, nonetheless slightly lower for scheelite, probably due to its high specific gravity compared to the other minerals (Figure 65). As for all the fatty acids, the carboxyl group of the rosin acids adsorbs onto the surface Ca^{2+} sites of the calcium minerals. It induces a surface hydrophobation of all the calcium minerals, however significantly lower than the one provided by classical fatty acids. This can be induced by the global configuration of the aliphatic chain of rosin acids, which contains several rings that are probably less efficient to establish chain-chain lateral interactions compared to linear chains. Moreover, their significant steric hindrance, resulting from the terpene rings, can be responsible for calcium sites to stay unoccupied on the surface. It erases the differences in terms of crystallographic properties between the four calcium salts, leading to similar microflotation recoveries.
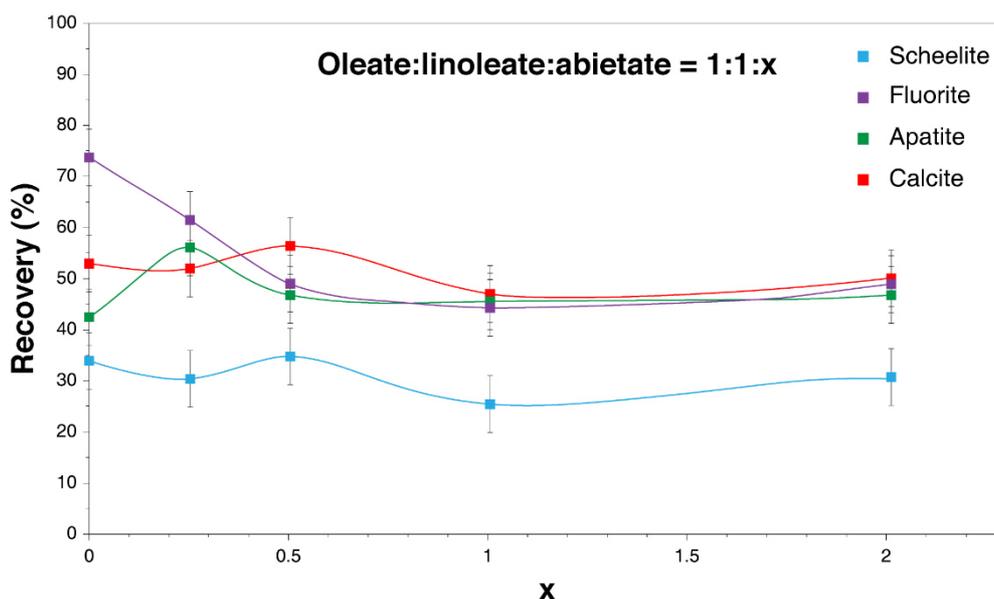
Figure 65. Effect of abietate/(oleate + linoleate) ratio on the efficiency of the flotation on pure minerals.

3. Batch scale flotation tests

Batch scale flotation tests were performed on the Tabuaço ore to confirm the conclusions drawn by microflotation studies or to develop new collector formulations. In particular, the optimal collector concentration for scheelite collection from the Tabuaço skarn was defined through preliminary tests. Then, the rosin acids content in the formulation, previously studied by microflotation, was investigated on the Tabuaço ore to discuss their effect on the selectivity. Besides, a new TOFA containing significant amounts of saturated fatty acids was tested on the tungsten skarn ore to assess the influence of the introduction of these latter in the unsaturated-fatty-acid-based formulations on the WO_3 grade and recovery. Finally, the introduction of a non-ionic co-collector was investigated in terms of flotation performances.

3.1 Collector concentration

First, the collector concentration was investigated and optimised. This study represented the very first tests performed on the Tabuaço ore and was conducted very early in this work which, therefore, induced that the depressing conditions were not yet optimised. Three tests were performed with 100 g/t, 150 g/t, and 200 g/t of RBD15. As stated previously, they were realised with only 500 g/t of Na_2SiO_3 as depressant since the collector concentration was the first operating parameter considered in the whole study. The results for the roughing stage are presented in a grade-recovery curve, see Figure 66. Consistently, a low collector concentration (100 g/t) provides a poor WO_3 recovery but a significant WO_3 grade (Figure 66). When the collector concentration is increased to 150 g/t and 200 g/t, the WO_3 recovery increases while the WO_3 grade decreases (Figure 66). At 200 g/t RBD15, the WO_3 recovery is 96.8%, which is a satisfactory value and motivated the choice to not further raise the collector concentration. Overall, these results demonstrate that 200 g/t of RBD15 are needed to collect most scheelite

particles. Also, this collector affords a poor selectivity since increasing the collector concentration induces a significant decrease in the WO_3 grade, indicating an increase of the gangue minerals recovery. Industrially, the WO_3 grade can be increased by other means and, most of the time, a WO_3 recovery as high as possible is required. Hence, the RBD15 concentration was set to 200 g/t for all the studies conducted hereafter.
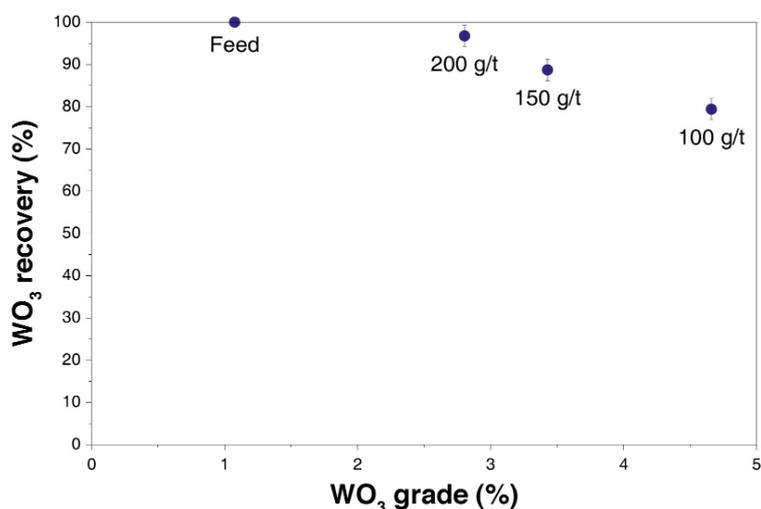
Figure 66. WO_3 recovery vs WO_3 grade for various concentration in RBD15 used alone on the Tabuaço Main Skarn ore, with 500 g/t of Na_2SiO_3 as depressant, at pH 9.5-10.

3.2 Rosin acids

TOFA are commonly used as industrial flotation collectors since they are by-products of the Kraft process and, therefore, very cheap and easy to provide. They usually contain rosin acids, which effect on minerals floatabilities has been investigated previously by microflotation tests. Hereafter, the impact of the rosin acids content on the scheelite flotation has been studied on the Tabuaço ore. For all the flotation tests, three different commercial TOFA, RBD2, RBD15, and RBD30, were used as collectors. The 2, 15, and 30 are the weight percentage of rosin acids contained in the mixture. Collector formulations were artificially created by mixing in various proportions the commercial formulations, in which oleic and linoleic acids predominated. The ratio between oleic and linoleic acids was maintained constant at 1.3-1.4, and the percentage of rosin acids in the mixture varied from 2 to 30% (Table 17).

Table 17. Composition of commercial and created collector formulations, with different contents in rosin acids.

Collector composition	BD2	2/3 BD2 + 1/3 BD30	RBD15	1/2 BD2 + 1/2 BD30	1/3 BD2 + 2/3 BD30	BD30
Oleic acid (%)	47.0	39.0	36.0	36.0	32.0	25.0
Linoleic acid (%)	34.0	28.0	25.0	26.0	23.0	18.0
Palmitic acid (%)	2.0	1.3	-	1.0	0.7	-

Linolenic acid (%)	-	0.7	2.0	1.0	1.3	2.0
Rosin acids (%)	2.0	11.3	15.0	16.0	20.7	30.0
Oleic acid/Linoleic acid	1.4	1.4	1.4	1.4	1.4	1.4
Oleic acid + Linoleic acid (%)	81.0	68.0	61.0	62.0	55.0	43.0

Since these tests were performed before the depressants optimisation, 1050 g/t of sole sodium silicate was used to depress the gangue minerals. The total collector dosage was set to 200 g/t, according to the previous optimisation tests (see section 3.1). The results of the roughing flotation tests are presented in Figure 67. Since the cleaning stage displayed the same trends, the results are not presented. The increase of the rosin acids content leads to a significant rise of all the recoveries, including the WO_3 recovery (Figure 67). This induces a decrease of the selectivity and, therefore, of the WO_3 grade, which is in good agreement with the microflotation tests performed in section 2.4. The WO_3 and F recoveries increase slightly while the P_2O_5 recovery increases significantly with the rosin acids content. Due to the action of Na_2SiO_3, the SiO_2 recovery is poorly affected by the rosin acids content. As mentioned previously (see section 2.4), rosin acids are large molecules containing several rings and, therefore, may play a role in the stabilisation of the oleate/linoleate adsorption layer on minerals surfaces. Their high steric hindrance, due to their aliphatic rings, probably reduces electrostatic repulsion between the carboxyl groups and induces high packing areas, which can explain the increase in the overall recoveries. In addition, the high packing areas of rosin acids could be responsible for calcium sites to stay unoccupied on the surface, which could result in higher availability for linear-chain carboxylates to adsorb on other minerals, leading to the loss of selectivity. Hence, a compromising is mandatory, between an acceptable WO_3 recovery, provided by a significant rosin acids content, and a good flotation selectivity, afforded by a low rosin acids content. Besides, the selectivity between scheelite and fluorite cannot be enhanced without impacting significantly the WO_3 recovery. Hence, rosin acids are not the key to float selectively the scheelite from a fluorite-rich gangue and other more selective reagents formulations must be developed. The optimal ratio between fatty acids and rosin acids is around six for one. A flotation test with this ratio, which roughly corresponds to the ratio of RBD15, produces a rougher concentrate assaying 7.2% WO_3 grade for 91.7% WO_3 recovery, from a feed assaying 0.9% WO_3. The P_2O_5 and SiO_2 recoveries are quite low, at 29.7% and 7.3%, respectively, while the F recovery is still as high as 55.2%.
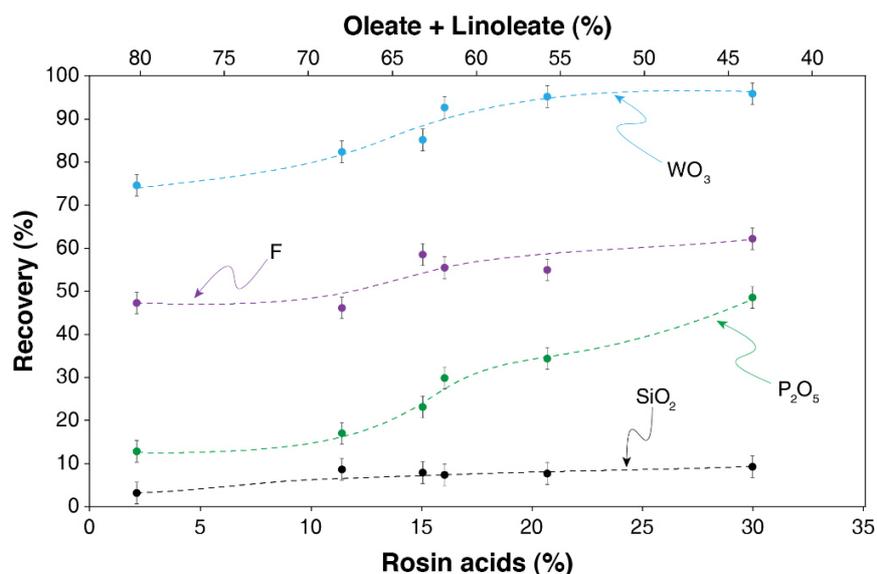
Figure 67. F, P_2O_5, SiO_2, and WO_3 recoveries versus the rosin acids content in the collector mixture.

3.3 Fatty acids

In microflotation tests, mixing fatty acids exhibited satisfactory results in terms of selectivity in favour of scheelite. This trend had to be validated by batch scale flotation tests performed on the Tabuaço ore. RBD15, the TOFA used for all the previous batch scale flotation tests was a mixture mainly comprising oleic and linoleic acids, *i.e.* unsaturated fatty acids. Hence, another TOFA, called LD, in which the palmitic acid content was significantly higher than in RBD15, was tested. As in the previous formulations, oleic and linoleic acids were the main constituting fatty acids, with a ratio oleate:linoleate of around 1.4, similar to that of RBD15. However, it was impossible to obtain more information, in particular about the ester/alcohols/rosin acids content, which can be considerable in TOFA. Under the best optimised depressing conditions determined in Chapter 4, LD induces very good results in terms of selectivity between scheelite and fluorite though it exhibits low WO_3 recoveries. Consequently, a study was carried out on this collector in order to define the best dosage required to maximise the WO_3 recovery (Figure 68).
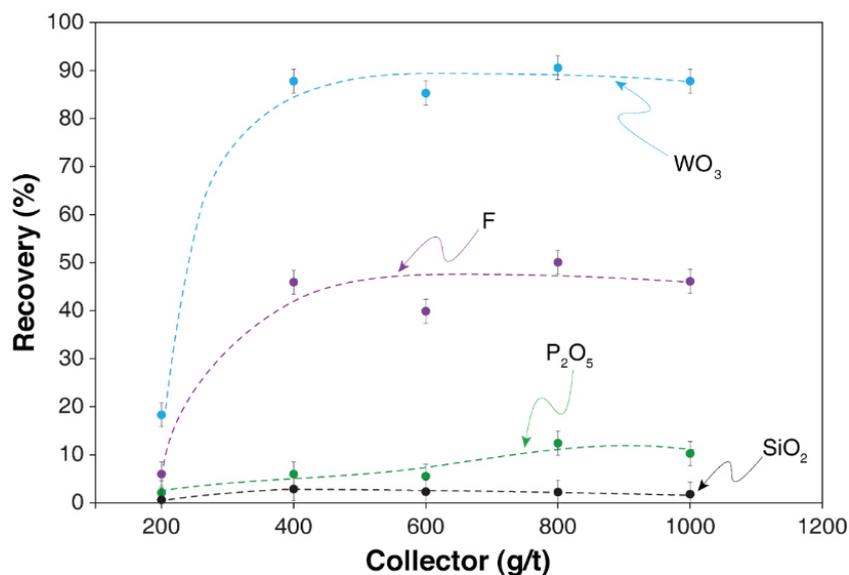
Figure 68. F, P_2O_5, SiO_2, and WO_3 recoveries versus LD dosage.

At 800 g/t, which seems to be the optimal dosage, still under the optimised depressing conditions, the rougher concentrate assays 14.2% WO_3 with 90.6% WO_3 recovery. The recoveries of silicates and apatite are low, which is promising (respectively 2.4% and 13.8%). Compared to test with RBD15, under the same depressing conditions, the fluorite recovery is decreased from 64.1% to 50.1% in the rougher stage. A cleaning stage allows to obtain a concentrate that assays 22.5% WO_3 with 84.7% WO_3 recovery, 30.9% F recovery, and 8.3% P_2O_5 recovery. A diminution of the WO_3 recovery of 6% between the rougher and the cleaner stage is acceptable, since it is associated with a satisfactory decrease of the F and P_2O_5 recoveries. The enhanced separation contrast could be explained by a better organisation of the adsorption layer when saturated fatty acids are introduced in the formulation. Nevertheless, since the ester/alcohols/rosin acids contents were not given by the producer, all the interpretations have to be taken carefully and no further explanation can be provided in terms of molecular mechanisms. The performances attained with the commercial mixture, LD, could not be matched by creating fatty acids mixtures in laboratory. This might be related to a pre-established organisation of the fatty acids in solution allowed for the commercial mixture since they are in contact during long times before being used in solution. For the mixtures prepared in this work, the fatty acids were pre-mixed during few minutes before their addition in the conditioning pulp. Besides, decreasing the collector dosage from 800 g/t to 600 g/t induces a preferred adsorption onto scheelite. Also, it would reduce the operating costs for industrial applications. With 600 g/t of LD, the flotation cleaner concentrate assays 25.2% WO_3 with a 73.7% WO_3 overall recovery.

3.4 Co-collectors

The synergistic effects between fatty acids with different structures (unsaturation degree, mostly), observed previously, is probably due to a better organisation of the adsorption layer when saturated fatty acids are introduced in the formulations. These observations were related to the theory on which the introduction of non-ionic reagents is based. Indeed, over the past

decades, several authors have demonstrated that the flotation selectivity between the calcium salts can be modulated by the use of non-ionic reagents (see Chapter 1). In particular, fatty alcohols afforded a good selectivity for scheelite flotation from calcite (Filippov et al., 1993; Filippov and Filippova, 2006) but no research was conducted on scheelite-fluorite systems. Hence, batch scale flotation tests were performed using the two main TOFA studied in this work, RBD15 and LD, combined with isotridecanol in various ratios. The choice was made to systematically keep the main collector (RBD15 or LD) concentration constant and, therefore, when the ratio between the main collector and the co-collector was changed, the total collector + co-collector concentration varied. Notably, within the framework of this theory, it is assumed that the co-collector does not provide a significant flotation recovery when it is used alone.

The tests were first performed with RBD15, the classical TOFA, which exhibited acceptable scheelite recovery at 200 g/t. Under the best depressing conditions defined in Chapter 4 (1,150 g/t Na_2CO_3 and 1,225 g/t Na_2SiO_3) and with the amount of RBD15 set to 200 g/t, various RBD15:isotridecanol ratios were tested. The results are presented in Figure 69a for the roughing stage and in Figure 69b for the cleaning stage. Surprisingly, in the roughing stage (Figure 69a), the WO_3 and P_2O_5 recoveries are constant at 100% regardless the RBD15:isotridecanol ratio. This can be related to a considerable increase of the flotation selectivity in favour of apatite, which is a well-known consequence of the use of non-ionic reagents (Filippov et al., 2019). Besides, when the isotridecanol amount is increased, the F recovery is significantly enhanced and stays quite high (>60%) until it decreases for higher isotridecanol amounts introduced. Finally, the SiO_2 recovery increases slightly when low amount of isotridecanol are added to the formulations but decreases significantly when this amount is increased. In the cleaning stage (Figure 69b), the magnitude of the responses are higher and allows to discuss more thoroughly the results. First, low amounts of isotridecanol introduced in the collector formulation induces a significant increase in the WO_3, P_2O_5, and F recoveries. This can be related to a non-selective stabilisation of the adsorption layer due to the introduction of the isotridecanol in the adsorption layer, which probably reduces the polar repulsion between the carboxylate groups. When the isotridecanol amounts are increased above 200 g/t, *i.e.* a 1:1 ratio with RBD15, all the recoveries decrease significantly with however a lower diminution for scheelite compared to apatite and fluorite. This can be attributed to the reduction of the collecting ability of the fatty acids due to a competitive adsorption between them and the isotridecanol, since this latter is assumed to adsorb onto Ca^{2+} sites but to have a lower hydrophobising effect.
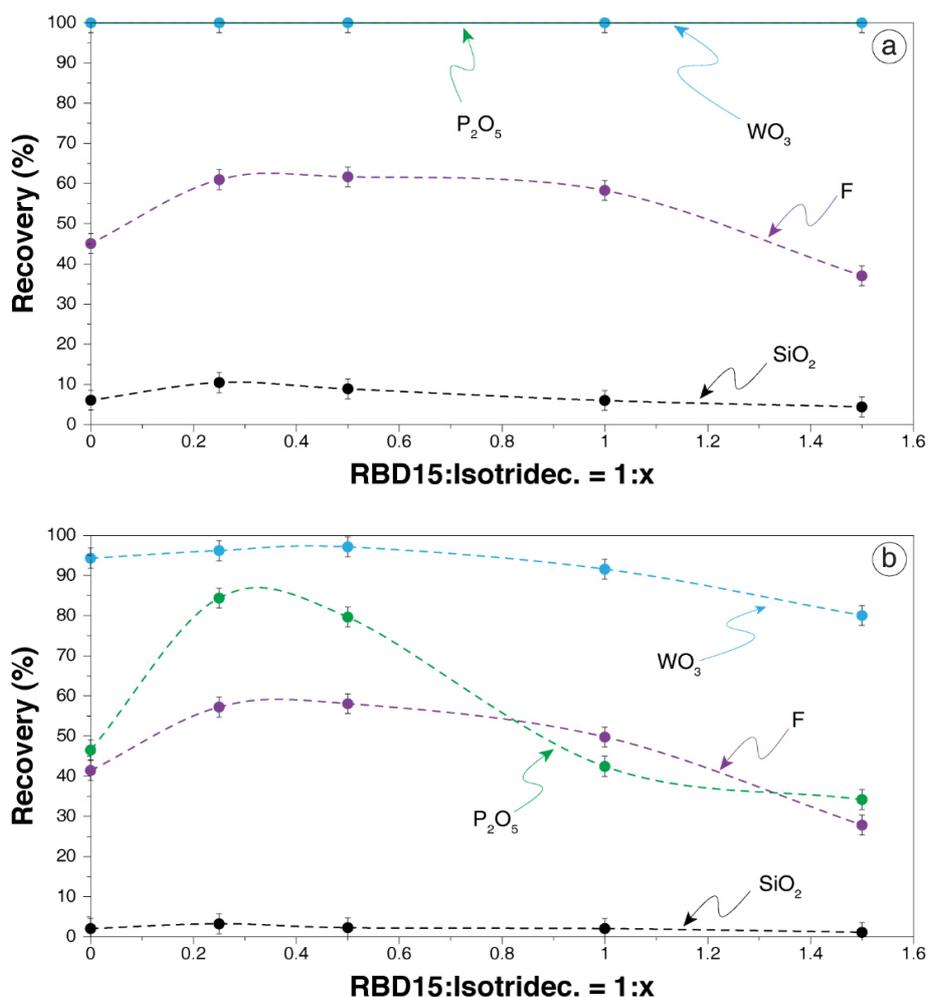
Figure 69. WO$_3$, P$_2$O$_5$, SiO$_2$, and F recoveries as a function of the RBD15:Isotridecanol ratio for a constant RBD15 amount set to 200 g/t, for the rougher (a) and the cleaning (b) stages. The point at 0 represents the reference test, *i.e.* without using isotridecanol.

The results are also presented in a grade-recovery curve for the roughing and cleaning stages together, see Figure 70. Consistently, the 1:1 ratio presents the best results in terms of WO$_3$ recovery and grade. The flotation roughing concentrate assays 13.0% WO$_3$ with 100% WO$_3$ recovery, which is significantly better than the test with sole RBD15 that produces a rougher concentrate assaying 8.8% WO$_3$ with 100% WO$_3$ recovery. These observations can also be made for the cleaning stage, which allows to reach 19.3% WO$_3$ in the concentrate for 91.6% WO$_3$ recovery. Although this WO$_3$ grade is still far from the required WO$_3$ grades for a typical scheelite concentrate (>60% WO$_3$), it is significantly higher than the grade obtained with sole RBD15 (13.2% WO$_3$). This demonstrates that the addition of isotridecanol modulates the flotation selectivity in favour of scheelite and allows to increase the WO$_3$ grade with a negligible impact on the WO$_3$ recovery (91.6% instead of 94.3%).
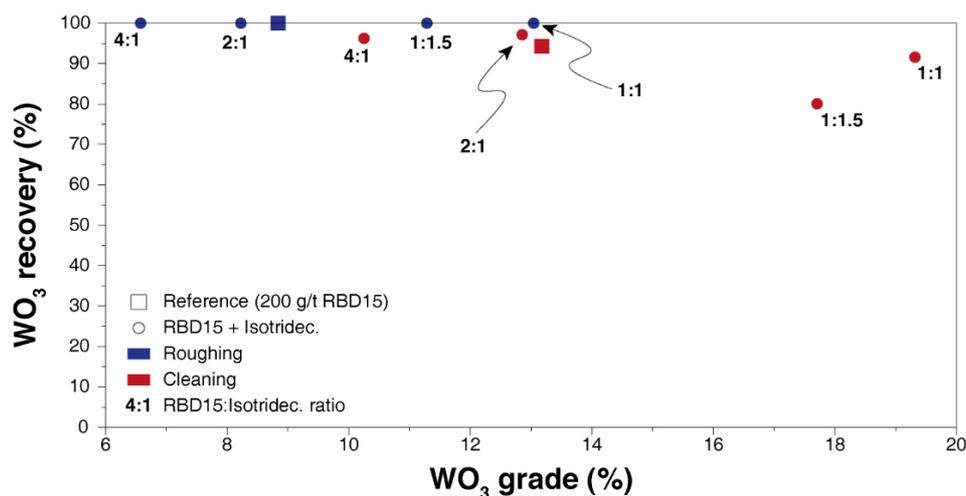
Figure 70. WO$_3$ recovery vs WO$_3$ grade for the tests performed with different RBD15:Isotridecanol ratios, showing together the roughing and the cleaning stages.

Besides, still under the best depressing conditions defined in Chapter 4, the RBD15 was replaced with LD and various LD:isotridecanol ratios were tested with the amount of LD set to 600 g/t. During the previous tests, conducted with RBD15, the 2:1 and 1:1 ratios exhibited the best performances. Hence, the tests performed with LD focussed on those two ratios. The results of both roughing and cleaning stages are presented in a grade-recovery curve, see Figure 71. First, the reference test, *i.e.* carried out without the addition of isotridecanol, exhibited lower performances than that obtained previously. This could be attributed to a higher temperature since this latter is known to influence considerably the adsorption process. When isotridecanol is introduced in the formulations at a 1:1 ratio, it induces a significant decrease of the recoveries, including the WO$_3$ recovery (Figure 71). Moreover, the WO$_3$ grade is strongly affected, which can be attributed to a lack of the main collector, *i.e.* fatty acids, compared to the low-hydrophobising fatty alcohol. Hence, a 2:1 ratio has been tested and, consistently, conducts to an increase of both WO$_3$ grade and recovery (Figure 71): the rougher concentrate assays 11.9% WO$_3$ with 53.5% WO$_3$ recovery. Interestingly, the F recovery in the concentrate is only 5.9%, which indicates a very satisfying selectivity between scheelite and fluorite. However, the WO$_3$ recovery is still low although the WO$_3$ grade is significantly increased compared to the 1:1 ratio; with the same LD:isotridecanol ratio, *i.e.* 2:1, the total collector concentration has been raised to attain 800 g/t of LD, therefore mixed with 400 g/t of isotridecanol. This test produces a flotation roughing concentrate that assays 14.8% WO$_3$ with 100.0% WO$_3$ recovery and 16.8% F recovery, which again constitutes an unprecedented selectivity between scheelite and fluorite. A cleaning stage performed on this rougher concentrate, without adding any reagent, produces a flotation cleaning concentrate assaying 45.2% WO$_3$ with 56.5% WO$_3$ recovery and 3.2% F recovery. This WO$_3$ grade, attained in only two flotation stages, is a very satisfactory value albeit the WO$_3$ recovery is still low. Hence, the use of fatty alcohols introduced in the formulations conducts to a considerable increase in the selectivity between scheelite and fluorite. This increase is however more pronounced with LD than with RBD15, which could highlight the existence of synergistic effects between unsaturated fatty acids, saturated fatty acids, and fatty alcohol in the

collector formulations. The selectivity increase could be related to a most favoured adsorption of the fatty alcohol on scheelite compared to fluorite along with a more efficient stabilisation of the adsorption layer on scheelite rather than on fluorite. Nonetheless, more fundamentals studies are required to unravel the mechanisms responsible for that synergistic effects.
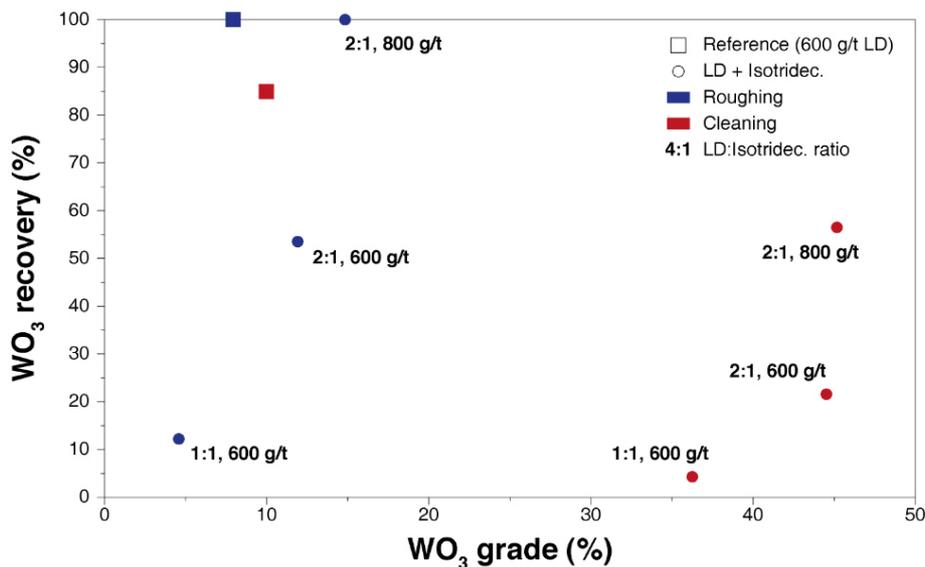
Figure 71. WO_3 recovery vs WO_3 grade for the tests performed with different LD:Isotridecanol ratios and total collector concentrations, showing together the roughing and the cleaning stages.

4. Spectroscopic analyses and DFT calculations

    4.1 Fatty acids mixtures

The spectra of oleate, linoleate, stearate and their mixture at 5×10^{-5} mol.L^{-1} adsorbed on fluorite and scheelite at pH 9 were acquired by DRIFTS. This aimed at discussing the nature and configuration of the species adsorbed on the two minerals to gain understanding in the mechanisms leading to the selectivity modulation observed in microflotation and flotation tests. The spectrum of the pure mineral conditioned in deionised water only has been systematically subtracted from the spectra presented in Figure 72. On FTIR spectra, fatty acids traditionally exhibit two regions of interest: the first domain, located between 3020 and 2800 cm^{-1}, is characteristic of the C-H bonds vibrations. Depending on the species, three or four peaks are present in this region, at 2855-2848 cm^{-1}, 2928-2915 cm^{-1}, 2957- 2955 cm^{-1}, and, in some instances, 3007-3005 cm^{-1}. The two first peaks are ascribed to the symmetric and asymmetric elongation vibrations (ν_s and ν_{as}) of the (-CH$_2$) group, respectively, while the two last bands are attributed to the asymmetric elongation vibration of the (-CH$_3$) and the (=C-H) groups, respectively. The peaks at 2928-2915 cm^{-1} and 2855-2848 cm^{-1} display a significant shift in wavenumbers between the three different fatty acids adsorbed (Figure 72). Notably, the peak ascribed to ν_{as}(-CH$_2$) is located at 2915 cm^{-1} for stearate, at 2922 cm^{-1} for oleate, and at 2928 cm^{-1} for linoleate. Lower wavenumbers for this peak are interpreted in the literature as the existence of stronger lateral interactions between aliphatic chains (Free and Miller, 1996; Kellar et al., 1991; Mielczarski et

171

al., 1998). The degree of unsaturation is therefore negatively correlated with the chain-chain interactions. This is attributed to a larger packing area and, therefore, a larger distance between the molecules within the adsorption layer for the unsaturated fatty acids, due to their double-bond-related bendings in their chains. When the three fatty acids are used in mixture, the v_{as}(-CH$_2$) peak is located at 2919 cm^{-1}, which demonstrates a tighter organisation of the adsorption layer when stearate is introduced into the unsaturated-fatty-acid-based formulations. The same phenomena can be observed for the peak attributed to v_s(-CH$_2$), within however a lower range of wavenumbers. Besides, this domain exhibits no significant difference between scheelite and fluorite and, overall, the same conclusions can be drawn for the two minerals.
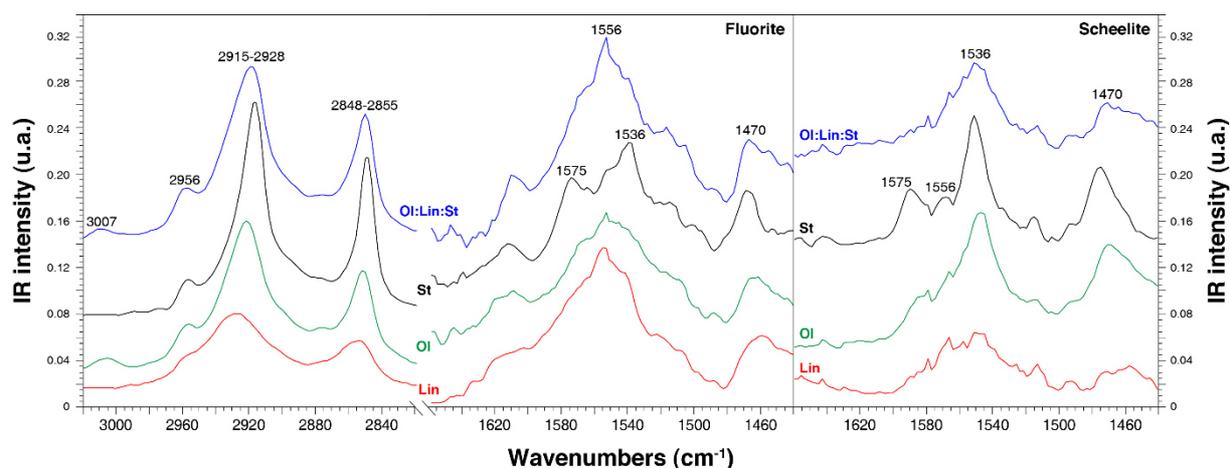
Figure 72. DRIFT spectra measured with linoleate (red), oleate (green), stearate (black), and a mixture of the three (blue) adsorbed on fluorite (left) and scheelite (right) surfaces. The total fatty acids concentration was maintained constant at 5 x 10^{-5} mol.L^{-1} and the pH was set to 9. The IR spectra of the pure minerals have been subtracted from the spectra presented here.

The second region of interest of the IR spectra is located between 1700 and 1400 cm^{-1}. The peak at around 1470 cm^{-1} is attributed to the bending vibration of the (-CH$_2$) group. As with the stretching vibrations, this peak shifts to higher wavenumbers in the case of stearate, indicating a smaller distance between the chains than in the case of oleate and linoleate. In the case of fluorite, the peak at 1556 cm^{-1} is significantly present for the sole oleate and linoleate but barely observed for the sole stearate (Figure 72). This peak is generally attributed to the chemical adsorption of carboxyl groups on the surface (Free and Miller, 1996; Hu et al., 1986a, 1986b; Lu and Miller, 2002; Rao et al., 1991b). Besides, a doublet at 1536 and 1575 cm^{-1} is clearly observed for stearate used alone on fluorite and under the forms of shoulders of the peak at 1556 cm^{-1} for sole oleate and linoleate. This doublet is traditionally ascribed to the adsorption of a calcium dicarboxylate precipitate (Free and Miller, 1996; Hu et al., 1986a, 1986b; Lu and Miller, 2002; Rao et al., 1991b) or to two different geometrical configurations possible during the surface chemisorption of fatty acids (Mielczarski et al., 1998). For further discussions, please report to Chapter 8. When the three fatty acids are mixed, the peak at 1556 cm^{-1} is present with shoulders at 1536 and 1575 cm^{-1}. Interestingly, the peak area is significantly increased compared to when the two unsaturated fatty acids are solely used. This observation demonstrates an increase in the

total amount of fatty acids adsorbed when the three fatty acids are used in mixture. This can be explained by a better stability of the adsorption layer when the saturated fatty acids are introduced. There is most probably a spontaneous organisation of the molecules in favour of lateral interactions between the chains.

For scheelite, the peak at 1556 cm^{-1} is present for the three fatty acids used alone, including stearate. Assessing that this peak is related to the fatty acids surface chemisorption, this indicates that stearate chemisorbs on scheelite and not on fluorite since this peak is not observed for fluorite. However, the intensity of this peak for oleate and linoleate is significantly lower for scheelite than for fluorite. In addition, the peak at 1536 cm^{-1} displays a higher intensity than the singlet at 1556 cm^{-1} (which is not very visible) in the case of scheelite. It could suggest different fatty acids adsorption modes between the two minerals, related to the different coordination of the surface calcium atoms or the different Ca-Ca distance on the surface. Nonetheless, for oleate, linoleate, and the mixture, the peak at 1536 cm^{-1} exhibits a significantly higher intensity than the peak at 1575 cm^{-1} while authors systematically described a doublet involving these two peaks. Finally, while the peak intensity increases when the fatty acids are used in mixture with fluorite, it is not significant with scheelite. Overall, the FTIR results could explain the increase of the selectivity by a better organisation of the adsorption layer but do not provide any response concerning the selectivity of this better organisation between scheelite and fluorite. Deeper investigations should, therefore, be undergone to gaining understanding in the synergistic effects observed during microflotation/flotation tests.

4.2 Co-collectors

Considering the above-described flotation tests, it was suggested that fatty alcohols such as isotridecanol adsorb onto cationic sites and reduce the polar repulsion between the carboxylate groups. It would allow a better organisation of the adsorption layer and, hence, a higher hydrophobation of the mineral surfaces. However, the fine mechanisms are poorly described. In particular, the selectivity of the stabilisation of the adsorption layer is not well understood. Hence, to gain understanding in the synergistic effects between fatty acids and fatty alcohols, FTIR experiments and DFT calculations were conducted. The DRIFT spectra of scheelite and fluorite conditioned during 15 min with sole sodium oleate and a mixture of sodium oleate and isotridecanol (premixed before adding it in the conditioning solution) at pH 9 are presented in Figure 73. Oleate species are adsorbed for both cases and both minerals, without any significant difference. Interestingly, only one singlet is exhibited for the carboxyl group asymmetric stretching vibration (for further discussions, see Chapter 8), at 1550-1560 cm^{-1} for fluorite and 1538 cm^{-1} for scheelite. This peak is located at 1551 cm^{-1} for fluorite conditioned with sole sodium oleate and at 1558 cm^{-1} for fluorite conditioned with sodium oleate + isotridecanol. Though little significance, this could indicate a variation in the adsorption mechanisms regarding the carboxylate group, due to the isotridecanol. Besides, no shift is observed in the –CH$_2$ stretching vibrations wavenumbers, indicating that the use of isotridecanol in combination with sodium oleate did not change the tightness of the adsorption layer.
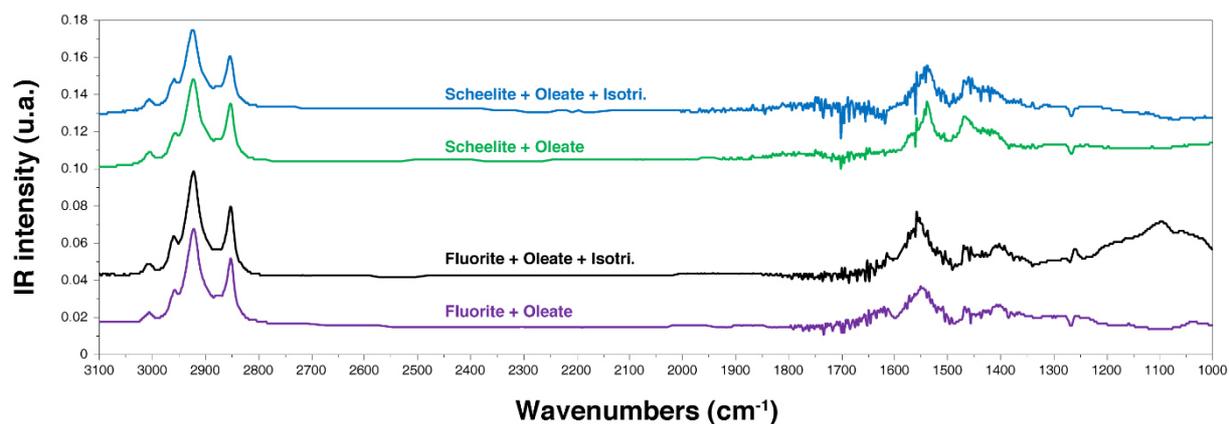
Figure 73. DRIFT spectra of fluorite (bottom) and scheelite (top) conditioned in a solution of sodium oleate at 5 x 10^{-5} mol.L^{-1} (purple for fluorite, green for scheelite) or in a solution of sodium oleate at 5 x 10^{-5} mol.L^{-1} and of isotridecanol at 2.5 x 10^{-5} mol.L^{-1} (black for fluorite, blue for scheelite). The IR spectra of the pure minerals have been subtracted from the spectra presented here.

DFT calculations were performed to gain understanding in the molecular mechanisms that are responsible for the synergistic effects observed in flotation between fatty acids and the fatty alcohol. First, the adsorption energies of isotridecanol onto fluorite and scheelite were calculated. The adsorption of isotridecanol is significantly favoured on scheelite compared to fluorite: it adsorbs with ΔE_{ads} = -120.7 kJ.mol^{-1} including ΔE_{disp} = -44.6 kJ.mol^{-1} on the (001) scheelite surface, with ΔE_{ads} = -149.8 kJ.mol^{-1} including ΔE_{disp} = -56.3 kJ.mol^{-1} on the (112) scheelite surface, and with only ΔE_{ads} = -79.5 kJ.mol^{-1} including ΔE_{disp} = -25.9 kJ.mol^{-1} on the (111) fluorite surface. Hence, the isotridecanol is more likely to adsorb on scheelite than on fluorite. Nonetheless, the adsorption energies of isotridecanol should be compared with adsorption energies of water molecules on the surfaces, since the adsorption of water is significantly more favoured on scheelite than on fluorite (see Chapter 7). Besides, to investigate the synergistic adsorptions between sodium oleate and isotridecanol, one, two, and three sodium oleate molecules were adsorbed sequentially on scheelite (001) and fluorite (111) surfaces, close to each other. The choice was made to model the adsorption of sodium oleate species rather than free oleate anion based on the previous FTIR results. Considering the high computational costs induced by the modelling of oleate species, the cells could not be filled with water molecules. The adsorption energies were systematically calculated by DFT at 0 K. Then, the sodium oleate molecule located between the two others was substituted with an isotridecanol molecule and the total energy of the system was calculated, for scheelite and fluorite. The energy difference between "Fluorite + 3 Na-Oleate" and "Fluorite + 2 Na-Oleate + 1 Isotridecanol" was roughly the same than for scheelite. Hence, energetic considerations cannot unravel the synergistic effects between fatty acids and fatty alcohols and further calculations should be performed.

5. Conclusion

In the present chapter, the fatty-acid-based formulations were investigated with the global aim to increase the selectivity between scheelite and gangue minerals, mostly fluorite. First, the

optimal pH for scheelite flotation was found to be 9-10, although it also corresponded to the optimal floatability of fluorite. Then, three main options were studied to improve the selectivity between scheelite and fluorite:

- The rosin acids content in fatty-acid-based formulations;
- The ratios between different fatty acids (saturated/unsaturated, short chain/long chain) in the formulations;
- The introduction of a fatty alcohol as a co-collector.

Microflotation and batch scale flotation tests demonstrated that the rosin acids are responsible for a decrease of the flotation selectivity along with an increase of the flotation recoveries. Hence, their content in the formulation should be thoroughly controlled and moderate contents are required (around 15% in the present study) to make a compromise between flotation selectivity and recovery. This optimal ratio corresponded to the main TOFA used in this work, RBD15, which was mainly composed of unsaturated fatty acids (oleic and linoleic) along with 15% rosin acids. Besides, fatty acids mixtures exhibited satisfactory results in terms of flotation selectivity in microflotation tests. Otherwise, in batch scale flotation tests, another TOFA, LD, which comprised higher amounts of saturated fatty acids exhibited a better selectivity between scheelite and fluorite than RBD15. Finally, the introduction of isotridecanol, a fatty alcohol, in RBD15 and LD commercial formulations displayed a significant increase in the flotation selectivity in favour of scheelite. Overall, under the best depressing conditions determined in Chapter 4 (1,150 g/t Na_2CO_3, 1,225 g/t Na_2SiO_3) and at pH 10, the attained achievements are presented in Table 18. For further experiments, according to Table 18, two choices are then suitable, namely with the co-collector, which provided high WO_3 grade with low WO_3 recovery, or without the co-collector, *i.e.* with sole LD, which afforded moderate WO_3 grade and recovery.

Table 18. WO_3 grade and recovery of the flotation roughing and cleaning stages for various steps of optimisation in terms of collector formulations.

	Roughing		Cleaning	
	WO_3 grade	WO_3 recovery	WO_3 grade	WO_3 recovery
Optimised rosin acids content	9.4%	93.8%	14.9%	85.4%
Optimised rosin acids content Optimised fatty-acids ratios	14.5%	85.4%	25.2%	73.7%
Optimised rosin acids content Optimised fatty-acids ratios Optimised co-collector	14.8%	100.0%	45.2%	56.5%

Development of a mobile, adaptable, efficient, and environment-friendly process for the beneficiation of complex tungsten skarns

1. Introduction

In the previous chapters, different processing operations were thoroughly investigated and optimised. Indeed, based on the mineralogical composition of the Tabuaço Main Skarn ore, described in Chapter 2, different processing options were suggested for the scheelite beneficiation from complex tungsten skarns such as Tabuaço skarn. In particular, enhanced gravity separation (Falcon), froth flotation, and high intensity magnetic separation were proposed in first approximation for tungsten skarns, see Chapter 1. The Falcon gravity separation was studied in Chapter 3, which aimed at rejecting as much gangue minerals and slimes as possible by a Falcon concentration. The two bowls, UF and SB, were tested through the DOE methodology to model the effect of the operating parameters on the studied responses. Based on these models, the operating parameters were optimised to maximise the gangue minerals rejection. Besides, in Chapter 4, a wide investigation was conducted to find the most suitable depressants for the selective scheelite flotation from Tabuaço tungsten skarn. The Na_2CO_3/Na_2SiO_3 system exhibited the best performances and their respective amounts were optimised following the DOE methodology. This allowed to define optimised depressing conditions for the scheelite flotation for the Tabuaço tungsten skarn. Finally, in Chapter 5, the collecting conditions were thoroughly investigated to increase the separation differential between scheelite and fluorite. Notably, the use of a new TOFA allowed to reach satisfactory WO_3 grades in the flotation concentrate with acceptable WO_3 recoveries.

This chapter presents the flowsheet development performed on the Tabuaço Main Skarn ore and has conducted to a publication in Minerals Engineering, entitled "Integrated Approach for the Processing of a Complex Tungsten Skarn Ore (Tabuaço, Portugal)". The three previous chapters allowed to define optimised parameters for the gravity concentration, the depressing conditions and the collector formulation, respectively. All these optimisations are combined and discussed hereafter with the global objective to develop an adaptable, mobile, efficient, and environment-friendly process for the production of a marketable scheelite concentrate. As previously, this work is still based on the mineralogical composition of the Tabuaço Main Skarn ore, presented in Chapter 2 and in Table 19. This latter summarises the Main Skarn's mineralogical association, sorting the identified minerals in 4 different classes and displaying their respective properties (magnetic susceptibility, specific gravity, and floatability with fatty acids). This serves as a basis for the process development presented hereafter. Considering its mineralogical properties (Table 19), several beneficiation routes were investigated to produce a scheelite concentrate from the Main Skarn:

- Gravity separation, which, based on the range of densities displayed by the various minerals, could provide efficient elimination of the light silicates (feldspars, quartz), reasonable rejection of calcium salts (fluorite, apatite), but poor rejection of the dense silicates (vesuvianite, zoisite, and grossular);
- Magnetic separation that would lead to an efficient rejection of the paramagnetic minerals, namely, the dense silicates (vesuvianite, zoisite, and grossular);

- Froth flotation with fatty acids, which would collect all the calcium minerals, namely, the calcium salts (scheelite, fluorite, and apatite) and the dense silicates (vesuvianite, zoisite, and grossular). However, the collection of the dense silicates and, to a lesser extent, of the unwanted calcium salts, can be addressed using specific depressants and new collector formulations.

Table 19. Comparison of the key mineralogical properties of the main minerals in the Main Skarn (magnetic susceptibility, specific gravity, and floatability with fatty acids) for the possible processing options for scheelite concentration. For each mineralogical property, the first sub-column gives the property value or class, while the second sub-column indicates the flow in which the mineral would be recovered. Dia.: diamagnetic, Conc.: concentrate, Para.: Paramagnetic, Tail.: Tailings, Mid.: Middlings.

Mineral	Class	Magnetic susceptibility		Specific gravity		Fatty-acids floatability	
		Class	Flow	Value	Flow	Value	Flow
Scheelite	Mineral of interest	Dia.	Conc.	6.1	Conc.	High	Conc.
Fluorite	Calcium salts	Dia.	Conc.	3.2	Mid.	High	Conc.
Apatite	Calcium salts	Dia.	Conc.	3.2	Mid.	High	Conc.
Vesuvianite	Dense silicates	Para.	Tail.	3.4	Mid.	Moderate	Mid.
Zoisite	Dense silicates	Para.	Tail.	3.4	Mid.	Moderate	Mid.
Grossular	Dense silicates	Para.	Tail.	3.7	Mid.	Moderate	Mid.
Quartz	Light silicates	Dia.	Conc.	2.7	Tail.	Low	Tail.
Feldspars	Light silicates	Dia.	Conc.	2.7	Tail.	Low	Tail.
Clay minerals	Light silicates	Para.	Tail.	2.6-3	Tail	Low	Tail.

The liberation size makes classical physical methods inefficient for scheelite beneficiation, so the use of a Falcon centrifugal concentrator was suggested for the Tabuaço skarn (see Chapter 1). Although the magnetic separation was also suitable for the Tabuaço skarn beneficiation, fine particles (-150+7 µm) cannot be processed in dry conditions, which is however appropriate for coarse particles only (>150 µm) and were then processed in wet conditions. Hence, magnetic separation was investigated on two different size fractions. Froth flotation was also tested on the fine particles (-150+7 µm), considering the fine liberation size. Since silicates represent 85-95 wt.% of the Tabuaço ore, the use of amines seemed inappropriate to attain good selectivity and the choice was made to work with fatty acids under the form of TOFA. However, the two mineralised layers of Tabuaço deposit, particularly the Main Skarn, displayed high amounts of calcium-bearing minerals, either calcium silicates or calcium semi-soluble salts (fluorite, apatite, calcite, and scheelite) which suggested the need for depressant optimisation and their dosage as well as the collector formulation.

2. Process optimisation for the Tabuaço skarn ore

Prior to the process optimisation, the crushing and milling stages were adapted, see Chapter 2. Based on the mineralogical compositions (see Chapter 2 and Table 19), the mineral properties (Table 19), and the previous discussions, 5 distinct beneficiation routes can be suggested and investigated for the Main Skarn processing (Figure 74):

1. Direct flotation;
2. Falcon UF gravity separation;
3. Falcon SB gravity separation;
4. Wet high intensity magnetic separation;
5. Dry high intensity magnetic separation performed on the unground -500+150 µm fraction.

Each route illustrated in Figure 74 was optimised in the previous chapters (Chapters 3, 4, and 5) and all the processing options investigated are compared hereafter in terms of separation performances, with the global objective of combining the best routes to produce a marketable scheelite concentrate.
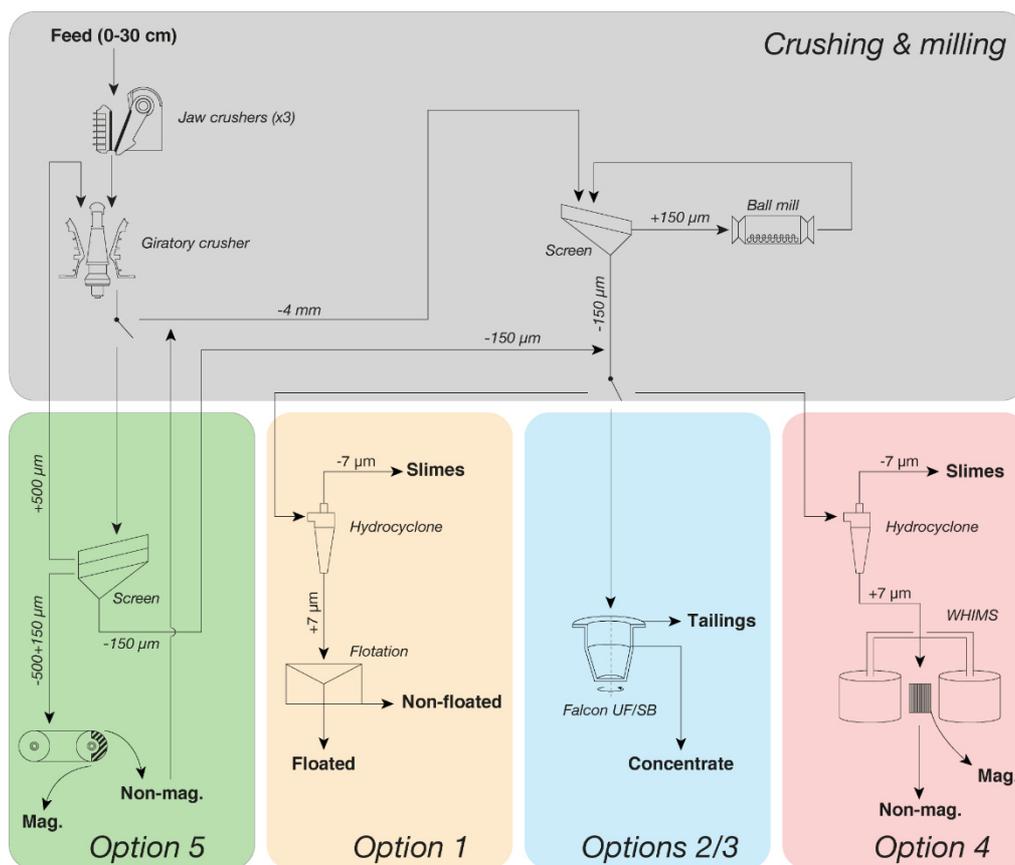
Figure 74. Global flowsheet displaying the optimised milling stage and the 5 different options investigated for processing the Main Skarn Tabuaço ore. Options 1 to 4 are performed on a milled ore (-150 µm) while option 5 is performed prior to the milling stage. Options numbers correspond to the numbers introduced in the text.

2.1 .Depressants in direct flotation

The flotation with fatty acids used without depressant led to flotation of all the minerals, including scheelite, fluorite, apatite, and silicates (see Chapter 4). Considering the very low separation efficiency between minerals, the use of depressants was mandatory in flotation. In Chapter 4, a wide study was conducted to find the best depressant(s) in terms of selectivity and WO_3 recovery. Among all the depressants investigated, the combination of Na_2CO_3 and Na_2SiO_3 exhibits the best efficiency, mainly attributed to strong positive synergistic effects existing between the two reagents. Both the WO_3 grade and recovery were optimised through a 4-level factorial DOE, commonly used for optimisation work. However, the approach using depressants is limited: fluorite and scheelite display very close distances between the surface calcium atoms inducing a very low selectivity of all the depressants, particularly when they occur in large molecules with high surface coverage. The optimised conditions for maximising both WO_3 grade and recovery were 1,150 g/t Na_2CO_3 and 1,225 g/t Na_2SiO_3 with 200 g/t of RBD15 as collector, according to Chapter 4. The whole flowsheet, including the test with optimised depressing conditions, has been performed again in the present chapter, see Table 20. First, slimes represent 6.3% WO_3 loss, which is an acceptable value indicating that no scheelite concentration occurs in the fine particles during grinding. The concentrate product of a one-stage flotation on this deslimed ore assays 9.2% WO_3 with 87.8% WO_3 recovery for a feed assaying 1.1% WO_3, which is in agreement with the validation test performed in the Chapter 4. Consistently, both dense and light silicates as well as apatite are efficiently depressed since the Fe_2O_3, K_2O, and P_2O_5 recoveries in the concentrate are 3.8%, 2.4%, and 26.9%, respectively (Table 20). Very few silicates and apatite particles can be observed in the flotation concentrate product (Figure 75). However, the fluorite recovery in the concentrate product remains unacceptably high at 55.1% (Table 20), illustrating that, even with high Na_2CO_3/Na_2SiO_3 concentrations, fluorite cannot be efficiently depressed and represents most of the concentrate product (Figure 75), diluting dramatically the WO_3 content. Particles are mostly free and no mineral association is observed between scheelite and fluorite: the flotation selectivity depends then only on the selectivity of the reagents. The following discussions will use the "optimised depressants" designation for the test performed with 1,150 g/t Na_2CO_3 and 1,225 g/t Na_2SiO_3.
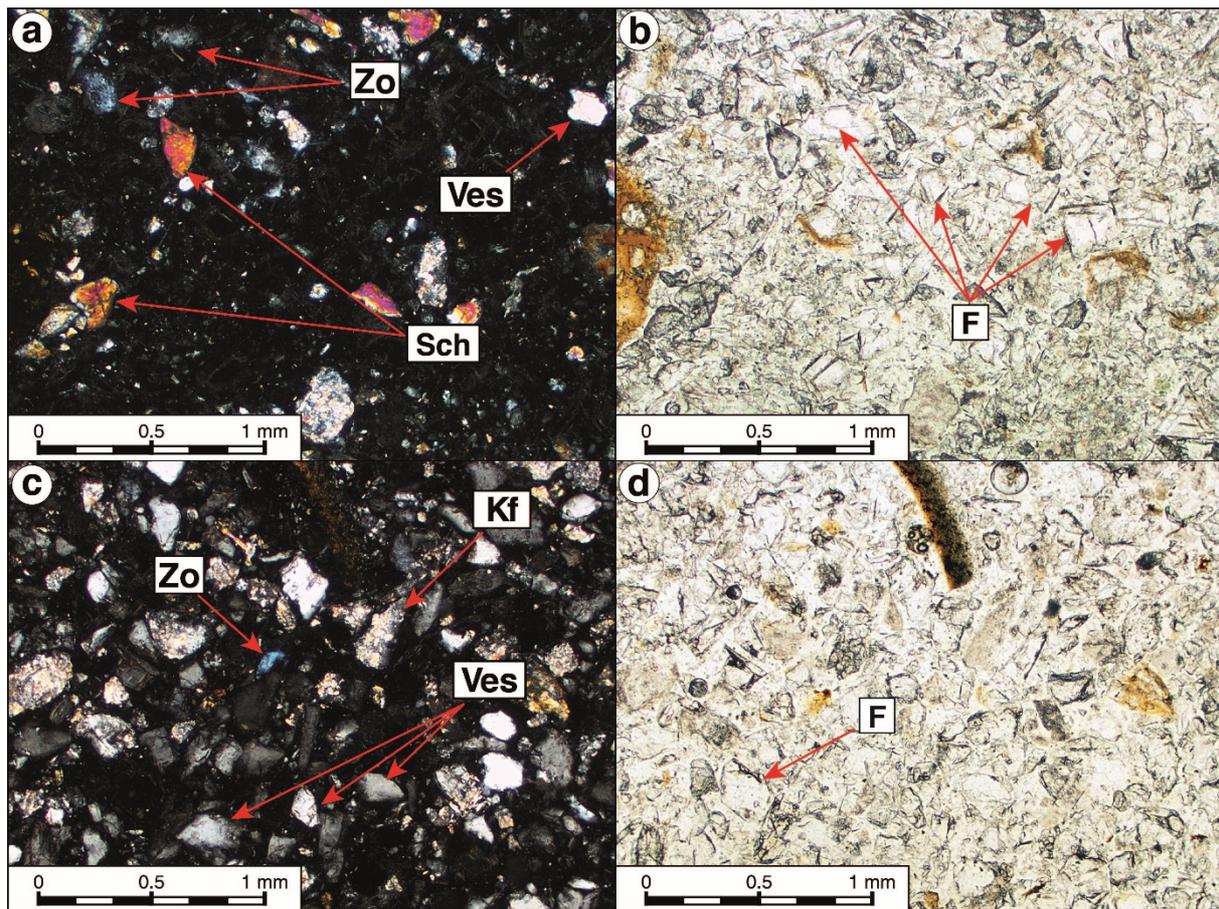
Figure 75. Micrographs of thin sections of the concentrate (a, b) and the tailings (c, d) of the flotation test with optimised depressants conditions observed with an optical microscope under cross-polarised light (a, c) and polarised light (b, d). F = Fluorite; Ves = Vesuvianite; Zo = Zoisite; Kf = K-feldspar; Sch = Scheelite.

2.2 Flotation collectors

Previous results suggest that the depressants currently available do not enhance significantly the selectivity between scheelite and fluorite. Hence, under the best depressing conditions, the main focus was put on the collectors in Chapter 5: a good separation contrast could not be attained with RBD15, mainly composed of oleic and linoleic acids. Consequently, LD, another TOFA containing a significant part of saturated fatty acids, has been tested. With the optimised depressants conditions, the collector quantity has been optimised in the Chapter 5, allowing optimal conditions at 600 g/t of LD. Besides, the addition of isotridecanol, a fatty alcohol, was investigated in Chapter 5. It resulted in a significant increase of the WO_3 grade, exclusively in the flotation cleaner stage, with a considerable decrease of the WO_3 recovery. However, the use of isotridecanol induces higher amounts of LD (800 g/t instead of 600 g/t), along with 400 g/t of isotridecanol, which would represent high operating costs for the flotation process. The choice was therefore made to not select this latter option and to use sole LD for flotation. Hence, the whole flowsheet, including the desliming stage and this optimised flotation test, has been performed again in the present chapter. It produces a flotation concentrate assaying 14.1% WO_3

with 77.1% WO₃ recovery for a feed assaying 1.1% WO₃ (Table 20). Compared to the test with RBD15, the WO₃ recovery in the concentrate is significantly reduced, from 87.9% to 77.1% while the F recovery is decreased from 55.1% to 32.9%, as well as the other gangue minerals recoveries, see Table 20. LD produces a WO₃ grade that is 1.5 times higher than when RBD15 is used (14.1% WO₃ instead of 9.2% WO₃). The following discussions will use the "fully-optimised flotation" or "optimised depressants and collectors" designations for the test performed with 1,150 g/t Na₂CO₃, 1,225 g/t Na₂SiO₃, and 600 g/t LD.

Table 20. Material balances of the two flotation schemes, using either RBD15 or LD as collectors with optimised depressants. Product names correspond to those defined in Figure 74. *Feed is back-calculated.

Product	wt.%	WO₃ grade (%)	WO₃ recovery (%)	P₂O₅ recovery (%)	K₂O recovery (%)	Fe₂O₃ recovery (%)	F recovery (%)
RBD15							
Slimes	7.5	0.9	6.3	5.0	14.9	11.3	7.3
Non-floated	82.5	0.1	5.8	68.1	82.7	84.9	37.6
Floated	10.0	9.2	87.9	26.9	2.4	3.8	55.1
Feed*	100.0	1.1	100.0	100.0	100.0	100.0	100.0
LD							
Slimes	7.5	0.9	6.9	5.3	13.4	12.0	7.7
Non-floated	87.3	0.2	16.0	89.1	85.8	85.5	59.4
Floated	5.2	14.1	77.1	5.6	0.8	2.4	32.9
Feed*	100.0	1.1	100.0	100.0	100.0	100.0	100.0

2.3 Falcon gravity separation

Another beneficiation route investigated for the Tabuaço ore was to take advantage of the significant specific gravity contrast existing between scheelite (6.1) and fluorite (3.2), the latter being the most problematic mineral in flotation with a recovery as high as 35.7% in the fully-optimised-flotation step. Hence, the use of a Falcon concentrator to eliminate the fluorite by gravity separation prior to or after flotation has been investigated in Chapter 3. The whole flowsheet, including the tests with optimised operating parameters defined in Chapter 3, have been performed again in this chapter, see Table 21.

Table 21. Material balances of the Falcon UF and Falcon SB optimised experiments. Product names correspond to those defined in Figure 74. *Feed is back-calculated.

Product	wt.%	WO_3 grade (%)	WO_3 recovery (%)	P_2O_5 recovery (%)	K_2O recovery (%)	Fe_2O_3 recovery (%)	F recovery (%)
Falcon UF							
Tailings	78.6	0.6	44.0	74.1	81.9	78.3	78.7
Concentrate	21.4	2.8	56.0	25.9	18.1	21.7	21.3
Feed*	100.0	1.1	100.0	100.0	100.0	100.0	100.0
Falcon SB							
Tailings	84.2	0.3	24.2	79.7	88.5	84.3	84.7
Concentrate	15.8	5.0	75.8	20.3	11.5	15.7	15.3
Feed*	100.0	1.1	100.0	100.0	100.0	100.0	100.0

The Falcon SB rejects 84.7% and 79.7% of the total amounts of fluorite and apatite, respectively, from the concentrate with 75.8% WO_3 recovery in the concentrate (Table 21). Although the silicates (both dense and light) are efficiently rejected, vesuvianite still represents, with scheelite, most of the Falcon SB concentrate (Figure 76). Consistently, the tailings mostly comprise fluorite, light silicates, and fine particles (Figure 76). The Falcon SB concentrate yields 15.8 wt.% of the total feed, which means that it rejects 84.2 wt.% of the total feed (Table 21). The Falcon UF exhibits lower performances in terms of WO_3 recoveries, gangue minerals' rejection, and, consequently, WO_3 grade (Table 21). Besides, Falcon bowls allow an efficient desliming of the pulp as Falcon UF displays slime rejection performance similar to a hydrocyclone (around 50% of desliming efficiency) while the Falcon SB eliminates 95% of the slimes, see Chapter 3.
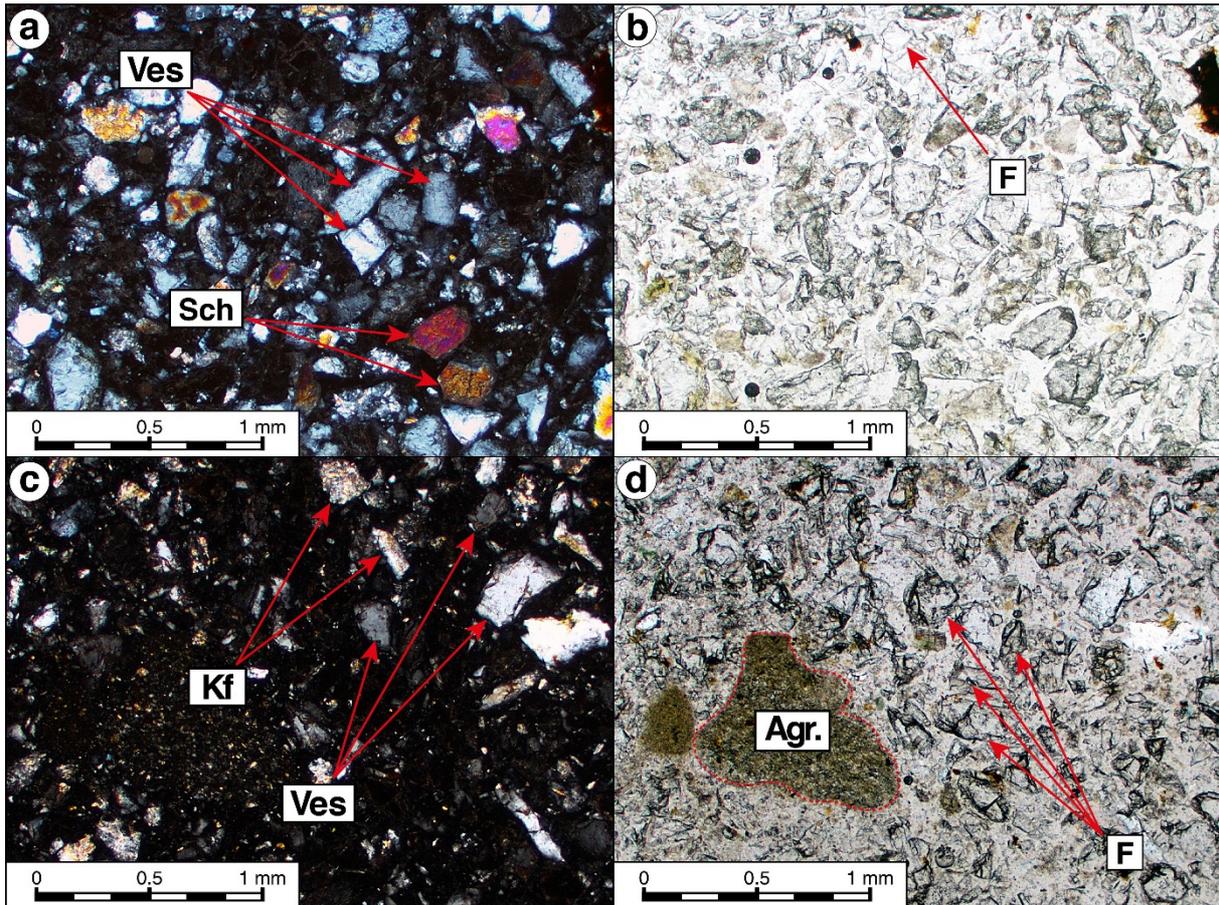
Figure 76. Micrographs of thin sections of the concentrate (a, b) and the tailings (c, d) of the Falcon SB test with optimised operating parameters observed with optical microscope under cross-polarised light (a, c) and polarised light (b, d). Abbreviations defined in Figure 75 captions, Agr = Aggregate, i.e. aggregates fine particles.

2.4 High intensity magnetic separation

The Tabuaço tungsten skarn contains high amounts of vesuvianite, which comprises iron and magnesium, and significant amounts of zoisite and grossular that also include iron and magnesium (see Chapter 2). Overall, more than 70 wt.% of the Main Skarn and 90 wt.% of the Lower Skarn are ferromagnesian minerals that are paramagnetic. These minerals corresponded to the dense silicates that are not eliminated by the Falcon separation but very efficiently by froth flotation, see section 2.1. Hence, magnetic separation is a possible option to eliminate the dense silicates in addition to the flotation stage. Both dry and wet high intensity magnetic separations have been tested on the Main Skarn. However, the dry magnetic separation is known to be inefficient on fine particles and has then been performed on the -500+150 µm fraction, prior to the milling stage, while the wet magnetic separation has been performed on the flotation feed, namely, the -150+7 µm fraction.

The results of the magnetic separation tests are presented in Table 22. The magnetic and non-magnetic products of the dry magnetic separation have been observed under optical microscope to estimate the behaviour of each mineral (Figure 77). The dry magnetic separation

exhibited satisfying results (Table 22): the magnetic fraction comprises mainly the ferromagnesian minerals, corresponding to the dense silicates, namely, vesuvianite, zoisite, and grossular (Figure 77). The non-magnetic fraction is composed of calcium salts (scheelite, fluorite, and apatite) and non-ferromagnesian silicates such as quartz and feldspars (Figure 77). As illustrated in Figure 74, the -150+0 µm fraction, separated prior to the dry magnetic separation, constitutes a part of the flotation/Falcon feed and is then not considered as tailings. Hence, only the magnetic fraction corresponds to a tailing product. It represents 44.5 wt.% of the total yield with 6.0% WO_3 recovery, 13.7% P_2O_5 recovery, 25.8% K_2O recovery, 59.6% Fe_2O_3 recovery, and 27.8% F recovery demonstrating an efficient rejection of the dense ferromagnesian silicates (Table 22). The P_2O_5, K_2O, and F recoveries in the magnetic fraction are significantly higher than the WO_3 recovery, suggesting that apatite, fluorite, and light silicates, which do not display paramagnetic properties, are more likely to be associated with ferromagnesian minerals than scheelite. Overall, this test demonstrates that a dry high intensity magnetic separation stage can reduce the mass fed to the milling stage by 44.5 wt.%, with limited scheelite losses, namely 6.0%. Moreover, most of the rejected minerals, *i.e.*, the dense ferromagnesian silicates, exhibit high hardness that would negatively impact the milling stage.

Table 22. Material balances of the dry and wet magnetic separation tests, which are performed on different feed products, as reported in Figure 74. Product names correspond to those defined in Figure 74. *Feed is back-calculated.

Product	wt.%	WO_3 grade (%)	WO_3 recovery (%)	P_2O_5 recovery (%)	K_2O recovery (%)	Fe_2O_3 recovery (%)	F recovery (%)
DHIMS							
-150+0 µm	35.6	1.0	33.6	43.4	26.2	33.6	22.7
Mag.	44.5	0.2	6.0	13.7	25.8	59.6	27.8
Non-mag.	19.9	3.3	60.4	42.9	48.0	6.8	49.5
Feed*	100.0	1.1	100.0	100.0	100.0	100.0	100.0
WHIMS							
Slimes	7.5	0.9	7.9	6.5	14.0	11.4	7.7
Mag.	33.4	0.2	7.2	10.4	10.7	45.5	15.6
Non-mag.	59.2	1.2	84.9	83.1	75.3	43.1	76.7
Feed*	100.0	0.9	100.0	100.0	100.0	100.0	100.0
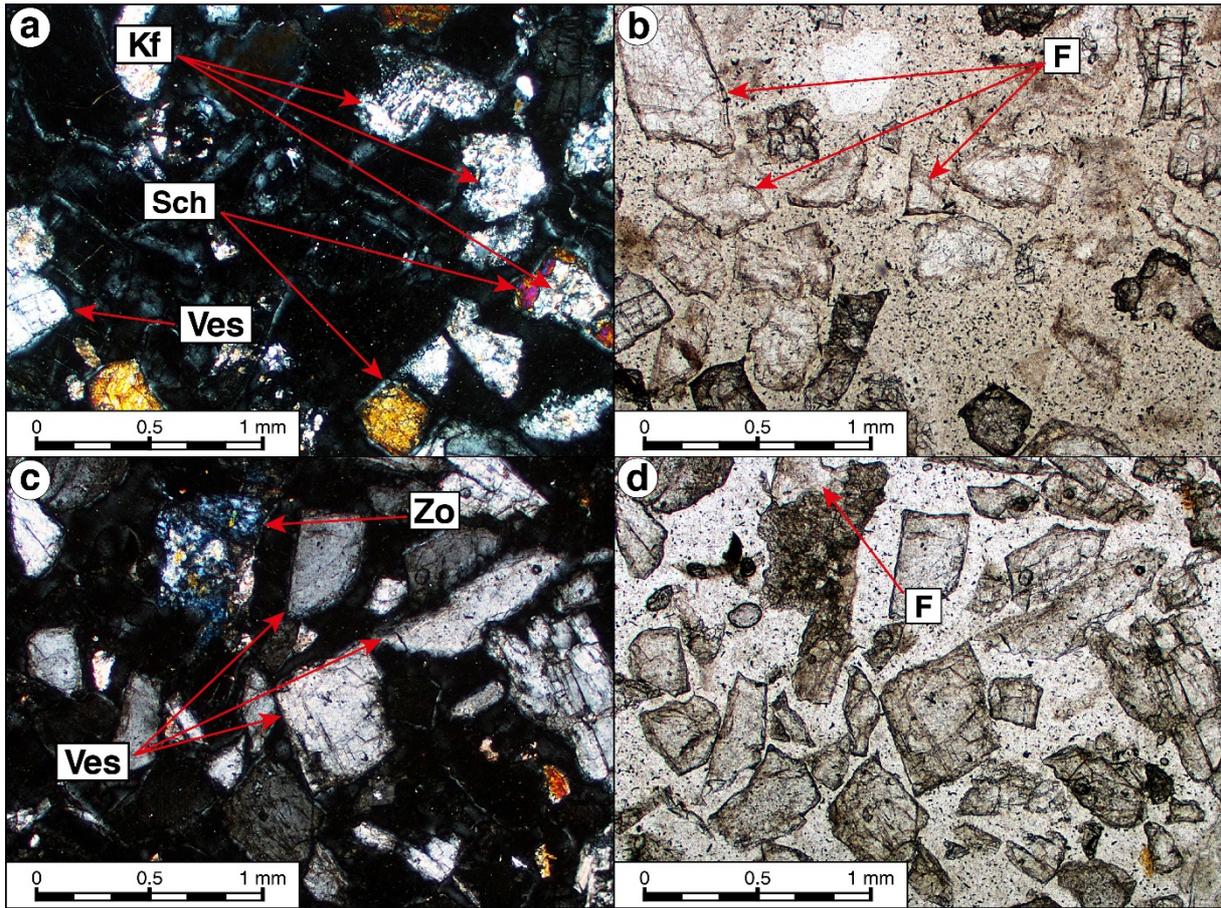
Figure 77. Micrographs of thin sections of the concentrate, *i.e.* the non-magnetic product, (a, b) and the tailings, *i.e.* the magnetic product, (c, d) of dry high intensity magnetic separation with optimised operating parameters observed with optical microscope under cross-polarised light (a, c) and polarised light (b, d). Abbreviations defined in Figure 75 captions.

The wet magnetic separation displays significantly lower performances compared to the dry magnetic separation, despite the different processed fractions (Table 22). Hereby, the slimes and the magnetic product are considered as tailings, as illustrated in Figure 74. The non-magnetic product represents 59.2 wt.% of the mass, with 84.9% WO_3 recovery, 83.1% P_2O_5 recovery, 75.3% K_2O recovery, 43.1% Fe_2O_3 recovery, and 76.7% F recovery (Table 22). The WO_3 recovery is lower compared to the dry magnetic separation, mainly due to losses in slimes, while the gangue minerals rejection compares poorly with the dry magnetic treatment option.

2.5 Combination of gravity and flotation

The Falcon UF exhibits performances significantly lower than the Falcon SB (see section 2.3), which, additionally, displays a very satisfying rejection of fluorite that is problematic in flotation with fatty acids according to Chapters 4 and 5. Consequently, the Falcon SB has been selected to be combined with flotation, as a pre-concentrating or a post-concentrating apparatus. Besides, flotation cleaning stages have been performed to enhance the WO_3 grade of the concentrate. Since the use of LD provides an increase in the WO_3 grade but a decrease in the WO_3 recovery, the choice has been made to test the two types of flotations, either with RBD15 or with LD, at

optimised depressing conditions for both. Finally, considering the performances of magnetic separation, this latter option is not able to supplant flotation and the choice has been made not to combine it with other separation techniques although it would provide rejection of 44.5 wt.% of the yield prior to the milling stage. Based on the results of each separation performed separately and the previous discussions, several global flowsheets were suggested and tested (Figure 78):

1. 2-steps flotation with optimised depressants;
2. 2-steps flotation with optimised depressants and collectors (*i.e.* LD);
3. Falcon SB concentration followed by flotation with optimised depressants;
4. Falcon SB concentration followed by flotation with optimised depressants and collectors (*i.e.* LD);
5. Flotation with optimised depressants followed by Falcon SB concentration.
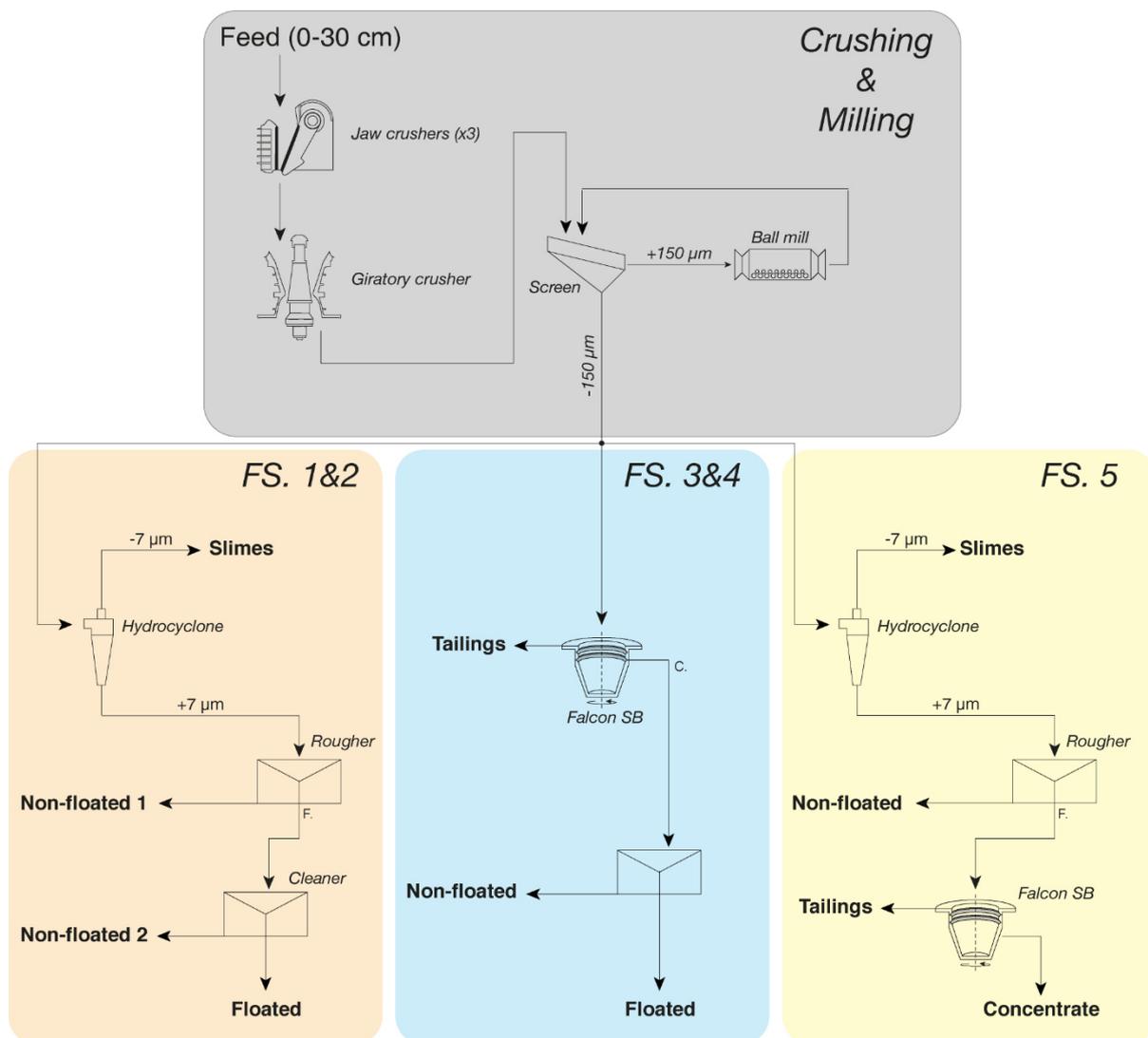
Figure 78. Overview of the 5 distinct flowsheet (FS) investigated in this study for the Tabuaço skarn ore.

Results in terms of WO_3 grade and recovery for each flowsheet are presented in Figure 79 while the detailed material balances are presented in Table 23. The flowsheets incorporating only froth flotation exhibit significantly higher WO_3 grade when LD is used, with similar WO_3 recovery (FS. 1&2). The Falcon SB pre-concentrate displays a significantly lower WO_3 grade and recovery than the flotation concentrate (Figure 79, Table 23). However, most of the fluorite and the apatite are eliminated from the pre-concentrate, as well as most of the slimes. It induces a very high efficiency, *i.e.* enrichment ratio, of the subsequent flotation stage, performed on the Falcon SB pre-concentrate. The final concentrate, after only two separation stages (Falcon SB followed by flotation with RBD15) assays 38.1% WO_3 with 62.5% WO_3 global recovery (Figure 79) from a feed assaying 1.1% WO_3 (Figure 79, Table 23). Moreover, the yield after the Falcon SB stage is 15.1-15.8 wt.%, meaning that around 85 wt.% of the total feed mass is rejected during this phase. When the flotation with LD is performed on the Falcon SB pre-concentrate, the results are roughly the same (Table 23), attributed to the fact that most of the fluorite is rejected by the Falcon separation. This prior rejection erases the selectivity differences between RBD15 and LD, producing then very similar concentrates. However, the use of LD increases slightly the WO_3 recovery, probably due to higher dosages compared to RBD15 (600 g/t instead of 200 g/t).
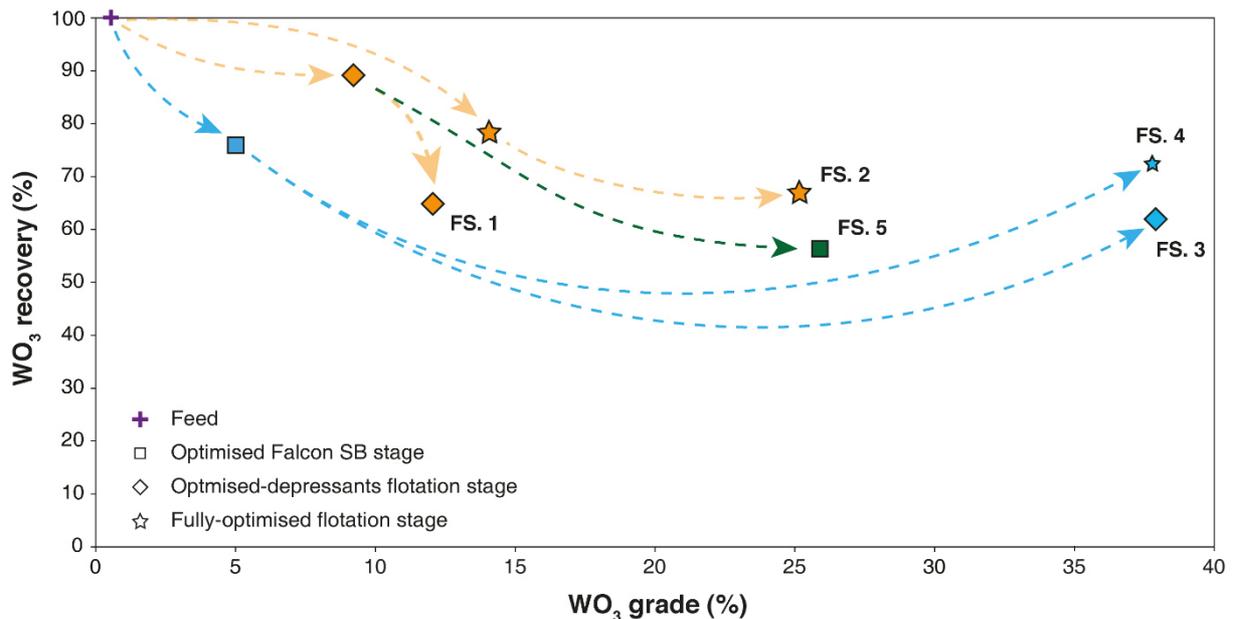
Figure 79. WO_3 recovery - WO_3 grade curve displaying the different flowsheets investigated for the beneficiation of the Main Skarn layer at Tabuaço deposit. The hydrocyclone stage is included in the flotation stage when this latter process is performed first, the WO_3 recoveries take into account the losses in the slimes. Flowsheets numbers and colours correspond to those of Figure 78.

The reverse flowsheet has also been tested where the final concentrate, after a flotation stage with RBD15 followed by a Falcon SB stage, assays 25.9% WO_3 with 55.9% WO_3 global recovery (Table 23, Figure 79). This option however presents fewer advantages:

1. When the flotation is performed first, the ore has to be deslimed and then requires the use of a hydrocyclone, implying more operations and scheelite losses in the slimes;
2. Since the Falcon represents lower operating costs compared to flotation, the highest flowrates should be processed with the Falcon;
3. The fatty acids do not desorb from the particles surfaces and make the scheelite and fluorite particles hydrophobic, which disturbs the separation mechanisms during the Falcon stage performed on the flotation concentrate.

Table 23. Material balances of the 5 different flowsheets investigated for the beneficiation of the Main Skarn layer. Flowsheets numbers and product names correspond to those defined in Figure 78. *Feed is back-calculated.

Product	wt.%	WO₃ grade (%)	WO₃ recovery (%)	P₂O₅ recovery (%)	K₂O recovery (%)	Fe₂O₃ recovery (%)	F recovery (%)
Flotation (RBD15)							
Slimes	7.5	0.9	6.3	5.0	14.9	11.3	7.3
Non-floated 1	82.5	0.1	5.8	68.1	82.7	84.9	37.6
Non-floated 2	4.4	5.7	23.7	18.1	2.1	2.9	14.7
Floated	5.6	12.0	64.2	8.8	0.3	0.9	40.5
Feed*	100.0	1.1	100.0	100.0	100.0	100.0	100.0
Flotation (LD)							
Slimes	7.5	0.9	6.9	5.3	13.4	12.0	7.7
Non-floated 1	87.26	0.2	16.0	89.1	85.8	85.5	59.4
Non-floated 2	2.7	3.9	11.2	1.9	0.8	1.8	16.7
Floated	2.5	25.2	66.0	3.7	0.0	0.6	16.2
Feed*	100.0	1.0	100.0	100.0	100.0	100.0	100.0
Falcon SB ➔ Flotation (RBD15)							
Falcon tailings	84.2	0.3	24.2	79.7	88.5	84.3	84.7
Non-floated	14.1	1.0	13.3	15.4	11.5	15.2	8.6
Floated	1.7	38.1	62.5	4.9	0.0	0.5	6.7
Feed*	100.0	1.1	100.0	100.0	100.0	100.0	100.0
Falcon SB ➔ Flotation (LD)							
Falcon tailings	84.9	0.3	23.7	79.0	89.4	85.2	85.0
Non-floated	13.1	0.3	3.7	13.0	10.4	14.2	8.0
Floated	2.0	37.8	72.6	8.0	0.2	0.6	7.0
Feed*	100.0	1.0	100.0	100.0	100.0	100.0	100.0
Flotation (RBD15) ➔ Falcon SB							
Slimes	7.5	0.9	6.1	6.2	13.2	11.9	7.8
Non-floated	81.6	0.1	10.2	66.7	83.4	82.4	37.3
Falcon tailings	8.6	3.5	27.8	18.8	3.1	4.8	44.7
Falcon conc.	2.3	25.9	55.9	8.3	0.3	0.8	10.2
Feed*	100.0	1.1	100.0	100.0	100.0	100.0	100.0

Based on the WO$_3$ grade and recovery, the flowsheet 4 (Falcon SB → Flotation with LD) has been selected as the best option for the Tabuaço Main Skarn processing since it produces a final concentrate assaying 37.8% WO$_3$ with an overall 72.6% WO$_3$ recovery. Several cleaning stages have been performed on the concentrate of this test, without additional reagent addition (Figure 80). Undoubtedly, successive cleaning stages increase the WO$_3$ grade with a moderate decrease of the WO$_3$ recovery. After four flotation stages performed on the Falcon SB pre-concentrate, the final concentrate assays 62.9% WO$_3$ for 59.4% WO$_3$ global recovery from the feed assaying 1.1% WO$_3$ (Figure 80), which constitutes a marketable scheelite concentrate.
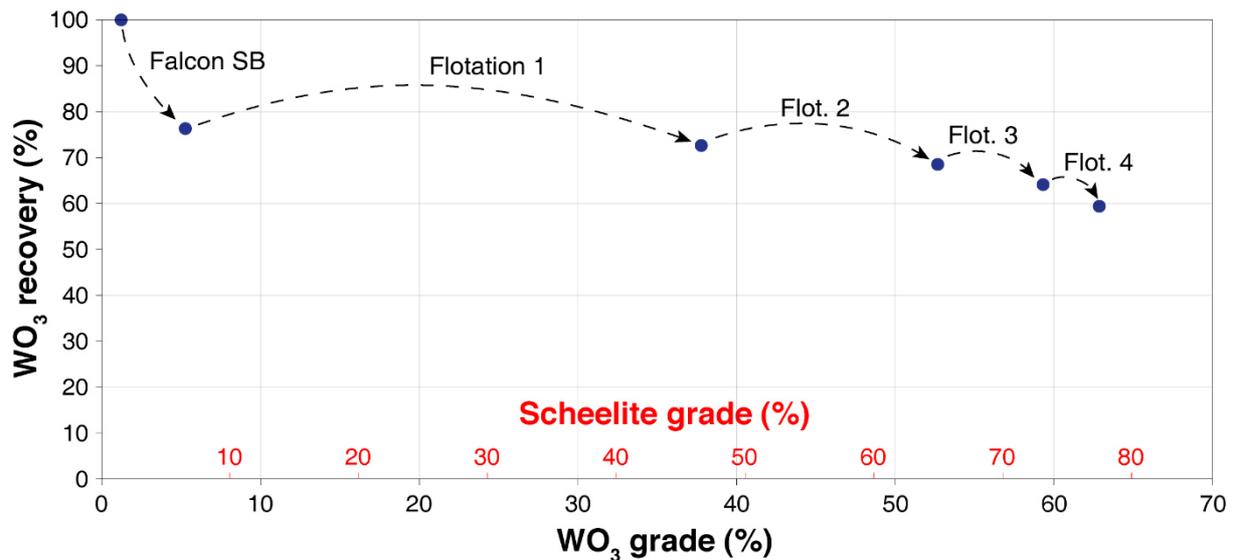
Figure 80. WO$_3$ recovery vs WO$_3$ and scheelite grades for the best flowsheet showing the influence of the Falcon SB and the flotation stages on the WO$_3$ grade and recovery.

3. Economic assessment and conclusions

The present chapter aimed to recover tungsten from a typical complex skarn ore, adapting the process to the mineralogy of the ore. The integrated flowsheet developed here is presented on Figure 81. First, a dry magnetic separation is a possible option on the crushed feed prior to fine grinding. It would lead to the rejection, prior to the milling stage, of around 45 wt.% of the yield that mainly contain the hardest minerals of the ore (dense ferromagnesian silicates), which would correspond to a significant energy saving. The magnetic fraction contains only 6.0% of the total scheelite distribution and can be considered as tailings.
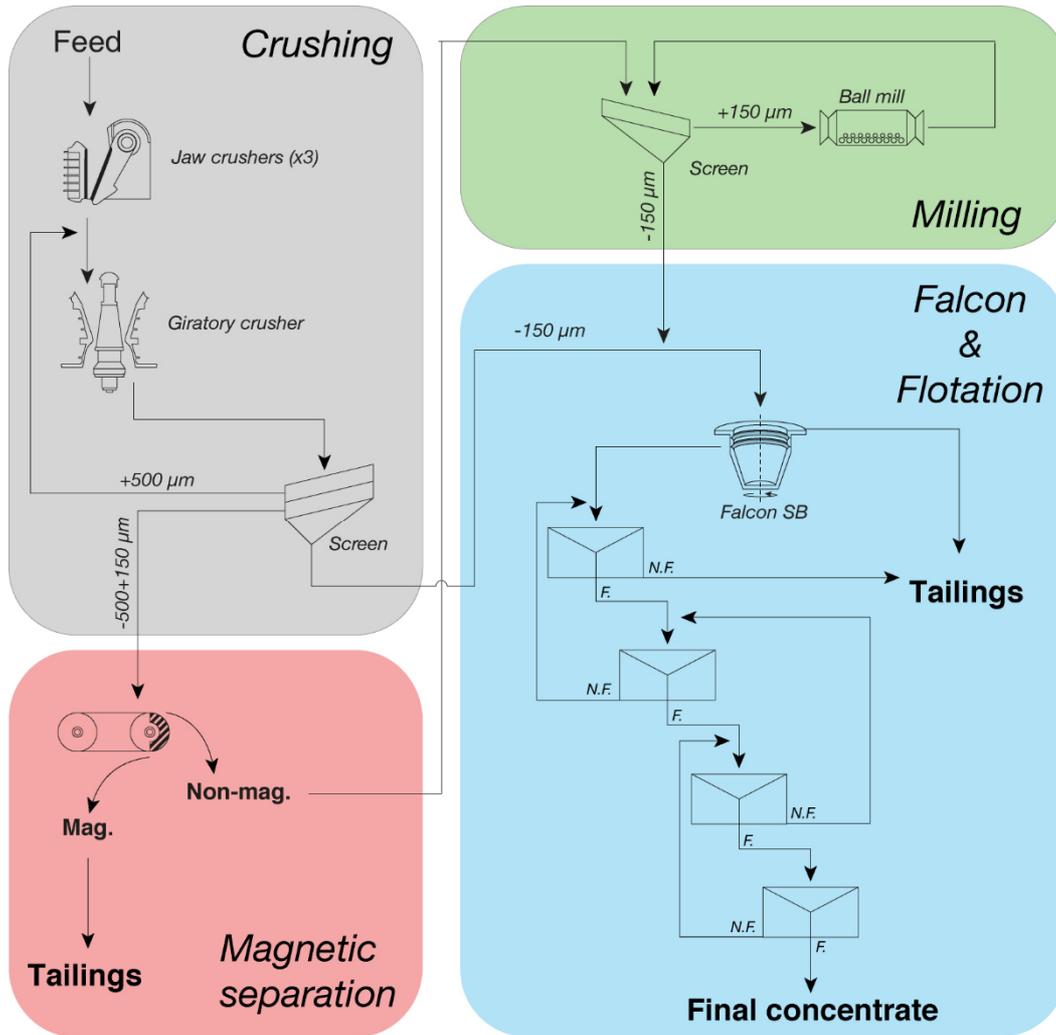
Figure 81. Suggested global flowsheet for the production of a marketable scheelite concentrate for the Main Skarn level.

Moreover, the use of a Falcon SB prior to flotation provides:

- Rejection of around 85 wt.% of the total milled feed;
- Desliming with a high efficiency for the flotation feed;
- After only one fully-optimised flotation stage, producing a concentrate assaying 37.8% WO_3 with 72.6% WO_3 global recovery.

This process route is better than a two-stage flotation that produces a concentrate assaying 12.0% with 64.2% WO_3 recovery with RBD15 or assaying 25.2% WO_3 with 66.0% WO_3 recovery for novel reagents formulations (LD), see Figure 79 and Table 23. Performing several flotation stages on the Falcon SB pre-concentrate produces a concentrate assaying 62.9% WO_3 with 59.4% WO_3 global recovery, which is a marketable scheelite concentrate. The WO_3 recovery will be significantly increased if the integrated process is scaled-up from batch tests, performed in the present study, to continuous scale (*i.e.* pilot scale) since the tailings products, containing significant amounts of scheelite, will be recirculated (Figure 81). Moreover, studies on the Falcon SB tailings, which still represents around 24% WO_3 distribution, can be undertaken to increase

the overall WO_3 recovery. The flowsheets developed here can be adapted to the targeted performance: the operating parameters used for the Falcon SB stage can be defined to maximise either the gangue minerals (mostly fluorite) rejection, *i.e.* the WO_3 grade or the WO_3 recovery (see Chapter 3). Furthermore, the number of flotation cleaning stages performed on the Falcon SB pre-concentrate can be optimised to maximise the WO_3 grade or the WO_3 recovery. Overall, the suggested flowsheets would:

- Reduce the energy consumption as more than half of the product is rejected before the mill;
- Reduce the reagents costs by decreasing the ore quantity processed by flotation;
- Reduce the energy/water consumption as less feed material is sent to flotation;
- Use only environmental benign chemicals in flotation (Na_2CO_3, Na_2SiO_3, fatty acids) as problematic gangue minerals are eliminated before flotation;
- Use no thermal treatment (Petrov process);
- Produce a marketable WO_3 concentrate (62.9% WO_3);
- Adapt the processing route to the product specifications or to the targeted performance (WO_3 grade or WO_3 recovery).

Approximatively 375 000 tons/year will be processed in the Tabuaço plant, which roughly represents 45 t/h. The adapted Falcon concentrator has a motor power of 30 kW which is equivalent, given the average electricity price of 0.21 €/kWh in Portugal, to 6.3 €/h and thus to 0.14 €/t. No water is required after the milling stage as the Falcon can process pulps at more than 30% wt. solids. It represents extremely low operating costs compared to the flotation stage. Even if the flotation cells energy consumption is similar to the Falcon one, flotation needs the addition of water to reach 30 % wt. solids in the pulp and requires reagents that constitute an important part of the operating costs. Globally, the implementation of a Falcon concentrator in the process would lead to the elimination of around 85 wt.% of the total feed flowrate, resulting in a flotation feed stream of only 7.2 t/h instead of 45 t/h. Assuming 250 €/ton for the Na_2CO_3, 150 €/ton for the Na_2SiO_3 and 700 €/ton for the TOFA, the gravity pre-concentration leads to a saving of approximatively 20 €/h and then 0.45 €/t. Further, the implementation of a dry magnetic separation prior to the milling stage would lead to the rejection of around 45 wt.% of the total feed flowrate, inducing that the energy consumed for the milling would be 2 times lower. Overall, the process choice should be adapted to the ore characteristics as new methods exist for on-line monitoring and for selective mining following integrated approaches.

Surface properties of fluorite and scheelite in presence of water: atomistic investigations

1. Introduction

The previous chapters, mostly Chapter 4 and 5, exhibited the importance of the synergistic effects between flotation reagents for modulating the flotation selectivity and/or recoveries. In particular, DFT calculations performed at 300 K (*ab initio* molecular dynamics simulations) allowed to unravel the molecular mechanisms involved in the synergistic adsorption of Na_2CO_3 and Na_2SiO_3, with strong experimental validations. Hence, the interactions between the flotation collector(s) and the mineral surfaces should be deeply investigated by means of DFT calculations. Nonetheless, during the cleavage process, the mineral surfaces are initially in contact with water molecules, which generally adsorb onto them, considering the surface reactivity induced by the cleavage process. In the Langmuir model, the adsorption of molecules in liquid phase onto solid surfaces is related to the desorption of the pre-adsorbed water molecules, prior to the strictly-speaking adsorption of the molecule. In view of these points, the general method for the study of adsorption of molecules in liquid phase onto mineral surfaces, presented in Chapter 1, requires, as a first step, an extensive investigation of the hydration mechanisms taking place on the surface.

At the moment, very few authors investigated the adsorption of water onto fluorite surface. DFT studies were conducted by de Leeuw and co-workers (2000) using VASP with the PW91 exchange-correlation functional in the generalised gradient approximation (De Leeuw et al., 2000). In particular, they found that water adsorbs under molecular form even if dissociated water (H^+ and OH^-) is set as input (De Leeuw et al., 2000). They reported average adsorption energies of -53.4 kJ.mol^{-1} per water molecule for 50 % surface coverage, decreasing to -41.4 kJ.mol^{-1} per water molecule for 100 % surface coverage (De Leeuw et al., 2000). Besides, the adsorption of water onto scheelite surfaces was investigated by interatomic potential methods (derived from DFT) by Cooper and de Leeuw (2003), who reported average molecular adsorption energies ranging from -22 kJ.mol^{-1} on the least reactive (001) surface to -78 kJ.mol^{-1} on the most reactive (103) surface (Cooper and de Leeuw, 2003). However, these studies did not take into account dispersive interactions, did not investigate in details the influence of the coverage, or did not have the accuracy provided by density functional theory, the most common method for molecular modelling currently. In the present chapter, the adsorption of water molecules onto the (111) fluorite surface and the (001) and (112) scheelite surfaces was investigated with the PBE exchange-correlation functional and including dispersive interactions correction. The global aim was to evaluate the hydration mechanisms on the aforementioned surfaces and the energies linked to the water adsorption, to serve as a basis for deeper studies on the adsorption of flotation reagents on these surfaces. **A part of this work, dealing with fluorite hydration, has been published in The Journal of Physical Chemistry B**, selected for the front cover page of the issue 26 of the volume 122 (05/07/2018) of this journal, and constituted a news-in-brief article in the journal of the *Institut National des Sciences de l'Univers* of the French National Scientific Research Centre (CNRS).

2. Fluorite

2.1 Surface

Following previous studies, a (111) cleavage surface has been created from the fully relaxed bulk. A supercell containing 144 atoms (48 Ca and 96 F) has been generated, made of four layers of calcium atoms, each of them separated by two successive layers of fluorine atoms (Figure 82a). Therefore, the (111) surface consists of a plane of 12 seven-coordinate calcium ions, each one being in a hexagonal array (Figure 82). The calcium atoms in the lattice fluorite are eight-coordinated, which induces that, on the (111) surface, each calcium atom has one dangling bond. Besides, the cell has been constructed so that a vacuum of 15 Å has been systematically kept between the surface and the upper limit of the cell, following the z axis, including the uppermost atom of the added molecule(s). This avoids any unwanted interaction due to the periodicity of the cell. Four layers of bottom atoms in the cell (one layer of calcium ions, three layers of fluorine ions) have been frozen to their bulk positions. As *ab initio* molecular dynamics simulations are numerically costly, in this case, the fluorite slab has been reduced to a thickness of six layers.
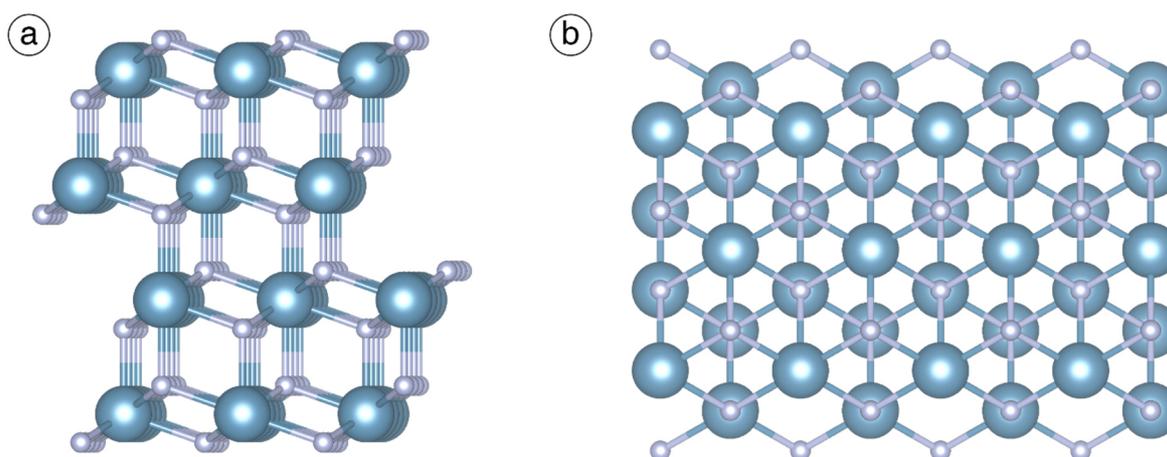
Figure 82. (111) fluorite surface seen from side (a) and from top (b). The blue balls represent the calcium atoms, whereas the grey balls represent the fluorine atoms.

2.2 Isolated water molecule on fluorite

2.2.1   Adsorption of dissociated water molecule

For the dissociated case, several configurations were explored. A hydroxyl group was placed above a calcium ion on the surface, with the O close to the calcium and the H oriented up, away from the surface. The lone H^+ ion was set at the vicinity of a fluorine ion. Various distances between the OH and H groups were tested. For those cases, the D3 correction method was used (Grimme et al., 2010).

Short OH-H distance

First, the H$^+$ and the OH$^-$ were set on respectively a fluorine atom and a calcium atom which are part of the same octahedron (*i.e.* Ca-F bond length is 2.37 Å). The H$^+$ ion is captured by the OH$^-$ and the water molecule is reformed. De Leeuw and co-workers (2000) have reported the same phenomena of recombination of molecular water (De Leeuw et al., 2000). After relaxation, the O-H$_1$ and O-H$_2$ bonds lengths are both 0.98 Å. The calculated adsorption energy is ΔE_{ads} = -55.6 kJ.mol^{-1} including ΔE_{disp} = -13.0 kJ.mol^{-1}. The O atom adsorbs on the calcium atom, the Ca-O bond length being 2.46 Å. The water molecule is in a plane sub-parallel to the surface (Figure 83). One H atom (H$_1$) is oriented towards one of the three surface fluorine atoms being around the Ca^{2+}, the H$_1$-F distance being 1.64 Å. Due to the vicinity of H$_1$, the Ca-F bond is broken, the distance between Ca and F is now 2.92 Å instead of 2.36-2.38 Å without H$_2$O adsorption. This fluorine atom is then bonded to only two Ca atoms, instead of three. The second hydrogen atom (H$_2$) is slightly pointing away from the surface, inducing a tilted configuration of the molecule (Figure 83). These results are in very good accordance with the DFT calculations performed previously, which reported an adsorption energy of -43 to -51 kJ.mol^{-1} (De Leeuw et al., 2000) The differences in the adsorption energies and in the H-F distances can be explained by the non-inclusion of dispersive energy correction in the previous DFT calculations and by the use of a different functional (PW91).
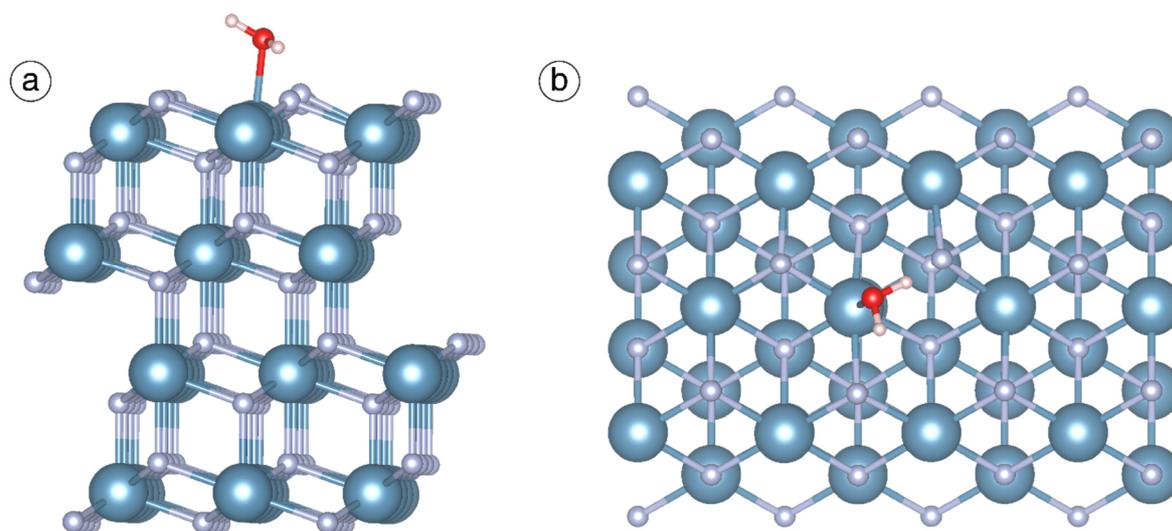
Figure 83. Adsorption of dissociated water molecule with H$^+$ and OH$^-$ close on the (111) fluorite surface after DFT relaxation, in side view (a) and in top view (b). The water molecule is reformed. The blue, grey, red, and white balls represent the calcium, fluorine, oxygen, and hydrogen atoms, respectively.

Medium OH-H distance

Then, the distance between OH$^-$ and H$^+$ was increased. The two ions were not set on atoms of the same octahedron. One fluorine atom was left between H$^+$ and OH$^-$, for an initial OH-H

distance of 4.73 Å. The distance was large enough to avoid the reformation of the water molecule. However, the hydrogen ion forms an H-F bond with the unoccupied fluorine ion, and both tilt so that the hydrogen ion becomes closer to the hydroxyl group. This latter moves and replace the unoccupied fluorine ion, forming a hydrogen bond with the hydrogen ion and two Ca-O bonds which lengths are 2.49 Å and 2.47 Å. This configuration is probably a local energy optimum found by the DFT calculation. The water molecule is not reformed and the calculated adsorption energy is $\Delta E_{ads} = +37.9$ kJ.mol^{-1}. It constitutes a significant endothermic value, indicating that the adsorption of dissociated water is disfavoured at 0 K.

High OH-H distance

When the proton is placed at 6 Å from the hydroxyl group, there is no interaction between them. The hydrogen ion forms H-F bonds with two surface fluorine atoms, which lengths are 1.21 Å and 1.08 Å (Figure 84). The OH$^-$ forms a Ca-O bond with a length of 2.04 Å. This value is small compared to the Ca-O bond length when the molecular water is reformed, which is 2.46 Å. It can be explained by the availability of three lone pairs of electrons for the hydroxyl group oxygen whereas the molecular water oxygen has only two available lone pairs. This configuration is very much disfavoured as the calculated adsorption energy is $\Delta E_{ads} = +247.8$ kJ.mol^{-1}.
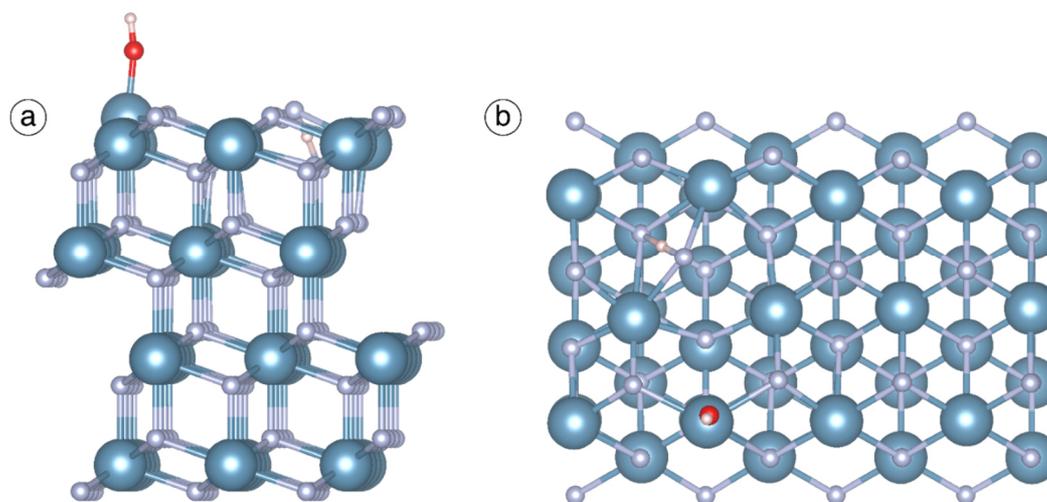
Figure 84. Adsorption of dissociated water molecule with H$^+$ and OH$^-$ far on the (111) fluorite surface after DFT relaxation, in side view (a) and in top view (b). The blue, grey, red, and white balls represent the calcium, fluorine, oxygen, and hydrogen atoms, respectively.

2.2.2   Adsorption of molecular water

As the molecular adsorption of water appears to be more stable than the dissociative adsorption, several configurations of adsorbed water were tested where a water molecule was directly set above a surface calcium ion. The D3 correction method was also used for this case. Three different spatial orientations were tested. The H of the water molecules were oriented towards the vacuum ("up" configuration), towards the fluorite crystal ("down" configuration), or within a plane parallel to the surface ("side" configuration). As fluorite is part of cubic system, a three-fold axe

is constituted by the calcium ions alignment, perpendicularly to the (111) surface. Then, the six fluorine ions coordinating each calcium ion are composed of two different fluorine ions being repeated three times by the three-fold axis. In these two different fluorine ions, one is part of the plane located below the calcium layer and the other is part of the plane located above the calcium layer. Thus, two different cases had to be tested in terms of spatial configuration in the (111) plane, even if all the Ca-F bond lengths are the same. All the different cases tested ("up", "down", "side" configurations and two planar orientations for each configuration) lead to the same final geometry. Also, the final configuration of the adsorbed water molecule is the same than after the reformation of the water molecule in the dissociative case: the molecule is adsorbed on a surface calcium, the oxygen atom forming a bond with the surface calcium (Figure 83). The molecule is nearly parallel to the (111) plane, being slightly tilted. The mean Ca-O bond length is 2.47 Å and the hydrogen atoms are oriented toward two fluorine ions of the plane located above the calcium layer (Figure 83). One of the two H is pointing away from the surface. The H-F bond lengths are respectively 1.79 Å and 2.59 Å. The calculated adsorption energy is loosely the same than for the reformed water molecule, being ΔE_{ads} = -55.9 kJ.mol^{-1}.

2.2.3   Substitution of F$^-$ by OH$^-$

Finally, the substitution of F$^-$ by OH$^-$ on the (111) fluorite surface was investigated, still with the D3 correction method. A hydroxyl group was set at the place of a surface fluorine atom. The substitution of F$^-$ by OH$^-$ on the (111) fluorite surface has been described by Shi and Lang (2012), who found that the most stable spatial configuration for a substitution of F$^-$ by OH$^-$ is when the OH$^-$ is placed in the first fluorine sublayer, with the H above the O (Shi et al., 2012). Then, the following reaction was studied for only one spatial configuration, the more energetically stable one after Shi and Lang (2012), calculating the energy of each component:

$$\text{Surface} + \text{H}_2\text{O} = \text{Surface}_{\text{F->OH}} + \text{HF} \qquad (36)$$

When the hydroxyl group is introduced in the fluorite structure, it forms Ca-O bonds with the three surrounding calcium ions (Figure 85). These calcium atoms, that coordinate the anion, are distending and the Ca-O bond lengths are 2.46 Å, while the usual Ca-F bond lengths are 2.38 Å. This difference can be explained by the difference of electronegativity between fluorine and oxygen atoms. The calculated reaction energy is ΔE_r = +71.1 kJ.mol^{-1}, including $\Delta E_{r\text{-disp}}$ = -8.4 kJ.mol^{-1}. This indicates that the substitution of F$^-$ by OH$^-$ on the surface is not thermodynamically favoured at 0 K. However, this result is crucial to understand the influence of the pH on the surface condition of fluorite. A high concentration of OH$^-$ in the solution will probably make possible the substitution of F$^-$ by OH$^-$ in the first layer. Indeed, the free energy of this reaction depends on the H$_2$O/HF concentration ratio. The solubility of fluorite is constant from pH 5 to pH 11, *i.e.* when the H$^+$ and OH$^-$ concentrations are still low (Roche, 1973). At pH<5, HF will be formed in solution as F$^-$ will be substituted by a solution anion onto the surface (SO$_4^{2-}$ if sulfuric acid is used for example) and the Ca^{2+} cation substituted by several protons (Roche, 1973; Zhang et al., 2006). Also, in alkaline medium (pH>11), the hydroxyl group, in high

concentration, will substitute more easily the surface fluorine ions, leading to a progressive destabilisation of the calcium cations and their solvation (Roche, 1973; Zhang et al., 2006). Dissolution of fluorite has been intensively investigated by researchers who showed that the defects percentage on the surface is, with the pH, one of the main parameter involved in the dissolution rate (Godinho et al., 2012; Jose R. A. Godinho et al., 2014; J.R.A. Godinho et al., 2014; Maldonado et al., 2013). This study, performed on a perfect (111) cleavage plane and with pure molecular water permits to conclude that the dissolution of fluorite, through the substitution of a fluorine ion by a hydroxyl group or the substitution of calcium ions by protons, needs an activation energy (brought by temperature) and/or high concentrations of pH-determining ions.
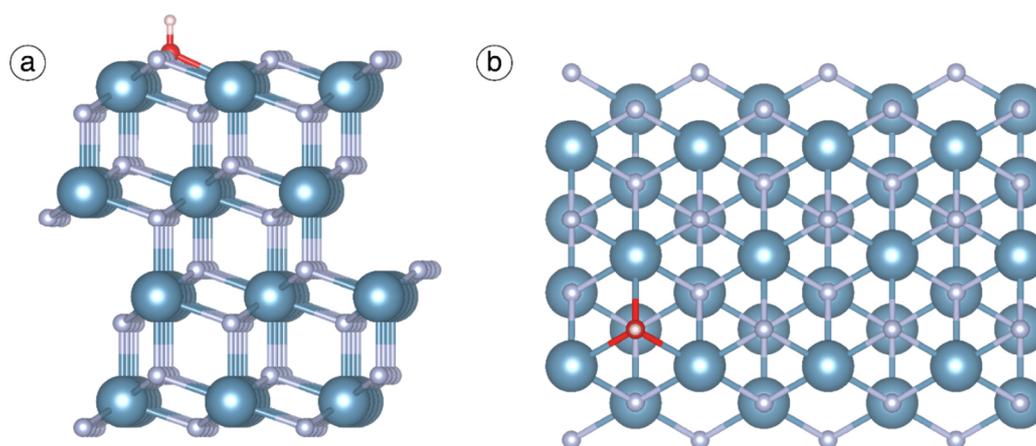
Figure 85. Side view (left) and top view (right) of the (111) fluorite surface after DFT relaxation of the system where a fluorine atom has been replaced by a hydroxyl group. The blue, grey, red, and white balls represent the calcium, fluorine, oxygen, and hydrogen atoms, respectively.

2.3 Towards a full hydration of the surface

Once the most favourable configuration for a single molecule of water determined, the progressive hydration of the surface was investigated. Then, two, three, six and 12 H_2O were placed on the surface composed of 12 calcium atoms. For each number of molecules, three different spatial configurations were tested:

1. A "surface" layout, where each water molecule is set on a calcium atom with $d_{Ca-O} \sim 2.50$ Å (Figure 86a);
2. A "partial clusters" layout, where the total number of water molecules is divided between an adsorbed layer ($d_{Ca-O} \sim 2.50$ Å) and a layer further from the surface, involved in hydrogen bonds with the first layer (Figure 86b);
3. A "full clusters" layout, where the geometry of the water molecules is set up following the cluster spatial organisation described by Temelso and co-workers (Temelso et al., 2011) (Figure 86c).

For each case, the water molecules can be set following different geometries, and only the most stable configuration and the corresponding adsorption energy per water molecule are presented hereafter (see Figure 87). Also, the PBE functional is compared with the D2 and D3 correction methods for each case and each number of water molecules. For the "surface" layout, the most stable case is, for each coverage, the configuration where water molecules are close of each other. The hydration energy per water molecule becomes less negative when the number of water molecules increases to 12. Hence, the configuration with six molecules, *i.e.* a 50% coverage of the surface, is the most stable, which is in accordance with what previous authors have shown (De Leeuw et al., 2000). However, the variation between all the coverages is limited: for instance, with the PBE functional, the calculated adsorption energies is ranging between -40 and -45 kJ.mol^{-1} while for the corrected functionals, it varies between -55 and -63 kJ.mol^{-1}, see Figure 87.
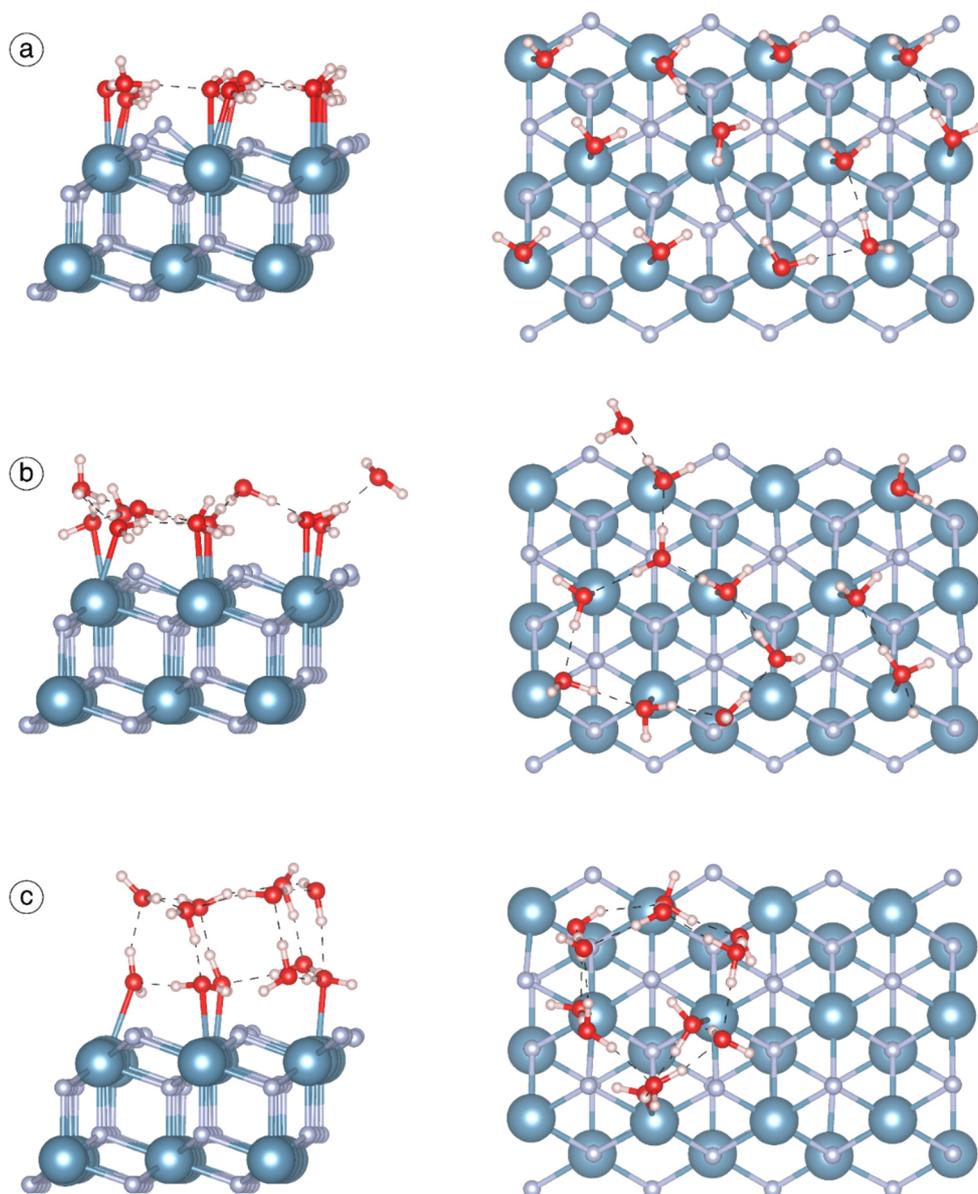
Figure 86. Side views (left) and top views (right) of the (111) fluorite surface showing the different spatial configurations investigated when the water coverage is increased, for instance 100 % coverage here. "Surface" (a), "partial clusters" (b), and "full clusters" (c) layouts were tested. Dashed lines represent H-bonds. The blue, grey, red, and white balls represent the calcium, fluorine, oxygen, and hydrogen atoms, respectively.

The "full clusters" layout is the less favoured case since a small number of water molecules is adsorbed directly on the surface, while the hydrogen bonds between water molecules do not compensate. While increasing the number of water molecules, the adsorption energy per molecule goes from a minimum of -37 to a maximum of -45 kJ.mol^{-1} with the PBE functional (Figure 87). However, using the D2 and D3 corrections, it ranges between -52 to -59 kJ.mol^{-1}. This corresponds to a progressive stabilisation of the system for an increasing number of molecules. Nevertheless, the "partial clusters" layout is the most stable configuration. The adsorption energy per water molecule decreases systematically when the number of molecules is increased. The calculated

adsorption energies are going from -61 kJ.mol^{-1} for two molecules to -64 kJ.mol^{-1} for 12 molecules, including a contribution of -12 to -14 kJ.mol^{-1} of dispersive energy (Figure 87). It demonstrates a stabilisation of the adsorbed molecules involved in some water clusters.
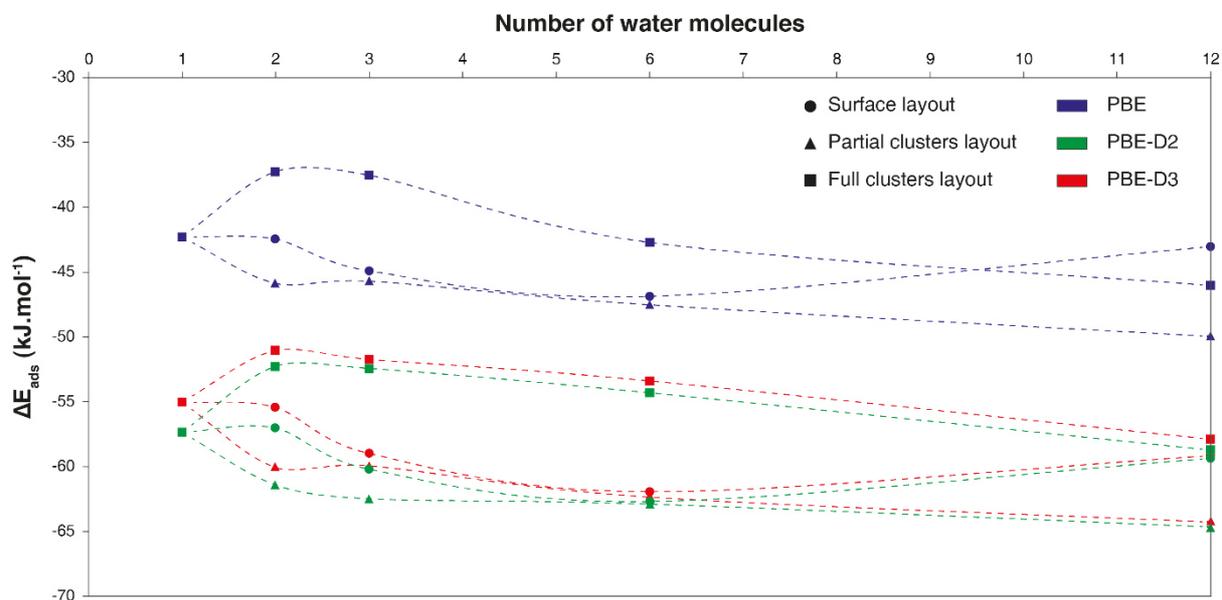
Figure 87. Adsorption energies per water molecule for the different spatial configurations tested when the water coverage is increased from one water molecule to 12 water molecules. D2 and D3 correction methods were tested for each case, as well as no correction method.

Overall, the energies obtained with the PBE functional are, in absolute values, significantly lower than the ones obtained with the corrected methods, which highlights their importance (Figure 87). Moreover, the energy ordering between the various layouts is sometimes different (see for instance the energy for 12 molecules in "full clusters" and "surface" layouts). Also, the two dispersion correction methods lead to very similar results.

2.4 Ab initio molecular dynamics calculations of the hydrated (111) fluorite surface

To complete the results obtained at T = 0 K, the hydration of the (111) fluorite surface was studied by *ab initio* molecular dynamics simulations at T = 300 K using PBE+D2 correction method. Molecular dynamics calculations were performed on the surface with one, two, three, six, and 12 water molecules, as before. The results show that the temperature does not change the hydration mechanisms determined at T = 0 K (Figure 88): the water molecules form spontaneously the "partial clusters" layout predicted at T = 0 K. Indeed, half of the water molecules are adsorbed on calcium atoms with d_{Ca-O} = 2.40-2.60 Å. The other half is a bit further from the surface with $d_{Surface-Molecule}$ = 3.00-3.50 Å. All the molecules are involved in clusters with four, five, or six water molecules in each cluster, where the stabilisation of the structure is due to H-bonds, with bond lengths ranging between 1.40 and 2.50 Å. For each number of water molecules, the computed internal energy of adsorption at T = 300 K follows the same trend than

the adsorption energy at T = 0 K, albeit with a shift of roughly -10 kJ.mol^{-1} due to the temperature (Figure 88).
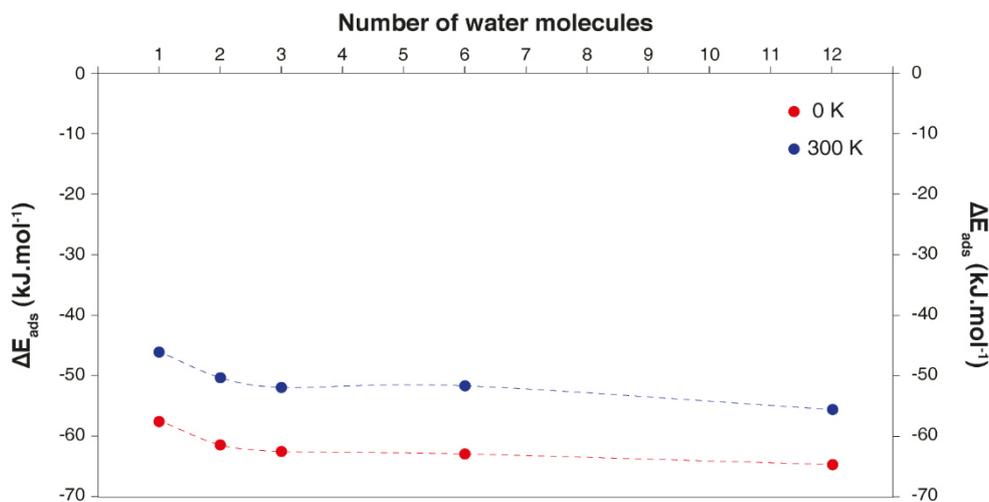
Figure 88. Internal adsorption energies calculated from the AIMD calculations for different water coverages, confirming the results obtained at 0 K.

Then, configurations with 24 molecules, 36 molecules, and the cell filled with water molecules have been simulated (Figure 89). For this last case, the number of water molecules was adapted to obtain a calculated water density close to 1.00 g.cm^{-3}. For all the configurations investigated, we have found that only 50% of the surface calcium ions are occupied by an adsorbed water molecule, with a distance of 2.46 Å (Figure 89). The other molecules are further from the surface with distances ranging 2.80 Å to more than 3 Å. Moreover, the presence of multiple water layers does not affect the specific geometric configuration of the first layer identified at T = 0 K previously.
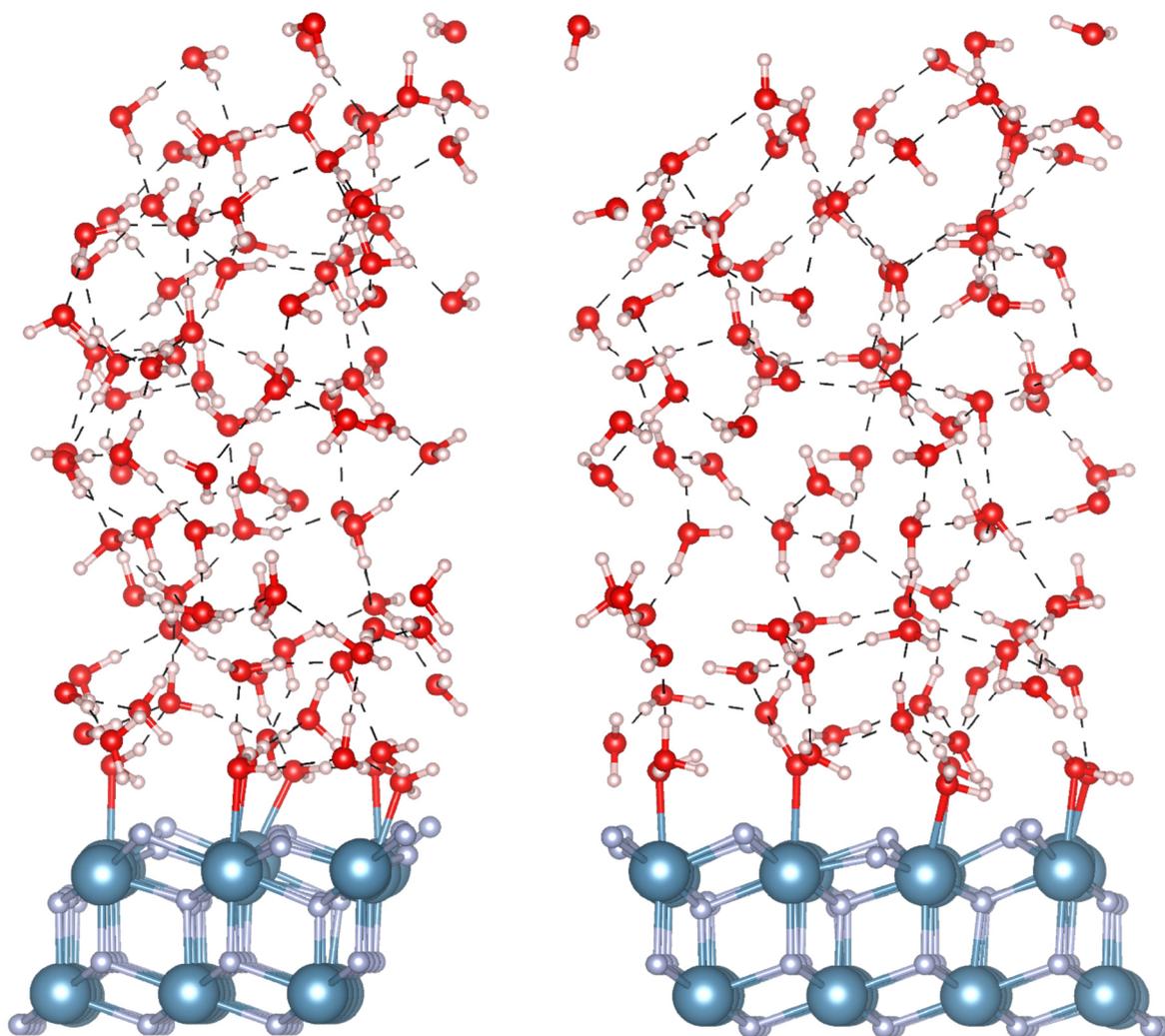
Figure 89. Snapshots of side views with 90° between each other of the (111) fluorite surface with the vacuum above the surface completely filled with water molecules so that the density is 1 g.cm⁻³. Dashed lines represent H-bonds. The blue, grey, red, and white balls represent the calcium, fluorine, oxygen, and hydrogen atoms, respectively.

Water molecules that are close to the surface are often part of non-planar pentamers from which one or two molecules are adsorbed onto a surface calcium. For the bulk of water, the geometries are structured in a way that the two H of two molecules point towards an oxygen of another molecule (Figure 89). The H of the two other molecules are establishing hydrogen bonds with other multi-molecular structures. This result is in accordance with water clusters that have been intensively described before (Liu et al., 1996; Ludwig, 2001; Perera, 2011; Roy et al., 2005; Skinner et al., 2014): clusters involving from two to 100 water molecules are well known in the literature (Anacker and Friedrich, 2014; Gillan et al., 2016; Ludwig, 2001; Maheshwary et al., 2001; Møgelhøj et al., 2011). The average H-bond length was calculated on the 96 water molecules set on the (111) fluorite surface. The mean H-bond length is 1.84 Å, all the H-bonds lengths ranging between 1.44 Å and 2.46 Å. Also, 100% of the oxygen atoms in the bulk establish one H-bond with another water molecule, and 90% of them establish two H-bonds with other water molecules.

3. Scheelite

    3.1 Surfaces

Following previous studies, (001) and (112) cleavage surfaces have been created from the fully relaxed scheelite bulk. Supercells containing 96 atoms (16 Ca, 16 W, and 64 O) for the (001) surface and 192 atoms (32 Ca, 32 W, and 128 O) have been generated. They were made of four layers of calcium/tungsten atoms, each of them separated by two or four successive layers of oxygen atoms for the (001) and the (112) surfaces, respectively (Figure 90 and Figure 91). Therefore, the (001) surface consists of a plane of four six-coordinated calcium atoms and four tungstate anions (WO_4^{2-}) that, considering the high energy of the W-O bond (see Chapter 1), remain unbroken during the cleavage process (Figure 90). Besides, the (112) surface consists of a plane of eight six-coordinated along with eight tungstate ions, which also remain unbroken during the cleavage process (Figure 91). On the (001) surface, the calcium atoms are separated by 5.21 Å in all directions while they are separated by 3.86 Å on one direction on the (112) surface. This value is very similar to that of fluorite, which, however, exhibits a Ca-Ca surface distance of 3.86 Å in all the directions (Figure 82). On both (001) and (112) scheelite surfaces, the calcium atoms are six-coordinated while they are eight-coordinated in the scheelite lattice, inducing two dangling bonds per calcium atom. This is significantly higher than for fluorite, in which each calcium atom exhibits only one dangling bond that probably results in a lower reactivity. Occasionally, larger surfaces had to be generated for specific requirements such as large distances needed between two adsorbed atoms. Besides, the same methodology applied for fluorite was used here (see section 2.1). In the previous part (see section 2.3), the D2 and D3 correction methods exhibited very similar results with close structures, adsorption energies, and dispersion contributions. Hence, the choice was made in the present part to use only the D2 correction as it is computationally cheaper than the D3 method.
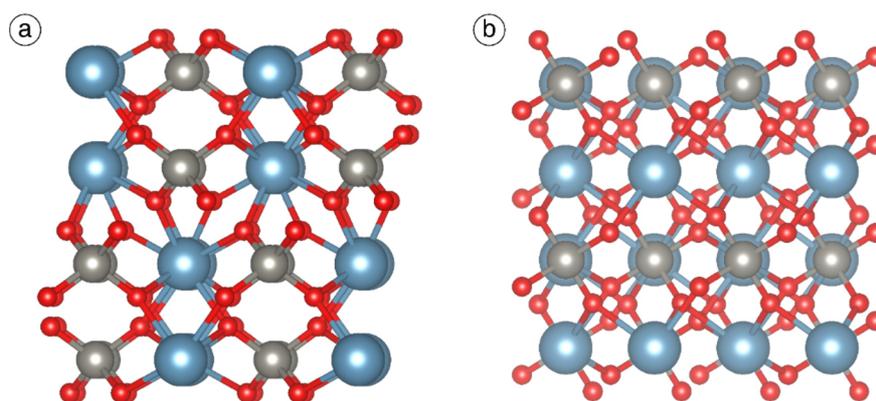
Figure 90. (001) scheelite surface seen from side (a) and from top (b). The blue, dark grey, and red balls represent the calcium, tungsten, and oxygen atoms, respectively.
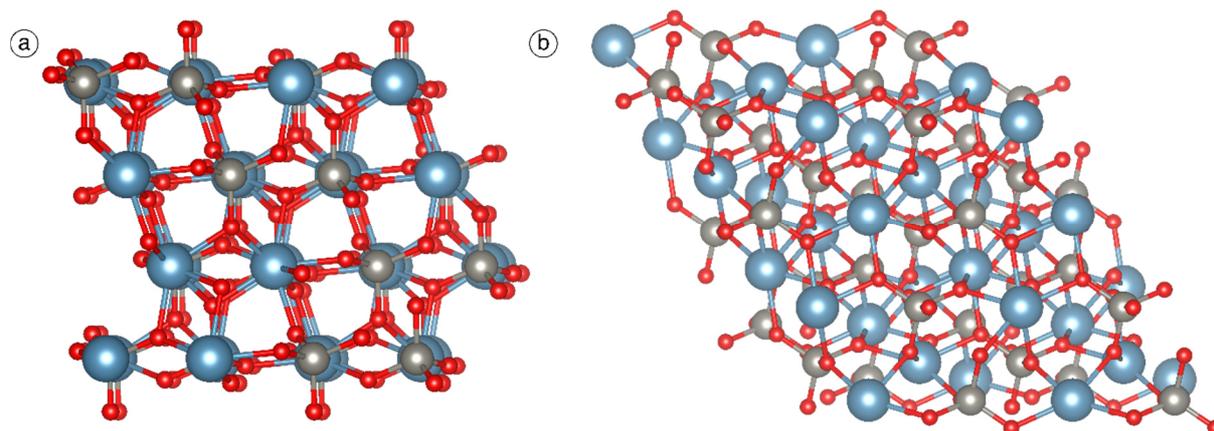
Figure 91. (112) scheelite surface seen from side (a) and from top (b). The blue, dark grey, and red balls represent the calcium, tungsten, and oxygen atoms, respectively.

3.2 Isolated water molecule on scheelite surfaces

3.2.1   Adsorption of dissociated water molecule

For the dissociated case, several configurations have been explored following the same procedure than for fluorite, as described in section 2.2.1: a hydroxyl group was placed above a calcium ion on the surface, with the O close to the calcium and the H oriented up, away from the surface. The lone H^+ ion was set at the vicinity of an oxygen atom part of a tungstate ion. Various distances between the OH and H groups were tested.

Short OH-H distance

As for fluorite, the H^+ and the OH^- were set on respectively an oxygen atom of a tungstate ion and a neighbouring calcium atom. For both surfaces, the H^+ ion is captured by the OH^- and the water molecule is reformed (Figure 92), indicating that the adsorption of water under molecular form is favoured compared to under dissociated form. However, significant differences can be observed between the two surfaces: on the (001) surface, the reformed water molecule adsorbs onto a lone calcium atom with $d_{Ca-O} = 2.29$ Å and establishes a hydrogen bond with an oxygen atom of the closest tungstate ion with $d_{H-O} = 1.58$ Å (Figure 92a). For this configuration, the calculated adsorption energy is $\Delta E_{ads} = -87.6$ kJ.mol^{-1} including $\Delta E_{disp} = -15.2$ kJ.mol^{-1}, indicating a significantly strong adsorption. Besides, on the (112) surface, the reformed water molecule adsorbs between two calcium atoms with Ca-O bond lengths of 2.60 Å and 2.66 Å (Figure 92b). One hydrogen atom of the water molecule is oriented towards the closest oxygen atom with $d_{H-O} = 1.88$ Å. This adsorption occurs with $\Delta E_{ads} = -127.3$ kJ.mol^{-1} including $\Delta E_{disp} = -25.2$ kJ.mol^{-1}, which represents a significant value. The difference in terms of adsorption energies between the two surfaces can be attributed to the Ca-Ca distance difference: on the (112) surface, the calcium atoms are close enough to allow the adsorption of the water molecule between two calcium atoms, which is impossible on the (001) surface considering the higher Ca-Ca distance. Overall, the high adsorption energies found for both surfaces for the adsorption

of a sole water molecule are probably induced by the significant reactivity of surface calcium atoms, resulting from the two above-mentioned two dangling bonds per calcium atom.

$\Delta E_{ads} = -87.60 \text{ kJ.mol}^{-1}$ $\Delta E_{ads} = -127.30 \text{ kJ.mol}^{-1}$
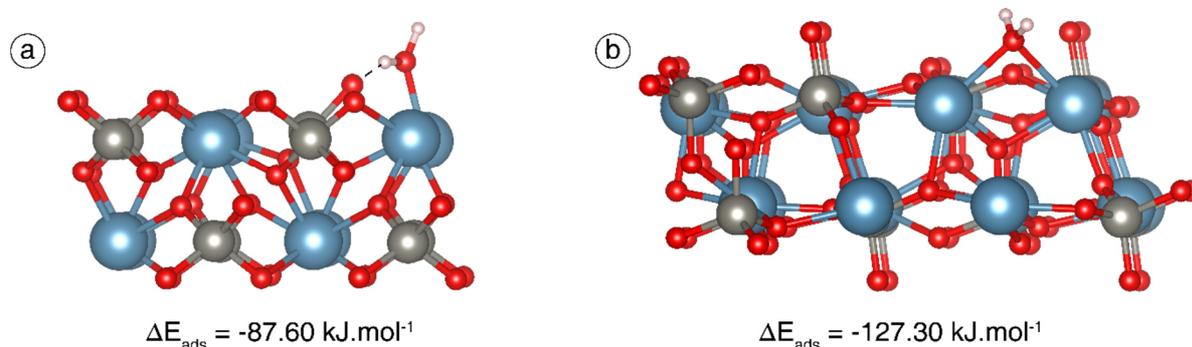
Figure 92. Adsorption of dissociated water molecule with short OH-H distance onto (001) (a) and (112) (b) scheelite surfaces. Only the upper part of the surfaces are displayed here. The blue, dark grey, red, and white balls represent the calcium, tungsten, oxygen, and hydrogen atoms, respectively.

High OH-H distance

For both (001) and (112) surfaces, when the proton is placed far from the hydroxyl group (>6 Å), *i.e.* with no interaction between them, the hydrogen ion forms a H-O bond with an oxygen atom part of a tungstate anion, which length is 1.01 Å. The H establishes a hydrogen bond with the closest oxygen atom, part of another tungstate ion, with $d_{H-O} \sim 1.70$ Å (Figure 93). For the (001) surface, the OH⁻ adsorbs between a calcium and a tungsten, establishing a Ca-O and a W-O bonds with $d_{Ca-O} = 2.27$ Å and $d_{W-O} = 2.08$ Å (Figure 93a). Hence, the tungsten is five-coordinated since it displays five W-O bonds in this configuration, which is slightly disfavoured as the calculated adsorption energy is $\Delta E_{ads} = +11.4 \text{ kJ.mol}^{-1}$. However, this means that, for a moderate OH⁻ activity, *i.e.* a slightly alkaline pH, the water molecule can adsorb under dissociated form onto the (001) scheelite surface. Besides, for the (112) surface, the OH⁻ group adsorbs between two calcium atoms (Figure 93b) since, on the considered surface, they are separated by only 3.86 Å. The lengths of the two created Ca-O bonds are 2.23 Å and 2.26 Å. The calculated adsorption energy for this configuration is $\Delta E_{ads} = -47.3 \text{ kJ.mol}^{-1}$ including $\Delta E_{disp} = -19.9 \text{ kJ.mol}^{-1}$, which indicates that the adsorption of water molecules under their dissociate form is possible spontaneously, albeit it is significantly less favoured than the adsorption under their molecular form (occurring with $\Delta E_{ads} = -127.3 \text{ kJ.mol}^{-1}$).

ΔE_{ads} = +11.40 kJ.mol^{-1} ΔE_{ads} = -47.30 kJ.mol^{-1}
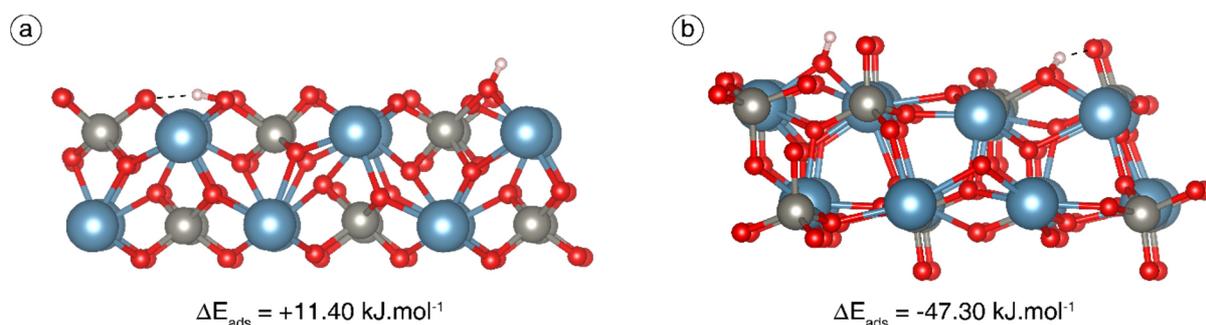
Figure 93. Adsorption of dissociated water molecule with high OH-H distance onto (001) (a) and (112) (b) scheelite surfaces. The (001) surface has been extended to have a large enough distance between the OH group and the H atom. Only the upper part of the surfaces are displayed here. The blue, dark grey, red, and white balls represent the calcium, tungsten, oxygen, and hydrogen atoms, respectively.

3.2.2   Adsorption of molecular water

Since the molecular adsorption of water appeared to be more stable than the dissociative adsorption, a water molecule was directly set above a surface calcium ion. Several configurations were tested, with different orientations of the hydrogen atoms of the water molecule. All the input configurations lead to the same final geometries. For the (001) surface, the water molecule adsorbs onto a calcium atom with d_{Ca-O} = 2.29 Å and establishes a hydrogen bond with an oxygen atom of the closest tungstate ion with d_{H-O} = 1.58 Å, as described previously when the water molecule is reformed (Figure 92a). The adsorption energies are roughly the same than those given previously, namely ΔE_{ads} ~ -87 kJ.mol^{-1} including ΔE_{disp} ~ -15 kJ.mol^{-1}. Significantly lower adsorption energies were however reported by Cooper and de Leeuw (2003), who found -22.1 kJ.mol^{-1} for the adsorption of water molecules on the (001) scheelite surface (Cooper and de Leeuw, 2003). For the (112) surface, the water molecule adsorbs onto a calcium atom with d_{Ca-O} = 2.45 Å while the two hydrogen atoms establish hydrogen bonds with two oxygen atoms from two different tungstate anions (Figure 94). This configuration results in a calculated adsorption energy of ΔE_{ads} = -102.3 kJ.mol^{-1} including ΔE_{disp} = -23.1 kJ.mol^{-1}, which is significantly lower in absolute value than when the molecular water is reformed from a dissociate molecule.
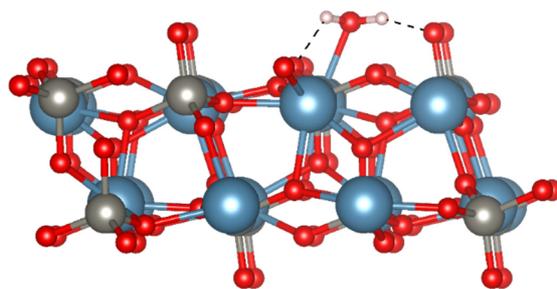
$$\Delta E_{ads} = -102.30 \text{ kJ.mol}^{-1}$$

Figure 94. Adsorption of molecular water on the (112) scheelite surface. Only the upper part of the surfaces are displayed here. The blue, dark grey, red, and white balls represent the calcium, tungsten, oxygen, and hydrogen atoms, respectively.

3.2.3 Substitution of WO_4^{2-} by OH^-

Finally, as for fluorite, the substitution of WO_4^{2-} by 2 OH^- on the (001) and (112) scheelite surfaces was investigated. Two hydroxyl groups were set at the place of a surface tungstate anion. Then, the following reaction was studied by calculating the energy of each component:

$$\text{Surface} + H_2O = \text{Surface}_{WO4->2OH} + H_2WO_4 \qquad (37)$$
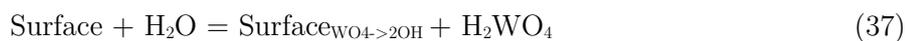
In the scheelite lattice, tungstate anions are eight-coordinated, *i.e.* each oxygen atom of the tungstate anion is bonded to two calcium atoms and the global tungstate anion is bonded to eight different calcium atoms. On both (001) and (112) surfaces, tungstate anions are only six-coordinated, *i.e.* they are bonded to six different calcium atoms. However, when a tungstate anion is substituted by two OH groups, these latter cannot establish six Ca-O bonds due to their low steric hindrance compared to a WO_4^{2-} anion. Hence, the substitution reaction is highly endothermic, with $\Delta E_r = +424.5$ kJ.mol^{-1} for the (112) surface and $\Delta E_r = +321.2$ kJ.mol^{-1} for the (001) surface. This mechanism seems therefore very unlikely to occur on scheelite surface, which is consistent with the fact that scheelite dissolution is favoured at acidic pH rather than at alkaline pH (Atademir et al., 1979; K. I. Marinakis and Kelsall, 1987).

3.3 Towards a full hydration of the scheelite surfaces

As for fluorite, once the most favourable configuration for a single molecule of water determined, the progressive hydration of the surfaces was investigated. Then, two, four, and eight H_2O molecules were placed on the surfaces composed of four calcium atoms and four tungstate anions. For that study, the (112) surface was reduced to be comparable to the (001) surface that originally consisted of a plane of four calcium atoms. For the (001), the first four water molecules were placed sequentially on the four surface calcium atoms while the last four molecules were set on tungstate anions, their hydrogen atoms pointing towards the surface. For the (111) surface, the first two water molecules were placed in the most favoured configuration, *i.e.* each water molecule between two calcium atoms. Then, for four water molecules, each molecule was set on

a calcium atom while the last four molecules were set on tungstate anions, in a similar way to the (001) surface. On fluorite, temperature did not change significantly the adsorption mechanisms but only shifted the adsorption energies of around -10 kJ.mol^{-1}. Hence, the choice was made to study the constitution of a water monolayer at 0 K. The results are presented in Figure 95. On the (001) surface, the surface coverage has no significant impact on the average adsorption energy per water molecule, which stays constant at around -75 to -80 kJ.mol^{-1} (Figure 95). This indicates that, although the first four water molecules occupy the four surface calcium atoms, the last four water molecules adsorb with similar adsorption energies than the first ones. Interestingly, on the final geometries, two water molecules adsorb onto a same calcium atom, with however different Ca-O distances, 2.45 Å and 2.84 Å. This phenomenon was observed by Cooper and de Leeuw (2003), who reported the adsorption of two water molecules on each surface calcium atom of the (001) scheelite surface (Cooper and de Leeuw, 2003). The same authors mentioned average molecular adsorption energies for a full surface coverage of -22.1 kJ.mol^{-1}, which is significantly lower than the values calculated here (Cooper and de Leeuw, 2003). This is probably due to the use of different methods, since these authors employed interatomic potentials derived from DFT but, strictly speaking, not DFT. Besides, on the (112) surface, the average adsorption energy per water molecule decreases between two and four molecules, which results from the change in the adsorption, going from each water molecule adsorbed between two calcium atoms to each water molecule adsorbed onto a lone calcium atom. For eight water molecules, *i.e.* 100% coverage, the average adsorption energy per molecule is the same between the (001) and the (112) surfaces, due to the two above-mentioned phenomena.
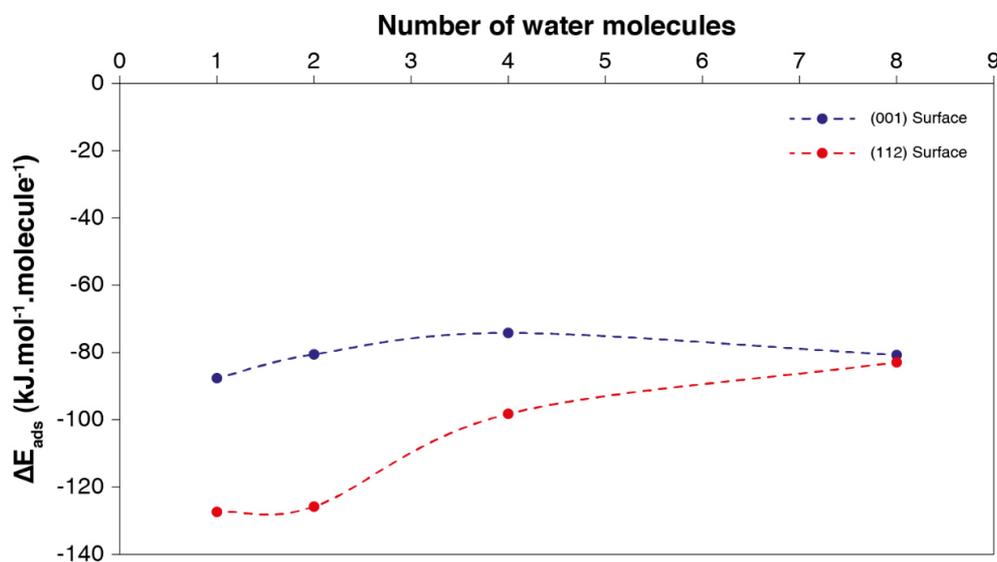
Figure 95. Adsorption energies per water molecule for the (001) and (112) scheelite surfaces when the water coverage is increased from one water molecule to eight water molecules.

Then, for each surface, the cell was completely filled with water molecules to reach a density of 1.00 g.cm^{-3}. Moreover, to investigate the influence of the temperature on the hydration mechanisms, the calculation was performed at T = 300 K. Snapshots of the *ab initio* molecular dynamics simulations are presented in Figure 96. For the (001) surface, the adsorption of two

water molecules per calcium atom, observed previously, also occurs for a full hydrated cell at 300 K. Indeed, the four calcium atoms constituting the surface are occupied by seven water molecules adsorbed onto them (Figure 96a). Also, three water molecules are adsorbed by hydrogen bonds established with oxygen atoms of surface tungstate anions. For the bulk of water, the geometries are structured in a way that the two H of two molecules point towards an oxygen of another molecule (Figure 96a). The H of the two other molecules are establishing hydrogen bonds with other multi-molecular structures, establishing the same water molecules clusters described for fluorite and intensively characterised in the literature, see section 2.3. The four calcium atoms of the (112) surface are occupied by six water molecules adsorbed (Figure 96b): four water molecules are adsorbed onto the four surface calcium atoms while two additional molecules are adsorbed between two calcium atoms, as observed at 0 K and for low coverage (see Figure 92b). Also, three water molecules adsorb by establishing hydrogen bonds with surface tungstate anions. The bulk of water is organised in a same way than for the (001) surface or for fluorite, see previously.
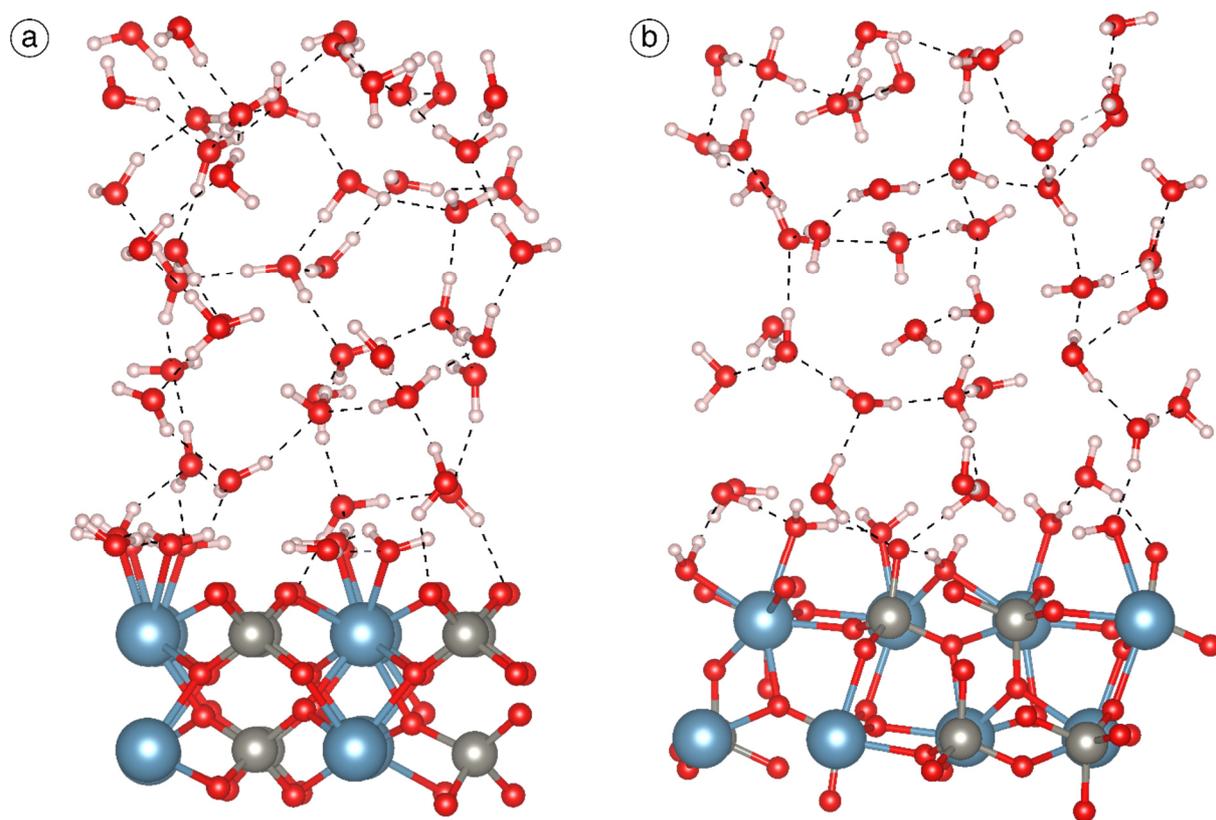
Figure 96. Snapshots of side views of the (001) (a) and (112) (b) scheelite surfaces with the vacuum above the surface completely filled with water molecules so that the density is 1.00 g.cm^{-3}. The blue, dark grey, red, and white balls represent the calcium, tungsten, oxygen, and hydrogen atoms, respectively.

4. Conclusions

In this chapter, the interplay between the (111) surface of fluorite, the (001) and the (112) surfaces of scheelite, and water molecules has been investigated using density functional theory calculations including a correction for van der Waals interactions at 0 K and at 300 K. The results demonstrated that water adsorbs in its molecular form on a lone calcium atom in the case of fluorite and the (001) scheelite surface and between two calcium atoms in the case of (112) scheelite surface. The calculated adsorption energies are of $\Delta E_{ads} \approx$ -55 kJ.mol^{-1} for fluorite, of $\Delta E_{ads} \approx$ -87 kJ.mol^{-1} for (001) scheelite, and of $\Delta E_{ads} \approx$ -127 kJ.mol^{-1} for (112) scheelite, indicating that the adsorption of water on scheelite is significantly more favoured than on fluorite (Figure 97). In addition, the adsorption of dissociate water is favourable on both scheelite surfaces with, nonetheless, an exothermic adsorption only for the (112) surface. This indicates a strong ability of scheelite surfaces to be hydroxylated, which probably results in a lower required pH to adsorb hydroxyl groups onto scheelite calcium atoms compared to fluorite. Besides, since fluorite and scheelite are semi-soluble salts, the substitution of F$^-$ or WO$_4^{2-}$ by OH$^-$ on the surface was investigated and was found to be energetically significantly disfavoured, for all surfaces. Then, the interaction of the surfaces with several water molecules was studied at 0 K and confirmed at 300 K by *ab initio* molecular dynamics simulations. Interestingly, on fluorite, half of the surface calcium atoms are occupied by an adsorbed water molecule while, on the (001) scheelite surface, each surface calcium atom exhibits two adsorbed water molecules and, on the (112) scheelite surface, each surface calcium atom displays one water molecule adsorbed with a water molecule adsorbed between two surface calcium atoms, resulting in three water molecules adsorbed on two calcium atoms.
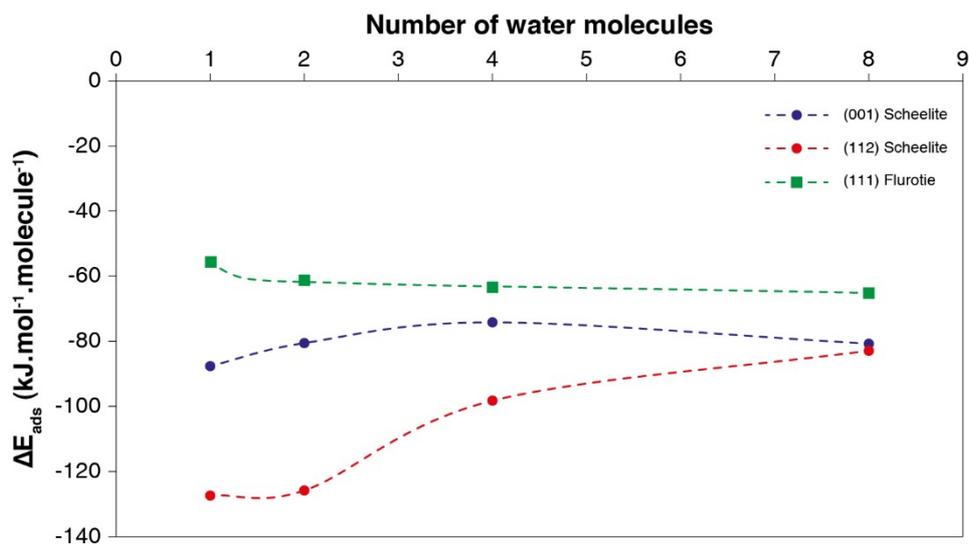
Figure 97. Comparison of the surface coverage with water molecules on the three different studies surfaces.

Fundamentals of the adsorption of fatty acids onto calcium minerals

1. Introduction

In previous chapters, mostly Chapter 5, considerable synergistic effects between fatty acids with different structures or between fatty acids and a fatty alcohol have been exhibited. At the moment, they are poorly understood in terms of molecular mechanisms and DFT was used to gain understanding in these systems. However, one main scientific questioning was raised when fatty acids were set on surfaces: how do they adsorb? Indeed, several adsorption configurations for fatty acids on calcium minerals were suggested in the literature, see Chapter 1, but supported only by indirect experiments. For decades, this hot topic has been intensively discussed without the emergence of a final theory for the adsorption of carboxylates on calcium minerals and, more generally, of anionic collectors on semi-soluble minerals. However, recent developments in the calculations devices allow now to perform DFT calculations on systems with moderate to large sizes, including mineral surfaces with organic molecules adsorbed. Hereafter, the fundamentals of the adsorption of fatty acids on fluorite, considered as an archetype of calcium minerals, are investigated by means of DFT calculations performed at 0 K and 300 K, under vacuum and hydrated conditions. In Chapter 7, the hydration state of fluorite was investigated to serve as a basis for the study of fatty acids adsorption, presented in the present chapter, since the calcium minerals surfaces are systematically hydrated prior the adsorption of flotation reagents. Also, to obtain experimental validations, IR spectra are simulated and compared to experimental ones. For most of the simulations presented in this chapter, octanoic acid/octanoate anion are used since it exhibits a long enough chain to avoid any influence of the induction effect and short enough to limit the computational costs by reducing the cell size. **A part of this work has been published in the Journal of Physical Chemistry B under the title "Molecular Insight into Fatty Acid Adsorption on Bare and Hydrated (111) Fluorite Surface".**

2. Adsorption of carboxylic acids in vacuum conditions

2.1 Adsorption under molecular form

Depending on the pH, the carboxyl group can be under –COOH form or under –COO$^-$ form. It is assumed that for pH < pKa -1, the main form is –COOH while for pH > pKa + 1, it is the -COO$^-$. However, most of the minerals can be floated at acidic and alkaline pH (Fuerstenau and Healy, 1972), proving that both acidic and anionic form of the carboxyl group can adsorb onto minerals surface. It is assumed that a physisorption occurs for the carboxylic acid (Fuerstenau and Bunge, 2006; Fuerstenau and Healy, 1972; Fuerstenau and Palmer, 1976) while the carboxylate chemisorbs (Fa et al., 2003; Lovell et al., 1974; Marinakis and Shergold, 1985a; Mielczarski et al., 1998, 1999; Rao et al., 1991b, 1991a). At the moment, the adsorption mechanisms are not well understood for both forms although some authors confirmed the adsorption of the methanoic acid onto the (111) fluorite surface, reporting adsorption energies of -56.3 to -75.9 kJ.mol^{-1} but without a dispersion correction (Cooper and Leeuw, 2002). The first step in the investigation of fatty acids adsorption onto mineral surfaces is to gain understanding in the fundamentals of their adsorption and, therefore, simulations in vacuum conditions can be performed. It allows, in first approximation, to unravel the molecular mechanisms involved in

the adsorption processes by freeing the study from the influence of water. Methanoic acid was used to study the geometry of an adsorbed carboxyl group on the (111) fluorite surface. Six different configurations were possible to set the molecule on the surface:

1. Each oxygen atom is set on a calcium atom, doing a bidentate binuclear adsorption;
2. The two oxygen atoms are placed on the same calcium atom, forming a bidentate adsorption;
3. The double-bonded oxygen is placed on a calcium atom, the –O-H pointing away to the surface;
4. The –O-H is set on a calcium atom, the double-bonded oxygen pointing away to the surface.
5. The double-bonded oxygen is placed between two calcium atoms, the –O-H pointing away to the surface;
6. The –O-H is set between two calcium atoms, the double-bonded oxygen pointing away to the surface.

Among all the tested cases, the bidentate binuclear adsorption (1) is the most favoured (Figure 98). The calculated adsorption energy is ΔE_{ads} = -78.2 kJ.mol^{-1}, which can be decomposed in ΔE_{disp} = -17.6 kJ.mol^{-1} and ΔE_{PBE} = -60.6 kJ.mol^{-1}. The PBE contribution obtained here is in nice agreement with the computed adsorption energy of -56.3 kJ.mol^{-1} with the PW91 functional without dispersion correction reported in the literature (Cooper and Leeuw, 2002). In this configuration, the double-bonded oxygen atom adsorbs onto the calcium atom with d_{Ca-O} = 2.44 Å while the hydrogen of the –OH group points towards the closest fluorine atom with d_{H-F} = 1.48 Å (Figure 98).

The same geometry is reformed during the relaxation when the methanoic acid is set in a bidentate configuration (2) and in configuration 6 (Figure 98). The adsorption energies are very similar. For cases 4 and 5, the methanoic acid becomes sub-parallel to the surface, and the two oxygen atoms are in interaction with two calcium atoms with both d_{Ca-O} = 2.84 Å. The H of the –OH group also points towards the closest fluorine atom with d_{H-F} = 1.48 Å. The calculated adsorption energies are ΔE_{ads} ≈ -58.4 kJ · mol^{-1} including ΔE_{disp} ≈ -29.4 kJ · mol^{-1}. The absolute value of the energy is lower than for the cases 1, 2 and 6 whereas the dispersive forces contribution is significantly higher. It can be explained by the increase of the induced dipole-induced dipole forces when the oxygen of the –OH group interacts with the calcium atom. Finally, the case 3 is the least favoured, with ΔE_{ads} = -41.3 kJ.mol^{-1} including ΔE_{disp} = -15.4 kJ.mol^{-1}. Even if the double-bonded oxygen atom adsorbs onto a calcium atom, the H atom of the –OH group cannot interact with any fluorine atom, which could explain the low adsorption energy in absolute value. Overall, the adsorption energies obtained for the adsorption of the methanoic acid are consistent with a physisorption of this species onto the (111) fluorite surface, which has been suggested in the literature by French and co-workers (1954) and confirmed later on by many authors (French et al., 1954; Fuerstenau and Bunge, 2006; Fuerstenau and Healy, 1972; Fuerstenau and Palmer, 1976).
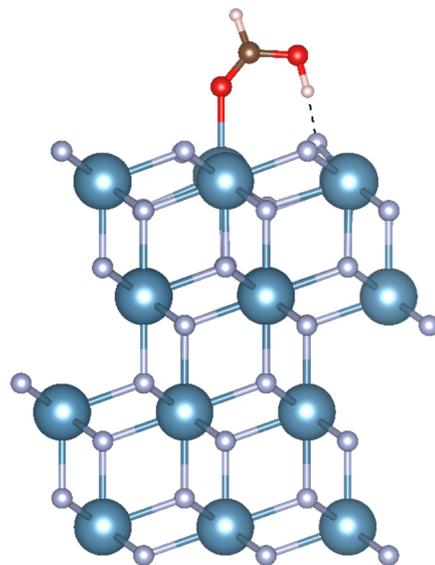
Figure 98. Adsorption of a methanoic acid molecule on the (111) fluorite surface after DFT relaxation, in side view. The blue, grey, red, marron, and white balls represent the calcium, fluorine, oxygen, carbon, and hydrogen atoms, respectively. The dashed line corresponds to a hydrogen bond.

2.2 Adsorption under dissociate form

The adsorption of the methanoic acid could be also possible by the dissociation of HCOOH into HCOO$^-$ and H$^+$ at the vicinity of the surface. This dissociation was investigated, comparing the system where the carboxylate and the hydrogen atom are both adsorbed to the system where the HCOOH is set far from the surface. The methanoate was set on the surface with the most favoured configuration determined previously, namely the bidentate binuclear configuration. The proton was set between two fluorine atoms, at different distances of the carboxyl group. When it is placed close to the carboxyl group, at $d_{Carboxyl-H} = 2.5$ Å, the carboxylic acid is reformed and adsorbs as described previously, in a monodentate configuration, see Figure 98. When the H is placed far enough, at $d_{Carboxyl-H} = 7.1$ Å, it establishes two H-F bonds, while the carboxylate adsorbs onto calcium atoms with the bidentate binuclear configuration as displayed in Figure 99. Nonetheless, the adsorption does not compensate the dissociation as the global reaction energy is $\Delta E_r = 75.2$ kJ.mol^{-1} including $\Delta E_{r-disp} = -29.2$ kJ.mol^{-1}. This indicates that, when the carboxylic acid is under acidic form, it adsorbs as it, without dissociating at the vicinity of the surface.

3. Adsorption of carboxylates in vacuum conditions

In flotation, carboxylic acids are mostly used at alkaline pH, in the range where pH>pKa+1. Hence, for most flotation flowsheets used worldwide, the carboxylic acids are under their anionic form, *i.e.* the carboxylate anion. Considering the preparation of the fatty acids prior to flotation, it can be assessed that the carboxylate anion adsorb on the calcium minerals surfaces either bonded with a sodium cation (Na$^+$) or free. This problematic will be discussed further, see section

4.1.2. Also, different chain lengths can be used for the fatty acids and their influence is still poorly understood albeit it exhibited, in Chapter 5, significant effects on the flotation performances. Hereafter, the various adsorption mechanisms for carboxylates are deeply investigated in vacuum conditions as well as the effect of the chain length onto the adsorption.

3.1 The carboxyl group during the adsorption at 0 K

3.1.1   Free carboxylate on the surface

In first approximation, it was assessed that the carboxylate molecule adsorbs freely, under its anionic form, with an additional valence electron due to the deprotonation reaction. Hence, in the calculations described hereafter, the carboxylate molecules were modelled by adding an extra valence electron in the cell, which was subsequently localised during the DFT calculation. Overall, different configurations were tested for the adsorption of the methanoate molecule, $HCOO^-$:

1. Each oxygen atom is set on a calcium atom, doing a bidentate binuclear adsorption;
2. The two oxygen atoms are placed on the same calcium atom, forming a bidentate adsorption;
3. One oxygen is placed on a calcium, the other one is pointing away to the surface, forming a monodentate adsorption;
4. One oxygen is placed between two calcium atoms, the other one is pointing away to the surface;

The most favoured case is the bidentate binuclear adsorption (1). The calculated adsorption energy is ΔE_{ads} = -226.4 kJ.mol^{-1} including ΔE_{disp} = -18.5 kJ.mol^{-1}. Each oxygen atom establishes a bond with a surface calcium atom, with d_{Ca-O} = 2.33 Å for both (Figure 99a). The hydrogen atom of the C-H is pointing away the surface. The bidentate adsorption (2) and the case (4) reform the same geometry with very similar adsorption energies. The case (3) leads to a different configuration. Only one oxygen atom establishes a bond with a surface calcium atom, the other oxygen pointing away the surface (Figure 99b). However, the bond is shorter, d_{Ca-O} = 2.19 Å and the adsorption energy is lower in absolute value, ΔE_{ads} = -167.6 kJ.mol^{-1} including ΔE_{disp} = -11.2 kJ.mol^{-1}. The significantly lower adsorption energy in absolute value indicates that this adsorption is possible but occurs more rarely than the bidentate binuclear one. Two possible configurations for the carboxylate adsorption onto the fluorite surface were reported in the literature using spectroscopic methods (Mielczarski et al., 2002, 1998). The first identified configuration was a monodentate adsorption, which is accordance with what was found in the present study. The second one was a bidentate (mononuclear) adsorption, a configuration which was not possible to get from the simulations performed in the present study, in vacuum. However, these experimental investigations were conducted in aqueous medium at room temperature while this section was realised without water and at 0 K.
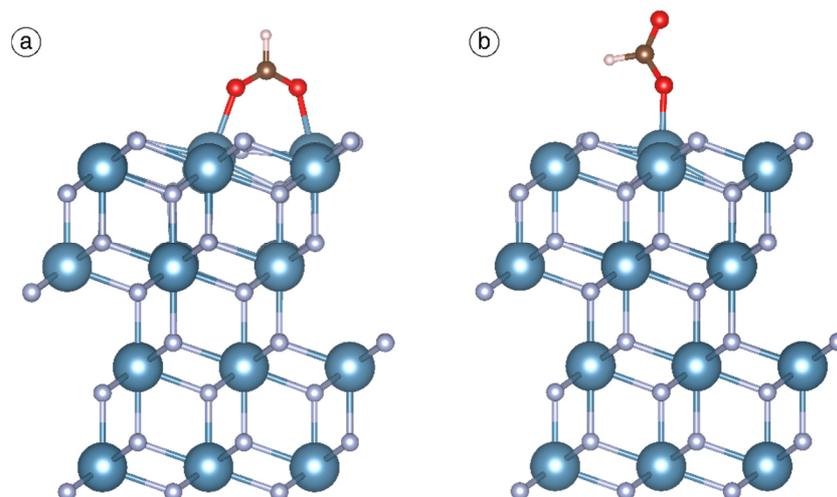
Figure 99. Two possible configurations for the adsorption of a methanoate molecule onto the (111) fluorite surface after DFT relaxation, in side views: bidentate binuclear configuration (a) and monodentate adsorption (b). The blue, grey, red, marron, and white balls represent the calcium, fluorine, oxygen, carbon, and hydrogen atoms, respectively.

Nevertheless, the methanoate molecule does not describe satisfactorily the carboxylate anions since its aliphatic chain is very short, induction phenomena being restricted to beyond four carbon atoms in the chain (Kanicky and Shah, 2002). Hence, an octanoate molecule, representing a good compromise between the chain length and the calculation cost, was considered and used for all the calculations presented hereafter. First, the above-described calculations were performed again with octanoate instead of methanoate. Interestingly, due to the higher chain length, the monodentate adsorption configuration cannot be observed. Hence, octanoate adsorbs under the sole bidentate binuclear mode, see Figure 100a. The calculated adsorption energies are very similar to that of methanoate, namely ΔE_{ads} = -234.9 kJ.mol^{-1} including ΔE_{disp} = -24.2 kJ.mol^{-1}, with also very similar Ca-O bond lengths (around 2.33 Å for both).

3.1.2   Sodium carboxylate

The carboxylate anion can also approach the surface bonded to a Na$^+$ that comes from the NaOH used for the deprotonation reaction. Hence, the carboxylate can adsorb onto calcium surface atoms but with the Na$^+$ staying at the vicinity of the carboxyl group and the surface. This system was modelled by DFT calculations. After the relaxation, the carboxylate anion is adsorbed in bidentate binuclear mode (Figure 100b): each oxygen atom is bonded to a different surface calcium atom with d_{Ca1-O1} = 2.45 Å and d_{Ca2-O2} = 2.54 Å. In addition, the Na$^+$ is bonded to two surface fluorine atoms with d_{Na-F1} = d_{Na-F2} = 2.33 Å and to the two oxygen atoms of the carboxylate with bond lengths of 2.38 Å and of 2.35 Å (Figure 100b). The calculated adsorption energy for this system is ΔE_{ads} = -122.3 kJ.mol^{-1} including ΔE_{disp} = -58.4 kJ.mol^{-1}, which is significantly lower than when the carboxylate is without the Na$^+$ on the surface.

If the carboxylate anion approaches the surface bonded to a Na^+, it can also adsorb with this latter acting as a bridging cation. This mechanism has been explicitly suggested by few authors (Rao et al., 1990) albeit, for many authors, the chemisorption of carboxylate can be related to the adsorption of sodium carboxylate, displaying the peak at 1555-1560 cm^{-1} in IR (see Chapter 1 for further explanations). Hence, this system was also modelled by DFT calculations to compare it with other adsorption possibilities for the carboxylate anion. After the relaxation, the carboxylate anion is adsorbed in bidentate (mononuclear) mode onto the bridging Na^+ with $d_{Na-O1} = d_{Na-O2} = 2.26$ Å (Figure 100c). This latter is adsorbed onto a fluorine atom of the fluorite surface with $d_{Na-F} = 2.25$ Å. For this system, the calculated adsorption energy is $\Delta E_{ads} = -56.5$ kJ.mol^{-1} including $\Delta E_{disp} = -19.9$ kJ.mol^{-1}, which represents significantly lower value compared to the previous adsorption configurations.

3.1.3 Substitution of a surface fluorine atom

Besides, the adsorption of carboxylate anions onto fluorite surface (and calcium minerals surfaces in general) can be depicted as an anion exchange. It was first postulated by Nixon and Cook (1950), later on by Peck and Wadsworth (1965), and more recently by Finkelstein (1989), who suggested this reaction for the anion exchange (Finkelstein, 1989; Nixon and Cook, 1950; Peck and Wadsworth, 1965; Young and Miller, 2000):

$$Ca|X(H_2O)_n + NaOl = Ca|Ol(H_2O)_{n-m} + mH_2O + NaX \qquad (38)$$
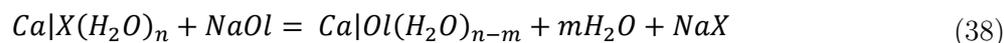
This reaction was investigated by means of DFT calculations with octanoate: the energy of each component of the previous equation was calculated in vacuum conditions and the total reaction energy was calculated. However, this reaction was investigated in vacuum, *i.e.* without water molecule in the system, which did not represent a problem since the desorption of water molecules from the surface has been described in Chapter 7. Assessing that the desorption energy of a water molecule is equivalent to the adsorption energy, the desorption of a water molecule from a calcium atom would represent around 55 kJ.mol^{-1}. Moreover, this reaction is an anion exchange and it was demonstrated in Chapter 7 that water molecules are physisorbed onto half of the surface calcium atoms on the (111) fluorite surface and only by means of hydrogen bonds onto surface fluorine atoms. Overall, reaction (38) is endothermic, displaying a reaction free energy of $\Delta E_r = +66.0$ kJ.mol^{-1} including $\Delta E_{r-disp} = -16.0$ kJ.mol^{-1}. The carboxylate anion adsorbs with one oxygen atom substituting the fluorine atom, establishing two Ca-O bonds with two different surface calcium atoms while the second oxygen atom establishes a Ca-O bond with a third calcium atom (Figure 100d).

3.1.4 Summary and discussion

In this part, four different adsorption modes were investigated for the adsorption of carboxylate onto the (111) fluorite surface in vacuum conditions. The presence of the Na^+ seems crucial since it adsorbs with the carboxylate anion and, consequently, decreases the adsorption energies in absolute value. Interestingly, when the Na^+ acts a bridging cation, the carboxylate adsorbs onto

a surface fluorine and not on a surface calcium as it is the case for the other adsorption modes. This induces that no water molecule should be desorbed from calcium atom to allow the carboxylate adsorption, increasing the global adsorption energy, *i.e.* the adsorption energy taking into account the prior water desorption. Moreover, the adsorption through a bridging Na$^+$ could result in a higher density of carboxylate in the adsorption layer since the surface cations are still available for adsorption. Overall, the four relaxed systems are presented in Figure 100 with their respective adsorption energies. Besides, authors also suggested the adsorption of carboxylates species onto fluorite by bridging onto a calcium atom coming from the mineral dissolution and re-adsorbed onto surface fluorine atom(s). Nonetheless, this assumption was not considered in the present study since it would not represent a realistic adsorption model regarding the low dissolution kinetics.
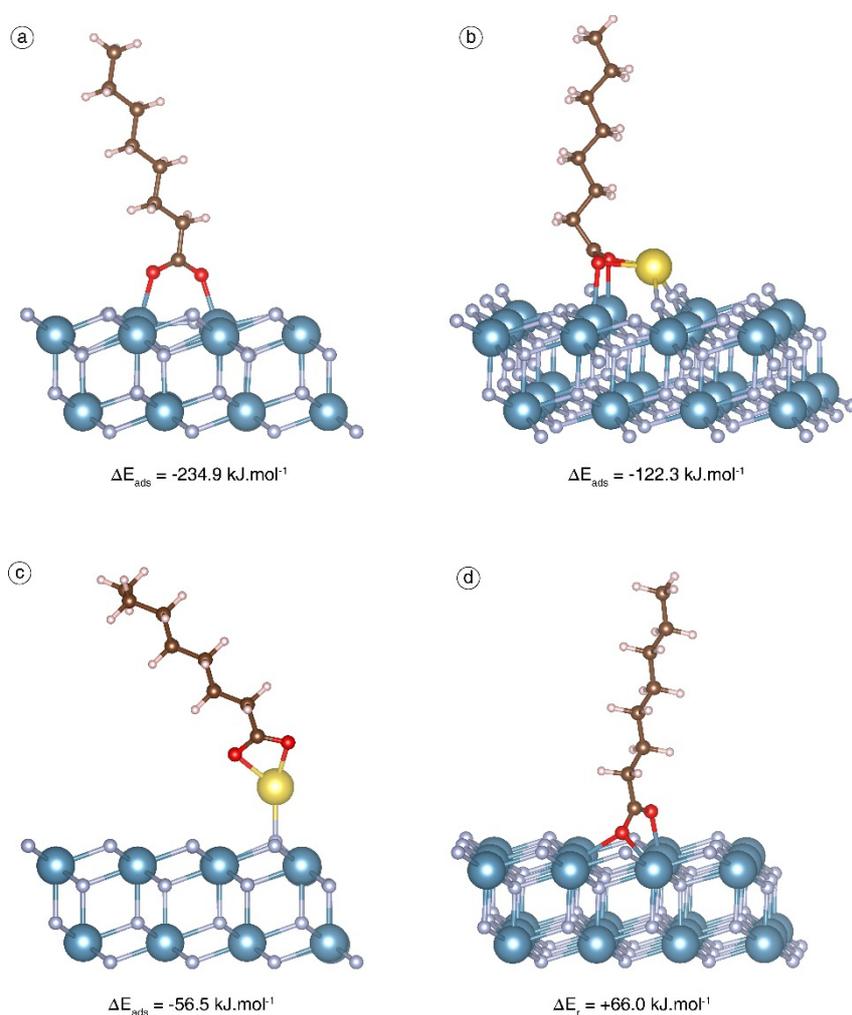
Figure 100. The four adsorption modes investigated after DFT relaxation and their respective adsorption (or reaction) energy for the adsorption of octanoate, with or without a neutralising Na$^+$, on the (111) fluorite surface in side views. The blue, grey, red, yellow, marron, and white balls represent the calcium, fluorine, oxygen, sodium, carbon, and hydrogen atoms, respectively.

3.2 The global molecule configuration during the adsorption at 0 K

The fatty acids used as flotation collectors can be written as R-COO⁻, R being a linear aliphatic chain composed of between 11 and 17 carbons. This parameter can impact strongly the global configuration of the adsorption. Hence, the adsorption of fatty acids with different chain lengths on the (111) fluorite surface was investigated, in vacuum conditions. The choice was made to study only the carboxylate forms as they are the stable form in flotation conditions. The most favoured adsorption mode was used for this study, *i.e.* the adsorption of free carboxylate species (without Na⁺). For each saturated-chain length, the adsorption with the molecule being perpendicular to the surface ("vertical" adsorption) was compared to the case where the molecule is parallel to the surface ("flat" adsorption). Results are presented in Figure 101.
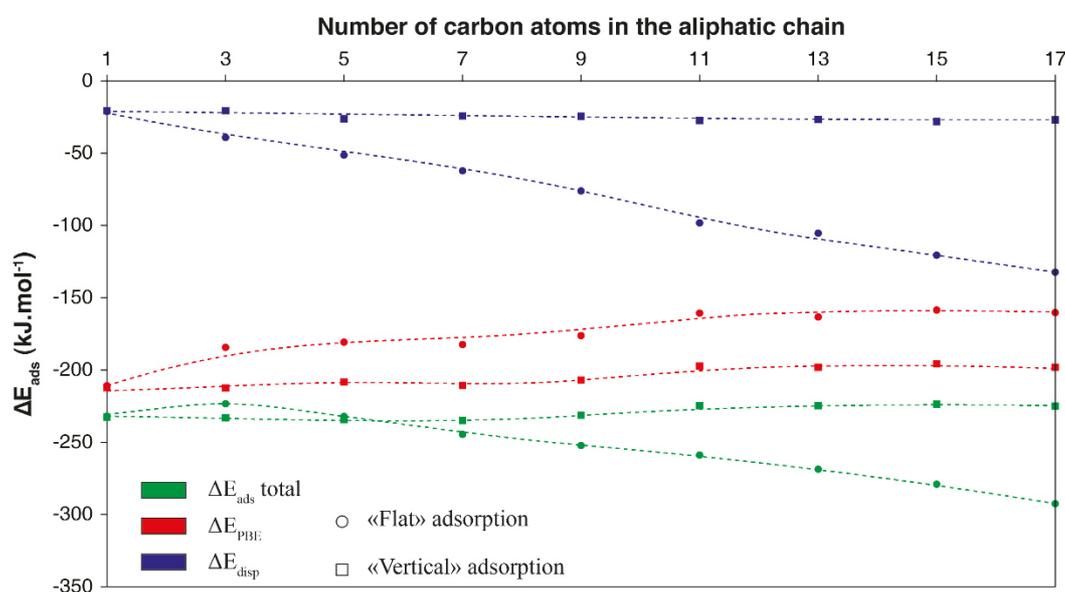
Figure 101. Evolution of the total adsorption energy and its PBE and dispersive components as a function of the number of carbon atoms in the aliphatic chain for vertical and flat adsorptions. One carbon means the ethanoate molecule, four means the butanoate...

The chain length does not impact significantly the adsorption energies when the molecules are adsorbed in "vertical" configuration, which are around -240 kJ.mol⁻¹. The corresponding contribution of dispersion interactions to the total adsorption energies are also similar whatever the chain length, around -20 kJ.mol⁻¹. It can be concluded that for the "vertical" adsorption mode, the adsorption is mainly controlled by the short range interaction between the carboxylate group and the surface.

Regarding the "flat" adsorptions, the adsorption energies increase in absolute values when the chain length is increased, ranging between -200 kJ.mol⁻¹ for R = CH₃ to -292.5 kJ.mol⁻¹ for R = C₁₇H₃₅. Moreover, the contribution of dispersive energy increases in absolute values with the chain length, from -21.0 kJ.mol⁻¹ for R = CH₃ to -132.3 kJ.mol⁻¹ for R = C₁₇H₃₅. It demonstrates that induced dipole-induced dipole interactions exist between the hydrogen atoms of the chain and the surface fluorine atoms. These forces are the main parameter explaining the increase of

the global adsorption energies when the chain length increases, the adsorption energies and the contribution from dispersion following the same trend. Also, the PBE contribution decreases slightly when the chain length is increased. It can be explained by a twist of the first C-C bond following the carboxyl group that occurs to allow the "flat" adsorption (Figure 102).
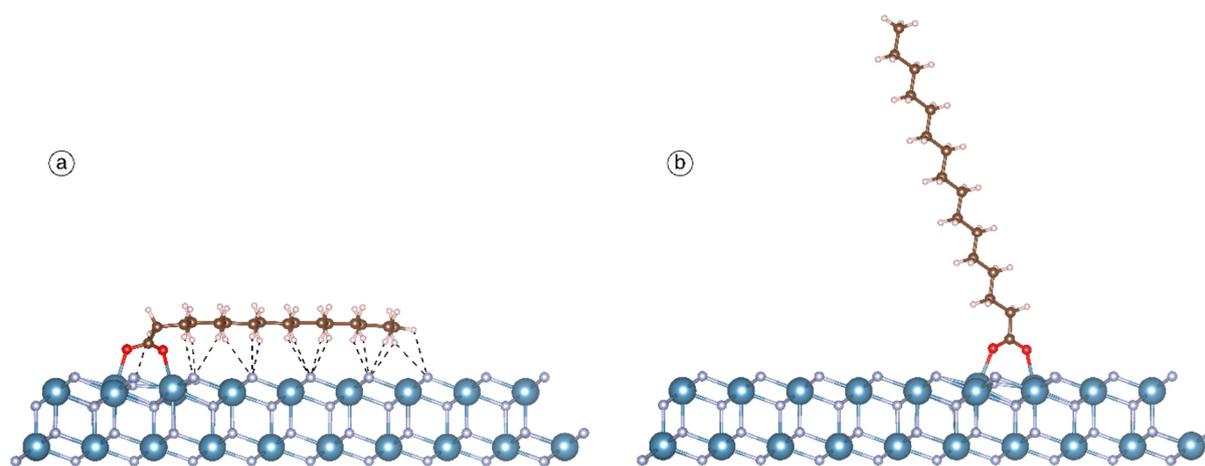
Figure 102. Adsorption of a hexadecanoate (palmitate) molecule (15 carbon atoms in the chain) in "flat" adsorption (a) and in "vertical" adsorption (b) after DFT relaxation. The blue, grey, red, marron, and white balls represent the calcium, fluorine, oxygen, carbon, and hydrogen atoms, respectively.

Dispersion forces make the "flat" adsorption much more favoured than the "vertical" adsorption for chain length longer than $R = C_5H_{11}$. For short chains, there is no difference in terms of adsorption energy between the "vertical" and the "flat" configurations. Also, the chain length and the adsorption mode ("flat" or "vertical") do not impact the geometry of the carboxyl group as it systematically adsorbs in the double-monodentate configuration with $d_{Ca1-O1} = d_{Ca2-O2} = 2.33$ Å (Figure 102). After the relaxation, the distances between the hydrogen atoms of the chain and their closest fluorine atom were measured for the different chain lengths in "flat" adsorption (Figure 102). The d_{H-F} ranges between 2.35 Å and 3 Å with a mean value of 2.59 Å.

3.3 The carboxyl group during the adsorption at 300 K

The previous calculations were conducted at T = 0 K. Therefore, to approach more realistic conditions and to assess the influence of the temperature on the adsorption energies and configurations, *ab initio* molecular dynamics simulations were performed at T = 300 K. Calculations with the methanoic acid and with the methanoate (R = H) were performed and, to gain understanding on the influence of the chain length, with the ethanoate ($R = CH_3$), the butanoate ($R = C_3H_7$) and the octanoate ($R = C_7H_{15}$). The objectives were to determine the geometries of the carboxyl group and the chain as well as the adsorption energies when they adsorb onto the (111) fluorite bare surface at T = 300 K. The most favoured adsorption mode was used for this study, *i.e.* the adsorption of free carboxylate species (without Na^+).

At 300 K, the carboxylate adsorbs in bidentate binuclear configuration as found for T = 0 K, whatever the chain length. Each oxygen atom adsorbs on a different calcium atom with d_{Ca-O} = 2.40 Å on average and a standard deviation being only 0.12 Å. As at T = 0 K, the chain length impacts the global geometry of the collector: the octanoate molecule becomes sub-parallel to the surface over time as the hydrogen atoms are getting closer to the fluorine atoms, between 2 and 3 Å on average. Also, the calculated internal adsorption energies increase in absolute value with the chain length (Figure 103), highlighting the same phenomenon observed previously at T = 0 K: the hydrogen bonds between the chain hydrogen atoms and the surface fluorine atoms make the "flat" adsorption more favoured. Overall, at T = 300 K, the internal adsorption energies range from -175.6 kJ.mol^{-1} for the methanoate molecule to -189.5 kJ.mol^{-1} for the octanoate molecule.
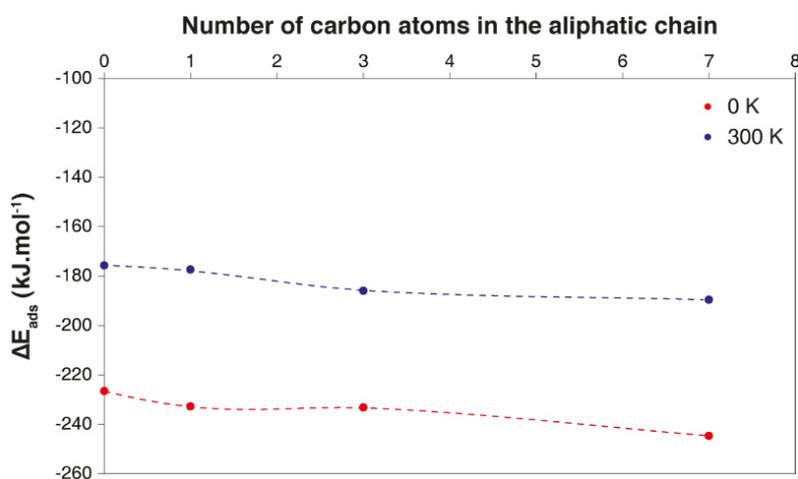
Figure 103. Evolution of the adsorption energy as a function of the aliphatic chain length at T = 0 K and T = 300 K.

4. Adsorption of carboxylates in hydrated conditions

The flotation process is conducted not only at room temperature (300 K) but also in aqueous phase and the fatty acids adsorb onto a hydrated surface, in presence of water. In the previous part, calculations at both 0 K and 300 K were performed in vacuum conditions. However, the presence of water may influence significantly the adsorption energies and geometries. Hence, this part of the study investigates the adsorption of fatty acids in hydrated conditions and systematically at 300 K, by means of AIMD simulations. Calculations have been conducted with the collector molecule placed at the vicinity of the surface and the cell filled with water molecules. In Chapter 7, the mechanisms leading to the hydration of the (111) fluorite surface were investigated but without the presence of the collector molecule. It allowed to create input configurations with the hydrated surface as determined by AIMD simulations in Chapter 7. Hereafter, when adsorption energies have been calculated, snapshots from AIMD simulations have been relaxed at 0 K by classical DFT calculations. Then, the total energy of the system where the collector is adsorbed have been compared to the total energy of the system where the collector molecule is placed in the bulk water at 10 Å far from the surface. These conditions (cells

completely hydrated and simulations at 300 K) represent the most realistic systems that can be modelled nowadays, as they consider the electronic density of each atom (DFT), the temperature (molecular dynamic simulations), and the water that surrounds the surface and the molecule.

4.1 Form of carboxylates/carboxylic acids in solution

4.1.1   Carboxylic acid

To investigate the solvation of fatty acids under their acidic forms, an octanoic acid molecule was set in a cell completely filled with water molecules to attain a density of 1 g.cm^{-3}, excluding a cylinder of 20 Å^2 of section around the octanoic acid molecule. To determine the most stable form of the molecule in solution, an *ab initio* molecular dynamics simulation was performed for a total duration of 50 ps. At 2 ps of simulation, the acidic H$^+$ ion of the carboxylic group is spontaneously transferred to a water molecule, forming the carboxylate anion and a H$_3$O$^+$ ion in the bulk of water (Figure 104). During the whole simulation, the proton is transferred from one water molecule to another while the octanoic acid stays under its carboxylate form, *i.e.* the octanoate anion. This result is in agreement with acid-base well-known concepts: the pKa of octanoic acid/octanoate couple is known to be around 5 (see Chapter 1) while, during this simulation, the cell was filled with water molecules, inducing a pH of 7. This confirms that, at the pH commonly used for calcium salts flotation, the carboxylic acids are mostly under their anionic form.
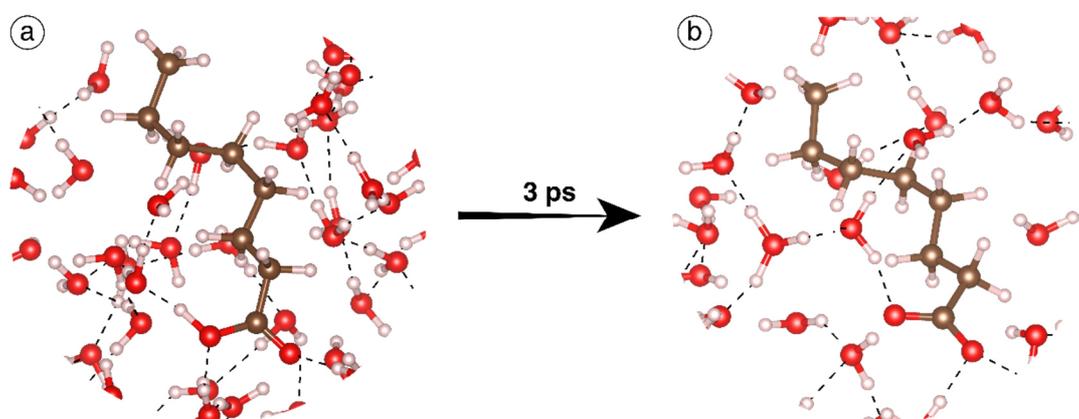
Figure 104. Octanoic acid in the bulk of water, at the very beginning of the simulation (a) and after 3 ps of AIMD simulation (b). A proton has been transferred to a water molecule. The red, marron, and white balls represent the oxygen, carbon, and hydrogen atoms, respectively.

4.1.2   Sodium carboxylate

During the collector preparation, before adding it in the conditioning stage, fatty acids are commonly treated with NaOH (or, in some cases, KOH). This treatment allows to improve the deprotonation reaction kinetics and, hence, to increase the solvation of the fatty acids, these latter being nearly insoluble under their acidic forms (see Chapter 1). The main scientific questioning that is raised by this treatment deals with the form of carboxylate in solution. Indeed,

when NaOH is added in solution, it is assumed that it completely dissociates to form Na^+ and OH^- ions. The OH^- ions react with the carboxylic acid to form a water molecule by receiving the acidic proton of the carboxylic group. After the deprotonation reaction, the only charged species remaining in solution are Na^+ and the carboxylate anion, which are not necessarily in close proximity. Is the carboxylate anion bonded to a sodium cation in the bulk of water, or are they separated with each of them surrounded by a water solvation shell? To answer this question, AIMD simulations were performed for the two above-mentioned cases, during 50 ps (Figure 105). The dissociation of the molecular sodium octanoate neither occurs spontaneously during the whole simulation nor the recombination of dissociated sodium octanoate. Since the number of water molecules was the same between the two systems, their total energy were calculated at 0 K by means of classical DFT calculations and compared. Interestingly, the molecular sodium octanoate is more favoured than the dissociate sodium octanoate, with $\Delta E_r = -33.7$ kJ.mol^{-1}. This indicates that, in solution, the carboxylate molecules are more likely to be linked to a sodium cation rather than be solely stabilised by the surrounding water molecules. Nevertheless, this reaction energy only assesses the thermodynamic stability of the molecular sodium octanoate but does not describe the binding between the octanoate anion and the sodium cation in terms of kinetics. Indeed, this reaction could be subject to a significant activation energy albeit, since the deprotonation reaction is experimentally conducted at T = 60°C, an activation energy could be provided to make this reaction possible. Notably, for the adsorption of fatty acids in hydrated conditions, two cases can be studied, as in vacuum conditions: the bond between Na^+ and R-COO^- can be broken before the adsorption process (or be inexistent in the case of free carboxylates in solution), leading to the adsorption of the lone R-COO^- anion or the whole R-COO-Na molecule can adsorb onto the surface, without dissociating before. Moreover, Na^+ cations can be already adsorbed on the surface when the carboxylate molecule approaches the surface, conducting to the same configuration to that when R-COO-Na adsorbs.
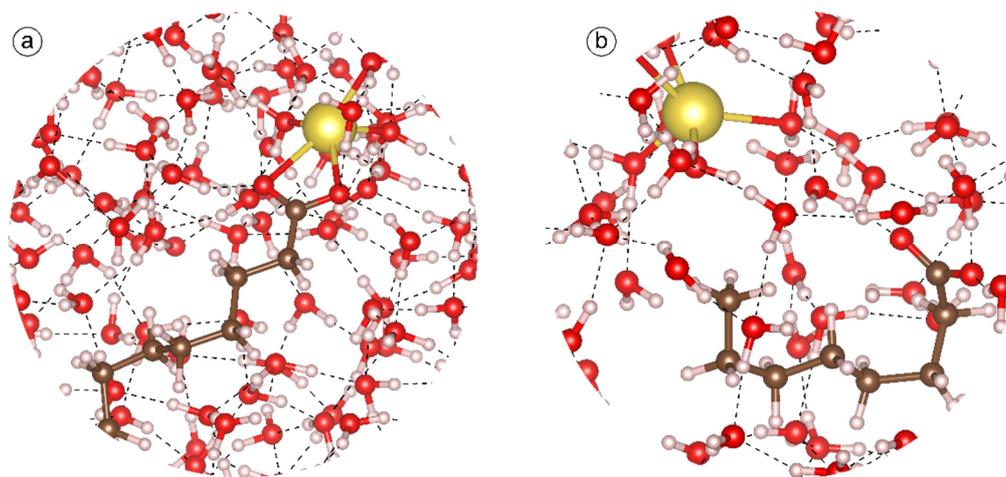
Figure 105. Snapshots at 15 ps of the molecular sodium octanoate (a) and the dissociate sodium octanoate (b) in the bulk of water. No spontaneous dissociation or recombination is observed. The red, marron, yellow, and white balls represent the oxygen, carbon, sodium, and hydrogen atoms, respectively.

4.1.3 Na^+ adsorption

The deprotonation reaction is commonly conducted with a slight excess of NaOH. Moreover, the adsorption and flotation processes are often realised at pH moderately alkaline (between 8 and 11). Since NaOH is one of the cheapest pH regulators for industrial applications, it is widely used in the flotation process. Finally, many flotation depressants are anionic depressants that are commonly neutralised with Na^+. Hence, either the fundamentals adsorption solutions or the industrial flotation pulps contain significant amount of Na^+, which can be likely to adsorb onto mineral surfaces, including fluorite. This adsorption was then studied by means of AIMD simulations: a Na^+ was set on the (111) fluorite surface with the cell completely filled with water molecules or in the water bulk. Once the global geometry was at its equilibrium, DFT calculations were performed at 0 K to determine an adsorption energy for the Na^+ onto the fluorite surface. In solution, the Na^+ has between four and six water molecules that surround it (solvation shell). When adsorbed, it is bonded to three water molecules from the bulk, to one water molecule adsorbed on the surface, and to three surface fluorine atoms. Overall, the calculated adsorption energy is $\Delta E_{ads} = $ -144.8 kJ.mol^{-1}, indicating a strong affinity of Na^+ for the fluorite surface. Hence, it can be assessed that, even for low sodium concentrations, the fluorite surface is covered by adsorbed Na^+ cations. Though a significant part of the carboxylate molecules can be under free carboxylate anions in solution, they are likely to adsorb on the pre-adsorbed sodium cations when approaching the surface.

4.2 The carboxyl group during the adsorption at 300 K in hydrated conditions

4.2.1   Free carboxylate on the surface

Under the carboxylate form, the octanoate molecule was set in a bidentate binuclear configuration, which represents the most favoured geometry found without water. In this configuration, each oxygen atom (O_1 and O_2) is close to a calcium atom (Ca_1 and Ca_2, respectively) with $d_{Ca1-O1} = d_{Ca2-O2} = 2.3$ Å. In the first 8 ps of the simulation, the two oxygen atoms are going away from their respective calcium atom. However, O_1 is getting closer to Ca_2 and the distance between the two atoms radically decreases from 4.0 Å to 2.5 Å between 8.4 ps and 8.7 ps. For the rest of the simulation, the distance between O_1 and Ca_2 oscillates around an average of 2.81 Å with a standard deviation of 0.30 Å, indicating that a bond is established between the two atoms. The other oxygen atom points towards the water bulk, forming H-bonds with the water molecules (Figure 106). It induces that the molecule is globally tilted, resulting to the existence of a global angle of around 20° between the surface and the line joining the two oxygen atoms (Figure 106). Overall, six water molecules are still adsorbed on the surface, composed of 12 calcium atoms, despite the adsorption of the octanoate molecule.
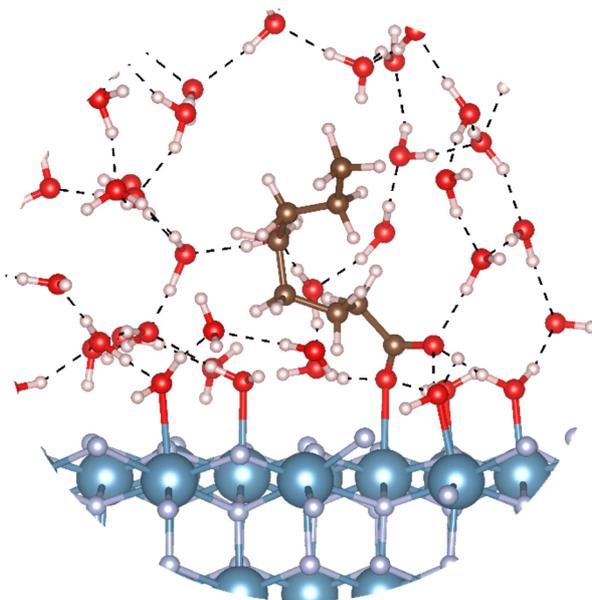
Figure 106. Snapshot of a side view of the (111) fluorite surface with an octanoate molecule adsorbed onto the surface after 58 ps, and with the cell completely filled with water molecules so that the density is 1 g.cm^{-3}. The blue, grey, red, marron, and white balls represent the calcium, fluorine, oxygen, carbon, and hydrogen atoms, respectively. Dashed lines represent H-bonds.

The results at T = 0 K and T = 300 K in the absence of the water demonstrated that each oxygen atom is bonded with a calcium atom while only one oxygen atom is bonded with a calcium atom in hydrated conditions. This indicates that the presence of water affects the geometry of the carboxyl group during the adsorption, changing the most favoured configuration from bidentate binuclear to monodentate. This adsorption has been described by FTIR through the internal reflection spectroscopy (IRS): authors demonstrated that a "uni-dentate" adsorption occurs for low fatty acids coverage onto the (111) fluorite surface (Mielczarski et al., 1998). They also reported that a global angle of around 10° exists between the line joining the two oxygen atoms and the surface (Mielczarski et al., 1998). Both of these statements are observed in the present study but, in addition, during the simulation, the global conformation of the molecule is changing due to the free rotation on the C-C axis (Figure 106). Several C-C bonds transform from –*trans* conformer to –*cis* conformer to maximise the van der Waals interactions between the hydrogen atoms of the chain, resulting in the folding up of the molecule on itself. This phenomenon has also been reported in the literature for low surface coverage by fatty acids (Kellar et al., 1991). Nevertheless, even if the molecule tilts over time, it does not desorb the water molecules from the surface so that the "flat" adsorption observed previously does not occur spontaneously under hydrated conditions, but is observed only on a bare surface. According to Chapter 7, the adsorption energies calculated for water are around -55 kJ·mol^{-1} while a "flat" adsorption of an octanoate molecule would result in the desorption of at least two water molecules, corresponding to -110 kJ.mol^{-1}. The difference between a "flat" and a "vertical" adsorption is lower than -110 kJ.mol^{-1}, inducing that the adsorption occurs in a sub-vertical configuration in presence of water. Also, it makes impossible the adsorption of a calcium dicarboxylate precipitate on the surface by the carboxylates chains since this would require the

233

desorption of water molecules from the surface. Hence, the adsorption of a calcium dicarboxylate precipitate, which have been suggested by many authors over the past decades, could only adsorb by the adsorption of their cation(s) on the surface, establishing a bridging mechanism.

In addition, the free energies of the two systems, *i.e.* where the octanoate anion is bonded to the surface and where the octanoate anion is in the water bulk, were determined by DFT simulations performed at 0 K and compared to calculate the total adsorption energy in hydrated conditions. Overall, the octanoate molecule adsorbs with ΔE_{ads} = -66.3 kJ.mol^{-1} in hydrated conditions. This value is significantly lower than the adsorption energy in vacuum conditions, indicating a considerable stabilisation of the free octanoate anion by the water molecules. This can be related to the existence of hydrogen bonds between three to four water molecules and the anionic carboxyl group in the water bulk. Moreover, the water molecules adsorbed on the surface calcium atoms probably decrease the total surface energy, inducing a diminution of the global surface reactivity, including the calcium atoms reactivity.

4.2.2   Sodium carboxylate

The results at T = 0 K and/or in vacuum conditions exhibited two possible configurations for the adsorption of a carboxylate molecule bonded with a sodium cation. Hence, the same configurations were tested at 300 K (through AIMD simulations) in hydrated conditions. Different input configurations were however tested for setting the octanoate molecule in presence of the Na$^+$, which was systematically adsorbed onto a surface fluorine atom regardless the adsorption configuration:

1.   Bidentate binuclear, with each oxygen atom on a different calcium atom, near the Na$^+$, similar to Figure 100b;
2.   Bidentate binuclear, with an oxygen atom on a calcium atom and the other one on the Na$^+$;
3.   Monodentate, with one oxygen on a calcium atom, the other oxygen pointing towards the bulk of water, still near the Na$^+$, similar to Figure 106;
4.   Bidentate bridging, with the two oxygen atoms adsorbed onto the Na$^+$, on the other side from the surface, similar to Figure 100c.
5.   Monodentate bridging, with one oxygen atom adsorbed onto the Na$^+$, the other one pointing towards the water bulk.

All the above-described configurations conducted to the same geometry after eight to ten picoseconds: the octanoate molecule adsorbs under a monodentate bridging configuration (Figure 107). One oxygen atom of the carboxyl group establishes a bond with the Na$^+$, its bond length being around 2.59 Å. The other oxygen atom of the collector points towards the bulk of water, establishing two H-bonds with water molecules. Besides, the Na$^+$ is adsorbed on a surface fluorine atom with d_{Na-F} = 2.31 Å and surrounded by four water molecules among which two are adsorbed on the surface (Figure 107). This configuration is therefore the most favoured geometry for the

adsorption of sodium carboxylate on the (111) fluorite surface at 300 K and under hydrated conditions.
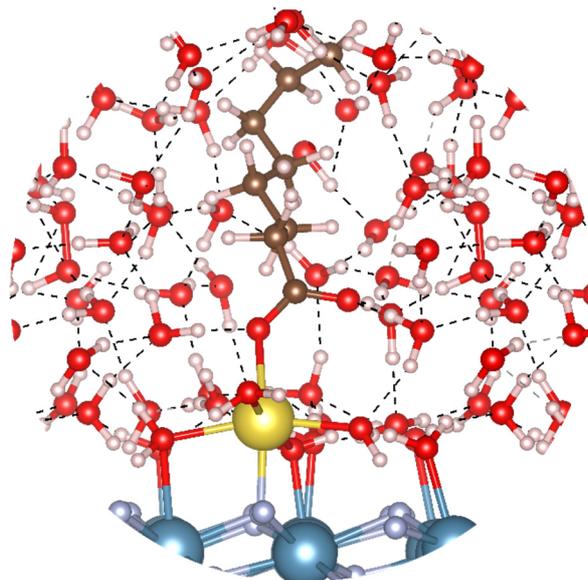
Figure 107. Snapshot of a side view of the (111) fluorite surface with a sodium octanoate molecule adsorbed onto the surface after 18 ps and with the cell completely filled with water molecules so that the density is 1 g.cm^{-3}. The blue, grey, red, yellow, marron, and white balls represent the calcium, fluorine, oxygen, sodium, carbon, and hydrogen atoms, respectively. Dashed lines represent H-bonds.

As previously, the free energies of the two systems, *i.e.* where the sodium octanoate molecule is bonded to the surface and where the sodium octanoate is in the water bulk, were determined by DFT simulations performed at 0 K. They were compared to calculate the total adsorption energy in hydrated conditions, which was, for the sodium octanoate adsorption, $\Delta E_{ads} = $ -154.2 kJ.mol^{-1} in hydrated conditions. This value is significantly higher than that of the free carboxylate, indicating a much more favoured adsorption under this form.

4.2.3   Substitution of a surface fluorine atom

The anion exchange between a fluorine atom and the carboxylate anion, previously investigated at 0 K under vacuum conditions, was also studied at 300 K under hydrated conditions. However, since NaF is a soluble salt, the formation of NaF when F$^-$ is released in the water bulk seems unlikely to occur. Moreover, if the adsorption of the carboxylate species is an anion exchange, the Na$^+$ probably stays in the water bulk. Hence, the choice was made hereafter to not include the Na$^+$ in the reaction. Overall, based on the reaction postulated originally (Finkelstein, 1989; Nixon and Cook, 1950; Peck and Wadsworth, 1965; Young and Miller, 2000), another reaction was suggested and investigated:

$$Surface + Oct^- = Surface - Oct + F^- \tag{39}$$
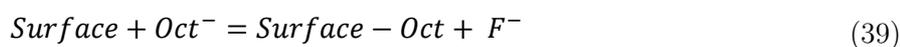
Each part of reaction (39) represented a lone system comprising the fluorite slab (with fluoride or with octanoate adsorbed on the surface) and the free anion at 10 Å far from the surface. The cell was then completely filled with water molecules inducing that the surface was hydrated and the anions (carboxylate and fluoride) were solvated in the bulk of water. The configuration obtained at 300 K in hydrated conditions for the carboxylate was the same than the one obtained at 0 K in vacuum conditions (Figure 108): one oxygen atom of the carboxylate adsorbs between two surface calcium atoms while the second oxygen atom forms a bond with a third calcium atom. The fluoride anion, in solution, is surrounded by three water molecules, with their hydrogen atoms oriented towards the fluoride anion (Figure 108).
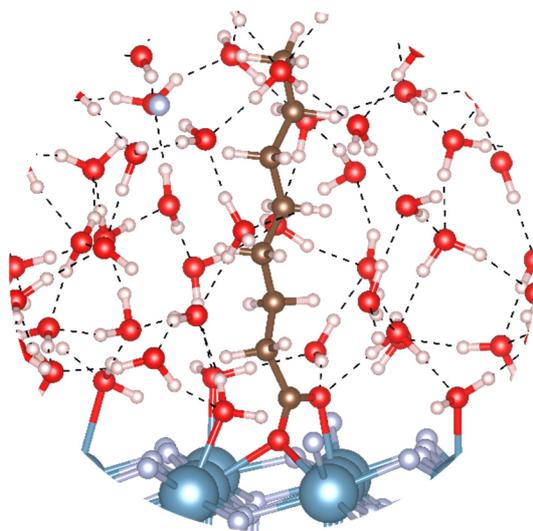
Figure 108. Snapshot of a side view of the (111) fluorite surface with an octanoate anion adsorbed on the surface by an anion exchange process, the fluoride anion, and the cell completely filled with water molecules so that the density is 1 g.cm^{-3}. The blue, grey, red, marron, and white balls represent the calcium, fluorine, oxygen, carbon, and hydrogen atoms, respectively. Dashed lines represent H-bonds.

In addition, the total energy of each system was determined by means of DFT calculations at 0 K on a snapshot taken from the AIMD simulation. The energies of the two systems (left side and right side of the equation) were compared to determine the free energy of this reaction. While reaction (38) was endothermic, reaction (39) is significantly exothermic in hydrated conditions with ΔE_r = -106.4 kJ.mol^{-1}. This indicates that an adsorption of carboxylate by anion exchange is likely to occur thermodynamically speaking and would be much more stable than the adsorption of free carboxylate. However, the anion exchange is only possible by solubilising a fluoride anion from the surface, which probably displays a significant activation energy considering the three Ca-F bonds that must be broken. Therefore, this configuration is possible for the adsorption of the carboxylate species onto fluorite but could be disfavoured kinetically speaking compared to a simple adsorption of sodium octanoate or free octanoate, which probably needs a low or zero activation energy.

5. Towards the formation of a monolayer

In the previous part (section 4), the adsorption mechanisms of a lone fatty acid molecule were investigated by means of DFT calculations, performed, in the last stage, at 300 K and under hydrated conditions. Nonetheless, an adsorption layer must form on the surface to make the mineral surface hydrophobic. The molecular mechanisms leading to the formation of an adsorption layer are poorly understood at the moment, albeit many options have been described in the literature over the past decades. It is well admitted that the adsorption of fatty acids (as well as other collector types) onto mineral surfaces follow a Langmuir behaviour with, however, lateral interactions between the adsorbed molecules (Cases and Mutaftschiev, 1968; Cases and Villieras, 1992; Dobiáš, 1984). These latter are considered by deriving a Frumkin-Fowler isotherm, which includes a term for lateral interactions between the aliphatic chains of the adsorbed molecules (Cases and Mutaftschiev, 1968; Cases and Villieras, 1992; Dobiáš, 1984). Besides, the impact of the adsorption of several carboxylate molecules on the adsorption mechanisms, mostly in terms of carboxyl group geometry, are still poorly understood. Hence, some AIMD calculations were performed with increasing surface coverage under hydrated conditions. Considering the high computational costs, an extensive study could not be realised and only a few simulations were performed to provide some insights in the mechanisms leading to the formation of an adsorption layer. Hereafter, the free carboxylates only were used for the study of the formation of an adsorption layer.

First, two collectors were set on the same (111) fluorite surface. When the two octanoate molecules are set far from each other, the water molecules between them screen the interactions which can exist between their aliphatic chains, making the two adsorptions completely independent from each other. Hence, the two molecules adsorb under monodentate configurations as if they were alone. Besides, when the two octanoate molecules are set close from each other on the surface, *i.e.* on neighbouring calcium atoms with $d_{Ca-Ca} = 3.86$ Å, one molecule adsorbs under the bidentate binuclear mode while the other adsorbs under the monodentate mode (Figure 109). The first one establishes two Ca-O bonds with $d_{Ca1-O1} = 2.82$ Å and $d_{Ca2-O2} = 2.55$ Å while the second one forms only one Ca-O bond with $d_{Ca-O} = 2.64$ Å, its other oxygen atom pointing towards the bulk of water (Figure 109). This demonstrates an interaction between the two carboxyl groups since the bidentate binuclear mode was observed spontaneously only under vacuum conditions. In addition, no water molecule is present between the aliphatic chains of the two octanoate molecules, demonstrating significant hydrophobic interactions between them. Four hydrogen atoms of each molecule interact (through dispersive forces) with their equivalent on the other molecule with H-H distances ranging from 2.07 Å to 2.31 Å.
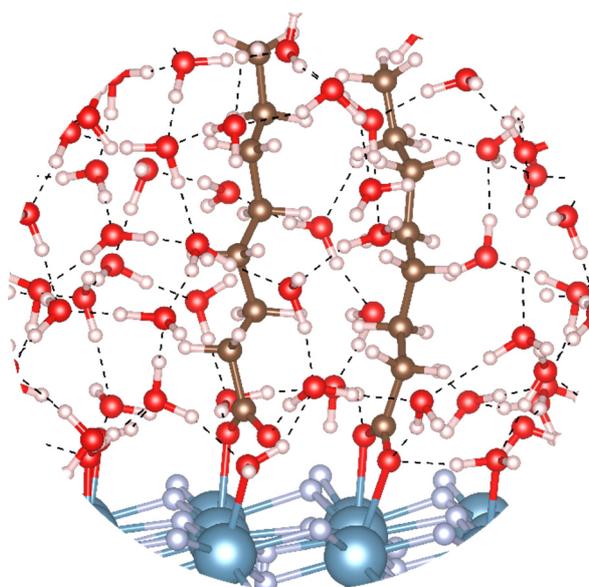
Figure 109. Snapshot of a side view of the (111) fluorite surface with two octanoate anions adsorbed on the surface after 20 ps, and with the cell completely filled with water molecules so that the density is 1 g.cm^{-3}. The blue, grey, red, marron, and white balls represent the calcium, fluorine, oxygen, carbon, and hydrogen atoms, respectively. Dashed lines represent H-bonds.

Furthermore, the coverage was increased to three octanoate molecules, representing roughly a 50% surface coverage considering 20 Å^2 of packing area for octanoate and a surface area of around 150 Å^2. Also, according to the above-mentioned results, the surface with 12 calcium atoms can be covered with six octanoate molecules if a bidentate binuclear configuration is assessed for the adsorption, 12 for a monodentate configuration. When three octanoate molecules are set on neighbouring calcium atoms (3.86 Å between each molecule), two of them adsorb under the monodentate mode with d_{Ca-O} = 2.68 Å while the third, located between the two latter, adsorb under the bidentate binuclear configuration (Figure 110). This molecule forms two Ca-O bonds, which lengths are 2.58 Å and 2.75 Å. No water molecules are present between the aliphatic chains and H-H distances in the same range than for two molecules are exhibited, see previously. However, a significant number of water molecules are still adsorbed on the surface, making this latter still quite hydrophilic.
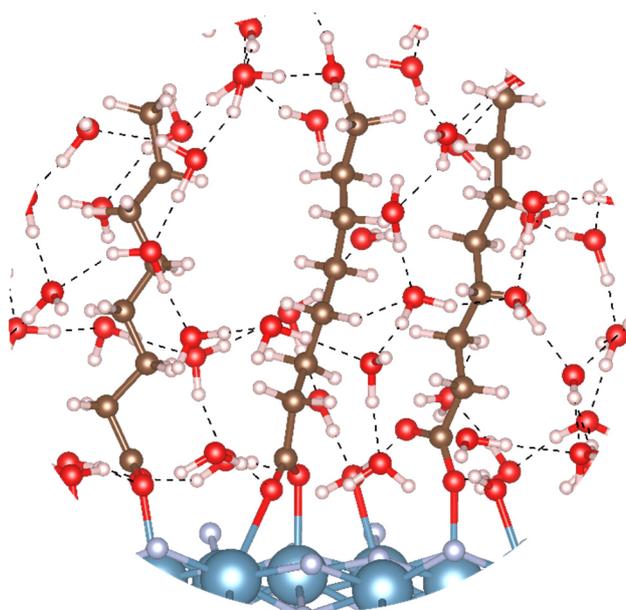
Figure 110. Snapshot of a side view of the (111) fluorite surface with three octanoate anions adsorbed on the surface and the cell completely filled with water molecules so that the density is 1 g.cm^{-3}. The blue, grey, red, marron, and white balls represent the calcium, fluorine, oxygen, carbon, and hydrogen atoms, respectively. Dashed lines represent H-bonds. Dashed lines represent H-bonds.

Finally, six octanoate anions were set on the (111) fluorite surface, corresponding to a 100% surface coverage if only bidentate binuclear adsorptions are assessed. During the AIMD simulation, several interesting phenomena occur (Figure 111):

- Two octanoate anions catch protons from water molecules and form the octanoic acid, while generating two OH^{-};
- One of the two octanoic acid adsorbs by forming the ion-molecular complex [R-COOH-OOO-R]$^{-}$;
- The octanoate involved in the above-mentioned ion-molecular complex adsorbs under monodentate configuration;
- Two octanoate anions adsorb under bidentate binuclear form;
- The last octanoate anion adsorbs by somewhat substituting a fluorine atom that is re-adsorbed on the neighbouring calcium atom;
- One of the OH^{-} substitutes a fluorine atom in the fluorite slab while the second one goes into the bulk of water;
- No more water molecule is adsorbed on the surface;
- A small number of water molecules are present in the adsorption layer;
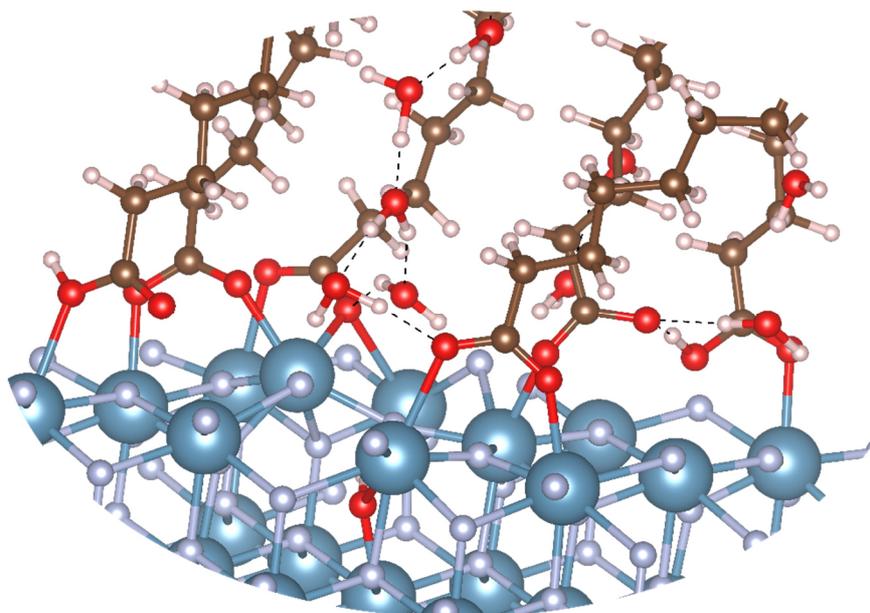
Figure 111. Snapshot of a side view of the (111) fluorite surface with three octanoate anions adsorbed on the surface and the cell completely filled with water molecules so that the density is 1 g.cm^{-3}. The blue, grey, red, marron, and white balls represent the calcium, fluorine, oxygen, carbon, and hydrogen atoms, respectively. Dashed lines represent H-bonds.

Considering the above-mentioned observations made in AIMD simulations under hydrated conditions, several conclusions can be drawn. Albeit ion-molecular forms are stable in solution and have been described by authors (Miller and Misra, 1984), the presence of 33% of the adsorbed molecules under their acidic form would induce the presence of a peak at around 1740 cm^{-1} in FTIR spectra, commonly ascribed to the C=O stretching vibration. According to literature, this peak has never been observed for fatty acids adsorption process conducted on fluorite (and other calcium salts) at pH 9, which invalidates the practicality of this system. Notably, it appears unlikely to attain a 100% coverage, *i.e.* a monolayer, with only free carboxylate molecules. This can be related to two main facts. First, in real systems, such monolayers may not be reached and adsorption layers are possibly more loosely, which would induce a lower basicity/negative charge at the vicinity of the surface. Moreover, the surface coverage was increased by using only free carboxylate forms while previous simulations demonstrated that, despite a possible considerable activation energy, the carboxylates are more stable in solution when they are bonded with a Na$^+$. Consistently, if the carboxylate approaches the surface bonded to a Na$^+$, this latter will adsorb on the surface anions (here, fluorine) and will probably stabilise the adsorption layer by decreasing the global negative charge at the vicinity of the surface.

Therefore, considering the previous results, the adsorption mechanisms leading to the formation of a monolayer are probably a mixture of the four main mechanisms highlighted in the previous parts: free carboxylate under monodentate configuration (Figure 106), free carboxylate under bidentate binuclear configuration (Figure 100a), anion-exchanged free carboxylate (Figure 108), and sodium carboxylate under bridging configuration (Figure 107).

6. Investigation on the adsorption modes by DFPT

To investigate deeply the adsorption mechanisms of fatty acids onto calcium minerals, among which fluorite constitutes the simplest archetype, the density functional perturbation theory (DFPT) was used. Within the DFT framework, DFPT allows the prediction of the relation existing between atomistic structures and experimentally detectable spectroscopic properties such as those observed in FTIR or Raman spectroscopies. These experimental methods are very sensitive to the local bonding and chemical structure. Notably, they can provide crucial information on the adsorption geometries and, therefore, on the fatty acids adsorption mechanisms. In particular, FTIR spectroscopy has been widely used over the past decades to discuss the adsorption modes of fatty acids onto various calcium minerals, including fluorite, apatite, calcite, and scheelite (see Chapter 1). The DFPT methodology applies an external electric field to the system, which induces changes in atoms polarisabilities. They correspond to the Born effective charges tensor that can be subsequently used for the determination of the IR vibrational frequencies and their respective intensities. Nowadays, DFPT is one of the most accurate method to simulate IR spectra from given geometries, including atomic structures determined by DFT calculations. In this study, to unravel the molecular mechanisms involved in the adsorption of fatty acids onto calcium minerals surfaces, DFPT calculations were performed on the systems obtained by DFT simulations conducted at 0 K or 300 K as well as under vacuum or hydrated conditions. In particular, the four mechanisms that are suggested to be at play for the formation of the adsorption layer were studied and IR spectra were simulated from their atomistic structures. The results are presented in Figure 112, which displays each configuration and its corresponding simulated IR spectra. The main vibration modes are well simulated with nonetheless a significant shift (around 100 cm^{-1}) for the vibrations (bending and stretching) of the –CH$_2$ groups. This can be attributed to the fact that C-H bond lengths are shorter in DFT calculations than in the reality, inducing higher wavenumbers for stretching vibrations and lower wavenumbers for bending vibrations. However, the vibration modes involving C-H bonds are not of interest here since they do not provide useful information about the adsorption configuration. Besides, the domain between 1500 and 1600 cm^{-1} corresponds to the asymmetric stretching vibration of the COO$^-$ group. It has been subject to considerable discussion in the field since it could give crucial information about the adsorption configuration.

Interestingly, the peak of the asymmetric stretching of the COO$^-$ group adsorbed in the bidentate binuclear configuration is located at 1573 cm^{-1} (Figure 112). As mentioned previously, this configuration has been observed only under vacuum conditions for a sole octanoate molecule or for two molecules under hydrated conditions. In addition, this peak is located at 1535 cm^{-1} for the octanoate adsorbed in monodentate configuration, observed under hydrated conditions (Figure 112). For the anion-exchange-based adsorption, this peak is located at 1586 cm^{-1} while, when the octanoate is adsorbed with a Na$^+$ acting as a bridging cation, it is located at 1557 cm^{-1} (Figure 112). Three of those four wavenumbers have been observed in the literature with different interpretations, including chemisorbed carboxylate, surface precipitated calcium dicarboxylate, or different adsorption modes.
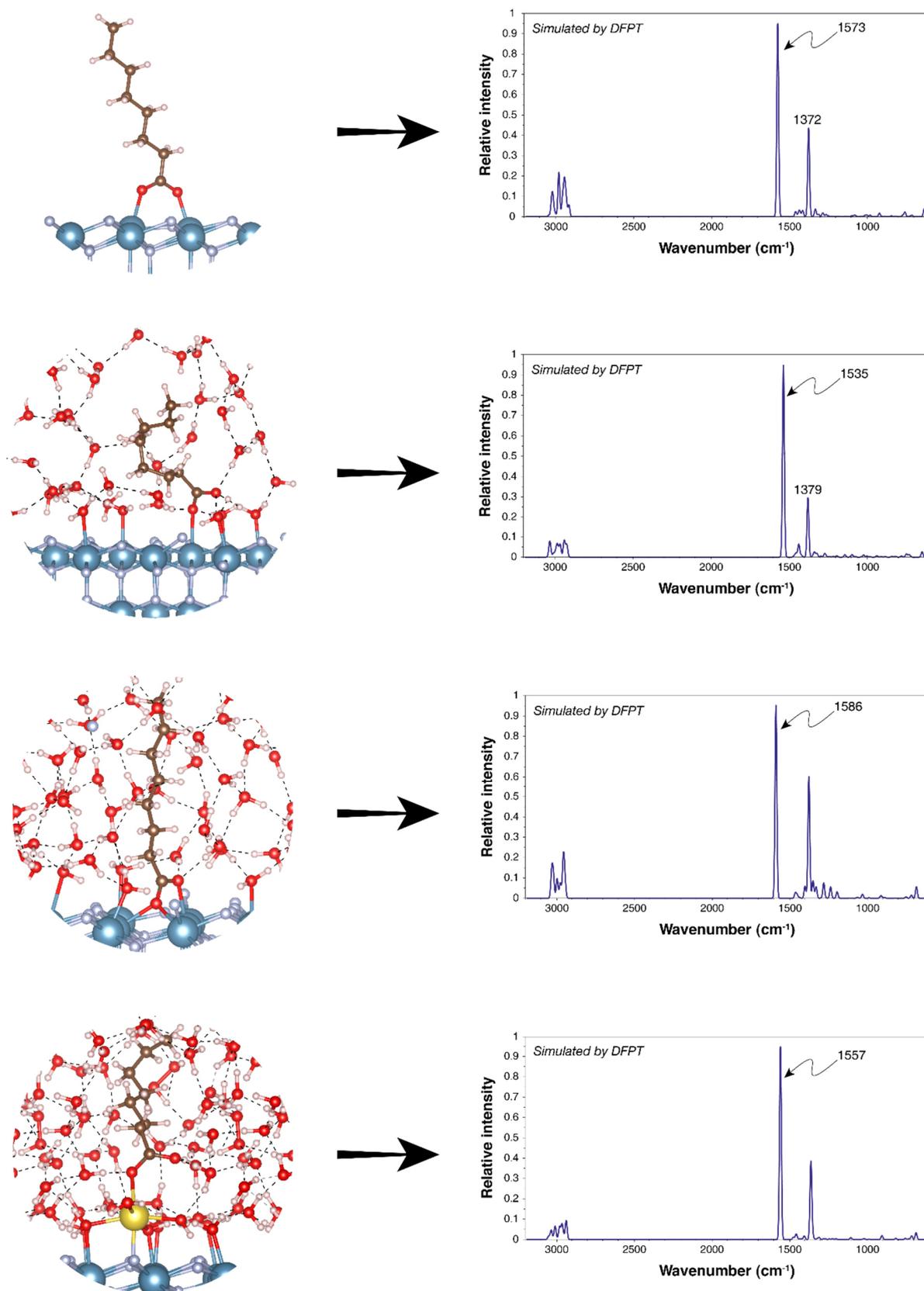
Figure 112. The four main adsorption mechanisms for fatty acids on the (111) fluorite surface and the corresponding IR spectra simulated by DFPT. The most intense peak is ascribed to the asymmetric stretching of the COO⁻ group, which gives information about the adsorption mechanism.

242

Hence, the DFPT simulations allow to ascribe with an unprecedented accuracy the different wavenumbers observed experimentally for the asymmetric stretching of the –COO$^-$ group to various adsorptions mechanisms that have been found by state-of-the-art molecular modelling simulations performed at 300 K and under hydrated conditions. In particular, the doublet at 1575 cm^{-1} and 1535 cm^{-1} observed systematically by some authors (Mielczarski et al., 2002, 2000, 1998, 1999) and only at high carboxylate concentrations for other authors (Free and Miller, 1996; Hu et al., 1986b, 1986a; Rao et al., 1991a, 1991b, 1990; Young and Miller, 2000) can be attributed to carboxylate species adsorbed in the bidentate binuclear and monodentate modes. These two modes occur in similar proportion since, when the surface coverage was increased (see section 5) to three molecules, one molecule was adsorbed under a monodentate mode, one under a bidentate binuclear mode, and the last under an intermediate configuration. Besides, the peak at 1555-1560 cm^{-1} observed by authors at low carboxylate concentrations correspond to the adsorption of the carboxylate molecule onto a bridging Na$^+$, itself adsorbed on the surface anion(s).

7. Experimental validations

7.1 Fluorite and sodium oleate

The DRIFT spectrum of pure fluorite (used hereafter) conditioned in deionised water is presented in Figure 113. To avoid any effect of a possible excess of Na$^+$ in solution due to NaOH, the choice was made to perform all the following experiments at natural pH. A little carbonation of the surface can be observed on the pure mineral resulting in a peak at 1610-1620 cm^{-1} (Figure 113). Hence, the choice was made to systematically subtract the IR spectrum of the pure fluorite from the spectra where fatty acids are adsorbed onto fluorite. Besides, the IR spectrum of pure sodium oleate (NaOl) is also presented in Figure 113. On this spectrum, the peak at 1470 cm^{-1} is attributed to –CH$_2$ bending while the peaks at 2852, 2921, 2955, and 3005 cm^{-1} are ascribed to the symmetric elongation vibrations of –CH$_2$, asymmetric elongation of –CH$_2$, asymmetric elongation of –CH$_3$, and elongation of =C-H, respectively. In addition, the strong absorption band at 1558 cm^{-1} is attributed to the asymmetric stretching vibration of the –COO$^-$ group. Interestingly, this band exhibits similar wavenumber than the carboxylate species adsorbed on the fluorite surface on a bridging Na$^+$. This demonstrates that, under this configuration, the carboxylate species displays an atomistic structure (bond lengths and bond angles) very close to its structure in the crystallised pure sodium oleate compound.
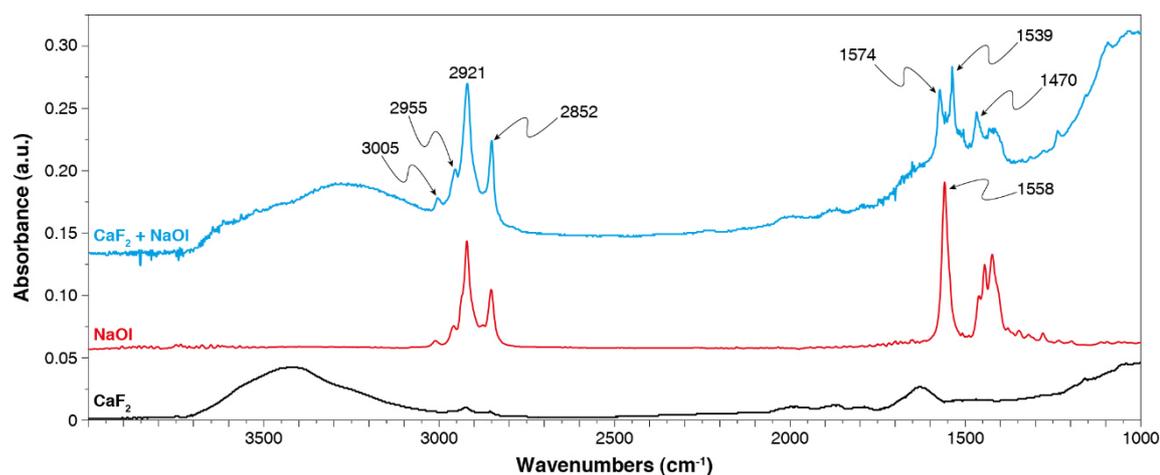
Figure 113. DRIFT spectra of fluorite conditioned in deionised water (black) and conditioned in a solution of sodium oleate at 1×10^{-4} mol.L^{-1} (blue) at pH 7. The IR spectrum of pure sodium oleate is also displayed (red).

Then, pure fluorite (0.5 g) was conditioned in 5 mL of a solution at 1×10^{-4} mol.L^{-1} of sodium oleate during 15 min at natural pH and washed three times in deionised water (Figure 113). All the peaks attributed to the aliphatic chain are present at similar wavenumbers than for pure sodium oleate (Figure 113). Nonetheless, the lone peak at 1558 cm^{-1} for pure sodium oleate, attributed to the asymmetric stretching vibration of -COO$^-$ group, is replaced with a doublet at 1539 and 1574 cm^{-1}, which, according to section 6, indicates the adsorption onto surface calcium atoms under monodentate and bidentate binuclear configurations. Interestingly, the peak at 1539 cm^{-1} seems to have a higher intensity than the peak at 1574 cm^{-1}, which could result from higher amount of oleate species adsorbed under monodentate configuration. This raises the question of the influence of the concentration and, therefore, the tightness of the adsorption layer on the relative intensity of the two peaks: a tighter adsorption layer would induce higher amount of carboxylate adsorbed under bidentate binuclear configuration (peak at 1574 cm^{-1}).

7.2 Effect of concentration

The conditioning time was then set to 24 h under vigorous shaking conditions to attain a thermodynamic equilibrium. The samples were also systematically washed three times before being filtrated. At low concentrations (1×10^{-5} mol.L^{-1}), a small peak can be observed for the asymmetric stretching of the -COO$^-$ group, at 1560 cm^{-1} (Figure 114). Though little significance, this could be attributed to the adsorption of sodium carboxylate on the surface by a bridging configuration, as demonstrated previously. Besides, the peaks attributed to the aliphatic chain are presented with low intensities. In particular, the asymmetric elongation of -CH$_2$ is at 2926 cm^{-1}, which indicates a loose organisation of the adsorption layer since authors demonstrated that this peak shifts towards the lower wavenumbers when the aliphatic chains are close from each other. When the concentration is increased to 5×10^{-5} mol.L^{-1}, a plateau is exhibited from 1535 to 1572 cm^{-1} while the peak at 2926 cm^{-1} previously observed shifts to 2923 cm^{-1}, indicating a tighter organisation of the adsorption layer, *i.e.* higher amounts of sodium oleate adsorbed. The

plateau could result from the coexistence of the three adsorption configurations for oleate species on the fluorite surface in similar proportions, which induce the presence of the three above-mentioned absorption bands. When the concentration is increased to 1×10^{-4} mol.L^{-1}, the doublet at 1572 and 1535 cm^{-1} and a slight peak at 1560 cm^{-1} are observed. Those peaks are all attributed to adsorbed oleate species. These results are consistent with the adsorption energies previously calculated by means of DFT (see section 4.2): at low sodium oleate concentration, sodium oleate adsorption occurs under the configuration exhibiting the higher adsorption energy while, when the concentration is increased the other adsorption modes, less favoured, are more likely to occur. Moreover, previous calculations demonstrated that, when water is absent, *i.e.* when the adsorption layer is being tighter, carboxylate species adsorb in a bidentate binuclear mode, which is significantly more favoured than the monodentate mode occurring at low surface coverage. Hence, it can be assessed that the very first carboxylate molecules adsorbed onto the surface adsorb bridged on a Na$^+$, itself adsorbed onto the surface anions.
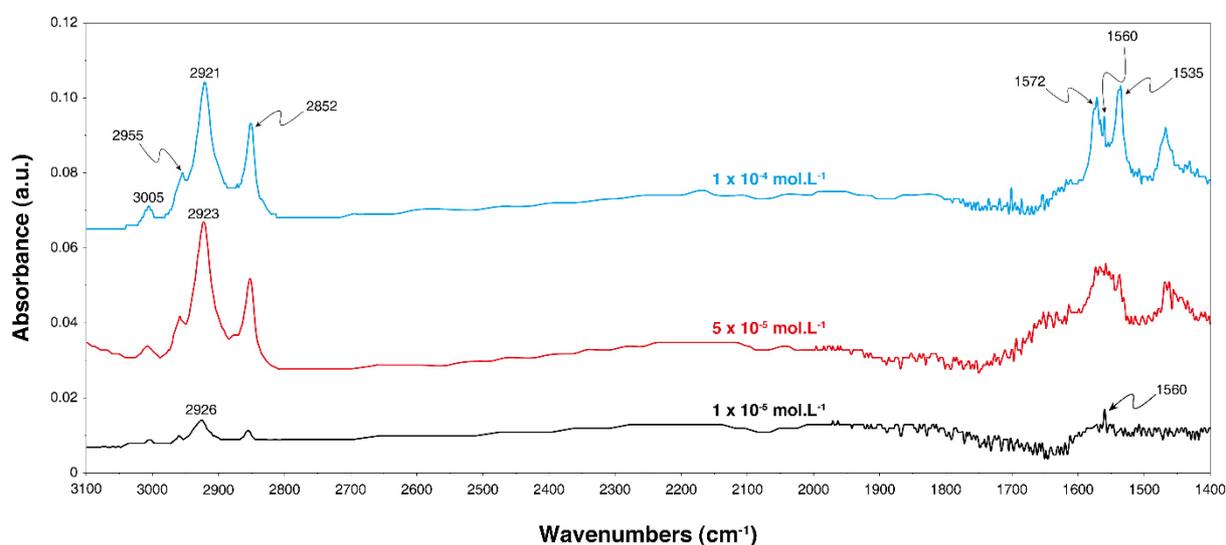
Figure 114. DRIFT spectra of fluorite conditioned in a solution of sodium oleate at 1×10^{-5} mol.L^{-1} (black), at 5×10^{-5} mol.L^{-1} (red), and at 1×10^{-4} mol.L^{-1} (blue). The IR spectrum of pure fluorite, presented in Figure 113, has been subtracted from the spectra presented here.

7.3 Effect of conditioning time

Besides, the conditioning time was reduced to 5 min to assess the kinetics of the formation of the adsorption layer as well as the effect of the mineral dissolution. Indeed, authors suggested that a calcium dicarboxylate precipitate is formed on the surface, responsible for the doublet at 1535 and 1575 cm^{-1} observed in IR spectra. The kinetics of fluorite dissolution is quite low and, in 5 min in contact with a solution of deionised water, fluorine concentration in solution is around 1×10^{-5} mol.L^{-1} (Roche, 1973). Considering the dissolution reaction, the equivalent concentration of calcium ions in solution is 1×10^{-10} mol.L^{-1}. Hence, a sodium oleate concentration of 1×10^{-4} mol.L^{-1} is not enough to attain the solubility product of calcium dioleate, which was measured around 1×10^{-15}-10^{-16} (Fuerstenau and Miller, 1967; Hu et al., 1986a; Irani and Callis, 1960). Hence, at a conditioning time set to 5 min, the formation of a calcium dioleate precipitate

on the surface is unlikely to occur. However, for a sodium oleate concentration of 1×10^{-4} mol.L^{-1}, the doublet is observed on IR spectrum whatever the conditioning time, including 5 min (Figure 115). This indicates that, under vigorous shaking conditions and at room temperature (25°C), the thermodynamic equilibrium is reached very fast, in 5 min. Moreover, according to the previous discussions, the doublet observed on IR spectra cannot be attributed to a calcium dioleate surface precipitate.
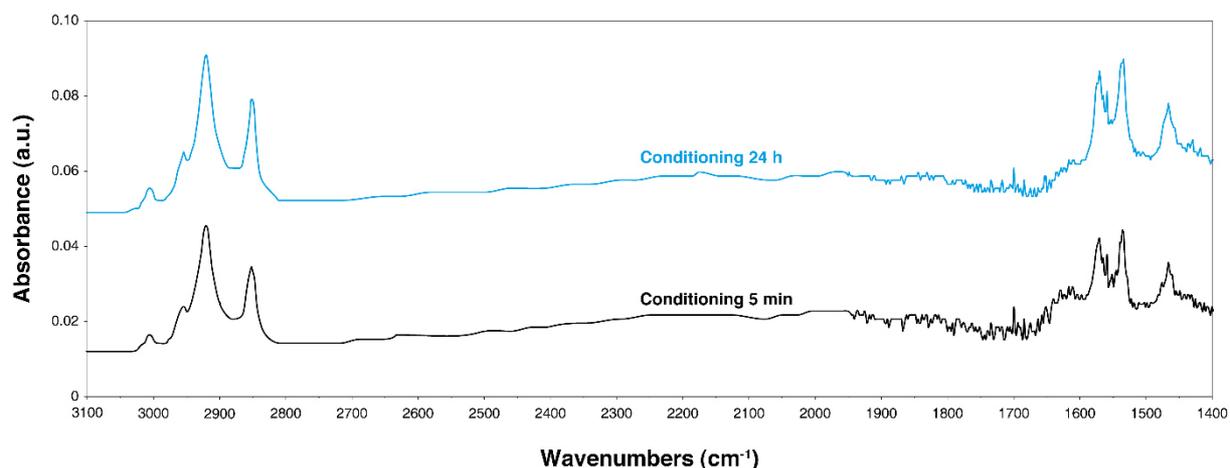
Figure 115. DRIFT spectra of fluorite conditioned in a solution of sodium oleate at 1×10^{-4} mol.L^{-1} during 5 min (black) and during 24 h (blue). The IR spectrum of pure fluorite, presented in Figure 113, has been subtracted from the spectra presented here.

7.4 Effect of temperature

To assess the influence of the temperature on the carboxylate adsorption on the surface, a pure fluorite sample was conditioned in a solution of sodium oleate at 1×10^{-4} mol.L^{-1}, washed three times in deionised water, filtrated, dried at room temperature for 1 hour and placed in a pressure-temperature-controlled apparatus for DRIFT acquisition. First, an IR spectrum at room temperature (25°C) and pressure (1 bar) has been recorded. Then, the pressure has been reduced to 1×10^{-6} bar (partial vacuum) and another IR spectrum has been acquired after 30 min in these conditions to assess the influence of the pressure on the IR spectrum. After that, the temperature has been increased continuously and IR spectra have been recorded regularly after 30 min at the same temperature to equilibrate the system. However, for high temperatures (>150°C), the spectra acquisition is not possible and, therefore, the temperature has been decreased back to room temperature to record the spectra. Results are presented in Figure 116. First, the pressure has no significant effect on the peaks, *i.e.* on the adsorption configurations, their wavenumbers, and their intensities. This confirms the chemisorption of oleate species on the fluorite surface since in partial vacuum (1×10^{-6} bar), oleate species do not desorb from the surface. Then, when the temperature is increased, a peak at 1560-1540 cm^{-1}, which can be attributed to sodium oleate species possibly mixed with oleate adsorbed on the surface, is observed. Hence, at 60°C, a transition occurs and sodium oleate probably crystallises on the surface. After that, at 250°C, the peak shifts towards 1530 cm^{-1} while the intensity of the peak at 3005 cm^{-1} is significantly

decreased, which indicates the degradation of the C=C double bond. Also, the intensities of the peaks related to the –CH$_2$ and –CH$_3$ groups are considerably reduced: the adsorbed species are being desorbed. At 300°C, the C=C double bonds are completely destroyed while the intensities of the peaks related to the aliphatic chain are still decreasing, as well as the peak at 1540 cm^{-1}. Finally, at 410°C, all the oleate species have been desorbed since no more absorbance band are observed on the whole domain.
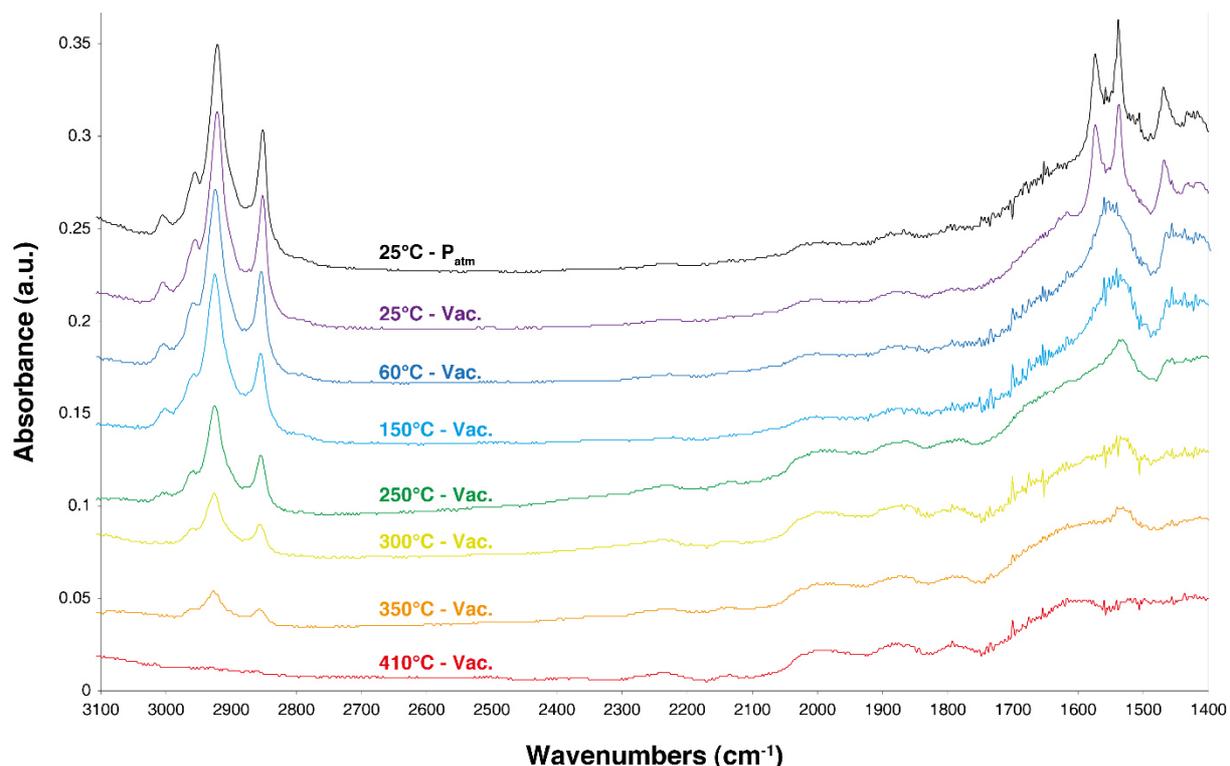
Figure 116. DRIFT spectra of a fluorite sample conditioned in a solution of sodium oleate at 1 x 10^{-4} mol.L^{-1} with different pressures and increasing temperatures. The IR spectrum of pure fluorite has not been subtracted here.

7.5 Effect of chain length and sodium concentration

Finally, to assess the influence of the chain length, IR spectra of fluorite conditioned with different fatty acids solutions at 1 x 10^{-4} mol.L^{-1} during 15 min and washed three times in deionised water were recorded. They are presented in Figure 117. For these experiments, the C12 to C18, *i.e.* sodium laurate to sodium stearate, were obtained from pure fatty acids prepared with NaOH in equimolar proportions at 60°C. However, the C8 (sodium octanoate) was acquired directly under sodium octanoate form and was, therefore, just dissolved in deionised water to prepare the conditioning solution. In this case, Na$^+$ was in significant excess since it was a commercial product. Figure 117 shows that for C12 to C18, the two peaks at 1537 and 1573 cm^{-1} are observed, indicating the adsorption of those fatty acids on the surface calcium atoms under monodentate and bidentate binuclear forms. Notably, the solubility product of calcium dilaurate is significantly higher than that of calcium dioleate, around 8.0 x 10^{-13} (Leja, 1981), which makes impossible the

precipitation of calcium dilaurate on the surface. The peak at 1558-1560 cm^{-1} is not present. Nonetheless, conditioning with sodium octanoate results in a singlet at 1558 cm^{-1}, which is ascribed to the adsorption of sodium octanoate on the surface fluorine atoms, with two small shoulders at 1537 and 1573 cm^{-1}. The sole difference between the sodium octanoate and the other solutions was the fact that sodium octanoate was prepared commercially with a significant excess of sodium in the solid product used for the preparation of the conditioning solution. Consequently, it can be assessed that the chain length (and unsaturation degree) does not impact significantly the adsorption configuration of the polar head on the surface. Also, it can be concluded that the sodium amount in solution most probably controls the main adsorption configuration of carboxylate species on the surface.
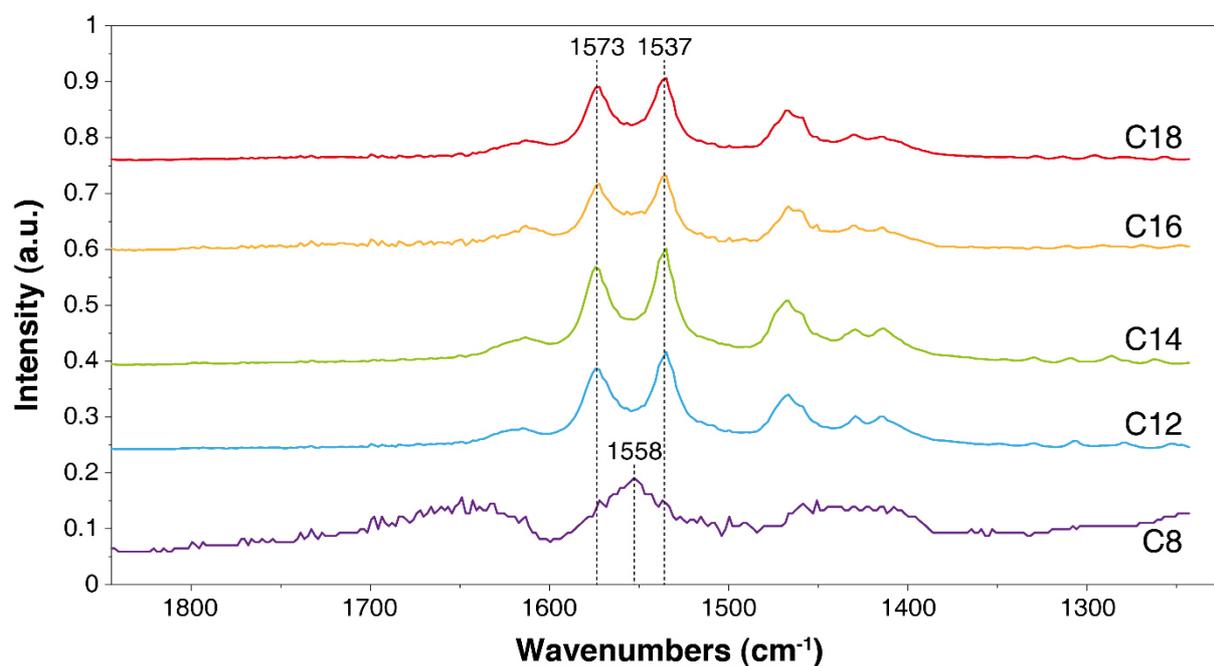
Figure 117. DRIFT spectra of fluorite conditioned in solutions of saturated fatty acids with different chain lengths (from C8 to C18) at 1 x 10^{-4} mol.L^{-1} and during 15 min. The IR spectrum of pure fluorite, presented in Figure 113, has been subtracted from the spectra presented here.

8.   Conclusion

In this chapter, the adsorption of fatty acids on the (111) fluorite surface was investigated by means of DFT calculations conducted at 0 K and 300 K under both dry and hydrated conditions. First, fatty acids under their acidic form adsorb on the fluorite surface with ΔE_{ads} = -78.2 kJ.mol^{-1} albeit their adsorption by dissociation is endothermic. Besides, fatty acids under their carboxylate form can adsorb directly under their anionic form or associated with a Na$^+$ for neutralisation. Hence, a single carboxylate without sodium chemisorbs under a bidentate binuclear configuration while, with Na$^+$, it adsorbs on the surface calcium atoms or bridged on the Na$^+$ that is bonded to surface fluorine atoms. In addition, the free carboxylate can adsorb through an anion-exchange reaction, which is however endothermic. Overall, under vacuum conditions, the adsorption of the free carboxylate form is significantly favoured over the other

possible modes. The configuration of the aliphatic chain was then studied: for chain lengths of typical fatty acids used in flotation, the "flat" adsorption is favoured, *i.e.* with the chain sub-parallel to the surface and interacting with these latter by means of dispersion forces. At 300 K, the same conclusions can be drawn with similar adsorption energies, slightly shifted due to the temperature.

The adsorption mechanisms were also studied under hydrated conditions, systematically at 300 K for the geometry determination and at 0 K for the energy calculation. First, the results demonstrated that, in solution, the bonding between the carboxylate and a Na^+ is thermodynamically favoured over the dissociated case. Moreover, the Na^+ is likely to adsorb on the surface with ΔE_{ads} = -144.8 kJ.mol^{-1}, which indicates that most of the surface fluorine atoms are probably occupied with Na^+. Hence, sodium atoms in solution are either linked to the carboxylate species or adsorbed onto the surface. Besides, for the adsorption of carboxylates under hydrated conditions, three adsorption modes were highlighted:

- Free carboxylate anion in a monodentate configuration (ΔE_{ads} = -66.3 kJ.mol^{-1})
- Sodium carboxylate adsorbed bridged to the surface by the Na^+ adsorbed onto surface fluorine atoms (ΔE_{ads} = -154.2 kJ.mol^{-1})
- Anion exchange between a fluorine atom and the free carboxylate (ΔE_r = -106.4 kJ.mol^{-1})

To confirm these results, the DFPT method was used to simulate IR spectra from the geometries determined by DFT at 300 K and under hydrated conditions. The results showed that the adsorption under bidentate binuclear and monodentate modes are responsible for the IR absorption band of the carboxyl group located at around 1575 and 1535 cm^{-1}, respectively. Interestingly, these two bands have been widely observed by authors in the literature and often attributed to the precipitation of calcium dicarboxylate on the surface. In addition, the adsorption of sodium carboxylate with the Na^+ acting as a bridging cation resulted in the IR absorption band of the carboxyl group located at 1558 cm^{-1}, also widely observed, while it is located at 1586 cm^{-1} for the anion-exchange case. The adsorption of carboxylate species under their anionic form (monodentate/bidentate binuclear) or bridged onto a Na^+ seems mostly controlled by the Na^+ concentration in solution.

Chapter 9

Discussion, conclusion, and perspectives

1. Overview and objectives

Tungsten has been classified as a CRM since 2011 in the EU, and, therefore, has significantly drawn worldwide attention since that. In particular, China holds 86% of the global tungsten production while this metal is crucial for the European economy, low recycled at the moment, and poorly substitutable. The FAME project, in which this work is included, aimed at relaunching the CRM mining industry in the EU by developing new flexible, economic, and environment-friendly processes for the beneficiation of complex European deposits. Notably, the EU owns many tungsten skarns in its underground, which exploitation could diminish the EU dependency to China. Nowadays, tungsten skarns account for more than 40% of the global tungsten resources. However, most of these deposits are non-economic, due to high amounts of calcium minerals that make their beneficiation by flotation very difficult. In addition, although the gangue minerals display a significant density contrast with scheelite, the fine textures commonly displayed by skarn deposits are problematic for classical gravity separation techniques. It is, therefore, of paramount interest to develop new environmental friendly, efficient, and adaptable processes for the beneficiation of tungsten skarns which could ensure, in the future, most of the tungsten world production.

In this work, the Tabuaço tungsten skarn represented an archetype of tungsten skarns: it comprised high amounts of calcium minerals, including dense calcium silicates and calcium salts such as fluorite, apatite, and calcite and displayed moderately fine textures, *i.e.* liberation size. The global objective was to develop an efficient, environment-friendly, and adaptable process for scheelite beneficiation by increasing the separation contrast between the scheelite and the gangue minerals, mostly the calcium-bearing ones. Considering the mineralogical composition, a flowsheet based on Falcon gravity separation and fatty-acid-based froth flotation was suggested. Falcon concentrators have been specifically designed for fine particles gravity processing and they are known to require low amounts of process water while processing high throughputs with high pulp densities. Moreover, gravity separation seemed a suitable option for pre-concentrating since it does not use any reagent. Besides, in flotation, the choice was made to employ only environment-benign reagents such as NaOH, Na_2CO_3, Na_2SiO_3, and fatty acids. In addition, all the fatty-acid-based commercial formulations used for batch scale flotation tests were TOFA, by-products of the Kraft process. Besides their high efficiency due to the presence of rosin acids, TOFA are very cheap (significantly cheaper than classical fatty acids), environmental benign, and do not require a specific production since they are by-products of an existing process. However, their high efficiency results from a high affinity of carboxylates for calcium atoms and, therefore, a very good collecting ability for all the calcium minerals, including the calcium silicates, the calcium salts, and the scheelite. The fatty-acid flotation selectivity can be improved by the Petrov process, which consists in a thermal treatment of the flotation rougher concentrate with a high Na_2SiO_3 concentration. This method has been widely used in Russia and China for decades but implies considerable energy consumption and, therefore, alternatives have been investigated in the present work. In particular, the use of depressants and their optimisation were studied to provide an as high as possible depression of calcium minerals with minimum scheelite

losses. Meanwhile, the collector formulations were considered to enhance the selectivity from a collector point of view. Notably, the influence of the pH, the rosin acids content, the ratios between fatty acids with different aliphatic chains (unsaturation degree, length), and the introduction of a fatty alcohol as a co-collector were studied. Finally, a high intensity magnetic separation appeared as a suitable option to reject some calcium minerals (mostly the calcium silicates) prior to the milling stage. Overall, the investigated processing options and the developments made are summarised in Figure 118.

Furthermore, to thoroughly investigate the molecular mechanisms involved in the adsorption of flotation reagents on minerals surfaces, DFT was suggested. This method allows to determine geometries and energies of systems with a very good accuracy and represents, nowadays, the most used method widely for molecular modelling (15,000 scientific articles per year include DFT). Also, *ab initio* molecular dynamics simulations (DFT performed at 300 K) allow to take into account the temperature and, therefore, the atoms motion as well as to observe reactions requiring low or no activation energy. Hence, a more fundamental part of this work has been dedicated to the study of the molecular mechanism taking place at the mineral/water interface. The main objectives are summarised in Figure 118. They consisted in gaining understanding in the synergistic effects observed at macroscopic scale during the process development, mostly in batch scale flotation tests or microflotation tests. Moreover, this study aimed at providing new insights in the adsorption mechanisms of fatty acids on calcium minerals surfaces by studying them on fluorite, an archetype of those minerals.
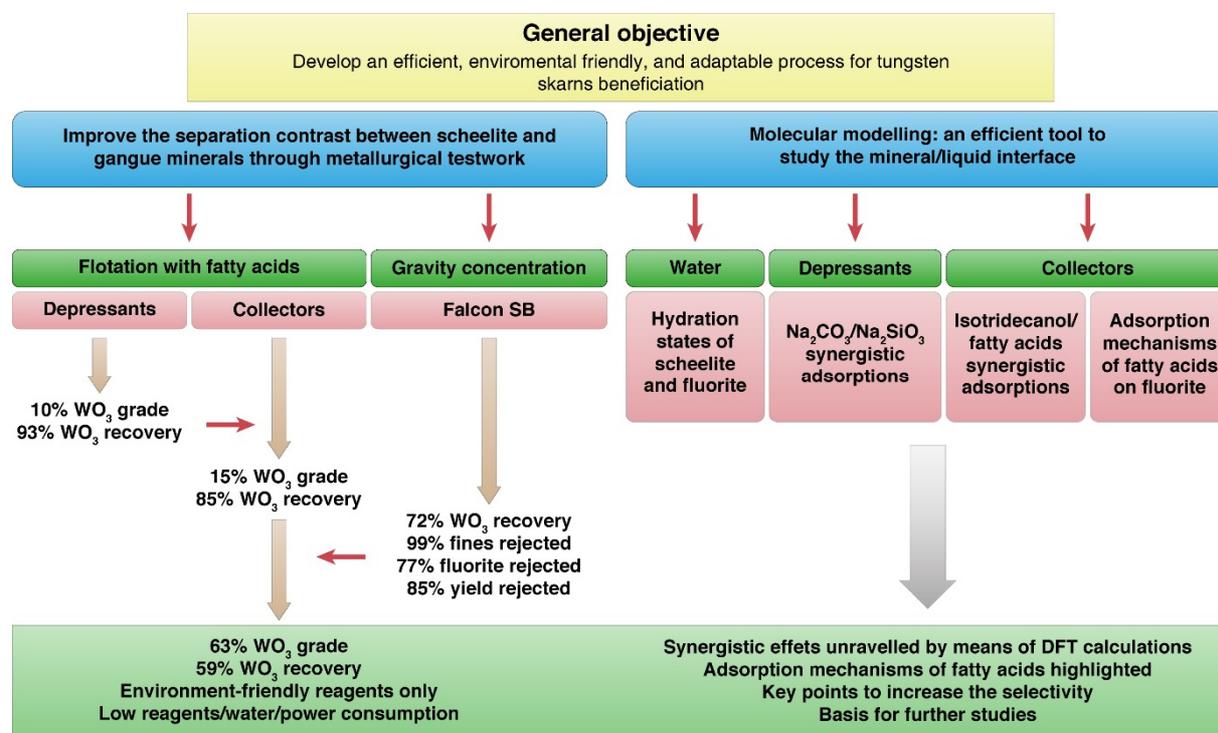
Figure 118. General schema summarising the main objectives and developments done in this work.

2. Process development

2.1 Gravity concentration

In Chapter 3, the beneficiation of the Tabuaço tungsten skarn by Falcon concentration has been investigated, with the aim to reject the problematic calcium minerals, mostly the calcium salts, and slimes prior to flotation. The two Falcon bowls, namely the Falcon UF and the fluidised Falcon SB, were used and compared. For each bowl, a DOE was employed to model the effect of each operating parameter on the gangue minerals recoveries, scheelite recovery, and desliming efficiency. Also, the DOE were used to define the optimal operating parameters that maximised the gangue minerals rejection without impacting significantly the scheelite recovery. Falcon SB allowed to obtain WO_3 recoveries ranging from 50% to 86%, WO_3 enrichment ratios ranging from 1.8 to 7.9, and desliming efficiencies ranging from 80% to 98%. Due to its optimised bowl design and the addition of a fluidisation pressure, the Falcon SB displayed better performances than the Falcon UF despite a slight decrease in WO_3 recoveries: this latter produced concentrates with WO_3 recovery ranging from 60% to 92%, WO_3 enrichment ratio ranging from 1.30 to 2.88, and desliming efficiencies ranging from 50% to 80%. The underflow of a classical hydrocyclone stage with a 10 µm cut-off displayed a 1.2 WO_3 enrichment ratio for 92% WO_3 recovery. The optimised Falcon SB test rejected 77.4% of apatite and fluorite and 98.8% of fine particles with a WO_3 recovery of 71.6%. Otherwise, the Falcon UF rejected 74.6% of apatite and fluorite and 72.5% of fine particles with a WO_3 recovery of 63.7%. Accordingly, the Falcon SB was selected for its better performances (higher calcium salts rejection, WO_3 recovery, and desliming efficiency). Also, it conducted to the elimination of 85 wt.% of the total feed mass, which was a satisfactory value for a pre-concentration stage since it would allow to reduce significantly the amounts of reagents used in the subsequent flotation stage. Overall, using a Falcon SB as a pre-concentrating apparatus would:

- Deslime efficiency the feed, significantly better than a hydrocyclone, hence substituting this latter;
- Reject 77.4% of the total amount of apatite + fluorite, which are problematic in the fatty-acid-based flotation process, thereby conducting to a scheelite concentration in the pre-concentrate;
- Eliminate 85 wt.% of the feed mass directly after the milling stage;
- Conduct however to the loss of 28.4% of the total amount of scheelite.

The scheelite losses will probably be significantly lower if industrial Falcon C are used since they are known to display better performances than laboratory-scale Falcon UF and SB. Although these latter can be operated industrially in batteries (parallel circuits), Falcon C are usually preferred. According to Sepro Mineral Systems (Sepro, 2015a, 2015b), the Falcon C efficiency at industrial scale can be assessed based on laboratory tests performed with semi-batch-operated Falcon SB/UF. Pilot-scale tests should now be performed with industrial-scale Falcon C units, which are designed to process from 1 ton/h to 100 tons/h with high pulp densities and low required areas considering the limited size of Falcon apparatuses. If the scheelite recoveries are

still as low as 71.6%, a scavenger Falcon unit can be set up to reduce the scheelite losses. Overall, replacing hydrocyclones by Falcon concentrators (SB or C) in flotation feed preparation circuits could lead to higher process performances while reducing the environmental impacts by allowing the replacement of usual ecotoxic reagents by the environmental-friendly fatty acids, reducing the reagent and energy consumptions. One main limitation of this work is the adaptability: the models developed in Chapter 3 predict quite efficiently the separation performances of Falcon UF and Falcon SB apparatuses for the Tabuaço tungsten skarn. Nonetheless, albeit the mineralogical characteristics are commonly close from one tungsten skarn to another (Dawson, 1996; Kwak, 1987), the prediction performances of the models developed here could be dramatically reduced for another skarn due to slight variations in the mineralogical and textural features. Therefore, it is of paramount interest to develop fluid-dynamics-based models that are able to predict the separation performances with Falcon UF or Falcon SB from the mineralogical and textural characteristics. Some studies have been undergone in the framework of FAME project and this work with the global aim to build strong models to predict the evolution of the separation over time as a function of the ore washability. However, these preliminary works, which are not presented in the present work, should be continued to consider all phenomena acting on the separation performances over time.

2.2 Flotation depressants

The flotation depressants were then investigated to attain suitable depressing conditions for scheelite without impacting too much its recovery. In particular, Na_2SiO_3 was tested and compared to different organic molecules, namely tannin, CMC, lignosulfonate, citric acid, and starch. All these molecules exhibited very low selectivity compared to sole Na_2SiO_3. Next, the addition of various metallic cations (Al^{3+}, Zn^{2+}, and Fe^{2+}) followed by Na_2SiO_3 demonstrated little improvement in the selectivity, with significant loss in scheelite. Most of the depressants tested in this study afforded poor selectivity between scheelite and fluorite, inducing low WO_3 grades in the concentrates. The combination of Na_2CO_3 added prior to the addition of Na_2SiO_3 afforded the best results in terms of WO_3 recovery and gangue minerals rejection. This combination was then studied in deeper detail by using the DOE methodology to assess the effect of each reagent as well as their interactions. It allowed to highlight strong synergistic effects between the two reagents, mainly on scheelite, fluorite, and, to a lesser extent, silicates. These effects were attributed to surface carbonation that makes silica species adsorption more favourable. Overall, the DOE allowed the setting of the best experimental conditions in terms of reagent concentration, thereby leading to optimised gangue mineral depression in the flotation process. These conditions were established as: 1,150 g/t Na_2CO_3 with 1,225 g/t Na_2SiO_3. This proposed method produced a flotation rougher concentrate assaying 10.1% WO_3 with 93.2% WO_3 recovery. Besides, the Na_2CO_3/Na_2SiO_3 system was deeply characterised by spectroscopic studies (FTIR and XPS) combined with state-of-the-art AIMD simulations performed on fluorite, considered as an archetype of the calcium minerals. They all demonstrated that the use of Na_2CO_3 conducts to the formation of a carbonate layer on the fluorite surface. These adsorbed species subsequently induce an acid-base reaction on the surface involving the silica species: a proton is

transferred from $Si(OH)_4$ to a CO_3^{2-} ion from the pre-adsorbed carbonate layer, forming $SiO(OH)_3^-$. The same proton transfer occurs for the dimer silica and, most probably, for the n-mers. This leads to a significantly more favoured adsorption of the silica monomers [-100.7 kJ.mol^{-1} for $Si(OH)_4$ on bare surface compared to -180.8 kJ.mol^{-1} on carbonated surface] and dimers [-165.1 kJ.mol^{-1} for $SiO(OH)_6$ on bare surface compared to -261.6 kJ.mol^{-1} on carbonated surface]. Also, experimental evidences of depolymerisation of silica species were observed exclusively on the carbonated surface. Although this reaction was not spontaneously observed by AIMD simulations, these latter demonstrated a preferred adsorption of monomeric over polymerised silica on the fluorite surface (carbonated or not). Hence, in flotation, when Na_2CO_3 is used to modulate the pH instead of NaOH, it conducts to the spontaneous formation of a carbonate layer on the surface. Silica species, regardless their polymerisation degree, turn into their basic, *i.e.* anionic, form(s) and into less polymerised forms by reaction with the carbonated surface and subsequently adsorb with higher adsorption energies. This allowed to unravel the molecular mechanisms responsible for the strong synergistic effects that have been observed for decades between Na_2CO_3 and Na_2SiO_3. Also, it highlighted the benefits of using DFT simulations for gaining understanding in the molecular mechanisms involved in the flotation process. Nonetheless, this study has been conducted on a single mineral, fluorite, which somewhat constitutes an archetype of the calcium salts. The DOE methodology demonstrated that the use of Na_2CO_3 modulates the depression selectivity since scheelite is slightly depressed compared to other minerals. Hence, the selectivity of the carbonation should be investigated by means of theoretical and experimental studies as differences in the affinities could be exhibited between carbonate species and the various minerals contained in typical tungsten ores. Indeed, the surface carbonation is most probably related to the surface properties, mainly the Ca-Ca distance, which can be very different from one mineral to another, especially between the calcium silicates and the calcium salts. Besides, the selectivity between fluorite and scheelite remains a strong problematic in terms of depressing conditions since none of the depressants tested in this work afforded an acceptable depression of fluorite without impacting significantly scheelite, including the Na_2CO_3/Na_2SiO_3 system. Indeed, under the optimised depressing conditions, the fluorite recovery was still 63.6% in the flotation roughing concentrate, which is considered high. Hence, new depressants with a high affinity for fluorite should be found or developed; they can be based on their interaction with fluorine atoms rather than with calcium atoms as it was case for most of the depressants tested. Moreover, such depressants could be found or designed based on DFT modelling studies, which allow an efficient determination of the adsorption energies and, hence, of the affinities of a given molecule for the minerals surfaces.

2.3 Flotation collectors

Meanwhile, the collector formulations were investigated to improve the global flotation selectivity, mostly between scheelite and fluorite. First, microflotation tests were performed to assess the floatabilities of each mineral considered separately as well as the two minerals mixed together. Fluorite and scheelite exhibit similar behaviours regarding the pH: their optimal floatabilities are between pH 8 and 11, which corresponds to the stability domain of the anionic

form of fatty acids (carboxylate) with however low OH⁻ activities. When the pH is raised, the floatabilities significantly decrease due to the competitive adsorption between OH⁻ and carboxylate anions on the surface cationic sites. Overall, scheelite exhibits lower floatability than fluorite with sodium oleate, most probably due to its higher specific gravity, its higher surface Ca-Ca distance, and its lower surface cationic sites density. For industrial flotation processes, TOFA formulations are commonly used. They are co-products of the Kraft paper process, which makes their price significantly low. They contain considerable amounts of rosin acids, terpene-derivative molecules displaying several rings and a carboxylic group. The influence of these compounds on the flotation performances was investigated by microflotation and batch scale flotation tests. The increase in rosin acids content provided better recoveries but lower selectivity between scheelite and the gangue minerals. These molecules probably adsorb as fatty acids on the surface calcium sites. However, their highly hindered aliphatic chain, containing several rings, may induce a high packing area and, therefore, a poor organisation of the adsorption layer and a significant loss of the control Ca-Ca distance has on this organisation. Moreover, according to their large aliphatic chain, some calcium sites are probably unoccupied on the surface, which conducts to higher amounts of collector (fatty acids or rosin acids) available to adsorb on the gangue minerals, resulting in the loss of selectivity. Hence, a comprise had to be done between a good selectivity in favour of scheelite, provided by low amounts of rosin acids, and a good scheelite recovery, afforded by high amounts of rosin acids. The optimised rosin acids content was determined at 15%, which corresponded to the RBD15, the classical TOFA used in this study, including for the optimisation of the depressing conditions. This study proved the importance of the steric hindrance and, therefore, of the packing area, on the organisation of the adsorption layer since, according to the previous results, the selectivity seems inversely correlated with packing area. Then, the classical sodium oleate was replaced with three other fatty acids with different chain lengths and unsaturation degrees, *i.e.* packing areas, in microflotation tests and their performances were compared. These tests were conducted on sole minerals or on scheelite + fluorite mixtures to estimate the real selectivity. The microflotation tests exhibited systematically a selectivity in favour of fluorite while, interestingly, the unsaturation degree erased those differences; sodium linoleate afforded similar recoveries for scheelite and fluorite. Again, this is due to the decrease of the control Ca-Ca distance has on the organisation of the adsorption layer when the unsaturation degree, *i.e.* the packing area, is increased. Besides, mixing the fatty acids exhibited synergistic effects that increased significantly the selectivity in favour of scheelite in microflotation tests. These results served as a basis to tests new formulations containing unsaturated and saturated fatty acids in various proportions on the Tabuaço tungsten skarn. Non-commercial formulations did not provide satisfactory results in terms of selectivity and recoveries, which were both decreased when fatty acids with different molecular structures were mixed. However, when a TOFA containing significant amounts of saturated fatty acids with similar oleate:linoleate and fatty acids:rosin acids ratios similar to those of RBD15, LD, was used, it afforded a better selectivity between scheelite and fluorite, allowing to attain higher WO₃ grades in the concentrate. The differences observed between non-commercial and commercial fatty acids mixtures could be due to a pre-organisation of the different fatty acids in solution in

the case of commercial mixtures. Indeed, these latter undergo chemical processes such as distillation and liquid-solid states transformation that might be responsible for an optimal organisation of the fatty acids, maximising the chain-chain interactions in solution. Under the optimised depressing conditions, LD produced flotation concentrates that assayed 14.5% WO_3 for 85.4% WO_3 recovery for the rougher stage and 25.2% WO_3 for 73.7% WO_3 recovery for the cleaning stage. The WO_3 grades were significantly higher than with RBD15, under the same depressing conditions, while the WO_3 recovery was decreased by around 10%. Finally, the introduction of isotridecanol, a fatty alcohol, in RBD15 and LD commercial formulations displayed a significant increase in the flotation selectivity in favour of scheelite. Overall, under optimised depressing conditions, LD mixed with isotridecanol at a ratio of 2:1 produced a flotation rougher concentrate assaying 14.8% WO_3 for 100.0% WO_3 recovery while the cleaner concentrate assayed 45.2% WO_3 for 56.5% WO_3 recovery. Interestingly, the isotridecanol did not enhance significantly the WO_3 grade in the rougher concentrate but considerably in the cleaner concentrate. This can be attributed to a stronger hydrophobation of scheelite particles compared to fluorite particles; these latter do not attach to (or detach from) bubbles during the cleaning stage. This stronger hydrophobation can be ascribed to a better organisation of the adsorption layer on scheelite compared to fluorite. Nonetheless, the molecular mechanisms involved in this selective stabilisation are poorly understood and could not be unravelled by DFT calculations, which proved that isotridecanol adsorbs onto surface calcium sites by establishing a Ca-O bond with its terminal alcohol group. Although the adsorption energy of isotridecanol is significantly higher on scheelite than on fluorite, it has been demonstrated in Chapter 7 that the adsorption of water molecule is also more favoured on scheelite compared to fluorite. Considering the water molecule(s) desorption, the adsorption of isotridecanol is not considerably favoured on scheelite compared to fluorite. Moreover, when isotridecanol was introduced between two sodium oleate molecules, the energy difference was similar between scheelite and fluorite. These calculations were performed for the (001) scheelite surface while the (112) is part of the most exposed surfaces for scheelite. Also, the Ca-Ca distances on the (001) and the (112) scheelite surfaces are different, which could induce significant differences in the mechanisms involved in the stabilisation of the adsorption layer. Hence, the above-mentioned atomistic simulations should also be performed on the (112) surface. Furthermore, calculations were performed using sodium oleate molecules while, in Chapter 8, it has been demonstrated that free carboxylate anions, *i.e.* without a Na^+, can adsorb on the surface. This configuration would result in higher polar repulsion between the carboxylate groups since no cation would be present on the surface to stabilise the polar heads as it is the case when Na^+ are included in the simulations. In this case, the introduction of a neutral (non-ionic) co-collector such as isotridecanol could lead to a decrease of the polar repulsion between the carboxylate thereby conducting to a stabilisation of the adsorption layer. Based on previous results and discussions from Chapter 8, the adsorption of several carboxylate anions on neighbouring calcium sites on the surface is neither favoured nor realistic. One solution would be to include some Na^+ in the adsorption layer to stabilise the polar head and reduce the basicity/electron density on the surface. Besides, non-ionic molecules could also be introduced in the adsorption layer to reduce the polar repulsions and the electron density on the surface. The

weight ratios between the fatty acids and the fatty alcohol that provided satisfactory results were between 1:1 and 2:1, which, considering the molar weight of isotridecanol, roughly corresponded to molar ratios ranging from 1.5:1 to 3:1. Hence, assessing a periodic organisation of the adsorption layer, this indicates that two carboxylate molecules are adsorbed for one isotridecanol, which probably induce a screening of the electron density on the surface. Moreover, in Chapter 8, it has been proven that the location of the IR absorption bands of the asymmetric stretching of the carboxyl group gives useful information about the adsorption configuration. When isotridecanol was added with sodium oleate, no significant change was observed in FTIR compared to system where sole sodium oleate was used. Hence, it can be assessed that isotridecanol does not affect the fatty acids adsorption mechanisms and, therefore, that it only adsorbs on cationic sites that are unoccupied for systems with only fatty acids. Overall, deeper investigations are required to unravel the molecular mechanisms that are responsible for the considerable synergistic effects observed in batch scale flotation tests. Gaining understanding in such details could allow to design new collectors/co-collectors, not necessarily fatty acids/alcohols, to improve further the scheelite flotation performances. On a broader level, it could provide new insights in the adsorption processes that conduct to the formation of the adsorption layer. Hence, this methodology could afford the development and the adaptation of co-collectors/collectors to a wide range of minerals contained in low separation contrast ores, with the global aim to increase the selectivity in favour of the valuable mineral. For the Tabuaço skarn process development, two choices were then suitable, namely with isotridecanol, which provided high WO_3 grade with somewhat low WO_3 recovery, or without, *i.e.* with sole LD, which afforded moderate WO_3 grade and recovery. Notably, the use of isotridecanol induced a higher consumption of LD (800 g/t with isotridecanol instead of 600 g/t without) along with the 400 g/t of isotridecanol. Hence, the operating costs would be considerably higher if isotridecanol is used and, in Chapter 6, the flotation flowsheets were tested with sole TOFA. However, the introduction of fatty alcohols would be a suitable option for only-flotation flowsheets, *i.e.* without the gravity pre-concentration developed in Chapter 3.

2.4 Flowsheet development

Based on the previous discussions, the global flowsheet for the Tabuaço tungsten skarn was developed by combining the Falcon gravity separation, optimised in Chapter 3, and the flotation, optimised in Chapter 4 and Chapter 5. A final concentrate assaying 62.9% WO_3 with 59.4% WO_3 recovery was produced from a feed assaying 1.1% WO_3 after one optimised Falcon SB stage and four optimised flotation stages. These latter were performed at pH 10 using 1,150 g/t Na_2CO_3 and 1,225 g/t Na_2SiO_3 as depressants and 600 g/t LD as collector. This product constituted a marketable scheelite concentrate, which can be processed by hydrometallurgy. Moreover, a dry magnetic separation was a possible option on the crushed feed prior to fine grinding. Although it would lead to the rejection, prior to the milling stage, of around 45 wt.% of the yield with only 6.0% scheelite losses, this option was not implemented in the global flowsheet for the Tabuaço tungsten skarn. Notably, it would correspond to a significant energy saving since the rejected part mainly contains the hardest minerals of the ore (dense ferromagnesian silicates). Besides,

the DOE methodology used for the flowsheets development allows to adapt the operating parameters to the targeted performance, *i.e.* to maximise either the gangue minerals (mostly fluorite) rejection, *i.e.* the WO_3 grade or the WO_3 recovery (see Chapter 3 and Chapter 4). Furthermore, the number of flotation cleaning stages performed on the Falcon SB pre-concentrate as well as the collector formulation can be optimised to maximise the WO_3 grade or the WO_3 recovery. Overall, the suggested flowsheets would:

- Provide low energy consumption as more than half of the product is rejected before the mill;
- Induce low reagents costs by decreasing as much as possible the ore quantity processed by flotation;
- Afford low energy/water consumption as a low part of the feed material is sent to flotation;
- Use only environmental benign chemicals in flotation (Na_2CO_3, Na_2SiO_3, fatty acids) as problematic gangue minerals are eliminated before flotation;
- Conduct the whole process at room temperature, avoiding the use of the Petrov's process to increase the selectivity between calcium minerals in flotation;
- Produce a marketable WO_3 concentrate (62.9% WO_3);
- Adapt the processing route to the product specifications or to the targeted performance (WO_3 grade or WO_3 recovery).

The developed flowsheets should be implemented with the dry high intensity magnetic separation to assess the influence of this latter on the subsequent process. Moreover, tests at pilot scale should be performed to calculate the material balance on the developed flowsheets as well as to estimate the effect of a continuous process and the re-circulations between the different separations. Overall, a global model should be constructed by implementing the models developed for each separation (Falcon, flotation, and magnetic separation) with the global aim to predict the separation performances (WO_3 grade and recovery) in the final concentrate as well as the operating costs. Finally, this process should be tested on other tungsten skarns to validate its adaptability and to demonstrate the mineral processing feasibility of such low separation contrast ores, still considered as complex.

3. Surface phenomena applied to flotation

Besides from the process development, a wide work has been undergone to model the surface phenomena applied to the froth flotation. Since anionic collectors involve chemisorption and are usually employed for calcium minerals flotation, an accurate description of the surface chemical reactions was required. Hence, the use of density functional theory was suggested to model the solid/liquid interface corresponding to the mineral/solution interface. First, DFT calculations were performed on fluorite, which represent a simple (cubic) mineral exhibiting one most exposed surface and containing only two different atoms types (Ca and F). The hydration state of fluorite was first studied to serve as a basis for the investigation of the fatty acids adsorption. It has been demonstrated, in Chapter 7, that only half of the surface calcium atoms are occupied with water

molecules adsorbed, which is consistent with the moderate hydrophobicity of fluorite observed experimentally. Besides, the hydration state of scheelite was also modelled on its two main surfaces, the (112) and (001). The adsorption of hydroxyl groups onto calcium atoms was possible, although the adsorption of molecular water was significantly favoured. Overall, the adsorption energies for molecular water are -55 kJ.mol⁻¹ for fluorite, -87 kJ.mol⁻¹ for (001) scheelite, and -127 kJ.mol⁻¹ for (112) scheelite. This is consistent with the higher reactivity of surface calcium atoms for scheelite induced by the existence of two dangling bonds per calcium atom instead of only one dangling bond per calcium atom for fluorite. Also, this reactivity difference results in the adsorption of two water molecules per surface calcium atoms or three water molecules on two surface calcium atoms for the (001) and the (112) scheelite surfaces, while only one water molecule is adsorbed per two surface calcium atoms in the case of fluorite. This can explain the moderate hydrophobicity of the (111) fluorite surface, resulting in significant contact angles (~ 20°) reported by authors (Jańczuk et al., 1993; Kowalczuk et al., 2017; Zhang et al., 2015). Considering their significant number of water molecules adsorbed per unit area, scheelite surfaces should be hydrophilic, albeit contact angles of 73.1° and 62.7° were reported for the (001) and (112) surfaces (Gao et al., 2013). Indeed, assessing that (111) fluorite has a calcium sites density two times higher than (001) and (112) surfaces (see Chapter 1), two water molecules per surface calcium atoms [for the (001) surface] and three water molecules per two surface calcium atoms [for the (112) surface] still represent higher numbers of water molecules adsorbed per unit area compared to one water molecule per two surface calcium atoms (for fluorite). Besides, in the Langmuir model, the adsorption of molecules in liquid phase onto solid surfaces comprises the pre-adsorbed water molecule(s) desorption, before the strictly-speaking adsorption process. Hence, the higher adsorption energies of water molecules onto scheelite compared to fluorite probably induce a higher difficulty for flotation reagents to adsorb onto scheelite, since water molecules need higher energies to be desorbed. This can explain the lower floatability exhibited by scheelite compared to fluorite, along with its lower calcium sites density and its higher Ca-Ca distance. The results about hydration state contributed to a better understanding of the properties of fluorite and scheelite in aqueous phase and were crucial to understand to subsequent adsorption of flotation collectors. Namely, the next step was be to study the fundamentals of fatty acids adsorption onto different mineral surfaces, mostly fluorite, to gain understanding in the molecular mechanisms involved in their adsorption.

Based on octanoate molecules, the different possible configurations for the adsorption of carboxylate onto fluorite surface were investigated by DFT calculations at 0 K and 300 K, under vacuum or hydrated conditions. Moreover, DFPT allowed to simulate IR spectra from given atomic structures, to establish a link with experimental data. It was shown that, at 300 K and under hydrated conditions:

- Sodium atoms are likely to adsorb onto fluorite surface (ΔE_{ads} = -144.8 kJ.mol⁻¹);
- The bonding between carboxylate species and sodium atoms in solution is slightly favoured (ΔE_r = -33.7 kJ.mol⁻¹);

- One free carboxylate anion adsorbs under hydrated conditions in a monodentate configuration (ΔE_{ads} = -66.3 kJ.mol^{-1}), which corresponds to the peak at 1535 cm^{-1} in IR;
- Two free carboxylate anions adsorb under hydrated conditions with one in a monodentate configuration and the other in a bidentate binuclear configuration, this latter corresponds to the peak at 1575 cm^{-1} in IR;
- Sodium carboxylate adsorbs bridged to the surface by the sodium atom adsorbed onto surface fluorine atoms (ΔE_{ads} = -154.2 kJ.mol^{-1}), which corresponds to the peak at 1558 cm^{-1} in IR;
- Anion exchange between a fluorine atom and the free carboxylate (ΔE_r = -106.4 kJ.mol^{-1}).
- An adsorption monolayer cannot be formed by only carboxylate anions.

DFT calculations performed in this work did not provide the activation energies of the investigated reaction since they depend on kinetics consideration. However, it can be assessed that the bonding between carboxylate species and sodium cation in solution is subject to a slight activation energy since the hydration shell of sodium cation has to be partly destroyed. Besides, the adsorption of sodium on the surface requires low or no activation energy since it adsorbs onto surface fluorine atoms which are occupied by one water molecule interacting through a hydrogen bond. Among the three above-described adsorption modes, the anion exchange probably requires a significant activation energy considering the breakage of three Ca-F bonds to eject the fluorine atom from the surface. Hence, at room temperature, this reaction seems unlikely to occur although some researchers suggested it (Finkelstein, 1989; Nixon and Cook, 1950; Peck and Wadsworth, 1965; Young and Miller, 2000). The two other modes probably implies low activation energy since water molecules are adsorbed onto fluorine atoms only by means of hydrogen bonds (*i.e.* few kJ.mol^{-1} to desorb one) and only half of the calcium atoms are occupied by water molecules under hydrated conditions (see Chapter 7), which induces around 23 kJ.mol^{-1} of activation energy per carboxylate, *i.e.* one water molecule desorbed for two carboxylates.

The mechanisms leading to the formation of a complete adsorption layer were then investigated by means of AIMD simulations performed at 300 K and under hydrated conditions. The assumption was made, in first approximation, that the adsorption layer is formed only by carboxylate anions, *i.e.* without sodium atoms. Interestingly, when the coverage is increased, some molecules adsorb under the monodentate configuration while other ones adsorb under the bidentate binuclear mode which, for a sole molecule, was stable only under vacuum conditions (see Chapter 8). These two adsorption configurations correspond to the peaks at 1535 and 1575 cm^{-1} in IR, which is consistent with what was observed experimentally by many authors and in this work (Free and Miller, 1996; Hu et al., 1986b, 1986a; Lovell et al., 1974; Mielczarski et al., 2002, 2000, 1998, 1999; Rao et al., 1991a, 1991b, 1990; Young and Miller, 2000). This is in accordance with previous works performed by IRS, which attributed those two peaks to two different adsorption configurations of carboxylate anions on the surface (Mielczarski et al., 2002, 2000, 1998, 1999). Hence, it can be assessed that, in the adsorption layer, most species are under their anionic form and adsorbed under both monodentate and bidentate binuclear configurations.

Nevertheless, the global system must be electrically neutral when species are adsorbed on the surface and, therefore, cations must be present in the adsorption layer to ensure the neutrality. However, when a carboxylate anion is adsorbed onto surface calcium atoms and close to a sodium atom adsorbed on a surface fluorine atom, at 300 K and under hydrated conditions, it spontaneously desorb from the calcium atoms and adsorb bridged on the sodium atom. This is consistent with the adsorption energies calculated for sodium carboxylate adsorption, which are significantly higher in absolute value than those for carboxylate anion. This result is also in agreement with the fact that, at low sodium carboxylate concentrations, a singlet at 1558 cm^{-1} is observed (see Chapter 8), attributed by DFPT to the adsorption of carboxylate bridged on a sodium atom. Moreover, when a full surface coverage is set with carboxylate anions, carboxylic acids are reformed (two out of six molecules), which is not consistent with the IR experiments since no peak at 1740 cm^{-1} is observed (corresponding to the C=O). Nonetheless, for higher carboxylate concentrations, the two peaks at 1535 and 1575 cm^{-1} are observed, previously ascribed to the chemisorption of carboxylate anions onto the surface calcium atoms under both monodentate and bidentate binuclear configurations. This means that carboxylate species are first adsorbed bridged on a sodium atom and, when the coverage is increased, they adsorb onto surface cations. However, this doublet has been attributed to the precipitation of calcium dicarboxylate on the surface by several authors (Free and Miller, 1996; Hu et al., 1986b, 1986a; Rao et al., 1991a, 1991b, 1990; Young and Miller, 2000). To investigate this hypothesis, IR experiments were conducted with different chain lengths and conditioning times. Indeed, in the calcium dicarboxylate surface precipitation theory, the calcium is provided by the dissolution of the calcium minerals, which displays a moderately slow kinetics. At short conditioning times (5 min) or short chains (C12), the doublet is still observed while the solubility product of calcium dilaurate is not attained. Besides, the adsorption of commercial sodium octanoate was studied; this species exhibits a single peak at 1558 cm^{-1} when it is adsorbed on fluorite, which indicates its adsorption on a bridging sodium atom. Furthermore, most of the IR experiments presented in this study were conducted at pH 7 for the adsorption of the collector, except in Chapter 5, where they were performed at pH 9, obtained by the addition of sodium hydroxide. At pH 7, the doublet was systematically observed except for low concentrations, as mentioned previously. When the IR experiments were conducted at pH 9, the singlet was always observed, see Chapter 5. This indicates that the sodium atoms, provided by the use of sodium hydroxide, play a role in the adsorption mechanisms of carboxylate species on the fluorite surface. Most probably, the sodium cations adsorb on the surface fluorine atoms and constitute adsorption sites that allow the adsorption of carboxylate species. When the concentration is raised, the carboxylate species start to adsorb on surface calcium atoms under the two modes exhibited previously. Some responses could be provided by experiments conducted with different sodium atoms concentrations as well as with different alkaline cations (potassium, sodium, lithium…). It can be assessed that the IR peak corresponding to alkali carboxylate will be shifted between potassium, sodium, and lithium carboxylate. If the adsorption of carboxylate species is controlled by the adsorption of alkali cations on the surface anion atoms, changing the alkali type could conduct to a modulation of the flotation selectivity. The use of other strong bases than alkali hydroxides

could provide useful information about the role of the sodium cations in the adsorption mechanisms and eventually modulate the selectivity. In particular, CaO or $Ca(OH)_2$ are widely used in the industrial flotation process and they would allow to have no sodium atom in the whole system, thereby discussing the differences in adsorption mechanisms and floatabilities. Besides, the solubility product of calcium dioleate can be attained for conditioning times around 30 min, which provide high enough calcium concentration due to the mineral dissolution. Hence, to assess the validity of this hypothesis, some XRD experiments could be conducted to identify a precipitate, *i.e.* a crystallised phase, adsorbed on the surface. However, within this assumption, the adsorption of the precipitate cannot be done by interactions between the oleate chains and the surface since it has been demonstrated in Chapter 8 that the "flat" adsorption is not enough favoured to desorb enough water molecules. Hence, the adsorption of such precipitate would necessarily occur by the cations contained in the precipitate, which would imply the formation of bonds between the calcium atoms of the precipitate and the surface anions. Deep investigations can therefore be undergone to discuss that points.

References

Abd El-rahman, M.K., Youssef, M.A., Helal, N.H., El-Rabiei, M.M., Elsaidy, S.R., 2009. Experimental Design Technique on Recovery of Fine Cassiterite from Igla Placer Ore of Egypt.

Abeidu, A.M., 1973. Selective depression of calcite from fluorite. Transactions of the Institution of Mining and Metallurgy, Section C 49–50.

Abela, R.L., 1997. Centrifugal concentrators in gold recovery and coal processing, in: Extr. Metall. Africa' 97, The South African Institute of Mining and Metallurgy, Randburg, South Africa, 1997.

Agar, G.E., 1984. Scheelite Flotation Process. US Patent. 4,488,959.

Ahmed, A.A., Gypser, S., Leinweber, P., Freese, D., Kühn, O., 2019. Infrared spectroscopic characterization of phosphate binding at the goethite–water interface. Phys. Chem. Chem. Phys. 21, 4421–4434. https://doi.org/10.1039/C8CP07168C

Alekseev, V.S., Morozov, G.G., 1975. Rate of flotation of kyanite, quartz, and muscovite. Soviet Mining Science 11, 62–64. https://doi.org/10.1007/BF02501018

Alp, I., Celep, O., Deveci, H., Vicil, M., 2008. Recovery of gold from a free-milling ore by centrifugal gravity separator. Iranian Journal of Science & Technology, Transaction B, Engineering, 32(B1). pp. 67–71.

Anacker, T., Friedrich, J., 2014. New accurate benchmark energies for large water clusters: DFT is better than expected. Journal of Computational Chemistry 35, 634–643. https://doi.org/10.1002/jcc.23539

Ancia, P., Frenay, J., Dandois, P., 1997. Comparison of Knelson and Falcon centrifugal separators. In: Mozeley, R. (Ed.), Innovation in Physical Separation Technologies, Richard Mozely Symposium Volume. IMM, Falmouth, UK, pp. 53–62.

Angadi, S.I., Eswaraiah, C., Jeon, H.-S., Mishra, B.K., Miller, J.D., 2017. Selection of Gravity Separators for the Beneficiation of the Uljin Tin Ore. Mineral Processing and Extractive Metallurgy Review 38, 54–61. https://doi.org/10.1080/08827508.2016.1262856

Angadi, S.I., Sreenivas, T., Jeon, H.-S., Baek, S.-H., Mishra, B.K., 2015. A review of cassiterite beneficiation fundamentals and plant practices. Minerals Engineering 70, 178–200. https://doi.org/10.1016/j.mineng.2014.09.009

Aquino, A.J.A., Tunega, D., Haberhauer, G., Gerzabek, M.H., Lischka, H., 2007. Quantum Chemical Adsorption Studies on the (110) Surface of the Mineral Goethite. J. Phys. Chem. C 111, 877–885. https://doi.org/10.1021/jp0649192

Araujo, A.C., Viana, P.R.M., Peres, A.E.C., 2005. Reagents in iron ores flotation. Minerals Engineering 18, 219–224. https://doi.org/10.1016/j.mineng.2004.08.023

Arnold, R., Brownbill, E.E., Ihle, S.W., 1978. Hallimond tube flotation of scheelite and calcite with amines. International Journal of Mineral Processing 5, 143–152. https://doi.org/10.1016/0301-7516(78)90011-X

Arnold, R., Warren, L.J., 1974. Electrokinetic properties of scheelite. Journal of Colloid and Interface Science 47, 134–144.

Atademir, M.R., Kitchener, J.A., Shergold, H.L., 1981. The surface chemistry and flotation of scheelite, II. Flotation "collectors." International Journal of Mineral Processing 8, 9–16.

Atademir, M.R., Kitchener, J.A., Shergold, H.L., 1979. The surface chemistry and flotation of scheelite. I. Solubility and surface characteristics of precipitated calcium tungstate. Journal of Colloid and Interface Science 71, 466–476.

Audion, A.S., Labbé, J.F., 2012. Panorama 2011 du marché du tungstène.

Aydogan, N.A., Kademli, M., 2019. Effect of operational conditions on Falcon concentrator performance with different particle size fractions. Particulate Science and Technology 1–5. https://doi.org/10.1080/02726351.2019.1573867

Azizi, D., Larachi, F., 2018. Surface interactions and flotation behavior of calcite, dolomite and ankerite with alkyl hydroxamic acid bearing collector and sodium silicate. Colloids and Surfaces A: Physicochemical and Engineering Aspects 537, 126–138. https://doi.org/10.1016/j.colsurfa.2017.09.054

Bachér, J., Mrotzek, A., Wahlström, M., 2015. Mechanical pre-treatment of mobile phones and its effect on the Printed Circuit Assemblies (PCAs). Waste Management, Urban Mining 45, 235–245. https://doi.org/10.1016/j.wasman.2015.06.009

Badawi, M., Cristol, S., Paul, J.-F., Payen, E., 2009. DFT study of furan adsorption over stable molybdenum sulfide catalyst under HDO conditions. Comptes Rendus Chimie 12, 754–761. https://doi.org/10.1016/j.crci.2008.10.023

Badawi, Michael, Paul, J.-F., Cristol, S., Payen, E., 2011. Guaiacol derivatives and inhibiting species adsorption over MoS2 and CoMoS catalysts under HDO conditions: A DFT study. Catalysis Communications 12, 901–905. https://doi.org/10.1016/j.catcom.2011.02.010

Badawi, M., Paul, J.F., Cristol, S., Payen, E., Romero, Y., Richard, F., Brunet, S., Lambert, D., Portier, X., Popov, A., Kondratieva, E., Goupil, J.M., El Fallah, J., Gilson, J.P., Mariey, L., Travert, A., Maugé, F., 2011. Effect of water on the stability of Mo and CoMo hydrodeoxygenation catalysts: A combined experimental and DFT study. Journal of Catalysis 282, 155–164. https://doi.org/10.1016/j.jcat.2011.06.006

Badawi, M., Paul, J.-F., Payen, E., Romero, Y., Richard, F., Brunet, S., Popov, A., Kondratieva, E., Gilson, J.-P., Mariey, L., Travert, A., Maugé, F., 2013. Hydrodeoxygenation of Phenolic Compounds by Sulfided (Co)Mo/Al $_2$ O $_3$ Catalysts, a Combined Experimental and Theoretical Study. Oil Gas Sci. Technol. – Rev. IFP Energies nouvelles 68, 829–840. https://doi.org/10.2516/ogst/2012041

Bahr, A., Clement, M., Surmatz, H., 1968. On the effect of inorganic and organic substances on the flotation of some non-sulfide minerals by using fatty-acid-type collectors. In: VIIIth International Mineral Processing Congress. Leningrad, Russia.

Baral, K., Li, A., Ching, W.-Y., 2017. Ab Initio Modeling of Structure and Properties of Single and Mixed Alkali Silicate Glasses. The Journal of Physical Chemistry A 121, 7697–7708. https://doi.org/10.1021/acs.jpca.7b06530

Barr, T.L., 1978. An ESCA study of the termination of the passivation of elemental metals. The Journal of Physical Chemistry 82, 1801–1810. https://doi.org/10.1021/j100505a006

Bass, J.L., Turner, G.L., 1997. Anion Distributions in Sodium Silicate Solutions. Characterization by ^{29} SI NMR and Infrared Spectroscopies, and Vapor Phase Osmometry. The Journal of Physical Chemistry B 101, 10638–10644. https://doi.org/10.1021/jp9715282

Bel'kova, O.N., Leonov, S.B., Shcherbakova, E.V., 1993. Intensification of beneficiation of scheelite ores by flotation. Journal of Mining Science 28, 480–485. https://doi.org/10.1007/BF00711134

Bennewitz, R., Reichling, M., Matthias, E., 1997. Force microscopy of cleaved and electron-irradiated CaF2(111) surfaces in ultra-high vacuum. Surface Science 387, 69–77. https://doi.org/10.1016/S0039-6028(97)00268-9

Berlinskii, I.I., 1962. Electrokinetic analysis of the reaction of flotation reagents with certain minerals of non-sulphide ores. Tr. Tsentr. Nauchno-Issled. Gornorazved. Inst. Isvetn., 47: 124--133, CA 59:2426b.

Bittarello, E., Bruno, M., Aquilano, D., 2018. Ab Initio Calculations of the Main Crystal Surfaces of Baryte (BaSO $_4$). Crystal Growth & Design 18, 4084–4094. https://doi.org/10.1021/acs.cgd.8b00460

Bjørheim, T.S., Besikiotis, V., Haugsrud, R., 2012. Hydration thermodynamics of pyrochlore structured oxides from TG and first principles calculations. Dalton Trans. 41, 13343. https://doi.org/10.1039/c2dt31517c

Blazy, P., Joussemet, R., 2011. Concentration par gravité - Différentes technologies.

Blöchl, P.E., 1994. Projector augmented-wave method. Physical Review B 50, 17953–17979. https://doi.org/10.1103/PhysRevB.50.17953

Bo, F., Xianping, L., Jinqing, W., Pengcheng, W., 2015. The flotation separation of scheelite from calcite using acidified sodium silicate as depressant. Minerals Engineering 80, 45–49. https://doi.org/10.1016/j.mineng.2015.06.017

Box, G.E., Wilson, K.G., 1951. On the Experimental Attainment of Optimum Conditions. Journal of the Royal Statistical Society 1–45.

Brandao, P.R.G., 1982. Adsorption of oleate on magnesite and its influence on flotation. Ph.D. Thesis, University of British Columbia.

Brandao, P.R.G., Poling, G.W., 1988. Flotation of magnesite with sodium oleate as collector; an infrared spectrophotometric study. In: K.S.E. Forssberg (Editor), 16th Int. Miner. Process. Cong. Elsevier, Amsterdam, pp. 1463-1475.

References

Briggs, D., 1981. Handbook of X-ray Photoelectron Spectroscopy C. D. Wanger, W. M. Riggs, L. E. Davis, J. F. Moulder and G. E.Muilenberg Perkin-Elmer Corp., Physical Electronics Division, Eden Prairie, Minnesota, USA, 1979. 190 pp. $195. Surface and Interface Analysis 3, v–v. https://doi.org/10.1002/sia.740030412

Bučko, T., Chibani, S., Paul, J.-F., Cantrel, L., Badawi, M., 2017. Dissociative iodomethane adsorption on Ag-MOR and the formation of AgI clusters: an ab initio molecular dynamics study. Phys. Chem. Chem. Phys. 19, 27530–27543. https://doi.org/10.1039/C7CP05562E

Bučko, T., Hafner, J., Lebègue, S., Ángyán, J.G., 2010. Improved Description of the Structure of Molecular and Layered Crystals: Ab Initio DFT Calculations with van der Waals Corrections. J. Phys. Chem. A 114, 11814–11824. https://doi.org/10.1021/jp106469x

Bučko, T., Lebègue, S., Ángyán, J.G., Hafner, J., 2014. Extending the applicability of the Tkatchenko-Scheffler dispersion correction via iterative Hirshfeld partitioning. The Journal of Chemical Physics 141, 034114. https://doi.org/10.1063/1.4890003

Bučko, T., Lebègue, S., Gould, T., Ángyán, J.G., 2016. Many-body dispersion corrections for periodic systems: an efficient reciprocal space implementation. J. Phys.: Condens. Matter 28, 045201. https://doi.org/10.1088/0953-8984/28/4/045201

Bučko, T., Lebègue, S., Hafner, J., Ángyán, J.G., 2013a. Tkatchenko-Scheffler van der Waals correction method with and without self-consistent screening applied to solids. Physical Review B 87. https://doi.org/10.1103/PhysRevB.87.064110

Bučko, T., Lebègue, S., Hafner, J., Ángyán, J.G., 2013b. Improved Density Dependent Correction for the Description of London Dispersion Forces. Journal of Chemical Theory and Computation 9, 4293–4299. https://doi.org/10.1021/ct400694h

Bulatovic, S.M., 2015. Handbook of flotation reagents: chemistry, theory and practice. Volume 3, Volume 3,.

Bulatovic, S.M., 2010. Handbook of flotation reagents: chemistry, theory and practice. Vol. 2: Flotation of gold, PGM and oxide minerals, 1. ed. ed. Elsevier, Amsterdam.

Bulatovic, S.M., 2007. Handbook of flotation reagents: chemistry, theory and practice, 1st ed. ed. Elsevier, Amsterdam ; Boston.

Buonvino, M., 1993. A study of the Falcon concentrator, PhD Thesis McGill University, 1993.

Burdukova, E., Van Leerdam, G.C., Prins, F.E., Smeink, R.G., Bradshaw, D.J., Laskowski, J.S., 2008. Effect of calcium ions on the adsorption of CMC onto the basal planes of New York talc – A ToF-SIMS study. Minerals Engineering 21, 1020–1025. https://doi.org/10.1016/j.mineng.2008.03.017

Burt, R., 1999. The role of gravity concentration in modern processing plants. Minerals Engineering 12, 1291–1300.

Burt, R.O., 1987. Gravity Concentration Methods, in: Yarar, B., Dogan, Z.M. (Eds.), Mineral Processing Design. Springer Netherlands, Dordrecht, pp. 106–137. https://doi.org/10.1007/978-94-009-3549-5_5

Burt, R.O., Korinek, G., Young, S.R., Deveau, C., 1995. Ultrafine tantalum recovery strategies. Minerals Engineering 8, 859–870. https://doi.org/10.1016/0892-6875(95)00048-U

Burt, R.O., Mills, C., 1984. Gravity concentration technology, Developments in mineral processing. Elsevier, Amsterdam.

Calvo, G., Mudd, G., Valero, Alicia, Valero, Antonio, 2016. Decreasing Ore Grades in Global Metallic Mining: A Theoretical Issue or a Global Reality? Resources 5, 36. https://doi.org/10.3390/resources5040036

Campatelli, G., Lorenzini, L., Scippa, A., 2014. Optimization of process parameters using a Response Surface Method for minimizing power consumption in the milling of carbon steel. Journal of Cleaner Production 66, 309–316. https://doi.org/10.1016/j.jclepro.2013.10.025

Carniato, S., Gallet, J.-J., Rochet, F., Dufour, G., Bournel, F., Rangan, S., Verdini, A., Floreano, L., 2007. Characterization of hydroxyl groups on water-reacted Si $(001) - 2 \times 1$ using synchrotron radiation O 1 s core-level spectroscopies and core-excited state density-functional calculations. Physical Review B 76. https://doi.org/10.1103/PhysRevB.76.085321

Cases, J.M., Mutaftschiev, B., 1968. Adsorption et condensation des chlorhydrates d'alkylamine à l'interface solide-liquide. Surface Science 9, 57–72. https://doi.org/10.1016/0039-6028(68)90163-5

Cases, J.M., Villieras, F., 1992. Thermodynamic model of ionic and nonionic surfactants adsorption-abstraction on heterogeneous surfaces. Langmuir 8, 1251–1264. https://doi.org/10.1021/la00041a005

Chang, L.L.Y., Howie, R.A., Zussman, J., Deer, W.A., Chang, L.L.Y., 1996. Non-silicates: sulphates, carbonates, phosphates, halides, 2. ed., reprinted. ed, Rock-forming minerals. Geological Society, London.

Changgen, L., Yongxin, L., 1983. Selective flotation of scheelite from calcium minerals with sodium oleate as a collector and phosphates as modifiers. II. The mechanism of the interaction between phosphate modifiers and minerals. International Journal of Mineral Processing 10, 219–235. https://doi.org/10.1016/0301-7516(83)90012-1

Chebbi, M., Chibani, S., Paul, J.-F., Cantrel, L., Badawi, M., 2017. Evaluation of volatile iodine trapping in presence of contaminants: A periodic DFT study on cation exchanged-faujasite. Microporous and Mesoporous Materials 239, 111–122. https://doi.org/10.1016/j.micromeso.2016.09.047

Cheetham, A.K., Fender, B.E.F., Cooper, M.J., 1971. Defect structure of calcium fluoride containing excess anions: I. Bragg scattering.

Chen, C., Zhu, H., Qin, W., Chai, L., Jia, W., 2018. Improving collecting performance of sodium oleate using a polyoxyethylene ether in scheelite flotation. J. Cent. South Univ. 25, 2971–2978. https://doi.org/10.1007/s11771-018-3967-5

Chen Chen, Hailing Zhu, Wei Sun, Yuehua Hu, Wenqing Qin, Runqing Liu, 2017. Synergetic Effect of the Mixed Anionic/Non-Ionic Collectors in Low Temperature Flotation of Scheelite. Minerals 7, 87. https://doi.org/10.3390/min7060087

Chen, J., Chen, Y., 2010. A first-principle study of the effect of vacancy defects and impurities on the adsorption of O2 on sphalerite surfaces. Colloids and Surfaces A: Physicochemical and Engineering Aspects 363, 56–63. https://doi.org/10.1016/j.colsurfa.2010.04.013

Chen, J., Chen, Y., Long, X., Li, Y., 2017. DFT study of coadsorption of water and oxygen on galena (PbS) surface: An insight into the oxidation mechanism of galena. Applied Surface Science 420, 714–719. https://doi.org/10.1016/j.apsusc.2017.05.199

Chen, J., Long, X., Zhao, C., Kang, D., Guo, J., 2014. DFT calculation on relaxation and electronic structure of sulfide minerals surfaces in presence of H2O molecule. J. Cent. South Univ. 21, 3945–3954. https://doi.org/10.1007/s11771-014-2382-9

Chen, J.-H., Li, Y.-Q., Lan, L.-H., Guo, J., 2014. Interactions of xanthate with pyrite and galena surfaces in the presence and absence of oxygen. Journal of Industrial and Engineering Chemistry 20, 268–273. https://doi.org/10.1016/j.jiec.2013.03.039

Chen, W., Feng, Q., Zhang, G., Yang, Q., Zhang, C., 2017. The effect of sodium alginate on the flotation separation of scheelite from calcite and fluorite. Minerals Engineering 113, 1–7. https://doi.org/10.1016/j.mineng.2017.07.016

Chen, Y., Bylaska, E.J., Weare, J.H., 2017. Weakly bound water structure, bond valence saturation and water dynamics at the goethite (100) surface/aqueous interface: ab initio dynamical simulations. Geochem Trans 18, 3. https://doi.org/10.1186/s12932-017-0040-5

Chen, Z., Ren, Z., Gao, H., Zheng, R., Jin, Y., Niu, C., 2019. Flotation studies of fluorite and barite with sodium petroleum sulfonate and sodium hexametaphosphate. Journal of Materials Research and Technology 8, 1267–1273. https://doi.org/10.1016/j.jmrt.2018.10.002

Cheng, Y., 2016. Petrogenesis of skarn in Shizhuyuan W-polymetallic deposit, southern Hunan, China: Constraints from petrology, mineralogy and geochemistry. Transactions of Nonferrous Metals Society of China 26, 1676–1687. https://doi.org/10.1016/S1003-6326(16)64277-2

Cheng, Y.L., Kuz'kin, S.F., Solynshkin, V.I., 1963. Infrared spectra of calcite, scheelite and apatite after treatment with flotation regulators. Izv. Vyssh. Uchebn. Zaved., Tsvetn. Metall., 6(5): 28--32, CA 60:3617b.

Chernyshova, I.V., Ponnurangam, S., Somasundaran, P., 2011. Adsorption of Fatty Acids on Iron (Hydr)oxides from Aqueous Solutions. Langmuir 27, 10007–10018. https://doi.org/10.1021/la2017374

Chibani, S., Badawi, M., Loiseau, T., Volkringer, C., Cantrel, L., Paul, J.-F., 2018. A DFT study of RuO 4 interactions with porous materials: metal–organic frameworks (MOFs) and zeolites. Phys. Chem. Chem. Phys. 20, 16770–16776. https://doi.org/10.1039/C8CP01950A

Cooper, T.G., de Leeuw, N.H., 2004. A Computer Modeling Study of the Competitive Adsorption of Water and Organic Surfactants at Surfaces of the Mineral Scheelite. Langmuir 20, 3984–3994. https://doi.org/10.1021/la049796w

References

Cooper, T.G., de Leeuw, N.H., 2003. A combined ab initio and atomistic simulation study of the surface and interfacial structures and energies of hydrated scheelite: introducing a CaWO4 potential model. Surface Science 531, 159–176. https://doi.org/10.1016/S0039-6028(03)00362-5

Cooper, T.G., Leeuw, N.H. de, 2002. Co-adsorption of surfactants and water at inorganic solid surfacesElectronic supplementary information (ESI) available: potential parameters. See http://www.rsc.org/suppdata/cc/b2/b204110c/. Chemical Communications 1502–1503. https://doi.org/10.1039/b204110c

Coulter, T., Subasinghe, G.K.N., 2005. A mechanistic approach to modelling Knelson concentrators. Minerals Engineering 18, 9–17. https://doi.org/10.1016/j.mineng.2004.06.035

Cramer, C.J., 2004. Essentials of computational chemistry: theories and models, 2nd ed. ed. Wiley, Chichester, West Sussex, England ; Hoboken, NJ.

Csonka, G.I., Perdew, J.P., Ruzsinszky, A., Philipsen, P.H.T., Lebègue, S., Paier, J., Vydrov, O.A., Ángyán, J.G., 2009. Assessing the performance of recent density functionals for bulk solids. Phys. Rev. B 79, 155107. https://doi.org/10.1103/PhysRevB.79.155107

Dai, P., Mao, J., Wu, S., Xie, G., Luo, X., 2018. Multiple dating and tectonic setting of the Early Cretaceous Xianglushan W deposit, Jiangxi Province, South China. Ore Geology Reviews 95, 1161–1178. https://doi.org/10.1016/j.oregeorev.2017.11.017

Das, A., Sarkar, B., 2018. Advanced Gravity Concentration of Fine Particles: A Review. Mineral Processing and Extractive Metallurgy Review 39, 359–394. https://doi.org/10.1080/08827508.2018.1433176

Dawson, K.M., 1996. Skarn tungsten. Geology of Canadian Mineral Deposit Types, Geological Survey of Canada, Geology of Canada, No. 8, 495-502.

de Leeuw, N.H., Cooper, T.G., 2007. Surface simulation studies of the hydration of white rust Fe(OH)2, goethite α-FeO(OH) and hematite α-Fe2O3. Geochimica et Cosmochimica Acta 71, 1655–1673. https://doi.org/10.1016/j.gca.2007.01.002

de Leeuw, N.H., Cooper, T.G., 2003a. The layering effect of water on the structure of scheelite. Phys. Chem. Chem. Phys. 5, 433–436. https://doi.org/10.1039/b210461j

de Leeuw, N.H., Cooper, T.G., 2003b. A computational study of the surface structure and reactivity of calcium fluoride. Journal of Materials Chemistry 13, 93–101. https://doi.org/10.1039/b208004d

de Leeuw, N.H., Parker, S.C., 1998. Surface Structure and Morphology of Calcium Carbonate Polymorphs Calcite, Aragonite, and Vaterite: An Atomistic Approach. J. Phys. Chem. B 102, 2914–2922. https://doi.org/10.1021/jp973210f

de Leeuw, N.H., Parker, S.C., 1997. Atomistic simulation of the effect of molecular adsorption of water on the surface structure and energies of calcite surfaces. Faraday Trans. 93, 467–475. https://doi.org/10.1039/a606573b

De Leeuw, N.H., Purton, J. a A., Parker, S.C., Watson, G.W., Kresse, G., 2000. Density functional theory calculations of adsorption of water at calcium oxide and calcium fluoride surfaces. Surface science 452, 9–19.

Dean, K.C., Schack, C.H., 1964. Flotation of Calcareous Scheelite ores. In: Report of investigation. U.S. Bureau of Mines; 1964. p. 15.

Dehaine, Q., Filippov, L.O., 2015. Rare earth (La, Ce, Nd) and rare metals (Sn, Nb, W) as by-product of kaolin production, Cornwall: Part1: Selection and characterisation of the valuable stream. Minerals Engineering 76, 141–153. https://doi.org/10.1016/j.mineng.2014.10.006

Dehaine, Q., Filippov, L.O., Glass, H.J., Rollinson, G., 2019a. Rare-metal granites as a potential source of critical metals: A geometallurgical case study. Ore Geology Reviews 104, 384–402. https://doi.org/10.1016/j.oregeorev.2018.11.012

Dehaine, Q., Filippov, L.O., Joussemet, R., 2017. Rare earths (La, Ce, Nd) and rare metals (Sn, Nb, W) as by-products of kaolin production – Part 2: Gravity processing of micaceous residues. Minerals Engineering 100, 200–210. https://doi.org/10.1016/j.mineng.2016.10.018

Dehaine, Q., Foucaud, Y., Kroll-Rabotin, J.-S., Filippov, L.O., 2019b. Experimental investigation into the kinetics of Falcon UF concentration: Implications for fluid dynamic-based modelling. Separation and Purification Technology 215, 590–601. https://doi.org/10.1016/j.seppur.2019.01.048

Detienne, J.-L., 1978. Valorisation par flottation d'un minerai de scheelite finement exprimée. Institut National Polytechnique de Lorraine, Nancy.

Deveau, C., 2006. Improving Fine Particle Gravity Recovery through Equipment Behavior Modification 18.

Dewulf, J., Blengini, G.A., Pennington, D., Nuss, P., Nassar, N.T., 2016. Criticality on the international scene: Quo vadis? Resources Policy 50, 169–176. https://doi.org/10.1016/j.resourpol.2016.09.008

Dias, R., Ribeiro, A., Coke, C., Moreira, N., Romão, J., 2014. Arco Ibero-Armoricano: indentação versus auto-subducção Ibero-Armorican Arc: indentation versus self-subduction 4.

Dimas, D., Giannopoulou, I., Panias, D., 2009. Polymerization in sodium silicate solutions: a fundamental process in geopolymerization technology. Journal of Materials Science 44, 3719–3730. https://doi.org/10.1007/s10853-009-3497-5

Djoudi, W., Aissani-Benissad, F., Bourouina-Bacha, S., 2007. Optimization of copper cementation process by iron using central composite design experiments. Chemical Engineering Journal 133, 1–6. https://doi.org/10.1016/j.cej.2007.01.033

Dobiáš, B., 1984. Surfactant adsorption on minerals related to flotation, in: New Developments. Springer Berlin Heidelberg, Berlin, Heidelberg, pp. 91–147. https://doi.org/10.1007/BFb0111655

Drielsma, J., Allington, R., Brady, T., Guinée, J., Hammarstrom, J., Hummen, T., Russell-Vaccari, A., Schneider, L., Sonnemann, G., Weihed, P., 2016. Abiotic Raw-Materials in Life Cycle Impact Assessments: An Emerging Consensus across Disciplines. Resources 5, 12. https://doi.org/10.3390/resources5010012

Du, Z., de Leeuw, N.H., 2006. Molecular dynamics simulations of hydration, dissolution and nucleation processes at the α-quartz (0001) surface in liquid water. Dalton Trans. 2623–2634. https://doi.org/10.1039/B516258K

Duan, C., Wen, X., Shi, C., Zhao, Y., Wen, B., He, Y., 2009. Recovery of metals from waste printed circuit boards by a mechanical method using a water medium. Journal of Hazardous Materials 166, 478–482. https://doi.org/10.1016/j.jhazmat.2008.11.060

Ebadnejad, A., Karimi, G.R., Dehghani, H., 2013. Application of response surface methodology for modeling of ball mills in copper sulphide ore grinding. Powder Technology 245, 292–296. https://doi.org/10.1016/j.powtec.2013.04.021

Edraki, M., Baumgartl, T., Manlapig, E., Bradshaw, D., Franks, D.M., Moran, C.J., 2014. Designing mine tailings for better environmental, social and economic outcomes: a review of alternative approaches. Journal of Cleaner Production 84, 411–420. https://doi.org/10.1016/j.jclepro.2014.04.079

Einaudi, M.T., Burt, D.M., 1982. Introduction; terminology, classification, and composition of skarn deposits. Economic Geology 77, 745–754. https://doi.org/10.2113/gsecongeo.77.4.745

Ejtemaei, M., Irannajad, M., Gharabaghi, M., 2012. Role of dissolved mineral species in selective flotation of smithsonite from quartz using oleate as collector. International Journal of Mineral Processing 114–117, 40–47. https://doi.org/10.1016/j.minpro.2012.09.004

El-Midany, A.A., Ibrahim, S.S., 2011. Does calcite content affect its separation from celestite by Falcon concentrator? Powder Technology 213, 41–47. https://doi.org/10.1016/j.powtec.2011.07.003

Engelhardt, L.G., Zeigan, D., Jancke, H., Wieker, W., Hoebbel, D., 1975. 29Si-NMR-Spektroskopie an Silicatl◆sungen. II. Zur Abh◆ngigkeit der Struktur der Silicatanionen in w◆◆rigen Natriumsilicatl◆sungen vom Na : Si-Verh◆ltnis. Zeitschrift f◆r anorganische und allgemeine Chemie 418, 17–28. https://doi.org/10.1002/zaac.19754180103

Epstein, N., 2005. Teetering. Powder Technology 151, 2–14. https://doi.org/10.1016/j.powtec.2004.11.026

Epstein, S., 2014. The variation method in quantum chemistry. Elsevier Science, Saint Louis.

Escamilla-Roa, E., Sainz-Díaz, C.I., Huertas, F.J., Hernández-Laguna, A., 2013. Adsorption of Molecules onto (101¯4) Dolomite Surface: An Application of Computational Studies for Microcalorimetry. J. Phys. Chem. C 117, 17583–17590. https://doi.org/10.1021/jp404529e

Espiritu, E.R.L., da Silva, G.R., Azizi, D., Larachi, F., Waters, K.E., 2019. Flotation behavior and electronic simulations of rare earth minerals in the presence of dolomite supernatant using sodium oleate collector. Journal of Rare Earths 37, 101–112. https://doi.org/10.1016/j.jre.2018.04.016

Espiritu, E.R.L., da Silva, G.R., Azizi, D., Larachi, F., Waters, K.E., 2018. The effect of dissolved mineral species on bastnäsite, monazite and dolomite flotation using benzohydroxamate collector. Colloids and Surfaces A: Physicochemical and Engineering Aspects 539, 319–334. https://doi.org/10.1016/j.colsurfa.2017.12.038

Espiritu, Eileen Ross L., Naseri, S., Waters, K.E., 2018. Surface chemistry and flotation behavior of dolomite, monazite and bastnäsite in the presence of benzohydroxamate, sodium oleate and phosphoric acid ester collectors.

References

Colloids and Surfaces A: Physicochemical and Engineering Aspects 546, 254–265. https://doi.org/10.1016/j.colsurfa.2018.03.030

European Commission, 2014. Report on Critical Raw Materials for the EU, Report of the Ad hoc Working Group on defining critical raw materials. Technical Report, European Commision, DG Enterprise and Industry, Brussels.

European Commission, 2010. Critical raw materials for the EU: Report of the Ad-hoc Working Group on defining critical raw materials.

European Commission, 2008. The raw materials initiative–meeting our critical needs for growth and jobs in Europe. Communication from the Commission to the European Parliament and the Council, COM (2008) 699. Technical report.

European Commission, Directorate-General for Internal Market, I., Entrepreneurship and SMEs, Deloitte Sustainability, British Geological Survey, Toegepast natuurwetenschappelijk onderzoek, 2017. Study on the review of the list of critical raw materials final report.

Evans, J.D., Fraux, G., Gaillac, R., Kohen, D., Trousselet, F., Vanson, J.-M., Coudert, F.-X., 2017. Computational Chemistry Methods for Nanoporous Materials. Chem. Mater. 29, 199–212. https://doi.org/10.1021/acs.chemmater.6b02994

Evans, J.D., Huang, D.M., Hill, M.R., Sumby, C.J., Sholl, D.S., Thornton, A.W., Doonan, C.J., 2015. Molecular Design of Amorphous Porous Organic Cages for Enhanced Gas Storage. J. Phys. Chem. C 119, 7746–7754. https://doi.org/10.1021/jp512944r

Fa, K., Jiang, T., Nalaskowski, J., Miller, J.D., 2003. Interaction forces between a calcium dioleate sphere and calcite/fluorite surfaces and their significance in flotation. Langmuir 19, 10523–10530.

Falconer, A., 2003. Gravity Separation: Old Technique/New Methods. Physical Separation in Science and Engineering 12, 31–48. https://doi.org/10.1080/1478647031000104293

Fatahi, M.R., Farzanegan, A., 2018. An analysis of multiphase flow and solids separation inside Knelson Concentrator based on four-way coupling of CFD and DEM simulation methods. Minerals Engineering 126, 130–144. https://doi.org/10.1016/j.mineng.2018.07.004

Fatahi, M.R., Farzanegan, A., 2017. DEM simulation of laboratory Knelson concentrator to study the effects of feed properties and operating parameters. Advanced Powder Technology 28, 1443–1458. https://doi.org/10.1016/j.apt.2017.03.011

Feng, B., Guo, W., Xu, H., Peng, J., Luo, X., Zhu, X., 2017. The combined effect of lead ion and sodium silicate in the flotation separation of scheelite from calcite. Separation Science and Technology 52, 567–573. https://doi.org/10.1080/01496395.2016.1260590

Fenter, P., Kerisit, S., Raiteri, P., Gale, J.D., 2013. Is the Calcite–Water Interface Understood? Direct Comparisons of Molecular Dynamics Simulations with Specular X-ray Reflectivity Data. J. Phys. Chem. C 117, 5028–5042. https://doi.org/10.1021/jp310943s

Filho, L.S.L., Seidl, P.R., Correia, J.C.G., Cerqueira, L.C.K., 2000. Molecular modelling of reagents for flotation processes. Minerals Engineering 13, 1495–1503. https://doi.org/10.1016/S0892-6875(00)00133-3

Filippov, L.O., Dehaine, Q., Filippova, I.V., 2016. Rare earths (La, Ce, Nd) and rare metals (Sn, Nb, W) as by-products of kaolin production – Part 3: Processing of fines using gravity and flotation. Minerals Engineering 95, 96–106. https://doi.org/10.1016/j.mineng.2016.06.004

Filippov, L.O., Duverger, A., Filippova, I.V., Kasaini, H., Thiry, J., 2012. Selective flotation of silicates and Ca-bearing minerals: The role of non-ionic reagent on cationic flotation. Minerals Engineering 36–38, 314–323. https://doi.org/10.1016/j.mineng.2012.07.013

Filippov, L.O., Filippova, I.V., 2006. Synergistic effects in mix collector systems for non-sulfide mineral flotation. In: Onal, G., et al. (Eds.), Proc. of XXIII Int. Min Proc. Congress, Istanbul, Turkey, pp. 631–634.

Filippov, L.O., Filippova, I.V., Lafhaj, Z., Fornasiero, D., 2019. The role of a fatty alcohol in improving calcium minerals flotation with oleate. Colloids and Surfaces A: Physicochemical and Engineering Aspects 560, 410–417. https://doi.org/10.1016/j.colsurfa.2018.10.022

Filippov, L.O., Houot, R., 1997. Synergistic effects of a nonionic reagent with heteropolar collectors on the nonsulfide ores flotation. In: Proceedings of the XX International Mineral Processing Congress, Aachen, vol. 3, pp. 427–436.

Filippov, L.O., Severov, V.V., Filippova, I.V., 2013. Mechanism of starch adsorption on Fe–Mg–Al-bearing amphiboles. International Journal of Mineral Processing 123, 120–128. https://doi.org/10.1016/j.minpro.2013.05.010

Filippov, L.O., Shokhin, V.N., Yenbaeva, L.I., Ignatkina, V.A., 1993. Improvement of engineering data for flotation of scheelite using combination of sodium oleate and Exol-B. Tsvetnye Metally 1, 60–64.

Filippova, I.V., Filippov, L.O., Duverger, A., Severov, V.V., 2014. Synergetic effect of a mixture of anionic and nonionic reagents: Ca mineral contrast separation by flotation at neutral pH. Minerals Engineering 66–68, 135–144. https://doi.org/10.1016/j.mineng.2014.05.009

Filippova, I.V., Filippov, L.O., Lafhaj, Z., Barres, O., Fornasiero, D., 2018. Effect of calcium minerals reactivity on fatty acids adsorption and flotation. Colloids and Surfaces A: Physicochemical and Engineering Aspects 545, 157–166. https://doi.org/10.1016/j.colsurfa.2018.02.059

Finkelstein, N.P., 1989. Review of Interactions in Flotation of Sparingly Soluble Calcium Minerals with Anionic Collectors. Trans. Inst. Min. Metall. 1989, 98, 157–177.

Fleet, M.E., Liu, X., 2008. Accommodation of the carbonate ion in fluorapatite synthesized at high pressure. American Mineralogist 93, 1460–1469. https://doi.org/10.2138/am.2008.2786

FLSmidth, 2015. FLSmidth Knelson's website. http://www.flsmidth.com/en-US/About+FLSmidth/Our+History/Our+Product+Brands/Knelson.

Freddolino, P.L., Arkhipov, A.S., Larson, S.B., McPherson, A., Schulten, K., 2006. Molecular Dynamics Simulations of the Complete Satellite Tobacco Mosaic Virus. Structure 14, 437–449. https://doi.org/10.1016/j.str.2005.11.014

Free, M.L., Miller, J.D., 1997. Kinetics of 18-Carbon Carboxylate Adsorption at the Fluorite Surface. Langmuir 13, 4377–4382. https://doi.org/10.1021/la960329r

Free, M.L., Miller, J.D., 1996. The significance of collector colloid adsorption phenomena in the fluorite/oleate flotation system as revealed by FTIR/IRS and solution chemistry analysis. International Journal of Mineral Processing 48, 197–216. https://doi.org/10.1016/S0301-7516(96)00027-0

French, R.O., Wadsworth, M.E., Cook, M.A., Cutler, I.B., 1954. The Quantitative Application of Infrared Spectroscopy to Studies in Surface Chemistry. J. Phys. Chem. 58, 805–811. https://doi.org/10.1021/j150520a002

Fuerstenau, D.W., Bunge, R.C., 2006. The complex behavior of fatty acids in fluorite flotation, in: XXXIII Mineral Processing Congress. pp. 510–515.

Fuerstenau, D.W., Healy, T.W., 1972. CHAPTER 6 - PRINCIPLES OF MINERAL FLOTATION, in: Lemlich, R. (Ed.), Adsorptive Bubble Separation Techniques. Academic Press, pp. 91–131. https://doi.org/10.1016/B978-0-12-443350-2.50011-3

Fuerstenau, D.W., Miller, J.D., 1967. The role of the hydrocarbon chain in anionic flotation of calcite, Trans. AIME 238, 153-160.

Fuerstenau, M.C., Gutierrez, G., Elgillani, D.A., 1972. The influence of sodium silicate in non-metallic flotation systems. Trans. AIME, 241: 348--352.

Fuerstenau, M.C., Palmer, B.R., 1976. Anionic flotation of oxides and silicates. in Flotation. A.M. Gaudin Memorial Volume, Ed. M.C. Fuerstenau, AIME:New York 1, 148–196.

Fukazawa, K., 1977. Froth flotation process for recovering sheelite. US Patent 4,040,519.

Fushun, Y., Yuhua, W., Jinming, W., Zhenfu, X., 2014. Investigation on different behavior and mechanism of Ca2+, Fe3+ adsorption on spodumene surface. Physicochemical Problems of Mineral Processing; ISSN 2083-3989. https://doi.org/10.5277/ppmp140210

Gaggiano, R., De Graeve, I., Mol, J.M.C., Verbeken, K., Kestens, L.A.I., Terryn, H., 2013. An infrared spectroscopic study of sodium silicate adsorption on porous anodic alumina: An FTIR study of sodium silicate adsorption on porous anodic alumina. Surface and Interface Analysis 45, 1098–1104. https://doi.org/10.1002/sia.5230

Gao, Y., Gao, Z., Sun, W., Yin, Z., Wang, J., Hu, Y., 2018. Adsorption of a novel reagent scheme on scheelite and calcite causing an effective flotation separation. Journal of Colloid and Interface Science 512, 39–46. https://doi.org/10.1016/j.jcis.2017.10.045

Gao, Z., Bai, D., Sun, W., Cao, X., Hu, Y., 2015a. Selective flotation of scheelite from calcite and fluorite using a collector mixture. Minerals Engineering 72, 23–26. https://doi.org/10.1016/j.mineng.2014.12.025

References

Gao, Z., Fan, R., Ralston, J., Sun, W., Hu, Y., 2019. Surface broken bonds: An efficient way to assess the surface behaviour of fluorite. Minerals Engineering 130, 15–23. https://doi.org/10.1016/j.mineng.2018.09.024

Gao, Z., Gao, Y., Zhu, Y., Hu, Y., Sun, W., 2016a. Selective Flotation of Calcite from Fluorite: A Novel Reagent Schedule. Minerals 6, 114. https://doi.org/10.3390/min6040114

Gao, Z., Hu, Y., Sun, W., Drelich, J.W., 2016b. Surface-Charge Anisotropy of Scheelite Crystals. Langmuir 32, 6282–6288. https://doi.org/10.1021/acs.langmuir.6b01252

Gao, Z., Li, C., Sun, W., Hu, Y., 2017. Anisotropic surface properties of calcite: A consideration of surface broken bonds. Colloids and Surfaces A: Physicochemical and Engineering Aspects 520, 53–61. https://doi.org/10.1016/j.colsurfa.2017.01.061

Gao, Z., Sun, W., Hu, Y., 2015b. New insights into the dodecylamine adsorption on scheelite and calcite: An adsorption model. Minerals Engineering 79, 54–61. https://doi.org/10.1016/j.mineng.2015.05.011

Gao, Z., Sun, W., Hu, Y., 2014. Mineral cleavage nature and surface energy: Anisotropic surface broken bonds consideration. Transactions of Nonferrous Metals Society of China 24, 2930–2937. https://doi.org/10.1016/S1003-6326(14)63428-2

Gao, Z., Sun, W., Hu, Y., Liu, X., 2013. Surface energies and appearances of commonly exposed surfaces of scheelite crystal. Transactions of Nonferrous Metals Society of China 23, 2147–2152. https://doi.org/10.1016/S1003-6326(13)62710-7

Gao, Z., Sun, W., Hu, Y., Liu, X., 2012. Anisotropic surface broken bond properties and wettability of calcite and fluorite crystals. Transactions of Nonferrous Metals Society of China 22, 1203–1208. https://doi.org/10.1016/S1003-6326(11)61306-X

Gaudin, A.M., Fuerstenau, D.W., 1956. Minerals Beneficiation - Quartz Flotation with Anionic Collectors. The American Institute of Mining, Metallurgical, and Petroleum Engineers.

Ghaffari, A., Farzanegan, A., 2018. An investigation on laboratory Knelson Concentrator separation performance: Part 3: Multi-component feed separation modelling. Minerals Engineering 122, 185–194. https://doi.org/10.1016/j.mineng.2018.03.043

Ghaffari, A., Farzanegan, A., 2017. An investigation on laboratory Knelson Concentrator separation performance: Part 2: Two-component feed separation modelling. Minerals Engineering 112, 114–124. https://doi.org/10.1016/j.mineng.2017.07.009

Ghatee, M.H., Koleini, M.M., 2017. Bonding, structural and thermodynamic analysis of dissociative adsorption of H3O+ ion onto calcite $\left(10\overline{1}4\right)$ surface: CPMD and DFT calculations. J Mol Model 23, 331. https://doi.org/10.1007/s00894-017-3499-1

Gillan, M.J., Alfè, D., Michaelides, A., 2016. Perspective: How good is DFT for water? The Journal of Chemical Physics 144, 130901. https://doi.org/10.1063/1.4944633

Glembotskii, V.A., Uvarov, V.S., 1964. The mechanism of action of sodium silicate during the flotation of several on-sulphide minerals. Dokl. Akad. Nauk., Tadzh. SSSR, 7(2): 29--32, CA 61:7979C.

Godinho, J.R.A., Piazolo, S., Balic-Zunic, T., 2014. Importance of surface structure on dissolution of fluorite: Implications for surface dynamics and dissolution rates. Geochimica et Cosmochimica Acta 126, 398–410. https://doi.org/10.1016/j.gca.2013.11.017

Godinho, J.R.A., Piazolo, S., Evins, L.Z., 2012. Effect of surface orientation on dissolution rates and topography of CaF2. Geochimica et Cosmochimica Acta 86, 392–403. https://doi.org/10.1016/j.gca.2012.02.032

Godinho, Jose R. A., Putnis, C.V., Piazolo, S., 2014. Direct Observations of the Dissolution of Fluorite Surfaces with Different Orientations. Crystal Growth & Design 14, 69–77. https://doi.org/10.1021/cg401119p

Gong, G., Han, Y., Liu, J., Zhu, Y., Li, Y., Yuan, S., 2017. In Situ Investigation of the Adsorption of Styrene Phosphonic Acid on Cassiterite (110) Surface by Molecular Modeling. Minerals 7, 181. https://doi.org/10.3390/min7100181

González, M.A., 2011. Force fields and molecular dynamics simulations. JDN 12, 169–200. https://doi.org/10.1051/sfn/201112009

González-Martín, M.L., Bruque, J.M., González-Caballero, F., Perea-Carpio, R., Janczuk, B., 1996. The mechanism of adsorption of sodium dodecylsulfonate on fluorite and its surface free energy. Applied Surface Science 103, 395–402. https://doi.org/10.1016/S0169-4332(96)00540-5

Goupy, J., Creighton, W.L., 2007. Introduction to design of experiments with JMP examples, 3rd ed. ed, SAS Press series. SAS Institute, Cary, N.C.

Goverapet Srinivasan, S., Shivaramaiah, R., Kent, P.R.C., Stack, A.G., Riman, R., Anderko, A., Navrotsky, A., Bryantsev, V.S., 2017. A comparative study of surface energies and water adsorption on Ce-bastnäsite, La-bastnäsite, and calcite via density functional theory and water adsorption calorimetry. Phys. Chem. Chem. Phys. 19, 7820–7832. https://doi.org/10.1039/C7CP00811B

Grimme, S., 2006. Semiempirical GGA-type density functional constructed with a long-range dispersion correction. Journal of Computational Chemistry 27, 1787–1799. https://doi.org/10.1002/jcc.20495

Grimme, S., Antony, J., Ehrlich, S., Krieg, H., 2010. A consistent and accurate *ab initio* parametrization of density functional dispersion correction (DFT-D) for the 94 elements H-Pu. The Journal of Chemical Physics 132, 154104. https://doi.org/10.1063/1.3382344

Grosman, L.I., 1962. Separation of non-sulphide minerals in acidified medium, Tr. Vses. Nauchno Issled. Proektno Inst. Mekh. Obrab. Polezn. Iskop., 131 (1962) 208-218.

Grosman, L.I., Sukhoval'skaya, S.D., 1955. Flotation separation of calcium and barium minerals, Tsvetn. Met., 28 (1955) 7-13.

Guichen, G., Jie, L., Yuexin, H., Yimin, Z., 2018. An atomic scale investigation of the adsorption of sodium oleate on Ca2+ activated quartz surface. Physicochemical Problems of Mineral Processing; ISSN 2084-4735. https://doi.org/10.5277/ppmp18173

Gutierrez, C., 1979. Influence of calcium ion and quebracho in the oleate flotation of fluorite and calcite. Trans. AIME 266, 1918–1924.

Hafner, J., 2008. *Ab-initio* simulations of materials using VASP: Density-functional theory and beyond. J. Comput. Chem. 29, 2044–2078. https://doi.org/10.1002/jcc.21057

Haider, S., Roldan, A., de Leeuw, N.H., 2014. Catalytic Dissociation of Water on the (001), (011), and (111) Surfaces of Violarite, FeNi $_2$ S $_4$: A DFT-D2 Study. J. Phys. Chem. C 118, 1958–1967. https://doi.org/10.1021/jp409522q

Halasz, I., Agarwal, M., Li, R., Miller, N., 2007. Vibrational spectra and dissociation of aqueous Na2SiO3 solutions. Catalysis Letters 117, 34–42. https://doi.org/10.1007/s10562-007-9141-6

Hammond, J.S., Holubka, J.W., deVries, J.E., Dickie, R.A., 1981. The application of x-ray photo-electron spectroscopy to a study of interfacial composition in corrosion-induced paint de-adhesion. Corrosion Science 21, 239–253. https://doi.org/10.1016/0010-938X(81)90033-0

Han, H., Hu, Y., Sun, W., Li, X., Cao, C., Liu, R., Yue, T., Meng, X., Guo, Y., Wang, J., Gao, Z., Chen, P., Huang, W., Liu, J., Xie, J., Chen, Y., 2017. Fatty acid flotation versus BHA flotation of tungsten minerals and their performance in flotation practice. International Journal of Mineral Processing 159, 22–29. https://doi.org/10.1016/j.minpro.2016.12.006

Han, Y., Liu, W., Chen, J., 2016. DFT simulation of the adsorption of sodium silicate species on kaolinite surfaces. Applied Surface Science 370, 403–409. https://doi.org/10.1016/j.apsusc.2016.02.179

Hanna, H., Somasundaran, P., 1976. Flotation of salt-type minerals. In: Flotation – A. M. Gaudin Memorial. New York: AIME; 1976. p. 197–272.

Hanumantha Rao, K., Forssberg, K.S.E., 1991. Mechanism of fatty acid adsorption in salt-type mineral flotation. Minerals Engineering 4, 879–890. https://doi.org/10.1016/0892-6875(91)90071-3

Hartree, D.R., Hartree, W., 1935. Self-consistent field, with exchange, for beryllium. Proc. R. Soc. Lond. A 150, 9–33. https://doi.org/10.1098/rspa.1935.0085

He, G.-C., Xiang, H.-M., Jiang, W., Kang, Q., Chen, J.-H., 2014. First-principles theory on electronic structure and floatability of spodumene. Rare Met. 33, 742–748. https://doi.org/10.1007/s12598-014-0317-0

Heikkila, R.E., Deamer, D.W., Cornwell, D.G., 1970. Solution of fatty acids from monolayers spread at the air-water interface: identification of phase transformations and the estimation of surface charge. J. Lipid Res. 11, 195–200.

Helbig, C., Baldauf, H., Mahnke, J., Stöckelhuber, K.W., Schulze, H.J., 1998. Investigation of Langmuir monofilms and flotation experiments with anionic/cationic collector mixtures. International Journal of Mineral Processing 53, 135–144. https://doi.org/10.1016/S0301-7516(97)00077-X

References

Heydari, H., Elahifard, M., Behjatmanesh-Ardakani, R., 2019. Role of oxygen vacancy in the adsorption and dissociation of the water molecule on the surfaces of pure and Ni-doped rutile (110): a periodic full-potential DFT study. Surface Science 679, 218–224. https://doi.org/10.1016/j.susc.2018.09.014

Hiçyìlmaz, C., Atalay, ü., Özbayoglu, G., 1993. Selective flotation of scheelite using amines. Minerals Engineering 6, 313–320. https://doi.org/10.1016/0892-6875(93)90039-P

Hicyilmaz, C., Özbayoglu, G., 1992. The effects of amine and electrolytes on the zeta-potential of scheelite from Uludag, Turkey. Minerals engineering 5, 945–951.

Hohenberg, P., Kohn, W., 1964. Inhomogeneous Electron Gas. Physical Review 136, B864–B871. https://doi.org/10.1103/PhysRev.136.B864

Honaker, R.Q., 1998. High capacity fine coal cleaning using an enhanced gravity concentrator. Minerals Engineering 11, 1191–1199. https://doi.org/10.1016/S0892-6875(98)00105-8

Honaker, R.Q., Wang, D., Ho, K., 1996. Application of the Falcon Concentrator for fine coal cleaning. Minerals Engineering 9, 1143–1156. https://doi.org/10.1016/0892-6875(96)00108-2

Hoover, W.G., 1985. Canonical dynamics: Equilibrium phase-space distributions. Physical Review A 31, 1695–1697. https://doi.org/10.1103/PhysRevA.31.1695

Hu, J.S., Misra, M., Miller, J.D., 1986a. Effect of temperature and oxygen on oleate adsorption by fluorite. International Journal of Mineral Processing 18, 57–72. https://doi.org/10.1016/0301-7516(86)90007-4

Hu, J.S., Misra, M., Miller, J.D., 1986b. Characterization of adsorbed oleate species at the fluorite surface by FTIR spectroscopy. International Journal of Mineral Processing 18, 73–84. https://doi.org/10.1016/0301-7516(86)90008-6

Hu, Y., Gao, Z., Sun, W., Liu, X., 2012. Anisotropic surface energies and adsorption behaviors of scheelite crystal. Colloids and Surfaces A: Physicochemical and Engineering Aspects 415, 439–448. https://doi.org/10.1016/j.colsurfa.2012.09.038

Hu, Y., Yang, F., Sun, W., 2011. The flotation separation of scheelite from calcite using a quaternary ammonium salt as collector. Minerals Engineering 24, 82–84. https://doi.org/10.1016/j.mineng.2010.08.023

Huang, Z., Zhong, H., Wang, S., Xia, L., Zou, W., Liu, G., 2014. Investigations on reverse cationic flotation of iron ore by using a Gemini surfactant: Ethane-1,2-bis(dimethyl-dodecyl-ammonium bromide). Chemical Engineering Journal 257, 218–228. https://doi.org/10.1016/j.cej.2014.07.057

Hünenberger, P.H., 2005. Thermostat Algorithms for Molecular Dynamics Simulations, in: Dr. Holm, C., Prof. Dr. Kremer, K. (Eds.), Advanced Computer Simulation. Springer Berlin Heidelberg, Berlin, Heidelberg, pp. 105–149. https://doi.org/10.1007/b99427

Hung, A., Yarovsky, I., Russo, S.P., 2004. Density-functional theory of xanthate adsorption on the pyrite FeS_2 (100) surface. Philosophical Magazine Letters 84, 175–182. https://doi.org/10.1080/09500830310001628248

Hung, A., Yarovsky, I., Russo, S.P., 2003. Density-functional theory studies of xanthate adsorption on the pyrite FeS2(110) and (111) surfaces. The Journal of Chemical Physics 118, 6022–6029. https://doi.org/10.1063/1.1556076

Irani, R.R., Callis, C.F., 1960. METAL COMPLEXING BY PHOSPHORUS COMPOUNDS. II. SOLUBILITIES OF CALCIUM SOAPS OF LINEAR CARBOXYLIC ACIDS [1]. J. Phys. Chem. 64, 1741–1743. https://doi.org/10.1021/j100840a034

Jabraoui, H., Hessou, E.P., Chibani, S., Cantrel, L., Lebègue, S., Badawi, M., 2019. Adsorption of volatile organic and iodine compounds over silver-exchanged mordenites: A comparative periodic DFT study for several silver loadings. Applied Surface Science 485, 56–63. https://doi.org/10.1016/j.apsusc.2019.03.282

Jańczuk, B., Bruque, J.M., González-Martín, M.L., del Pozo, J.M., 1993. Wettability and surface tension of fluorite. Colloids and Surfaces A: Physicochemical and Engineering Aspects 75, 163–168. https://doi.org/10.1016/0927-7757(93)80427-G

Janeček, J., Netz, R.R., Flörsheimer, M., Klenze, R., Schimmelpfennig, B., Polly, R., 2014. Influence of Hydrogen Bonding on the Structure of the (001) Corundum–Water Interface. Density Functional Theory Calculations and Monte Carlo Simulations. Langmuir 30, 2722–2728. https://doi.org/10.1021/la500149s

Jang, W.H., Miller, J.D., 1993. Verification of the internal reflection spectroscopy adsorption density equation by Fourier transform infrared spectroscopy analysis of transferred Langmuir-Blodgett films. Langmuir 9, 3159–3165. https://doi.org/10.1021/la00035a068

Jansson, H., Bernin, D., Ramser, K., 2015. Silicate species of water glass and insights for alkali-activated green cement. AIP Advances 5, 067167. https://doi.org/10.1063/1.4923371

Jébrak, M., Marcoux, É., Laithier, M., 2016. Geology of mineral resources, Second edition. ed. Geological Association of Canada, St. John's, NL.

Jensen, F., 2007. Introduction to computational chemistry, 2nd ed. ed. John Wiley & Sons, Chichester, England ; Hoboken, NJ.

Jiao, F., Qin, W., Liu, R., Wang, X., 2015. Adsorption mechanism of 2-mercaptobenzothiazole on chalcopyrite and sphalerite surfaces: Ab initio and spectroscopy studies. Transactions of Nonferrous Metals Society of China 25, 2388–2397. https://doi.org/10.1016/S1003-6326(15)63854-7

Jin, J., Long, Y., Gao, H., Ren, Z., 2019. Flotation behavior and mechanism of andalusite and kyanite in the presence of sodium oleate. Separation Science and Technology 54, 1803–1814. https://doi.org/10.1080/01496395.2018.1540636

Johnson, B.G., Gill, P.M.W., Pople, J.A., 1993. The performance of a family of density functional methods. The Journal of Chemical Physics 98, 5612–5626. https://doi.org/10.1063/1.464906

Jorgensen, W.L., Maxwell, D.S., Tirado-Rives, J., 1996. Development and Testing of the OPLS All-Atom Force Field on Conformational Energetics and Properties of Organic Liquids. J. Am. Chem. Soc. 118, 11225–11236. https://doi.org/10.1021/ja9621760

Kadau, K., Germann, T.C., Lomdahl, P.S., 2006. MOLECULAR DYNAMICS COMES OF AGE: 320 BILLION ATOM SIMULATION ON BlueGene/L. Int. J. Mod. Phys. C 17, 1755–1761. https://doi.org/10.1142/S0129183106010182

Kademli, M., Gulsoy, O., 2012. THE ROLE OF PARTICLE SIZE AND SOLID CONTENTS OF FEED ON MICA-FELDSPAR SEPARATION IN GRAVITY CONCENTRATION. Physicochemical Problems of Mineral Processing 48, 645–654. https://doi.org/10.5277/ppmp120227

Kahlenberg, V., 2010. Structural Chemistry of Anhydrous Sodium Silicates – A Review. CHIMIA International Journal for Chemistry 64, 716–722. https://doi.org/10.2533/chimia.2010.716

Kanicky, J.R., Poniatowski, A.F., Mehta, N.R., Shah, D.O., 2000. Cooperativity among Molecules at Interfaces in Relation to Various Technological Processes: Effect of Chain Length on the p K_a of Fatty Acid Salt Solutions [†]. Langmuir 16, 172–177. https://doi.org/10.1021/la990719o

Kanicky, J.R., Shah, D.O., 2002. Effect of Degree, Type, and Position of Unsaturation on the pKa of Long-Chain Fatty Acids. Journal of Colloid and Interface Science 256, 201–207. https://doi.org/10.1006/jcis.2001.8009

Kellar, J.J., Young, C.A., Knutson, K., Miller, J.D., 1991. Thermotropic phase transition of adsorbed oleate species at a fluorite surface byin situ FT-IR/IRS spectroscopy. Journal of Colloid and Interface Science 144, 381–389. https://doi.org/10.1016/0021-9797(91)90404-V

Kellar, J.J., Young, C.A., Miller, J.D., 1992. In-situ FT-IR/IRS investigation of double-bond reactions of adsorbed oleate at a fluorite surface. International Journal of Mineral Processing 35, 239–251. https://doi.org/10.1016/0301-7516(92)90036-V

Kent, J.A., Bommaraju, T.V., Barnicki, S.D. (Eds.), 2017. Handbook of industrial chemistry and biotechnology. Springer, Cham.

Kerisit, S., Bylaska, E.J., Felmy, A.R., 2013. Water and carbon dioxide adsorption at olivine surfaces. Chemical Geology 359, 81–89. https://doi.org/10.1016/j.chemgeo.2013.10.004

Khatib, R., Backus, E.H.G., Bonn, M., Perez-Haro, M.-J., Gaigeot, M.-P., Sulpizi, M., 2016. Water orientation and hydrogen-bond structure at the fluorite/water interface. Scientific Reports 6. https://doi.org/10.1038/srep24287

Khuwijitjaru, P., Adachi, S., Matsuno, R., 2002. Solubility of Saturated Fatty Acids in Water at Elevated Temperatures. Bioscience, Biotechnology, and Biochemistry 66, 1723–1726. https://doi.org/10.1271/bbb.66.1723

Kincl, M., Turk, S., Vrečer, F., 2005. Application of experimental design methodology in development and optimization of drug release method. International Journal of Pharmaceutics 291, 39–49. https://doi.org/10.1016/j.ijpharm.2004.07.041

References

Klepeis, J.L., Lindorff-Larsen, K., Dror, R.O., Shaw, D.E., 2009. Long-timescale molecular dynamics simulations of protein structure and function. Current Opinion in Structural Biology 19, 120–127. https://doi.org/10.1016/j.sbi.2009.03.004

Kohn, W., Sham, L.J., 1965. Self-Consistent Equations Including Exchange and Correlation Effects. Physical Review 140, A1133–A1138. https://doi.org/10.1103/PhysRev.140.A1133

Kökkılıç, O., Langlois, R., Waters, K.E., 2015. A design of experiments investigation into dry separation using a Knelson Concentrator. Minerals Engineering 72, 73–86. https://doi.org/10.1016/j.mineng.2014.09.025

Kowalczuk, P.B., Akkaya, C., Ergun, M., Janicki, M.J., Sahbaz, O., Drzymala, J., 2017. Water contact angle on corresponding surfaces of freshly fractured fluorite, calcite and mica. Physicochemical Problems of Mineral Processing; ISSN 2084-4735 538 kB. https://doi.org/10.5277/ppmp170116

Kresse, G., Furthmüller, J., 1996. Efficient iterative schemes for *ab initio* total-energy calculations using a plane-wave basis set. Physical Review B 54, 11169–11186. https://doi.org/10.1103/PhysRevB.54.11169

Kresse, G., Hafner, J., 1993. *Ab initio* molecular dynamics for liquid metals. Physical Review B 47, 558–561. https://doi.org/10.1103/PhysRevB.47.558

Kresse, G., Joubert, D., 1999. From ultrasoft pseudopotentials to the projector augmented-wave method. Physical Review B 59, 1758–1775. https://doi.org/10.1103/PhysRevB.59.1758

Kristoffersen, H.H., Vegge, T., Hansen, H.A., 2018. OH formation and H_2 adsorption at the liquid water–Pt(111) interface. Chem. Sci. 9, 6912–6921. https://doi.org/10.1039/C8SC02495B

Kroll-Rabotin, J.-S., 2010. Analyse physique et modélisation de la séparation centrifuge de particules ultrafines en film fluant: Application au séparateur industriel Falcon.

Kroll-Rabotin, J.-S., Bourgeois, F., Climent, É., 2013. Physical analysis and modeling of the Falcon concentrator for beneficiation of ultrafine particles. International Journal of Mineral Processing 121, 39–50. https://doi.org/10.1016/j.minpro.2013.02.009

Kroll-Rabotin, J.-S., Bourgeois, F., Climent, É., 2010. Fluid dynamics based modelling of the Falcon concentrator for ultrafine particle beneficiation. Minerals Engineering 23, 313–320. https://doi.org/10.1016/j.mineng.2009.10.001

Kroll-Rabotin, J.-S., Climent, E., Bourgeois, F., 2011. Beneficiation of concentrated ultrafine suspensions with a Falcon UF concentrator. Canadian Institute of Mining Journal 2, 189–198.

Kühne, T.D., 2014. Second generation Car-Parrinello molecular dynamics: Second-generation Car-Parrinello molecular dynamics. WIREs Comput Mol Sci 4, 391–406. https://doi.org/10.1002/wcms.1176

Kupka, N., Rudolph, M., 2018a. Froth flotation of scheelite – A review. International Journal of Mining Science and Technology 28, 373–384. https://doi.org/10.1016/j.ijmst.2017.12.001

Kupka, N., Rudolph, M., 2018b. Role of sodium carbonate in scheelite flotation – A multi-faceted reagent. Minerals Engineering 129, 120–128. https://doi.org/10.1016/j.mineng.2018.09.005

Kwak, T.A.P., 1987. W-Sn skarn deposits and related metamorphic skarns and granitoids, Developments in economic geology. Elsevier : Distributors for the United States and Canada, Elsevier Science Pub. Co, Amsterdam ; New York.

Lagaly, G., Tufar, W., Minihan, A., Lovell, A., 2000. Silicates, in: Wiley-VCH Verlag GmbH & Co. KGaA (Ed.), Ullmann's Encyclopedia of Industrial Chemistry. Wiley-VCH Verlag GmbH & Co. KGaA, Weinheim, Germany. https://doi.org/10.1002/14356007.a23_661

Laplante, A., Nickoletopoulos, N., 1997. Validation of a falcon model with a synthetic ore. Canadian Metallurgical Quarterly 36, 7–13. https://doi.org/10.1016/S0008-4433(96)00031-6

Laplante, A.R., Buonvino, M., Veltmeyer, A., Robitaille, J., Naud, G., 1994. A Study of the Falcon Concentrator. Canadian Metallurgical Quarterly 33, 279–288. https://doi.org/10.1179/cmq.1994.33.4.279

Laplante, A.R., Shu, Y., Marois, J., 1996. Experimental Characterization of a Laboratory Centrifugal Separator. Canadian Metallurgical Quarterly 35, 23–29. https://doi.org/10.1179/cmq.1996.35.1.23

Lassner, E., Schubert, W.-D., 1999. Tungsten: Properties, Chemistry, Technology of the Element, Alloys, and Chemical Compounds. Springer US, Boston.

Lauri, L., Brown, T., Gunn, G., Kalvig, P., Sievers, H., 2018. Identification and quantification of primary CRM resources in Europe.

Lebègue, S., Eriksson, O., 2009. Electronic structure of two-dimensional crystals from *ab initio* theory. Phys. Rev. B 79, 115409. https://doi.org/10.1103/PhysRevB.79.115409

Lee, S.G., Choi, J.I., Koh, W., Jang, S.S., 2013. Adsorption of β-d-glucose and cellobiose on kaolinite surfaces: Density functional theory (DFT) approach. Applied Clay Science 71, 73–81. https://doi.org/10.1016/j.clay.2012.11.002

Leja, J., 1981. Surface Chemistry of Froth Flotation. Springer US, Boston, MA. https://doi.org/10.1007/978-1-4615-7975-5

Lejaeghere, K., Bihlmayer, G., Bjorkman, T., Blaha, P., Blugel, S., Blum, V., Caliste, D., Castelli, I.E., Clark, S.J., Dal Corso, A., de Gironcoli, S., Deutsch, T., Dewhurst, J.K., Di Marco, I., Draxl, C., Du ak, M., Eriksson, O., Flores-Livas, J.A., Garrity, K.F., Genovese, L., Giannozzi, P., Giantomassi, M., Goedecker, S., Gonze, X., Granas, O., Gross, E.K.U., Gulans, A., Gygi, F., Hamann, D.R., Hasnip, P.J., Holzwarth, N.A.W., Iu an, D., Jochym, D.B., Jollet, F., Jones, D., Kresse, G., Koepernik, K., Kucukbenli, E., Kvashnin, Y.O., Locht, I.L.M., Lubeck, S., Marsman, M., Marzari, N., Nitzsche, U., Nordstrom, L., Ozaki, T., Paulatto, L., Pickard, C.J., Poelmans, W., Probert, M.I.J., Refson, K., Richter, M., Rignanese, G.-M., Saha, S., Scheffler, M., Schlipf, M., Schwarz, K., Sharma, S., Tavazza, F., Thunstrom, P., Tkatchenko, A., Torrent, M., Vanderbilt, D., van Setten, M.J., Van Speybroeck, V., Wills, J.M., Yates, J.R., Zhang, G.-X., Cottenier, S., 2016. Reproducibility in density functional theory calculations of solids. Science 351, aad3000–aad3000. https://doi.org/10.1126/science.aad3000

Lentz, C.W., 1964. Silicate Minerals as Sources of Trimethylsilyl Silicates and Silicate Structure Analysis of Sodium Silicate Solutions. Inorganic Chemistry 3, 574–579. https://doi.org/10.1021/ic50014a029

Li, C., Gao, Z., 2017. Effect of grinding media on the surface property and flotation behavior of scheelite particles. Powder Technology 322, 386–392. https://doi.org/10.1016/j.powtec.2017.08.066

Li, L., Hao, H., Yuan, Z., Liu, J., 2017. Molecular dynamics simulation of siderite-hematite-quartz flotation with sodium oleate. Applied Surface Science 419, 557–563. https://doi.org/10.1016/j.apsusc.2017.05.069

Li, X., Zhao, Z.-J., Zeng, L., Zhao, J., Tian, H., Chen, S., Li, K., Sang, S., Gong, J., 2018. On the role of Ce in CO_2 adsorption and activation over lanthanum species. Chem. Sci. 9, 3426–3437. https://doi.org/10.1039/C8SC00203G

Li, Y., Chen, J., Chen, Y., Zhu, Y., Liu, Y., 2019. DFT Simulation on Interaction of H_2O Molecules with ZnS and Cu-Activated Surfaces. J. Phys. Chem. C 123, 3048–3057. https://doi.org/10.1021/acs.jpcc.8b12273

Lins, F.F., Veiga, M.M., Stewart, J.A., Papalia, A., Papalia, R., 1992. Performance of a new centrifuge (Falcon) in concentrating a gold ore from texada island, BC, Canada. Minerals Engineering 5, 1113–1121.

Liu, A., Fan, J., Fan, M., 2015. Quantum chemical calculations and molecular dynamics simulations of amine collector adsorption on quartz (0 0 1) surface in the aqueous solution. International Journal of Mineral Processing 134, 1–10. https://doi.org/10.1016/j.minpro.2014.11.001

Liu, C., Feng, Q., Zhang, G., Chen, W., Chen, Y., 2016. Effect of depressants in the selective flotation of scheelite and calcite using oxidized paraffin soap as collector. International Journal of Mineral Processing 157, 210–215. https://doi.org/10.1016/j.minpro.2016.11.011

Liu, J., Gong, G., Han, Y., Zhu, Y., 2017. New Insights into the Adsorption of Oleate on Cassiterite: A DFT Study. Minerals 7, 236. https://doi.org/10.3390/min7120236

Liu, J., Wang, Y., Luo, D., Zeng, Y., Wen, S., Chen, L., 2018. DFT study of SDD and BX adsorption on sphalerite (1 1 0) surface in the absence and presence of water molecules. Applied Surface Science 450, 502–508. https://doi.org/10.1016/j.apsusc.2018.04.194

Liu, J., Wen, S., Chen, X., Bai, S., Liu, D., Cao, Q., 2013. DFT computation of Cu adsorption on the S atoms of sphalerite (110) surface. Minerals Engineering 46–47, 1–5. https://doi.org/10.1016/j.mineng.2013.03.026

Liu, J., Wen, S., Deng, J., Chen, X., Feng, Q., 2014. DFT study of ethyl xanthate interaction with sphalerite (110) surface in the absence and presence of copper. Applied Surface Science 311, 258–263. https://doi.org/10.1016/j.apsusc.2014.05.052

Liu, K., Cruzan, J.D., Saykally, R.J., 1996. Water Clusters. Science 271, 929–933. https://doi.org/10.1126/science.271.5251.929

Liu, T., Luo, W., Cole, D.R., Asthagiri, A., 2019. Water adsorption on olivine(010) surfaces: Effect of alkali and transition metal cation doping. J. Chem. Phys. 150, 044703. https://doi.org/10.1063/1.5058770

References

Liu, X., Luo, H., Cheng, R., Li, C., Zhang, J., 2017. Effect of citric acid and flotation performance of combined depressant on collophanite ore. Minerals Engineering 109, 162–168. https://doi.org/10.1016/j.mineng.2017.03.010

Liu, X., Tang, Y., Shen, M., Li, W., Chu, S., Shan, B., Chen, R., 2018. Bifunctional CO oxidation over Mn-mullite anchored Pt sub-nanoclusters *via* atomic layer deposition. Chem. Sci. 9, 2469–2473. https://doi.org/10.1039/C7SC05486F

Logan, R.L., 1979. Tall oil fatty acids. J Am Oil Chem Soc 56, 777A-779A. https://doi.org/10.1007/BF02667443

Long, X., Chen, J., Chen, Y., 2016a. Adsorption of ethyl xanthate on ZnS(110) surface in the presence of water molecules: A DFT study. Applied Surface Science 370, 11–18. https://doi.org/10.1016/j.apsusc.2016.02.094

Long, X., Chen, Y., Chen, J., Xu, Z., Liu, Q., Du, Z., 2016b. The effect of water molecules on the thiol collector interaction on the galena (PbS) and sphalerite (ZnS) surfaces: A DFT study. Applied Surface Science 389, 103–111. https://doi.org/10.1016/j.apsusc.2016.07.084

Lopez-Berganza, J.A., Diao, Y., Pamidighantam, S., Espinosa-Marzal, R.M., 2015. Ab Initio Studies of Calcium Carbonate Hydration. J. Phys. Chem. A 119, 11591–11600. https://doi.org/10.1021/acs.jpca.5b09006

Losch, P., Joshi, H.R., Vozniuk, O., Grünert, A., Ochoa-Hernández, C., Jabraoui, H., Badawi, M., Schmidt, W., 2018. Proton Mobility, Intrinsic Acid Strength, and Acid Site Location in Zeolites Revealed by Varying Temperature Infrared Spectroscopy and Density Functional Theory Studies. J. Am. Chem. Soc. 140, 17790–17799. https://doi.org/10.1021/jacs.8b11588

Lovat, G., Doud, E.A., Lu, D., Kladnik, G., Inkpen, M.S., Steigerwald, M.L., Cvetko, D., Hybertsen, M.S., Morgante, A., Roy, X., Venkataraman, L., 2019. Determination of the structure and geometry of N-heterocyclic carbenes on Au(111) using high-resolution spectroscopy. Chem. Sci. 10, 930–935. https://doi.org/10.1039/C8SC03502D

Lovell, V.M., 1976. Froth characteristics in phosphate flotation, In: Fuerstenau, M.C. (Ed.), Flotation: Gaudin Memorial Volume, vol. 1, pp. 597-621.

Lovell, V.M., Goold, L.A., Finkelstein, N.P., 1974. Infrared studies of the adsorption of oleate species on calcium fluoride. International Journal of Mineral Processing 1, 183–192. https://doi.org/10.1016/0301-7516(74)90014-3

Lu, D., Wang, Y., Jiang, T., Sun, W., Hu, Y., 2016. Study on pre-concentration efficiency of wolframite from tungsten ore using gravity and magnetic separations. Physicochemical Problems of Mineral Processing; ISSN 2084-4735 362 kB. https://doi.org/10.5277/ppmp160216

Lu, H.-Z., Liu, Y., Wang, C., Xu, Y., Li, H., 2003. Mineralization and Fluid Inclusion Study of the Shizhuyuan W-Sn-Bi-Mo-F Skarn Deposit, Hunan Province, China. Economic Geology 98, 955–974. https://doi.org/10.2113/gsecongeo.98.5.955

Lu, Y., Drelich, J., Miller, J.D., 1998. Oleate Adsorption at an Apatite Surface Studied by Ex-Situ FTIR Internal Reflection Spectroscopy. Journal of Colloid and Interface Science 202, 462–476. https://doi.org/10.1006/jcis.1998.5466

Lu, Y., Miller, J.D., 2002. Carboxyl Stretching Vibrations of Spontaneously Adsorbed and LB-Transferred Calcium Carboxylates as Determined by FTIR Internal Reflection Spectroscopy. Journal of Colloid and Interface Science 256, 41–52. https://doi.org/10.1006/jcis.2001.8112

Ludwig, R., 2001. Water: From Clusters to the Bulk. Angewandte Chemie International Edition 40, 1808–1827. https://doi.org/10.1002/1521-3773(20010518)40:10<1808::AID-ANIE1808>3.0.CO;2-1

Ma, L., Wei, L., Pei, X., Zhu, X., Xu, D., 2019. CFD-DEM simulations of particle separation characteristic in centrifugal compounding force field. Powder Technology 343, 11–18. https://doi.org/10.1016/j.powtec.2018.11.016

Ma, L., Wei, L., Zhu, X., Xu, D., Pei, X., Xue, H., 2018. Numerical Studies of Separation Performance of Knelson Concentrator for Beneficiation of Fine Coal. International Journal of Coal Preparation and Utilization 1–11. https://doi.org/10.1080/19392699.2018.1434165

Ma, X., Xia, L., Wang, S., Zhong, H., Jia, H., 2017. Structural Modification of Xanthate Collectors To Enhance the Flotation Selectivity of Chalcopyrite. Ind. Eng. Chem. Res. 56, 6307–6316. https://doi.org/10.1021/acs.iecr.6b04566

Maheshwary, S., Patel, N., Sathyamurthy, N., Kulkarni, A.D., Gadre, S.R., 2001. Structure and Stability of Water Clusters (H$_2$O)$_n$, $n = 8-20$: An Ab Initio Investigation. The Journal of Physical Chemistry A 105, 10525–10537. https://doi.org/10.1021/jp013141b

Majumder, A.K., Barnwal, J.P., 2006. MODELING OF ENHANCED GRAVITY CONCENTRATORS–PRESENT STATUS. Mineral Processing and Extractive Metallurgy Review 27, 61–86. https://doi.org/10.1080/08827500500339307

Maldonado, P., Godinho, J.R.A., Evins, L.Z., Oppeneer, P.M., 2013. Ab Initio Prediction of Surface Stability of Fluorite Materials and Experimental Verification. The Journal of Physical Chemistry C 117, 6639–6650. https://doi.org/10.1021/jp312645f

Marinakis, Kelsall, G.H., 1987. The surface chemical properties of scheelite (CaWO4) II. Collector adsorption and recovery of fine scheelite particles at the iso-octane/water interface. Colloids and Surfaces 26, 243–255. https://doi.org/10.1016/0166-6622(87)80119-1

Marinakis, K.I., 1980. THE ACTION OF SODIUM SILICATE ON THE FLOTATION OF SALT-TYPE MINERALS WITH OLEIC ACID.

Marinakis, K.I., Kelsall, G.H., 1987. The surface chemical properties of scheelite (CaWO4) I. The scheelite/water interface and CaWO4 solubility. Colloids and surfaces 25, 369–385.

Marinakis, K.I., Shergold, H.L., 1985a. The mechanism of fatty acid adsorption in the presence of fluorite, calcite and barite. International journal of mineral processing 14, 161–176.

Marinakis, K.I., Shergold, H.L., 1985b. Influence of sodium silicate addition on the adsorption of oleic acid by fluorite, calcite and barite. International Journal of mineral processing 14, 177–193.

Martins, J.I., Amarante, M.M., 2013. Scheelite Flotation From Tarouca Mine Ores. Mineral Processing and Extractive Metallurgy Review 34, 367–386. https://doi.org/10.1080/08827508.2012.657022

Masan Resources, 2012. Update on Nui Phao Project in Northern Vietnam. ITIA. September 2012.

McAlister, S., Armstrong, K., 1998. Development of the Falcon concentrators, in: Soc. Mining, Metall. Explor. Annu. Meet., Orlando, Florida, 1998. http://www.seprosystems.com/images/falcon-s/pdf/fcd.pdf (accessed February 10, 2014).

Mcarthur, J.M., 1985. Francolite geochemistry—compositional controls during formation, diagenesis, metamorphism and weathering. Geochimica et Cosmochimica Acta 49, 23–35. https://doi.org/10.1016/0016-7037(85)90188-7

Meinert, L.D., 1992. Skarns and Skarn Deposits. Geoscience Canada, 19(4).

Meinert, L.D., Dipple, G.M., Nicolescu, S., 2005. World Skarn Deposits. Economic Geology 100th Anniversary Volume, 299-336.

Mercade, V.V., 1975. RECOVERY OF SCHEELITE FROM ORES BY FLOTATION. 3,915,391.

Merlen, E., Lynch, J., Bisiaux, M., Raatz, F., 1990. Surface modifications during Y zeolite dealumination. Surface and Interface Analysis 16, 364–368. https://doi.org/10.1002/sia.740160177

Methfessel, M., Paxton, A.T., 1989. High-precision sampling for Brillouin-zone integration in metals. Physical Review B 40, 3616–3621. https://doi.org/10.1103/PhysRevB.40.3616

Mielczarski, E., de Donato, Ph., Mielczarski, J.A., Cases, J.M., Barres, O., Bouquet, E., 2000. Solution Chemistry in Adsorption Layer Formation of Oleate on Fluorite. Journal of Colloid and Interface Science 226, 269–276. https://doi.org/10.1006/jcis.2000.6793

Mielczarski, E., Mielczarski, J.A., Cases, J.M., 1998. Molecular Recognition Effect in Monolayer Formation of Oleate on Fluorite. Langmuir 14, 1739–1747.

Mielczarski, E., Mielczarski, J.A., Cases, J.M., Rai, B., others, 2002. Influence of solution conditions and mineral surface structure on the formation of oleate adsorption layers on fluorite. Colloids and Surfaces A: Physicochemical and Engineering Aspects 205, 73–84.

Mielczarski, J., Nowak, P., Strojek, J.W., 1983. Correlation between the adsorption of sodium dodecyl sulphate on calcium fluoride (fluorite) and its floatability — An infra-red internal reflection spectrophotometric study. International Journal of Mineral Processing 11, 303–317. https://doi.org/10.1016/0301-7516(83)90051-0

Mielczarski, J.A., Cases, J.M., Bouquet, E., Barres, O., Delon, J.F., 1993. Nature and structure of adsorption layer on apatite contacted with oleate solution. 1. Adsorption and Fourier transform infrared reflection studies. Langmuir 9, 2370–2382. https://doi.org/10.1021/la00033a020

References

Mielczarski, J.A., Mielczarski, E., Cases, J.M., 1999. Dynamics of Fluorite—Oleate Interactions. Langmuir 15, 500–508. https://doi.org/10.1021/la980593f

Miller, F.A., Wilkins, C.H., 1952. Infrared Spectra and Characteristic Frequencies of Inorganic Ions. Analytical Chemistry 24, 1253–1294. https://doi.org/10.1021/ac60068a007

Miller, J.D., Hiskey, J.B., 1972. Electrokinetic behavior of fluorite as influenced by surface carbonation. Journal of Colloid and Interface Science 41, 567–573. https://doi.org/10.1016/0021-9797(72)90378-5

Miller, J.D., Hu, J.S., Jin, R., 1989. Thermochemistry of oleate adsorption at the fluorite/water interface. Colloids and Surfaces 42, 71–84. https://doi.org/10.1016/0166-6622(89)80078-2

Miller, J.D., Misra, M., 1984. The Hydrophobic Character of Semisoluble Salt Minerals with Oleate as Collector. International Conference on Recent Advances in Mineral Sciences and Technologic, Johannesburg, South Africa 259–267.

Mishra, R.K., Chander, S., Fuerstenau, D.W., 1980. Effect of ionic surfactants on the electrophoretic mobility of hydroxyapatite. Colloids and Surfaces 1, 105–119. https://doi.org/10.1016/0166-6622(80)80040-0

Misra, K.C., 2000. Understanding Mineral Deposits. Springer Netherlands, Dordrecht. https://doi.org/10.1007/978-94-011-3925-0

Mizuniwa, T., Hotta, Y., Shimoiizaka, J., 1979. Adsorption Mechanism of Sodium Oleate on Scheelite. J. Mining and Metallurgical Inst. Jap. 95 (1093), 149-153.

Mkhonto, D., Ngoepe, P.E., Cooper, T.G., de Leeuw, N.H., 2006. A computer modelling study of the interaction of organic adsorbates with fluorapatite surfaces. Phys Chem Minerals 33, 314–331. https://doi.org/10.1007/s00269-006-0080-3

Møgelhøj, A., Kelkkanen, A.K., Wikfeldt, K.T., Schiøtz, J., Mortensen, J.J., Pettersson, L.G., Lundqvist, B.I., Jacobsen, K.W., Nilsson, A., Nørskov, J.K., 2011. Ab initio van der Waals interactions in simulations of water alter structure from mainly tetrahedral to high-density-like. The Journal of Physical Chemistry B 115, 14149–14160.

Mogilevsky, P., Parthasarathy, T.A., Petry, M.D., 2004. Anisotropy in room temperature microhardness and fracture of CaWo4 scheelite. Acta Materialia 52, 5529–5537. https://doi.org/10.1016/j.actamat.2004.08.022

Montgomery, D.C., 2013. Design and analysis of experiments, Eighth edition. ed. John Wiley & Sons, Inc, Hoboken, NJ.

Mudd, G.M., 2007. Global trends in gold mining: Towards quantifying environmental and resource sustainability. Resources Policy 32, 42–56. https://doi.org/10.1016/j.resourpol.2007.05.002

Nakamura, T., Ogawa, M., 2012. Attachment of the Sulfonic Acid Group in the Interlayer Space of a Layered Alkali Silicate, Octosilicate. Langmuir 28, 7505–7511. https://doi.org/10.1021/la300390s

Nakhaei, F., Irannajad, M., 2018. Reagents types in flotation of iron oxide minerals: A review. Mineral Processing and Extractive Metallurgy Review 39, 89–124. https://doi.org/10.1080/08827508.2017.1391245

Napier-Munn, T.J., 1997. Invention and innovation in mineral processing. Minerals Engineering 10, 757–773. https://doi.org/10.1016/S0892-6875(97)00055-1

Neiman, A., 1996. Cooperative transport in oxides: Diffusion and migration processes involving Mo(VI), W(VI), V(V) and Nb(V). Solid State Ionics 83, 263–273. https://doi.org/10.1016/0167-2738(95)00247-2

Nesbet, R.K., 2002. Variational Principles and Methods in Theoretical Physics and Chemistry. Cambridge University Press, Cambridge. https://doi.org/10.1017/CBO9780511535161

Nikiforov, K.A., Skobeev, I.K., 1968. Infrared spectroscopic study of fluorite and calcite after treatment of minerals by water glass. Nauchn. Tr. Irkutsk. Gos. Nauchno- Issled. Inst. Redk. Tsvetn. Met., 19: 153-158, CA 72:72744e.

Nixon, J.C., Cook, M.A., 1950. Fluorite flotation III: Improvement of selectivity of oleic acid by the use of vitamin D type addition agents, Vol. 40. Bulletin of the University of Utah, Utah Engineering Experiment Station, Salt Lake City, UT.

Nordström, J., Nilsson, E., Jarvol, P., Nayeri, M., Palmqvist, A., Bergenholtz, J., Matic, A., 2011. Concentration- and pH-dependence of highly alkaline sodium silicate solutions. Journal of Colloid and Interface Science 356, 37–45. https://doi.org/10.1016/j.jcis.2010.12.085

Nosé, Shūichi, 1984. A molecular dynamics method for simulations in the canonical ensemble. Molecular Physics 52, 255–268. https://doi.org/10.1080/00268978400101201

Nosé, Shuichi, 1984. A unified formulation of the constant temperature molecular dynamics methods. The Journal of Chemical Physics 81, 511–519. https://doi.org/10.1063/1.447334

Ogawa, T., Aonuma, T., Tamaki, T., Ohashi, H., Ushiyama, H., Yamashita, K., Yamaguchi, T., 2014. The proton conduction mechanism in a material consisting of packed acids. Chem. Sci. 5, 4878–4887. https://doi.org/10.1039/C4SC00952E

Oliveira, J.F., Sampaio, J.A., 1988. Development studies for the recovery of Brazilian scheelite fines by froth flotation, in: Production and Processing of Fine Particles. A.J. Plumpton, pp. 209–2017.

Ozcan, O., Bulutcu, A.N., 1993. Electrokinetic, infrared and flotation studies of scheelite and calcite with oxine, alkyl oxine, oleoyl sarcosine and quebracho. International Journal of Mineral Processing 39, 275–290. https://doi.org/10.1016/0301-7516(93)90020-B

Ozcan, O., Bulutcu, A.N., Sayan, P., Recepoglu, O., 1994. Scheelite flotation: a new scheme using oleoyl sarcosine as collector and alkyl oxine as modifier. International Journal of Mineral Processing 42, 111–120. https://doi.org/10.1016/0301-7516(94)90023-X

Pareek, A., Torrelles, X., Angermund, K., Rius, J., Magdans, U., Gies, H., 2009. Competitive Adsorption of Glycine and Water on the Fluorapatite (100) Surface. Langmuir 25, 1453–1458. https://doi.org/10.1021/la802706y

Pareek, A., Torrelles, X., Angermund, K., Rius, J., Magdans, U., Gies, H., 2008. Structure of Interfacial Water on Fluorapatite (100) Surface. Langmuir 24, 2459–2464. https://doi.org/10.1021/la701929p

Parks, T.C., Barker, W.W., 1977. The ordered dispersal of point defects over cubic lattices: Application to fluorite-related structures. Journal of Solid State Chemistry 20, 397–407. https://doi.org/10.1016/0022-4596(77)90177-3

Pastor, H., 2000. Métallurgie et recyclage du tungstène. Procédés.

Patil, D.P., Nayak, U.B., 1985. Selective flotation of scheelite and calcite. Proceeedings of National Seminar on Mineral Processing and IX Annual Technical Convention of Indian Institute of Mineral Engineers, 11th & 12th March 1985, National Metallurgical Laboratory (CSIR), Jamshedpur 10.

Pauling, L., 2000. The nature of the chemical bond and the structure of molecules and crystals: an introduction to modern structural chemistry, 3. ed., 17. print. ed. Cornell Univ. Press, Ithaca, New York.

Pearse, M.J., 2005. An overview of the use of chemical reagents in mineral processing. Minerals Engineering 18, 139–149. https://doi.org/10.1016/j.mineng.2004.09.015

Peck, A.S., 1963. Infrared studies of oleic acid and sodium oleate adsorption on fluorite, barite, and calcite. U.S. Bureau of Mines Report of Investigation No. 6202.

Peck, A.S., Wadsworth, M.E., 1965. Infrared study of the depression effect of fluoride, sulfate, and chloride on chemisorption of oleate on fluorite and barite. In: Arbiter, N. _Ed.., Proc. of VII Int. Miner. Process. Congr., Gordon and Breach Science Publishers, New York, NY, pp. 259–267.

Pedone, A., Malavasi, G., Cormack, A.N., Segre, U., Menziani, M.C., 2007. Insight into Elastic Properties of Binary Alkali Silicate Glasses; Prediction and Interpretation through Atomistic Simulation Techniques. Chemistry of Materials 19, 3144–3154. https://doi.org/10.1021/cm062619r

Peltonen, J.P.K., Rosenholm, J.B., 1989. The influence of light on the properties of fatty acid-poly(3-octylthiophene) Langmuir-Blodgett films. Thin Solid Films 179, 543–547. https://doi.org/10.1016/0040-6090(89)90234-4

Peng, C., Min, F., Liu, L., Chen, J., 2016. A periodic DFT study of adsorption of water on sodium-montmorillonite (001) basal and (010) edge surface. Applied Surface Science 387, 308–316. https://doi.org/10.1016/j.apsusc.2016.06.079

Perdew, J.P., Burke, K., Ernzerhof, M., 1996. Generalized Gradient Approximation Made Simple. Physical Review Letters 77, 3865–3868. https://doi.org/10.1103/PhysRevLett.77.3865

Perdew, J.P., Wang, Y., 1992. Accurate and simple analytic representation of the electron-gas correlation energy. Phys. Rev. B 45, 13244–13249. https://doi.org/10.1103/PhysRevB.45.13244

Perdew, J.P., Zunger, A., 1981. Self-interaction correction to density-functional approximations for many-electron systems. Phys. Rev. B 23, 5048–5079. https://doi.org/10.1103/PhysRevB.23.5048

Perera, A., 2011. On the microscopic structure of liquid water. Molecular Physics 109, 2433–2441. https://doi.org/10.1080/00268976.2011.617712

Perry, T.D., Cygan, R.T., Mitchell, R., 2007. Molecular models of a hydrated calcite mineral surface. Geochimica et Cosmochimica Acta 71, 5876–5887. https://doi.org/10.1016/j.gca.2007.08.030

References

Petrov, I.S., 1940. A new method for flotation of poor scheelite ores.

Pfeiffer-Laplaud, M., Gaigeot, M.-P., 2016. Electrolytes at the Hydroxylated (0001) α-Quartz/Water Interface: Location and Structural Effects on Interfacial Silanols by DFT-Based MD. J. Phys. Chem. C 120, 14034–14047. https://doi.org/10.1021/acs.jpcc.6b01819

Pinto, C.A.F., Yarar, B., Araujo, A.C., 1991. Apatite flotation kinetics with conventional and new collectors, Prerint 91-80, SME Annual Meeting, Denver, Colorado, February 25-28.

Pinto, M.D., Ribeiro, M.A., Noronha, F., 2016. Rochas calcossilicatadas e metagrauvaques da Formação de Bateiras (CXG – Grupo do Douro) 5.

Píš, I., Magnano, E., Nappini, S., Bondino, F., 2019. Under-cover stabilization and reactivity of a dense carbon monoxide layer on Pt(111). Chem. Sci. 10, 1857–1865. https://doi.org/10.1039/C8SC04461A

Pitfield, P., Brown, T., Gunn, G., Rayner, D., 2011. Tungsten profile. London: British Geological Survey [Online], 2011. https://www.bgs.ac.uk/downloads/start.cfm?id=1981.

Plaksin, I., 1959. Interaction of minerals with gases and reagents in flotation. Min. Eng., 214: 319-324.

Pradip, Fuerstenau, D.W., 1985. Adsorption of hydroxamate collectors on semisoluble minerals Part II: Effect of temperature on adsorption. Colloids and Surfaces 15, 137–146. https://doi.org/10.1016/0166-6622(85)80061-5

Pradip, Fuerstenau, D.W., 1983. The adsorption of hydroxamate on semi-soluble minerals. Part I: Adsorption on barite, Calcite and Bastnaesite. Colloids and Surfaces 8, 103–119. https://doi.org/10.1016/0166-6622(83)80079-1

Prigiobbe, V., Suarez Negreira, A., Wilcox, J., 2013. Interaction between Olivine and Water Based on Density Functional Theory Calculations. J. Phys. Chem. C 117, 21203–21216. https://doi.org/10.1021/jp403271e

Pugh, R., Stenius, P., 1985. Solution chemistry studies and flotation behaviour of apatite, calcite and fluorite minerals with sodium oleate collector. International journal of mineral processing 15, 193–218.

Qi, G.W., Klauber, C., Warren, L.J., 1993. Mechanism of action of sodium silicate in the flotation of apatite from hematite. International Journal of Mineral Processing 39, 251–273. https://doi.org/10.1016/0301-7516(93)90019-7

Raatz, S., 1992. THE INFLUENCE OF MULTIVALENT CATIONS ON THE FLOATABILITY OF SCHEELITE, FLUORITE AND CALCITE, in: Innovations in Flotation Technology. P. Mavros and K.A. Matis.

Rahimi, S., Irannajad, M., Mehdilo, A., 2017. Effects of sodium carbonate and calcium chloride on calcite depression in cationic flotation of pyrolusite. Transactions of Nonferrous Metals Society of China 27, 1831–1840. https://doi.org/10.1016/S1003-6326(17)60206-1

Rakotonarivo, E., Bottero, J.Y., Cases, J.M., Leprince, A., 1985. Study of the adsorption of long chain sodium soaps from aqueous solutions on aluminum hydroxide gels. Colloids and Surfaces 16, 153–173. https://doi.org/10.1016/0166-6622(85)80249-3

Rao, D.S., VijayaKumar, T.V., Rao, S.S., Prabhakar, S., Raju, G.B., 2011. Effectiveness of sodium silicate as gangue depressants in iron ore slimes flotation. International Journal of Minerals, Metallurgy, and Materials 18, 515–522. https://doi.org/10.1007/s12613-011-0471-4

Rao, K.H., Antti, B.-M., Forssberg, E., 1990. Mechanism of oleate interaction on salt-type minerals, Part II. Adsorption and electrokinetic studies of apatite in the presence of sodium oleate and sodium metasilicate. International Journal of Mineral Processing 28, 59–79. https://doi.org/10.1016/0301-7516(90)90027-V

Rao, K.H., Antti, B.-M., Forssberg, E., 1988. Mechanism of oleate interaction on salt-type minerals part I. Adsorption and electrokinetic studies of calcite in the presence of sodium oleate and sodium metasilicate. Colloids and Surfaces 34, 227–239. https://doi.org/10.1016/0166-6622(88)80101-X

Rao, K.H., Cases, J.M., De Donato, P., Forssberg, K.S.E., 1991a. Mechanism of oleate interaction on salt-type minerals. Journal of Colloid and Interface Science 145, 314–329. https://doi.org/10.1016/0021-9797(91)90364-E

Rao, K.H., Cases, J.M., Forssberg, K.S.E., 1991b. Mechanism of oleate interaction on salt-type minerals. Journal of Colloid and Interface Science 145, 330–348. https://doi.org/10.1016/0021-9797(91)90365-F

Rao, K.H., Forssberg, K.S.E., 1991. Mechanism of oleate interaction on salt-type minerals Part III. Adsorption, zeta potential and diffuse reflectance FT-IR studies of scheelite in the presence of sodium oleate. Colloids and Surfaces 54, 161–187. https://doi.org/10.1016/0166-6622(91)80058-V

Rath, S.S., Sahoo, H., Das, B., Mishra, B.K., 2014a. Density functional calculations of amines on the (101) face of quartz. Minerals Engineering 69, 57–64. https://doi.org/10.1016/j.mineng.2014.07.007

Rath, S.S., Sinha, N., Sahoo, H., Das, B., Mishra, B.K., 2014b. Molecular modeling studies of oleate adsorption on iron oxides. Applied Surface Science 295, 115–122. https://doi.org/10.1016/j.apsusc.2014.01.014

Richards, R.G., MacHunter, D.M., Gates, P.J., Palmer, M.K., 2000. Gravity separation of ultra-fine (−0.1mm) minerals using spiral separators. Minerals Engineering 13, 65–77. https://doi.org/10.1016/S0892-6875(99)00150-8

Richards, R.G., Palmer, M.K., 1997. High capacity gravity separators a review of current status. Minerals Engineering 10, 973–982. https://doi.org/10.1016/S0892-6875(97)00071-X

Rietjens, M., 1998. Decomplexation of aluminium±⁻uoride complexes by citrate-based buffers as a function of pH, aluminium and ⁻uoride concentrations. Analytica Chimica Acta 9.

Rignanese, G.-M., Charlier, J.-C., Gonze, X., 2004. First-principles molecular-dynamics investigation of the hydration mechanisms of the (0001) α-quartz surface. Phys. Chem. Chem. Phys. 6, 1920–1925. https://doi.org/10.1039/B311842H

Roche, M., 1973. Caractérisation de l'état de surface des fluorines et application à la flottation des minerais de fluorine du district du Tarn (Montroc - Le Burc). Université de Nancy I.

Roller, P.S., Ervin, G., 1940. The System Calcium Oxide-Silica-Water at 30°. The Association of Silicate * Ion in Dilute Alkaline Solution. Journal of the American Chemical Society 62, 461–471. https://doi.org/10.1021/ja01860a001

Roy, R., Tiller, W.A., Bell, I., Hoover, M.R., 2005. The Structure Of Liquid Water; Novel Insights From Materials Research; Potential Relevance To Homeopathy. Materials Research Innovations 9, 98–103. https://doi.org/10.1080/14328917.2005.11784911

Rutledge, J., Anderson, C., 2015. Tannins in Mineral Processing and Extractive Metallurgy. Metals 5, 1520–1542. https://doi.org/10.3390/met5031520

Sakuma, H., Kondo, T., Nakao, H., Shiraki, K., Kawamura, K., 2011. Structure of Hydrated Sodium Ions and Water Molecules Adsorbed on the Mica/Water Interface. J. Phys. Chem. C 115, 15959–15964. https://doi.org/10.1021/jp111936s

Sarvaramini, A., Azizi, D., Larachi, F., 2016a. Hydroxamic acid interactions with solvated cerium hydroxides in the flotation of monazite and bastnäsite—Experiments and DFT study. Applied Surface Science 387, 986–995. https://doi.org/10.1016/j.apsusc.2016.07.044

Sarvaramini, A., Larachi, F., 2017. Understanding the interactions of thiophosphorus collectors with chalcopyrite through DFT simulation. Computational Materials Science 132, 137–145. https://doi.org/10.1016/j.commatsci.2017.02.027

Sarvaramini, A., Larachi, F., Hart, B., 2016b. Collector attachment to lead-activated sphalerite – Experiments and DFT study on pH and solvent effects. Applied Surface Science 367, 459–472. https://doi.org/10.1016/j.apsusc.2016.01.213

Schmidt, S., 2012a. From Deposit to Concentrate: The Basics of Tungsten Mining Part 1: Project Generation and Project Development. ITIA June 2012.

Schmidt, S., 2012b. From Deposit to Concentrate: The Basics of Tungsten Mining Part 2: Operational Pratices and Challenges. ITIA June 2012.

Schubert, H., Baldauf, H., Kramer, W., Schoenherr, J., 1990. Further development of fluorite flotation from ores containing higher calcite contents with oleoylsarcosine as collector. International Journal of Mineral Processing 30, 185–193. https://doi.org/10.1016/0301-7516(90)90014-P

Schubert, W.-D., Lassner, E., Walser, P., 2006. Geology of Tungsten. International Tungsten Industry Association (ITIA) Newsletter, pp12. Available at: http://www.itia.info/FileLib/Newsletter_2006_12.pdf.

Schulz, R., Lindner, B., Petridis, L., Smith, J.C., 2009. Scaling of Multimillion-Atom Biological Molecular Dynamics Simulation on a Petascale Supercomputer. J. Chem. Theory Comput. 5, 2798–2808. https://doi.org/10.1021/ct900292r

Sepro, 2015a. Falcon UF Gravity Concentrators brochure, Sepro Miner. Syst. Website. (2015). http://www.seprosystems.com/images/brochures/sepro-falcon-uf-concentrators.pdf.

References

Sepro, 2015b. Falcon SB Gravity Concentrators brochure, Sepro Miner. Syst. Website. (2015). http://www.seprosystems.com/images/brochures/sepro-falcon-sb-concentrators.pdf.

Shchukarev, A., Korolkov, D., 2004. XPS Study of group IA carbonates. Open Chemistry 2. https://doi.org/10.2478/BF02475578

Shelby, J.E., 2005. Introduction to glass science and technology, 2nd ed. ed. Royal Society of Chemistry, Cambridge.

Shen, C., Cebula, I., Brown, C., Zhao, J., Zharnikov, M., Buck, M., 2012. Structure of isophthalic acid based monolayers and its relation to the initial stages of growth of metal–organic coordination layers. Chem. Sci. 3, 1858. https://doi.org/10.1039/c2sc20087b

Shergold, H.L., 1972. Infra-red study of adsorption of sodium dodecyl sulphate by CaF2. Bull. Inst. Mining Met. Sect. C 81, C 148 (1972).

Shi, H., Chang, L., Jia, R., Eglitis, R.I., 2012. Ab Initio Calculations of Hydroxyl Impurities in CaF_2. The Journal of Physical Chemistry C 116, 6392–6400. https://doi.org/10.1021/jp211075g

Sholl, D.S., Steckel, J.A., 2009. Density functional theory: a practical introduction. Wiley, Hoboken, N.J.

Sis, H., Chander, S., 2003. Reagents used in the flotation of phosphate ores: a critical review. Minerals Engineering 16, 577–585. https://doi.org/10.1016/S0892-6875(03)00131-6

Sivamohan, R., De Donato, P., Cases, J.M., 1990. Adsorption of oleate species at the fluorite-aqueous solution interface. Langmuir 6, 637–644. https://doi.org/10.1021/la00093a019

Skelton, A.A., Wesolowski, D.J., Cummings, P.T., 2011. Investigating the Quartz (101̄0)/Water Interface using Classical and Ab Initio Molecular Dynamics. Langmuir 27, 8700–8709. https://doi.org/10.1021/la2005826

Skinner, L.B., Benmore, C.J., Neuefeind, J.C., Parise, J.B., 2014. The structure of water around the compressibility minimum. The Journal of Chemical Physics 141, 214507. https://doi.org/10.1063/1.4902412

Slater, J.C., 1930. Note on Hartree's Method. Phys. Rev. 35, 210–211. https://doi.org/10.1103/PhysRev.35.210.2

Soloviev, S.G., Krivoshchekov, N.N., 2011. Vostok-2 gold-base-metal-tungsten skarn deposit, Central Sikhote-Alin, Russia. Geol. Ore Deposits 53, 478–500. https://doi.org/10.1134/S1075701511060080

Somasundaran, P., 1969. Adsorption of starch and oleate and interaction between them on calcite in aqueous solutions. Journal of Colloid and Interface Science 31, 557–565. https://doi.org/10.1016/0021-9797(69)90056-3

Somasundaran, P., Xiao, L., Vasudevan, T.V., 1991. Separation of salt-type minerals by flotation using structurally modified collectors, In: Proceedings of the XVIIth International Mineral Processing Congress, Bergakademie, Freiberg, 2, 379-391.

Song, S., Lopez-Valdivieso, A., Martinez-Martinez, C., Torres-Armenta, R., 2006. Improving fluorite flotation from ores by dispersion processing. Minerals Engineering 19, 912–917. https://doi.org/10.1016/j.mineng.2005.10.005

Sørensen, E., 1973. On the adsorption of some anionic collectors on fluoride minerals. Journal of Colloid and Interface Science 45, 601–607. https://doi.org/10.1016/0021-9797(73)90177-X

Souvi, S.M.O., Badawi, M., Paul, J.-F., Cristol, S., Cantrel, L., 2013. A DFT study of the hematite surface state in the presence of H2, H2O and O2. Surface Science 610, 7–15. https://doi.org/10.1016/j.susc.2012.12.012

Souvi, S.M.O., Badawi, M., Virot, F., Cristol, S., Cantrel, L., Paul, J.-F., 2017. Influence of water, dihydrogen and dioxygen on the stability of the Cr_2O_3 surface: A first-principles investigation. Surface Science 666, 44–52. https://doi.org/10.1016/j.susc.2017.08.005

Srinivasan, S.G., Shivaramaiah, R., Kent, P.R.C., Stack, A.G., Navrotsky, A., Riman, R., Anderko, A., Bryantsev, V.S., 2016. Crystal Structures, Surface Stability, and Water Adsorption Energies of La-Bastnäsite via Density Functional Theory and Experimental Studies. J. Phys. Chem. C 120, 16767–16781. https://doi.org/10.1021/acs.jpcc.6b04747

Srour, J., Badawi, M., El Haj Hassan, F., Postnikov, A., 2018. Comparative study of structural and electronic properties of GaSe and InSe polytypes. The Journal of Chemical Physics 149, 054106. https://doi.org/10.1063/1.5030539

Stack, A.G., Stubbs, J.E., Srinivasan, S.G., Roy, S., Bryantsev, V.S., Eng, P.J., Custelcean, R., Gordon, A.D., Hexel, C.R., 2018. Mineral–Water Interface Structure of Xenotime (YPO_4) {100}. J. Phys. Chem. C 122, 20232–20243. https://doi.org/10.1021/acs.jpcc.8b04015

Suárez Sánchez, A., Krzemień, A., Riesgo Fernández, P., Iglesias Rodríguez, F.J., Sánchez Lasheras, F., de Cos Juez, F.J., 2015. Investment in new tungsten mining projects. Resources Policy 46, 177–190. https://doi.org/10.1016/j.resourpol.2015.10.003

Sun, H., 1998. COMPASS: An ab Initio Force-Field Optimized for Condensed-Phase ApplicationsOverview with Details on Alkane and Benzene Compounds. J. Phys. Chem. B 102, 7338–7364. https://doi.org/10.1021/jp980939v

Sun, W., Hu, Y., Qiu, G., Qin, W., 2004. Oxygen adsorption on pyrite (100) surface by density functional theory. J Cent. South Univ. Technol. 11, 385–390. https://doi.org/10.1007/s11771-004-0080-8

Swenson, J., Adams, S., 2003. Mixed Alkali Effect in Glasses. Physical Review Letters 90. https://doi.org/10.1103/PhysRevLett.90.155507

Tasker, P.W., 1980. The structure and properties of fluorite crystal surfaces. Le Journal de Physique Colloques 41, C6–488.

Temelso, B., Archer, K.A., Shields, G.C., 2011. Benchmark Structures and Binding Energies of Small Water Clusters with Anharmonicity Corrections. The Journal of Physical Chemistry A 115, 12034–12046. https://doi.org/10.1021/jp2069489

Tian, M., Zhang, C., Han, H., Liu, R., Gao, Z., Chen, P., He, J., Hu, Y., Sun, W., Yuan, D., 2018. Novel insights into adsorption mechanism of benzohydroxamic acid on lead (II)-activated cassiterite surface: An integrated experimental and computational study. Minerals Engineering 122, 327–338. https://doi.org/10.1016/j.mineng.2018.04.012

Tomas, H., 1985. Le traitement des minerais de tungstène à Salau.

Tomoaia-Cotişel, M., Zsako´, J., Mocanu, A., Lupea, M., Chifu, E., 1987. Insoluble mixed monolayers. Journal of Colloid and Interface Science 117, 464–476. https://doi.org/10.1016/0021-9797(87)90407-3

Torem, M.L., Peres, A.E., Adamian, R., 1992. On the mechanisms of beryl flotation in the presence of some metallic cations. Minerals Engineering 5, 1295–1304. https://doi.org/10.1016/0892-6875(92)90166-7

Tozsin, G., Acar, C., Sivrikaya, O., 2018. Evaluation of a Turkish Lignite Coal Cleaning by Conventional and Enhanced Gravity Separation Techniques. International Journal of Coal Preparation and Utilization 38, 135–148. https://doi.org/10.1080/19392699.2016.1209191

Tripathy, S.K., Ramamurthy, Y., Kumar, C.R., 2010. Modeling of high-tension roll separator for separation of titanium bearing minerals. Powder Technology 201, 181–186. https://doi.org/10.1016/j.powtec.2010.04.005

Ulian, G., Moro, D., Valdrè, G., 2018. Probing the interaction of (001) carbonated hydroxylapatite surfaces with water: a density functional investigation. Micro & Nano Letters 13, 4–8. https://doi.org/10.1049/mnl.2017.0058

U.S. Department of the Interior, 2018. Final List of Critical Minerals 2018.

U.S. Geological Survey, 2019. Mineral Commodity Summaries 2019. Technical report, United States Geological Survey, Reston, Virginia, USA.

van Duin, A.C.T., Dasgupta, S., Lorant, F., Goddard, W.A., 2001. ReaxFF: A Reactive Force Field for Hydrocarbons. J. Phys. Chem. A 105, 9396–9409. https://doi.org/10.1021/jp004368u

Varshneya, A.K., 1994. Fundamentals of Inorganic Glasses. Elsevier. https://doi.org/10.1016/C2009-0-21359-6

Veloso, C.H., Filippov, L.O., Filippova, I.V., Ouvrard, S., Araujo, A.C., 2018. Investigation of the interaction mechanism of depressants in the reverse cationic flotation of complex iron ores. Minerals Engineering 125, 133–139. https://doi.org/10.1016/j.mineng.2018.05.031

Villegas-Jiménez, A., Mucci, A., Whitehead, M.A., 2009. Theoretical Insights into the Hydrated (10.4) Calcite Surface: Structure, Energetics, and Bonding Relationships. Langmuir 25, 6813–6824. https://doi.org/10.1021/la803652x

Walsh, K.A., Vidal, E.E., 2009. Beryllium chemistry and processing. ASM International, Materials Park , Ohio.

Wang, J., Kalinichev, A.G., Kirkpatrick, R.J., Cygan, R.T., 2005. Structure, Energetics, and Dynamics of Water Adsorbed on the Muscovite (001) Surface: A Molecular Dynamics Simulation. J. Phys. Chem. B 109, 15893–15905. https://doi.org/10.1021/jp045299c

Wang, J., Somasundaran, P., 2005. Adsorption and conformation of carboxymethyl cellulose at solid–liquid interfaces using spectroscopic, AFM and allied techniques. Journal of Colloid and Interface Science 291, 75–83. https://doi.org/10.1016/j.jcis.2005.04.095

References

Wang, J., Zhou, Z., Gao, Y., Sun, W., Hu, Y., Gao, Z., 2018. Reverse Flotation Separation of Fluorite from Calcite: A Novel Reagent Scheme. Minerals 8, 313. https://doi.org/10.3390/min8080313

Wang, L., Sun, W., Liu, R., 2014. Mechanism of separating muscovite and quartz by flotation. J. Cent. South Univ. 21, 3596–3602. https://doi.org/10.1007/s11771-014-2341-5

Wang, X., Zhang, Q., Li, X., Ye, J., Li, L., 2018. Structural and Electronic Properties of Different Terminations for Quartz (001) Surfaces as Well as Water Molecule Adsorption on It: A First-Principles Study. Minerals 8, 58. https://doi.org/10.3390/min8020058

Wang, Y., Yu, F., 2007. Effects of Metallic Ions on the Flotation of Spodumene and Beryl. Journal of China University of Mining and Technology 17, 35–39. https://doi.org/10.1016/S1006-1266(07)60008-X

Wei, Z., Hu, Y., Han, H., Sun, W., Wang, R., Wang, J., 2018. Selective flotation of scheelite from calcite using Al-Na 2 SiO 3 polymer as depressant and Pb-BHA complexes as collector. Minerals Engineering 120, 29–34. https://doi.org/10.1016/j.mineng.2018.01.036

Wei, Z., Hu, Y., Han, H., Sun, Wei, Wang, R., Sun, Wenjuan, Wang, J., Gao, Z., Wang, L., Zhang, C., Sun, L., Liu, R., 2019. Selective Separation of Scheelite from Calcite by Self-Assembly of H2SiO3 Polymer Using Al3+ in Pb-BHA Flotation. Minerals 9, 43. https://doi.org/10.3390/min9010043

Wells, A., 1991. Some experiences in the design and optimisation of fine gravity concentration circuits. Minerals Engineering 4, 383–398. https://doi.org/10.1016/0892-6875(91)90143-J

Werner, A.B.T., Sinclair, W.D., Amey, E.B., 1998. International Strategic Mineral Issues Summary Report - Tungsten. U.S. Geological Survey Circular 930-O, pp71. Available at: http://pubs.usgs.gov/pdf/circular/c930-o.html.

Wheeler, A., 2015. Technical report on the mineral resources and reserves of the Los Santos mine project, Spain. 31st October 2015.

Whittaker, E.J.W., 1982. Cleavage energies of minerals. Mineral. mag. 46, 398–399. https://doi.org/10.1180/minmag.1982.046.340.17

Wills, B., Finch, J., Safari, an O.M.C., 2015. Wills' Mineral Processing Technology, 8th Edition.

Wills, B.A., Finch, J.A., 2016. Froth Flotation, in: Wills' Mineral Processing Technology. Elsevier, pp. 265–380. https://doi.org/10.1016/B978-0-08-097053-0.00012-1

Wolthers, M., Di Tommaso, D., Du, Z., de Leeuw, N.H., 2012. Calcite surface structure and reactivity: molecular dynamics simulations and macroscopic surface modelling of the calcite–water interface. Phys. Chem. Chem. Phys. 14, 15145. https://doi.org/10.1039/c2cp42290e

Wungu, T.D.K., Agusta, M.K., Saputro, A.G., Dipojono, H.K., Kasai, H., 2012. First principles calculation on the adsorption of water on lithium–montmorillonite (Li–MMT). J. Phys.: Condens. Matter 24, 475506. https://doi.org/10.1088/0953-8984/24/47/475506

Xia, L., Zhong, H., Liu, G., Li, X., 2009. Electron bandstructure of kaolinite and its mechanism of flotation using dodecylamine as collector. J. Cent. South Univ. Technol. 16, 73–79. https://doi.org/10.1007/s11771-009-0012-8

Xia, S., Pan, G., Cai, Z.-L., Wang, Y., Reimers, J.R., 2007. The Manganite−Water Interface. J. Phys. Chem. C 111, 10427–10437. https://doi.org/10.1021/jp068842t

Xian-Ping, L., Bo, F., Xianwen, Z., Li-Ying, L., Zheng-He, X., 2017. Flotation separation of wolframite from quartz using N-oleoyl sarcosine acid as collector. Physicochemical Problems of Mineral Processing; ISSN 2084-4735 341 kB. https://doi.org/10.5277/ppmp170103

Xie, J., Li, X., Mao, S., Li, L., Ke, B., Zhang, Q., 2018. Effects of structure of fatty acid collectors on the adsorption of fluorapatite (0 0 1) surface: A first-principles calculations. Applied Surface Science 444, 699–709. https://doi.org/10.1016/j.apsusc.2018.03.105

Xiong, X., Hua, X., Zheng, Y., Lu, X., Li, S., Cheng, H., Xu, Q., 2018. Oxidation mechanism of chalcopyrite revealed by X-ray photoelectron spectroscopy and first principles studies. Applied Surface Science 427, 233–241. https://doi.org/10.1016/j.apsusc.2017.08.047

Xu, L., Hu, Y., Tian, J., Wu, H., Yang, Y., Zeng, X., Wang, Z., Wang, J., 2016. Selective flotation separation of spodumene from feldspar using new mixed anionic/cationic collectors. Minerals Engineering 89, 84–92. https://doi.org/10.1016/j.mineng.2016.01.013

Xu, L., Peng, T., Tian, J., Lu, Z., Hu, Y., Sun, W., 2017a. Anisotropic surface physicochemical properties of spodumene and albite crystals: Implications for flotation separation. Applied Surface Science 426, 1005–1022. https://doi.org/10.1016/j.apsusc.2017.07.295

Xu, L., Tian, J., Wu, H., Deng, W., Yang, Y., Sun, W., Gao, Z., Hu, Y., 2017b. New insights into the oleate flotation response of feldspar particles of different sizes: Anisotropic adsorption model. Journal of Colloid and Interface Science 505, 500–508. https://doi.org/10.1016/j.jcis.2017.06.009

Xu, Y., Liu, Y.-L., He, D.-D., Liu, G.-S., 2013. Adsorption of cationic collectors and water on muscovite (001) surface: A molecular dynamics simulation study. Minerals Engineering 53, 101–107. https://doi.org/10.1016/j.mineng.2013.07.006

Yang, F., Sun, W., Hu, Y., Long, S., 2015. Cationic flotation of scheelite from calcite using quaternary ammonium salts as collector: Adsorption behavior and mechanism. Minerals Engineering 81, 18–28. https://doi.org/10.1016/j.mineng.2015.07.014

Yang, X., 2018. Beneficiation studies of tungsten ores – A review. Minerals Engineering 125, 111–119. https://doi.org/10.1016/j.mineng.2018.06.001

Yang, Y., Xie, B., Wang, R., Xu, S., Wang, J., Xu, Z., 2016. Extraction and separation of tungsten from acidic high-phosphorus solution. Hydrometallurgy 164, 97–102. https://doi.org/10.1016/j.hydromet.2016.05.018

Yehia, A., Miller, J.D., Ateya, B.G., 1993. Analysis of the adsorption behaviour of oleate on some synthetic apatites. Minerals Engineering 6, 79–86. https://doi.org/10.1016/0892-6875(93)90165-J

Yin, W., Wang, J., 2014. Effects of particle size and particle interactions on scheelite flotation. Transactions of Nonferrous Metals Society of China 24, 3682–3687. https://doi.org/10.1016/S1003-6326(14)63515-9

Yin, W.-Z., Wang, J.-Z., Sun, Z.-M., 2015. Structure–activity relationship and mechanisms of reagents used in scheelite flotation. Rare Metals 34, 882–887. https://doi.org/10.1007/s12598-014-0381-5

Yongxin, L., Changgen, L., 1983. Selective flotation of scheelite from calcium minerals with sodium oleate as a collector and phosphates as modifiers. I. Selective flotation of scheelite. International Journal of Mineral Processing 10, 205–218. https://doi.org/10.1016/0301-7516(83)90011-X

Young, C.A., Miller, J.D., 2001. Conformation of chemisorbed oleate at a calcite surface. Mining, Metallurgy & Exploration 18, 38–44. https://doi.org/10.1007/BF03402869

Young, C.A., Miller, J.D., 2000. Effect of temperature on oleate adsorption at a calcite surface: an FT-NIR/IRS study and review. International Journal of Mineral Processing 58, 331–350. https://doi.org/10.1016/S0301-7516(99)00057-5

Yu, F., Wang, Y., Zhang, L., Zhu, G., 2015. Role of oleic acid ionic−molecular complexes in the flotation of spodumene. Minerals Engineering 71, 7–12. https://doi.org/10.1016/j.mineng.2014.10.001

Yue, T., Han, H., Hu, Y., Wei, Z., Wang, J., Wang, L., Sun, W., Yang, Y., Sun, L., Liu, R., Sultan Ahmed, K., 2018. Beneficiation and Purification of Tungsten and Cassiterite Minerals Using Pb–BHA Complexes Flotation and Centrifugal Separation. Minerals 8, 566. https://doi.org/10.3390/min8120566

Zachara, J.M., Kittrick, J.A., Harsh, J.B., 1988. The mechanism of Zn2+ adsorption on calcite. Geochimica et Cosmochimica Acta 52, 2281–2291. https://doi.org/10.1016/0016-7037(88)90130-5

Zahn, D., Hochrein, O., 2003. Computational study of interfaces between hydroxyapatite and water. Phys. Chem. Chem. Phys. 5, 4004. https://doi.org/10.1039/b306358e

Zhang, B., 1998. Recovering gold from high density gangues with Knelson concentrators, M. Eng. Thesis, 1998, McGill University.

Zhang, R., Hu, S., Zhang, X., 2006. Experimental Study of Dissolution Rates of Fluorite in HCl–H2O Solutions. Aquatic Geochemistry 12, 123–159. https://doi.org/10.1007/s10498-005-3658-3

Zhang, X., Wang, X., Miller, J.D., 2015. Wetting of selected fluorite surfaces by water. Surface Innovations 3, 39–48. https://doi.org/10.1680/si.14.00004

Zhang, Y., He, Y., Zhang, T., Zhu, X., Feng, Y., Zhang, G., Bai, X., 2018. Application of Falcon centrifuge in the recycling of electrode materials from spent lithium ion batteries. Journal of Cleaner Production 202, 736–747. https://doi.org/10.1016/j.jclepro.2018.08.133

Zhang, Y., Li, Y., Chen, R., Wang, Y., Deng, J., Luo, X., 2017. Flotation Separation of Scheelite from Fluorite Using Sodium Polyacrylate as Inhibitor. Minerals 7, 102. https://doi.org/10.3390/min7060102

References

Zhao, G., Peng, J., Zhong, H., Wang, S., Liu, G., 2016. Synthesis of Novel Ether Thionocarbamates and Study on Their Flotation Performance for Chalcopyrite. Minerals 6, 97. https://doi.org/10.3390/min6030097

Zhao, G., Wang, S., Zhong, H., 2015. Study on the Activation of Scheelite and Wolframite by Lead Nitrate. Minerals 5, 247–258. https://doi.org/10.3390/min5020247

Zhao, G., Zhong, H., Qiu, X., Wang, S., Gao, Y., Dai, Z., Huang, J., Liu, G., 2013. The DFT study of cyclohexyl hydroxamic acid as a collector in scheelite flotation. Minerals Engineering 49, 54–60. https://doi.org/10.1016/j.mineng.2013.04.025

Zheng, R., Ren, Z., Gao, H., Qian, Y., 2018. Evaluation of Sulfonate-Based Collectors with Different Hydrophobic Tails for Flotation of Fluorite. Minerals 8, 57. https://doi.org/10.3390/min8020057

Zheng, X., Smith, R.W., 1997. Dolomite depressants in the flotation of apatite and collophane from dolomite. Minerals Engineering 10, 537–545. https://doi.org/10.1016/S0892-6875(97)00031-9

Zhou, P., Hou, X., Chao, Y., Yang, W., Zhang, W., Mu, Z., Lai, J., Lv, F., Yang, K., Liu, Y., Li, J., Ma, J., Luo, J., Guo, S., 2019. Synergetic interaction between neighboring platinum and ruthenium monomers boosts CO oxidation. Chem. Sci. 10, 5898–5905. https://doi.org/10.1039/C9SC00658C

Zhou, W., Moreno, J., Torres, R., Valle, H., Song, S., 2013. Flotation of fluorite from ores by using acidized water glass as depressant. Minerals Engineering 45, 142–145. https://doi.org/10.1016/j.mineng.2013.02.017

Zhu, G., Wang, Y., Wang, X., Yu, F., Miller, J.D., 2018. States of coadsorption for oleate and dodecylamine at selected spodumene surfaces. Colloids and Surfaces A: Physicochemical and Engineering Aspects 558, 313–321. https://doi.org/10.1016/j.colsurfa.2018.08.083

Zhu, X., Tao, Y., Sun, Q., Man, Z., 2017a. Enrichment and migration regularity of fine coal particles in enhanced gravity concentrator. International Journal of Mineral Processing 163, 48–54. https://doi.org/10.1016/j.minpro.2017.04.007

Zhu, X., Tao, Y., Sun, Q., Man, Z., 2017b. The low efficiency of lignite separation by an enhanced gravity concentrator. Energy Sources, Part A: Recovery, Utilization, and Environmental Effects 39, 835–842. https://doi.org/10.1080/15567036.2016.1270373

Récupération du tungstène à partir d'un skarn à faible contraste de séparation – Apport de la modélisation moléculaire dans la flottation des minéraux calciques

Aujourd'hui, plus de 40 % des ressources mondiales en tungstène sont contenues dans les skarns, dont le gisement de Tabuaço (Portugal) constitue un archétype. Ce minerai contient de fortes teneurs en minéraux calciques (fluorite, apatite et vésuvianite) en association fine avec la scheelite ($CaWO_4$) qui, étant donné leurs propriétés de surface proches, sont difficiles à séparer par flottation aux acides gras. Au cours de cette étude, ancrée dans le projet européen H2020 FAME, un procédé économique, écologique et transférable a été développé sur le minerai de Tabuaço afin de prouver la faisabilité minéralurgique de l'exploitation des skarns à tungstène, classé parmi les métaux critiques en Europe. En flottation, le système Na_2CO_3/Na_2SiO_3 a montré la meilleure efficacité en matière de dépression, obtenue grâce à des effets synergiques considérables. Ces derniers ont été décrits par des méthodes statistiques, spectroscopiques et atomistiques. En parallèle, l'influence des ratios entre différents acides carboxyliques au sein des formulations de collecteurs (huiles de tall) a été évaluée avec pour objectif d'améliorer la sélectivité de la flottation. La séparation par gravité augmentée (concentrateur centrifuge Falcon) a été examinée, optimisée puis combinée avec la flottation afin de produire un concentré commercialisable de scheelite titrant 63 % WO_3 pour 59 % de récupération. Par ailleurs, en vue d'appréhender les mécanismes moléculaires impliqués dans la flottation, les interfaces de la fluorite et de la scheelite ont été modélisées en utilisant la théorie de la fonctionnelle de la densité. Cette étude a permis de caractériser l'état d'hydratation des deux minéraux, qui présentent des affinités différentes pour les molécules d'eau. En outre, l'adsorption des acides gras sur la fluorite a été étudiée afin de fournir des éléments de réponse, confirmés expérimentalement, au sujet des mécanismes d'adsorption de ces molécules sur les minéraux calciques.

Mots-clés : Acides gras, Concentré par gravité, Effets synergiques, Théorie de la Fonctionnelle de la Densité, Scheelite, Fluorite

Tungsten recovery from a skarn with a low separation contrast – Contribution of molecular modelling in the flotation of calcium minerals

Nowadays, skarns represent more than 40% of the global resources in tungsten, which has been classified as a critical raw material in the European Union. In particular, the Tabuaço deposit constitutes an archetype of tungsten skarns and contains high amounts of calcium minerals, including fluorite, apatite, and vesuvianite, in close association with scheelite ($CaWO_4$). According to their similar surface properties, the separation of these minerals by flotation with fatty acids is significantly difficult and, therefore, remains a scientific challenge. In this study, which has been conducted within the framework of the FAME H2020 European project, an economic, environment-friendly, and transferable process has been developed for the Tabuaço ore to demonstrate the feasibility of the tungsten skarns processing. In the froth flotation process, the Na_2CO_3/Na_2SiO_3 system has exhibited the best efficiency in terms of gangue minerals depression due to considerable synergistic effects that have been subsequently described by statistical, spectroscopic, and atomistic methods. Meanwhile, the influence of the ratios between different carboxylic acids in the collector formulations (Tall Oil Fatty Acids) has been assessed to improve the flotation selectivity. In addition, the enhanced gravity separation (Falcon centrifuge concentrator) has been investigated, optimised, and combined with the flotation to produce a marketable scheelite concentrate assaying 63% WO_3 with 59% recovery. Besides, to gain understanding in the molecular mechanisms involved in the flotation process, the fluorite and scheelite interfaces have been modelled using the density functional theory. This study has allowed to characterise the hydration state of these minerals, which display different affinities for water molecules. Furthermore, the adsorption of fatty acids on fluorite has been studied to unravel the adsorption mechanisms of these molecules on calcium minerals, confirmed by experimental investigations.

Keywords: Fatty acids, Gravity separation, Synergistic effects, Density Functional Theory, Scheelite, Fluorite